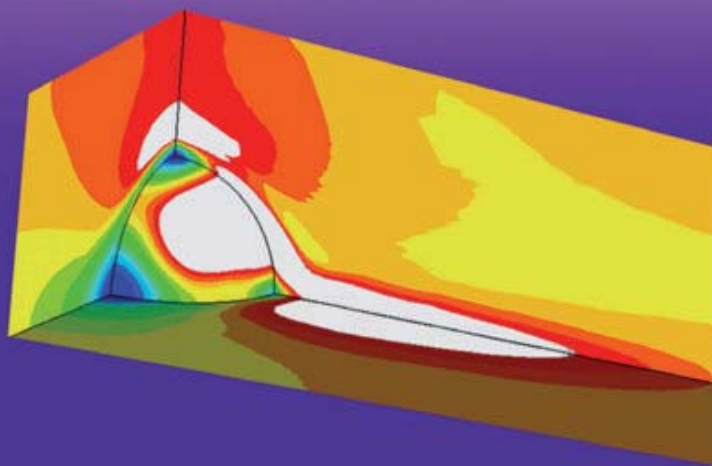
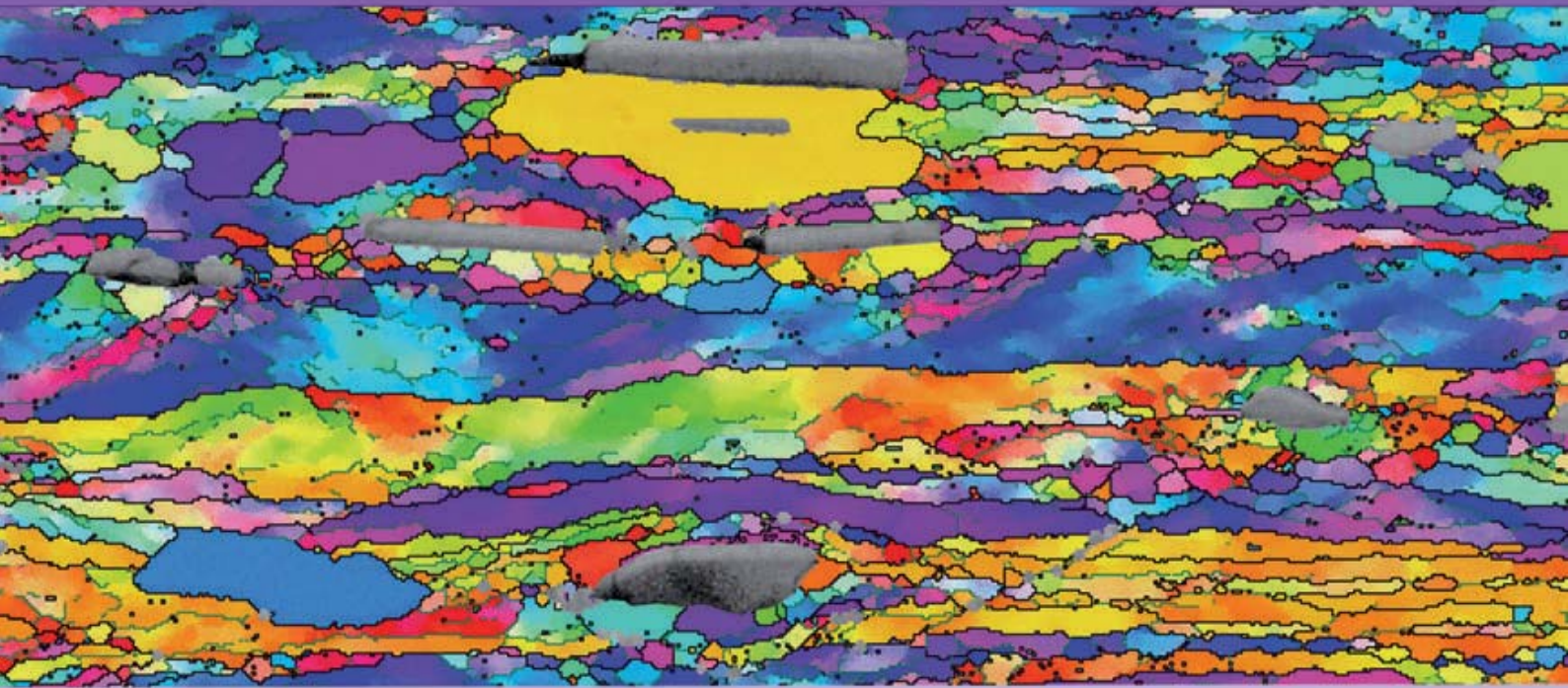


Recrystallization Modeling considering Second-Phase Particles

Carmen Schäfer



Cuvillier Verlag Göttingen
Internationaler wissenschaftlicher Fachverlag

Recrystallization Modeling considering Second-Phase Particles

Von der Fakultät für Georessourcen und Materialtechnik
der Rheinisch-Westfälischen Technischen Hochschule Aachen

zur Erlangung des akademischen Grades eines
Doktors der Ingenieurwissenschaften
genehmigte Dissertation

vorgelegt von

Dipl.-Ing. Carmen Schäfer

aus Saarbrücken

Berichter: Univ.-Prof. Dr. rer. nat. Dr. h. c. Günter Gottstein
Priv. Doz. Dr. rer. nat. Volker Mohles

Tag der mündlichen Prüfung: 02. August 2010

Bibliografische Information der Deutschen Nationalbibliothek

Die Deutsche Nationalbibliothek verzeichnet diese Publikation in der Deutschen Nationalbibliografie; detaillierte bibliografische Daten sind im Internet über <http://dnb.d-nb.de> abrufbar.

1. Aufl. - Göttingen : Cuvillier, 2010

Zugl.: (RWTH) Aachen, Univ., Diss., 2010

978-3-86955-560-7

© CUVILLIER VERLAG, Göttingen 2010

Nonnenstieg 8, 37075 Göttingen

Telefon: 0551-54724-0

Telefax: 0551-54724-21

www.cuvillier.de

Alle Rechte vorbehalten. Ohne ausdrückliche Genehmigung des Verlages ist es nicht gestattet, das Buch oder Teile daraus auf fotomechanischem Weg (Fotokopie, Mikrokopie) zu vervielfältigen.

1. Auflage, 2010

Gedruckt auf säurefreiem Papier

978-3-86955-560-7

Meinen Eltern

Danksagung

Die vorliegende Arbeit entstand am Institut für Metallkunde und Metallphysik (IMM) der RWTH Aachen.

Mein herzlichster Dank gilt Herrn Prof. Dr. rer. nat. Günter Gottstein für die freundliche fachliche und persönliche Unterstützung, das mir entgegengebrachte Vertrauen und vor allem den mir gewährten wissenschaftlichen Freiraum.

Herrn Priv.-Doz. Dr. rer. nat. Volker Mohles danke ich für die Übernahme des Koreferates und für seine Hilfe und Unterstützung während meiner Zeit am Institut.

Frau Priv.-Doz. Dr. rer. nat. Myriam Winning möchte ich ganz herzlich für ihre Kommentare und Anmerkungen zu meiner Arbeit danken.

Herrn Prof. Dr.-Ing. Jürgen Hirsch von der Hydro Aluminium Deutschland GmbH gilt mein aufrichtiger Dank für die wertvollen Hinweise im Rahmen verschiedener Aufgabenstellungen, sowie für die fortwährende Diskussionsbereitschaft. Darüber hinaus danke ich Herrn Prof. Olaf Engler und Frau Dr. Galyna Lapyeva, ebenfalls von der Hydro Aluminium Deutschland GmbH, für die gute Zusammenarbeit im Rahmen des Transferbereichs 63. Der Hydro Aluminium Deutschland GmbH möchte ich ferner für die Bereitstellung von Material und die Durchführung der thermoelektrischen, sowie Widerstandsmessungen ganz herzlich danken. Weiterhin möchte ich allen Mitarbeitern im Rahmen des SFB 370 / TFB 63 für die gute Kooperation danken, insbesondere Herrn Xiaoli Li für wertvolle Diskussionen bezüglich der Umformrechnungen.

The financial support of the Netherlands Institute of Metals Research is gratefully acknowledged. Part of this research was carried out under projectnumber MC4.03176 „Quantitative Recrystallization Texture Modeling for Hot Rolling of Aluminum Alloys“ in the framework of the Strategic Research programme of the Netherlands Institute of Metals Research (www.NIMR.nl/ www.M2I.nl/). In this respect, I would also like to thank Dr. Cheng Liu (Corus Technology BV) for providing sample material and process-relevant data.

Großer Dank geht auch an die German Research School for Simulation Sciences für die finanzielle Unterstützung aber vor allem auch für die nette Zeit im Kreise ihrer Mitglieder.

Der deutschen Forschungsgemeinschaft danke ich für die finanzielle Förderung der Arbeit im Rahmen des Sonderforschungsbereiches 370 „Integrative Werkstoffmodellierung“, sowie des Transferbereichs 63 „Praxisrelevante Modellierungswerkzeuge“.

Den Kollegen vom technischen Dienst danke ich für die stete Hilfsbereitschaft und das große Engagement, insbesondere David Beckers, Arndt Ziemons, Thomas Burllet und Barbara Eigelshoven. Herrn Dr.-Ing. Weiping Hu möchte ich für die Hilfe bei der Transmissionselektronenmikroskopie danken. Ein besonderer Dank geht an die Computergruppe, insbesondere an Gerda Pomana für ihre Hilfe und Unterstützung bei allen software-technischen Fragen. Des Weiteren, möchte ich Matthias Loeck und Sergej Laiko für ihre stetige Hilfsbereitschaft im EDV Bereich danken.

Dem kompetenten Team unserer feinmechanischen Werkstatt, Detlef Fuchs, Alex Teschner, Gerd Schütz, möchte ich für all die Jahre der unermüdlichen Unterstützung bei der Probenherstellung, sowie der Zeichnung und Fertigung diverser Bauteile danken.

Den Studierenden, die durch Studien-, Diplom- und Masterarbeiten sowie als studentische Hilfskräfte zum Gelingen dieser Arbeit beigetragen haben sei herzlich gedankt. Insbesondere Dipl.-Ing. Dorothee Praum, MSc. Jia Song, MSc. Hu Lei, Dipl.-Ing. Björn Rotmann, BSc. Eva Gumbmann, MSc. Simon Averlant, MSc. Shunhua Yang und MSc. Xiaoyu Li.

Lieben Dank an meine Freunde und Kollegen während meiner Zeit am Institut. Ganz besonders möchte ich hier MSc. Jia Song danken, die mich auch im Privaten sehr unterstützt hat. Ich danke Dr. Luis Antonio Barrales-Mora, meinem langjährigen Bürokollegen, für die nette Zeit und seine Hilfsbereitschaft bei anfänglichen Programmierfragen, Dr. Emmanuel Jannot, Peter Konijnenberg, sowie Dipl.-Ing. Olga Sukhopar für die wöchentliche Motivation zum Kontakthüpfen, die ebenso dankend angenommen wurde, wie unsere Sushi-Pausen.

For Ivan Lazić I have only words of gratitude for his unconditional love and support during this last period of my thesis. Mein größter Dank gilt jedoch meiner Familie, die mich zu jeder Zeit bedingungslos unterstützt und ausgehalten hat, und mich immer wieder motiviert hat. Ganz besonders möchte ich meinen Eltern Margit und Josef Schäfer, sowie meinen beiden Schwestern Sarah und Marion für ihre Liebe und Unterstützung während all der vergangenen Jahre danken.

Content

1. Introduction	1
2. Recrystallization	5
2.1 Introduction	5
2.2 Recrystallization Nucleation	6
2.2.1 Instability criteria	6
2.2.2 Types of nucleation	7
2.2.3 Influences on nucleation	11
2.3 Nucleus Growth	12
2.3.1 Grain boundary migration	12
2.3.2 Influence of recovery	13
2.3.3 Influence of small particles - Zener drag	14
2.3.4 Influence of solutes - solute drag	16
2.4 Recrystallization Models	18
2.4.1 Phenomenological models	19
2.4.2 Geometric microstructure models	21
2.4.3 Vertex models	21
2.4.4 Discrete models	22
2.4.5 Recrystallization texture models	23
3. Simulation of Recrystallization using Cellular Automata	25
3.1. Introduction	25
3.2 Fundamentals	26
3.3 Theory of the Cellular Operator for Recrystallization CORE	27
3.3.1 History of CORE	27
3.3.2 A nucleation model for CORE	28
3.3.3 Modifications of the CORE model	29
3.3.4 Theory of CORE	29
3.4 Model Input	33
3.5 Model Output	36
3.6 Coupling to the Softening Model CORE-3IVM+	37
3.7 Coupling to the Precipitation Model CORE-ClaNG	42

3.8	Modifying the Real-Time Scaling	44
3.9	Quantitative Nucleation Modeling in CORE - Modifications	45
3.9.1	Nucleation – and the importance of the absolute nucleus number	46
3.9.2	Nucleation at grain boundaries	47
3.9.3	Nucleation in orientation gradients	48
3.9.4	Influence of Zener drag on nucleation	50
3.9.5	The total nucleus number	51
4.	Parameter Studies	55
4.1	Introduction	55
4.2	Influence on Recrystallization Texture	55
4.2.1	Influence of pre-deformation texture	56
4.2.2	Influence of dislocation density on growth	58
4.2.3	Influence of strain	59
4.2.4	Influence of alloy composition	62
4.2.5	Influence of particle-stimulated nucleation	64
4.2.6	Influence of Zener drag	64
4.2.7	Influence of the arrangement in GIA-Aggregates	65
4.3	Influence on Recrystallization Kinetics	66
4.3.1	Comparison with JMAK Theory	66
4.3.2	Influence of the number of nuclei	67
4.3.3	Influence of the shape of the deformed grains	68
4.3.4	Influence of the nucleation rate	69
4.3.5	Influence of dislocation density on growth	69
4.3.6	Influence of strain	70
4.3.7	Influence of inhomogeneities during growth	71
4.3.8	Influence of mobility on growth	74
4.3.9	Influence of Zener drag	76
4.3.10	Influence of heating rates	80
4.3.11	Influence of particle-stimulated nucleation	83
4.3.12	Influence of solute drag	84
4.4	Influence on Grain Size Distribution	86
4.4.1	Influence of the nucleus number	86
4.4.2	Influence of strain	89
4.4.3	Influence of inhomogeneities	90
4.4.4	Influence of mobility distribution	92
4.4.5	Influence of particle-stimulated nucleation	92
4.4.6	Influence of Zener drag	94

4.5	Precision and Errors	95
4.5.1	Input parameters	95
4.5.2	Inaccuracies during the simulation	96
4.5.3	Evaluation & Interpretation	97
4.6	Classification of Effects on Recrystallization	98
5.	Model for Particle-Stimulated Nucleation	101
5.1	Introduction	101
5.2	Evolution of the Deformation Zone (fcc) – Experiments	101
5.2.1	Appearance of the deformation zone	101
5.2.2	Subgrain size	103
5.2.3	Microtexture in the deformation zone	105
5.2.4	P- and 22° ND rotated Cube texture component	108
5.2.5	Nucleus texture and frequency	109
5.3	The GIA-DZ model for In-Grain Deformation Zone Evolution	111
5.3.1	Model Setup and general model behavior	111
5.3.2	FEM modeling	113
5.3.3	Strain evolution in the particle vicinity	113
5.3.4	Texture evolution in the particle vicinity	115
5.3.5	Texture evolution in ideal orientations	119
5.4	Modeling the Evolution of the Deformation Zone (fcc)	121
5.4.1	Influence of deformation degree, temperature and initial texture	121
5.4.2	Comparison to experiments	123
5.5	A nucleation Model for Particle-Stimulated Nucleation	125
5.5.1	Implementation of particle-stimulated nucleation	125
5.5.2	Precipitation free zone	126
5.6	Conclusions	128
6.	Influence of Recovery on Recrystallization	129
6.1.	Introduction	129
6.2	Appearance of Recovery accompanying Recrystallization	130
6.2.1	Temperature dependence of recovery	130
6.2.2	Orientation dependence of recovery	131
6.2.3	Effect of recovery on recrystallization growth	131
6.2.4	Comparison to empirical approaches for recovery	134
6.3	Modeling Incubation Times	135
6.3.1	Two models for incubation times	136

6.3.2	Application of the incubation time criterion	137
6.3.3	Modeling nucleation rates	139
6.4	Conclusions	140
7	Recrystallization Behavior influenced by Precipitation Effects	143
7.1	Introduction	143
7.2	Experimental Data and Evaluation	144
7.2.1	Homogenization treatment for initial material	144
7.2.2	Cold rolling of the homogenized material	144
7.2.3	Characterization of the heat treated material	145
7.2.4	Data for recrystallization kinetics	147
7.2.5	Precipitation during annealing	149
7.3	Input for Recrystallization Modeling	149
7.3.1	Deformation simulations	149
7.3.2	Sub-structural quantities and nucleation	150
7.3.3	Precipitation behavior	152
7.3.4	Growth and recovery parameters	153
7.4	Results of the Recrystallization Predictions	154
7.4.1	Simulated grain size and grain size distributions	154
7.4.2	Simulated recrystallization textures	156
7.4.3	Simulated recrystallization kinetics	157
7.5	Discussion of Recrystallization Kinetics	158
7.5.1	The influence of recovery	159
7.5.2	Accuracy of ClaNG predictions	159
7.5.3	Particle coarsening	160
7.5.4	Concurrent progress of precipitation coarsening and recovery	161
7.5.5	Introducing a new kinetics	162
7.6	Conclusions	166
8	Influence of Heating Rates on the Recrystallization Behavior	169
8.1	Introduction	169
8.2	Experimental Data	170
8.2.1	Characterization of the industrially processed material	170
8.2.2	Considered time-temperature curves	171
8.2.3	Characterization of the heat-treated material	172
8.2.4	Data for recrystallization kinetics	173
8.2.5	Precipitation during annealing	174
8.2.6	Growth selection of P-oriented nuclei	175

8.3	Input for Recrystallization Modeling	177
8.3.1	Deformation Modeling	178
8.3.2	Sub-structural quantities and nucleus orientations	178
8.3.3	Precipitation input	180
8.4	Recrystallization Simulations	183
8.4.1	Recrystallization textures	183
8.4.2	Recrystallization kinetics	185
8.4.3	Grain size distribution	187
8.5	Effect of Orientation Dependent Growth Rates	190
8.6	Conclusions	191
9.	Through-Process Modeling of AA3103 Sheet Fabrication	193
9.1	Introduction	193
9.1.1	Process description	193
9.1.2	Modeling setup	194
9.2	Work-hardening Behavior	195
9.3	Hot Rolling	197
9.4	Coil Cooling	201
9.5	Cold Rolling	202
9.6	Final Annealing	205
9.6.1	Precipitation modeling	205
9.6.2	Modeling of recovery	209
9.6.3	Modeling of recrystallization kinetics	209
9.6.4	Modeling of recrystallized grain sizes	212
9.6.5	Modeling of recrystallization textures	215
9.7	Assessment of through-process predictions	219
10.	Summary	221
11.	Zusammenfassung	225
	References	229
	Curriculum Vitae	

Chapter 1

Introduction

The recrystallization of deformed metals has been the subject of research for almost 70 years. Although there is now a reasonable understanding of many aspects of the process, many important areas require further elucidation. Two of these areas, which are addressed in this thesis, are the recrystallization nucleation and the modeling of recrystallization in commercial alloys considering the vast number of possible influences.

During plastic deformation, e.g. rolling, defects are introduced into the material. These defects are removed during a subsequent annealing treatment by recrystallization and recovery. Recrystallization is the complete regeneration of the microstructure by creation and migration of high angle grain boundaries during a heat treatment of deformed materials. The complete change of microstructure is further accompanied by severe texture changes. Texture and microstructure essentially determine the properties of metallic materials. This motivates the interest of industry in this particular process. Since texture and microstructure can be changed within wide margins by respective processing, optimum processing conditions and best materials chemistry have to be found for low cost and high performance products. The ever decreasing product life cycles, and the rising demand for advanced materials and low cost production render empirical practices ineffective. They require reliable models of materials development during processing for prediction of terminal material properties and the optimum processing window. The complication is that materials modeling means microstructure modeling, and microstructure changes during processing. Thus, physical based models are required rather than empirical ones.

From relevant literature on recrystallization it is known that for recrystallization modeling the physical mechanisms of nucleation and their specific growth relationships need to be implemented. This is the consequence of an extensive discussion on the topic of recrystallization being controlled by oriented nucleation and oriented growth during recent years. The common consensus in this respect is that recrystallization is most likely the selected growth (oriented growth) out of a set of nuclei originating at preferred nucleation sites (oriented nucleation). Against this background nucleation is of special importance since it not only influences the orientation, and thus the texture of the material, but also the final grain size. The approaches for nucleation in literature being mostly of empirical nature are not very useful for the application in through-process modeling

since they require very often parameters or experimental data, which is, in general, difficult to access. As a result, a comprehensive description of nucleation is not available. However, the trend in modeling nucleation goes towards models that link the deformation with the recrystallization behavior finding meaningful parameters which allow a more universal application of such models. A model of this type is, for instance, the ReNuc model developed at IMM (Institute of Metal Physics and Physical Metallurgy, RWTH Aachen) for the description of various nucleation mechanisms in Al alloys. However, one of the most important nucleation mechanisms in commercial alloys, the nucleation at second phases or so-called particle stimulated nucleation, was not considered up to now. This nucleation mechanism, if understood, can be used to control texture and microstructure, and thus the final properties by adjusting the number and the distribution of the nucleation stimulating particles.

In the present work, a model was developed, based on experimental observations, to describe the deformation and nucleation around particles. To investigate particle-stimulated nucleation experimentally, high-resolution SEM/EBSD was applied to collect the great amount of statistical data required. With nowadays obtainable high resolutions of the electron microscopes down to the order of 10 nm this provides a good technique to collect statistical data in a reasonable amount of time. The main purpose of this investigation was to understand the development of individual grain orientations in the particle vicinity during deformation and subsequent annealing. This is of special importance since these newly developed grain orientations will significantly determine the final texture. Based on the experimental observations, a model to describe the deformation and nucleation around particles was developed. For the description of the inhomogeneous deformation in the particle vicinity FEM (Finite Element Method) was utilized. This new nucleation model for particles is introduced in Chap. 5, together with the results of the experimental studies. The model for particle-stimulated nucleation was then incorporated in an existing recrystallization model for description of annealing treatments during thermo-mechanical processing (Chaps. 4, 7-9).

For the modeling and simulation of recrystallization various models are available from the literature (Chap. 2), such as phenomenological models, geometric microstructure models, vertex models, statistical models and discrete models, such as Monte Carlo and cellular automata methods [Raabe 1998]. For the present work, a cellular automaton approach was chosen due to the possibility to resolve microstructure inhomogeneities in sufficient detail. With respect to the recrystallization modeling on different time and length scales cellular automata are a promising modeling technique (able to bridge a large scale 10^{-10} to 100 m, for comparison MC only 10^{-9} - 10^{-5} m) [Raabe 1998]. The first who applied cellular automata to model the recrystallization phenomenon were Hesselbarth and Göbel in 1991 [Hesselbarth 1991].

Whereas the recrystallization models available in the literature are mostly restricted to the validated range, to single-phase materials or to the prediction of only kinetics, microstructures or textures; this work was dedicated to create a recrystallization model which is able to capture the full set of physical micro-scale mechanisms occurring during a heat treatment in commercial alloys as well as to reach reasonable predictions of kinetics, grain size and texture in equal measure. The recrystallization modeling is therefore focused on sub-structural quantities, e.g. orientation-resolved dislocation densities, which are traced along the process chain. The cellular automaton for recrystallization (CORE) as used in the present work is outlined in detail in Chap. 3. In contrast to an earlier version of the CORE model developed at the IMM [Mukhopadhyay 2007], the present model was extended for the application to commercial alloys including the required micro-scale mechanisms. In commercial alloys, such micro-scale mechanisms are recovery (Chap. 6), which reduces the driving force for recrystallization, and all effects connected to second-phases (Chaps. 7, 8). Those can be the development, coarsening or dissolving of particles, which hinder or even suppress recrystallization. These processes can occur prior to recrystallization, concurrent to it or even after it is completed. Chap. 4 presents a validation of the recrystallization model limiting the number of simultaneous influence factors.

Beside the growth, the correct description of nucleation is essential for the quantitative texture and grain size prediction. A further transfer to industrial problems proves itself even more complicated due to the use of non-isothermal heat treatments as well as more complicated alloying systems. Therefore, extensive validations for the recrystallization model were carried out for two commercial aluminum alloys AA3103 (Chap. 7) and AA8079L, applying, e.g. non-isothermal heat treatments (Chap. 8). The required experimental data was provided using X-ray diffraction, metallographic, optical - and electron microscopic techniques.

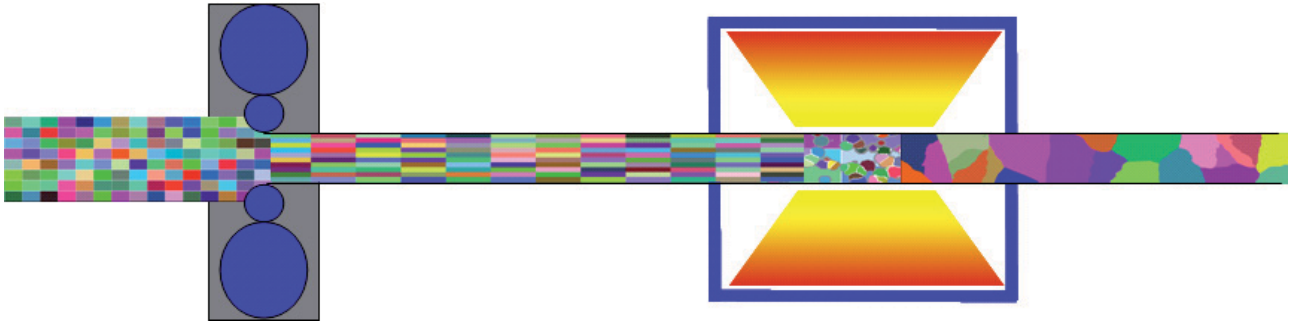


Fig. 1.1: Scheme of the modeling setup for predicting recrystallization. Prior to recrystallization a deformation simulation (rolling) is required to provide the major inputs for CORe. Microchemistry simulations are accompanying the process.

The main interest in the above introduced recrystallization model was its implementation into an existing through-process modeling setup displayed in Fig. 1.1. After deformation (rolling) the material, displaying elongated grains, is subjected to annealing treatment after which the microstructure is completely renewed. Here, the interaction of different models used for describing different parts of the system is the crucial problem to solve. The different incorporated phenomena do not necessarily take place on the same time-scale and it is not ensured that the parameters obtained from one model can be directly transferred to the subsequent model. This was particularly important in Chaps. 7-9 where alternating cycles of deformation and annealing are modeled on grain scale. The thesis is concluded by addressing a through-process modeling exercise for the application to a commercial Al-alloy AA3103 alloy (Chap. 9), considering simultaneously all introduced effects, i.e. recovery, recrystallization and precipitation.

Chapter 2

Recrystallization

2.1 Introduction

Recrystallization is the complete regeneration of the microstructure during annealing of a deformed material. In the process of deformation various defects (vacancies, dislocations, grain boundaries etc.) have been introduced into the material. Their amount and type are strongly dependent on the prior deformation degree and type. The defects transfer the material into a thermodynamically unstable state. At low temperatures, this material state is maintained, since the material is in a mechanical equilibrium. However, if the temperature is raised above a critical temperature, the thermodynamical equilibrium is approached by transferring the material to successively lower energy states. The gradual softening that is obtained if a deformed polycrystal is annealed at elevated temperatures is caused by two competing physical mechanisms: recovery and recrystallization. Recovery is the rearrangement and annihilation of dislocations, during which microstructure and texture are only slightly affected. In contrast, recrystallization is the replacement of the prior deformed microstructure by a new, strain free microstructure by the generation and migration of high-angle grain boundaries. Furthermore, the microstructure changes are accompanied by a complete change in texture. To distinguish between processes appearing during an annealing treatment after a prior deformation or during the deformation process itself, we distinguish dynamic and static mechanisms. The present work refers exclusively to static recovery and static recrystallization. Static recrystallization is further known as discontinuous or primary recrystallization to distinguish it from types of extended recovery (continuous recrystallization, recrystallization in-situ) or abnormal grain growth (secondary recrystallization). So-called secondary recrystallization occurs after recrystallization has been completed and is no actual recrystallization mechanism. It is abnormal grain growth which resembles in its appearance the microstructure changes during primary recrystallization. However, the energetic reasons for both processes are totally different. During primary recrystallization the stored dislocation density is reduced, whereas during secondary recrystallization, the interface area, connected with the specific interface energy, is reduced.

The occurrence of recrystallization is dependent on several factors: the normalized stacking fault energy, the deformation degree and type, the initial texture, type and distribution of second phases, solute contents and the grain size. The temperature at which recrystallization is initiated depends beside various other factors, on the melting temperature of the material and its purity.

The importance of recrystallization originates in its strong influence on the microstructure and texture evolution during industrial processing cycles and thus on the final properties of the material. This was for instance vividly demonstrated with respect to simulations in the SFB project 370 “Integral Materials Modeling”.

2.2 Recrystallization Nucleation

The importance of recrystallization nucleation is based on its influences on the final recrystallization texture and microstructure. Whereas the nucleus orientations have a very pronounced influence on the final recrystallization texture, the nucleus number basically determines the final recrystallized grain size, if effects such as grain boundary impingement by dispersoids are neglected.

The first researchers, who suggested applying the classical nucleation theory developed for phase transformations to recrystallization, were Burke and Turnbull [Burke 1952]. By theoretical considerations it was later shown that the origin of a nucleus cannot be described by the classical nucleation theory. The development of a nucleus by thermal fluctuations can be excluded, since the driving force for recrystallization, caused by the stored dislocations, is by orders of magnitude too low compared to the interface energy between the recrystallized region and the non-recrystallized matrix. A calculation according to classical nucleation theory would lead to unrealistic nucleus sizes in the order of $\sim 1 \mu\text{m}^3$ or 10^{10} atoms. Such huge nucleus radii are not found in the microstructure of metals which supports that the nuclei for recrystallization must already be present in the deformed state as first postulated by Burgers [Burgers 1941]. This leads to the so-called *preformed nucleus model*. At present, the preformed nucleus model seems to be the most accepted. In this case, it is assumed that the nuclei are already present in the deformed microstructure and a thermal formation of a nucleus is not required. This becomes obvious when discussing the instability criteria which lead to a viable nucleus as discussed below.

2.2.1 Instability criteria

During deformation, defects are introduced into the material. Those defects increase the internal energy of the material and therefore distance it from the thermodynamical equilibrium. The immediate reduction of the system energy towards the thermodynamical equilibrium is prevented since the structure is in a mechanical equilibrium. During annealing, it was observed e.g. by Ray et al. [Ray 1975] that prior to the appearance of recrystallized grains sub-boundary migration takes place. This means that a nucleus becomes overcritical as soon as the sub-boundary mobility suddenly increases, which corresponds to the transformation of a cell structure into a substructure and further to the generation of higher angle misorientations in the course of recovery. Based on such experimental observations the following nucleation criteria were stated:

Thermodynamic Instability

According to classical nucleation theory, a nucleus can grow only if the gain of transformation energy at least compensates the increase in surface energy. From this condition the radius of a critical nucleus r_{crit} with spherical shape can be obtained to:

$$r_{crit} = \frac{2\gamma}{p} \quad (2.1)$$

where γ is the interface energy and p the driving force. Since this critical nucleus leads to vanishing nucleus rates under the driving forces typically found in a deformed microstructure, a nucleus of critical size must already be present in the deformed state.

Mechanical Instability

To initiate nucleation, a local imbalance of the driving forces is required in the microstructure. This can be provided by a sufficiently large subgrain, which contains a comparatively low dislocation density surrounded by smaller subgrains with a higher dislocation density. Another possibility, are different recovery rates within different subgrains which could reduce drastically the dislocation density within certain grains; and hence lead to a heterogeneous dislocation density distribution.

Kinetic Instability

The presence of a mobile grain boundary is required for the successful growth of a preformed nucleus. The boundary mobility is depending on temperature via a Boltzmann term $\exp(-Q/kT)$. Hence a recrystallization temperature can be defined, which is required for recrystallization to appear in a reasonable time frame, usually one hour. This recrystallization temperature is for pure and strongly deformed metals proportional to the melting temperature ($T_R \cong 0.4T_m$) [Gottstein 1998]. Beside the temperature dependence there is also a strong dependence on the misorientation between adjacent grains or subgrains. It was found that with increasing misorientation the boundary mobility increases significantly [Gottstein 1992a].

In a deformed microstructure, in general, no sharp changes of orientation are observed, which would lead to a highly mobile boundary. Instead strong misorientation gradients can be found in highly deformed parts of the microstructure. Subsequently, recovery during annealing leads to polygonization, respectively to the development of a subgrain network. Subgrain networks within orientation gradients are characterized by boundaries with much higher misorientation than elsewhere in the matrix. Since nucleation is in particular favored in such orientation gradients only the creation of a mobile boundary out of the subgrain structure is required further. This was first proposed by Dillamore [Dillamore 1972]. For the initiation of nucleation it is already sufficient if parts of the boundary are highly mobile [Bailey 1962].

2.2.2 Types of nucleation*Nucleation at grain boundaries*

One of the first nucleation mechanisms identified as such is the *Strain Induced Boundary Migration (SIBM)* [Beck 1950, Cahn 1950, Cottrell 1953, Faivre 1979]. The first who investigated and proposed *SIBM* were Beck and Sperry 1950 [Beck 1950]. *SIBM* is the bulging of a part of a pre-existing boundary leaving a region behind the migrating boundary with a lower energy, respectively lower dislocation density. The condition for the occurrence of this process is a favorable energy-balance between the decrease of stored energy due to the elimination of defects caused by the passage of the boundary, and the increase in total grain boundary surface due to bulging.

The mechanism of nucleation at grain boundaries was revised by Bailey and Hirsch in 1962 [Bailey 1962]. They assumed, that not the whole boundary, but rather a part of the boundary, is mobile. This mobile part of the boundary is pinned by the immobile parts of the boundary. Since the

migration of a part of the grain boundary is connected with an increase of the grain boundary area, and therefore with an increase of the integral grain boundary energy, bulging will only appear if this energy is compensated by the elastic deformation energy, which was stored before in the volume swept by the boundary. This leads in 2D to a critical length of a mobile boundary section of two times r_{crit} (Eq. (2.1)).

Nucleation at grain boundaries is however most probable to happen by strain-induced boundary migration. SIBM fulfills most of the nucleation criteria outlined above. The demand of a large orientation gradient and thus, a high mobile interface, is basically fulfilled at high-angle grain boundaries, which are present from the prior deformed state. Furthermore, the dislocation density in real microstructures is mostly not homogeneously distributed within the grain boundary regions in two adjacent grains. This ensures the fulfillment of the criterion of mechanical instability, since a directed driving force across the boundary is obtained. Whereas high orientation gradients are developed near the boundary, a more homogeneous structure can be found in the grain interiors [Bailey 1960, Faivre 1979]. Furthermore, in most materials a specific substructure develops dependent on the initial orientation as described e.g. by Bellier [Bellier 1977].

The rearrangements occurring prior to the bulging were described by Jones et al. [Jones 1977]. They observed that during the earliest stages of a recrystallization anneal, the structure of the boundaries between deformed grains undergoes rapid and extensive rearrangements, which are the annihilation of all boundary dislocation components of antiparallel burgers vector and the incorporation of the remaining dislocations into a modified intrinsic grain boundary structure. The rearrangement of dislocations in the grain boundary surrounding area into a subgrain structure is required to create an imbalance of the driving forces on both sides of the boundary. They further observed that a boundary can bulge out between two pinning points, which are represented by narrow regions of higher dislocation density.

Recent investigations show that in particular at higher strains Eq. (2.1) requires some modifications [Bate 1997], since the changing density of substructure behind the boundary was not considered in the original approach.

The nuclei originating from SIBM show in general orientations related to the orientation of the mother grain. The strengthening of the $\{100\}\langle 001\rangle$ Cube texture during recrystallization of aluminum after high temperature deformation is attributed to SIBM. For nucleation at grain boundaries also orientations not close to the mother grains can be found [Beck 1950, Humphreys 2004]. Driver et al. [Driver 2000] observed in plane strain compression tests on Al bicrystals nucleus orientations with a $\sim 30^\circ\langle 111\rangle$ relation to the deformed matrix.

Nucleation in orientation gradients

As already mentioned earlier, the basic requirements for nucleation are a critical size of the nucleus which is at least partly bounded by a high-angle grain boundary within the deformed matrix. Further a driving force needs to act on this grain boundary to lead to migration. These conditions are especially fulfilled in the heterogeneously deformed parts of the material. Such inhomogeneities are, for instance, deformation bands [Hu 1962, Walter 1963, Faivre 1979, Inokuti 1978, Bellier 1977], transition bands [Ridha 1982, Hjelen 1991, Dillamore 1972] or particles after sufficiently high deformation. These inhomogeneities are, in general, preferred sites for nucleation since high misorientations between adjacent subgrains are locally present.

A transition band develops when neighboring volumes of a grain deform on different slip systems and rotate to different end orientations. This was studied in detail by Dillamore and Katoh [Dillamore 1974]. The nucleus orientations observed with respect to this mechanism are related to the initial mother grain. Deformation bands are thin regions across which the orientation of one part of a deformed grain changes rapidly to that of a differently oriented part of the same grain. During annealing a substructure can rapidly evolve in the present orientation gradients by processes such as recovery, so that boundaries with a higher mobility are locally developed. Bellier and Doherty [Bellier 1977] investigated nucleation in an aluminum alloy. It was observed that the dominating nucleation mechanism up to a strain of 20 % was SIBM, but after deformations of 40 % the

nucleation was observed to originate within the grains at deformation bands as dominating nucleation mechanism. Other preferred nucleation sites involving orientation-gradients are Brass-shear bands, since they comprise a high stored energy, and due to the almost random orientation distribution within the band any possible nucleus orientation can be found. Hence, at such locations a highly mobile boundary can be created easily with the surrounding matrix, so that all nucleation criteria are fulfilled and a viable nucleus is obtained.

Another advantage of the inhomogeneous regions in the deformed matrix is the presence of a non-homogeneous subgrain size distribution. A subgrain, which is misoriented by more than the average value, would tend to shrink, because of the energy penalty of its higher-energy boundary. Only in combination with a larger than average subgrain size, as present in a non-homogeneous subgrain size distribution a nucleus can develop [Humphreys 2004a]. During its growth the orientation difference to the surrounding environment is increasing rapidly, providing boundaries with a higher mobility. This makes those regions with large local misorientations preferred nucleation sites, in addition to the reasons already outlined above. Another example for nucleation in orientation gradients is particle-stimulated nucleation, which is described subsequently.

Nucleation at particles

An example of heterogeneous nucleation is particle-stimulated nucleation (PSN). Second-phase particles have a large effect on the evolution of the microstructure developed during deformation, and this in turn affects the recrystallization nucleation. If a particle-containing material is deformed, the material will not deform homogeneously throughout the crystal. Since the second-phase particles ($> 1 \mu\text{m}$) often have a higher strength than the surrounding matrix, the material will rather deform inhomogeneously. During deformation, at first the matrix material will deform whereas the constituent particles (incoherent) remain almost undeformed. This causes a material flow around the particles and leads, e.g. during compression or rolling of a two-phase material, to the development of so-called deformation zones as indicated in Fig. 2.1a.

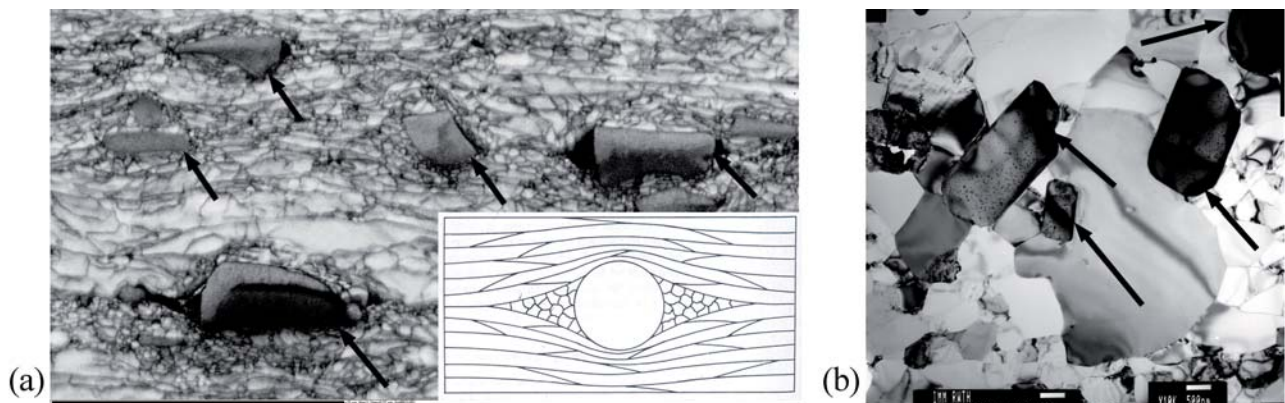


Fig. 2.1: (a) Deformation zones in the vicinity of particles after 70% cold rolling (alloy AA3103, Chap. 7-9) with schematic subgrain structure around particle [Porter 1979] ; (b) particle stimulated nucleation in a commercial Al-1 wt% Mn alloy (AA3103) after annealing for $t = 25 \text{ min}$ at $T = 290^\circ\text{C}$. The particles are indicated by arrows.

These zones are characterized by an increased dislocation density in combination with very high misorientation gradients. From experimental studies [Russell 1970, Brown 1971, Humphreys 1979, Humphreys 1983] maximum misorientations up to 40° with respect to the matrix were measured. The dislocation density and misorientations can be further increased if several deformation zones overlap, which will happen if the second-phase particles are closely located. The interaction of particle deformation zones was studied, for instance, by [Sircar 1994].

The local orientations found within the deformation zones are of major importance for particle-stimulated nucleation during subsequent annealing. Ashby [Ashby 1970] studied the lattice rotation geometry in the vicinity of particles in single crystals during tensile tests. He found that the rotation

axis is at the same time perpendicular to the primary slip direction and to the slip plane normal. From his observation he concluded that in fcc lattices the orientations in the deformation zones are related by a rotation around a $\langle 121 \rangle$ -direction to those in the initial matrix. This was reported by Humphreys, e.g. for Al-Cu and Al-Si single crystals deformed in tension and compression using TEM and X-ray measurements, and other authors [Russell 1970, Brown 1971, Humphreys 1979, Humphreys 1983]. More commonly these rotations are also described by rotations around the transverse direction, e.g. for rolling [Engler 1997a]. The transverse direction is closely related to the $\langle 121 \rangle$ axis as suggested by Humphreys [Humphreys 1979, Engler 1997a]. For higher rolling reductions, the deformation is not based on single slip any more. Hence, the above mentioned considerations are not valid any more and more complex dislocation structures are developed. It was found that the subgrains in the deformation zones were, however, not randomly oriented but showed characteristic orientation relationships to the deformed matrix, which can be related to the operative slip systems [Humphreys 2004]. With respect to polycrystalline microstructures systematic investigations of the deformation zones are hardly reported in literature.

During subsequent annealing of those deformation zones new nuclei develop from the orientation spectrum present. Nucleation at particles is promoted by the locally higher stored dislocation density. A first insight on the mechanism of PSN was given by Humphreys [Humphreys 1977], Herbst and Huber [Herbst 1978] and Bay [Bay 1979]. They found that recrystallization originates at pre-existing subgrains within the deformation zone, but not necessarily on the particle surface. It was further observed that nucleation occurs by rapid boundary migration and that growth may cease when the deformation zone is consumed, leaving behind so-called island grains in the fully recrystallized microstructure.

A necessary criterion for nucleation within the deformation zone is a high enough misorientation to form a mobile boundary as previously discussed. This requires a critical particle size as well as a critical strain [Humphreys 1977]. It was found that the nucleus orientations found at particles lay within the scatter of those found in the deformation zone, e.g. by Ferry who studied annealing of oriented particle-containing single crystals which had been deformed in plane strain compression [Ferry 1996a, Ardakani 1994, Ferry 1996b]. In general, weak recrystallization textures are reported in connection to particle-stimulated nucleation [Humphreys 2004]. The range of orientations observed in case of polycrystals is much larger. A single grain will give rise to a nucleus scatter over a large range, since it contains more than one particle and therefore numerous deformation zones. As a result a weakening of the overall texture is obtained. In some cases, however characteristic orientations, such as the P and ND rotated Cube texture components are observed which accompany PSN [Engler 1995a, Engler 1995b, Engler 1996, Lücke 1990]. Engler et al. [Engler 1996] investigated the formation of recrystallization textures in a binary Al-1.3% Mn. They found that within the orientation spectrum also the P orientation and ND rotated Cube orientation were present, which were found to originate from the deformation zones.

From literature it is known that the critical size for incoherent isolated particles in order to initiate PSN is larger than $1\ \mu\text{m}$ [Humphreys 2004]. Further in some cases, nucleation at particles was observed below this particle size if particles were arranged so closely that their deformation zones overlapped [Herbst 1978, Gawne 1971, Weiland 1995]. In such cases PSN can be initiated below the critical size of $1\ \mu\text{m}$. The reported nucleus efficiency of particles is in general about one nucleus per particle, for larger particles or particle clusters also multiple nucleation was observed [Herbst 1978].

Nucleation by subgrain coalescence

Another possibility for nucleation beside the inhomogeneous subgrain growth in an orientation gradient is subgrain coalescence. The possibility of subgrain coalescence was first thoroughly examined by Hu [Hu 1963] and Li [Li 1962]. Nucleation by subgrain coalescence is favored at lower annealing temperatures. It is a mechanism that promotes subgrain growth, disappearance of sub-boundaries and is changing at the same time the orientation with the neighboring subgrains. The increase in orientation difference leads to the appearance of a high-angle grain boundary

capable of high-speed migration, forming the nucleus of recrystallization [Favre 1979]. It is a non dominant recovery mechanism.

Nucleation by twinning

A nucleation mechanism in particular observed in metals with low stacking fault energy is nucleation by twinning [Gleiter 1969, Meyers 1978, Karduck 1983]. It is connected to characteristic orientation changes and can be described by a lattice transformation, by which a certain volume of an orientation is transformed into a mirror-symmetrical orientation. This can be described with an exact 60° rotation around a $\langle 111 \rangle$ axis. The first twinning generations lead not yet to the creation of high-angle grain boundaries. By further twinning of the already developed twins up to several subsequent twinning generations so-called twinning chains are developed, with an almost unlimited number of new orientations with any orientation relation to the original orientation. This was in more detail investigated in [Gottstein 1984a]. These twinning chains, or continued twinning, lead not only to large orientation differences but also to preferred growth relationships with the deformed microstructure.

Nucleation by “Inverse Rowland Transformation”

Another nucleation mechanism operating by lattice transformation is the nucleation by “Inverse Rowland Transformation”. It was proposed specifically for the cube texture in copper. It is also referred to as “martensitic” nucleation model. This model was postulated by Burgers and Verbraak [Burgers 1957, Verbraak 1960a, Verbraak 1960b] and describes nucleation by a quasi-martensitic shear within small regions of the deformed lattice.

In this case two adjacent twin-related lattices transform via lattice shearing by elimination of an incoherent twin boundary into a joint orientation, which results for instance in the Cube orientation in case of a $\{112\}\langle 111 \rangle$ starting orientation. Hence, a new region within the crystal is created which is entirely bounded by high-angle interfaces. This theory explains the orientation relationship between the Cu-deformation and Cu-recrystallization texture (Cube texture) correctly. Some very important reasons seem to be against the existence of such a mechanism. One of them is that similar orientations are also observed in aluminum, where the development of deformation twins is very restricted due to the high stacking fault energy.

2.2.3 Influences on nucleation

Most commercial alloys contain second-phase particles. Second-phase particles can be either present from casting, the so-called constituents, or they appear during an annealing treatment as dispersoids. The effect of second-phase particles on recrystallization is manifold. Large particles, which were present before deformation, can cause particle-stimulated nucleation during an annealing treatment; the same treatment might lead to the precipitation of dispersoids, which can have a completely contrary effect. Dispersoids can strongly hinder recrystallization up to complete suppression if they have small particle spacings (high volume fraction and small sizes).

Nucleation influenced by impurities

From literature it is known that impurity atoms influence the recrystallization behavior significantly [Masing 1956]. This means that the nucleation process, as well as the following growth is influenced by impurity atoms. Recovery processes are required to activate a potential nucleus. For pure metals the activation energy for climbing of dislocations is in the order of the activation energy for self-diffusion. This value, can be increased by more than one order of magnitude due to the segregation of impurity atoms, e.g. in Al-Fe [Holm 1970]. This suggests that the rearrangement during recovery is strongly controlled by particle growth.

In [Messenger 1960] it was shown that during nucleation especially the cell growth and to a lesser extent the dislocation rearrangement is influenced. The impurity atoms cause a decrease in the

stacking fault energy, which corresponds to easier dislocation dissociation. This can hinder climb and cross slip and therefore nucleation.

Nucleation influenced by fine particles

The presence of small particles prior to recrystallization leads to an interference with the free movement of dislocations. At low strains, small particles stimulate dislocation loop formation and enhance cross slip [Hirsch 1969, Brown 1971]. This leads to homogeneous dislocation distribution and hence reduction in local misorientations [Humphreys 1967]. The presence of a distribution of small particles suppresses or delays the cell formation and hence the subgrain growth [Hutchinson 1978, Detert 1965]. The result can be either a reduced rate of nucleation or a reduction in the total density of nuclei formed in such materials [Jones 1980]. The drastic retardation of nucleation in the presence of fine dispersions is described by Doherty and Martin [Doherty 1962]. They observed that the mean free distance for subgrain growth in between the dispersoids plays a very important role for the retardation of recrystallization. They further observed a coarsening of the microstructure with finer particle dispersions. In case the fine dispersoids are distributed with very large spacings, the influence on recrystallization can be neglected. In case of cuttable particles, bands of massive local slip can develop which enhances the nucleation. At the same time the size of the particle is reduced, which again leads to a hindering of the recrystallization nucleation. In case larger particles ($> 0.5 \mu\text{m}$) are present in the material, locally a zone of higher deformation develops around the particle which promotes nucleation at particles.

During recovery particles of a second phase influence not only the movement of single dislocations, but also the migration of low angle grain boundaries and hence influence the nucleation of recrystallization. If the sub-boundary has not reached a high enough misorientation before impingement with the particle, nucleation will be very difficult.

In extreme cases, especially at low temperatures recrystallization in-situ can occur [Engler 1995c]. In this case precipitates form at large grain boundaries, subgrain boundaries and sometimes on dislocations and dislocation networks. It was further reported in literature that precipitation is dependent on the initial grain orientation, respectively substructure [Chan 1984, Engler 1995c], which leads to specific effects on texture. In case precipitation starts before the onset of recrystallization softening becomes much more delayed [Saeter 1997]. In this context a strengthening of the Cube orientation was observed (concurrent precipitation). This was also observed by other authors [Furrer 1978].

2.3 Nucleus Growth

2.3.1 Grain boundary migration

The mechanism of the migration of high-angle grain boundaries can be derived as the diffusion jumps of atoms from one side of the boundary to the other under the applied driving force p .

The velocity of such a boundary can then be written as:

$$v = b \nu_D c_v \left(\exp\left(-\frac{G_m}{k_B T}\right) - \exp\left(-\frac{G_m + p\Omega}{k_B T}\right) \right) \quad (2.2)$$

where G_m is the free activation enthalpy for self diffusion, T the absolute temperature, p the driving pressure, Ω the atomic volume, b the Burgers vector, ν_D the Debye frequency, c_v the concentration of vacancies in the boundary, and k_B the Boltzmann factor.

Since $p\Omega/k_B T \ll 1$ a Taylor series can be truncated after the linear term.

$$v \approx b v_D c_v \left(\exp \left(- \frac{G_m}{k_B T} \right) \left(\frac{p \Omega}{k_B T} \right) \right) \quad (2.3)$$

Hence, in first approximation a linear dependence between driving force and velocity is obtained. This can be expressed as

$$v = m \cdot p \quad (2.4)$$

where m is the mobility and p the driving force [Gottstein 1992a]. The driving force during recrystallization is essentially given by dislocations. The mobility of the grain boundaries m is according to Eq. (2.3) described as a function of the temperature:

$$m = \frac{b^2 D_0^{Gb}}{k_B T} \exp \left(- \frac{Q_m}{k_B T} \right) \quad (2.5)$$

where D_0^{Gb} is the temperature independent pre-exponential coefficient for diffusion through the interface, and Q_m the activation energy of the mobility. It is known from the literature that the activation energy strongly depends on the misorientation and type of the boundary and on the concentration of foreign atoms in the interface [Gottstein 1999, Molodov 1999, Winning 2007].

2.3.2 Influence of recovery

The term recovery refers to changes in a deformed material which occur prior to recrystallization, and which partially restore the properties to their values before deformation. Recovery and recrystallization are competing processes as both are driven by the stored energy of the deformed state. If a certain amount of recovery occurs prior to recrystallization it may influence the nature and the kinetics of recrystallization. Recovery has further influences on the recrystallization nucleation since it is the main mechanisms to activate a nucleus during the incubation time.

The appearance of recovery depends strongly on the stacking fault energy. Materials with low stacking fault energy, such as Cu, hardly recover, whereas aluminum and most of its alloys, which have high stacking fault energies recover rapidly. The stacking fault energy affects the extent to which dislocations dissociate, and thus determines the rate of cross slip. Together with climb these mechanisms control the rate of recovery. This material property makes such materials with high stacking fault energy very prone to recovery because undissociated dislocations can easily cross slip; respectively dissociated dislocations can easily recombine prior to cross slip. Climb and cross slip are further thermally activated processes and depend on the applied strain.

The kinetics of recovery, being measured immediately after deformation is significantly different from the recrystallization kinetics, which proceeds very rapidly to completion as soon it is initiated after an incubation time. It is reported by Vandermeer [Vandermeer 1963] that decreasing growth rates during recrystallization are due to competing recovery processes which lower the available driving force in the unrecrystallized portions of the microstructure. The appearance of recovery was measured by calorimetric measurements in copper-doped, polycrystalline zone-refined aluminum, which was cold rolled to a thickness reduction of 40 % [Vandermeer 1963]. Two recovery stages were suggested corresponding to (a) the reduction in dislocation density within subgrains and the rearrangement in lower energy configurations, the so-called polygonization, and (b) the gradual growth of those subgrains with small misorientations to their neighbors.

The presence of dispersoids prior to recovery tends to retard the formation of dislocation cell structures and leads to smaller cell sizes compared to the same material without dispersoids after the same strain applied. The effect on recrystallization nucleation is that the onset of recrystallization is shifted to longer times, what leads to a further reduction of the stored energy respectively the

driving force. This results in an increasing critical size of the nucleus and reduces therefore the probability of nucleation.

It is further known from the literature that recovery depends also on the orientation. In general, a very heterogeneous recovery behavior is observed in the prior deformation substructure. Experimental investigations in literature also indicate that the level of stored energy in cold worked materials varies not only with the total strain imposed but also as a function of individual grain orientation [Taoka 1965]. It is further reported that the cell shape is a function of the grain orientation [Every 1974] and that increased stored energy was associated with both a smaller cell size and a larger average cell boundary misorientation [Dillamore 1967].

In cases of very pronounced recovery, recrystallization can be completely suppressed and recrystallization in-situ (continuous recrystallization) is observed. The recovery behavior is further detailed in Sec. 3.6.

2.3.3 Influence of small particles - Zener drag

The recrystallization growth after completed nucleation can be strongly hindered by fine distributed particles [Doherty 1962, Cotterill 1976b, Hornbogen 1978, Chan 1984, Nes 1985, Engler 1997d, Tangen 2002]. Zener [Zener 1949] is credited for first suggesting the interacting force between a boundary and an inclusion. If a boundary moves through a particle the grain boundary area is reduced, which is related to a drop in the grain boundary energy (Fig. 2.2). During a continued movement of the boundary, the saved surface energy needs to be provided again, which results in a back-driving force. For spherical particles the back-driving force p_Z can be calculated [Zener 1949]:

$$p_Z = -\frac{3}{2} \cdot \gamma \cdot \frac{f_p}{r_p} \quad (2.6)$$

where f_p , r_p are the dispersoid volume fraction, respectively radius and γ is the interface energy. Eq. (2.6) assumes a uniform distribution of the particles. If the particles are precipitated at grain boundaries, the given equation is no longer valid and the retarding force is much larger [Hornbogen 1978]. Nes et al. [Nes 1985] re-evaluated this equation. Considered were different types of distribution, but it was found that the back-driving forces obtained in various cases were not much different from the one originally proposed by Zener. The back-driving force is determined by the dispersion degree f_p/r_p . With increasing dispersion degree the back-driving force is increased. This can be caused by an increasing particle volume f_p or a decreasing particle radius r_p .

Doherty and Martin [Doherty 1962] investigated the effect of a dispersed second phase on recrystallization in Al-Cu alloys. They observed that recrystallization depends very sensitively upon the characteristics of the dispersion. With finer dispersions the recrystallization became increasingly retarded. Further, the nucleation rate was increasingly retarded with increased fineness of the dispersion due to pinning of sub-grain boundaries. It is reported that recrystallization in the presence of a dispersed second phase is either accelerated or opposite, retardation is observed. A close examination of those results suggests that the inter-particle spacing is the controlling factor, acceleration occurring at wide spacings and retardation at close spacings.

It is very often observed that as soon as a grain boundary is pinned by Zener drag, it can not move any further until the particles have significantly coarsened. However, it was proposed by Gottstein and Shvindlerman [Gottstein 1993] that in case of mobile particles the transition from the free boundary to the loaded one is more continuous (Fig. 2.3b). In a real material this behavior is more probable, since in most cases a grain size distribution is present in the material rather than an average one and particularly the small particles are mobile.

Besides recrystallization being influenced by dispersoids, it is also important when the dispersoids are effective with respect to recrystallization. Precipitation can take place either (a) before recrystallization, (b) during recrystallization or (c) after recrystallization is finished. In case precipitation takes place before the onset of recrystallization, a pinning of the boundaries due to Zener Drag as described above, is observed. In case (c) no influence of the precipitation is observed. In case (b), which is also referred to as concurrent precipitation the precipitation is favored by the moving boundary and recrystallization is strongly retarded. This behavior has been found in many supersaturated and deformed alloys [Hornbogen 1978].

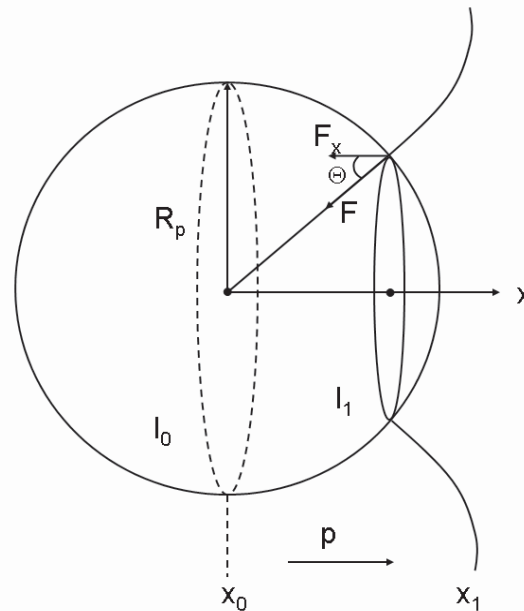


Fig. 2.2: Schematic sketch of the interaction of a grain boundary with a dispersoid.

If precipitation occurs concurrent to recrystallization strong effects on grain size and texture can be expected [Doherty 1962, Nes 1975, Engler 1997d, Tangen 2002]. In case precipitation occurs prior or concurrent to recrystallization, the grain structure becomes coarse and elongated in rolling direction, but if the material recrystallizes prior to precipitation, a fine, and equiaxed grain structure is obtained. Tangen et al. [Tangen 2002] for instance, present an investigation describing critical heating rates depending on the solute content of manganese in aluminum in order to prevent the occurrence of concurrent precipitation.

In many cases a strong Cube texture was observed along with heavy precipitation preferential in super-saturated solid solutions [Vatne 1997, Higginson 1997]. The preference of Cube was explained by the size advantage of Cube grains, which may even develop before the precipitation takes place. Further explanations are a reduced energy of Cube band boundaries or sub-boundaries within the Cube grains or even less segregation at Cube boundaries [Daaland 1996]. Humphreys and Ardakani [Humphreys 1996] proposed further an orientation dependence of Zener drag. They observed from corresponding experiments in Cu-Al single crystals that at intermediate strains grains with misorientations of $\sim 40^\circ$ about axes close to $\langle 111 \rangle$ with respect to the deformed matrix penetrate the two-phase regions, whereas other grains are stopped in their growth.

In contrast, during concurrent precipitation also P- and ND-rotated Cube texture components connected with a large elongated grain size were observed. The long elongated grains result from the precipitation preferential at high-angle grain boundaries before the onset of recrystallization. With increasing temperature, the grain size became more equiaxed, and the P-texture was decreased. In contrast, if no precipitation took place, the Cube texture component was dominant accompanied by a small grain size [Liu 2005]. They observed in the case of concurrent precipitation

Avrami exponents of $n = 0.4 - 0.6$ and for precipitation prior to the anneal values of 1.8 to 2.3. This is quite opposite to the aforementioned behavior.

Also the occurrence of a precipitation free zone (PFZ) was described by several authors [Morris 1978, Furrer 1979, Lloyd 1982]. They are in contrast to the observation of a preferred Cube texture. They are explained by precipitates dissolving in the particle vicinity, leaving a PFZ which allows recrystallization nucleation to take place at particles.

For fine dispersions present before the annealing treatment the final texture is characterized by a retained rolling texture on recrystallization [Humphreys 1986, Jazaeri 2004]. This process is also referred to as continuous recrystallization [Engler 1995c].

Summarizing, it is stated that the outlined influences of particles at the early nucleation stage are responsible for the effect on recrystallization texture.

2.3.4 Influence of solutes - solute drag

Beside fine dispersoids the recrystallization is also influence by elements in solid solution. It is reported that the recrystallization behavior is slowed down, e.g. in the presence of solutes in case of aluminum-manganese alloys [Lens 2005].

The influence of impurity atoms on grain boundary migration is described by the solute drag theory as proposed by Cahn, Lücke and Stüwe [Detert 1956, Lücke 1957, Cahn 1962, Gottstein 1999]. It is assumed that solute atoms experience close to the grain boundary a lower energy than in the comparatively perfect lattice. The reason for this is that grain boundaries are defect structures compared to the interior of a grain. Hence, in the grain boundary, free volumes are available which can be filled with solute atoms. Therefore, the local distortion of the lattice in the vicinity of a solute atom which is connected with an elastic energy is reduced in the grain boundary environment. A chemical interaction with the lattice can be neglected compared to this elastic energy. From the energy reduction an attractive force between a solute impurity atom and the grain boundary can be defined.

$$F(x) = - \frac{dU(x)}{dx} \quad (2.7)$$

where $U(x)$ is the free interaction energy and x the distance between the impurity atom and the grain boundary. From this attractive force follows, that the impurities are accumulated in a cloud next to the grain boundary. The concentration of the impurity atoms is dependent on the temperature.

$$c_{GB} = c_0 \cdot \exp\left(\frac{U}{kT}\right) \quad (2.8)$$

where c_0 is the equilibrium concentration of impurity atoms, U the interaction energy between solute atom and grain boundary, k is the Boltzmann constant and T the temperature. The solute atoms stored close to the boundary need to do a coupled motion together with the grain boundary. Since their speed is determined by the diffusion of the impurity atoms in the matrix, the boundary motion is influenced. They apply a back-driving force on the boundary induced by the energy gain caused by the interaction energy between solute atom and boundary. The velocity of a grain boundary can be written in this case as

$$v = m \cdot (p - p(v, c)) \quad (2.9)$$

Due to the impurities a back-driving force $p(v, c)$ is applied to the boundary, which is dependent on the speed of the moving boundary v and the impurity concentration c in the boundary.

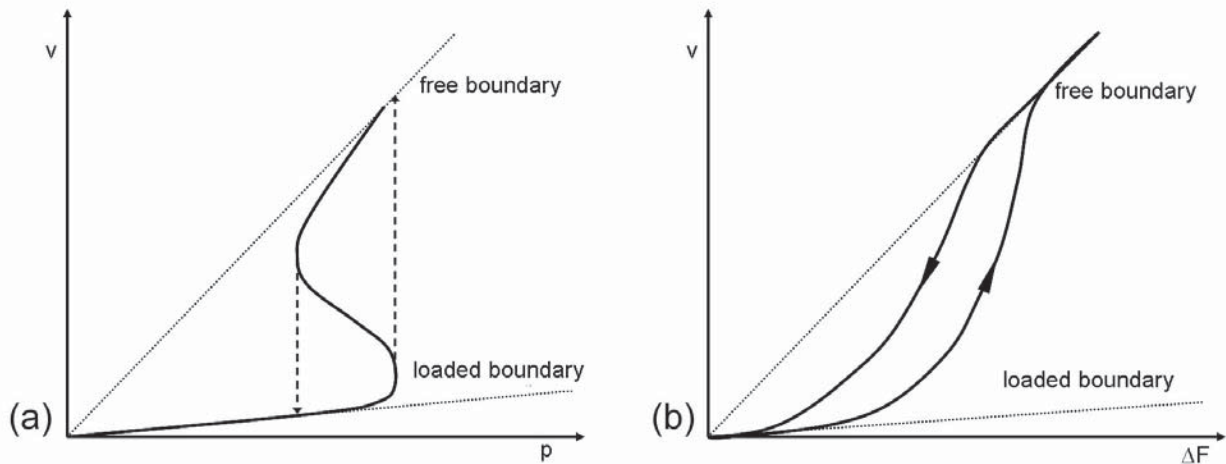


Fig. 2.3: (a) Dependence of the grain boundary migration rate on driving force in the presence of impurity drag. The transition from the loaded to the free boundary and vice versa occurs discontinuously [Lücke 1957]. (b) Schematic dependency of grain boundary velocity on driving force for grain boundary motion through a particle containing volume [Gottstein 1993].

With increasing concentration also the back-driving force is increased until by a further increase of impurity concentration an unstable range is reached as shown in Fig. 2.3a. The reason for this is the sudden break-free of the boundary from the impurity cloud [Gottstein 1999]. This is reflected in a discontinuous change of the grain boundary velocity. During the switch of the boundary from the free to the loaded stage, the driving force for an attachment is smaller than the one for the detachment. That means a range of driving forces exists where two different velocities can be observed.

Recrystallization Kinetics

Each recrystallization process has certain kinetics. This kinetics is determined by the kinetics of the development of nuclei and their subsequent growth. Other influences on the recrystallization kinetics are the deformation degree, temperature, initial texture and microstructure, activated nucleation mechanisms and the presence of solute atoms, respectively second-phases. The recrystallization kinetics is of major importance for industrial applications, e.g. to obtain a certain recrystallized volume fraction. The quantitative description of the recrystallization process is based on the nucleation rate and the growth velocity. As a quantitative description in most cases the Avrami-Johnson-Mehl-Kolmogorov-equation is applicable, as introduced in more detail in Sec. 2.4 (Eq. (2.18)). After the onset of recrystallization (incubation time), the nuclei are starting to grow, at first independently, later on the grains impinge and the free growth is increasingly hindered. This naturally slows down the recrystallization process towards the end, until after a certain time the system has reached a stagnation (in some cases this equals a strain free microstructure). More detailed information on the JMAK kinetic can be found in [Avrami 1939, 1940, 1941, Kolmogorov 1937, Gottstein 1998, Humphreys 2004].

Recrystallization textures in fcc metals

Since the present work is focused on fcc alloys, the presentation of recrystallization textures is restricted to fcc metals. In fcc metals and alloys basically two limiting textures are observed: the Cube texture $\{001\}\langle 100\rangle$ and the Brass-recrystallization texture $\{236\}\langle 385\rangle$. The Cube texture is bound to a copper type deformation texture and the Brass recrystallization texture to a brass type deformation texture. In pure materials, with copper type deformation texture, mostly a Cube texture component is observed, which leads owing to its high symmetry to over-proportional high intensities. Adding impurities leads to the occurrence of the R-orientation $\{123\}\langle 63\bar{4}\rangle$ often connected to the deformation texture component S.

In the past two rivaling theories for the development of recrystallization textures have been developed. In the case of oriented nucleation it is assumed that the preferred formation of special orientations determines the final recrystallization texture [Burgers 1931]. In the case of oriented growth or growth selection it is assumed, that starting from a broad spectrum of nucleus orientations, those with the best growth conditions with respect to the deformed matrix grow the fastest and hence dominated the recrystallization texture [Liebmann 1956, Lücke 1974, Molodov 1995]. Beside these theories there is also the theory of Lee [Lee 1995, Lee 1996, Park 1997], which explains the relation between deformation and recrystallization textures to be based on the directional stress distribution due to anisotropic dislocation arrangement.

Recrystallized grain size distributions

The final grain size after recrystallization might be the result of various influences during nucleation and growth. It further depends on the initial grain size, deformation history, deformation temperature and alloy composition which all cause influences on the nucleation and growth process. The grain sizes, as measured e.g. from a plane section are found to be usually close to a log normal distribution (Fig. 2.4). In the case, that extended recovery or strong changes in microchemistry may occur (e.g. during heating rates), the grain size distribution will be significantly influenced. Such influences lead in most cases to a heterogenization of the nucleation and growth process and thus, for instances, wider grain size distributions are observed.

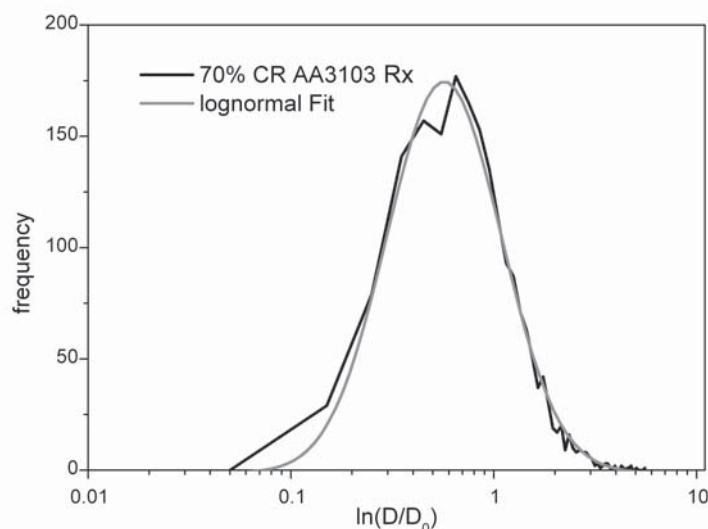


Fig. 2.4: An experimentally measured grain size distribution after completed recrystallization in a commercial Al-Mn alloy.

2.4 Recrystallization Models

The phenomenon of recrystallization introduced in the previous chapter, has an incredible impact on industrial processing. It mostly involves heat treatments leading to the occurrence of recrystallization. Recrystallization is a very complex phenomenon as introduced in Secs. 2.1-2.3 involving a number of interactions of lattice defects causing a complete change in material microstructure and texture. The modeling and simulation of recrystallization is nowadays an inevitable task in order to control texture and microstructure evolution in industrial processes. With the ever increasing capability of computers, in terms of higher speed and information storage, the modeling and simulation of material science phenomena became more and more feasible. Another reason for this evolution is the establishment of experimental data sets for empirical modeling, which is laborious and time-extensive and even not accessible to experiments in some cases over the required huge parameter ranges. In the past, several attempts have been undertaken to model recrystallization of which some are highlighted in the following section. During the past few years,

it became increasingly obvious that in order to provide reliable predictions for recrystallization, physical based models are urgently required. However, most of the presented approaches are basically growth models which lack a physically based description of the recrystallization nucleation and hence require separate sub-models.

The models developed for modeling recrystallization are mostly based on Monte Carlo simulations, Cellular Automata, Computer Avrami Models or statistical approaches. Models such as Molecular Dynamics or Vertex models are used to a lesser extent. A Cellular Automaton for modeling and simulation of recrystallization will be introduced in Chap. 3.

2.4.1 Phenomenological models

Johnson, Mehl, Avrami [Avrami 1939, 1940, 1941] and Kolmogorov [Kolmogorov 1937] (JMAK-theory) developed in the late 1930s independently of each other a theory, which provided the first analytical model to describe the kinetics of phase transformations, which was later on applied for recrystallization. It is one of the most famous analytical approaches to describe growth phenomena. The calculation of the recrystallized volume fraction as function of time is based on the following assumptions

- statistical and homogeneously distributed recrystallization nuclei,
- the recrystallization growth rate is constant and isotropic,
- upon impingement growth ceases Eq. (2.10)

For the description of phase transformations the extended volume fraction X^{ext} was introduced, which describes the growth of the nuclei independent of each other. Hence, each nucleus sees per time interval dt always a still hundred percent unrecrystallized volume. In reality however, this is not the case, since at one point the growing nuclei will impinge and overlap. It is assumed that the real recrystallized volume fraction dX at any time is proportional to the untransformed volume fraction $1-X$. Hence, we can write

$$dX^{\text{ext}} = \frac{dX}{1-X} \quad (2.10)$$

Eq. (2.10) was proven to be correct by Cahn [Cahn 1996]. Accordingly, the volume V_s of a spherical nucleus at the time t , which nucleated at $t=\tau$ is described in case of isotropic growth by

$$V_s(t, \tau) = \frac{4}{3}\pi \cdot r(t, \tau)^3 \quad (2.11)$$

Under the assumption of site saturation (all nuclei are developed at $t=0$, i.e. nucleation rate $N\delta(t)$) the extended volume can be written as

$$dX^{\text{ext}} = N \cdot 4\pi \cdot r(t)^2 \cdot dr \quad (2.12)$$

where N is the number of nuclei and r the radius of the nucleus. If we assume a constant growth rate v we obtain $r = v \cdot t$ and hence

$$dX^{\text{ext}} = N \cdot 4\pi \cdot v^3 \cdot t^2 dt \quad (2.13)$$

with v being at the same time the velocity of the moving grain boundary independent of time. Integration of Eq. (2.13) leads to the extended volume fraction X^{ext}

$$X^{\text{ext}}(t) = N \cdot \frac{4\pi}{3} \cdot v^3 \cdot t^3 \quad (2.14)$$

From Eq. (2.10) we can deduce the recrystallized volume fraction X

$$X_{\text{ext}} = \ln \frac{1}{1-X} \quad (2.15)$$

$$X(t) = 1 - e^{-X^{\text{ext}}(t)} \quad (2.16)$$

If we insert Eq. (2.14) in Eq. (2.16) we obtain the JMAK equation for isotropic growth and site saturation with an Avrami exponent of 3.

$$X(t) = 1 - e^{-\frac{4}{3}\pi \cdot N \cdot v^3 \cdot t^3} \quad (2.17)$$

In the case of deviations from homogeneity and isotropy, the exponent changes. For 2D growth it is reduced to 2. If instead a constant nucleation rate and isotropic growth is assumed it is increased to 4. In general the Avrami or JMAK equation can be written as

$$X(t) = 1 - e^{-\left(\frac{t}{t_R}\right)^q} \quad (2.18)$$

where q is the Avrami exponent and t_R is the characteristic recrystallization time ($X(t_R) = 1 - 1/e = 0.63$ recrystallized volume fraction).

The application of the JMAK theory for more realistic cases (non homogeneous nucleation and no spatially and temporally constant growth rate) requires substantial mathematical efforts [Rios 2009a, Rios 2009b]. The JMAK approach is restricted to the description of recrystallization kinetics, while microstructure and texture predictions require more substantial input. Nevertheless, the estimation of a recrystallized grain size is possible with this approach.

With respect to industrial application, heating rates are of interest. The consideration of heating rates was incorporated into the JMAK equations by several authors [Ruitenbergh 2001, Woldt 1992, Henderson 1978, Vázquez 2000]. Ruitenbergh has related the JMAK parameters under isothermal conditions to those in case of linear heating rate conditions. For constant linear heating rate the JMAK equation can be written as

$$X(t) = 1 - e^{-\left(\frac{t}{t'_R}\right)^{2q}} \quad (2.19)$$

with

$$t'^{2-q}_R = t'_{R,0} \cdot \beta^n \cdot \exp\left(\frac{\Delta H}{kT}\right) \quad (2.20)$$

Where β is the heating rate, $T = \beta t$, q is the Avrami exponent, and ΔH the activation energy for the recrystallization process. It was found that the Avrami exponent differs by a factor of two from the Avrami exponent under isothermal condition.

2.4.2 Geometric microstructure models

Since phenomenological models such as the JMAK approach, describing solely the recrystallization kinetics, are limited to homogeneous nucleation and growth processes, models based on geometrical considerations were developed to describe real microstructures. The first approach in this field was the geometrical and topological model of Malin, Hanson and Morris in 1976 [Malin 1976] and Frost, Whang and Thompson [Frost 1986] which is mainly based on incorporating the elementary geometry of nucleation, growth and impingement. To generate microstructures the space is discretized and a system of equations for any point in space is solved to obtain 2D microstructures. This method allowed studying different effects of various nucleation and growth theories on the microstructure and texture evolution. These models consist basically of three steps: nucleation, nucleus growth to impingement and sometimes subsequent grain coarsening. During nucleation, the nuclei are either distributed initially (site saturated) or constantly added according to a nucleation rate. In the model of Frost [Frost 1987] neighboring grains nucleate at the same time, expand with the same constant growth rate in radius. As a result the intermediate interface is a straight line. If further three neighboring grains grow under these conditions a triple junction is created. This model was applied for thin films. Deficiencies in these models refer to the prediction of grain size distribution for which the consideration of grain boundary surface tensions is inevitable. Latter enhancements are for instance the Trondheim Avrami Machine [Marthinsen 1989] or the RISØ-component model [Jensen 1992] which consider the grain boundary surface tensions. In these models conventional analytical growth expressions are further extended with respect to more spatially resolved data on texture components, nucleation rates and growth rates.

2.4.3 Vertex models

For the modeling of materials which display a cellular microstructure, the use of vertex models is recommendable. *Network* or *Vertex* models were originally developed for the description of grain growth phenomena [Bragg 1947]. Grain growth is driven by the curvature of the boundaries, and this curvature is due to the establishment of force equilibrium at the grain boundary junctions, the vertices. Since vertex models solely consider interfaces, the behavior of a connected boundary system can be best modeled by such approaches. Vertex models allow a better treatment of boundary properties than for instance Monte Carlo models. Vertex models are basically working as follows: the microstructure is constructed as a network of nodes between grains of different orientation. The interface energies apply forces to the nodes and hence lead to boundary migration. The kinetics is determined by the grain boundary mobility and the grain boundary surface tension. During the simulation the orientation information is used to calculate the driving forces and mobilities. Vertex models can in principle be applied to the modeling of recrystallization phenomena. The basic requirement is the possibility to describe the deformed microstructure in terms of a cellular or subgrain structure. During the simulation of recrystallization this subgrain structure in the deformed state is represented by a network, in case a pronounced cell structure is developed for the considered material. Hence, the applicability of the model is restricted to alloys with a pronounced subgrain structure after deformation. But also for such cellular structures it is questionable if the consideration of ideal low angle grain boundaries corresponds to the real microstructure. Already small deviations of the ideal structures of a low angle grain boundary have large effects on the grain boundary energies and mobilities. Humphreys [Humphreys 1992] considered a variety of 2D microstructures with regard to stability and found arrangements that would produce discontinuous subgrain growth which could also be interpreted as a nucleation event.

2.4.4 Discrete models

The heterogeneity of microstructure requires the consideration of a local and temporal variation of the physical processes of recrystallization. This can be provided by models which discretize the microstructure in space and time on a sufficiently small scale. Those models require high computational power and large storage capacity, which are nowadays available.

Two main approaches have been developed in recent years for the spatial and temporal modeling of recrystallization phenomena, the first being thermodynamic approaches such as Monte Carlo (MC) models and the second being kinetic approaches, such as cellular automata (CA). The common feature of both model types is the transition rule determining the irreversible switching of previously deformed or recovered volume entities into a recrystallized state.

In *Monte-Carlo-Potts Models* [Pott 1952, Srolovitz et al.1986, Rollet et a. 1989] the material is divided into a number of discrete points which represent the center of small areas or volumes (such as grains). Each of these areas is associated with some parameters, e.g. the crystallographic orientation. This information is then stored by a number and attributed to the respective grain. A grain might be composed of several sub-volumes containing exactly the same information. The model is run by selecting blocks at random (such as the roulette in Monte-Carlo). If e.g. two adjacent blocks are picked at random, they are compared with respect to their energy as for instance stored in a deformed grain in terms of dislocation density. In case of a recrystallization simulation it might therefore lead to a change of the grain orientation, in case a deformed area is transformed into a recrystallized area. The probability of the transition depends on the costs of the energy change (ΔE), if

$$\Delta E \begin{cases} \leq 0 & \text{transition accepted} \\ > 0 & \text{transition accepted, with probability distribution } e^{\left(\frac{-\Delta E}{kT}\right)} \end{cases} \quad (2.21)$$

Monte-Carlo models are in general preferred due to their simplicity. They are most powerful for simulation of grain growth. However a weakness of these types of models is the inherent scaling of time, which is based on Monte Carlo steps, where one Monte Carlo step represents the successive or simultaneous attention handling once for each block with respect to the transition to be undertaken. As for most of the recrystallization models, data on nucleation needs to be provided from outside. That means certain blocks are defined as nuclei prior to the simulation. However, a quantity that MC is incapable of considering is the effect of boundary plane [Bate 2001].

Cellular automata (CA) are closely related to the MC method, but they enable the consideration of more complex aspects of recrystallization in a more efficient and flexible way. They are also discrete in space and time like MC models, except that the transformation rule is different. Instead of being based on a probable change of state as depending on the energy effort required for the change, the transformation in cellular automata is deterministic, just defined by the states of the neighboring cells. The change of cell status can be reversible, but in case of recrystallization the transformation rule is one-directional while describing an irreversible process in a thermodynamical sense. Details on this approach are introduced in more detail in Chap. 3. Both types of models, cellular automata (CA) as well as Monte Carlo (MC) models are pure growth models, which require input from separate nucleation models. In this context, in particular nucleation criteria based on location or physical conditions are favorable. Compared to the MC models, the main advantage of cellular automata is the spatial resolution and their real-time scaling.

2.4.5 Recrystallization texture models

For a pure consideration of texture evolution special texture models are available. They are fast and require low computational power, since there is no need for a detailed microstructure description. In more recent models the evolution of all recrystallization texture components is considered and determined by their nucleation and growth probability. These texture models use approaches for the formulation of nucleation and growth probabilities from literature, such as proposed by Vatne [Vatne 1996a] and Engler [Engler 1997b, Engler 1999] e.g. for aluminum alloys.

The models, e.g. for aluminum assume that the recrystallization texture evolution can be explained by a growth selection of grains with an approximate 40° $\langle 111 \rangle$ orientation relationship out of a limited spectrum of preferentially formed nucleus orientations. The recrystallization textures can be modeled according to

$$f(g)^{\text{sim}} = f(g)^{\text{nuc}} \cdot f(g)^{\text{grow}} \quad (2.22)$$

where $f(g)^{\text{nuc}}$ is a function representing the nucleation probability of new grains with their growth probability function $f(g)^{\text{grow}}$. Information on individual nucleation mechanisms can be gained e.g. from EBSD-data, which is a very time-consuming procedure. The consideration of various nucleation mechanisms and their respective contribution to the overall nucleation distribution function $f(g)^{\text{nuc}}$ can be considered by weighting the contributions of the different nucleation sites

$$f(g)^{\text{nuc}} = x_{\text{Cube}} \cdot f(g)_{\text{Cube}}^{\text{nuc}} + x_{\text{GB}} \cdot f(g)_{\text{GB}}^{\text{nuc}} + x_{\text{PSN}} \cdot f(g)_{\text{PSN}}^{\text{nuc}} \quad (2.23)$$

The weight factors x_i denote the efficiency of nucleation at the corresponding site (Cube = at Cube bands, GB = at grain boundaries, PSN = at particles).

A more flexible treatment was introduced by Sebald [Sebald, 2002a, Sebald 2002b]. He suggested a space integrated but temporally resolved approach. Nuclei are set at random and assumed to grow according to the Avrami hypothesis. In contrast to other statistical models the growth approach also considers the temporal evolution of the growth surrounding of the nuclei. Different nuclei are initially competing for the same deformed orientation which is also referred to as competitive growth (Fig. 2.5a). After reaching a nucleus size comparable to the smallest grain dimension the nucleus starts to grow simultaneously into several deformed grains. This is called compromise growth (Fig. 2.5b).

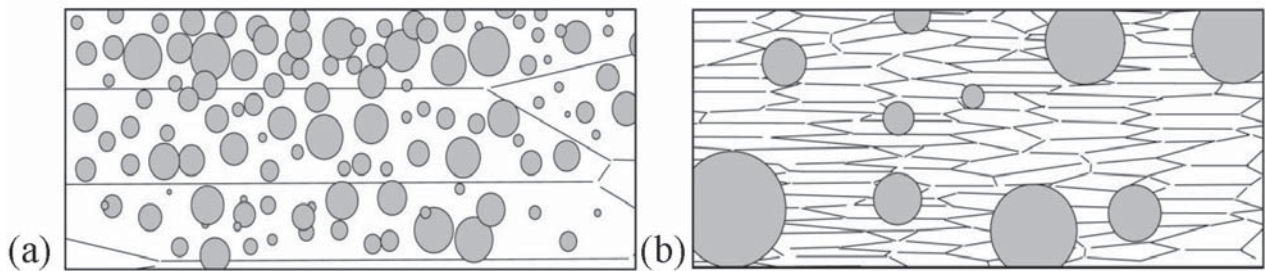


Fig. 2.5: (a) Microstructure during competitive growth, every nucleus (shaded) grows into one deformed grain (white); (b) microstructure during compromise growth. Every nucleus (shaded) grows simultaneously into several deformed grains (white) [Sebald 2002].

Chapter 3

Simulation of Recrystallization using cellular automata

3.1. Introduction

The scope of this work is the prediction of microstructure and texture evolution in fcc metals during industrial annealing treatments. During the thermal processing of aluminum alloys in general material softening is observed, which is due to the physical mechanisms of recovery and recrystallization. Further, also changes in microchemistry are observed, particularly in *commercial* alloys. They are caused by the precipitation, coarsening or dissolution of second-phases. The modeling of these meso-scale phenomena can be accomplished by the use of time and space resolved models, such as cellular automata, vertex or network models, and space discretized dislocation dynamics. As mentioned earlier the vertex or network models are restricted to the application to cellular substructures. Since cellular automata are not restricted to cellular structures only, they are favored for the present work. The popularity of cellular automata originates in their simplicity and the high potential in modeling complex systems. Cellular automata (CA) are not intrinsically calibrated, which allows their use over a wide range of scales: starting from diffusion simulations at the atomic level to the description of bushfires on the macroscale. Their definition as a meso-scale simulation method is therefore a little arbitrary. However, in the current work they are used as such. CA are simple models of a spatially extended decentralized system build up of a number of components (cells). The communication between the cells is in case of recrystallization limited to local interaction. It is assumed that recrystallization is influencing just the local surrounding which is swept by the migrating high angle grain boundary. Each cell has a specific state which changes over time depending on the predefined rules. CA allow the time and spatial resolved description of the recrystallization phenomenon. This includes further the consideration of local microstructure inhomogeneities, which makes this tool preferred for modeling of strongly heterogeneous phenomena such as recrystallization. The first who applied cellular automata to the phenomenon of recrystallization were Hesselbarth and Göbel in 1991 [Hesselbarth 1991].

3.2 Fundamentals

Cellular automata are discrete in time and space. In the present case, space represents the real space. They are built up either of a fixed number of points which span a regular lattice or of smallest units, the so-called cells (Fig. 3.1a). A cellular automaton evolves in discrete time steps.

The local interaction of neighboring sites is specified through a set of deterministic or stochastic transformation rules. The value of an arbitrary state variable ξ assigned to a particular site at a time $(t_0 + \Delta t)$ is determined by its present state (t_0) (or its last few states $t_0, t_0 - \Delta t$, etc.) and the state of its neighbors.

$$\xi_j^{t_0 + \Delta t} = f(\xi_{j-1}^{t_0 - \Delta t}, \xi_j^{t_0 - \Delta t}, \xi_{j+1}^{t_0 - \Delta t}, \xi_{j-1}^{t_0}, \xi_j^{t_0}, \xi_{j+1}^{t_0}) \quad (3.1)$$

where $\xi_j^{t_0}$ is the value of the variable at a time t_0 at the node j . The indexes $j+1$ and $j-1$ represent the position of the next neighbors in a one-dimensional simulation. The function f describes the set of transformation rules.

The description of the local neighborhood affects the local transformation rates. In the following a Moore neighborhood [Chopard 2005, Wolfram 2001] is considered in 3D. If the underlying material properties are isotropic, the use of a special cell shape (e.g. cubic) requires the scaling of the transformation rates which is 1 in the $\langle 100 \rangle$ directions, $1/\sqrt{2}$ for the $\langle 110 \rangle$ direction and $1/\sqrt{3}$ for the $\langle 111 \rangle$ direction. The developing morphology is strongly dependent on the definition of the neighborhood. Eq. (3.1) can thus be rewritten for a Moore neighborhood. For sake of simplicity a Moore neighborhood in 2D was assumed:

$$\xi_j^{t_0 + \Delta t} = f(\xi_{j-2}^{t_0 - \Delta t}, \xi_{j-1}^{t_0 - \Delta t}, \xi_j^{t_0 - \Delta t}, \xi_{j+1}^{t_0 - \Delta t}, \xi_{j+2}^{t_0 - \Delta t}, \xi_{j-2}^{t_0}, \xi_{j-1}^{t_0}, \xi_j^{t_0}, \xi_{j+1}^{t_0}, \xi_{j+2}^{t_0}) \quad (3.2)$$

Another way to define the neighborhood is according to von Neumann [Chopard 2005, Wolfram 2001]. Compared to the Moore neighborhood only the neighbors in $\langle 100 \rangle$ direction are considered. If we assume in case of a von Neumann neighborhood a very simple transformation rule, so that two states are possible $\xi_j = 0$ or $\xi_j = 1$, we can already define 2^8 possible deterministic or probabilistic transformation rules f . In case of a one-dimensional automaton, one cell has only two neighbors. The new function value then only depends on the current cell state of these two neighbors:

$$\xi_j^{t_0 + \Delta t} = f(\xi_{j-1}^{t_0}, \xi_j^{t_0}, \xi_{j+1}^{t_0}) \quad (3.3)$$

One out of the mainly possible rules is given in Tab. 3.1. This rule is encoded by 10001010_2 . Transforming the binary code into decimal numbers leads to the decimal code number 138_{10} . This digital coding system is used for compactly describing common transformation rules. The rule used in the present work for recrystallization will be specified later on. By the way, these cellular automata provide the basic concept on which each computer operates and some of them - chaotic cellular automata- show even artificial life.

Tab. 3.1: Example of a cellular automaton rule for the consideration of a von Neumann neighborhood.

$\xi_{j-1}^{t_0}$	$\xi_j^{t_0}$	$\xi_{j+1}^{t_0}$	$\xi_j^{t_0+\Delta t} = f(\xi_{j-1}^{t_0}, \xi_j^{t_0}, \xi_{j+1}^{t_0})$
1	1	1	1
1	1	0	0
1	0	1	0
1	0	0	0
0	1	1	1
0	1	0	0
0	0	1	1
0	0	0	0

3.3 Theory of the Cellular Operator for Recrystallization CORE

3.3.1 History of CORE

As mentioned above, the first approach to model recrystallization by a CA approach was made by Hesselbarth and Göbel [Hesselbarth 1991]. They discretized space and time into small volume elements and time increments. The recrystallization step comprised a whole number step during any considered increment of time. The cells could only assume two different states – either deformed or fully recrystallized. This model produced a behavior resembling to the process of recrystallization, but hardly contained any physics that could affect microstructure; and texture prediction was completely impossible. In order to integrate a physical base to a CA, the cellular operator approach of recrystallization (CORE) was founded at the Institute of Physical Metallurgy and Metal Physics (IMM), Aachen. The aim of the CORE model [Mukhopadhyay 2007] is the physical based modeling of recrystallization. Hereby, the transformation rule of a cell depends not on preset rules, but is rather a functional of local conditions. The CORE model underwent a long development during recent years. It was first introduced by Reher [Reher 1998]. Reher et al. refined the approach of Hesselbarth and Göbel by introducing the so-called modified cellular automata. In this approach the transformation rule was modified to take local and temporal variations of velocity into account, as based on driving force and boundary mobility, to accommodate local variations of microstructure evolution. This allows the consideration of other than just homogeneous systems. A dependence on microchemistry was in principle possible but not yet introduced. A problem in these predictions was basically the rough grain morphologies developed as based on the minimum displacement approach. In this approach, the lowest velocity in one time step is represented by the sweeping of one whole cell. Correspondingly the representation of highest velocities could easily comprise the sweeping of several cells at once in the considered direction, which inevitably leads to the observed rough grain morphologies. An approach to solve this problem was the use of a probabilistic CA as suggested by Raabe [Raabe 1999, Raabe 2000]. However, this introduces a probabilistic aspect in the deterministic approach of cellular automata and leads to the loss of the real-time scaling.

Marx et al. [Marx 1995a, 1995b, 1996, 1999] developed the CA further for application to the recrystallization phenomena. They replaced the existing model by an improved modified cellular automaton. The new model considered more distant neighbors than just the immediate neighborhood, because experience showed that the shape of the growing grains reflected the geometry of the spatial grid in case of just nearest and second-nearest neighbors. For modeling recrystallization already the influences of deformation, texture and precipitation, in terms of a Zener drag as a scalar variable, were introduced.

The problem of rough grain morphologies was finally solved by introducing a partial recrystallized volume fraction within the cells in the work of Mukhopadhyay [Mukhopadhyay 2007]. Each cell has the possibility to store the recrystallized volume fraction in terms of an unsigned integer variable and hence allow 65535 ($2^{16}-1$) possible recrystallized states. In one time step maximum one cell can recrystallize as defined by the maximum velocity, lower velocities are hence leading to a partial recrystallized volume fraction within one cell. Besides the accuracy of misorientation representation was refined, thus currently 262143 ($2^{18}-1$) different orientations can be considered, which corresponds to an angular spacing of 1.4° . Mukhopadhyay et al. [Mukhopadhyay 2007] created the CORE model in its first appearance in 2005 [Mukhopadhyay 2005]. Within this work a real-time scaling for the cellular automata was introduced which enabled a first comparison to real experiments. Furthermore, Loeck introduced 2007 a collision free hashing algorithm to rapidly process the large number of data required and reduce the computational efforts. Mukhopadhyay further improved the model and a first approach to interface the model with other microstructure models like a deformation texture model and a precipitation model was intended. Up to now, a basic validation of the model was demonstrated [Mukhopadhyay 2005, 2007]. Since CORE is a pure growth model, nucleation relevant data need to be provided separately by a nucleation model as outlined in the following.

3.3.2 A nucleation model for CORE

The CORE model is a pure growth model, so that nucleation is either dealt with as a boundary condition or is imported from other models. With respect to nucleation nowadays the ReNuc model [Crumbach 2005, 2006a] is used. A predecessor of the ReNuc model was developed by Marx. Marx considered physical nucleation mechanisms at first by empirical equations. For this purpose empirical nucleation models were used to describe the nucleus number resulting from the different nucleation mechanisms. The nucleus texture was obtained by weighting the different nucleation events with their corresponding texture components. Nucleation at Cube grains, grain boundaries and particles or random nucleation was considered. The total number of nuclei was hence calculated according to

$$N_{\text{tot}} = N_{\text{PSN,rand}} + N_{\text{GB}} + N_{\text{TB,CB}} \quad (3.4)$$

With being $N_{\text{rand,PSN}}$, N_{GB} , $N_{\text{TB,CB}}$ the numbers for random nucleation (nucleation at particles or shear bands), GB (grain boundary)-nuclei and TB (transition band)-or Cube nuclei. To obtain the orientation distribution function the different contributions were weighted and super-positioned.

$$f_{\text{nuc}}(\mathbf{g}) = F_{\text{Rand,PSN}} \cdot f_{\text{RND,PSN}}(\mathbf{g}) + F_{\text{GB}} \cdot f_{\text{GB}}(\mathbf{g}) + F_{\text{TB,CB}} \cdot f_{\text{CB,TB}}(\mathbf{g}) \quad (3.5)$$

$$\text{Where } F_i = \frac{n_i \cdot f_i}{\sum_{k=1}^3 n_k \cdot f_k} \quad (3.6)$$

And n_i being the number of deformed grains contributing to the respective nucleation mechanism. The model variables f_i were introduced by Crumbach to suppress or promote the respective nucleation mechanism. Crumbach further refined the model by replacing the empirical approaches for the nucleation mechanisms (transition bands, grain boundaries and shear band nucleation) by criteria that link the prior deformation microstructure to the later recrystallization texture. He

introduced the GIA-Split Up model [Crumbach 2005] to describe the split up behavior of grains. During deformation the deformed grains either remained stable or became unstable providing large orientation gradients (split up). This information was very valuable with respect to the prediction of nucleus textures. However because of the lack of a physical misorientation gradient, only the average values have been considered so far. With respect to grain boundary nucleation the number of activated slip systems was used as an indicator. He further introduced an orientation-dependence of the individual grains with respect to the average number of slip systems per grain.

To integrate nucleation in CORE, the nucleus texture predictions from ReNuc [Crumbach 2005, 2006a] were implemented. With ReNuc the nucleus efficiencies (for grain boundaries, transition and shear bands) can be provided locally resolved with respect to each single orientation. Mukhopadhyay [Mukhopadhyay 2005] further replaced the so far unknown nucleus number N_{tot} by a calculation of absolute quantities based on an approach developed by Derby and Ashby 1989 for dynamic recrystallization. This idea was transferred to all types of nucleation mechanisms considered at that time (nucleation at grain boundaries, transitions bands, and shear bands). Particle-stimulated nucleation was treated in a statistical sense further assuming that only random orientations are developed.

3.3.3 Modifications of the CORE model

These prior developments brought the CORE model to the *status quo* when the present work started. Since the CORE model requires quite a lot of inputs an overview of the model itself including its inputs is presented in the following chapter (Sec. 3.4). As output, the CORE model provides the possibility to compute recrystallization kinetics, grain size and texture (Sec. 3.5). The main developments of the Core model include the incremental coupling to the work-hardening / softening model 3IVM+ in order to describe softening processes due to recovery (Sec. 3.6), the successive coupling to ClaNG (Sec. 3.7), the introduction of temperature profiles for recrystallization (Sec. 3.8, Chap. 8) and a modification of the growth as influenced by Zener drag (Chap. 7). Modifications of the compound of nucleation sub-models (ReNuc) are described at the end of Sec. 3.9. Further a new nucleation model for particle-stimulated nucleation was proposed based on a newly developed model for the description of deformation inhomogeneities within a deformation zone (GIA-DZ, Chap. 5). The main task of the current work with respect to simulations with the CORE model was an extended validation and application to real experiments. An attempt was undertaken to consider particularly also those effects which significantly influence the recrystallization behavior. These are in commercial alloys beside recovery, effects caused by the presence, precipitation, dissolving or evolving of particles. For example, the amount of special alloying elements such as manganese or iron in solid solution, were shown to have an extremely strong influence upon the recrystallization behavior. According to papers e.g. by Masing et al. [Masing 1956] and Lücke and Detert [Detert 1956, Lücke 1957], additions of the order of 0.01% of manganese or iron can decrease the rate of recrystallization of high-purity aluminum by factors of 10^{12} or 10^{16} .

3.3.4 Theory of CORE

The recrystallization model CORE (Cellular Operator for Recrystallization) is a three-dimensional cellular automaton as introduced in Sec. 3.2. In the present case the space is subdivided in cubic cells (Fig. 3.1a). The model considers an initial microstructure consisting of block-shaped grains as provided by an advanced cluster-type deformation model (Grain-Interaction model GIA). For consideration of boundary effects in the model periodic boundary conditions were assumed.

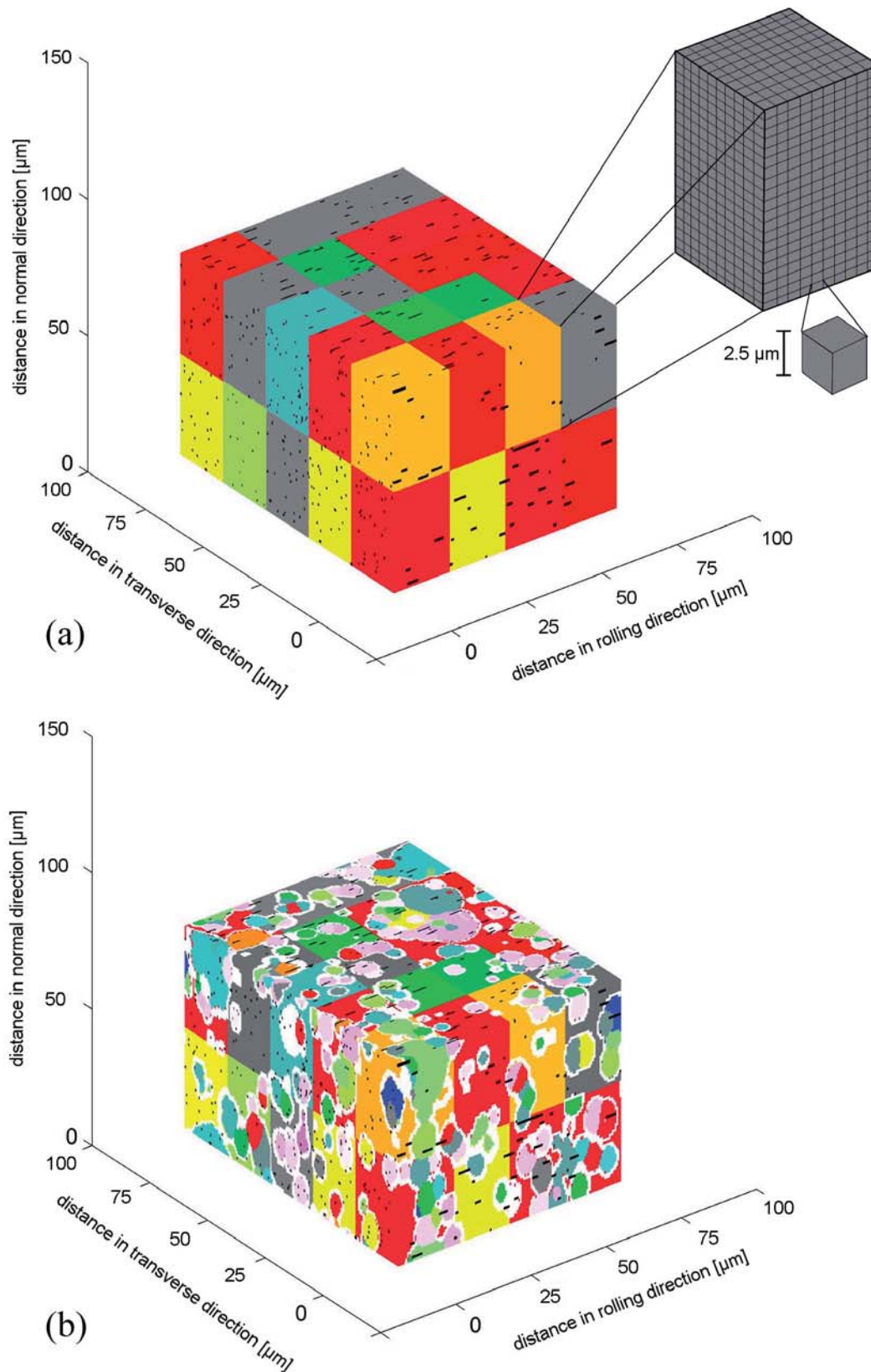


Fig. 3.1: COrE simulation of a volume element, showing (a) cubic grains of uniform size (original deformed grains) and (b) new grains consuming the deformed microstructure. In (a) the unit cell is indicated. The white area in (b) represents the recrystallization front consisting of cells with a recrystallized volume fraction between 0% and 100%. These are actually the calculating cells in process. The colors of the individual grains refer to the crystallographic orientations (red = Copper, green = S/R, yellow = Brass, blue = Cube, grey = remaining other orientations).

The transformation rule as introduced in Sec. 3.2 is defined by a physical description of the recrystallization growth. The state of the cells is introduced as float variable, so that a high number of possible states are allowed (previously defined as sub-grid). A cell contains thus a quasi-continuous developing recrystallized fraction, instead of a purely deformed “0” or recrystallized state “1”. In the course of recrystallization, each cell will be infected sooner or later by a fully recrystallized cell. As soon as a cell is contacted by an already recrystallized cell, it is infected, i.e. recrystallization is initiated in the respective grain. The overshoot of the before mentioned recrystallized cell is transferred to the newly infected one. As neighborhood, it was assumed that each cell is surrounded by 26 neighboring cells. To reduce the computational effort in general only those cells on the surface of a new grain are considered in the calculation. Already recrystallized cells will at first infect their neighborhood and will then immediately retire, i.e. will be erased from the memory.

The growth velocity is calculated according to Pythagoras $v = \sqrt{v_x^2 + v_y^2 + v_z^2}$ whereas v_x is the velocity in x-direction, v_y the velocity in y direction and v_z the corresponding velocity in z-direction. The consideration of this velocity calculation leads to an isotropic growth of the new grains. In the present work 18 nearest neighbors were considered (neighbors in $\langle 100 \rangle$ and $\langle 110 \rangle$ directions). In this case, the growth velocity in different spatial directions needs to be normalized by the corresponding factors in $\langle 100 \rangle$ by α and in $\langle 110 \rangle$ by β ($\beta = 0.1$, $\alpha = \sqrt{1 - 8\beta^2} - 4\beta$, where α the factor in $\langle 100 \rangle$ and β in $\langle 110 \rangle$ direction [Mohles 2007b]) to guarantee isotropic growth. But it was recently shown that the consideration of the next nearest neighbors ($x_-, x_+, y_-, y_+, z_-, z_+$) is sufficient for isotropic growth. Due to the three-dimensional growth sometimes very twisted grain shapes can result. The velocity with which recrystallization proceeds is defined by the equations outlined in the following. The recrystallization process is an irreversible process comprising the recrystallization nucleation and the subsequent growth of those nuclei. The velocity of the growth process can be derived from diffusion jumps over a grain boundary. The basics of grain boundary migration were introduced in more detail in Chap. 2. The grain boundary velocity v can be written in a simplified fashion as:

$$v = m \cdot p \quad (3.7)$$

where m is the boundary mobility and p the driving force. The driving force is determined by the stored dislocation density within the deformed grains. In the present model the stored energy is orientation-dependent and averaged within the respective grain volume. The driving force for primary recrystallization is given by

$$p(\rho) = \frac{1}{2} G b^2 \rho(t, g_i) \quad (3.8)$$

where p is the driving force, G the shear modulus, b the Burgers vector and ρ the dislocation density. The driving force is further reduced by softening mechanisms such as recovery, which is reducing the dislocation density by annihilation and rearrangement of dislocations. Recovery was implemented in the present work by incrementally coupling of CORE to a model describing recovery (the improved work-hardening model 3IVM+ [Gurla 2007, Mohles 2008], Sec. 3.6). According to this coupling recovery takes place dependent on time t and dependent on the individual orientation g_i of the initial deformed grains.

The mobility of a boundary was considered as indicated by Fig. 3.2. The migration rate of the boundaries was classified into different regimes, i.e. low angle boundaries, high angle boundaries and special boundaries to account for the preference of the $40^\circ \langle 111 \rangle$ relationship with enhanced mobility [Beck 1950, Kohara 1958, Parthasarathi 1961, Liebmann 1956, Yoshida 1959, Ibe 1966]. The values for the mobility m are based on literature data [Gottstein 1999, Molodov 1999, Winning

2007] for the preexponential factor m_0 and the activation enthalpies H_m . The mobility can be described as follows:

$$m = m_0 \exp\left(-\frac{H_m}{kT}\right) \quad (3.9)$$

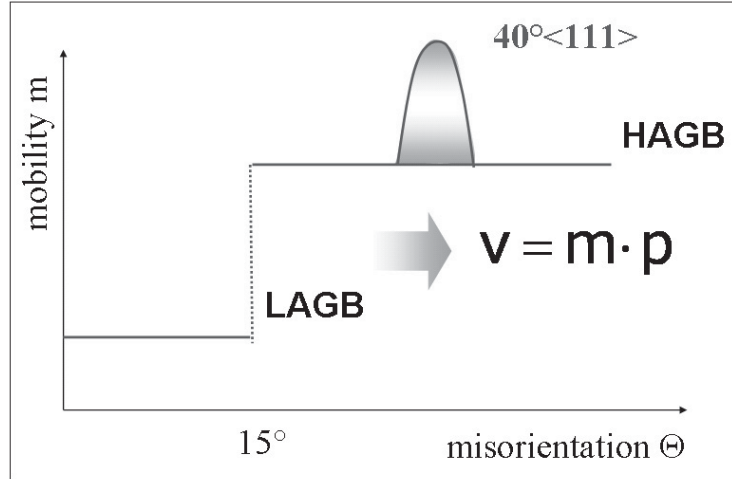


Fig. 3.2: Mobility Function defining the growth within the CORE mode, (LAGB = low angle grain boundary, HAGB = high angle grain boundary; $40^\circ\langle 111 \rangle$ = misorientation relationship which denotes the fastest boundaries, also referred to as growth selection GS).

Back-driving forces are active if the material contains elements in solid solution (Impurity drag – Lücke and Detert 1957, Lücke and Stüwe 1962) or as dispersoids (Zener drag- Zener 1949, Cotterill 1962, Haessner 1978, Gottstein 1984, Nes 1985, Humphreys 2004). This is the case in most commercial aluminum alloys. In the presence of a fine dispersion of second-phase particles the driving force can be affected by Zener drag as follows:

$$v = m \cdot (p - p_Z) \quad (3.10)$$

where p is the driving force, p_Z the Zener drag and m the boundary mobility, which is assumed to be independent of v in the present approach. In Chap. 7 a dependency of the velocity is introduced. The Zener drag p_Z was assumed to be exerted by spherical particles statistically distributed throughout the microstructure. The dragging force is then given by:

$$p_Z = \frac{3}{2} \cdot \gamma \cdot \frac{f_p}{r_p} \quad (3.11)$$

where, γ is the grain boundary energy, f_p is the volume fraction of dispersoids, and r_p the average dispersoid radius. Since the boundary mobility m is a function of temperature, misorientation and affected by segregation, it varies according to the following equation [Gottstein 1999]:

$$m = \frac{m_{HAGB}}{1 + c_s \cdot \beta \cdot z \cdot \frac{D_{self}}{D_{im}}} \quad (3.12)$$

where m_{HAGB} is the mobility in the absence of solute drag, D_{self} and D_{im} are the self and impurity diffusion coefficients, respectively, c_s is the solute concentration (Mn, respectively Fe in the current work), z is the number of adsorption sites in the boundary, and β is the grain boundary enrichment [Gottstein 1999].

A major improvement was the direct coupling with the precipitation model ClaNG, which allowed the consequent tracking of microchemistry changes during the recrystallization process (Sec. 3.7). The influence of precipitation on nucleation was considered in a first approach as well (Sec. 3.9, Chap. 8). Up to now the model was scaled according to the maximum mobility and the smallest cell size according to

$$\Delta t_{Rx} = \frac{d_{cell}}{v_{max}} = \frac{d_{cell}}{m_{max} \cdot p_{max}} \quad (3.13)$$

Where d_{cell} is the cell size and v_{max} the maximum grain boundary velocity, which is determined by the mobility m and the driving force p . The maximum mobility depends further on the solute type and solute content in the alloy [Mukhopadhyay 2005].

3.4 Model Input

The CORE model as improved in the present work is on one hand capable of describing very complex recrystallization behavior, but requires on the other hand a vast of input parameters to model such complex situation. Fig. 3.3 shows the flow chart for the modeling of recrystallization using CORE.

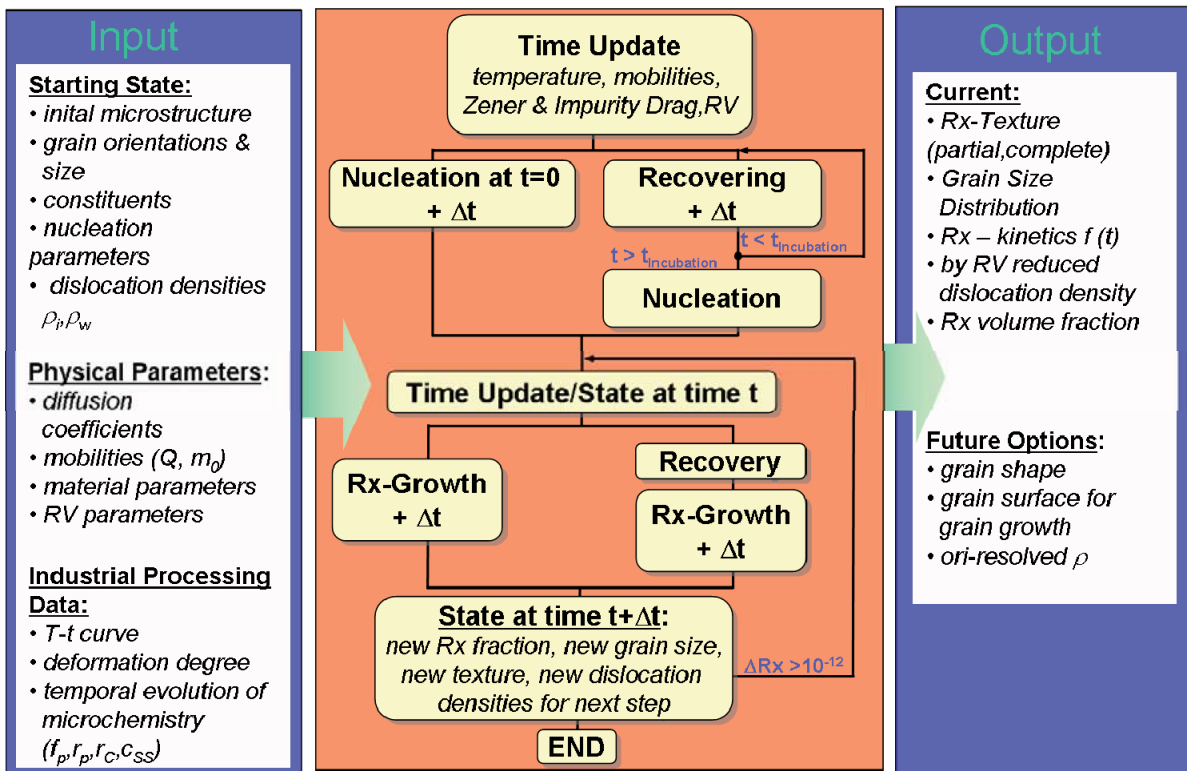


Fig. 3.3: Modeling scheme of CORE with required inputs and outputs in case site saturation is considered. (Rx = recrystallization, RV = recovery, ρ = dislocation density).

At the beginning the program is initialized. The input required for this can be sub-divided in several groups: material parameters (Tab. 3.2), parameters describing the initial discretization of the microstructure (Tab. 3.3), parameters describing the process history (Tab. 3.4), more specific parameters describing the growth (Tab. 3.3) and parameters describing nucleation for the considered alloy (Tab. 3.5). To make the model applicable for different scenarios, e.g. with or without recovery, so-called switches were introduced in the model. These switches are controlled by the parameter set given in Tab. 3.7.

Hence, different mechanisms can be activated during recrystallization, ranging from recovery to microchemistry related effects, if necessary. The required material parameters (Tab. 3.2) are partly available from literature, but are derived otherwise from additional models (recovery model 3IVM+, precipitation model ClaNG). The recrystallization model CORE was coupled in the present work with the work-hardening / softening model 3IVM+ (Sec. 3.6). The consideration of recovery requires the prior fitting of experimental flow curves with 3IVM+ for the same material. The obtained fitted parameter set is then utilized in CORE. In case microchemistry changes are observed during annealing, ClaNG simulations are carried out to describe the temporal and orientation-dependent evolution of solute content c , dispersoid radius r_p and volume fraction f_p . Nevertheless, it is possible to use also experimental data instead.

The major inputs for CORE, such as the dislocation density, are obtained from a deformation simulation with the Grain Interaction model GIA [Crumbach 2005]. Other input data for CORE as obtained from GIA is the number of slip systems activated during deformation and the average deformed grain size in rolling, transverse and normal direction.

Tab. 3.2: Material parameters in the recrystallization model CORE (EXP = from experiments, FEM = from finite element method).

Parameter	Source	Description
b		Burgers vector
G		Shear modulus
3IVM+ parms	3IVM+	3IVM+ physical parameters in case of CORE-3IVM+ coupling for calculation of dislocation densities ρ
c_a, c_b	ClaNG/EXP	Solute concentration of two elements (e.g. Fe, Mn) (coupling CORE-ClaNG : Solute Drag)
r_p, V_p	ClaNG/EXP	Mean radius of precipitates and volume fraction (coupling CORE-ClaNG : Zener Drag)
Starting texture	GIA-3IVM+/EXP	List of N grains representing ODF of input material
Initial ρ	GIA-3IVM+	averaged dislocation densities in the cell walls ρ and cell interior ρ resolved for each grain N
V_c	EXP	Volume fraction of constituents
$d_{DZ, RD}, d_{DZ, TD}, d_{DZ, ND}$	EXP/FEM/CPFEM	Size of the deformation zone in RD, TD, ND surrounding constituent particles after deformation
PSN nucleus tex.	EXP/GIA-DZ	Nucleus spectrum for particle-stimulated nucleation from experiment or resolved on grain scale from GIA-DZ
f_{DZ}	EXP/FEM	Factor of increase in dislocation density in the particle vicinity due to strain localization

For the description of nucleation in CORE the ReNuc model [Crumbach 2005], a collection of sub-models was used. To describe e.g. local inhomogeneities in case of transition bands the GIA-Split-Up model was used [Crumbach 2004, Crumbach 2005, and Crumbach 2006a]. It

describes the split up tendency of individual grains during deformation. The ReNuc model was extended for the consideration of particle-stimulated nucleation as detailed in Chap. 5.

The nucleation-relevant parameters are summarized in Tab. 3.6. Nucleation can be assumed either site-saturated (Fig. 3.3) or with a nucleation rate as detailed in Chap. 6. In case of site-saturation, recovery takes place when the incubation time for recrystallization is exceeded. Nucleation is then initiated and the actual recrystallization process starts. The concurrent modeling of recovery and recrystallization was realized in each time step by updating first recovery in all deformed grains, and then the individual recrystallized volume fractions in the calculating cells. Previously, also the microchemistry state and temperature are updated.

Tab. 3.3: Parameters describing the initial microstructure discretization in CORE.

Parameter	Source	Description
d_{RD}, d_{TD}, d_{ND}	GIA-3IVM+/EXP	Average grain size in three sample directions
number of initial microstructure grains	GIA-3IVM+/EXP	Number of initial microstructure grains (e.g. 4000)
number of CA cells		Number of cells in the cellular automaton (defines the resolution, in general 1-100 million cells)

The growth during recrystallization is determined by the influences of microchemistry and recovery, but all these processes are temperature-dependent (Tab. 3.4). The dependency of the mobility on temperature and misorientation was introduced in Sec. 3.3, Fig. 3.2. The corresponding parameters that define the mobility can be found in Tab. 3.5.

Tab. 3.4: Parameters describing the process history in CORE.

Parameter	Source	Description
T, t	Process	Temperature and process time for each step

Tab. 3.5: Parameters defining the growth behavior in CORE.

Parameter	Source	Description
GrowSelect_ActEnergy	EXP	Activation energy for growth in case of a $40^\circ\langle 111 \rangle$ growth selection, e.g. 1.0eV
GrowSelect_Mob0	EXP	Preexponential factor for the mobility in case of a $40^\circ\langle 111 \rangle$ growth selection, e.g. $3 \text{ m}^4/\text{Js}$
HAGB_ActEnergy	EXP	Activation energy for the growth in case of a high-angle grain boundary, e.g. 1.05eV
HAGB_Mob0	EXP	Preexponential factor for the mobility in case of a high-angle grain boundary, e.g. $3 \text{ m}^4/\text{Js}$
LAGB_ActEnergy	EXP	Activation energy for growth in case of a low-angle grain boundary, e.g. 1.6eV
LAGB_Mob0	EXP	Preexponential factor for growth in case of a low-angle grain boundary, e.g. $1000 \text{ m}^4/\text{Js}$

The exact meaning of the nucleation relevant parameters is further detailed in Sec. 3.9 ([Crumbach 2005]).

Tab. 3.6: Parameters describing nucleation relevant data in CORE

Parameter	Value	Description
GBNucleation_consider	0/1	“0” means no nuclei at grain boundaries, “1” considers grain boundary nucleation according to ReNuc
GB_Efficiency	0.001-0.01	Efficiency for nucleation at grain boundaries
GB_Scatter	0°-7.5°	Angle for scattering the grain boundary nuclei
TBNucleation_consider	0/1	“0” means no nuclei at transition boundaries, “1” considers transition band nucleation according to ReNuc &-GIA-SplitUp
TB_Efficiency	0.1-0.4	Efficiency for nucleation at transition bands
TB_Scatter	0°-7.5°	Angle for scattering the transition band nuclei
SBNucleation_consider	0/1	“0” means no nuclei at shear bands, “1” considers shear band nucleation according to ReNuc in each grain
SB_Efficiency	0.1-0.5	Efficiency for nucleation at shear bands
PSNucleation_consider	0/2	“0” means no nuclei at particles, “2” considers nuclei at particles

Tab. 3.7: Parameters in CORE to switch between different modi with respect to precipitation.

Parameter	Value	Description
CubeS_Sort	0/1	“1” Sorting of <i>Cube</i> grains close to <i>S</i> oriented grains for enhanced nucleation at <i>Cube</i> bands; “0” no sorting
Recovery_Consider	0/1	“0” means no nucleation is considered, “1” reduction of dislocation density due to recovery and incubation time
ZenerDrag_Consider	0/1/2	“0” means Zener Drag not considered, “1” consider time-independent Zener Drag, “2” a time-dependent Zener Drag is considered
ImpurityDrag_Consider	0/1/2	“0” means Impurity Drag not considered, “1” consider time-independent Impurity Drag, “2” a time-dependent Impurity Drag is considered
Particle_Consider	0/2	“0” no particles are considered, no PSN possible, “2” constituent particles are considered, PSN possible

3.5 Model Output

As output the recrystallization model CORE provides the recrystallization textures, the recrystallized volume fraction and microstructure information. Further, information on the local evolution of dislocation densities, the various nucleus spectra and partial recrystallized states is available.

Tab. 3.8: Most important output parameters of the recrystallization model CORE (ODF = orientation distribution function).

Parameter	Description
d_{av}	Grain Size and Grain Size Distribution
$X(t)$	Recrystallized Volume Fraction and Recrystallization Kinetics
g_i	Recrystallization Texture as single orientation list or ODF

3.6 Coupling CORE-3IVM+

As outlined in the previous chapters the recrystallization behavior significantly depends on the recovery behavior prior and during the recrystallization process. The recovery behavior is determined by the climbing and cross slip of dislocations. Prior to the recrystallization it basically determines the incubation time in high stacking fault materials. During this time the rearrangement of the dislocation structure takes place which activates the recrystallization nuclei for the latter recrystallization growth. During static recrystallization, recovery reduces the driving force for recrystallization, in this case the climbing is more pronounced. Recovery is strongly material dependent via the stacking fault energy. The recovery rate is further influenced by microchemistry effects and the previous deformation.

These effects were up to now not considered in the CORE model but are required due to the impact on recrystallization. Since recently the work-hardening model 3IVM was replaced by the improved 3IVM+ [Gurla 2007, Mohles 2008], which lead to an improved description of the total amounts of dislocation densities, a direct coupling with 3IVM+ was intended. The work-hardening model 3IVM+, respectively the former 3IVM (Fig. 3.4) distinguishes three types of dislocation densities: immobile dislocations in the cell walls and cell interiors, and mobile dislocations. Some of the dislocation interactions are demonstrated in Fig. 3.4.

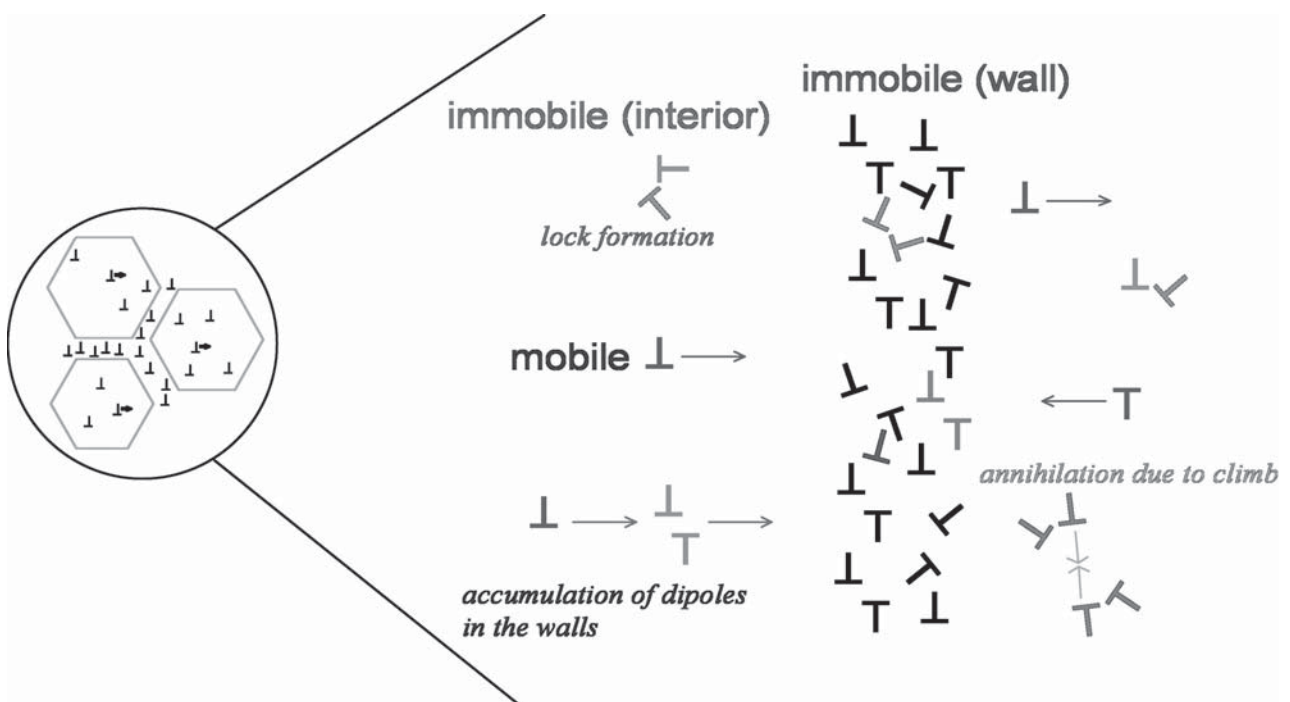


Fig. 3.4: Scheme of the work-hardening model 3IVM/3IVM+. In the model three types of dislocation densities are considered: mobile dislocations and immobile dislocations in cell interiors and cell walls [Goerdeler 2007].

In the following the equations implemented in CORE-3IVM+ are discussed in more detail. During recovery the cell walls sharpen while their interiors become further diminished in dislocations. The dislocations in walls and interior are both immobile dislocations. With respect to static recovery the structural evolution equations from 3IVM+ can be diminished, since all terms containing a strain rate dependency are eliminated in the case of static recovery. The recovery can be physically described by climbing and cross slip of dislocations. The climbing of dislocations to another slip plane, where they can annihilate with dislocations of opposite sign, can be described by the following equation:

$$\dot{\rho}_{i,w}^- = 2 \cdot d_{climb} \cdot v_{climb} \cdot \frac{1}{N} \cdot \rho_{i,w}^2 \quad (3.14)$$

An immobile dislocation in the cell interior or the cell wall can annihilate with other dislocations of opposite sign on other slip systems N , in case of a distance up to a maximum of about $2 d_{climb}$, where d_{climb} is the critical distance for dislocation annihilation by climb. The factor $1/N$ considers the probability for the reaction with a dislocation of opposite sign, which is located on another slip system N .

$$v_{climb} = \frac{D}{kT} \cdot \tau_{i,w} \cdot A \quad (3.15)$$

v_{climb} is the climbing speed of the dislocation which is dependent on the internal stresses $\tau_{i,w}$ created by the dislocation structure after deformation in the cell interior, respectively the cell wall. A is the activation area ($\sim b^2$).

$$D = D_0 \cdot \exp\left(-\frac{Q_{climb}}{kT}\right) \quad (3.16)$$

Climbing of dislocations is a thermally activated process according to Eq. (3.16) where D is the diffusion coefficient, which is determined by the formation and migration of vacancies ($Q_{climb} = Q_f + Q_m = 0.67 \text{ eV} + 0.7 \text{ eV} = 1.4 \text{ eV}$). D_0 is the pre-exponential factor. The dislocation annihilation rate by climb can thus be written as:

$$\dot{\rho}_{i,w}^- = 2 \cdot d_{climb} \cdot b^2 \cdot \frac{D_0}{kT} \cdot \frac{1}{N} \cdot \tau_{i,w} \cdot \rho_{i,w}^2 \cdot \exp\left(-\frac{Q_{climb}}{kT}\right) \quad (3.17)$$

The other important mechanism causing a diminishment of dislocations during recovery is cross slip. Also for cross slip, only the strain rate independent rate-controlling equations are considered, in case of static recovery. The reduction of dislocation density by annihilation via cross slip depends on the current dislocation density in the cell interiors, respectively the cell walls and the probability P_x by which cross slip occurs. ν_0 is the vibration frequency of dislocations which is known to be of the order of 10^{10} 1/s.

$$\dot{\rho}_{i,w}^- = \rho_{i,w} \cdot \nu_0 \cdot P_x^{i,w} \quad (3.18)$$

The probability for cross slip P_x depends on the activation energy for cross slip Q_x , the activation volume V and on the effective stress $\tau_{i,w}$.

$$P_x^{i,w} = \exp\left(-\frac{Q_x - V \cdot \tau_{i,w}}{kT}\right) \quad (3.19)$$

where

$$\tau_{i,w} = \tau_{T,i,w} + \tau_{chem} \quad (3.20)$$

The effective stress on a dislocation $\tau_{i,w}$ is given by the stress of the surrounding dislocation structure (Taylor stress) as well as on a stress caused by the presence of solutes and dispersoids. It was assumed in the following that the stress caused by the dislocation structure on an individual dislocation is affected by additional interactions with dispersoids or solutes. Dispersoids can pin the cell walls, solutes can suppress or hinder dislocation motion. The chemical stress is the push of the substructure on a partial dislocation waiting to overcome a particle. By this additional pressure the dislocation can convert to a perfect dislocation and cross slip.

The incremental coupling of the recrystallization model CORE and the work-hardening / softening model 3IVM+ is indicated in Fig. 3.5. The exchange of information is basically one-way. The CORE model provides parameters to 3IVM+, such as the number of slip systems N_{GLS} activated during the previous deformation, the actual temperature T and the dislocation density in the cell interiors ρ_i and walls ρ_w . The work-hardening model 3IVM+ provides based on this data and the updated microchemistry data the new dislocation density ρ_{i+1} in the cell walls and cell interior for the next recrystallization time step. From the original work-hardening model only those equations were implemented which relate to the case of static recovery, hence where the strain rate amounts to zero. Since CORE is a spatial resolved model the dislocation densities are resolved on grain scale, so that each grain has its *own recovery kinetics*. Based on the orientation-dependent recovery rates further grain-dependent incubation times can be defined (Chap. 6.3).

The introduction of orientation-dependent recovery rates further requires adjustment of the time scaling in each time step as dependent on the recovery kinetics in each grain. The time scaling is described in Sec. 3.8 in case of recovery being the time-controlling process. Other important parameters exchanged between CORE and 3IVM+ are microchemistry related parameters such as dispersoid volume fraction f_p , dispersoid radius r_p , and the solid solution content c_{SS} of e.g. manganese, iron.

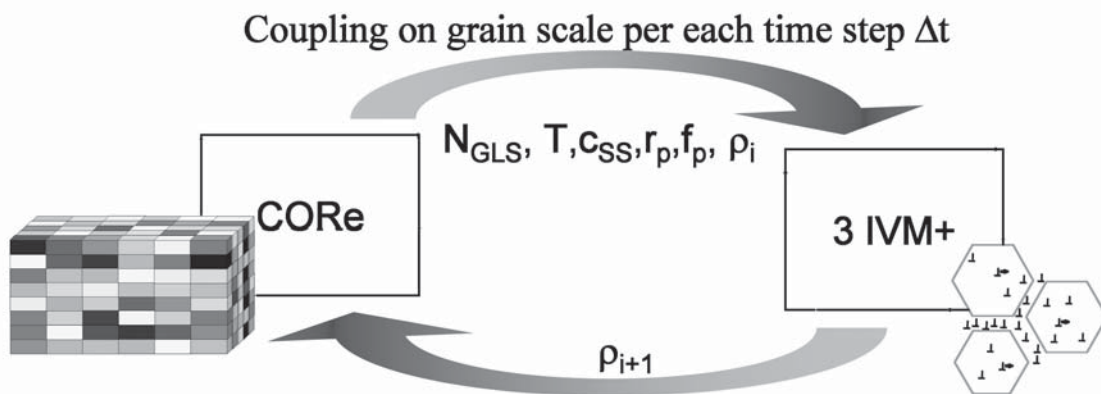


Fig. 3.5: Incremental coupling to the work-hardening model to obtain dislocation densities ρ_i for each grain per each time step Δt . (N_{GLS} = number of active slip systems during deformation, T = temperature, c_{SS} = solute level, r_p = average radius of precipitates, f_p = average volume fraction of precipitates).

The coupling of CORE and 3IVM+ (Fig. 3.5) as introduced here renders several benefits:

- The orientation resolved description of recrystallization with important effects on the recrystallization texture evolution.

- The possibility to describe an incubation time for recrystallization, which is inevitable for industrial processes with a fixed T-t-profile (see Chap. 6.3).
- The transfer of CORE output on grain scale is required for more advanced through-process modeling on grain scale and the remaining dislocation density in not fully recrystallized areas will definitely influence the deformation behavior and texture evolution in a subsequent deformation step.

At the beginning of a recrystallization simulation with CORE the number of activated slip systems N_{GLS} and the dislocation density in the cell walls ρ_w and interiors ρ_i is initialized with the value obtained after the last deformation step (GIA). These values are different for each individual grain, and thus orientation-dependent. Hence for each grain an individual recovery behavior is described by the coupling CORE-3IVM+ as mentioned above. This shall represent the link between the individual substructure obtained after deformation and its individual evolution during annealing as found from experiments.

Fig. 3.6 shows an example of the orientation dependent stored dislocation densities after cold and hot rolling and the number of activated slip systems (calculated with GIA-3IVM+ for the alloy AA3103). The data was analyzed with respect to twelve ideal orientation classes as indicated in the graphs (see also Tab. 3.9).

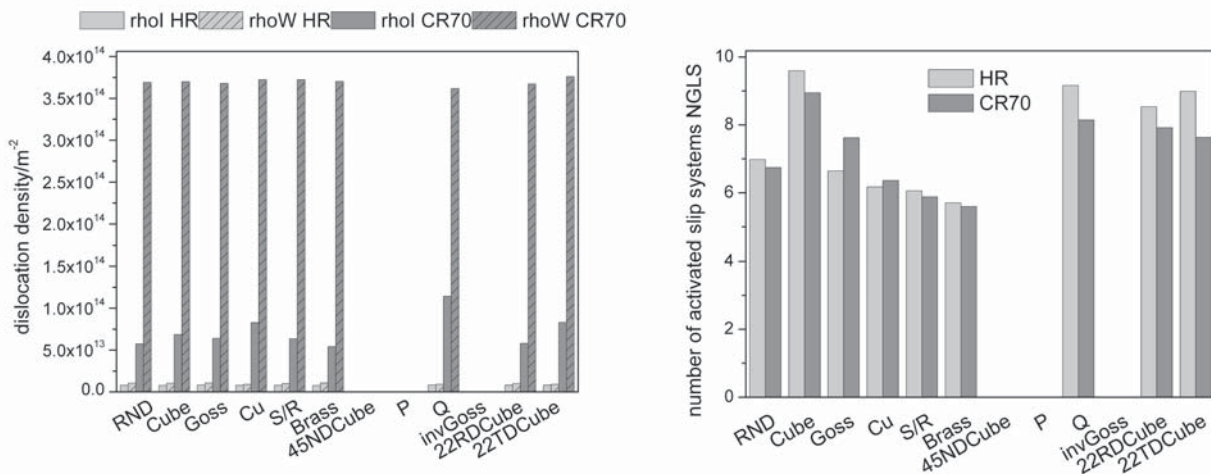


Fig. 3.6: (a) Dislocation density and (b) number of activated slip systems N_{GLS} dependent on the initial grain orientation (HR = hot rolled, CR70 = 70% cold rolled, ρ_i = dislocation density in cell interior, ρ_w = dislocation density in cell wall).

The consideration of orientation-dependent recovery rates as introduced allows orientation-dependent incubation times, and thus nucleation rates. Hence, a selection of preferred orientations is already possible at the nucleation stage with significant influences on the final recrystallization texture (Chap. 8). The consideration of recovery leads further to growth kinetics that proceed with a lower rate and under the condition of additional back-driving forces such as Zener pinning, lead to a local or complete suppression of recrystallization. So there are a number of very important aspects of recovery on recrystallization which can in general not be neglected in a high stacking fault material such as aluminum, but which are accounted for by the coupling CORE-3IVM+. The coupling of CORE-3IVM+ was used throughout this thesis and in particular for the Chaps. 7-9. The recovery behavior and the incubation times as modeled with CORE-3IVM+ are further detailed in Chap. 6.

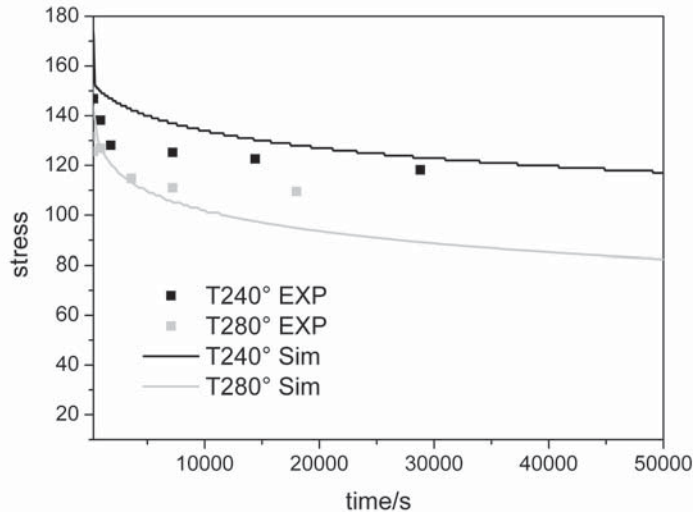


Fig. 3.7: Stress Evolution over time in order to compare the recovery behavior from experiment and simulation. The experimental values were obtained from hardness measurements which were related to the yield stress. The simulated curves were obtained from a simulation with CORE-3IVM+ for the same parameter set. Therefore the obtained dislocation density was transformed via $\alpha \cdot G \cdot b \cdot \sqrt{\rho}$ into a stress value. Two different temperatures where recovery takes place were investigated. The initial state of the material is 70% cold rolled AA3103 alloy.

The main advantage of the work-hardening / softening model 3IVM+ over 3IVM can be directly seen if the dislocation densities after deformation are compared. Whereas 3IVM gives values of the order of 10^{16} m^{-2} , the values obtained with 3IVM+ are respectively lower and of the order of 10^{13} - 10^{14} m^{-2} in case of for a cold rolling reduction of 70%. These more reasonable dislocation densities obtained with 3IVM+ were another reason for the preference of this model. It is further demonstrated in Fig. 3.7 that the 3IVM+ model provides a sufficient description of the recovery behavior if compared to experimental data.

In addition, a new model for improved softening kinetics for commercial fcc materials is currently under development for the prediction of better quantitative agreement. Nevertheless, the logarithmic decrease of dislocation density as predicted from the coupling CORE-3IVM+ allows a prediction of tendencies in grain size distribution, kinetics and textures under consideration of recovery that is in agreement with experiments.

The ulterior motive for consideration of a softening model such as 3IVM+ is the application of CORE-3IVM+ in a through-process model. Hence, some of the outputs of the recrystallization model CORE-3IVM+ will then be further input, e.g. for a subsequent deformation simulation. For the alternating modeling of annealing and deformation cycles, the required output parameters from the recrystallization model are the grain size, the recrystallization texture and the stored dislocation density in the remaining deformed grains. Those input parameters are used rather indirectly, but due to the strong influences on the deformation texture evolution they will also contribute to the flow stress development in the next deformation step.

The phenomenon of dynamic recrystallization was not considered in the present work, as it may be required for the modeling of copper or austenitic steels.

3.7 Coupling to a statistical model of precipitation kinetics CORE-ClaNG

ClaNG is a model based on the classical concepts of nucleation and growth of precipitates. It describes the microchemistry, in terms of solute contents and precipitates of aluminum alloys during thermo-mechanical treatment and was developed at the Institute of Physical Metallurgy and Metal Physics (IMM) by Schneider and Löchte [Schneider 2006, Löchte 2004]. Among the input parameters for ClaNG are the dislocation density and the time-temperature profile. The dislocation density influences significantly the nucleation rate of new precipitates as well as the growth of existing precipitates by diffusion (Fig. 3.8). Details on the influences of this quantity can be found in literature [Löchte 2004, Schneider 2006]. Major outputs of the ClaNG model with respect to recrystallization are the solute content in the matrix of the considered alloy and the size distribution of existing phases in the alloy. These phases can be either retained intermetallic constituents or precipitates formed during the heat treatment. The size distribution of these different phases can be analyzed to obtain an average overall radius and volume fraction.

The coupling with CORE was carried out in a successive way in the current work (Fig. 3.8), since an incremental coupling requires step wise communication which would slow down the recrystallization simulation enormously. The successive coupling, however, requires an a priori modeling of the microchemistry evolution for the chosen heat treatment before the actual recrystallization simulation is started. This indirectly assumes that an interaction of precipitation and recrystallization, e.g. by pipe diffusion at the high angle grain boundaries, does not take place.

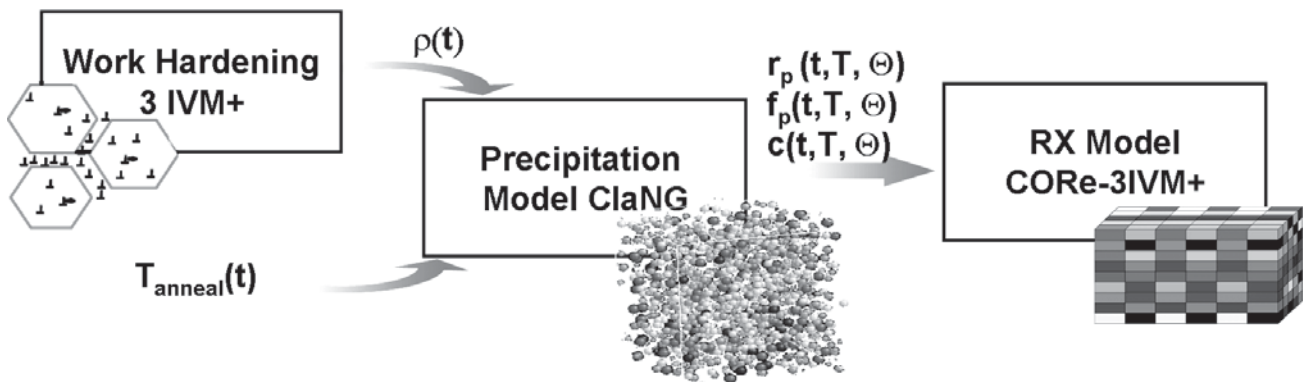


Fig. 3.8: Scheme of successive coupling of CORE and ClaNG. (ρ = dislocation density, r_p = particle radius, f_p = particle volume fraction, c = solute content, $T(t)$ = temperature profile, Θ = orientation).

However, during recrystallization the average dislocation density is gradually reduced due to recovery in the remaining deformed volumes. This in turn reduces the number of potential nucleation sites for precipitation and thus cannot be neglected. To consider the gradual softening of the material during annealing, the temporal evolution of dislocation density in the remaining deformed volumes is predicted with CORE-3IVM+, e.g. that means with 3IVM+ considering only those terms which concern static recovery. The obtained dislocation density reduction can be validated in a first approach with the relative decrease in the yield stress as directly measured or interpreted from hardness measurements.

The CORE model requires basically the time-dependent evolution of dispersoid volume fraction f_p , dispersoid radius r_p , and the solid solution content c_{SS} of e.g. manganese, iron.

CORE distinguishes between different solute elements in the matrix, but does not consider differences in composition of the dispersoids. Different solute elements have different diffusion coefficients in the matrix and therefore can cause differently strong effects in case of solute drag at

the grain boundaries. Dispersoids are considered with respect to their pinning ability of grain boundaries, why in this respect only an average volume fraction and dispersoid radius is required. In previous work [Mukhopadhyay 2005] only a time-dependent change of one element in solid solution (e.g. iron) was considered, the Zener drag was up to date always considered as being constant. In the present work instead of one element in solid solution several elements in solid solution were considered, each of them contributing differently in accordance to their diffusivity in the aluminum matrix. Further, since with a temporal change of the solute content always a change in the dispersoid size and volume fraction is obtained, this was also considered. This enables the consideration of phenomena such as concurrent precipitation, not only dependent on temperature but also on orientation (see below).

As input to the ClaNG simulation currently dislocation densities from the new GIA-3IVM+ approach are used, which lead to more reliable results in particle volume fractions. Due to the successive coupling prior to the recrystallization simulation the precipitation simulation is carried out for the chosen heat treatment. The output of ClaNG is provided as a time-dependent evolution of the aforementioned parameters in terms of precipitate size distributions. Since only the smaller particles have an influence on the recrystallization kinetics only those particles were considered which have a size in the range of 10 nm to 1 μm . By this coupling it is possible to consider the whole microstructure as homogeneous with an average dislocation density. The coupling between CORE and ClaNG has been further extended in this work for effects such as orientation dependent precipitation. In this sense the precipitation evolution was considered per grain. To reduce the computational effort the grains were further subdivided in relevant texture groups, so that in general twelve orientation classes exist according to the texture components displayed in Tab. 3.9. Hence, the individual structure evolution as dependent on the local stored dislocation density within the respective grains can be accounted for. This enables the modeling of orientation-dependent effects like substructure-dependent Zener pinning.

Tab. 3.9: Ideal orientation classes considered in the successive CORE-ClaNG coupling; for each orientation class a separate ClaNG simulation is required. This allows the effect of orientation-dependent precipitation during recrystallization simulation.

<i>Ori Class Index</i>	<i>Miller Indices</i>	<i>Euler angles phi1, PHI, phi2</i>	<i>Ideal Orientation</i>
1	{001}<100>	0, 0, 0	Cube $\pm 15^\circ$
2	{011}<100>	0, 45, 0	Goss $\pm 15^\circ$
3	{112}<11 $\bar{1}$ >	90, 35, 45	Copper $\pm 15^\circ$
4	{123}<63 $\bar{4}$ >	59, 37, 63	S/R $\pm 15^\circ$
5	{011}<21 $\bar{1}$ >	35, 45, 0	Brass $\pm 15^\circ$
6	{001}<110>	45, 0, 0	45°ND rotated Cube $\pm 15^\circ$
7	{011}<111>	55, 45, 0	P $\pm 11^\circ$
8	{0 3 10}<392>	70, 15, 0	Q $\pm 11^\circ$
9	{011}<01 $\bar{1}$ >	90, 45, 0	Inverse Goss $\pm 11^\circ$
10	{025}<100>	0, 22, 0	22° RD rotated Cube $\pm 15^\circ$
11	{001}<5 $\bar{2}0$ >	90, 22, 0	22° TD rotated Cube $\pm 15^\circ$

The effect of precipitation is not only considered on the recrystallization kinetics but also on the nucleation as detailed in Sec. 3.9.

3.8 Modifying the Real-Time Scaling

The real time scaling required some adjustment due to the new modifications in CORE (coupling to 3IVM+). In order to describe recovery and incubation times which enable more universal recrystallization simulations (Chap. 6), the recrystallization model CORE was coupled to the work-hardening / softening model 3IVM+ (Sec. 3.6). This required a further specification of the time-scaling to allow a reasonable time frame for the calculations. In addition, since the model should be applied to commercial materials under real processing conditions, a time-dependent temperature history was introduced, e.g. heating rates, which have an enormous influence on the microstructure and texture evolution in terms of precipitation and recovery. The following time-scaling differs therefore from the previous approaches in the work of Mukhopadhyay [Mukhopadhyay 2005], since basically the recrystallization time step was required in those models.

The maximum driving force p_{max} however is in each time-step reduced due to concurrent recovery, so that the time step Δt is dynamically calculated in each time step. Since recovery is the dominating process prior to the onset of recrystallization a specific time step for recovery was introduced in this work.

$$\Delta t_{Rv} = 0.05 \cdot \frac{\rho_{min}}{\dot{\rho}_{max}} \quad (3.21)$$

where ρ_{min} is the overall minimum dislocation density within the grains at a certain time step of the cellular automata. $\dot{\rho}_{max}$ is the corresponding overall maximum dislocation reduction rate. However, in case the temperature is not constant during the modeled recrystallization process, another time-step, dependent on the heating, respectively cooling rate, needs to be considered, in order to prevent large errors in the recrystallization kinetics.

$$\Delta t_{HR} = \frac{1 \text{ K}}{\dot{\Phi}} \quad (3.22)$$

where $\dot{\Phi}$ is the heating – or cooling rate. As soon as recrystallization is initiated also the recrystallization time step is calculated. The overall minimum time step of those introduced above determines the time step for the simulation.

3.9 Quantitative Nucleation Modeling in CORE - Modifications

Since CORE is a pure growth model, it requires input from separate nucleation models to provide the respective nucleus spectrum and the corresponding nucleus numbers.

In the past, two rivaling theories have been discussed for the modeling of recrystallization: the theories of oriented nucleation [Burgers 1951, Dillamore 1974] and oriented growth [Barrett 1940, Beck 1952, Beck 1953, Beck 1954, Liebmann 1956, Ibe 1966, Lücke 1974, Gottstein 1992, Molodov 1995]. During the last couple of years it became more and more obvious that the truth lies somewhere in between, implying that there are a few nucleation sites producing a range of orientations, of which a few have preferred growth conditions due to their location and corresponding growth environment. Since simulation can give a better insight in this regard, the influence of oriented growth has been discussed in literature correspondingly [Jensen 1997, Engler 1998, Gottstein 2001]. By this means, the range and effect on the texture and microstructure evolution due to oriented growth are more accessible. The results allow drawing the conclusion that the most significant effects on the microstructure and texture evolution originate from recrystallization nucleation.

The nucleation models available from literature are mostly empirical describing the nucleus spectrum at the beginning of a recrystallization texture simulation. The difficulty in predicting nucleation, and thus describe it by equations originates from the fact that most frequently the required sub-structural information is below any limit of resolution of experimental techniques or even the lack of those techniques for a 3D representation of the problem.

Engler et al. [Engler 1997b, Engler 1998] utilized measured nucleation spectra resolved according to different nucleation mechanisms for recrystallization simulations in aluminum alloys. Jensen [Jensen 1995] used experimentally determined growth rates, for individual orientations, for the simulation of recrystallization. From the substructure model developed by Hurley and Humphreys [Hurley 2003] a nucleation event is described as the result of subgrain growth, but without further consideration of the individual nucleus orientations. Such a model is restricted to cell-forming alloys only. Other approaches try to relate the deformation structure to the key parameters for nucleation, e.g. Wauthier et al. [Wauthier 2007] analyzed the deformed substructure in an IF steel in this respect. Liu et al. [Liu 1998] related the deformation substructure to the initial grain orientation. However, the key for recrystallization nucleation lies in the deformed structure. A detailed literature overview on recent investigations in this field was given in Chap. 2. In the present work the ReNuc model developed by Crumbach [Crumbach 2005] was utilized for analyzing the sub-structural quantities as key parameters for the subsequent nucleation. The ReNuc model is a compound of three sub-models for prediction of nucleation textures in aluminum alloys. It is analyzing the deformed microstructure in order to determine the efficiency of a certain grain orientation with respect to its nucleation behavior in terms of grain boundary, transition band and shear band nucleation [Crumbach 2005, 2006a]. However, a shortcoming of the model is the lack of treatment of particle influences (particle stimulated nucleation, Zener Drag), which are common in most commercial aluminum alloys. The effect of PSN was modeled up to now indirectly, and only for the case of a random nucleus spectrum originating at particles. During this work especially the model for particle-stimulated nucleation (PSN) has been developed, which will be presented in Chap. 5. Especially, in case of concurrent precipitation a strongly particle-dominated recrystallization texture is obtained. The modeling of such specific cases requires a new model for PSN and is further detailed in Chaps. 7, 8. Currently, the CORE model distinguishes four typical nucleation mechanisms frequently observed in aluminum alloys. Those are nucleation at (1) grain boundaries, (2) at transition bands, (3) nucleation at shear bands and (4) nucleation at particles. However, for the modeling of nucleation not only the nucleus texture originating at different nucleation sites but

also the nucleus number is of outstanding importance, e.g. for the prediction of recrystallized grain sizes.

3.9.1 Nucleation – and the importance of the absolute nucleus number

The number of nuclei plays an important role for the recrystallized microstructure, in particular for the grain size and grain size distribution. In the work of Mukhopadhyay [Mukhopadhyay 2005] the nucleus number is calculated based on an approach developed by Derby and Ashby [Derby 1987] for dynamic recrystallization.

In this context it is assumed that the underlying mechanism for nucleation is strain induced grain boundary migration (SIBM). Hence during recrystallization a new nucleus will develop by bulging of the grain boundary. Fig. 3.9 displays a case, for which bulging of a grain boundary might occur. The grain boundary is intersected from both sides by subgrain boundaries in non-equidistant spacings. These sub-boundaries pin the grain boundary locally. Fig. 3.9 indicates the initial setup before bulging; two different grains adjacent to a high-angle boundary provided with different average subgrain sizes $d_{sub,1}$ and $d_{sub,2}$.

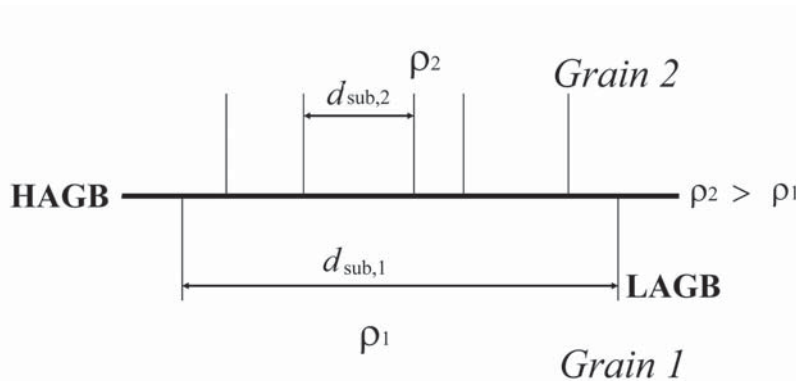


Fig. 3.9: The “Bulging Model” for nucleation at grain boundaries.

As suggested by Fig. 3.9 the microstructure prior to recrystallization is assumed to be a subgrain structure. Hence locally a very large subgrain in *grain 1* is observed facing very small subgrains across the grain boundary in *grain 2*. When this arrangement is overcritical, the subgrain with the diameter $d_{sub,1}$ will bulge into the adjacent grain (*grain 2*) (Figs. 3.9, 3.10). This bulging is considered as a nucleation event providing a single nucleus.

An arrangement becomes critical, as soon a critical boundary length is dragged by a sufficiently high number n_c of sub-boundaries ending in the high-angle grain boundary over a considered length. Interfaces considered in CORE are either grain boundaries, particle surfaces or the surface of shear bands, respectively transition bands.

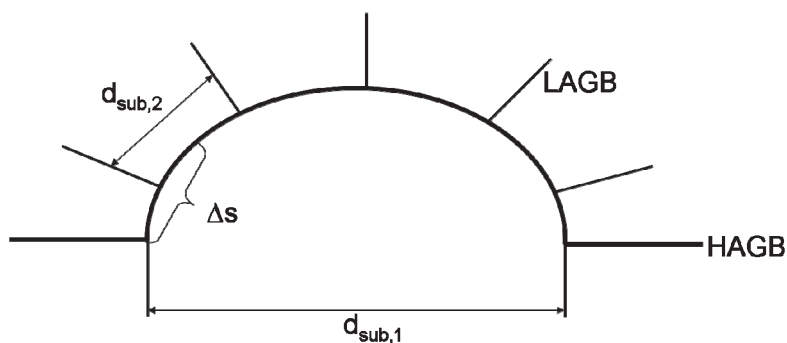


Fig. 3.10: Bulging of a high-angle grain boundary as caused by subgrain boundaries pinning a critical length segment.

Since subgrain sizes are not available from 3IVM / 3IVM+ they are interpreted via the principle of similitude. In contrast to [Mukhopadhyay 2005] who used the deformation texture model GIA-3IVM, in the present work the improved GIA-3IVM+ was utilized to provide the dislocation densities. From the GIA-3IVM+ output a homogeneous dislocation density is provided for each grain and thus for the respective cells (mathematical smallest discretization level). 3IVM+ distinguishes dislocation densities in the cell walls and cell interiors which are converted via the principle of similitude into a subgrain size:

$$\rho_{\text{tot}} = f_w \cdot \rho_w + (1 - f_w) \cdot \rho_i \quad (3.23)$$

$$d_{\text{Sub}} = \frac{C}{\sqrt{\rho_{\text{tot}}}} \quad (3.24)$$

where ρ_{tot} is the total dislocation density and, ρ_i , ρ_w the dislocation densities in the cell interior, respectively in the cell walls; f_w is the volume fraction of cell walls, C a geometrical constant of the order of 15 and d_{Sub} the subgrain size.

Hence, for each initial microstructure grain with the corresponding dislocation density an average subgrain size can be computed according to Eq. (3.24). The dislocation density evolution within the cell walls and interiors were further considered to model recovery as based on the 3IVM+ equations (Sec. 3.6). This is a significant improvement with respect to the approach by Mukhopadhyay [Mukhopadhyay 2005], where an exponential decrease of the average dislocation density was assumed, which was the same in each grain.

How can an absolute nucleus number be computed from an average subgrain size in each grain? Since an average subgrain size per initial microstructure grain is far from reality a subgrain size distribution was assumed (Fig. 3.11). To keep it simple an exponential decreasing function Eq. (3.25), with an average subgrain size d_2 or subgrain size area A_2 was utilized. In principle the nucleus numbers are calculated for each nucleation mechanism independently. The calculation of nucleus numbers is demonstrated first for the simplest case of nucleation at grain boundaries.

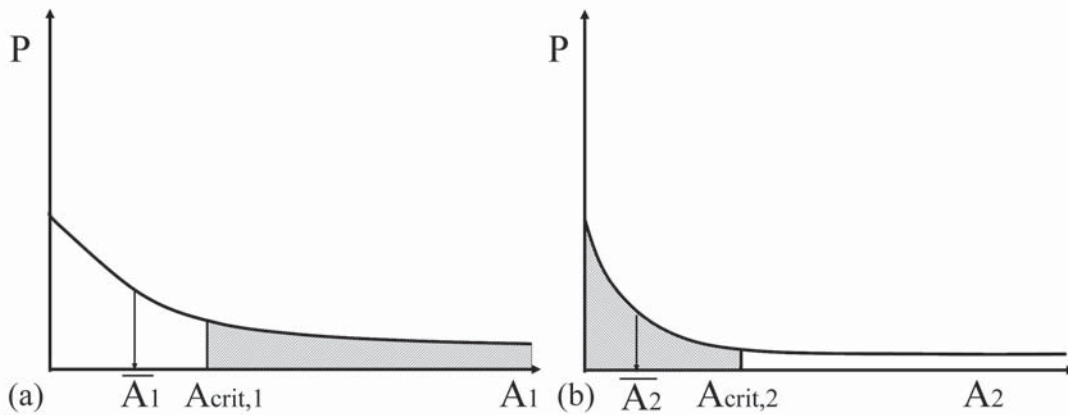


Fig. 3.11: Subgrain size distributions within grain 1 and grain 2 with the average values \bar{A} and the critical subgrain sizes A_{crit} . (a) Subgrain size distribution in grain 1 (low dislocation density-high average subgrain size); (b) Subgrain size distribution in grain 2 (high dislocation density-low average subgrain size).

3.9.2 Nucleation at grain boundaries

The current approach differs significantly from the former one by Mukhopadhyay, since a nucleus for recrystallization will be viable only if the nucleus has a critical size according to the thermodynamical instability criterion. In contrast, in the approach by Mukhopadhyay each nucleus was considered as a viable nucleus (also nuclei with sizes close to zero). The below outlined calculation of a nucleus number describes additionally the fulfillment of the mechanical instability criterion. To calculate the nucleus number for two adjacent grains, the subgrain size distributions in Fig. 3.11 are assumed. The average subgrain size is related according to Eq. (3.24) to the average dislocation density stored in both grains.

We can write the probability $P(A)$ to find a subgrain with the average size \bar{d} and the average area \bar{A} in the interval $[A, A+dA]$ as $P(A)dA$ with

$$P(A) = \frac{1}{\bar{A}} \cdot \exp\left(-\frac{A}{\bar{A}}\right) \quad (3.25)$$

If we assume that *grain 1* (Fig. 3.9) is the grain with the lower dislocation density and hence the larger average subgrain size, the nuclei density per area can be obtained from

$$N(n_c) = \frac{1}{\bar{A}_1} \cdot \int_{A_{crit,1}}^{\infty} \frac{1}{\bar{A}_1} \exp\left(-\frac{A_1}{\bar{A}_1}\right) dA_1 \cdot \int_0^{A_{crit,2}} \frac{1}{\bar{A}_2} \exp\left(-\frac{A_2}{\bar{A}_2}\right) dA_2 \quad (3.26)$$

Where $A_{crit,1}$ and $A_{crit,2}$ are the thermodynamic nucleus radii which are fixed for a certain dislocation density. The relation between A_1 and A_2 in particular for $A_{crit,1}$ and $A_{crit,2}$ reads as follows:

$$\frac{A_{1,crit}}{A_{2,crit}} = \frac{d_{1,crit}^2}{d_{2,crit}^2} = n_c \quad (3.27)$$

where n_c is the critical number of segments. $A_{crit,2}$ is not a fixed value but can be found for each valid A_1 . Summing up the nucleus number $N(n_c)$ for all different $n \geq n_c$ gives the total nucleus number N for this specific nucleation mechanism considered.

3.9.3 Nucleation in orientation gradients

For nucleation in orientation gradients, the approach is a little different. It is assumed that the orientation gradients (transition bands, shear bands, particle deformation zones) are located within one single grain. In contrast to grain boundaries, for all other nucleation mechanisms internal interfaces are considered. Hence, we have on one side of the interface a subgrain size distribution as in Fig. 3.11. On the other side of this interface we can describe the subgrain size distribution by a Poisson distribution (Eq. (3.29)). A Poisson-distribution Eq. (3.29) can be used for very small success probabilities in case of a large number of happenings, as it is certainly true for nucleation. Hence Eq. (3.29) describes the probability that n sub-boundaries are intersecting a critical length d_2 . The average subgrain size \bar{d}_2 is defined by the dislocation density in *grain 2* via Eq. (3.24).

$$P(A) = \frac{1}{\bar{A}_2} \cdot \exp\left(-\frac{A_2}{\bar{A}_2}\right) \quad (3.28)$$

$$P(n) = \frac{1}{n!} \cdot \left(\frac{A_2}{\bar{A}_2} \right)^n \cdot \exp\left(-\frac{A_2}{\bar{A}_2}\right) \quad (3.29)$$

The number of such critical nucleus events can be calculated by solving the following integral

$$N = \int_{A_{\text{crit}}}^{\infty} P(n)P(A_2) \frac{dA_2}{A_2} \quad (3.30)$$

to

$$N(n, A_{\text{crit}}) = \frac{1}{\bar{A} \cdot 2^{n_{\text{crit}}+1}} + \left[\frac{\exp\left(-2\frac{A_{\text{crit}}}{\bar{A}}\right) - 1}{2^{n+1} \cdot \bar{A}} + \frac{\exp\left(-2\frac{A_{\text{crit}}}{\bar{A}}\right)}{\bar{A}} \sum_{k=0}^{n-1} \frac{1}{(n-k)! \cdot 2^{k+1}} \left(\frac{A_{\text{crit}}}{\bar{A}}\right)^{n-k} \right] \quad (3.31)$$

$$N(n, A_{\text{crit}}) = \int_0^{\infty} P(n)P(A_2) \frac{dA_2}{A_2} - \int_0^{A_{\text{crit}}} P(n)P(A_2) \frac{dA_2}{A_2} \quad (3.32)$$

$$N_{\text{tot}} = \sum_{n=n_c}^{\infty} N(n, A_{\text{crit}}) \quad (3.33)$$

where N is the number of nuclei per area A and n is the number of critical intersections n_c over the critical length $d_{\text{Sub},l}$ in order to bulge the respective line element.

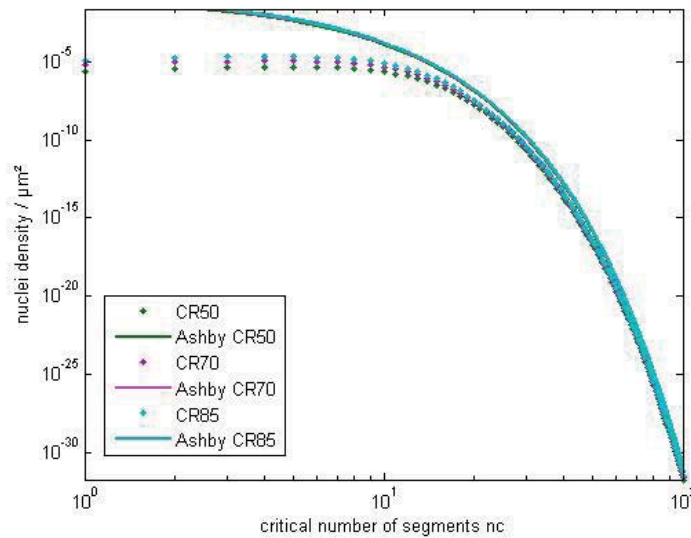


Fig. 3.12: Nuclei density in dependence on the rolling reduction calculated for an AA3013 alloy. (dotted line – approach presented in this thesis (Ashby approach); continuous line – approach based on Ashby, but as used in [Mukhopadhyay 2005]).

Fig. 3.12 compares the nucleation numbers computed above with those found from the approach of Mukhopadhyay. It was found that according to Mukhopadhyay approximately one nucleus per $3\mu\text{m} \times 3\mu\text{m}$ area was obtained. In the current approach one nucleus is obtained per $300\mu\text{m} \times 300\mu\text{m}$ area, which is lower. It is pointed out that this value holds for a single nucleation mechanism. Of course beside grain boundary nucleation in most commercial aluminum alloys also other types of nucleation mechanisms are observed. For particle stimulated nucleation the nucleus number is naturally higher than this value, since in the deformation zone a higher dislocation density and hence a higher nucleus number is obtained.

Calculation of critical segment length n_c

The number of critical intersections n_c required to lead to a bulging event can be calculated according to

$$n_c = \frac{A_{crit}}{A_{av}} = \frac{d_{crit}^2}{d_{av}^2} \quad (3.34)$$

where A_{crit} and A_{av} represent the critical and average grain size along the grain boundary. The average grain diameter d_{av} is calculated according to Eq. (3.34). d_{crit} is the critical grain diameter of a viable nucleus in accordance to the thermodynamical instability.

$$d_{crit} \geq \frac{4 \cdot \gamma_{HAGB}}{\frac{1}{2} \cdot G \cdot b^2 \cdot \rho_{av}} \quad (3.35)$$

where d_{crit} is the critical subgrain diameter, γ_{HAGB} the energy of a high-angle grain boundary, G the shear modulus, b the Burgers vector and ρ_{av} the average dislocation density in the grain.

3.9.4 Influence of Zener drag on Nucleation

A dispersion of dispersoids will provide a pinning pressure opposing the driving pressure on a boundary, which is in the process of bulging. Hence the calculation of the nucleus number according to the Eq. (3.30), Eq. (3.33) changes, since the lower limit of the integral, the critical grain size d_{crit} , respectively the critical grain area A_{crit} changes. The critical nucleus size in the presence of particles on the boundary can be derived in the following fashion. If we have N particles per unit volume with spherical size and radius r_p , the volume fraction can be written as

$$f = N \cdot \frac{4}{3} \cdot \pi \cdot r_p^3 \quad (3.36)$$

If the grain boundary area O is given, the number of particles in contact with the boundary can be derived to $O \cdot 4r_p \cdot N$. If the grain boundary area is in average covered by the area $\frac{1}{C^*} \pi r_p^2$ of a particle, the reduced surface area is

$$O \cdot 4r_p \cdot N \cdot \frac{1}{C^*} \pi r_p^2 = O \cdot \frac{3}{C^*} \cdot f \quad (3.37)$$

where C^* is a parameter to describe the statistical average of the intersected particle area. The energy balance can be written as follows

$$\Delta G = -\frac{4}{3} \pi r^3 \cdot p \cdot (1-f) + 4\pi r^2 \cdot \gamma \cdot \left(1 - \frac{3}{C^*} f\right) \quad (3.38)$$

The derivation of the critical nucleus size r_{crit} from $\left. \frac{d\Delta G}{dr} \right|_{r_{crit}} = 0$ leads to

$$r_{crit} = \frac{2\gamma}{p} \cdot \frac{\left(1 - \frac{3}{C^*} f\right)}{(1-f)} \quad (3.39)$$

where γ is the grain boundary energy and p the driving force. In the present work the volume fraction f is modeled independently with the precipitation model ClaNG. When nucleation is initiated the nucleus number is calculated based on the driving force including the effect of the precipitated volume fraction. The effect of Eq. (3.39) is comparatively small, since the critical radius is increased only slightly for $C^* > 3$.

3.9.5 The total nucleus number

The ReNuc model provides on one hand the efficiency of an individual grain for nucleation at grain boundaries, transition bands or shear bands, but on the other hand does not provide quantitative information, i.e. how many nuclei of which orientation. In the present work the ReNuc model was extended for PSN, which is further detailed in Chap. 5. The calculation of an absolute nucleus number per individual nucleation site was already outlined above.

The total number of nuclei N_{tot} per unit volume is assumed as

$$N_{tot} = N_{GB} + N_{TB} + N_{SB} + N_{PSN} \quad (3.40)$$

with N_{GB} , N_{TB} , N_{SB} and N_{PSN} being the number of grain boundary nuclei (*GB*), transition band nuclei (*TB*), shear band nuclei (*SB*) and nuclei at particles (*PSN*) per unit volume. In CORE the nucleus numbers are derived according to the above introduced nucleation procedure. The number of particle-stimulated nuclei is nucleated per particle p as follows

$$N_{PSN} = \sum_{p=1}^{p_{tot}} n_p \quad (3.41)$$

where p_{tot} is the total number of particles and n_p the number of nuclei calculated per particle. This number is influenced by the dislocation density within the respective grain. Hence, the number of nuclei per particle varies from grain to grain. Since a deformation gradient in the vicinity of the particle is implemented in the CORE model, the number of nuclei per particle also depends indirectly on the local increase of the dislocation density f_{DZ} (see Tab. 3.2), which is dependent on the strain localization within the deformation zones.

The nucleus number at other nucleation sites n_i is derived for each deformed grain k and for each nucleation mechanism i . As introduced above the corresponding nucleation mechanisms are considered: (1) nucleation at grain boundaries, (2) at transition bands, and (3) at shear bands. The total nucleus number N_i for each of those nucleation mechanisms i is then given as

$$N_i = \sum_{k=1}^{4000} n_{i,k} \cdot f_i \quad \text{with } i = 1,2,3 \quad \text{and } 1 = \text{GB}, 2 = \text{TB}, 3 = \text{SB} \quad (3.42)$$

with $n_{i,k}$ being the number of nuclei provided by the nucleation mechanism i in the grain k . The model constants f_{GB} , f_{TB} and f_{SB} are introduced to promote or suppress the respective mechanisms or for instance to account for the effect that grains with transition bands might form more nuclei than grains with shear bands. The total grain number of 4000 is the standard used in GIA-3IVM+ to compute statistically relevant output. In Fig. 3.13 it is exemplarily shown how the different nucleus numbers develop with increasing rolling reduction in the alloy AA3103. The critical (average values) of the respective quantities are displayed for comparison. The average number of activated slip systems N_{GLS} as predicted from the ReNuc model is stepwise increasing with increasing deformation degree. The average in-grain misorientation IGM as obtained by using the GIA-Split Up model [Crumbach 2004, Crumbach 2005, Crumbach 2006a] is continuously increasing with increasing rolling reduction. Furthermore, the evolution of the average *shear-relaxation* (Shear Relaxation Real Fig. 3.13) is indicated as well, however for the simulations a constant value of 0.18 (Crit Shear Relaxation Fig. 3.13) was assumed, as suggested by Crumbach [Crumbach 2005]. For the calculations within the present thesis, a value of 0.18 for cold rolling and 0.4 for hot rolling for the critical shear relaxation was used as suggested by Crumbach [Crumbach 2005].

The nucleus density is increasing with higher rolling reductions as to be expected. The number of PSN nuclei is continuously increasing due to the increasing dislocation density. The number of shear band nuclei is decreasing since the surface of the shear bands is decreasing with increasing rolling reduction. The numbers of grain boundary and transition band nuclei are both increasing with increasing deformation, since they are strongly dependent on interface area which is also increasing. However the relative frequency of transition band nuclei is strengthened at the expense of shear band nuclei. One interesting fact is that a cold rolling reduction of 20% is obviously too low to produce any nuclei. This agrees very well with experiments, since it is known that a minimum deformation degree is required to initiate recrystallization [Gottstein 1998].

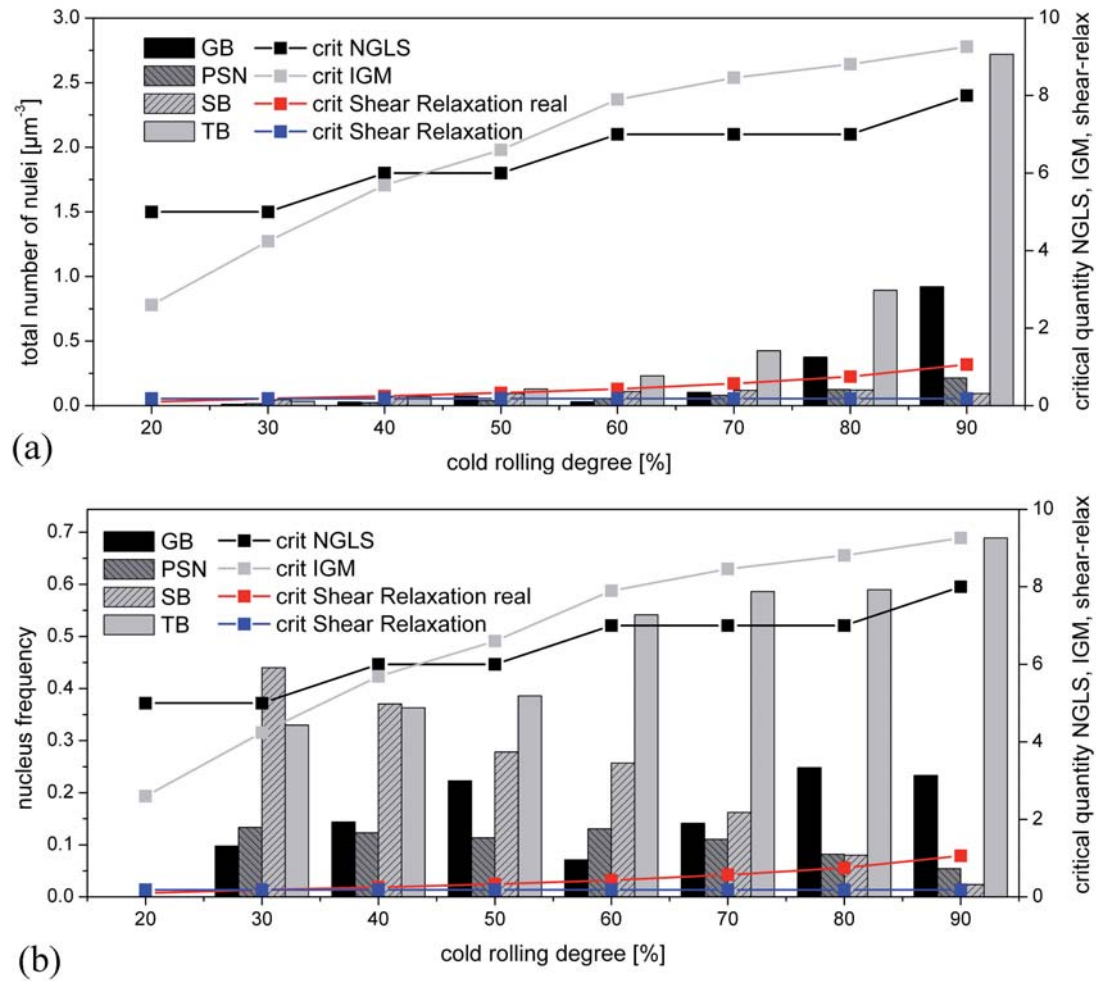


Fig. 3.13: Evolution of the critical parameters from the ReNuc model compared to the (a) absolute nucleus number and (b) relative nucleus number predicted with increasing deformation degree in the alloy AA3103. (IGM = in-grain misorientation, NGLS = number of activated slip systems, GB = grain boundary nucleation, PSN = particle-stimulated nucleation, SB = shear band nucleation, TB = transition band nucleation). These nucleus frequencies were obtained for a simulation based on 4000 initial deformed microstructure grains.

Chapter 4

Parameter Studies

4.1 Introduction

In this chapter the CORE model behavior will be analyzed with respect to its general dependency on process, material and model parameters. The main focus is to improve the understanding of various facets of the complex recrystallization behavior rather than elucidating so far undiscovered aspects. Different from experiments, simulations allow us to conduct single parameter studies. Such single-parameter variations allow confining their impact on recrystallization and thus categorizing them according to their importance. It further provides a better understanding of the individual response of the model, which is essential to evaluate more complex situations. The recrystallization behavior can be characterized by quantities such as the recrystallization texture, recrystallization kinetics and grain size distribution of the recrystallized grains. Hence, the influence of the above mentioned parameters was studied for each of them separately. The study of material parameters was restricted here to fcc materials, in particular aluminum alloys. Basically two alloys were studied, an Al-Mn alloy AA3103 and an AlFeSi alloy AA8079L. The input data for the alloy AA3103 is discussed in more detail in Chaps. 7-9 and the input data for the alloy AA8079L is presented in Sec. 4.2.4. As initial data sets, GIA-3IVM+ simulations were applied for the alloys AA3103 (Al-1wt%Mn) and AA8079L (AlFeSi).

4.2 Influence on recrystallization texture

In the following section the affection of the recrystallization texture by the outlined parameters is analyzed.

4.2.1 Influence of pre-deformation texture

It was already shown by [Crumbach 2005] that the pre-deformation texture (PDT) has an influence on the developing deformation texture. Due to the memory effect of texture, these initial texture components will reappear during later annealing in the recrystallization textures. To show this influence, at first deformation texture simulations were conducted with the advanced deformation texture model GIA-3IVM+ (Chap. 3) for different PDTs to provide CORE with required deformation data (Sec. 3.4). The material used for this study is the above mentioned aluminum alloy AA3103, containing about 1 wt% manganese. An overview of other input parameters required for the CORE simulations was given in Sec. 3.4. For a detailed description (parameter sets) of the virtual and real material processing of alloy AA3103 up to cold rolling, the reader is referred to Chap. 9. The detailed description of the cold rolling simulations is here of minor importance and thus not further detailed. Other input parameters of CORE-3IVM+ (Sec. 3.6) remained unaltered to guarantee comparability of the presented recrystallization textures. This includes besides the deformation condition, also the microchemistry options and parameters for the recrystallization simulations. In order to show an isolated influence of the PDT, it was further required to use the same nucleation parameter set for all present simulations.

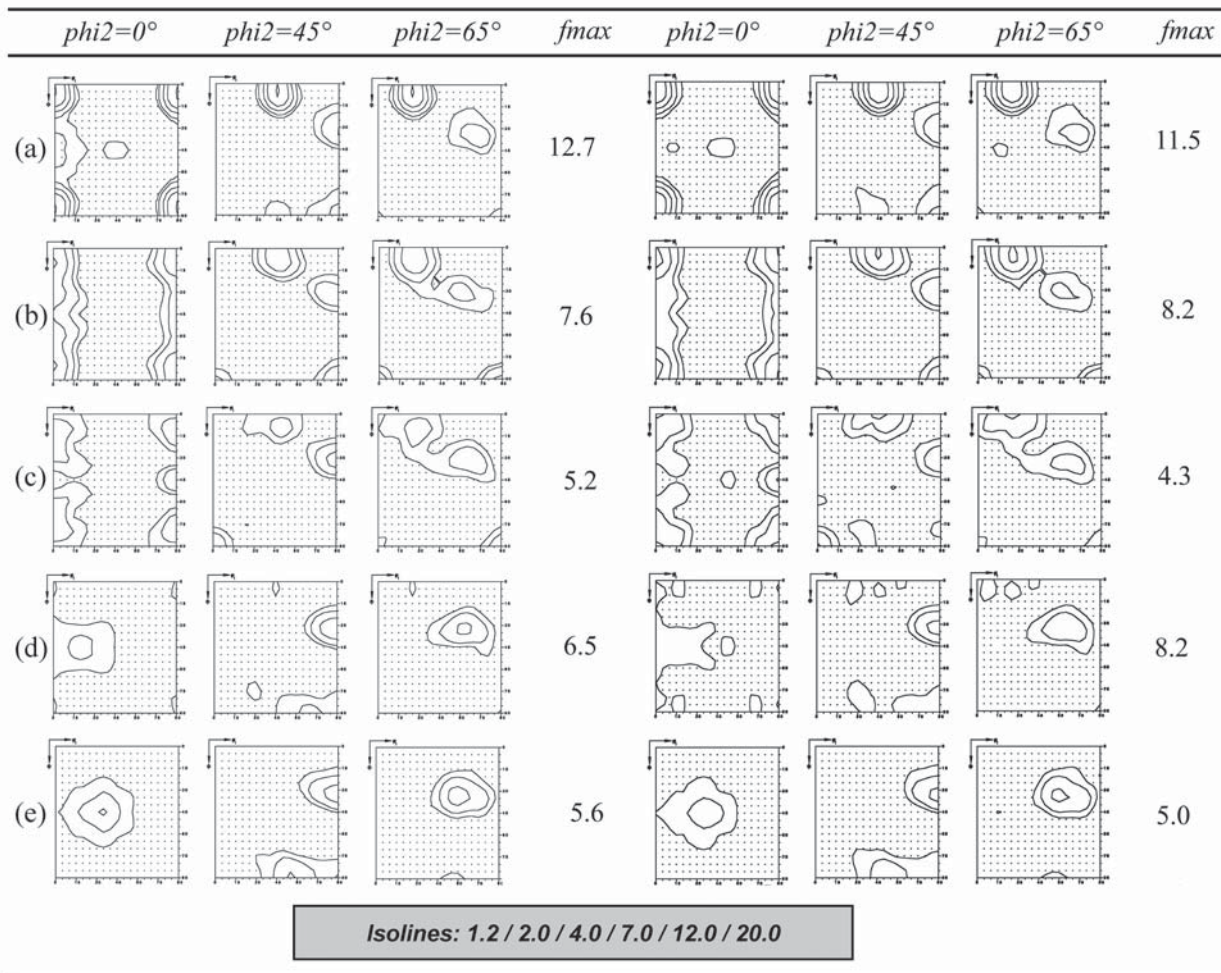


Fig. 4.1: CORE simulated nucleus textures (left) and recrystallization textures (right) by using different initial pre-deformation textures (PDTs): (a)- hot rolled, (b)-strong Cube, (c)-ND rotated Cube, (d)- random, (e)-cold rolled. The names denote the used pre-deformation texture. The textures are represented by selected sections through the Euler orientation space.

The different PDTs chosen for the investigation of their effect on the final recrystallization textures are as follows: (a) hot rolling texture, (b) strong Cube texture, (c) ND rotated Cube texture, (d) random texture, (e) cold rolling texture. These are typical PDTs frequently observed during sheet

metal fabrication of Al alloys. The effect of the different deformation textures, as resulting from a different PDT, on the nucleus texture and consequently on the recrystallization texture is shown in Fig. 4.1.

Depending on the PDT a quite different final recrystallization texture was obtained, which is characterized in particular by the intensity of the Cube component. In case of a hot rolling PDT a high intensity of the Cube and deformation texture components was found (Fig. 4.1a). If the PDT was dominated by a strong Cube texture (Fig. 4.1b), also a comparatively high amount of Cube oriented grains was retained in the simulated deformation texture. This resulted in a recurring comparatively strong Cube recrystallization texture (Fig. 4.1b). Other initial PDTs, such as a basically ND rotated Cube texture, over to a random and finally to a cold rolled texture, showed much weaker Cube texture components after finalization of recrystallization. This is related to the decreasing number of those Cube oriented grains which survived the deformation process. This is particularly pronounced, if the initial PDT contains already a low fraction of the Cube component, so that after a second cold rolling step hardly any Cube oriented nucleus remained in the GIA deformation texture (Fig. 4.1e). This has severe consequences for the recrystallization texture, which in this case is completely lacking the Cube component. It should be mentioned here that a very strong growth selection could in principle promote these small amounts of Cube oriented grains remaining after two subsequent cold rolling passes. However, a rather weak growth selection was assumed in the present case.

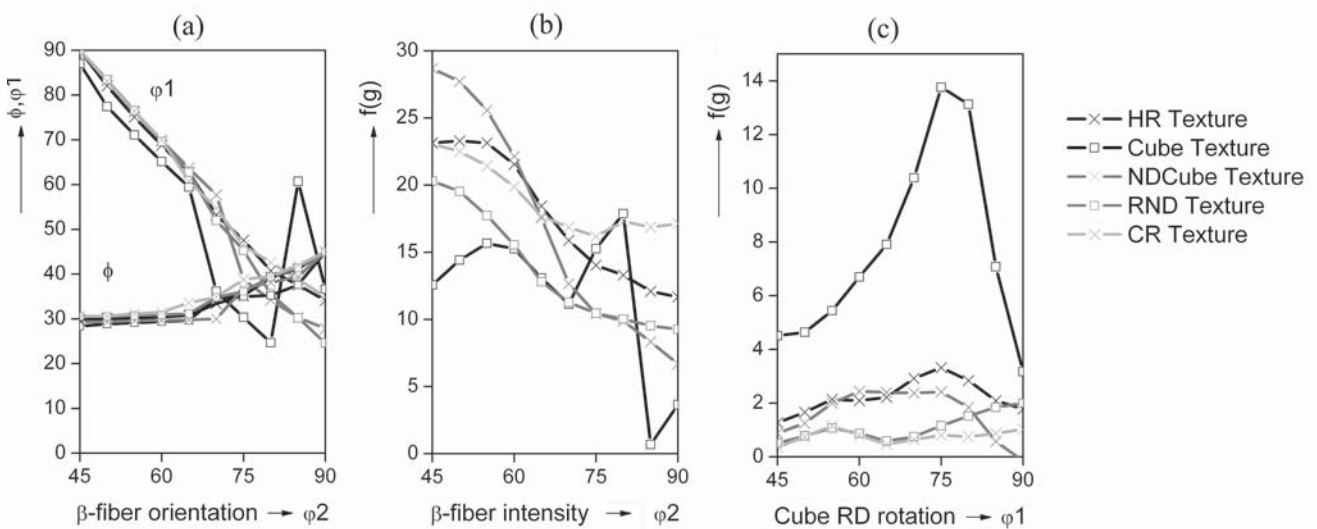


Fig. 4.2: GIA-3IVM+ simulated cold rolling textures of AA3103 for a thickness reduction of 70% using different types of input textures; (a) β -fiber orientation, (b) β -fiber intensity, (c) Cube RD rotation.

From the volume fraction plots and the skeleton plots (Figs. 4.2, 4.3) it is obvious that dependent on the PDT, slightly varying volume fractions of the deformation texture components along the β -fiber, as well as of the Cube texture component could be found after a simulated plane strain deformation of $\varepsilon_{vM} = 1.2$ corresponding to 70% rolling.

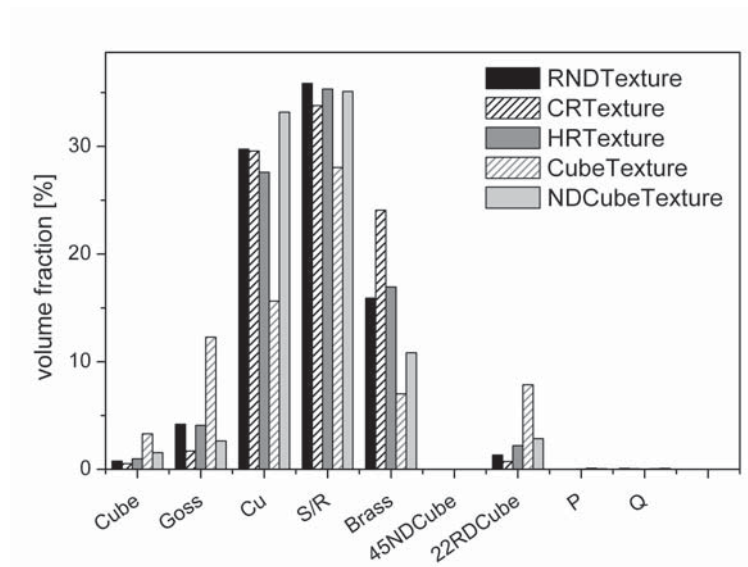


Fig. 4.3: GIA-3IVM+ simulated rolling textures of AA3103 for a thickness reduction of 70% using different types of input textures. The textures are represented as volume fractions of the mean texture components allowing for a maximum deviation of $\pm 15^\circ$.

4.2.2 Influence of dislocation density on growth

The dislocation density is one of the major inputs of the CORE model. The energy stored during deformation in terms of dislocation densities provides the driving force for primary recrystallization. Its influence on the evolution of the recrystallization texture is shown in Fig. 4.5. For these simulations the dislocation density present at the beginning of the simulation was modified: (1) it was averaged over all orientations, and (2) it was assumed to be orientation dependent as provided from a GIA-3IVM+ calculation, (3) it was assumed orientation dependent, but compared to case (2), with a larger scatter of the individual dislocation densities to make their original differences more pronounced. The different dislocation density distributions are shown in Fig. 4.4.

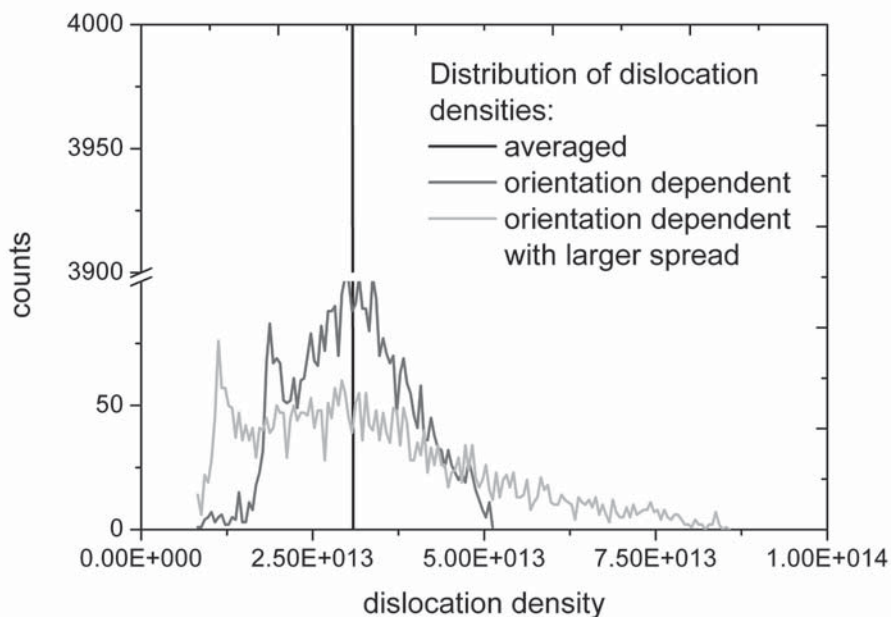


Fig. 4.4: Different distributions of the stored dislocation density in the initial microstructure of the recrystallization model CORE.

The predicted recrystallization textures as based on these modified dislocation density distributions are indicated in Fig. 4.5. It was found that the influence on texture is however, unexpectedly low. It seems that the orientation dependent growth selection by dislocations not only favored the Cube orientation, but also other components, such as e.g. the Goss orientation. Besides the minor variations observed in the texture components, also the texture intensities hardly changed.

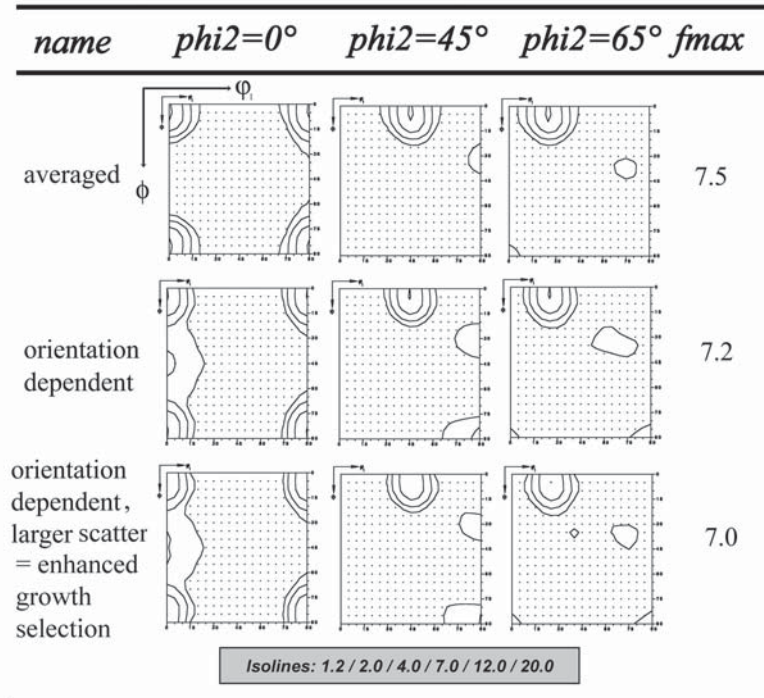


Fig. 4.5: Simulated recrystallization textures as obtained under the influence of different distributed dislocation densities within the initial microstructure.

The dislocation density as initial parameter was shown to have a minor effect on the recrystallization texture evolution by recrystallization growth.

4.2.3 Influence of strain

In the following section the influence of the prior deformation degree on recrystallization is demonstrated. The strain which the material experienced during deformation causes various effects on the subsequent recrystallization behavior. First of all, the dislocation density modeled with GIA-3IVM+ increased with increasing rolling reduction. However, the effect of dislocation density on texture was already discussed in Sec. 4.2.2 and classified as negligible. The pre-deformation texture as input for the deformation simulations plays a certain role in the final appearance of the recrystallization textures as previously demonstrated (Sec. 4.2.1). Besides these effects, the consideration of strain involves also additional influences such as the activation of various nucleation sites and the locally computed nucleation densities (dependent on the interface / volume ratio). It is stressed that these effects during deformation occur always in combination and are thus presented in this section accordingly. A special focus was laid on the consequences for the nucleus textures as a function of the applied strain (see nucleation-relevant quantities Fig. 4.7). The deformation texture simulations were conducted under the assumption of plane strain of $\epsilon_{VM} = 0.2 - 2.3$ corresponding to rolling reductions of 20% - 90%. The investigated material was the previously introduced Al-1 wt% Mn alloy AA3103 (see also Chap. 9). A constant cellular automaton volume was assumed for the simulations at different rolling reductions. As to be expected, an increasing total dislocation density was obtained with increasing deformation

(Fig. 4.6). While the dislocation density in the cell interior increased with increasing deformation, it remained almost constant in the cell walls.

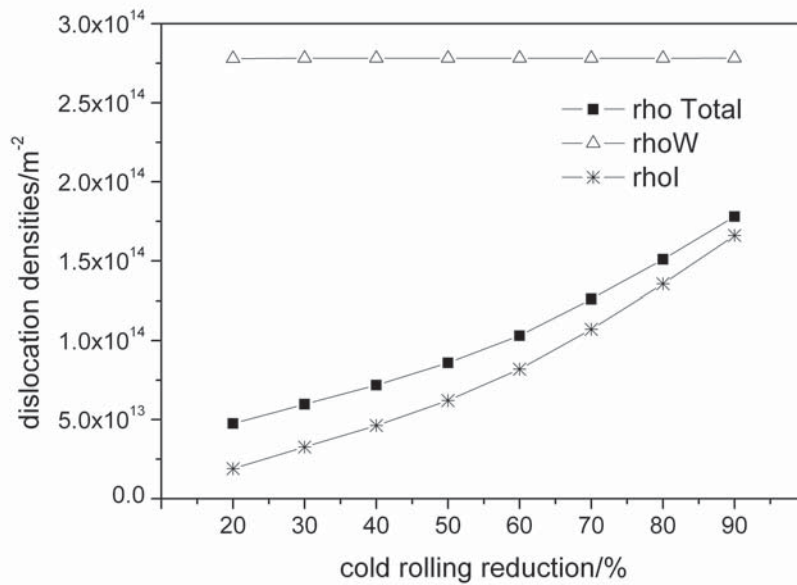


Fig. 4.6: Dislocation density evolution from GIA-3IVM+; the different types of dislocation densities in the wall, the cell interior and the total dislocation density depending on the cold rolling reduction.

The GIA-3IVM+ simulations were further analyzed with respect to sub-structural quantities to derive nucleation efficiencies during later recrystallization. Therefore, the nucleus spectrum was derived partly from an analysis of the GIA output (ReNuc [Crumbach 2006a]). The relevant parameters are the number of slip systems N_{GLS} activated during deformation, the in-grain misorientation gradient IGM and the critical shear relaxation $\varepsilon_{\text{crit}}^{\text{shear-relax}}$. The number of activated slip systems N_{GLS} during deformation is related to the substructure developed as dependent on orientation. The fact that a different subgrain size is evolved depending on the initial orientation can be interpreted with respect to grain boundary nucleation (GB) [Crumbach 2005]. The in-grain misorientation IGM was previously [Crumbach 2005] related to nucleation at transition bands (TB), and so was the critical shear relaxation $\varepsilon_{\text{crit}}^{\text{shear-relax}}$ to shear band nucleation (SB). The above outlined nucleation parameters and their change with increasing deformation degree are summarized in Fig. 4.7.

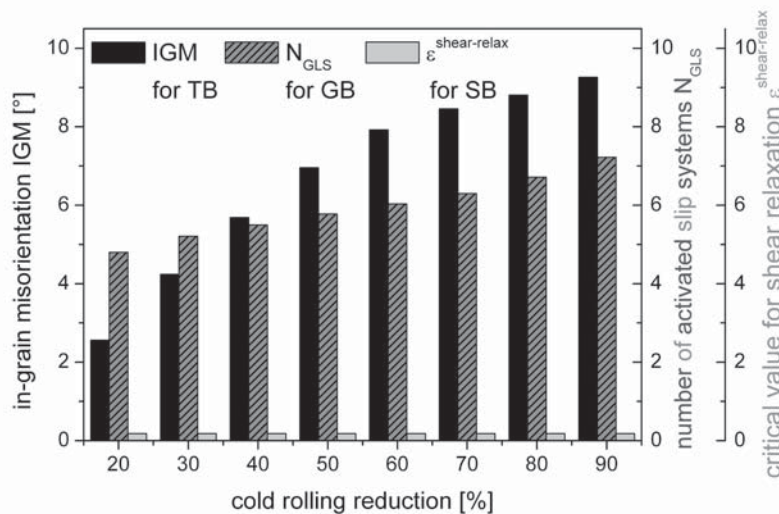


Fig. 4.7: Nucleation parameters as derived from GIA/ReNuc output. Represented are the critical numbers of activated slip systems N_{GLS} during deformation, the evolution of the critical in-grain misorientation IGM and the critical shear relaxation $\varepsilon_{\text{crit}}^{\text{shear-relax}}$. (TB = transition band nucleation, SB = shear band nucleation, GB = grain boundary nucleation).

It was found that with increasing deformation degree a higher number of activated slip systems N_{GLS} resulted. This number is closely related to the efficiency of an individual grain for grain boundary nucleation. Further, also the value for the in-grain misorientation IGM increased with increasing deformation degree (Fig. 4.7). With increasing deformation degree also higher critical misorientation gradients are required to initiate transition band nucleation in the respective grain. The value for shear band nucleation, the critical shear relaxation, was kept constant in all cases at 0.18 as suggested in [Crumbach 2005] for cold rolling. More detailed information on the ReNuc model can be found in Sec. 3.9, respectively in [Crumbach 2005, 2006a]. Beside the changes in nucleation quantities also the grain shape changed during deformation. The increasing rolling reduction lead thus to a higher grain interface area and therefore to a higher nucleus number (Fig. 4.8), for instance in case of transition band (TB) nucleation.

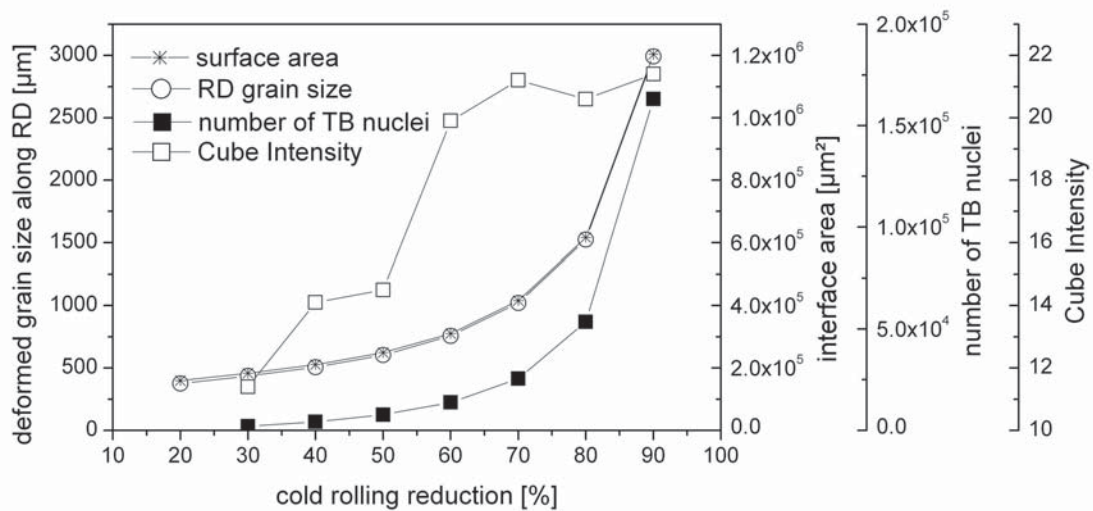


Fig. 4.8: Nucleus numbers and Cube texture intensities of the nucleus textures as a function of the deformation degree and in relation to the grain size, respectively grain interface evolution. All calculations were carried out using the Cube/S-Sort routine.

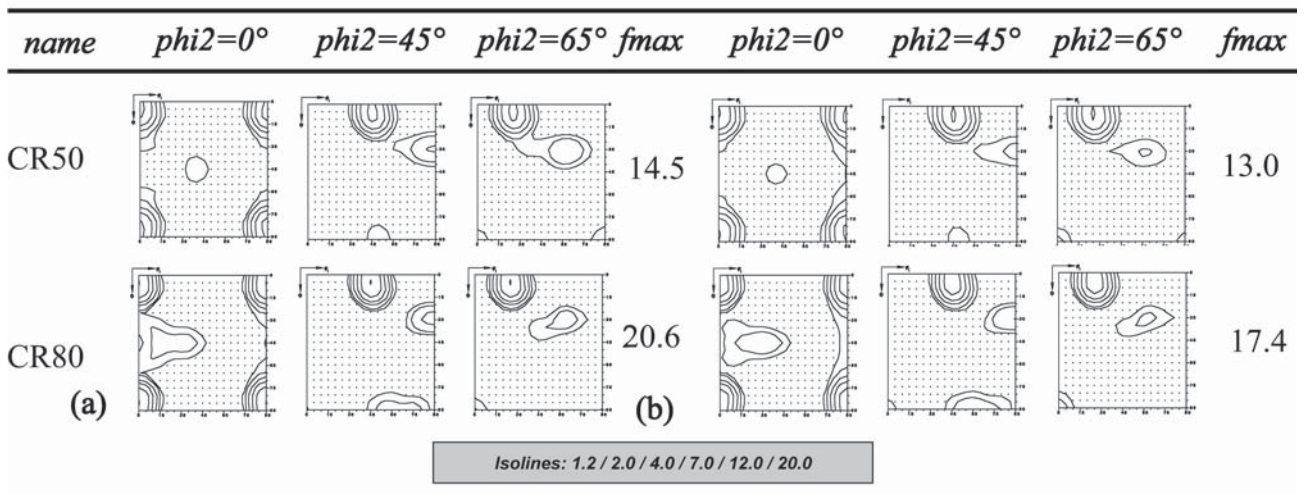


Fig. 4.9: (a) Nucleus textures and (b) recrystallization textures for two rolling reductions in the alloy AA3103. The corresponding recrystallization simulations were carried out for 50% and 80% cold rolling deformation. The calculations are based on an initial data set for the alloy AA3103.

Correspondingly, the main recrystallization texture component, the Cube component, showed a strong increase with increasing rolling reduction. After 70% cold rolling the Cube intensity reached a saturation value, which remained unchanged with further increasing deformation. The modeled

nucleus textures showed a high similarity to the simulated recrystallization textures. In Fig. 4.9 some nucleus and recrystallization textures are shown exemplarily. With increasing deformation the intensities of Cube as well as of the deformation texture components are slightly increased.

4.2.4 Influence of alloy composition

In this chapter mostly an Al-1 wt% Mn alloy was considered for parameter studies. In order to demonstrate that the alloy composition can have a significant influence on recrystallization texture evolution, in this section the recrystallization texture evolution in an AlFeSi alloy (8XXX series) is discussed. The material was taken from an industrial processing cycle and was available for different rolling reductions (50%, 70%, 90% and 95%). The experimental and with GIA-3IVM+ simulated deformation textures are shown in Fig. 4.10. More detailed information on the deformation texture simulations and work-hardening predictions can be found in [Schäfer 2009a, Mohles 2008].

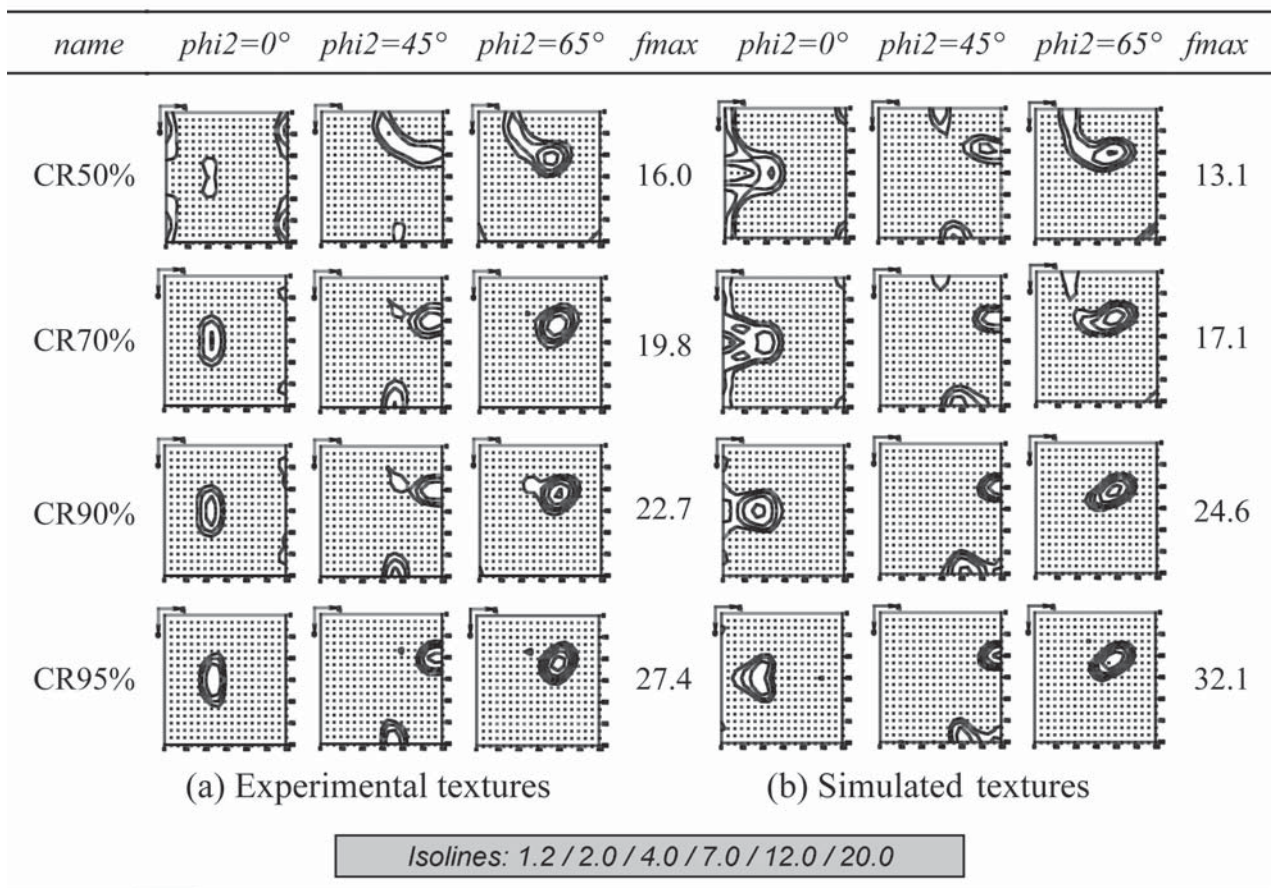


Fig. 4.10: Experimental (a) and simulated (b) macro textures close to the sheet center layer after cold rolling of the alloy AA8079L.

Based on the modeled deformation texture simulations, recrystallization was modeled with the recrystallization model CORE for the rolling reductions 50%, 70% and 90%. For comparison with modeled recrystallization textures the recrystallization textures of the fully recrystallized samples were measured near the sheet center layer. The results are shown in Fig. 4.11a. Beside an approximately constant intensity of the Cube components, the simulated and experimental textures displayed an increasing intensity in the S/R-component with increasing cold rolling reduction.

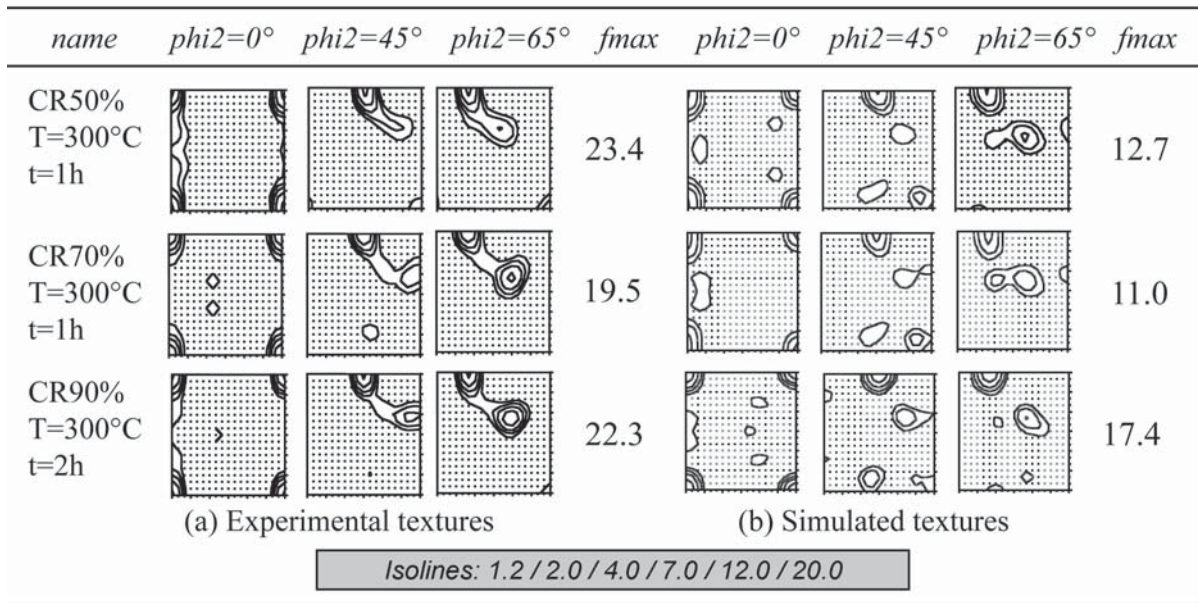


Fig. 4.11: Experimental (a) and simulated (b) macro textures for the sheet center layer after recrystallization in the alloy AA8079L for different initial rolling reductions.

The modeled textures showed basically the Cube texture component, however with a lower intensity in the case of the recrystallization texture after 50% cold rolling. Further, the S/R component was strengthened with increasing rolling reduction, which is in good agreement with the experimental observations (see also skeleton plots in Fig. 4.12a). Compared to the experimental textures, the modeled ones showed a slightly too weak intensity of the Cube component (Fig. 4.11a, b).

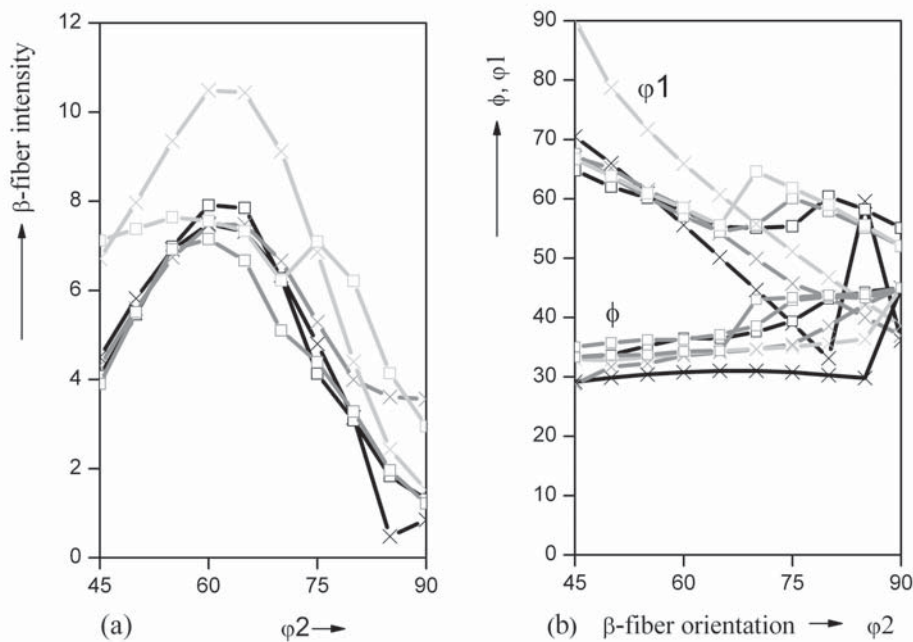


Fig. 4.12: (a) Intensity and (b) orientation of the β -fiber of experimental and simulated macrottextures for T=300°C. Black: CR50%; grey: CR70%; light-grey: CR90%; X EXP □ SIM

In contrast to the recrystallization texture simulations in the AA3103 alloy, the AA8079L alloy showed certain amounts of the S/R recrystallization texture component, which could be predicted with the chosen modeling setup as indicated in Figs. 4.11 and 4.12. Hence, the CORE model is able to account for different material behavior through the predictions of deformation textures with GIA.

4.2.5 Influence of particle-stimulated nucleation

The influence of particle-stimulated nucleation on the recrystallization texture can be in general described as a randomization of the texture [Humphreys 2004]. In some cases, e.g. for low heating rates (Chap. 8), specific texture components such as P- and ND-rotated Cube orientations occur, which are typically found in the presence of second-phase particles [Engler 1996]. The general influence of a high or low fraction of second-phase particles on texture as modeled with the CORE model is shown in Fig. 4.13b and c. Fig. 4.13a indicates the experimentally measured nucleation spectrum from particle-stimulated nucleation in the alloy AA3103 (see also Chap. 5).

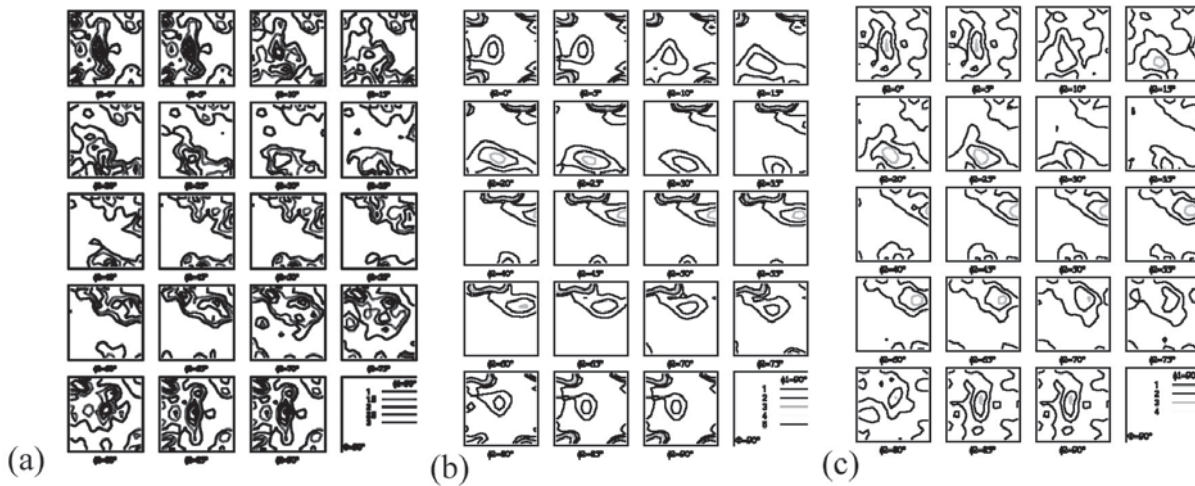


Fig. 4.13: (a) Nucleus orientations (ODF) related to particle stimulated nucleation – measured from experiment, (b) simulated recrystallization texture for a particle volume fraction of 0.01%, (c) simulated recrystallization textures for a particle volume fraction of 1%.

The higher the constituent particle volume fraction the more pronounced the occurrence of deformation-zone related texture components (Fig. 4.13c). Related to the appearance of texture components originating in the deformation zone is a drop in the overall texture intensities due to a randomization of the texture. This is in good agreement with experimental observations [Engler 1996, Humphreys 2004]. The occurrence of P- and ND-rotated Cube texture components is discussed in more detail in Chap. 8, since they are also observed in case of low constant heating rates.

4.2.6 Influence of Zener drag

Beside constituent particles, also finer dispersoids can be present prior to recrystallization. The presence of small particles leads in general to an interaction with the moving grain boundaries. It is further possible that such small particles are precipitated concurrent to recrystallization. This leads in the course of recrystallization inevitably to the pinning of grain boundaries and thus to a strong hindrance of the recrystallization process. In very severe cases recrystallization can be partially or completely inhibited. This leads to partially recrystallized microstructures, respectively recrystallization textures as indicated in Fig. 4.14. With increasing Zener drag the obtainable recrystallized volume fraction was lowered leading to an increasing amount of retained deformation texture component (i.e. orientations along the β -fiber). As to be expected, the strongest Cube component was found after 100% recrystallization. Depending on the Zener drag any texture from fully deformed to fully recrystallized can be obtained. This inhibition of recrystallization due to Zener drag can of course be only temporary, e.g. if the dispersoids developed during concurrent precipitation coarsen during further annealing and thus lose their retarding effect on grain boundary motion. This leads still to a fully recrystallized microstructure and texture, even if

recrystallization was slowed down or ceased for some time. Such effects are discussed later on in more detail (Chap. 7).

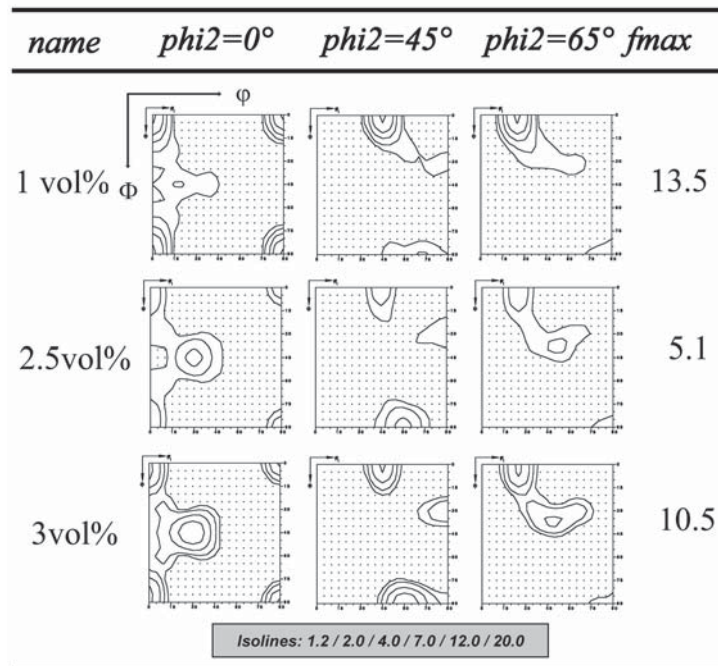


Fig. 4.14: Influence of constant Zener drag for different volume fraction of dispersoids. The material data set is based on AA3103 after 50% cold rolling reduction.

The observed partial recrystallized textures in Fig. 4.14 were obtained without the consideration of orientation-dependent Zener drag. In contrast to the observations in Fig. 4.14, also an increased Cube texture intensity in case of strong precipitation can be found in literature [Vatne 1996b]. However, those results referred to fully recrystallized material in all considered cases, and the underlying mechanism of Cube texture formation was different from the one considered here. The experimental results actually suggested an orientation-dependence of the Zener drag, which was not considered in the present simulations.

4.2.7 Influence of the arrangement in GIA-aggregates

Within the deformation model GIA a grain neighborhood is assigned. This misorientation distribution is, however, restricted to the considered individual 8-grain aggregate. The arrangement of grain aggregates in the GIA model suggests that this specific arrangement should be further kept during the recrystallization simulation, since the local deformation of a grain depends on its local environment in the cluster of the eight grains. It was described in [Crumbach 2005] that this arrangement in aggregates should be kept and transferred to the recrystallization model CORE, since significant effects were expected on recrystallization texture evolution but it remained untested. Hence, the initial microstructure in CORE should be built up of those aggregates, without destroying the local neighborhood. The effect of that local neighborhood was modeled with CORE. Simulations were carried out with a random arrangement of the 4000 initial microstructure grains. Further simulations were done with a random arrangement of the 500 “8-grain aggregates”. The individual “8-grain-aggregates” as obtained from GIA were hereby not destroyed. However, it was proven by various examples that the local arrangement, i.e. the grain neighborhood in the grain aggregate had a negligible influence on the texture and microstructure evolution. Even if the local nucleation efficiencies depend on this local arrangement, the global effect was negligible. Two reasons can be identified. Firstly, grain boundary nucleation is the only (out of 4) nucleation mechanism that is sensitive to the arrangements within the aggregates and thus the local neighborhood. And secondly, the number of interfaces within the GIA-aggregates (12) is smaller

than the number of outer surfaces (24). Hence, this effect is significantly weakened by nucleation at the external interfaces of the “8-grain-aggregate”.

For future improvements of the model, it is however strongly recommended that local gradients, e.g. at grain boundaries are considered. This requires an exact description of the grain neighbor relations (misorientation distribution function), since they influence the local evolution of such orientation gradients. In this context, the maintenance of the GIA-aggregates might be reasonable.

4.3 Influence on Recrystallization Kinetics

It is of interest to know, whether a material will recrystallize and by how much it will recrystallize under certain conditions, such as a given time-temperature profile (batch annealing cycles, coil cooling etc.) as used in industry. The evolution of the recrystallized volume fraction over time for homogeneous and isotropic conditions can be correctly described by the JMAK theory. The validity of the used cellular automaton was therefore tested by comparison with the predictions of the JMAK theory (Fig. 4.15). In the following section various effects on the recrystallization behavior are discussed. Such effects can have different origin. They are caused by different process parameters (temperature, heating rates etc.), material parameters (mobilities) or result from assumptions, respectively quantities considered in the CORE model (grain shape, nucleus number, nucleation rate, distribution of dislocation densities, distribution of inhomogeneities in the microstructures, etc.).

4.3.1 Comparison with JMAK theory

In order to determine the validity of the model, the outcome of the simulations of the recrystallization kinetics were compared with the classical JMAK theory (see Chap. 2) under equivalent conditions. The JMAK theory rests on some simplified basic assumptions. The new phase is nucleated by tiny “seed nuclei” already present in the deformed state. For the so-called site saturation case the number of nuclei are all present at time $t=0$ and are randomly distributed throughout the volume. The stored energy and mobility are assumed to be constant and isotropic. The overall growth rate is only influenced by the stored energy comprised by an average dislocation density. Effects from recovery and precipitation were switched off.

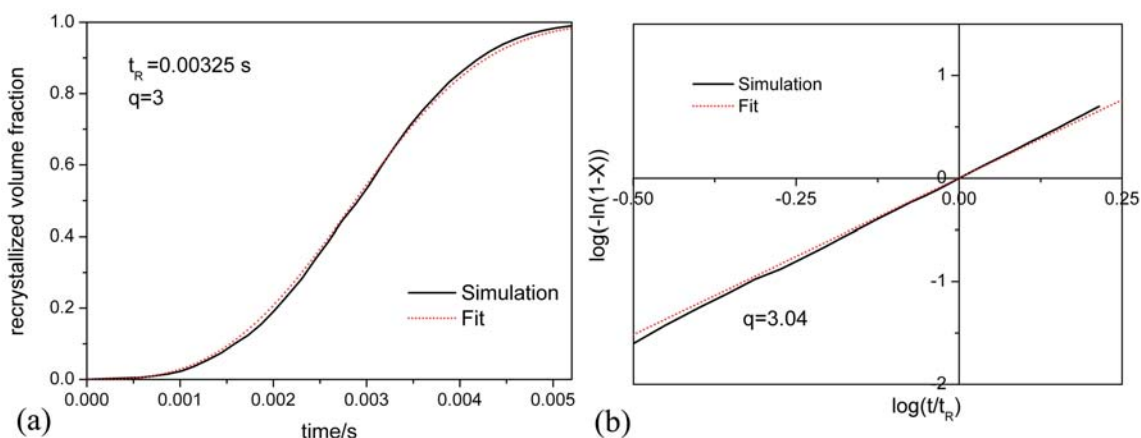


Fig. 4.15: Comparison of the simulation results with the prediction according to JMAK theory. (a) Recrystallization kinetics and (b) the corresponding Avrami plot. Equivalent conditions to the JMAK theory were assumed, such as: random distribution of nucleation sites, random oriented nuclei, an average homogeneous dislocation density, isotropic growth, and no recovery and microchemistry effects.

Fig. 4.15b shows that the Avrami exponent q obtained from the simulation shows a good agreement with JMAK theory for the considered case of isotropic growth and site saturation.

4.3.2 Influence of the number of nuclei

Since the recrystallization model used in this work is a pure growth model, the number and texture of nuclei need to be provided separately. For this purpose nucleation models are used as described in detail in Chaps. 3, 5. The nucleus number is determined indirectly by different processes and influences significantly the recrystallization kinetics and the final grain size, respectively the grain size distribution. Since the number of nuclei is calculated in dependence on the interface area, it is changed as soon as the deformation degree or the initial grain size is modified. The nucleus number depends further on the stored dislocation density during deformation, as well as on the local neighborhood. Other influences on the nucleus number can be caused by additional nucleation sites (such as at particles) or by a strong Zener drag during initial stages of recrystallization. Because of this variety of influences in the following simulations in Fig. 4.16 only shear band nucleation was considered, since those nuclei are distributed randomly within the grain. Nucleation was assumed to be site saturated. The nucleus density was assumed to be the same in all grains of the microstructure, and the efficiency for shear band nucleation in each grain was assumed to be one. With increasing number of nuclei per unit volume, the kinetics were accelerated. This is due to the faster consumption of deformed volume with increasing number of nuclei. An increase in the nucleus number is connected with an increase in the total interface area per unit of time and therefore a faster consumption of the still unrecrystallized volume (Fig. 4.16). The Avrami exponents observed in such case remained unchanged.

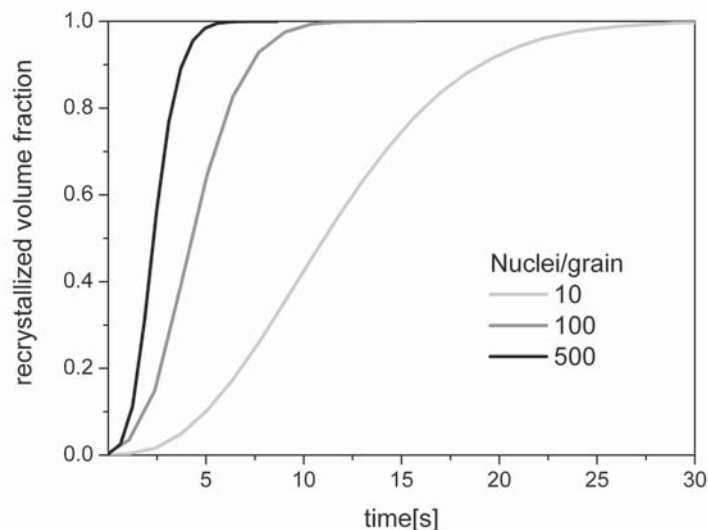


Fig. 4.16: Influence of the number of nuclei per grain on the recrystallization behavior.

In real microstructures, nucleation is not restricted to shear band nucleation only and does not appear homogeneously throughout the microstructure. Nucleation can, in general, occur also at preferred nucleation sites, such as at prior grain boundaries. The nucleus density is then directly related to the interface area. Thus, the grain size before deformation should have a pronounced effect on the recrystallization kinetics. This was tested by the use of different GIA calculations for 70% plane strain deformation in AA3103 with varying initial grain size. Subsequently, recrystallization was modeled with CORE for a representative volume. Naturally, a larger amount of interface area was obtained in the case of small pre-deformed grain sizes. Hence, with an increasing pre-deformed grain size, the interface area for nucleation is reduced and a lower nucleus number results for the consideration of grain boundary nucleation, of course. This corresponds to the tendency already presented in Fig. 4.16. Beside the pre-deformed grain size also the shape of the deformed grains prior to recrystallization could have an effect on the recrystallization kinetics. This is demonstrated in the following section.

4.3.3 Influence of the shape of the deformed grains

During deformation (not restricted to rolling only) very anisotropic grain structures can be obtained. With increasing deformation degree the surface to volume ratio increases significantly, in case rolling is considered as deformation type. This can have serious effects on the recrystallization behavior, because the nucleus number is related to the interfacial area. This investigation was confined to grain boundary nucleation, since for this mechanism the nucleus density is dependent on the grain boundary area. As described earlier grain boundary nucleation occurs only in such grains where the efficiency for grain boundary nucleation was larger than zero, and the dislocation density is higher than in the adjacent grain. The combined effect of an increasing surface leading to higher nucleus numbers and the heterogeneously occurring nucleation itself is demonstrated in Fig. 4.17.

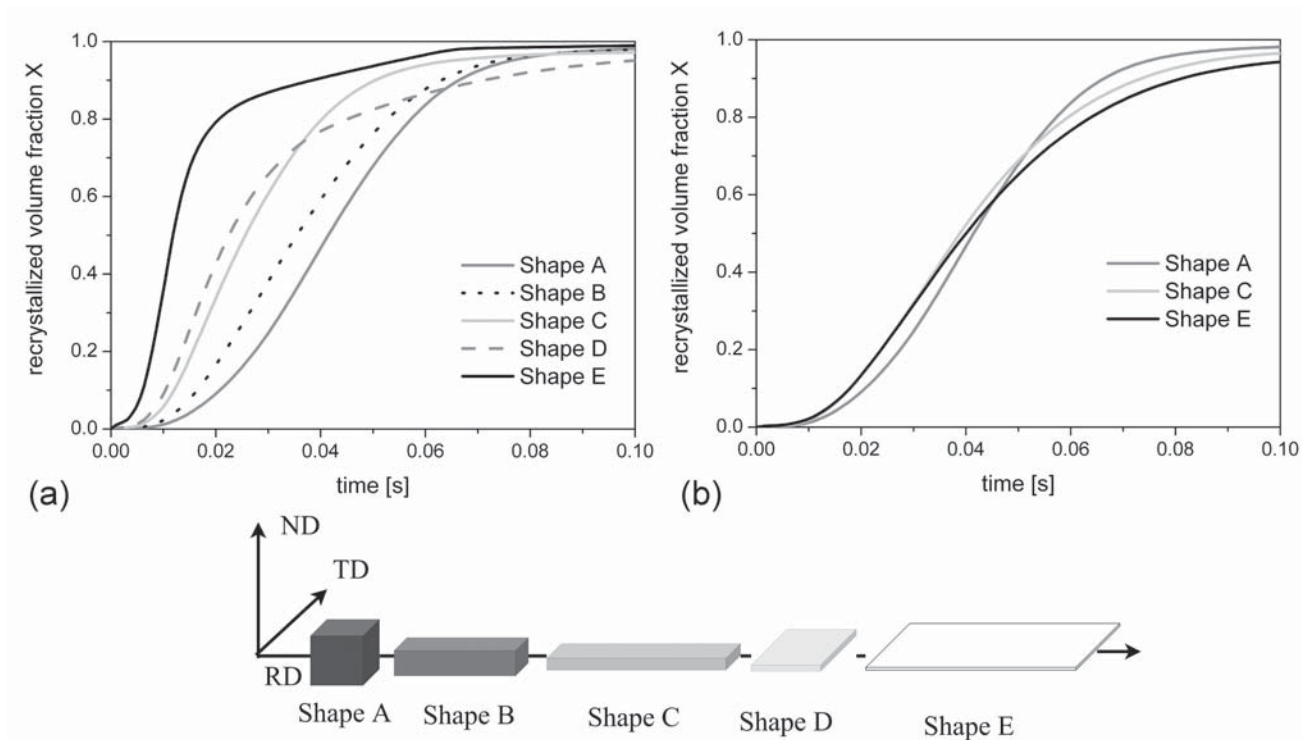


Fig. 4.17: Influence of grain shapes on recrystallization kinetics (only considering grain boundary nucleation), unvaried material data set of AA3103, 70% cold rolling reduction. (a) For a constant volume and varying interface area, (b) for a constant volume / interface ratio.

As can be seen from Fig. 4.17, recrystallization proceeded the slowest for an isotropic grain size, since it owned the smallest total surface. The more anisotropic the shape the larger the surface area and hence the nucleus number in those grains providing grain boundary nuclei. Since the nucleus density was zero in some grains and very high in other grains, this lead to a very inhomogeneous distribution of the nucleus density. Accordingly, the recrystallization kinetics were fast at the beginning of the simulation, since those grains where nucleation occurred were consumed first. Later on also those areas were consumed which did not cause grain boundary nucleation. In these areas recrystallization proceeded comparatively slow (slower recrystallization kinetics towards the end) due to the larger distances over which a nucleus needed to grow. This effect can be neglected, if nucleation occurs more homogeneously throughout the microstructure. In general, if an Avrami exponent is interpreted from a JMAK fit like in Sec. 4.3.1 a decrease with decreasing growth directionality is found.

4.3.4 Influence of the nucleation rate

In the previous sections site saturation had been assumed. In this section, the focus is laid on the variation of the nucleation rate. The case of different growth rates will be considered later on separately. For aluminum alloys the consideration of site saturated nucleation is in general valid for isothermal heat treatments. However, for industrial applications, in particular non-isothermal heat treatments are commonly in use leading to nucleation rates during recrystallization. A higher nucleation rate can be caused, for instance, by the fact that deformation in the material is not homogeneous and thus, locally high strains developed. Such preferred sites for nucleation can be found, e.g. in the vicinity of large particles. The high stored dislocation density and the high misorientation promote in general an early nucleation before other nucleation sites are activated.

Against this background the effect of different nucleation rates was investigated with the CORE model. It was shown that a different nucleation rate had a strong influence on the recrystallization kinetics as can be seen in Fig. 4.18a.

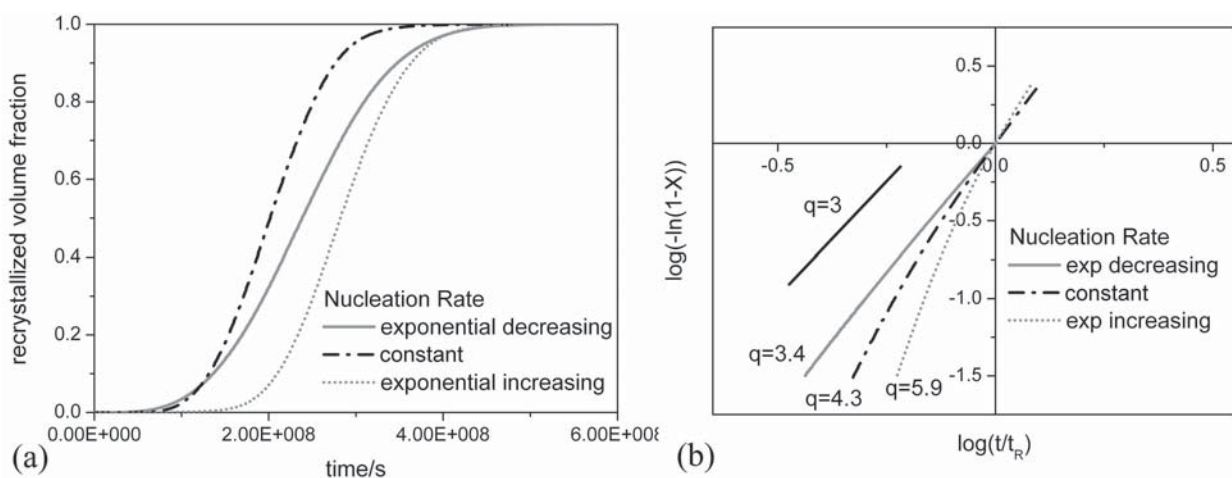


Fig. 4.18: (a) Recrystallization kinetics depending on the nucleation rate; (b) Avrami-plot for different nucleation rates, the slope $q=3$ is displayed for comparison.

It was found that with a constant nucleation rate in three dimensions, the Avrami exponent agreed very well with the exponent four as obtained from JMAK theory. An exponentially decreasing nucleation rate yielded similar Avrami exponents as predicted from the JMAK theory for the case of a constant nucleus number and hence, a nucleation rate of zero. The effect of heat treatments with linear heating rates and thus effective nucleation rates on recrystallization is demonstrated in Chap. 8.

4.3.5 Influence of dislocation density on growth

The driving force for static primary recrystallization is the energy stored in the microstructure after deformation. From the deformation model GIA-3IVM+ these quantities are available resolved on grain scale. In the recrystallization model CORE these grain-dependent stored energies in terms of dislocation densities are considered. The nucleus growth during recrystallization is determined by the mobility and the driving force and hence, strongly affected by the stored energy which is proportional to the dislocation density. This leads to different growth rates within different grains. In this section the effect of the spatial distribution of dislocation density on recrystallization is demonstrated. Besides an average dislocation density also orientation dependent stored dislocation densities were investigated. The scatter of the orientation dependent stored energies was varied by a factor of two. The corresponding dislocation density distributions were already presented in Fig. 4.4.

An orientation dependent stored dislocation density leads to an earlier onset of recrystallization. This is a direct consequence of the scatter of the dislocation densities, since with increasing scatter, comparatively lower but also higher dislocation densities can be found in the spectrum. In those grains with the highest dislocation densities the incubation time is the shortest and recrystallization is initiated earlier. However, the overall effect compared to other influences on recrystallization kinetics presented in this section was negligible.

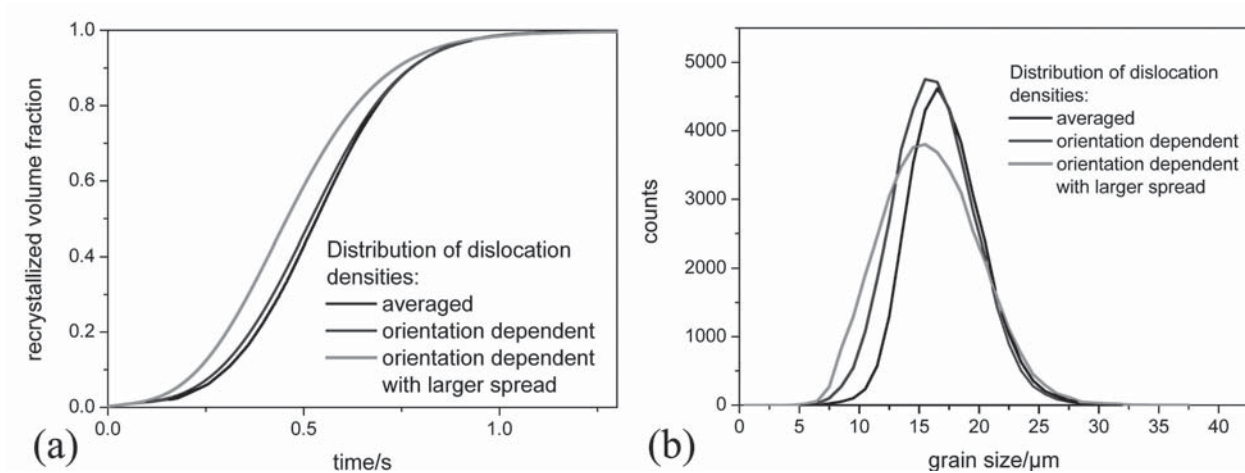


Fig. 4.19: (a) Recrystallization kinetics as influenced by different initial dislocation density distributions, (b) the corresponding effect on the grain size distribution. Data set for 70% cold rolled AA3103 alloy annealed at $T=350^{\circ}\text{C}$ (Chap. 9).

From the grain size distribution in Fig. 4.19b it can be seen that especially the orientation-dependent stored dislocation densities with the wider scatter lead to a wider grain size distribution. This is because some grains were favored sites for nucleation and were consumed fast during recrystallization whereas other grains had a higher resistance against recrystallization. In sum a wider distribution of grain sizes was obtained. This is in agreement with literature [Jensen 1992]. Jensen et al. modeled with their component model the microstructure evolution in 90% cold rolled aluminum. They assumed three texture classes (Cube, random and rolling texture components) and different growth rates as measured from experiment. The simulations were carried out under consideration of site-saturation. They found that the consideration of three different texture components over a single one, lead to the prediction of the desired wider grain size distributions comparable to experiments.

4.3.6 Influence of strain

During rolling two influences on the recrystallization kinetics can be identified. First of all, an increasing dislocation density is introduced with increasing deformation degree (Secs. 4.3.2, 4.3.5). Second, the increase of the dislocation density is further accompanied by an increase of the interface area with increasing rolling reduction. The total interface area is important for grain boundary nucleation and directly influences the nucleus number originating at these sites (Sec. 4.3.3). However, during rolling deformation these effects occur at the same time. With increasing rolling reduction an increasing dislocation density is combined with an increasing surface to volume ratio. To discuss the effect of strain, various GIA-3IVM+ calculations with different cold rolling reductions in the range of 20% up to 90% thickness reduction were carried out. Subsequently recrystallization was simulated based on the different deformation data sets. It was found that in the case of 20% cold rolling the model predicted no recrystallization at all, since the initial dislocation density was too low to initiate recrystallization. This agrees very well with literature [Gottstein 1998, Humphreys 2004] where for the initiation of recrystallization beside a critical temperature also a critical minimum deformation is required.

The simulated recrystallization kinetics indicated that with higher rolling reductions the kinetics were accelerated due to higher nucleus numbers and higher driving forces (Fig. 4.20a). Further, with increasing cold rolling reduction the Avrami exponent decreased (Fig. 4.20b). This is reasoned as follows. For low rolling reductions the initial grain volume is sufficiently extended in all three dimensions so that nucleus growth can proceed isotropic. For higher rolling reductions, however one grain dimension (in normal direction) becomes very small so that the grains can basically grow in the two remaining directions. Hence, a decreasing Avrami exponent with increasing rolling reduction is obtained. This behavior is however restricted to the deformation type rolling, and is for instance not true for channel die experiments.

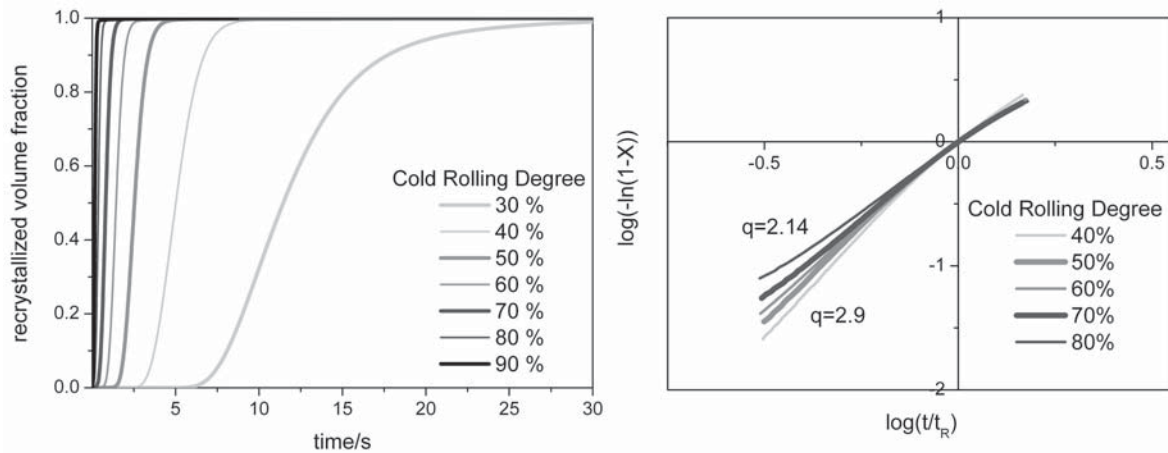


Fig. 4.20: (a) Recrystallization kinetics depending on the degree of deformation by cold rolling obtained with CORE. The influence of recovery was considered. The initial simulation data set is based on the material AA3103. (b) Avrami plots for different cold rolling reduction.

4.3.7 Influence of inhomogeneities during growth

The growth rate G during recrystallization as observed from experiments is in general not isotropic. Jensen et al. [Jensen 1995] observed in aluminum and copper that the Cube orientation had a higher growth rate than compared to other orientations. Besides variations in the growth rate also locally varying nucleus numbers N are observed in experiments which have their origin in structural inhomogeneities [Humphreys 2004]. The nucleus number N and the growth rate G depend both on the previous stored dislocation density and thus occur in combination only. The simulations in the present section show this combined effect of local varying growth rates G and nucleus number N on the recrystallization kinetics.

The dependency of the nucleus number on dislocation density in the CORE model is such that in regions with higher dislocation density automatically a larger nucleus number is calculated. This resulted in a locally faster consumption of the unrecrystallized microstructure. Further, the growth itself is influenced by the locally stored energy, which can be reduced during an annealing treatment by recovery as observed from experiments. Therefore, this section mainly demonstrates the effects of differences in the local driving force.

As initial parameter set for the simulations the already earlier introduced material data for AA3103, was used. As standard of comparison a plane strain deformation of $\varepsilon_{VM}=1.2$ was simulated corresponding to 70% rolling with GIA-3IVM+. In this case, the GIA predicted dislocation densities remained unmodified for the modeling of the curve (Fig. 4.21(e)). For the other simulations (Fig. 4.21 (a)-(d)), certain amounts of initial microstructure grains were provided with a higher growth rate G , respectively nucleus density N . For this purpose, the dislocation densities from the initial data set (curve (e)) were enlarged by a factor of 10 in the respective volume fraction. Those grains were then randomly distributed in between the other unmodified, deformed grains. The simulation results are presented in Fig. 4.21.

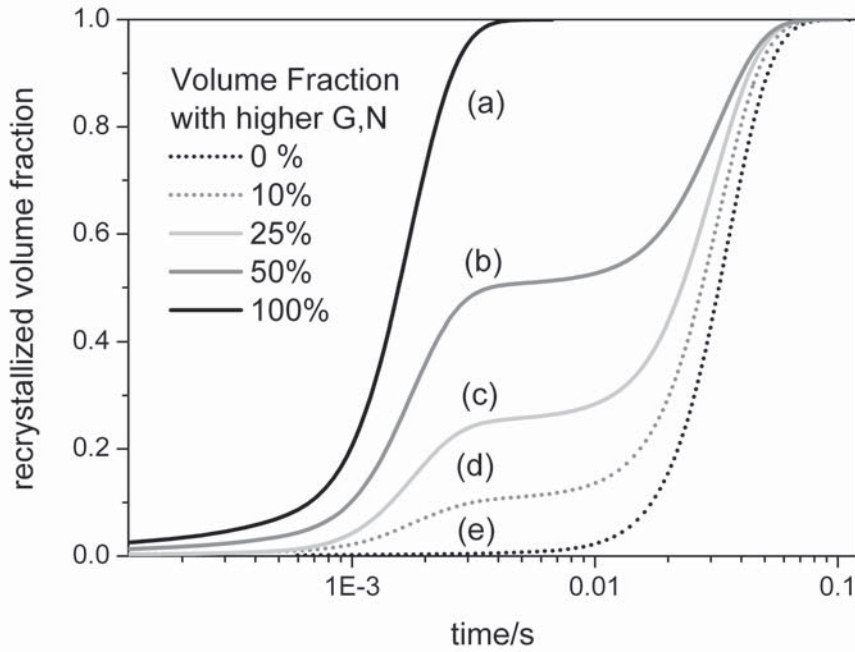


Fig. 4.21: Recrystallization kinetics dependent on the amount of volume with a higher nucleus number N and a higher growth rate G ; (a) 0% volume with higher G,N , (b) 10% (c) 25% (d) 50% (e) 100%. The cases (a) and (e) correspond to homogeneous growth conditions.

The simulations with a homogeneous nucleus number and growth rate (0%, 100%) showed the expected S-shaped curve. In between, several curves can be found which show a transition between the two S-shaped curves (0%, 100%). The areas with a higher growth rate G and nucleus density N recrystallized fast, and after that the overall growth rate slowed down during the consumption of the remaining volumes. The transition between the two ideal cases (0%, 100%) happened after the respective volume fraction was consumed. These results are in good agreement with literature [Hesselbarth 1992].

The structural inhomogeneities in a real material are, however, not so homogeneously distributed as assumed in the previous example by a random distribution (Fig. 4.21). It is more likely that there are preferred sites such as grain boundaries or transition bands. To account for this effect as well, in the following the structural inhomogeneities comprising a locally higher driving force and higher resulting nucleus number were distributed within the microstructure in different ways (Fig. 4.22). The cases (b)-(d) in Fig. 4.22 represent the same volume fraction with higher nucleus number N and growth rate G . The effect of the different distribution on recrystallization kinetics is demonstrated in Fig. 4.23.

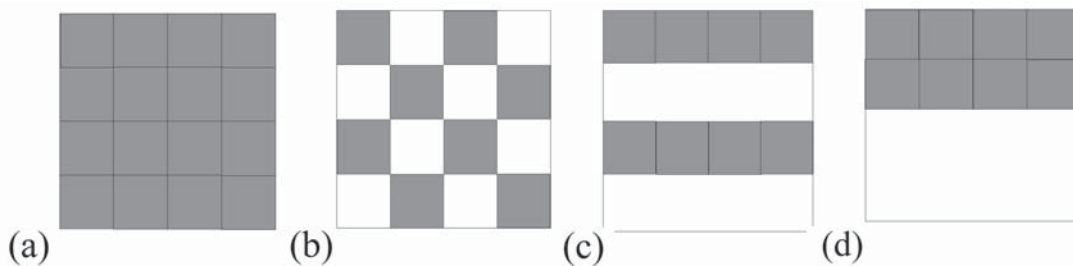


Fig. 4.22: Spatial distribution of areas with high (grey) and low (white) dislocation density; (a) homogeneous distribution (high G, N), (b) 3D chess-board distribution, (c) fine-layered structure (d) coarse-layered structure.

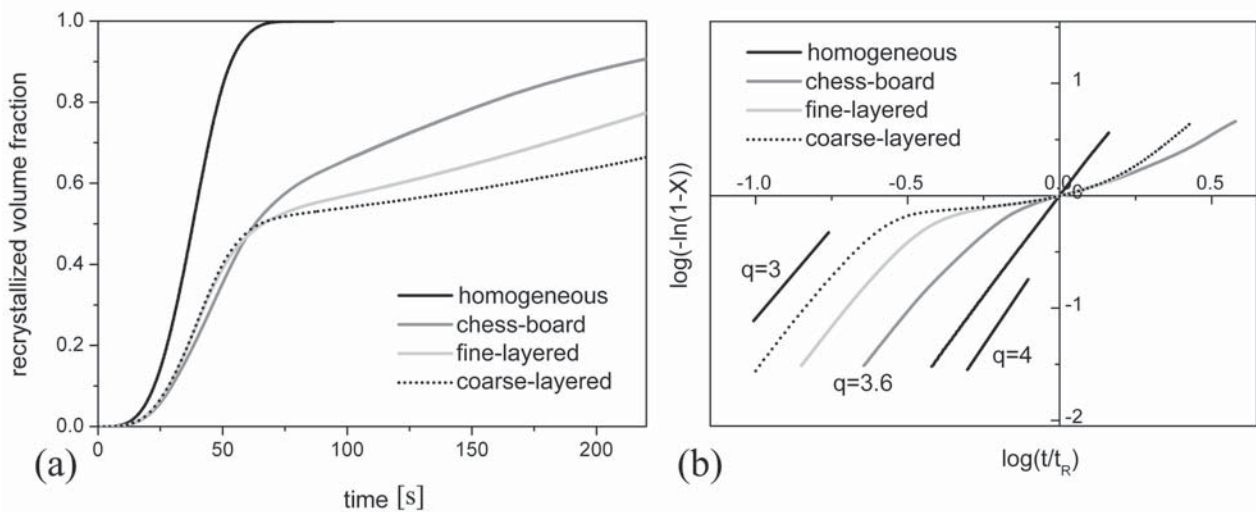


Fig. 4.23: Recrystallization kinetics in dependence on the spatial distribution of volumes with high and low dislocation density. (b) Corresponding Avrami plot in dependence on the spatial distribution of volumes with high and low dislocation density.

The effect of a chess-board distribution of structural inhomogeneities was not as pronounced as in the other cases (layered structures, Fig. 4.23a). But still a significant change in the recrystallization kinetics was observed. This can be also observed from the Avrami plot in Fig. 4.23b as indicated by the two different slopes for the different cases. At the beginning of the simulations the fastest growing grains dominated the recrystallization process; towards the end the more slowly growing grains took over. Such a recrystallization behavior corresponds to observations from real materials. It is stressed here that a certain minimum spatial resolution of the cellular automaton is required to capture such local variations of growth.

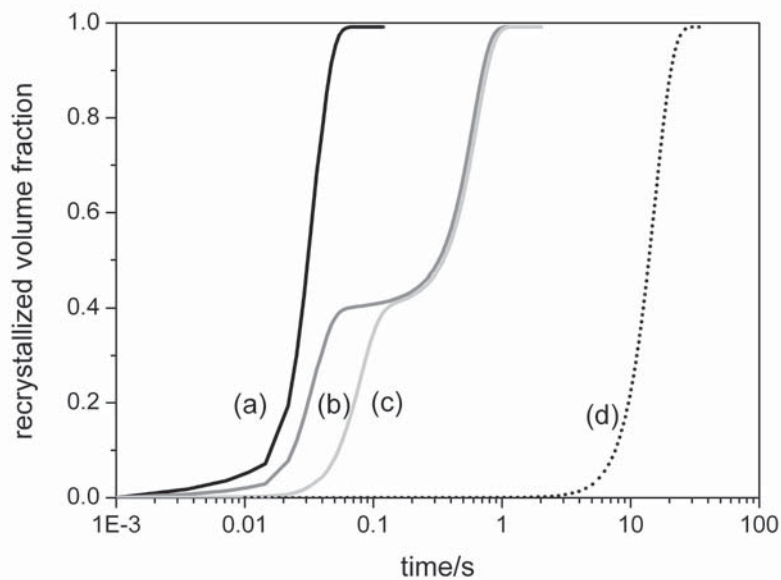


Fig. 4.24: Recrystallization kinetics showing the influence of a microstructure gradient; (a) no gradient with high growth velocity G and nucleus number N , (b) strong gradient, (c) weak gradient, (d) no gradient with low growth velocity G and nucleus number N .

The above presented inhomogeneous distribution of nucleus densities and driving forces is of technical relevance during sheet metal fabrication. Starting from break-down rolling after casting and homogenization, especially second-phases / segregations are accumulated in the material close to the center plane of the sheet. During break-down rolling and hot rolling an additional temperature

gradient from the sheet surface to the sheet center is introduced into the material providing different conditions for recrystallization and recovery. Those through-thickness gradients can be described in a similar fashion as above. The effect on recrystallization kinetics of such gradients is shown in Fig. 4.24. The corresponding microstructure changes in the presence of such gradients are presented in Fig. 4.25.

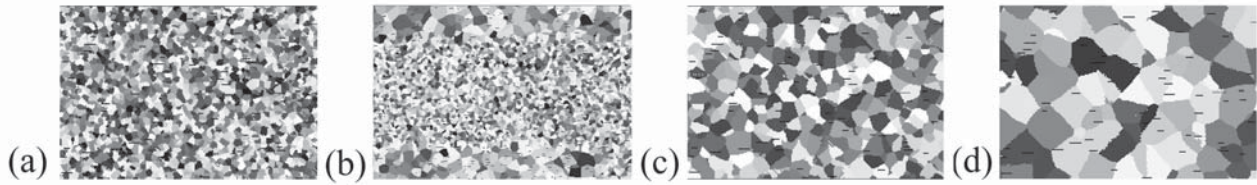


Fig. 4.25: Final microstructures after recrystallization in a through-thickness deformation structure gradient. Figures (b) and (c) show a gradient from the surfaces to the center; (a) and (d) show no gradient but different grain sizes.

Gradients such as demonstrated in Fig. 4.25b can be found in real materials such as e.g. in AA8079L after 50% cold rolling and subsequent annealing [Schäfer 2009a] (Fig. 4.26).

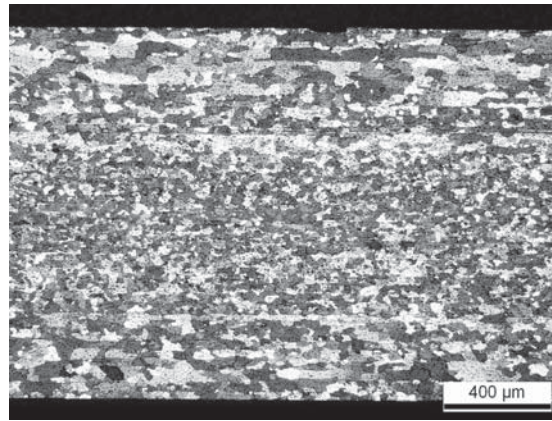


Fig. 4.26: Microstructure gradient after recrystallization of a 50% cold rolled AL-Fe-Si alloy AA8079L.

4.3.8 Influence of mobility on growth

Cellular automata models as applied in the present work for recrystallization are pure growth models. In CORE the growth rate v is described by the product of grain boundary mobility m and driving force p (see Chap. 3). The mobility depends according to Eq. (4.1) on the activation energy Q as

$$m_i = m_{0,i} \cdot e^{-\frac{Q_i}{kT}} \quad (4.1)$$

where m is the mobility, m_0 the preexponential factor, Q the activation energy, and i indicates the growth regime ($i = \text{GS, HAGB, LAGB}$). For the mobility different misorientation regimes are distinguished. A low mobility level is assumed for low-angle grain boundaries (LAGB), a medium mobility for high angle grain boundaries (HAGB), and the highest mobility was associated with $40^\circ < 111 >$ misorientations to take growth selection (GS) into account, which is very pronounced in aluminum alloys. The influence of the activation energy for grain boundary mobility at constant preexponential mobility factor is displayed in Fig. 4.27. In this case the same activation energy was assumed for misorientations in the different misorientation regimes.

For constant activation energy the recrystallization kinetics were accelerated by a higher temperature as indicated in Fig. 4.27. The change of the temperature for constant activation energies is equivalent to a reciprocal change of the activation energies. With decreasing activation energy, the recrystallization kinetics shifted to shorter annealing times, which is visualized as a parallel shift on a logarithmic time axis.

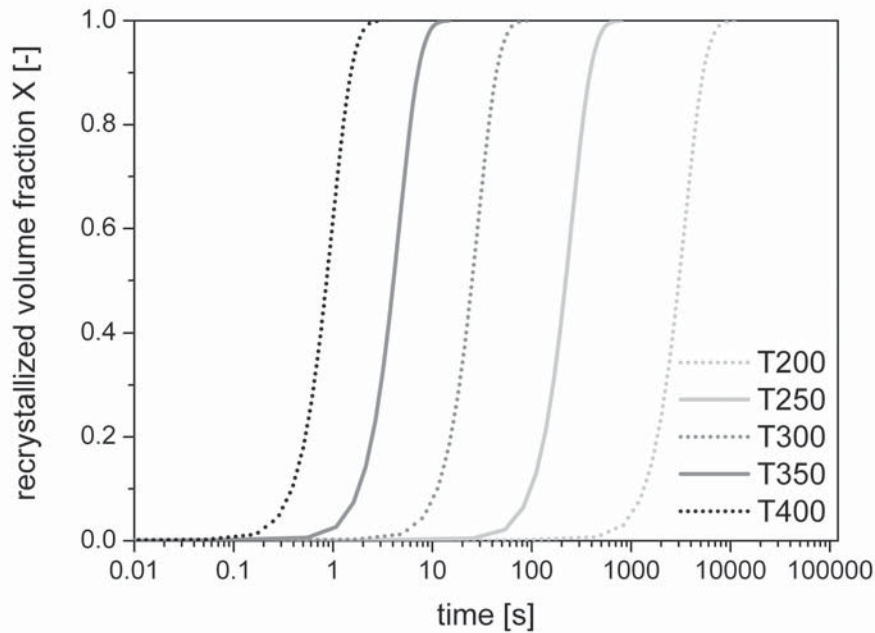


Fig. 4.27: Recrystallization kinetics in dependence on the annealing temperature in °C. this is equivalent to a reciprocal change of the activation energies. The activation energy used in the present case was $E_A=1.1\text{eV}$ and the preexponential factor was $m_0=1.6\text{ m}^4/\text{Js}$.

Fig. 4.28 reflects the dependency of the recrystallization kinetics on the ratio of the different mobilities. The simulations were carried out at a temperature of $T = 350\text{ °C}$ and were based on the data set for AA3103 with a cold rolling reduction of 70 % (see Chap. 9).

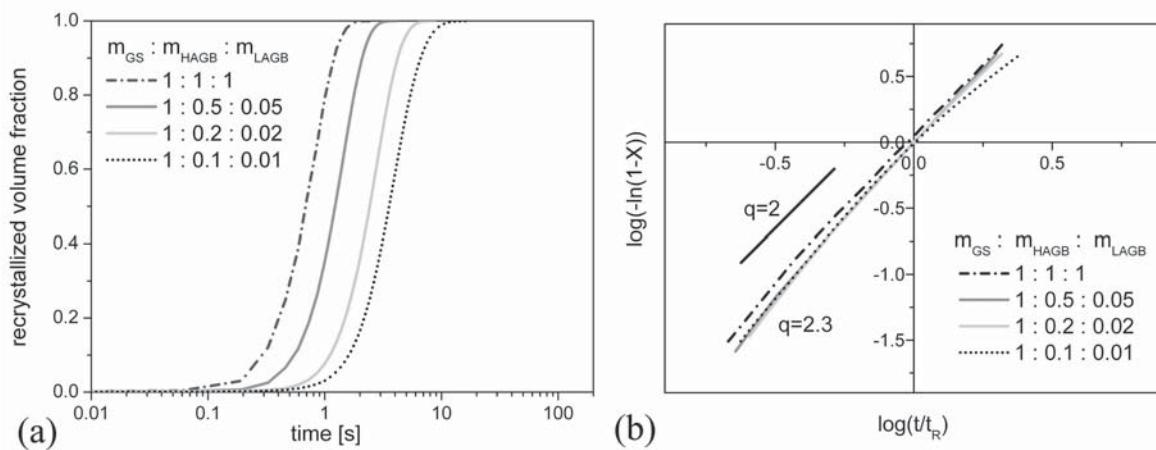


Fig. 4.28: (a) Recrystallization kinetics depending on the ratio of mobilities from low, high angle grain boundaries and growth selection, (b) respective Avrami plots. The mobility for growth selection serves as reference. For comparison a line with slope $q=2$ is displayed in the Avrami plot.

With increasing ratio of the different mobilities, the kinetics shifted to longer annealing times. This is still comparable to a behavior obtainable by consideration of in average decreasing mobilities (Fig. 4.28a). The Avrami exponent was found to be 2.3, as to be expected for site-saturation and non-random distribution of the nucleation sites. This is in good agreement with literature.

Marthinsen et al. [Marthinsen 1989] found for the case of differently growing grains combined with site-saturated nucleation Avrami exponents of 2.2.

In case of the mobility ratio 1 : 0.1 : 0.01, the Avrami exponent was slightly reduced towards the end of recrystallization (Fig. 4.28b). This is due to the large difference in the mobilities (factor 100). In some locations the remaining unrecrystallized volume present towards the end of recrystallization was reduced by grains having boundaries with minimum mobility. Thus the speed of recrystallization is diminished and a reduction of the Avrami-exponent is observed in this specific case (Fig. 4.28b – case 1 : 0.1 : 0.01).

For the above presented simulations the dislocation density was assumed orientation-independent, thus only the orientation distribution played a role (the different growth rates resulted basically from the orientation relationship between the nucleus and its local neighborhood). Nevertheless, also an orientation-dependent distribution of the dislocation density was tested, but no significantly different effect on the recrystallization kinetics was observed. Hence, the effect of orientation-dependent stored dislocation densities as predicted with GIA-3IVM+ for the present case can be neglected over the effect of different mobilities.

4.3.9 Influence of Zener drag

While constituent particles promote recrystallization, small particles, so-called dispersoids can strongly hinder recrystallization. In this work basically commercial aluminum alloys were investigated. Such alloys contain in general a variety of different alloying elements in variable amounts. As will be described in Chap. 8, also different thermo-mechanical treatments can lead to the precipitation of second-phase particles. In this section we restrict the consideration of particles to those with a size below 1 μm . Such dispersoids can be present after deformation, prior to recrystallization or develop concurrently to the recrystallization process. They might also coarsen or dissolve during the heat treatment. The effect of those particles on boundary migration is a back-driving force, the so-called Zener drag, which can hinder or even pin boundary movement. The influence of a Zener drag according to Eq. (3.11) on recrystallization kinetics is discussed in the following. At first, the effect of a time-invariant Zener drag on recrystallization kinetics is evaluated (Fig. 4.29). For this purpose a GIA-3IVM+ simulation was conducted assuming plane strain to $\varepsilon_{\text{VM}} = 0.7$ corresponding to 50% cold rolling in the alloy AA3103. It is noted that due to the orientation-dependent stored energies from GIA a local variation of the driving force for recrystallization is expected.

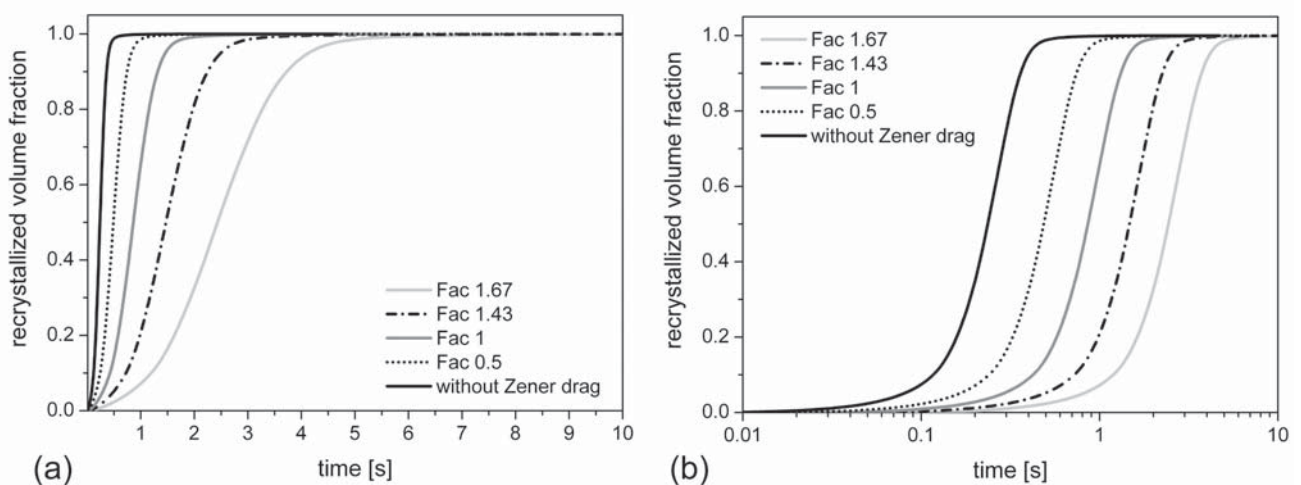


Fig. 4.29: Influence of a statistical Zener drag which is assumed to be time-invariant; (a) on a linear time scale, (b) on a logarithmic time scale. The black, solid curve represents the reference curve without Zener drag. The simulations were carried out for $T = 400^\circ\text{C}$.

For the simulations presented in Fig. 4.29 all particles had an invariant size r_p and volume fraction f_p . For the sake of simplicity in the following only the dispersion degree f_p/r_p will be discussed. The initial volume fraction was 0.3 vol% and the particle radius 135 nm, the various other values for a constant back-driving force were obtained by multiplying the dispersion degree with respective factors as indicated in Fig. 4.29. With increasing degree of dispersion a linear shift of the recrystallization kinetics on a logarithmic time-scale was observed (Fig. 4.29b). The recrystallization texture and grain size distribution remained unaffected by these variations. The influence of a constant Zener drag was also investigated after increasing the dispersion degree to such high values, that recrystallization was strongly hindered (Fig. 4.30). This was achieved by keeping the particle radius constant while increasing the particle volume fraction. With increasing volume fraction the recrystallization kinetics was increasingly affected, and recrystallization was even suppressed at particle volume fractions higher than 1 vol% (Fig. 4.30). The final recrystallized volume fraction decreased with increasing Zener drag. Essentially, this non-recrystallized volume fraction $I-X$ corresponds to those grains where the Zener drag p_Z is larger than the driving force.

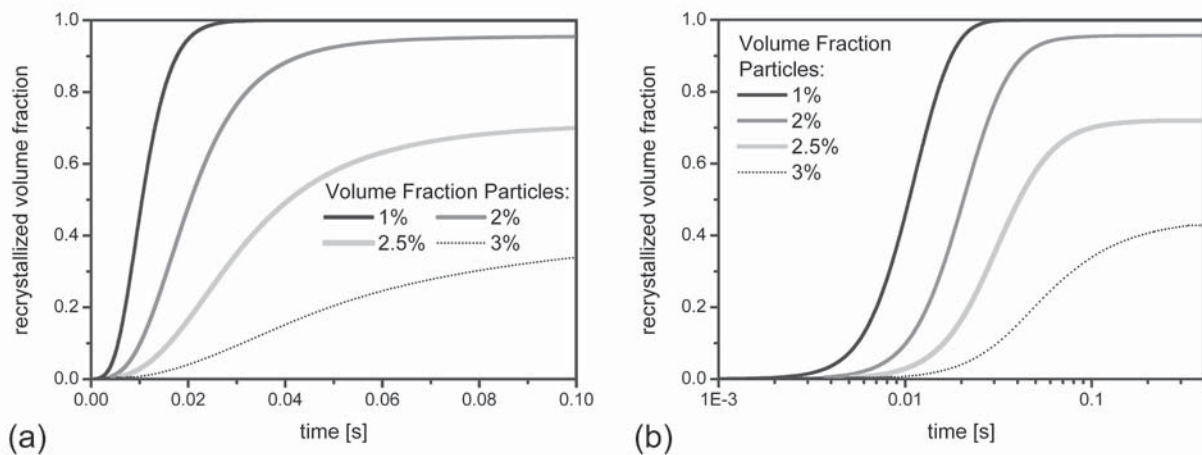


Fig. 4.30: Influence of a very high Zener drag disrupting the recrystallization kinetics with increasing volume fractions; (a) on a linear time scale, (b) on a logarithmic time scale. The corresponding material data set was based on an AA3103 alloy cold rolled to 50% reduction annealed at $T = 350^\circ\text{C}$; recovery was considered (see also Chap. 8).

The orientation dependent stored dislocation densities were in some grains so low that recrystallization was inhibited in the respective grains right from the beginning of the simulation. The higher the fraction of grains in which recrystallization growth ceased, the lower was the final recrystallized volume fraction. The simulations presented in Fig. 4.30 have also severe consequences for the final textures (Sec. 4.2.6).

The assumption of a time-invariant Zener drag, as considered for the previous simulations, is by far too simplified and in most cases not observed during industrial processing, since for most of the heat treatments a low heating rate is used. This can cause tremendous changes in the microchemistry, which suggests a time-dependent evolution of the precipitate size and volume fraction and thus, of the Zener drag. If particles were present before the annealing treatment they could under certain conditions coarsen or dissolve. If before the annealing a larger amount of elements was in solid solution it could possibly precipitate during an annealing treatment. Those different cases and their influences on recrystallization kinetics are exemplarily shown in the following graphs (Fig. 4.31, 4.32). Figs. 4.31a, b demonstrate for instance the coarsening of particles after precipitation. At first an increase of the Zener drag is observed due to formation of particles, which was replaced later on by a reduction of Zener drag due to particle coarsening. Fig. 4.31c reflects the case, which is obtained when an initially high Zener drag is reduced during

recrystallization due to particle coarsening or dissolution. For the three cases shown in Fig. 4.31 a fully recrystallized material was obtained in the end. The curves were plotted together in one graph (Fig. 4.31d) to show the relatively small influence on the final recrystallization kinetics. From these considerations, it can be concluded that the estimation of the real underlying precipitation behavior from e.g. experimental recrystallization kinetics is hardly possible since it was indicated in Fig. 4.31 that somehow different evolutions of Zener drag can result in pretty similar recrystallization kinetics.

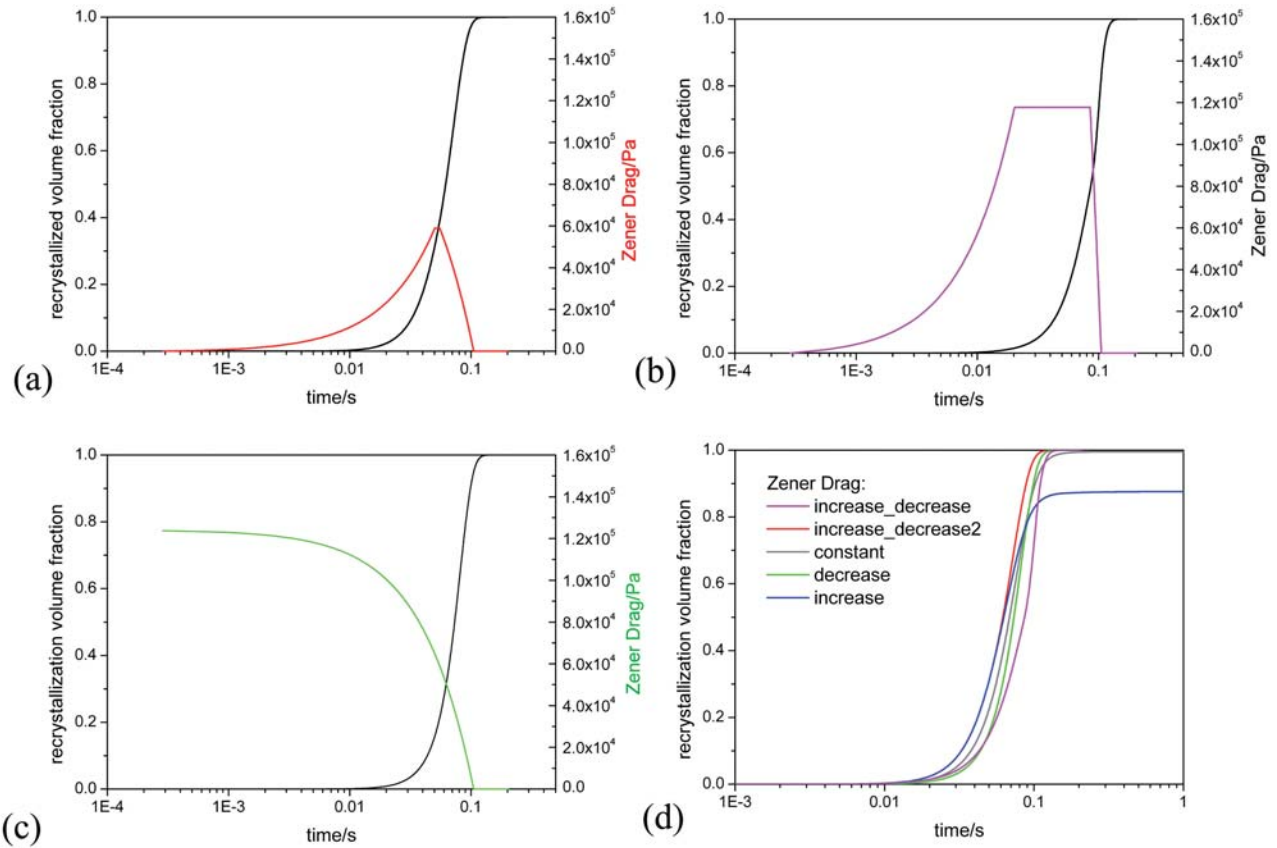


Fig. 4.31: Recrystallization kinetics influenced by precipitation causing back-driving forces (Zener drag) on the boundaries. Different evolutions of Zener drag were considered: (a) the precipitation of new particles and later on coarsening, (b) like in (a) but with an higher absolute Zener drag, (c) coarsening of particles. (d) Different variations of Zener drag and their effect on the recrystallization kinetics in comparison.

Beside a different precipitation, also the effect of precipitation at different times with respect to recrystallization can be studied. Fig. 4.32 reflects the recrystallization kinetics, if the evolution of Zener drag occurs at different stages of the recrystallization process. Therefore, Zener drag was assumed to increase linearly, but at different points in time. Three cases were distinguished: (a) particles of a critical size were already present before recrystallization and stayed invariant throughout the recrystallization process (Fig. 4.32a), (b) particles developed with the beginning of the annealing treatment, and recrystallization was initiated concurrently (Fig. 4.32b), (c) particles developed after recrystallization was completed (Fig. 4.32c).

As can be seen from Fig. 4.32d the smallest influence is found if the precipitation took place towards the end of recrystallization. *Concurrent precipitation* caused the *strongest* influence: it lead to a lower final recrystallized volume fraction and most importantly to a lower slope of the recrystallization kinetics. This can be ascribed to the locally varying growth rates, which are further dependent on time. This means for instance that the initially low fraction of grains inhibited to recrystallize is steadily increasing in the course of recrystallization. In other words, the growth rate of some nuclei is decreasing with time in selected grains. But it is also possible to find nuclei which

cannot grow at all ($p_{\text{driv}} < p_Z$) or such that are completely unaffected by the applied Zener drag ($p_{\text{driv}} \gg p_Z$). The effect of concurrent precipitation is picked up later on in Chaps. 7, 8.

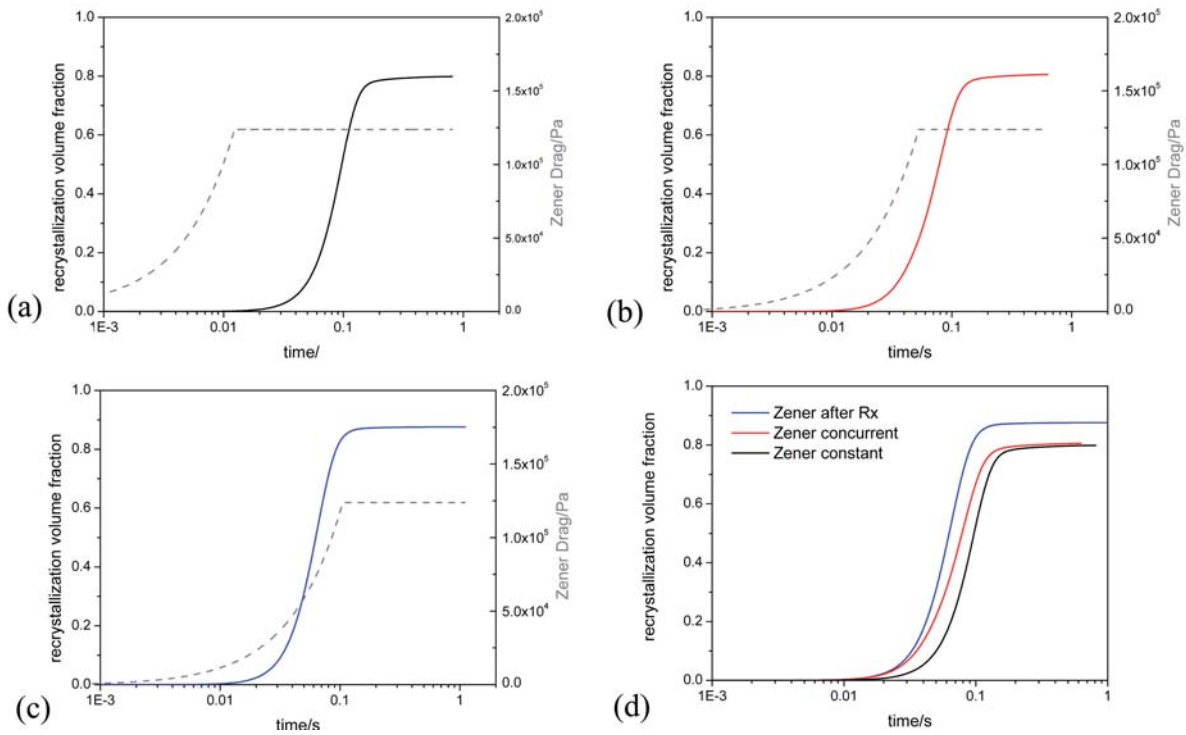


Fig. 4.32: Influence of Zener drag on recrystallization kinetics at different stages: (a) Zener drag reaches the maximum before the beginning of recrystallization, (b) concurrent precipitation, (c) onset of precipitation, when recrystallization was almost completed. (d) Comparison of the cases demonstrated in (a)-(c); concurrent precipitation leads to lower slopes of the recrystallization kinetics compared to both other cases.

In Fig. 4.33 the effect of selected Zener drag evolutions on recrystallization kinetics is compared. It can be clearly seen that a decreasing Zener drag leads to a steeper kinetics, which results in the present case even in a 100 % recrystallized volume fraction. When a constant Zener drag is applied, the final recrystallized volume fraction was strongly dependent on the absolute value of the Zener drag. For an increasing Zener drag, the material did not fully recrystallize since the Zener drag compensated at some point the driving force and thus disrupted the recrystallization process.

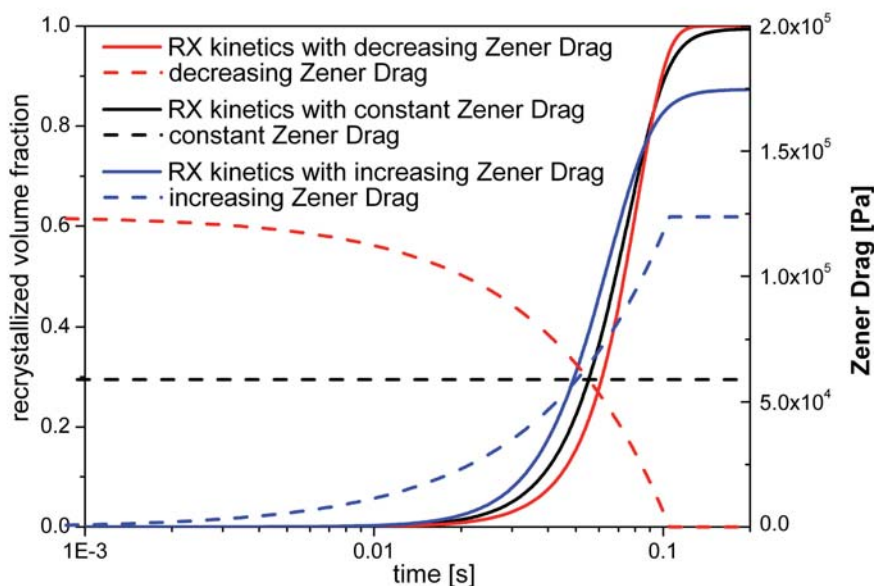


Fig. 4.33: Influence of different evolution of Zener drag during the recrystallization treatment.

Beside a time-dependent Zener drag, the Zener drag can also be considered to be orientation dependent [Lei 2008]. This influence leads to similar effects as caused by concurrent precipitation (Fig. 4.32), such as a lower slope of the recrystallization kinetics and correspondingly, a lower Avrami exponent.

An orientation-dependency of Zener drag was introduced into the CORE model motivated by experimental observations in literature, e.g. by Davison and West [Davidson 1979], who suggested a differently evolving substructure in the presence of fine particles. They further observed that the cold-worked substructures were modified in a manner that was dependent on the texture orientation. Such an orientation-dependence of precipitation can be understood from the orientation-dependent stored dislocation density during deformation.

Such orientation-dependent dislocation densities are a standard output of the GIA-3IVM+ model. From the evaluation of the orientation-dependent dislocation densities, it was very often found that orientations such as Copper and S/R texture component comprise much higher dislocation densities than for example the Cube and Brass orientation. Grains with higher dislocation densities are hence more preferred sites for precipitation than others. This means that precipitation would not be particularly favored in the Cube orientation due to lacking nucleation sites for precipitation (dislocation tangles). In CORE the subgrain size is related to the dislocation density via the principle of similitude (Eq. (3.24)). And thus a lower dislocation density in the Cube orientation would result in large subgrain sizes. Recrystallization simulations were carried out for orientation-dependent precipitation. The corresponding data required for the description of the different precipitation behavior in CORE was provided from ClaNG. For each orientation class a ClaNG simulation was carried out using the respective dislocation densities predicted with GIA as outlined above. The recrystallization simulations yielded under consideration of the different precipitation behavior in different orientation components a lower slope than if all orientations suffer from the same precipitation behavior. This is in agreement with experimental observations by Vatne et al. [Vatne 1996b]. They stated that the Cube oriented grains are less prone to precipitation, since larger subgrains were found in the Cube oriented regions. This tendency can be obtained from the simulations as well, since in general smaller dislocation densities accumulate during deformation in Cube oriented grains (GIA-3IVM+).

As shown in this section, the consideration of Zener drag in the order of the driving force can cause severe influences on recrystallization kinetics and the CORE model can be applied to study the various possibilities of interaction.

4.3.10 Influence of heating rates

The heat treatments applied for industrial processing are in general not iso-thermal. Unlike in laboratory sample production, in industry very often low heating rates are encountered. Such heat treatments can cause the material to behave quite differently than during an isothermal heat treatment, e.g. owing to the impact of recovery. The amount of recovery which increases with slower heating rates can significantly influence the recrystallization behavior. Other effects in case of low heating rates are caused by precipitation prior or concurrent to recrystallization (as demonstrated in Sec. 4.3.9).

To consider recrystallization during non-isothermal heat treatments, the temperature-dependencies of the different mechanisms were implemented in CORE: (1) The temperature-dependence of recovery as well as incubation times were introduced in Chap. 3 and are further detailed in Chap. 6. (2) The temperature-dependent modeling of microchemistry changes was presented in Chap. 3 and is applied to real material behavior in Chap. 8.

A simplified version of the influence of heating rates on recrystallization kinetics is shown in the following and further more detailed studies are presented in Chaps. 7-9. For the sake of simplicity, at first simulations are presented considering only the influence of recovery. Fig. 4.34a displays the different time-temperature profiles that were utilized for the simulation. The corresponding

recrystallization kinetics that were obtained for these heat treatments are displayed in Fig. 4.34b. The additional dotted lines indicate the reduction of the dislocation density in the remaining deformed volumes due to recovery (Fig. 4.34b).

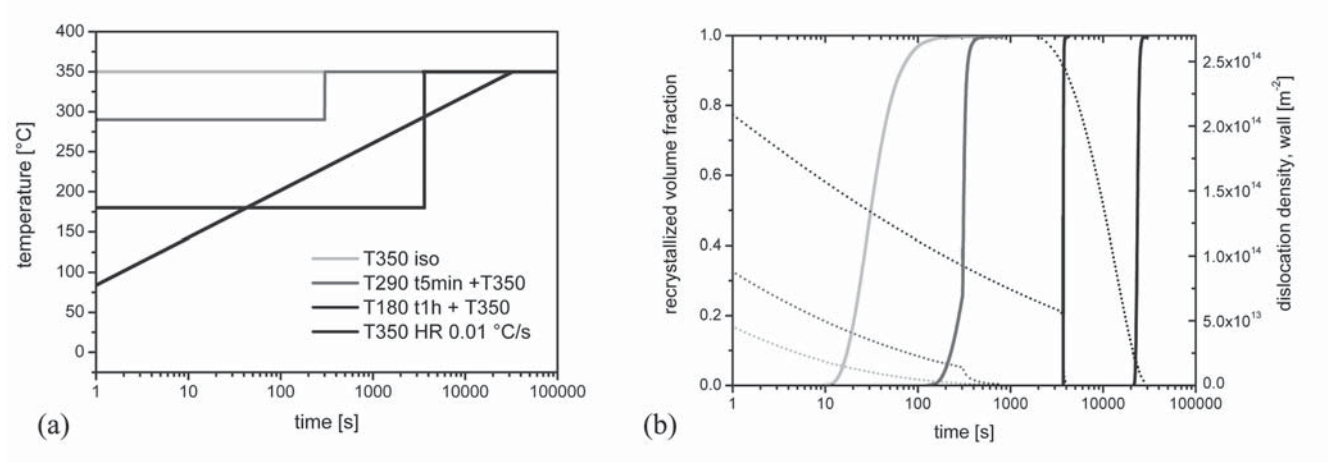


Fig. 4.34: Recrystallization kinetics obtained in case of different time- temperature profiles starting from the same initial state (AA3103 cold rolled 50%, random nuclei only). (a) The time-temperature profiles, (b) recrystallization kinetics (solid line) and corresponding dislocation density evolution (dotted line).

Recrystallization was initiated as soon as a sufficient annealing temperature was reached. Thus, for the different heat treatments (Fig. 4.34a) very different times for initiation of recrystallization were obtained (Fig. 4.34b). The prediction of the time window for recrystallization is of particular importance for industrial processes. It was found that beside a reduction of the growth rate $v(t)$ with increasing amount of recovery, also the grain size becomes slightly larger. This effect is of course much more pronounced if concurrently to recovery also precipitation reactions occur.

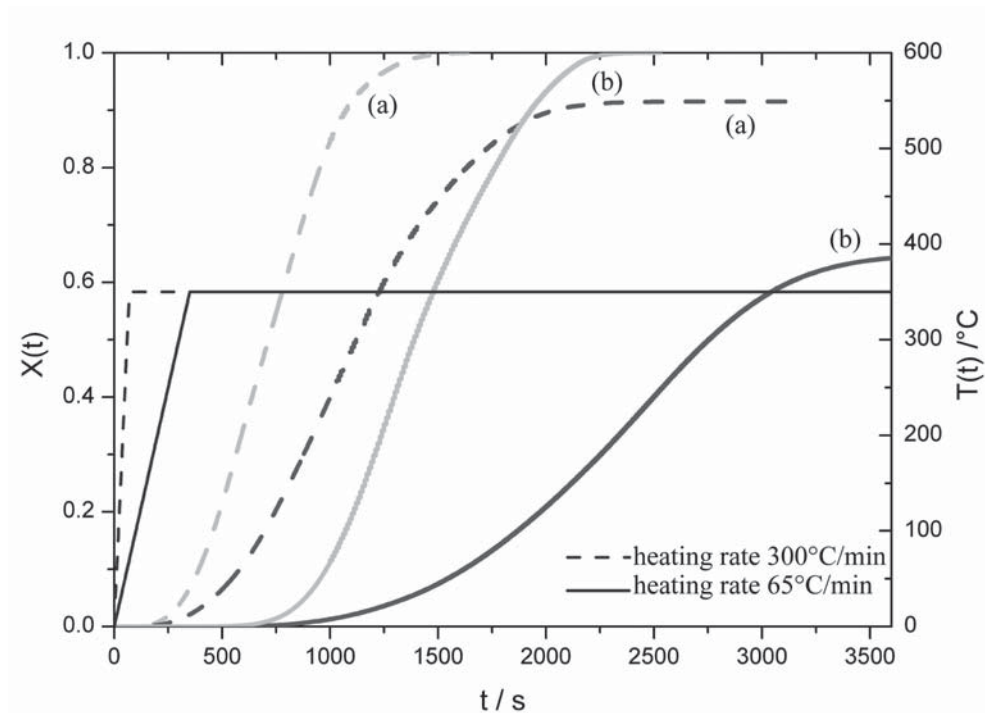


Fig. 4.35: Modeled recrystallized volume fraction of a AA3103 alloy for annealing with different heating rates [Mohles 2007a]. (a) Simulation without recovery and Zener drag; (b) Simulation with recovery and Zener drag $p_z(t)$ from ClaNG for the same $T(t)$. Dashed lines: Simulations with heating rate 300°C/min; solid lines: simulations with heating rate 65°C/min.

The case presented in Fig. 4.34 is rarely encountered in commercial alloys. It is more likely that recrystallization is influenced by a combination of recovery and precipitation. Whereas in the previous case (Fig. 4.34) only recovery was taken into account as a predominant effect during annealing with low heating rates, in the following also microchemistry effects were considered. Fig. 4.35 indicates the influence of recovery and an overlaid Zener drag for the consideration of linear heating rates. The Zener drag was calculated with the Classical Nucleation and Growth model for precipitation (ClaNG) [Schneider 2006] for the two different heating rates (the effect of solutes was neglected).

As to be expected, a lower heating rate hindered recrystallization more effectively (grey compared black in Fig. 4.35), since the maximum temperature was reached later on in the process. A reduction of the dislocation density $\rho(t)$ due to recovery and an increasing Zener drag $p_z(t)$ caused a reduction of the recrystallization rate dX/dt , hence a reduced slope of $X(t)$ was obtained (compare continuous and dashed lines in Fig. 4.35). The maximum recrystallized volume fraction after 1 hour annealing was lower for a lower heating rate (grey). Obviously the recrystallization nucleation was hindered more strongly by precipitation due to the lower heating rate so that the evolving Zener drag leads to a disruption of recrystallization.

The influence of the heating rate combined with the corresponding changes in microchemistry and recovery was investigated also for an AA8079L alloy. The most prominent element in these alloys is iron, which significantly influences the recrystallization behavior. In the following case study the iron content was modeled with ClaNG [Schneider 2006]. The corresponding effect of Zener drag on the recrystallization kinetics is shown in Figs. 4.36 and 4.37. The influence on recrystallization kinetics was investigated for different rolling reductions (50%, 70%) and temperatures ($T = 260^\circ\text{C}$, 300°C) [Laptyeva 2009]. The heat treatment was assumed as follows: the material was heated with a heating rate of 56°C/h and hold for $t = 8.4$ h and then cooled to room temperature with a cooling rate of 34°C/h . When considering a cold rolling reduction of 70% it was observed that the recrystallized volume fraction reached a maximum value of about 40% in the case of low ($p_{z,\text{low}} = 250$ Pa) or no Zener drag. This maximum value was dependent on the dwell time at $T = 260^\circ\text{C}$.

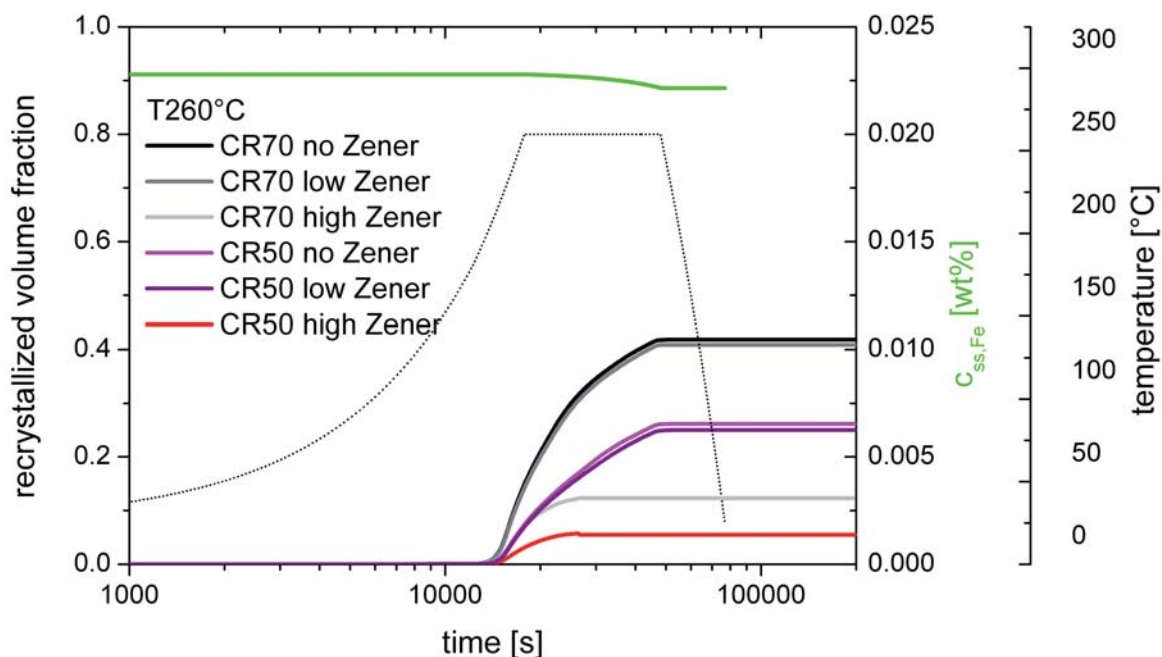


Fig. 4.36: Recrystallization kinetics modeled with CORE for material deformed to cold rolling reductions of 50% and 70% and annealed at $T=260^\circ\text{C}$ applying differently strong Zener drags and a changing solute content of iron as predicted by ClaNG. The material was heated according to a batch annealing cycle. ($p_{z,\text{high}} = 2.5 \cdot 10^3$ Pa, $p_{z,\text{low}} = 2.5 \cdot 10^2$ Pa).

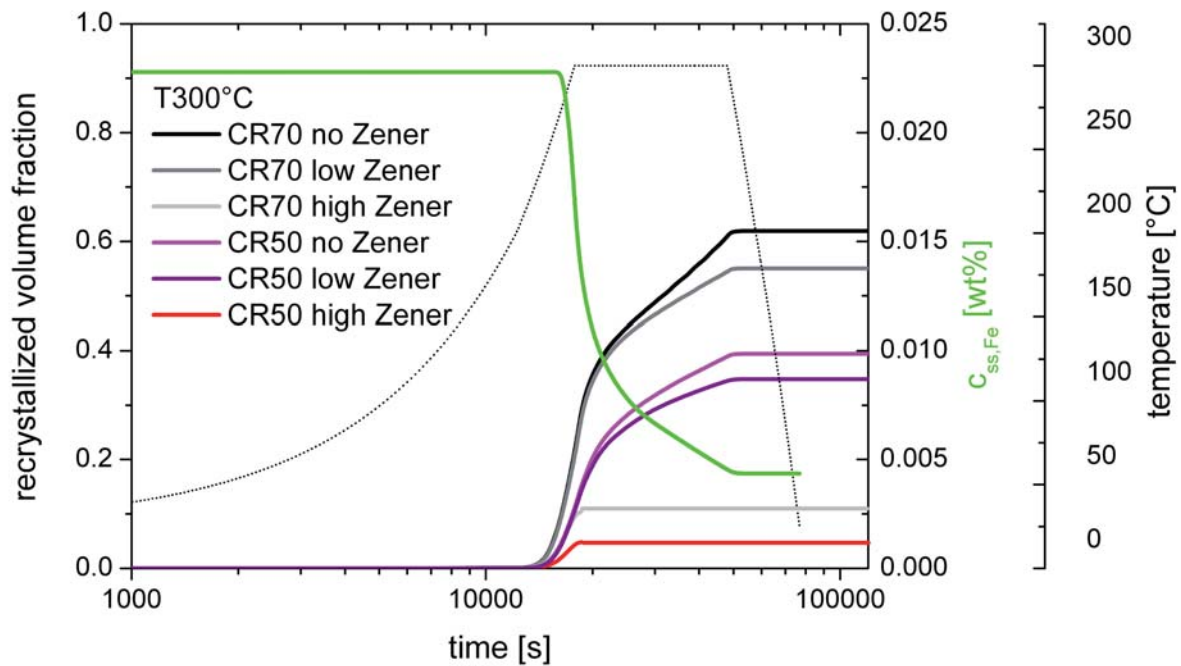


Fig. 4.37: Recrystallization kinetics modeled with CORE for material deformed to cold rolling reductions of 50% and 70 % and annealed at $T=300^{\circ}\text{C}$ applying differently strong Zener drags and a changing solute content of iron as predicted by ClaNG. The material was heated according to a batch annealing cycle. ($p_{z,\text{high}} = 2.5 \cdot 10^3 \text{ Pa}$, $p_{z,\text{low}} = 2.5 \cdot 10^2 \text{ Pa}$).

For the higher temperature of $T = 300^{\circ}\text{C}$ the maximum recrystallized volume fraction of 60% was obtained when no Zener drag was considered. If a low Zener drag ($p_{z,\text{low}} = 250 \text{ Pa}$) was assumed the final recrystallized volume fraction after the annealing treatment was decreased to 55% and, for very high Zener drag, to about 10%. It can be seen that with the beginning of the cooling process the recrystallized volume fraction remained almost unchanged. It can further be seen that the recrystallization kinetics were much faster towards the end at high temperatures compared to the lower temperature. This is caused by the significant drop in the iron content in solid solution at $T = 300^{\circ}\text{C}$, and hence a decreased impurity drag.

To demonstrate the influence of different rolling reductions the simulations were also carried out for a rolling reduction of 50%. The corresponding recrystallization kinetics are displayed for the batch annealing cycle in Fig. 4.36 for $T = 260^{\circ}\text{C}$ and Fig. 4.37 for $T = 300^{\circ}\text{C}$. The following differences to a rolling reduction of 70% can be pointed out: the kinetics were overall slower, and a lower final recrystallized volume fraction was obtained, by about 0.2 lower than in the 70% cold rolled material. The reason for this difference was the initially lower nucleus number owing to the lower rolling reduction and hence due to the lower total interface area providing grain boundary nuclei.

From this study it can be seen that with the amount of dwell time the amount of iron in solid solution and hence, the final recrystallized volume fraction, respectively the obtained grain size can be significantly tuned. This can be of importance in order to obtain a certain amount of recrystallization in-situ in industrial down-stream processing steps.

More detailed information on the influence of non-isothermal heat treatment on recrystallization in the alloy AA3103 can be found in Chap. 8.

4.3.11 Influence of particle-stimulated nucleation

Second-phase particles have various effects on recrystallization. The effect of dispersoids was previously discussed in Secs. 4.3.9 and 4.3.10 for Zener drag. In case the particles are above a

critical size and present prior deformation a deformation zone is formed in their vicinity during deformation. These deformation zones are during subsequent annealing preferred nucleation sites due to the local orientation and dislocation density gradient (Chaps. 5, 7). The model for consideration of particle-stimulated nucleation (PSN) in the cellular automaton is detailed in Chap. 5. For the following simulations, the simple presence of such additional nucleation sites is sufficient without going into further detail on the PSN-model and its implementation.

Fig. 4.38 demonstrates the effect of such additional nucleation sites at particles on recrystallization kinetics. In these simulations all nucleation mechanisms were activated: nucleation at particles, at grain boundaries, at transition bands and at shear bands. A particle distribution was considered similar to experimental findings, i.e. ranging from particle sizes of $0.25\ \mu\text{m}$ up to $19.8\ \mu\text{m}$ [Schäfer 2007].

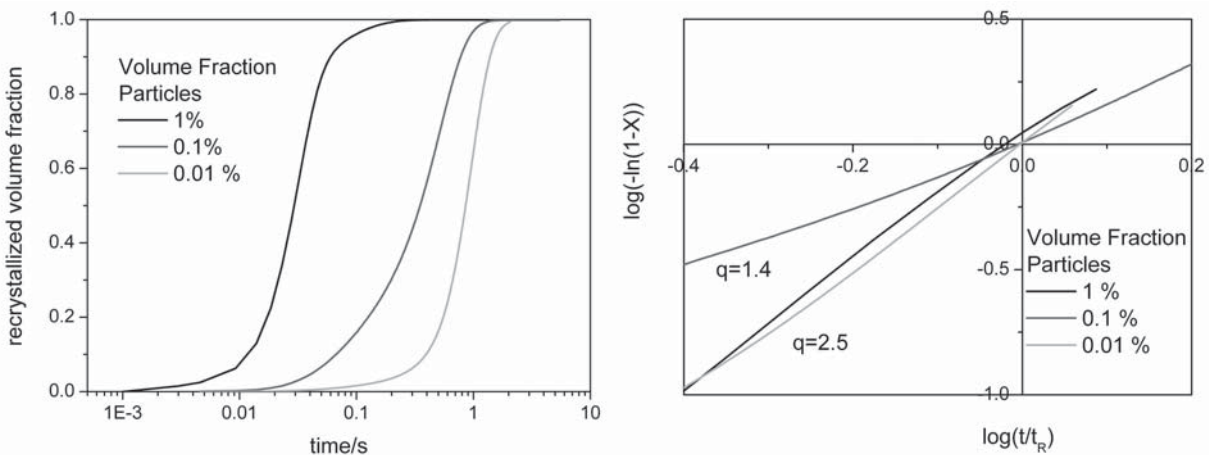


Fig. 4.38: (a) Recrystallization Kinetics influenced by the volume fraction of second-phase particles (constituents). (b) Avrami plots dependent on the volume fraction of second-phase particles.

Fig. 4.38 suggests that under consideration of particle-stimulated nucleation the recrystallization kinetics are accelerated. This can be, of course, attributed to an additional number of recrystallization nuclei introduced by the PSN model. For a high volume fraction of particles the number of nuclei strongly increased, leading to a smaller final grain size. For a constituent volume fraction of 0.01% the total amount of particles as nucleation sites was so small, that the recrystallization kinetics were basically determined by the nuclei developed at other nucleation sites, such as grain boundaries, transition bands and shear bands. In both cases recrystallization kinetics with an Avrami exponent of 2.5 were observed. At intermediate particle volume fractions a much lower slope of the recrystallization kinetics was obtained (Avrami exponent 1.4, Fig. 4.38b). Recrystallization was dominated initially by PSN and towards the end of recrystallization by nuclei developed at other nucleation sites. The initial growth advantage of particle-stimulated nuclei originates from the presence of the deformation zone, characterized by a higher dislocation density. Whereas at the beginning of recrystallization mostly nuclei at particles consumed the volume, towards the end of recrystallization the volume was consumed homogeneously by all nuclei. Accordingly, an overall lower Avrami exponent was obtained in this particular case.

4.3.12 Influence of solute drag

In commercial Al alloys, the recrystallization behavior is influenced beside second-phase particles also by another parameter concerning the microchemistry state, the solid solution content of the alloying elements. Those elements can significantly change the boundary mobility depending on their diffusivity by several orders of magnitude. It was found e.g. by [Detert 1956, Lücke 1957] that additions of the order of 0.01% of manganese or iron can decrease the rate of recrystallization of

high-purity aluminum by factors of 10^{12} or 10^{16} . In the following section the influence of the impurity or solid solution content is demonstrated. Solute drag was modeled as introduced in Chap. 3, Sec. 3.7. The simplest case is the consideration of a time-invariant solute drag (Fig. 4.39a). Fig. 4.39b shows the influence on recrystallization kinetics if the solute content of e.g. manganese in aluminum is varied time-dependent. The calculations were based on the dataset of a previously 50% cold rolled AA3103 alloy (Chap. 9), as introduced previously.

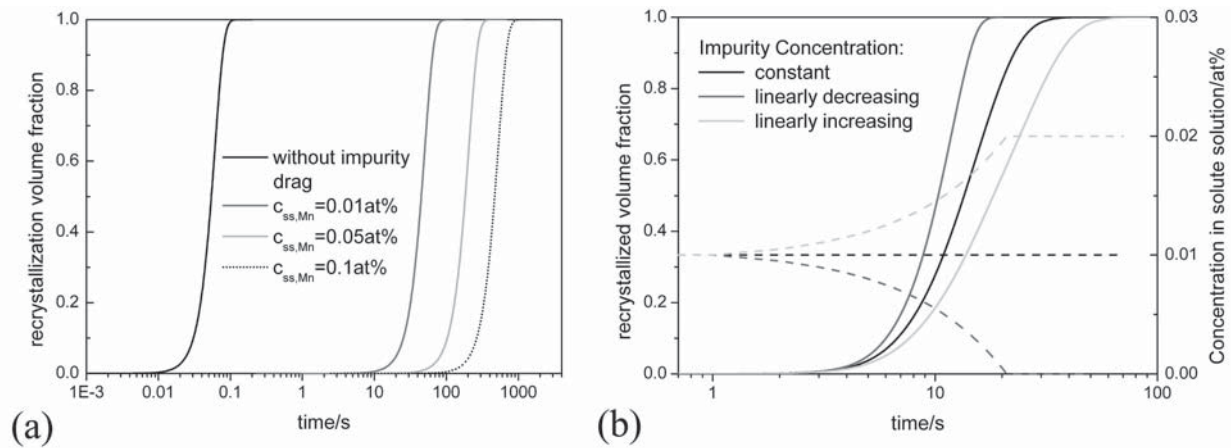


Fig. 4.39: Influence of (a) a time-invariant solute drag; (b) time-dependent solute drag for alloy AA3103.

In Fig. 4.39a it can be seen that with increasing solid solution content of manganese, the recrystallization kinetics shifted more and more to longer annealing times, due to the increasing hindrance of grain boundary motion.

Similarly to the evolution of Zener drag, the solid solution content will not always be time-invariant, it will rather decrease or increase during a heat treatment. The most pronounced effect will be obtained in case the time is sufficiently long for precipitation reactions to take place, such as during very low heating rates. In this case a time-dependent solute drag is expected. Fig. 4.39b shows the effect of a linearly decreasing, increasing and constant amount of manganese in solid solution. It was observed that the slope of the recrystallization kinetics can be significantly altered. This behavior is very similar to many effects observed during recrystallization in other commercial aluminum alloys, for instance in AA8079L [Schäfer 2009a].

Of course, the precipitation effects such as a back-driving force due to Zener drag or solute drag are usually not observed independently. Changes in solid solution content of the respective alloying elements are accompanied by a variation of the particle volume fraction, average size and size distribution. A consistent modeling of the microchemistry parameters was used in Chaps. 7, 8.

Modifications in the CORE model allow further the consideration of an orientation-dependent solute drag (Fig. 4.40). First it was assumed that the solute concentration in all orientations was independent of their substructure after deformation: in the two limiting cases a constant solute content of 0.01 at% respectively 0.15 at% manganese was assumed (light grey lines). It was observed that in case of a constant solute content basically the recrystallization kinetics shifted to longer annealing times as demonstrated in Fig. 4.39a. To consider the orientation-dependency of solute drag, locally a lower solute content was assumed in Cube oriented grains, providing in those grains a higher grain boundary mobility, whereas the non-Cube oriented grains recrystallized much more slowly due to a locally larger solute drag. If a rather heterogeneous distribution of an orientation dependent solute content was assumed, the mobility changed throughout the microstructure. In this case, a lower slope of the recrystallization kinetics is observed (dark line in Fig. 4.40). In real microstructures this effect is not only restricted to orientation sensitive precipitation and thus varying solute contents, but can also be the result of concentration gradients, such as caused by strain gradients e.g. in the vicinity of particles, or by temperature gradients.

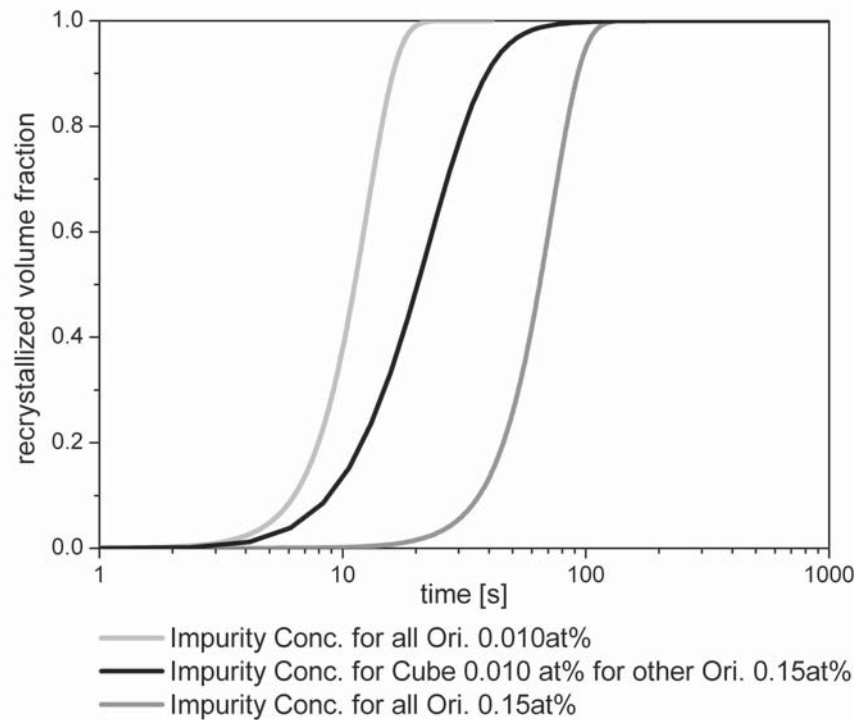


Fig. 4.40: Influence of an orientation dependent solute drag. It is assumed that the Cube orientation has the lowest solute content (dark line), two limiting cases for overall low or high solute content are indicated as well (light grey lines). The simulations were carried out without the consideration of Zener drag.

4.4 Influence on Grain Size Distribution

Beside the final texture and the recrystallization kinetics, also the distribution of grain sizes or the grain size itself is important. Certain phenomena, such as orientation dependent Zener drag and the resulting pinning of the grain boundaries can lead to very inhomogeneous grain structures [Furrer 1978, Bampton 1982, Tangen 2004, Liu 2008]. Also, an inhomogeneous strain distribution during deformation and the subsequent activation of nucleation sites, as well as their spatial distribution contribute significantly to such results. However, many industrial applications require a small, homogeneous grain size for good formability, e.g. foil production. Hence, the following section focuses on the investigation of various influences on the average grain size, respectively the grain size distribution.

4.4.1 Influence of the nucleus number

For the consideration of the effect of the nucleus density on grain size distribution, simulations were carried out with varying nucleus numbers per grain, considering a constant deformed grain size. Nucleation was assumed to occur site-saturated and randomly within the grain volumes. In case of homogeneous nucleation a finer average grain size was obtained with increasing nucleus number, as to be expected (Fig. 4.41). In real microstructures, such comparatively higher nucleus numbers can be caused, for instance by locally higher stored energy in terms of dislocation density, i.e. by increasing the degree of rolling reduction. The decrease in the nucleus density is further connected to a broadening of the grain size distribution. This can be understood from the microstructure simulations: with decreasing nucleus density increases the average free growth path in between adjacent nuclei. Hence, grains with preferred orientation relationships could grow in such cases to comparatively larger grain sizes, whereas unfavored grains remain small.

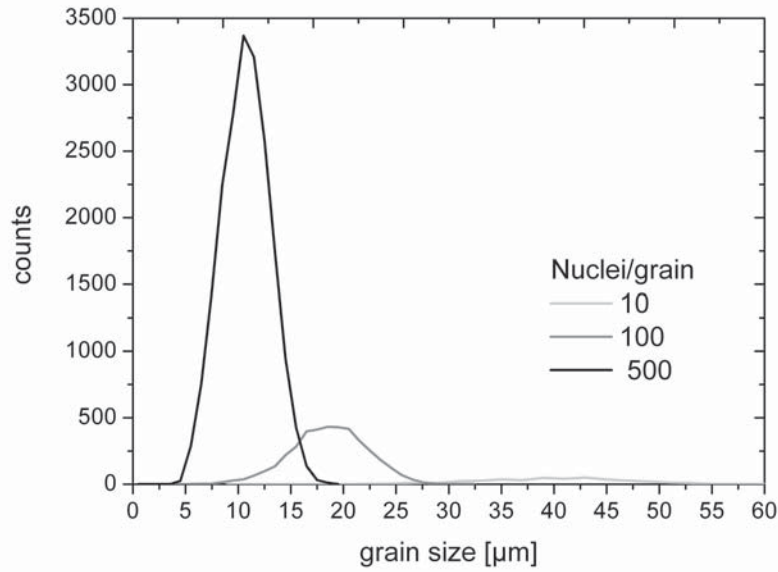


Fig. 4.41: Influence of the nucleus number on the grain size distribution for a completely recrystallized microstructure.

Fig. 4.41 reflects the effect of homogeneously distributed nuclei. However, for more realistic simulations the four typical nucleation mechanisms observed in aluminum alloys were considered, i.e. nucleation at grain boundaries, at transition bands, at shear bands and nucleation at large particles. The model for particle-stimulated nucleation will be introduced in detail in Chap. 5.

The calculation of the nucleus numbers depends strongly on the interface area (grain boundary area, interface area in case of transition band nuclei, etc.). Hence, in principle all nucleation mechanisms with exception of particle-stimulated nucleation are dependent via the interface area on the pre-deformed grain size. Fig. 4.42 demonstrates the effect of pre-deformed grain size on the final recrystallized grain size when the initial material is subjected to the same rolling reduction.

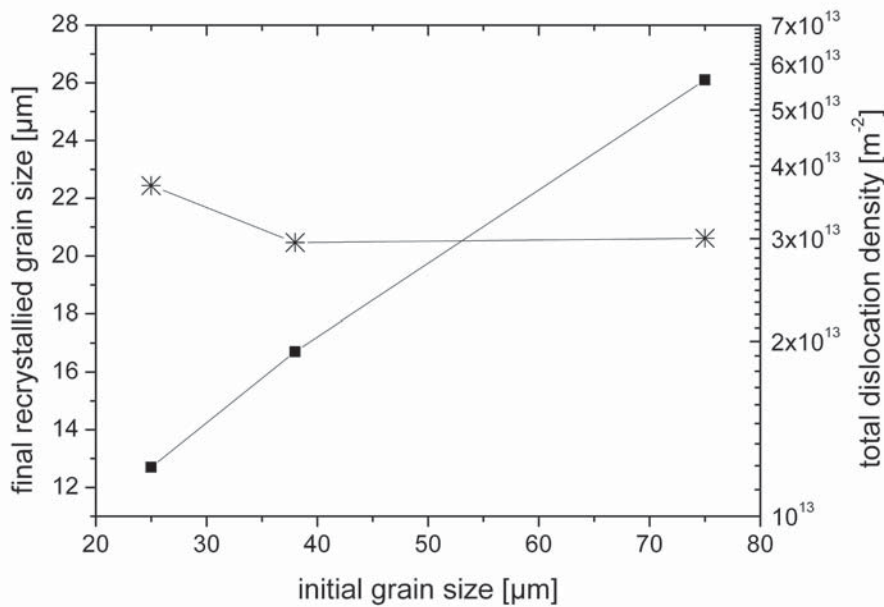


Fig. 4.42: Influence of the pre-deformed grain size on the final recrystallized grain size (solid squares); the corresponding averaged total dislocation densities as obtained from GIA-3IVM+ are presented as well (stars).

With decreasing pre-deformed grain size a lower recrystallized grain size was obtained. For this several causes can be identified: (1) a higher interfacial area per unit volume with decreasing initial grain size. This resulted in a higher total nucleus number and thus naturally in a finer recrystallized grain size. (2) The dislocation density introduced during deformation is slightly increasing with smaller initial grain size, and thus leads also to a higher nucleus number and smaller recrystallized grain size as well.

Also the pre-deformed grain shape, respectively the surface to volume ratio is important for the final recrystallized grain size. It does not only influence the total number of nuclei, which increases with the interfacial area as previously demonstrated, but can also result in a dimensional reduction of growth: while a homogeneous, equiaxed grain size allows growth in all three spatial dimensions, pancake shaped grains promote a one- or two-dimensional growth. This was commonly observed for highly rolled material, where the smallest grain size after recrystallization was obtained in the normal direction. In normal direction the moving grain boundary encounters more frequently high angle, higher energy grain boundaries (of the deformed grains). Thus, the recrystallization front proceeded slower in this direction and the resulting grains are smaller in normal direction.

The effect of the initial grain shape on the grain size distribution is presented in Fig. 4.43. In contrast to the previous cases where the initial grain shape and the total volume of the cellular automaton were kept unchanged, Fig. 4.43 indicates the effect of different grain shapes before deformation. The notation used for the shapes in Fig. 4.43 refers to the shapes introduced previously in Fig. 4.17.

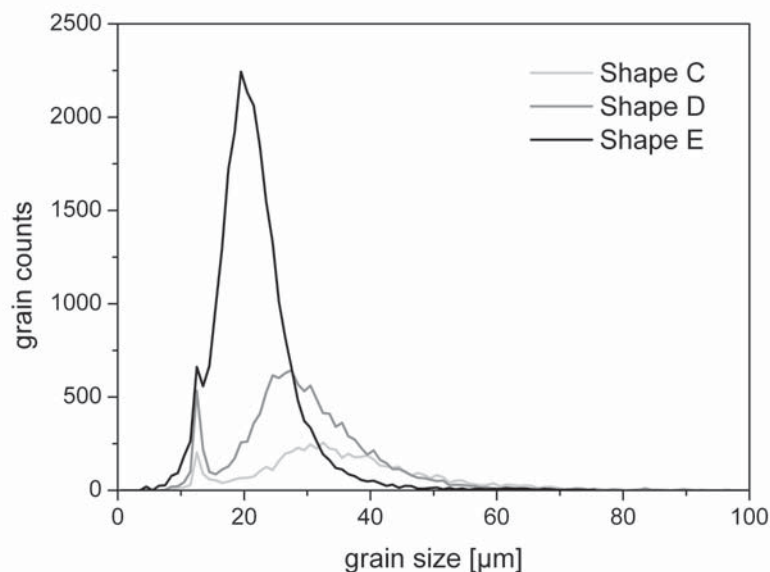


Fig. 4.43: Influence of iso-volume grain shapes on the grain size distribution of the recrystallized grains (only grain boundary nucleation is considered); unmodified material data set of AA3103 70% cold rolling reduction (for notation see Fig. 4.17).

With increasing surface to volume ratio (0.124 – shape C; 0.211 – shape D; 0.412 –shape E) a strong increase of the nucleus number was observed. This resulted in a smaller average grain size after complete recrystallization with a smaller scatter width of the grain size distribution. The smaller width of the grain size distribution is due to the in average reduced free growth length in case of very flat grains. It is pointed out that in case of very low nucleus numbers and additional strong Zener drag, very anisotropic recrystallized grain sizes will result. This case was not considered here. A reduction of the free growth length was also obtained with increasing nucleus density, as already demonstrated in Fig. 4.42. A combination of the above outlined influences, lead to smaller grain sizes and smaller scatter width of the grain size distributions.

4.4.2 Influence of strain

A combination of the above outlined effects is obtained during deformation. During rolling the interface area, grain shape and dislocation density are varied at the same time. With increasing rolling reduction an increase of the dislocation density was predicted by GIA-3IVM+ (Fig. 4.44). While the dislocation density in the cell interior increased with increasing deformation, a saturation density was reached in the cell walls at a certain rolling reduction. In Fig. 4.44 the evolution of the final recrystallized grain size is related to the deformed grain size, respectively to the interface area.

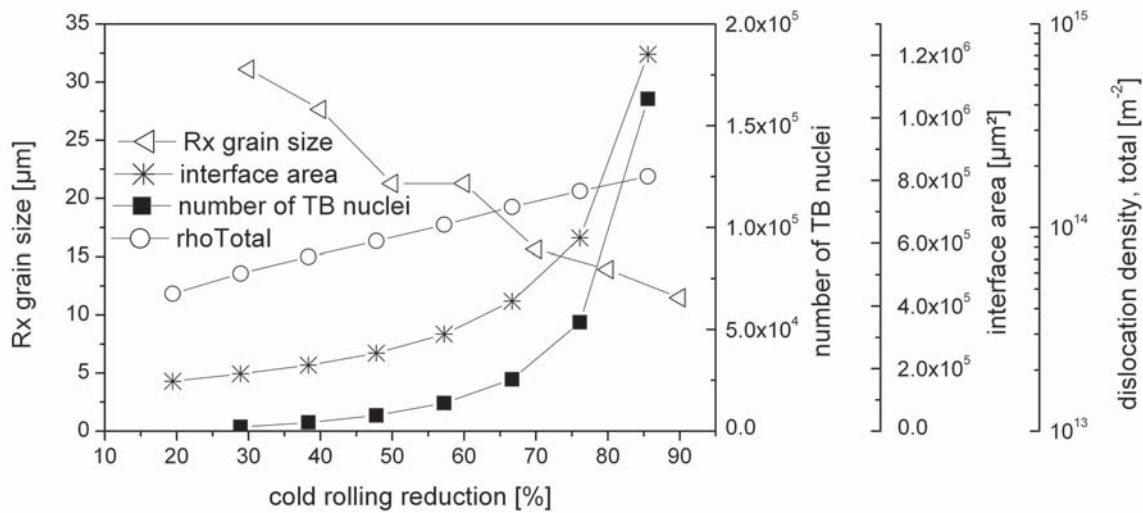


Fig. 4.44: Recrystallized grain size and nucleus number at transition bands as a function of the deformation degree and in relation to the evolution of the grain interface area.

With increasing rolling reduction a smaller recrystallized grain size was obtained. The decreasing grain size results from an increase of the stored dislocation density as well as from the increasing surface to volume ratio. The increasing rolling reduction is connected to a change of the ratio surface / volume and therefore, to a higher nucleus number (as indicated in Fig. 4.44 for transition band nuclei (TB)). The nucleus number calculation was based on the interface area as considered for the specific nucleation mechanisms (Chap. 3).

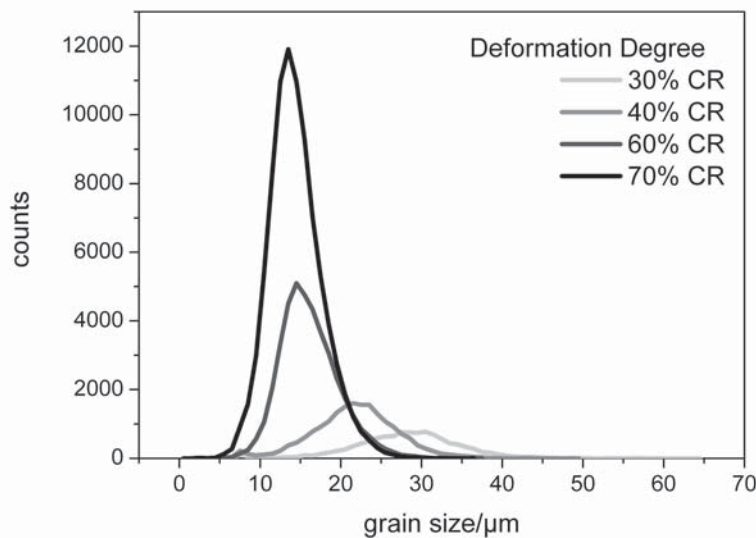


Fig. 4.45: Modeled grain size distribution in dependence of the degree of cold rolling reduction (CR) in alloy AA3103.

Fig. 4.45 indicates the development of the grain size distributions with increasing rolling reduction. It was found that the distribution width decreased significantly with increasing rolling reduction. This is mainly an effect of the increased nucleus density as discussed in Sec. 4.4.1. A wide distribution width means that some grains with preferred orientation grew much larger, whereas grains that were unfavored remained very small. This, however, implies that the free growth length at low rolling reductions was sufficiently larger than for high rolling reductions. This was certainly true since for low rolling reductions a much lower nucleus density was obtained. The final microstructures obtained after annealing for two different rolling reductions are presented in Fig. 4.46.

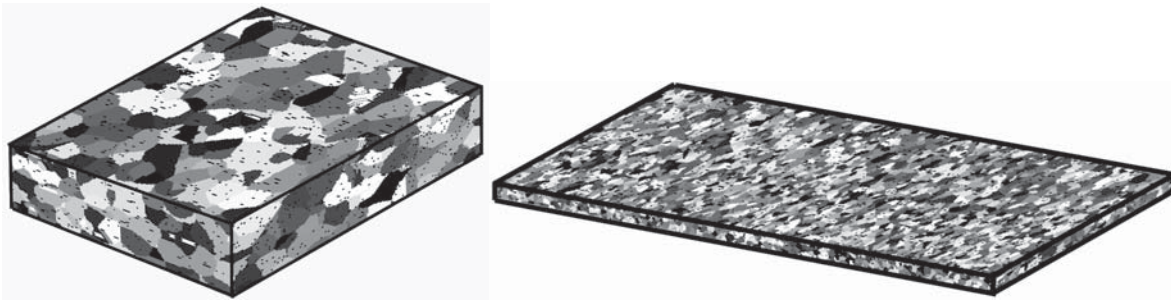


Fig. 4.46: Computed recrystallized microstructures for cold rolling reduction of (a) 30%, (b) 80% in the Alloy AA3103.

4.4.3 Influence of inhomogeneities – Effect of local variations in the nucleus frequency

One advantage of the cellular automaton compared to other - in particular statistical - models is its local resolution of the microstructure, and therefore the option to implement microstructural inhomogeneities up to small microstructural details. To probe the influence of inhomogeneities, a very inhomogeneously deformed microstructure was constructed as initial input for CORE. It was assumed that a certain fraction of the deformed grains developed a higher nucleus density than others: the nucleus number was increased in 0%, 30%, 50%, respectively 100% of all initial grains. The grains with a higher nucleus density were randomly distributed within the deformed microstructure. The initial slight variation in dislocation density due to different orientations remained unaltered, so that the growth rate was also influenced by the local misorientations. This setup represented, in a simplified fashion, structural inhomogeneities, resulting from the orientation-dependent stored energies during deformation. The nuclei originating from different nucleus mechanisms are, in general, not randomly distributed throughout the microstructure, but rather locally arranged. They occurred in grain boundary regions, at transition bands, at shear bands, and in the vicinity of particles. The simulations with inhomogeneities were compared to simulations with a homogeneous distribution of the respective nucleus numbers.

In contrast to the previous simulations, nucleation was assumed randomly (e. g. from shear bands) and with a constant nucleus number per grain. The observed effects on the recrystallized grain size, respectively the grain size distribution are shown in Figs. 4.47 and 4.48.

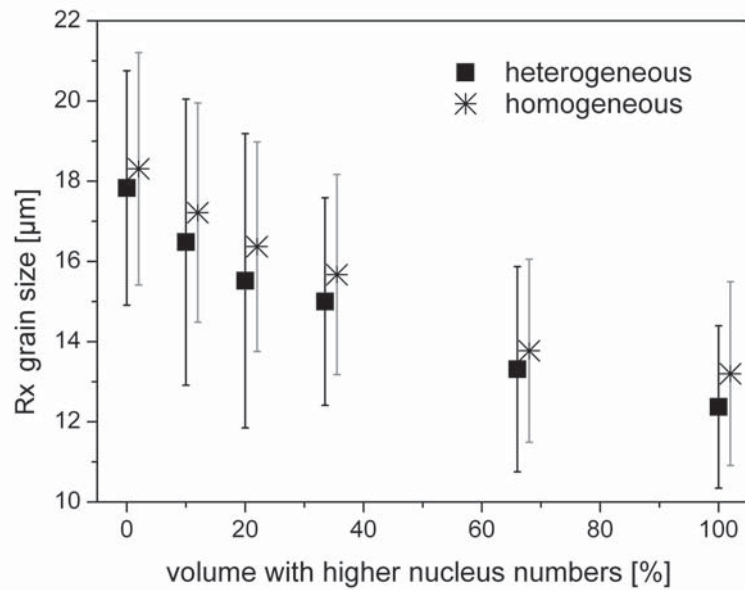


Fig. 4.47: Influence of an inhomogeneous distribution of nucleus numbers within the microstructure on the recrystallized grain size (solid squares). The corresponding average grain size obtained from simulations with a homogeneous nucleus distribution is indicated by stars. The average grain size decreased with increasing volume fraction of areas with high nucleus density. The scatter of the grain size is indicated by error bars.

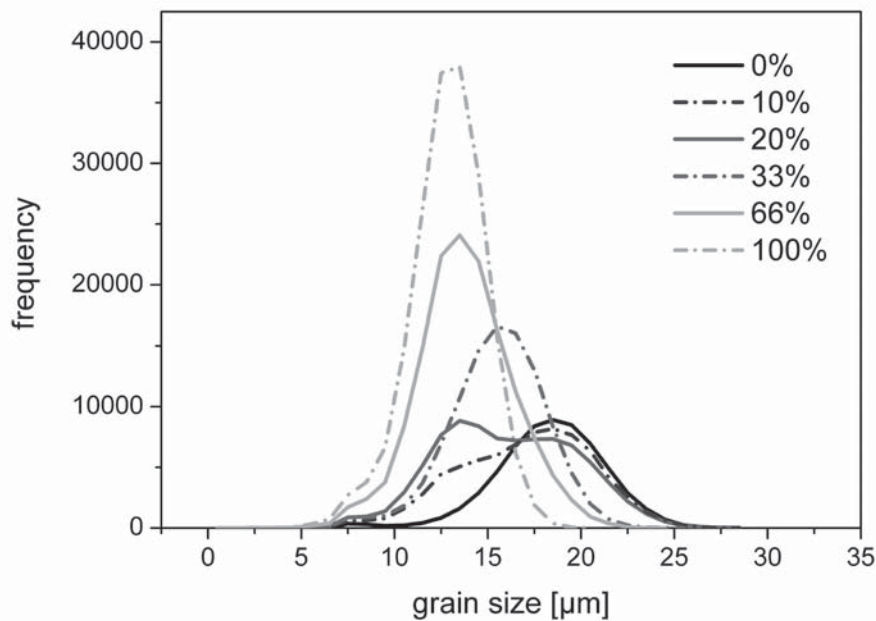


Fig. 4.48: Influence of an inhomogeneous distribution of nucleus numbers within the microstructure. The different percentages define the volume fraction within the cellular automata that carried by a factor 3 higher nucleus numbers. The number of initial grains was 400, the nucleus numbers ranged from 60000 to 180000 nuclei. For small volumes with a higher nucleus number (10%, 20%) a two-peak distribution was obtained.

With increasing total number of nuclei, respectively higher fractions of grains providing high nucleus numbers, the average recrystallized grain size decreased. The scatter of the average grain size is almost constant in case of the homogeneous nucleation. If, however, inhomogeneities during nucleation are considered a varying scatter of the average grain size is observed. This is particularly pronounced for the case of 10%, respectively 20% volume fraction with higher nucleus density (Fig. 4.47). In this case a two-peak distribution was obtained. The peak at larger grain size represented the average grain size in initially deformed grains with a low nucleus density. Accordingly, the peak at smaller grain sizes corresponded to the higher nucleus density in the

remaining volume. For low, respectively high volume fractions of areas providing higher nucleus numbers, a single-peak distribution developed (Fig. 4.48).

The consideration of local inhomogeneities in the nucleus density was shown to lead to the occurrence of grain size distribution with one or two peaks, accompanied by a wider scatter width. It can thus be concluded that the consideration of inhomogeneities (microstructure gradients) leads to the prediction of wider grain size distributions, which are in better agreement with experiments.

4.4.4 Influence of mobility distribution

The nucleus growth rate can be altered by changing the mobilities, e.g. caused by varying amounts of elements in solution (iron, manganese, etc.). The simulations in Fig. 4.49 demonstrate how the grain size distribution is affected by the ratio of the mobilities of high angle grain boundaries (HAGB), low angle grain boundaries (LAGB) and fast boundaries (FB). The notation *FB* for fast boundaries refers to the earlier used expression growth selection (*GS*) and was used in this context for better understanding.

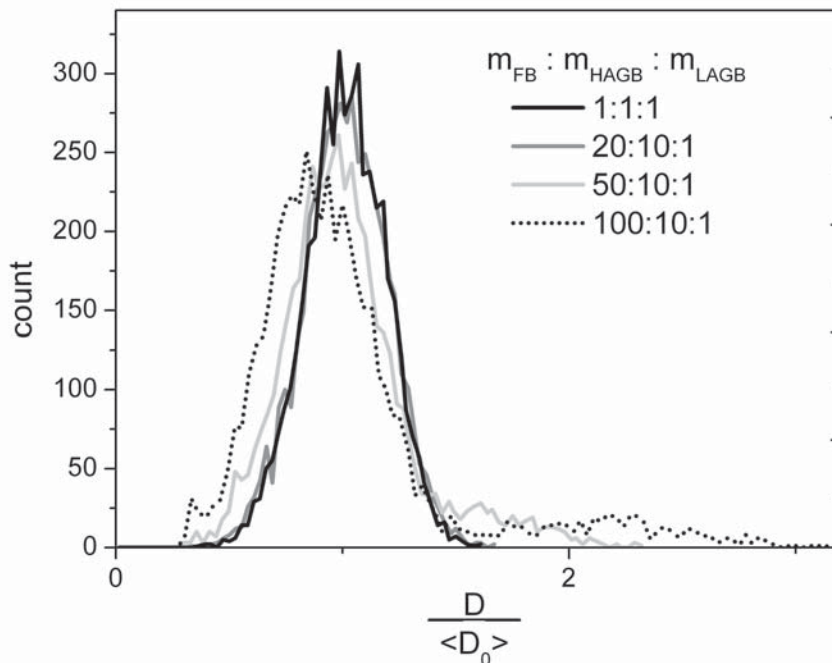


Fig. 4.49: Grain size distribution for different mobility ratios.

In general, a very small influence on the grain size distribution was obtained. If the mobility is modified by a factor of ten between fast boundaries and high angle grain boundaries more obvious changes in the grain size distribution are obtained. In this case occasionally very large grains appear which lead to a more inhomogeneous microstructure. The average grain size decreases with rising mobility ratio between high angle and fast boundaries.

4.4.5 Influence of particle-stimulated nucleation

Particle-stimulated nucleation (PSN) is most important for industrial applications to control the grain size. By adding additional nucleation sites at the particles the average grain size and grain size distribution can be altered significantly as shown below.

For the modeling of PSN the PSN model detailed in Chap. 5 was utilized. In the following only the basic effects of particles on microstructure are demonstrated. Fig. 4.50a indicates the effect of multiple nucleation at individual particles. As to be expected, with increasing number of nuclei per particles a decrease in the grain size was obtained (see also Fig. 4.51).

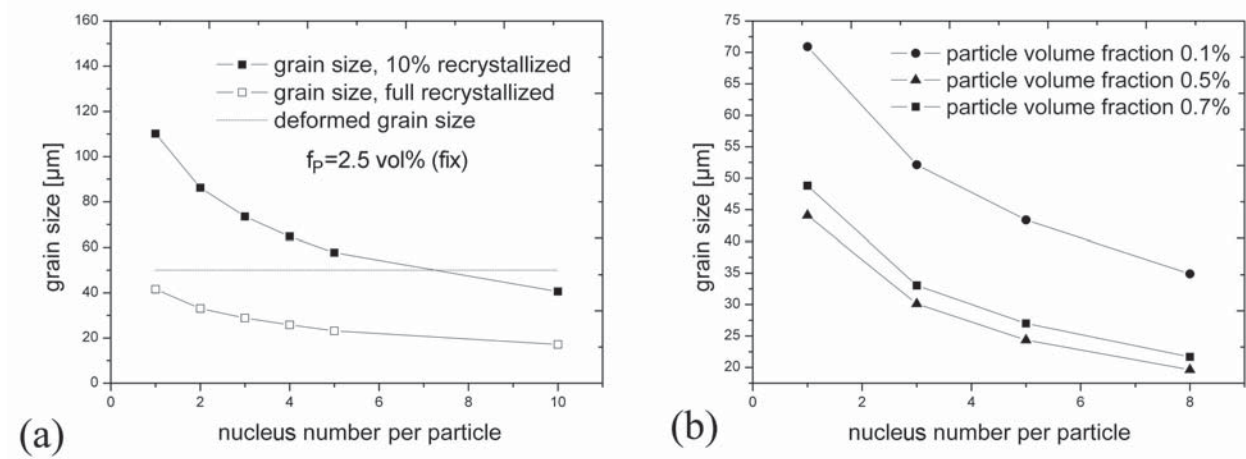


Fig. 4.50: (a) Average grain size in dependence on the nucleus frequency, (b) average full recrystallized grain size vs. number of nuclei per particle for different particle volume fractions.

Since it is known from experimental findings for the alloy AA3103 after 70% cold rolling (Chap. 5) that the number of nuclei per particle is in average one, simulations were carried using a fix nucleus number per particle of 1. Fig. 4.50b indicates the effect of an increasing particle volume fraction keeping the nucleus number per particle constant to 1. As to be expected, an increasing fraction of constituent particles lead to a decreasing average grain size.

The effect of a varying nucleus number per particle on microstructure evolution can be seen in Fig. 4.51. In the CORE model, a varying nucleus number per particle can result from different levels of the imposed deformation, which corresponds to a super elevation of the local dislocation density (Chap. 5).

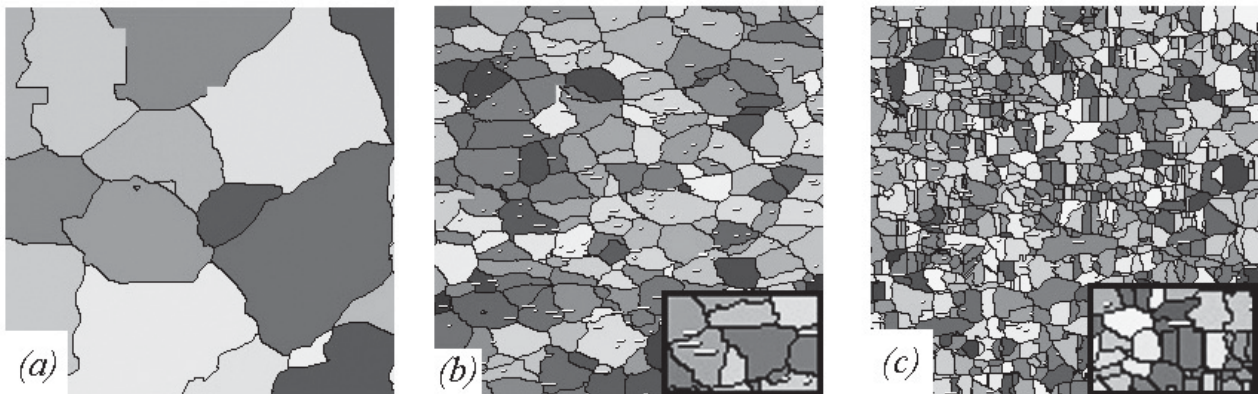


Fig. 4.51: Microstructure in transverse direction of a sheet for different nucleus frequencies (a) without particles, (b) one nucleus per particle, (c) 10 nuclei per particle (particles indicated as white rectangles).

Fig. 4.52 reveals the effect of different volume fractions of constituents (as nucleation sites) on the recrystallized grain size distribution. Besides the particles also other nucleation sites were activated in the respective simulations, such as grain boundaries, transition bands and shear bands.

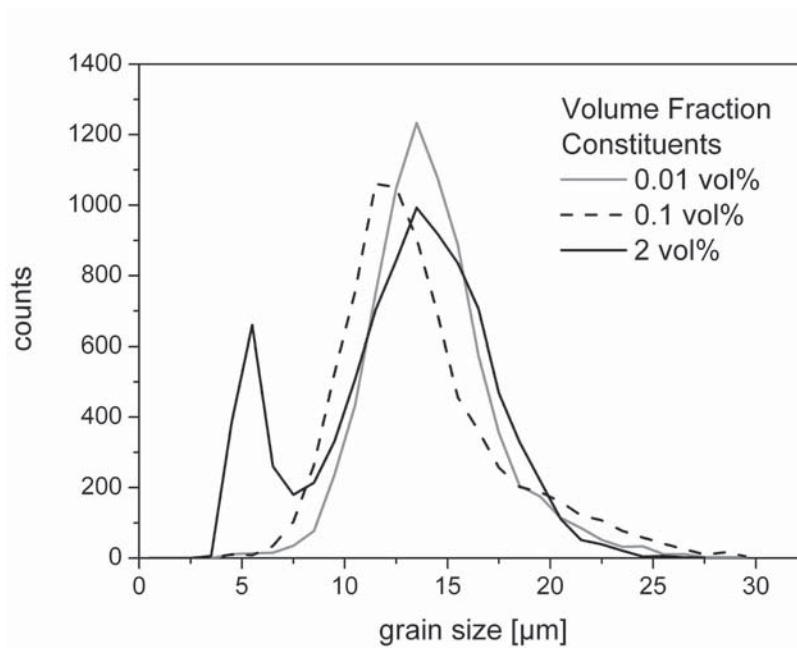


Fig. 4.52: Dependence of grain size distribution on the volume fraction of second-phase particles acting as nucleation sites.

Depending on the nucleus number resulting from the different nucleation sites, one peak or two-peak grain size distributions were obtained (Fig. 4.52). Starting from a very low fraction of particles (0.01 vol %) the average grain size was shifted to a lower average value. With further increasing volume fraction of particles a two-peak distribution is obtained, displaying small grains that originated at particles and larger grains originating at other nucleation sites.

The overall effect of particle-stimulated nucleation on recrystallization was investigated in more detail for non-isothermal annealing conditions (see Chap. 8).

4.4.6 Influence of Zener drag

Beside constituent particles which promote nucleation, smallest particles, the so-called dispersoids can hinder or even arrest grain boundary motion by Zener drag. This can lead to the suppression of recrystallization and hence, to only partially recrystallized microstructures. This effect on grain size distribution was investigated. If the driving force in the simulations was assumed much higher than the Zener drag, the grain size distribution remained unaffected by Zener drag. Therefore, the influence of Zener drag was strengthened by increasing the dispersion degree to such high values, that recrystallization was finally suppressed. The Zener drag for the individual simulations was assumed to be time-invariant. With increasing Zener drag a decreasing recrystallized grain size was obtained as reflected by the grain size distribution as indicated in Fig. 4.53. For low values of Zener drag, in case of 1 vol% dispersoids, a completely recrystallized microstructure was obtained with an average grain size of 14 μm . Thus, for 1 vol% dispersoids this did not influence the recrystallization process at all, but with increasing volume fraction of dispersoids the final recrystallized volume fraction was drastically reduced from 70% at 2.5 vol% to 20% at 3 vol% and hence partially recrystallized microstructures were obtained.

The Zener drag was kept constant during the simulations; however, the driving force was reduced with progressing recovery (Fig. 4.53b). The orientation-dependent recovery and hence locally varying driving forces, lead to the inhibition of recrystallization in those deformed grains where the driving force was compensated by the Zener drag. A decreasing grain size was obtained in case recrystallization was inhibited in each grain from some moment on and thus, the growth of already developed new grains ceased before they could impinge. Such a consideration of partial recrystallized microstructures is of importance for through-process modeling.

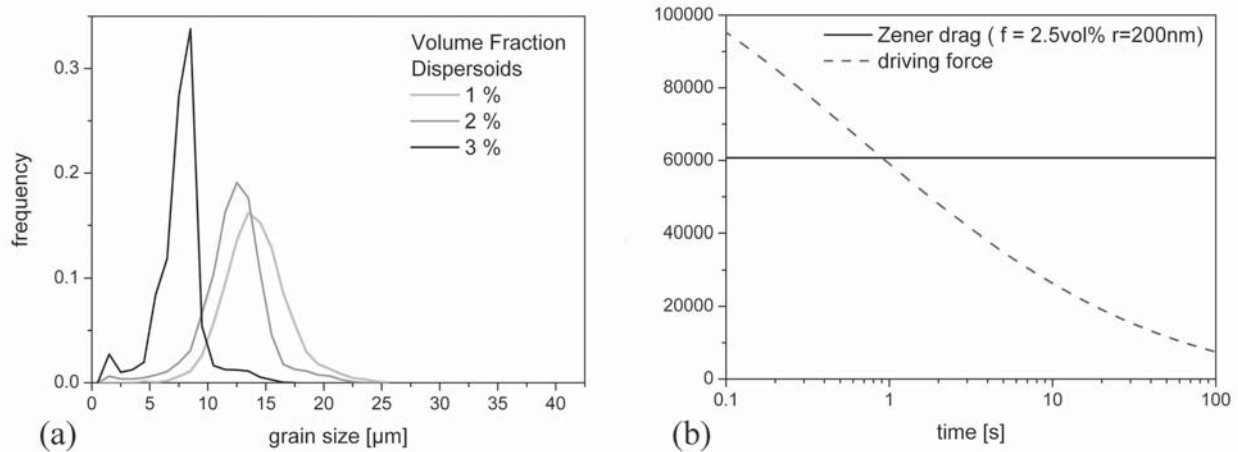


Fig. 4.53: Influence of a very high Zener drag on the grain size distribution after premature termination of recrystallization. Only the recrystallized grains were considered for the case of partial recrystallized microstructures. (a) Grain size distribution, (b) Zener drag and driving force as function of time. The corresponding material data set was based on an AA3103 alloy cold rolled to 50% reduction and annealed at $T = 350^{\circ}\text{C}$ (see Chap. 9).

4.5 Precision and Errors

The previously demonstrated modeling attempts carried out with a cellular automaton are, like all modeling approaches, also exposed to error influences. Errors can occur prior to the simulation, concurrent to the simulation. Two types of errors can be distinguished: systematic and statistical errors.

- Systematic errors occur as a consequence of approximations applied in CORE, e.g. the minimum cell size.
- Statistical errors are based on statistical fluctuations, e.g. arrangement.

Systematic errors should be prevented or if not possible, be considered in the interpretation of the results. Errors in the considered simulations can have various sources:

- Input parameters from other models, user etc.
- Inaccuracies during the simulation owing to the modeling technique.
- Evaluation and interpretation of the results using different methods with certain abstraction and hence, errors.

4.5.1 Input parameters

Input parameters can be of different nature. It can be distinguished between general parameters of the cellular automaton, parameters of physical nature and other parameters, which are in general unknown to the user or predefined by a previous simulation. Parameters that are predefined by a previous model (GIA-3IVM+, ClaNG, 3IVM+) require scrutiny and comparison with experiments, to prevent unrealistic cases during the recrystallization simulation.

Physical parameters are available from literature, but are sometimes not easily transferable to the model. For instance, published activation energies for growth are in most cases determined for bicrystals and very ideal cases (binary alloys, specific misorientations). In addition, it is in many cases not possible to estimate an accuracy of the physical parameters, because they are directly related to the measurement accuracy of the underlying experimental data, which is also often not known. For instance, the dislocation density as provided by a GIA-3IVM+ calculation can hardly be verified by experimental data (e.g. TEM).

In many cases experimental data is simply not available. In this case, it is necessary to find the optimum parameter set by a number of simulations or case studies with variation of the respective values over a critical range. A critical consideration and treatment by the user is therefore required (e.g. relating the flow stress to the dislocation density).

4.5.2 Inaccuracies during the simulation

Numerical Inaccuracies

Global parameters of the cellular automaton are for instance the cell size for the discretization of the initial mesh. A decreasing cell size is equivalent to an increasing resolution of the cellular automaton. The influence of the cell size on the recrystallization kinetics is shown in Fig. 4.54. It is found that for low cell numbers the onset as well as the whole recrystallization process is strongly influenced. For more than 7 million cells the problem already converges. From the Avrami plot in Fig. 4.54b significant deviations from the linear slope are observed particularly for low cell numbers.

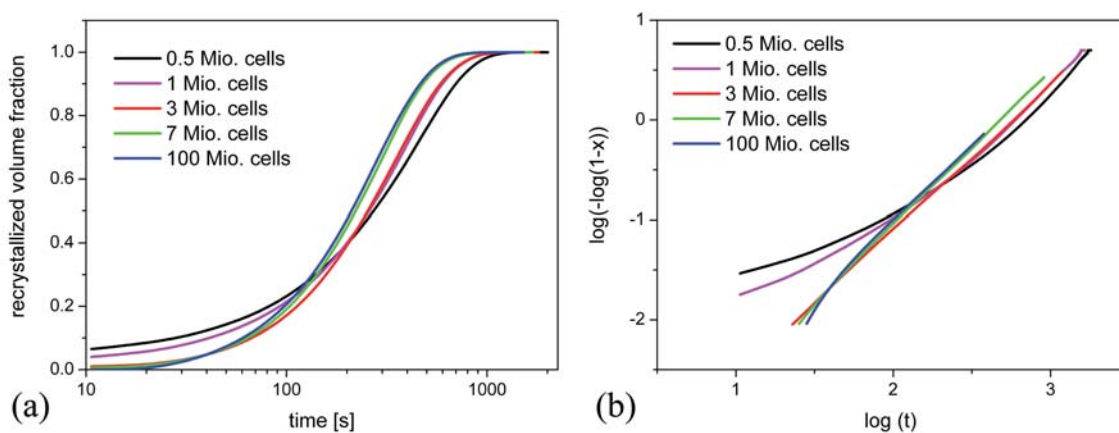


Fig. 4.54: (a) Recrystallization simulation assuming different initial cell sizes. (b) Corresponding Avrami plot showing the deviation from a linear dependency. The simulations were carried out for 400 grains. It was found from the graph in (a) that the optimum number of cells is 7 Mio. cells. For higher cell numbers no significant improvement was obtained. The grey shaded area in (b) corresponds to volume fractions smaller than 1 %.

The nucleus size is another global parameter, which could lead to a strong influence on the recrystallization simulation. The initial size of the nucleus is strongly dependent on the cell size, thus the discretization of the cellular automaton. In case the nucleus size is larger than the cell size of the automaton, no influence on the simulation is expected. However, in most cases this is not the case. It is more probable that the nucleus size is smaller than the grid size of the cellular automaton; in this case the recrystallized fraction at incipient nucleation will not be zero, more likely the nuclei have a finite size in accordance with the cell size. This can be considered by associating the nucleus size with a point in time, which corresponds to this finite nucleus size for the given growth rates. Correspondingly the time of zero nucleus size can be determined by back-extrapolation. The nucleus size will influence the recrystallization kinetics, the final grain size and grain size distribution.

Inaccuracies are also obtained dependent on the initial cell shape. This influence of the initially cubic cell grid in the cellular automaton on the final grain morphology was already considered by the introduction of partial recrystallized fractions within the cells [Mukhopadhyay 2007]. Nevertheless, very strange grain morphologies can be encountered now and then but purely as a result of the physical quantities, e.g. from locally varying boundary mobilities.

Statistical errors

Statistical errors in the outcome of the recrystallization simulations can be caused by the local arrangement of the initial microstructure grains. The following example (Figs. 4.55, 4.56)

demonstrates the effect of a random distribution of the initial microstructure grains in contrast to the preservation of prior GIA- '8 grain aggregates'. It was found that the influence of such statistical effects is comparatively small. This can be seen from the difference ODFs (texture with initial random configuration – texture with initial GIA-aggregates) indicated in Figs. 4.55c, 4.56c. After 50% recrystallization (Fig. 4.55) hardly any difference is reflected from the difference ODF (Fig. 4.55c). After 100% recrystallization a small difference is observed in the Cube intensity, which is slightly higher in case a random initial grain configuration is used. Nevertheless, the observed effects are of no significance compared to other effects studied in this chapter.

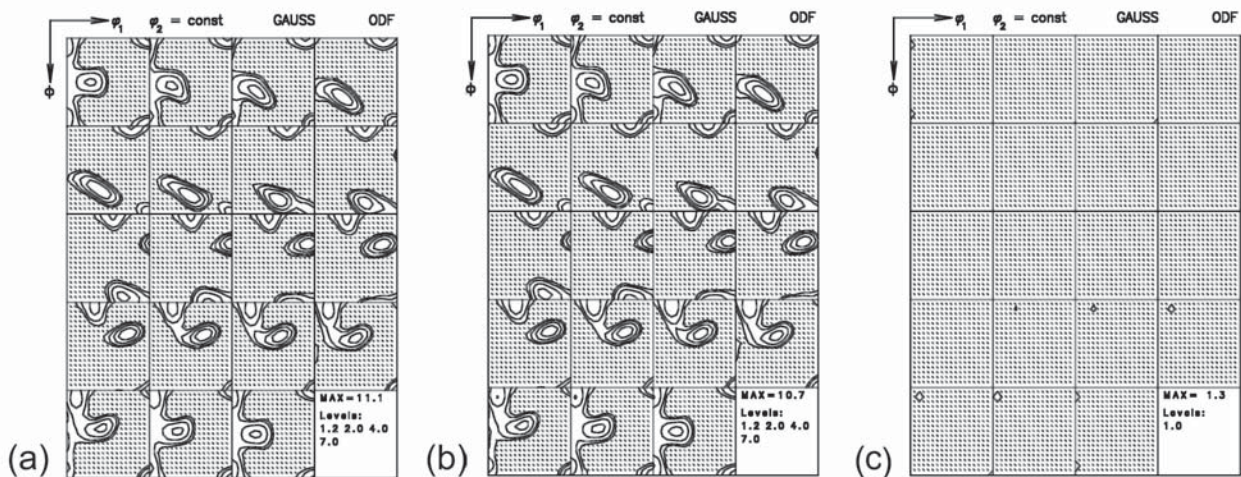


Fig. 4.55: Simulated recrystallization textures after a recrystallized volume fraction of 50 % (a) preserving the 8-grain aggregates obtained from a GIA-3IVM+ simulation; (b) without consideration of 8-grain aggregates; (c) difference ODF of (b)-(a). No differences between the shown textures can be identified.

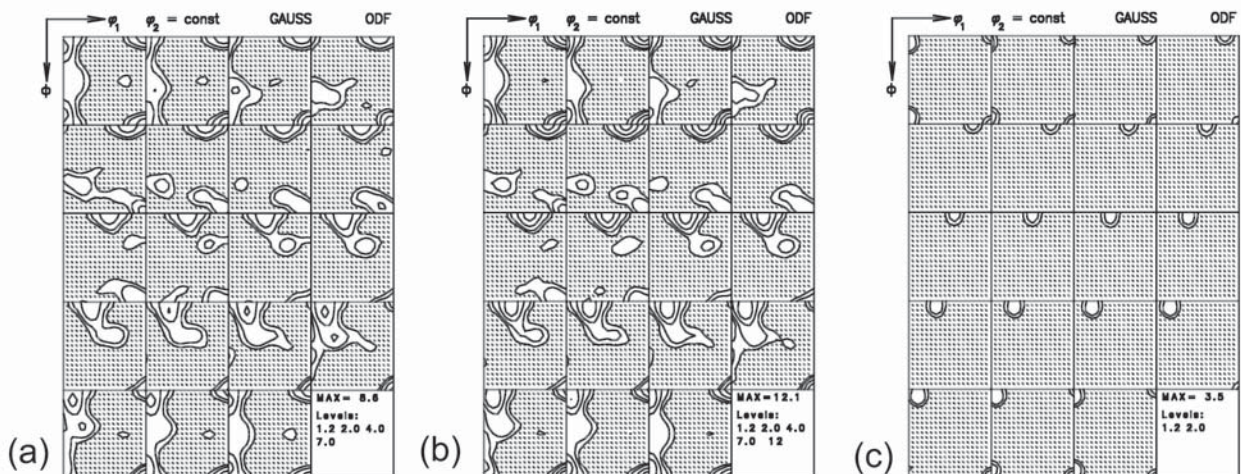


Fig. 4.56: Simulated recrystallization textures after a recrystallized volume fraction of 100 % (a) preserving the 8-grain aggregates obtained from a GIA-3IVM+ simulation; (b) without consideration of 8-grain aggregates; (c) difference ODF of (b)-(a). Only minor differences between the shown textures can be identified.

4.5.3 Evaluation & interpretation

After the simulation, the obtained results need to be interpreted for comparison with experimental data. The quantities that are compared to experiments are the recrystallization texture, kinetics and the grain size distribution. Errors or deviations can occur in the course of transferring the direct simulation output into such quantities. The recrystallized volume fraction is for instance a direct output, since each cell provides its own recrystallized volume fraction. The direct use of this

information does not lead to a loss of accuracy, e.g. for the determination of the *recrystallization kinetics*.

The *grain size* in CORE is computed from the total volume of a grain (sum of all cells that belong to the grain). This volume is associated with a sphere of radius $d_{\text{Grain}}/2$. A determination of the grain size corresponding to this approach will lead to larger errors in case the grain shape is not isotropic. The grain shape itself was not considered in the present work, due to the not yet sufficient quality of the grain size predictions.

The *recrystallization texture* is not a direct output of the recrystallization model CORE. To compute the orientation distribution function from the cellular automaton output each orientation is assigned a Gauss type orientation scatter. This procedure adds an additional uncertainty to the texture output [Reher 1998]. The volume fractions can be either evaluated according to the method of Lücke and Pospiech, or directly from the simulation by assigning a scatter of $\pm 11^\circ$, respectively $\pm 15^\circ$ depending on the texture component.

A potential disagreement of simulated data with experiments can also originate from the experimental data itself, since measurements also carry some uncertainty.

Experimental data for *recrystallization kinetics* can be obtained via various methods: hardness measurements, texture measurements, metallography etc. Hardness measurements for instance are fast and simple; they provide information on the material softening during annealing, but do not distinguish the various mechanisms involved. Hence, the calculation of the recrystallization kinetics from hardness data in case of pronounced recovery is subject to large error and is therefore not recommended. A better way is to track the evolution of the β -fiber volume fraction. The β -fiber volume fraction increases during recovery because of substructural rearrangements, which results in the reduction of dislocation density and at the same time to higher misorientation gradients accompanied by a texture sharpening. The onset of recrystallization can be identified from a drop in the β -fiber volume fraction. The additional determination of the recrystallized volume fraction from light-optical images or EBSD data ensures the construction of a reliable data set, as done in the present work.

The determination of the *grain size distribution* is strongly influenced by the used technique (light-microscopy, EBSD, etc.). It is known that EBSD data reveals, in general, smaller grain size classes than observed in a light-microscope. Further errors originate in the method used for evaluation. Whereas the grain size obtained by EBSD is based on the calculation of an equivalent circle diameter, the grain size from optical micrographs was measured with the Line Intercept method. The latter one is a reliable method for homogeneous grain size distributions only. In the present work, both methods were used and compared to simulated grain sizes.

4.6 Conclusions (classification of effects on recrystallization)

Tab. 4.1 summarizes the different effects on recrystallization that were studied in this chapter (Secs. 4.2-4.4). They are quantified with respect to their importance for the modeling of recrystallization kinetics, textures and grain sizes.

From Tab. 4.1, summarizing the effects investigated with CORE, it can be concluded that the most pronounced effects on recrystallization are caused by second-phase particles (Zener drag, particle-stimulated nucleation). Those effects are studied in more detail for real materials in Chaps. 7, 8 and 9. The effect of nucleation rates lead to surprisingly strong influences on the grain size distribution, hence in Chap. 6 a model for incubation times is introduced to mimic nucleation rates for application to real experiments.

The recrystallization model CORE provides further a new insight to gain a better understanding of annealing phenomena in deformed polycrystals, particularly to understand the complexity of the recrystallization phenomena being the result of a superposition of various effects.

Tab. 4.1: Effects on simulated recrystallization behavior quantified according to their impact (*Kin* = effect on recrystallization kinetics, *Tex* = effect on recrystallization texture, *GS* = effect on grain size or grain size distribution).

<i>Effects / Dependencies</i>	<i>Influence intensity</i>			<i>Chapter / section</i>
	<i>minor</i>	<i>medium</i>	<i>major</i>	
pre-deformation texture	<i>Kin, GS</i>	-	<i>Tex</i>	4.2.1
nucleus number / initial grain size	<i>Tex</i>	-	<i>GS, Kin</i>	4.3.2 / 4.4.1
Pre-deformed grain shape	<i>Tex</i>	<i>GS, Kin</i>	-	4.3.3
Dislocation density	<i>Tex, Kin</i>	-	<i>GS</i>	4.2.2 / 4.3.5 / Chaps. 7, 9
strain	<i>Tex</i>	-	<i>Kin, GS</i>	4.2.3 / 4.4.2 / 4.3.6 / Chaps. 7, 9
Alloy composition	-	<i>Kin, GS</i>	<i>Tex</i>	4.2.4
arrangements in GIA-aggregates	<i>GS, Tex, Kin</i>	-	-	4.2.7 / 4.6.2
Zener drag	<i>Tex, GS</i>	<i>Kin</i>	-	4.3.9 / Chap. 9
	-	-	<i>GS, Tex, Kin</i>	4.2.6 / 4.3.9 / 4.4.6 / Chaps. 7,8
Solute drag	<i>Tex**, GS**</i>	-	<i>Kin</i>	4.3.12
Particle-stimulated nucleation	-	-	<i>GS, Kin, Tex*</i>	4.2.5 / 4.3.11 / 4.4.5 / Chaps. 7,8
nucleation rate	-	<i>Tex</i>	<i>Kin, GS</i>	4.3.4 / Chap. 8
Inhomogeneities during growth	-	<i>Kin, GS</i>	-	4.3.7
mobility ratio on growth	<i>GS, Tex</i>	<i>Kin</i>	-	4.3.8, 4.4.4
Inhomogeneities during nucleation	<i>Kin, Tex</i>	<i>GS</i>	-	4.4.3
heating rates	-	-	<i>Kin, GS*, Tex*</i>	4.3.10, Chap. 8

* in case of concurrent precipitation; ** if orientation-independent

Chapter 5

Model for Particle-Stimulated Nucleation

5.1 Introduction

One of the major interests in recrystallization simulations is the calculation of the required nucleation spectra, since they significantly influence the outcome of the recrystallization texture predictions. The nucleation model used in the present work comprises various sub-models, such as for nucleation at grain boundaries, transition bands and shear bands. However, the influence of particle-stimulated nucleation was not considered in the recrystallization simulations up to now, but cannot be neglected in order to properly account for recrystallization of particle containing materials, i.e. most commercial aluminum alloys.

It seems certain that nuclei preferentially originate within the deformation zone around particles. Their orientations are therefore restricted to the orientations present in these zones. Thus, the focus of the present chapter is the detailed experimental investigation of the deformation zones and the subsequent nucleation behavior at particles during annealing. The evolving texture components are here of major importance. The obtained experimental results (Sec. 5.2) are modeled in Sec. 5.3 using the finite element method (FEM). The strain paths obtained from FEM were further utilized to create a deformation model to predict the inhomogeneities in the particle vicinity (Sec 5.4). At the end of this chapter a model for particle-stimulated nucleation is proposed for use in the recrystallization model CORE (Sec. 5.5) based on the collected experimental data and deformation simulations.

5.2 Evolution of the Deformation Zone in fcc Materials – Experiments

5.2.1 Appearance of the deformation zone

Most commercial alloys contain second-phase particles. Second-phase particles can be either present from casting, the so-called constituents or they appear during an annealing treatment as dispersoids. The effect of second-phase particles on recrystallization has many facets. Large particles, which were present before deformation, can cause particle-stimulated nucleation during an annealing treatment; at the same time the same treatment might lead to the appearance of dispersoids, which can have a completely opposite effect. While constituent particles enhance recrystallization nucleation, the small dispersoids can strongly hinder recrystallization up to complete suppression under certain processing conditions. In the following section the effect of second-phase particles during deformation and the consequences for subsequent annealing are discussed from an experimental point of view.

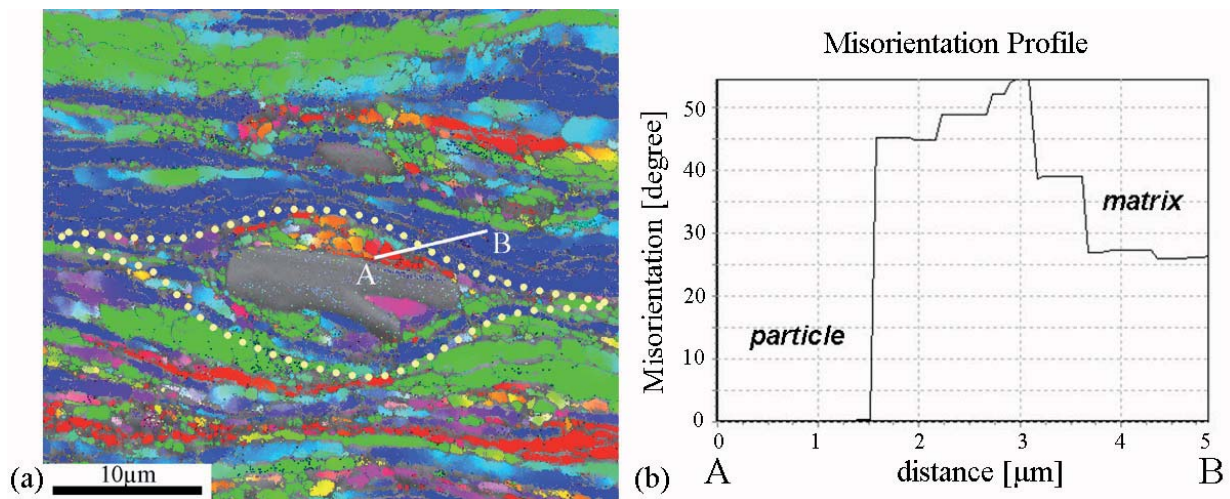


Fig. 5.1: (a) EBSD micrograph showing second-phase particles surrounded by a deformation zone (encircled by white dotted line). Displayed is the plane in transverse direction (b) Corresponding misorientation profile within the deformation zone from the particle surface to the surrounding matrix (70% cold rolled AA3103).

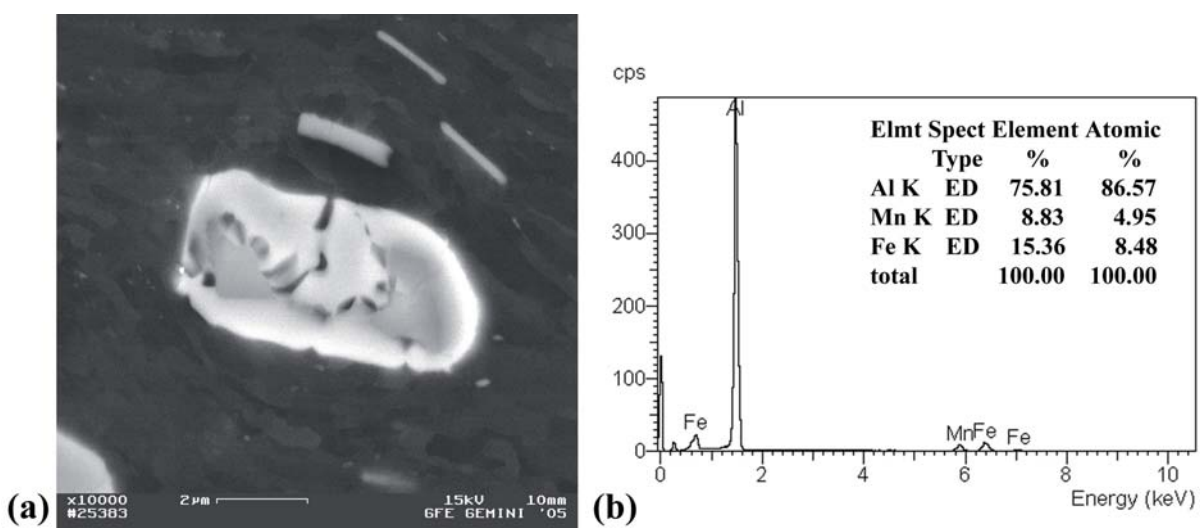


Fig. 5.2: (a) SEM micrograph of constituent particles in AA3103. (b) Results of an EDX (energy dispersive X-ray spectroscopy) analysis of the constituents. The corresponding composition is indicated as well. [courtesy of the GFE, RWTH Aachen].

The linking of nucleation to the prior deformed substructure is meaningful, since particularly the regions in the particle vicinity provide nucleus orientations which can significantly determine the final recrystallization textures.

The constituents observed in the Al-Mn alloy considered in the present work, had either the composition of Al_6Mn or $\alpha-AlMnSi$ and had no specific crystallographic relationship to the matrix (Fig. 5.2).

During deformation of a particle-containing material, the material will not deform homogeneously throughout the crystal (Fig. 5.1). The second-phase particles have usually a higher strength than the surrounding matrix. Thus, at first the matrix material will comply with the macroscopic deformation whereas the constituent particles remain almost undeformed. This causes inhomogeneous material flow behaviour during deformation and leads, for instance, during compression or rolling of a two-phase material to the development of so-called deformation zones (indicated by dotted line in Fig. 5.1a). Those are zones of increased dislocation density and very high orientation gradients (Fig. 5.1b). This is demonstrated exemplarily in Fig. 5.1b by a misorientation profile along the line AB indicated in Fig. 5.1a.

The particles are mostly spherical or ellipsoidal in shape; therefore an essentially symmetric influence on dislocation slip can be expected. The EBSD micrographs in Fig. 5.3a show a typical deformation zone observed after 70% cold rolling of industrially processed AA3103. Fig. 5.3b indicates new grains appearing in the vicinity of constituents, apparently developed by the mechanism of particle stimulated nucleation during an isothermal annealing treatment. Since in literature extended information is available for single crystals, but rather limited data for polycrystals, in the following a detailed investigation will be presented for a polycrystalline AA3103 alloy with respect to the orientations developing in the deformation zone and the related nucleation behavior. These orientations are of major importance since they strongly influence the recrystallization texture evolution in particle-containing alloys. The following investigations are all based on measurements by electron-back scatter diffraction (EBSD). The material considered is a commercial Al-Mn alloy AA3103 which was cold rolled to various cold rolling reductions (Fig. 5.5).

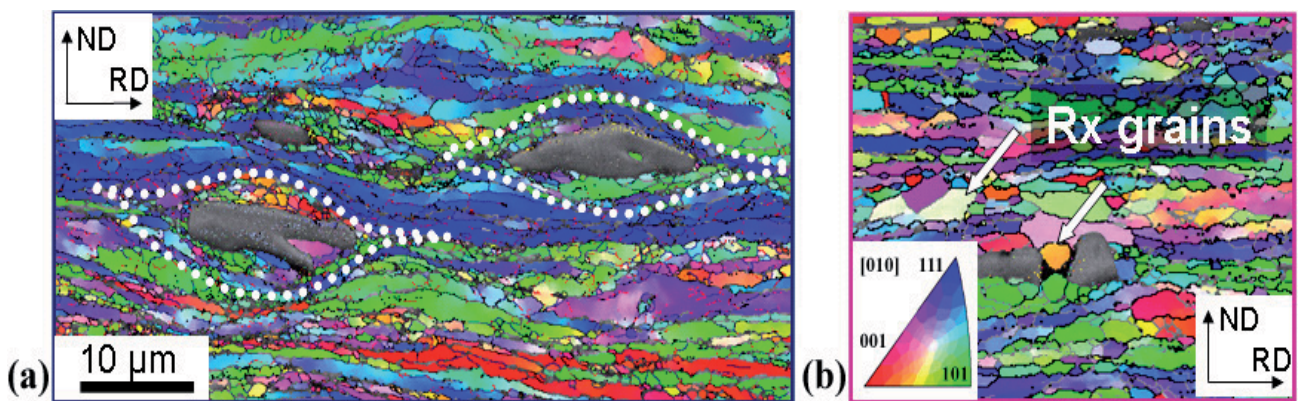


Fig. 5.3: (a) EBSD micrograph of a cold deformed microstructure showing the deformation zones surrounding constituent particles. (b) EBSD micrograph of nucleation within the deformation zone during annealing at $T=290^{\circ}C$ for 25 min of a 70% cold rolled Al alloy AA3103.

As introduced above, the material needs to flow around the particle during deformation, so that the macroscopic sample can comply with the imposed macroscopic shape change, creating that way a deformation zone in the particle vicinity. On a microscopic level this corresponds to an increase of the dislocation density in the surroundings of the particle. Complex dislocation networks develop, resulting in a much finer subgrain structure than observed in the matrix. In addition, the subgrains have a more equiaxed shape compared to the long elongated subgrains in the remaining matrix (Fig. 5.3a).

5.2.2 Subgrain size

For simulations the subgrain size within the deformation zone or, respectively, the corresponding dislocation density in the particle vicinity is important. The subgrain size inside and outside of the deformation zone was measured on samples cold rolled to 70% thickness reduction in the alloy AA3103. In order to define the corresponding deformation zone and, hence, the subsets for the analysis of the EBSD data (Figs. 5.4a,b), the extent of the deformation zone after 70% cold rolling reduction was taken from the FEM calculations in Sec. 5.3. In Fig. 5.4a,b, it is exemplarily shown how the deformation zones were defined. The measured subgrain size distribution in the matrix and within the deformation zones is displayed in Fig. 5.4c.

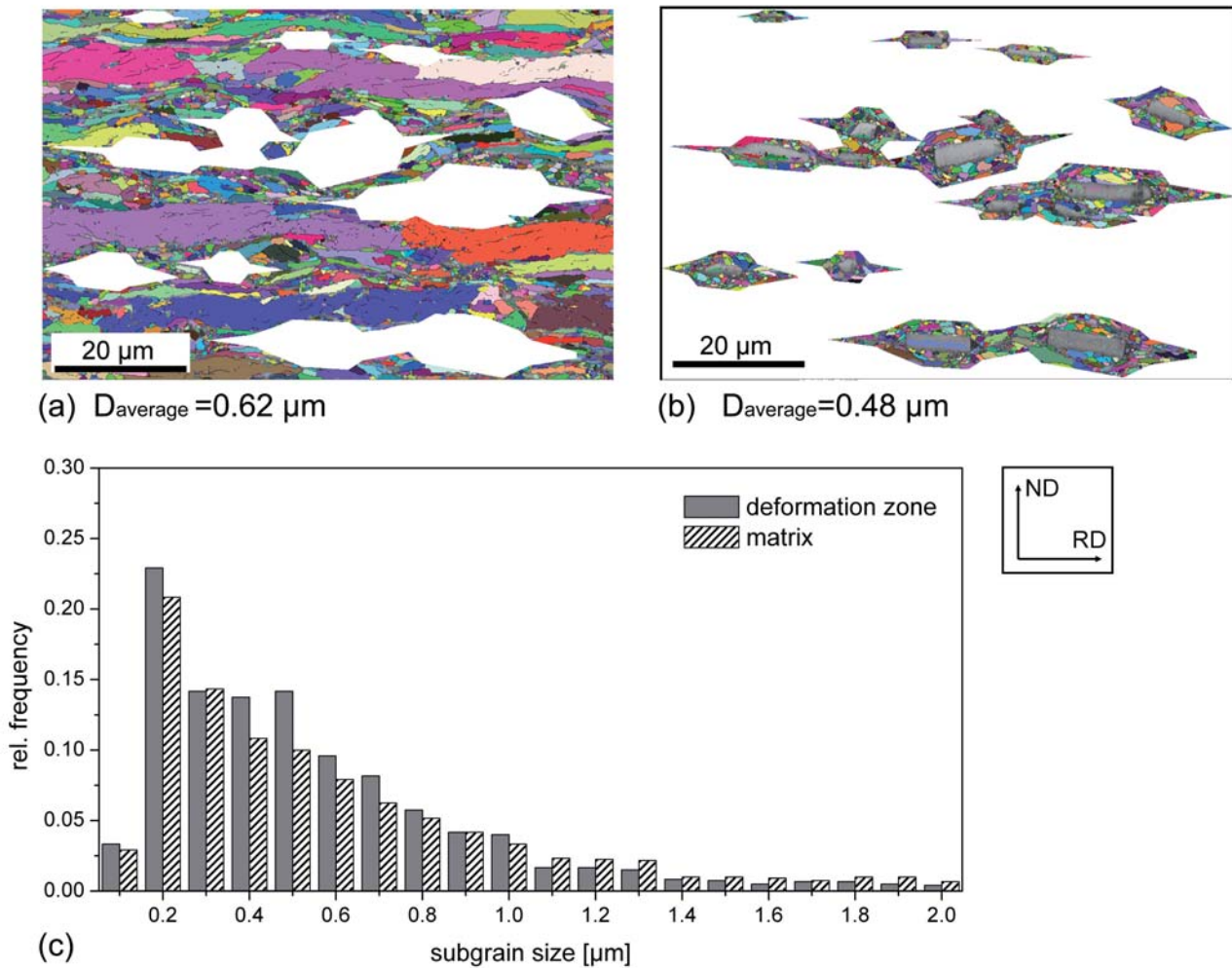


Fig. 5.4: (a) Subset of an EBSD micrograph of the subgrain structure within the deformation zone; (b) subset of the subgrain structure outside the deformation zone. (c) Subgrain size distribution within and outside the deformation zone. The investigated material is an AA3103 Al alloy cold rolled to 70% thickness reduction.

It was found from experiments that the subgrain size within the deformation zone after a cold rolling reduction of 70 % is by a factor 1.4 to 2 smaller than in the remaining matrix (Fig. 5.4). This is in agreement with literature [Humphreys 1977]. For application in recrystallization simulations this subgrain size was converted via the principle of similitude into a dislocation density.

$$d_{\text{Sub}} = \frac{C}{\sqrt{\rho_{\text{tot}}}} \quad (5.1)$$

where d_{sub} is the measured subgrain size, C a constant of the order of 15 [Blum 1993] and ρ_{tot} the total dislocation density. From this calculation an increase in dislocation density within the deformation zone was obtained.

5.2.3 Microtexture in the deformation zone

It is known from the literature [Russell 1970, Brown 1971, Humphreys 1979, Humphreys 1983] that in the vicinity of particles not only the subgrain size is smaller, but also the locally found orientations deviate significantly from the matrix orientation as shown in the following.

Fig. 5.5 indicates the evolution of deformation zones as depending on the deformation degree for material of the series RZ (see Chap. 7). After 50% cold rolling reduction the deformation zones are hardly visible. After cold rolling reduction 70% and beyond, the deformation zone is clearly visible, since the orientation in the near particle surrounding differs significantly from the orientation in the remaining grain (locally different color). The orientation spread is greatest at the very sharp edges of complex shaped particles. Those are the places where the compatibility problems between the matrix and the undeformable particles are greatest. This will be discussed in more detail by means of finite element simulations in Sec. 5.3. Due to that very large misorientations developed in the deformation zones. This agrees very well with findings from the literature [Herbst 1978].

The orientations developed in the vicinity of particles are crucial for further nucleation at these heterogeneities. It is justified to assume that nuclei which developed during recrystallization are similar to those found in the former deformation zone. Several investigations on single crystals are known [Herbst 1978, Chan 1984, Engler 1997a], which support this assumption. Therefore, in the following the deformation zones were investigated with special focus on the microtexture after cold rolling reductions of 50% and 70% (Figs. 5.6, 5.7).

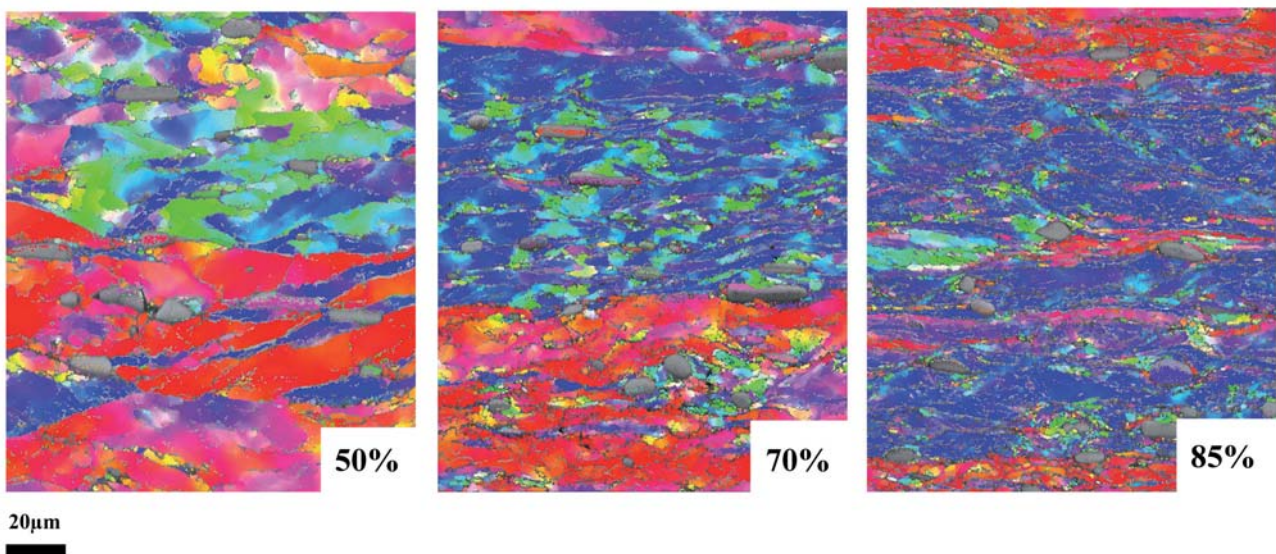


Fig. 5.5: EBSD micrographs of the microstructure after 50%, 70% and 85% cold rolling reduction displayed in transverse sheet direction. The initial material is an AA3103 which was homogenized before deformation.

For a better understanding the microtextures were considered inside and outside the deformation zones, separately. With the used software (HKL-Channel5) subsets for the deformation zones could be created and hence data collection in certain regions of the microstructure was independently possible. Only slight differences in the deformation zone textures can be observed with changing rolling reduction (Figs. 5.6a, 5.7a).

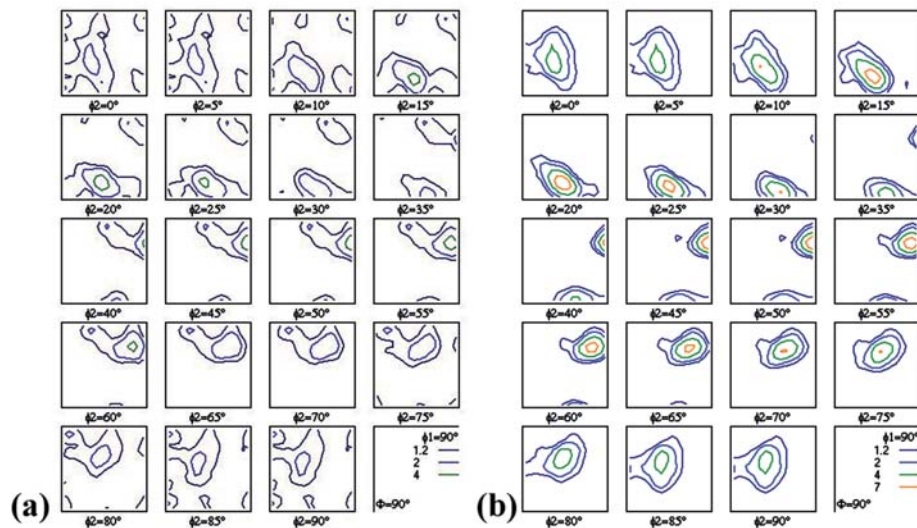


Fig. 5.6: (a) Microtexture inside the deformation zone based on one hundred measured deformation zones for 50% cold rolled AA3103, (b) Microtexture of the matrix- i.e. without the contribution of deformation zones for 50% cold rolled AA3103.

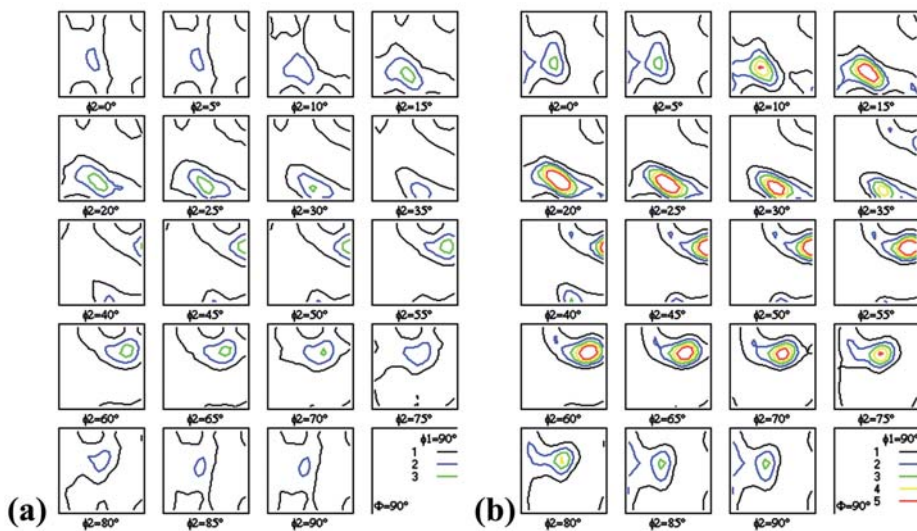


Fig. 5.7: (a) Microtexture inside the deformation zone based on one hundred measured deformation zones for 70% cold rolled AA3103, (b) Microtexture of the matrix- i.e. without the contribution of deformation zones for 70% cold rolled AA3103.

In the matrix in both cases a typical cold rolling texture was obtained, which is in agreement with macrotexture measurements in the same samples. A characteristic feature of the deformation zone is that the deformation texture components Cu, S and Brass have a much lower volume fraction than in the matrix which is in agreement with literature [Humphreys 2004]. This is due to the strong lattice rotations which lead to a much wider scatter of the deformation texture components. This can be clearly seen from the drop in the volume fractions of the deformation texture components (Fig. 5.8). Beside the textures measured from EBSD, which are referred to as microtexture, also the corresponding macrotextures were measured. The corresponding volume fractions are indicated in Fig. 5.8 for comparison. Within the deformation zone a higher volume fraction of 45° ND rotated Cube component was observed, which was not present in the remaining matrix. Also the macrotextures did not contain a significant volume fraction of the 45° ND Cube component. Beside the 45° ND rotated Cube texture component also the P- and the Q- texture component were observed within the deformation zones. If one compares Figs. 5.6a, 5.7a with Figs. 5.6b, 5.7b it can be observed that especially the peak of the Brass component seems to be smeared out up to the 45° ND

rotated Cube component. This effect can be attributed to a rotation of the Cu texture component around transverse direction [Engler 1997a, Humphreys 2004].

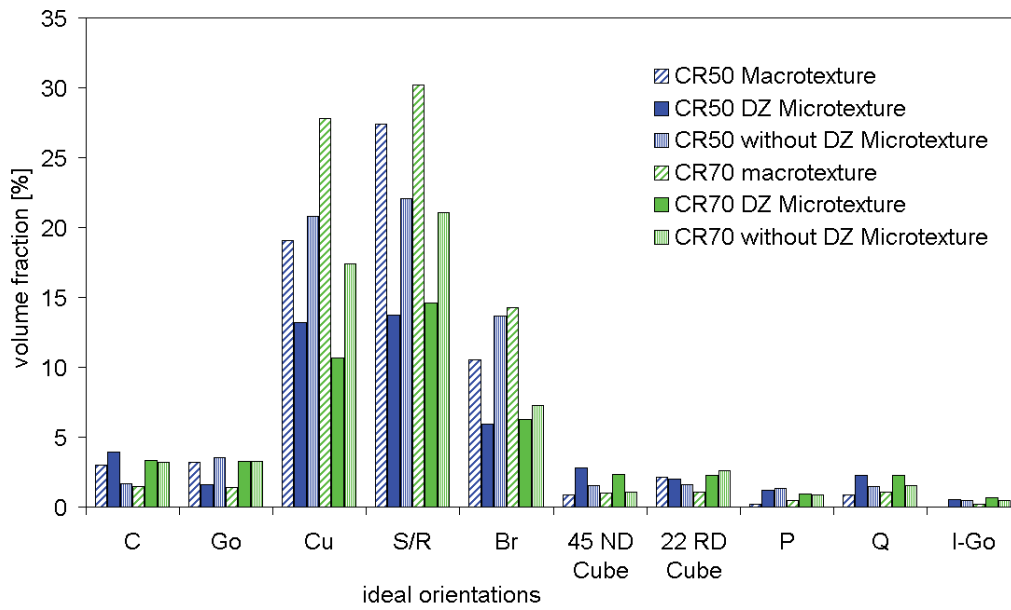


Fig. 5.8: AA3103 volume fractions in macro and microtexture; comparing the volume fractions of ideal components in the deformation zone and outside the deformation zone.

Fig. 5.8 shows the volume fractions of ideal texture components for the presented cases. In general weaker ideal deformation texture components are found in the deformation zone than in the adjacent matrix (see Fig. 5.8). It is observed that the Cube fraction and the fraction of the 45° ND rotated Cube component in the deformation zones is higher than in the surrounding matrix as measured from microtextures (EBSD). The overall misorientations measured within the deformation zones were much higher than those observed in the matrix.

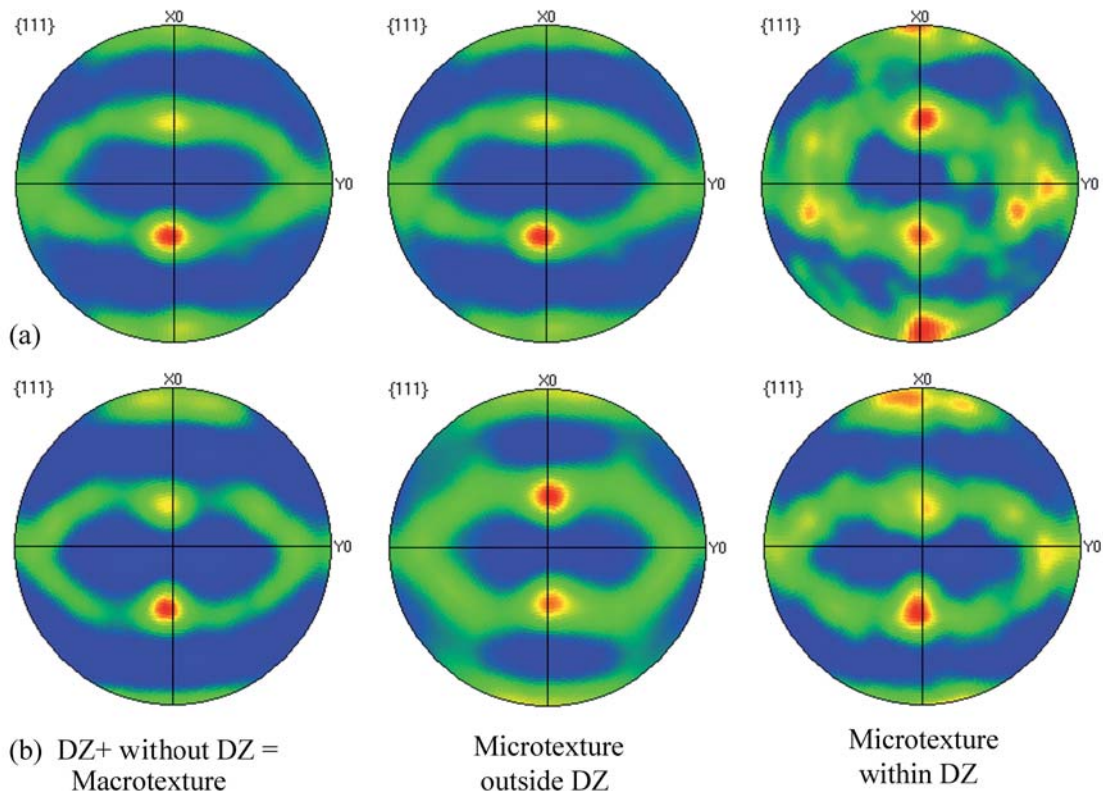


Fig. 5.9: Orientations measured from experiments inside/outside the deformation zone displayed in a {111} polefigure. (a) For 50% cold rolled material, (b) for 70% cold rolled AA3103. (DZ = deformation zone).

In Fig. 5.9 the texture change within the deformation zone compared to the matrix is visualized using $\{111\}$ polfigures. It can be observed that the macrotexture and the microtexture outside the deformation zone are basically the same. Contrary to most observations in literature, the microtexture within the deformation zones is far from being random. Basically the same components as in the matrix with a scatter up to 35° misorientation are observed. The actually observed successful nuclei have similar orientations, but with a much larger scatter than observed in the deformation zone (Fig. 5.13).

Another parameter which is important for simulations is the size of the deformation zone, since it determines under certain processing conditions the grain size in the fully recrystallized state, e.g. if precipitation reactions occur in the material during a chosen heat treatment. The size of the deformation zone is dependent on the particle size, shape and interparticle spacing. No detailed experimental study was carried out on this topic, but it will be considered for the modeling in Sec. 5.3.

5.2.4 P- and 22° ND rotated Cube texture component

For a better comparison with simulations, the location of specific texture components such as the P and 22° ND rotated Cube texture component within the deformation zone were analyzed in more detail. For this purpose the deformation zone was subdivided into different regions, which account for the symmetry of the deformation zone. The frequency of the P- and 22° ND Cube texture component was determined for the 50%, respectively 70% cold rolled AA3103 alloy introduced previously.

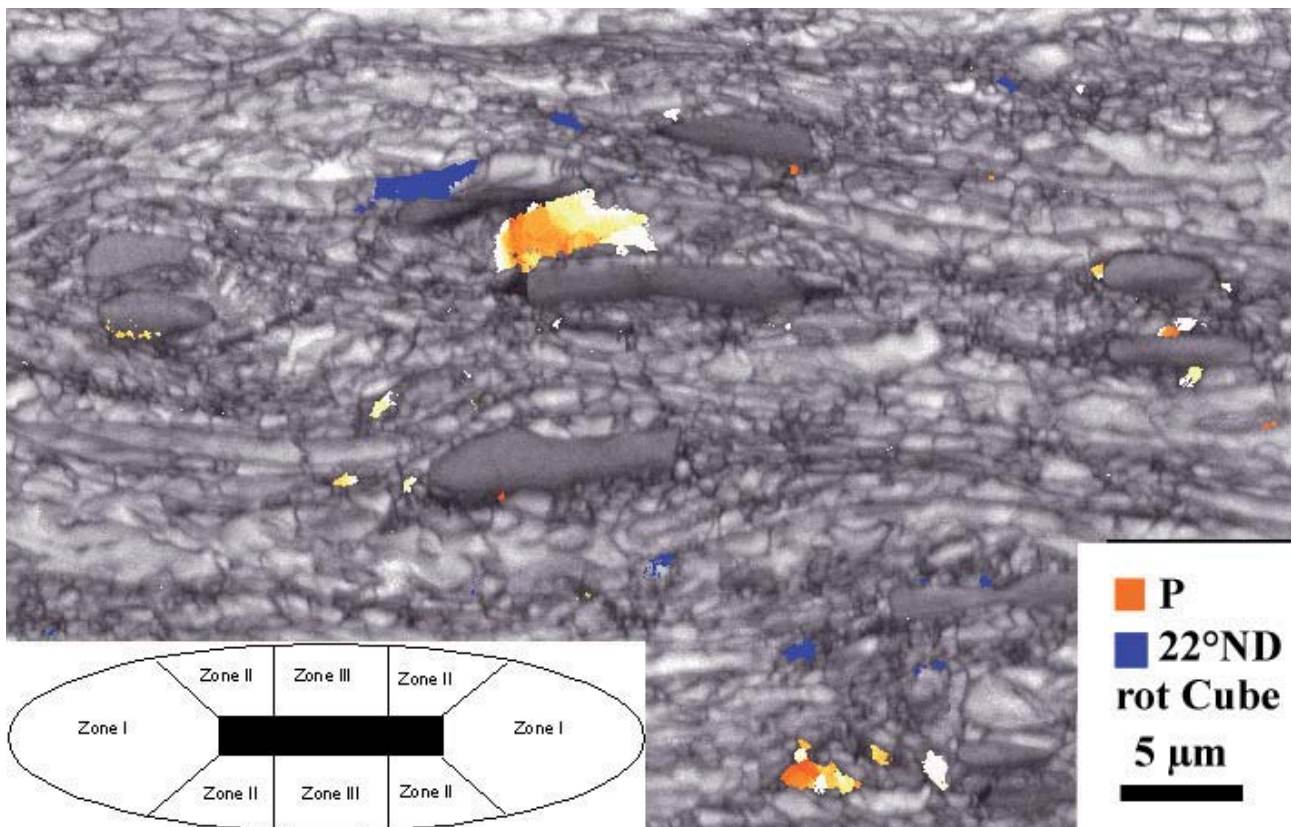


Fig. 5.10: EBSD micrograph showing P-oriented (orange) and 22° ND rotated Cube-oriented (blue) regions; scheme showing the subdivision of the deformation zone into different regions to characterize the location of special texture components.

Fig. 5.10 reflects the substructure in the particle vicinity displaying P and 22° ND rotated Cube texture components (highlighted in orange and blue). The deformation zone around the particles was subdivided in Zones I to III, to determine the exact location of the considered texture components. It was observed that most of the P and ND rotated Cube oriented nuclei were actually found at the tip of the particles in zone I, respectively II (Figs. 5.10, 5.11). The occurrence of the various components in the other zones can be attributed to the strong interaction of several deformation zones, as present in polycrystalline materials. This may not in general change the occurrence of these texture components but their location in the particle vicinity. The maximum probability for the occurrence of the investigated components is below 25%. This means that 25% of all investigated particles had either one or both components located in their vicinity.

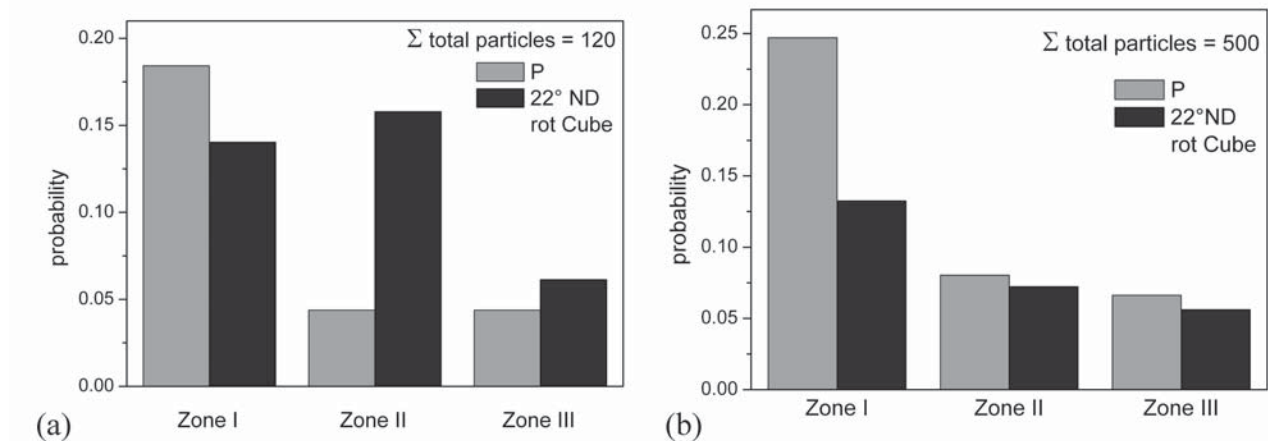


Fig. 5.11: Occurrence of the P component and ND rotated Cube component in the different zones within the deformation zone for (a) 50% and (b) 70% cold rolled AA3103.

5.2.5 Nucleus texture and frequency

So far we have only addressed the question as to whether, or not, a deformed grain will form a nucleus. For a quantitative treatment of the nucleation texture and also for grain size predictions, it is necessary to know how many nuclei are formed per considered nucleation site, since it is unlikely that each grain will form only a single nucleus. This problem has to be addressed for each nucleation mechanism separately. A very special case is particle stimulated nucleation (PSN). We have conducted an experimental investigation by EBSD into the nucleation frequency at large particles in a commercial aluminum alloy AA3103. For this purpose the material was first heat treated to initiate recrystallization. The number of new grains observed in the vicinity of particles was counted, and the dependency of nucleus frequencies on particle size was determined (Fig. 5.12b). There are particles without a recrystallization nucleus whereas other particles may be surrounded by several nuclei. On average approximately 1.06 recrystallization nuclei/particle were found. Therefore, the nuclei density at particles essentially corresponds to the particle density.

Since the particle distribution was measured in 2D the apparent particle size is smaller than the true particle size, so that an evaluation in 3D (e.g. [Nembach 1996, Fruhstorfer 2002]) would essentially cause a shift to larger particle sizes. The total constituent volume fraction was determined from BSE micrographs to 2.5 vol%.

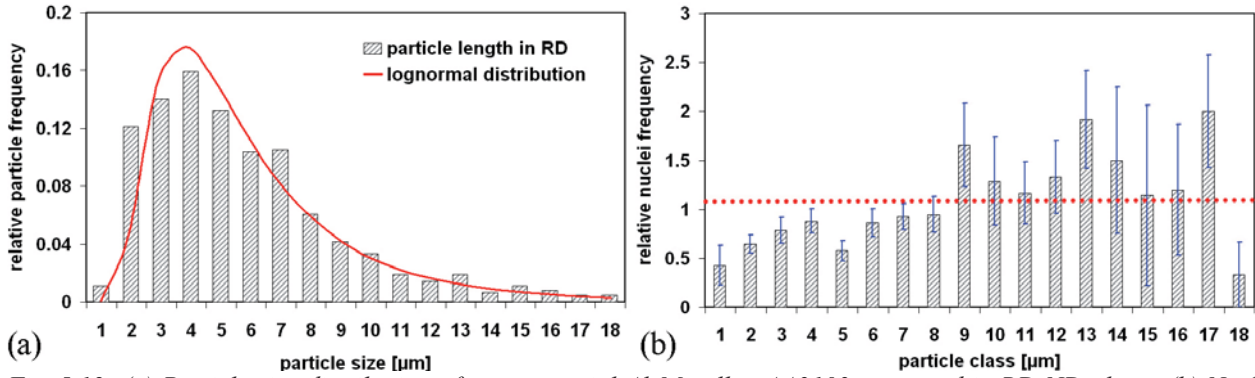


Fig. 5.12: (a) Particle size distribution of a commercial Al-Mn alloy AA3103 measured in RD-ND plane; (b) Nucleus frequency versus particle size.

For particle sizes smaller than 8 μm the nucleus frequency was less than one nucleus per particle. For particle sizes larger than 8 μm multiple nucleation was observed at the particles; on average each particle contributed about one nucleus. This is in good agreement with literature [Herbst 1978, Humphreys 2004]. Altogether about 500 particles were analyzed with respect to their nucleus frequency (Fig. 5.12b) and particle size distribution (Fig. 5.12a).

For more than 500 particles, located in different samples, the number of nuclei per particle and their orientation were measured (Fig. 5.13). The nucleus texture comprises orientations along the β -fiber with strong scatter as well as the RD rotated Cube orientation (Fig. 5.13).

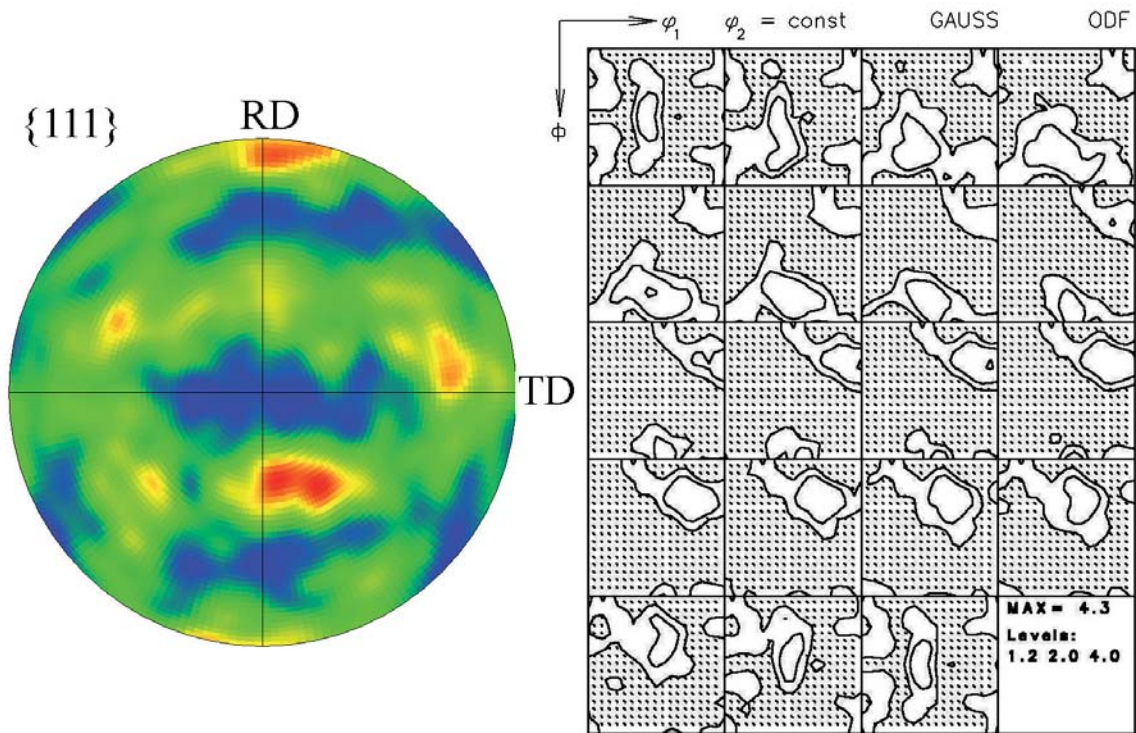


Fig. 5.13: (a) $\{111\}$ -polefigure of the successful nuclei originating in the vicinity of particles after 70% cold rolling deformation as measured from EBSD micrographs (in total 500 orientations); (b) Nucleus texture of commercial AA3103, 70% cold rolled, annealed for $t = 25$ min at 290° .

5.3 The GIA-DZ Model for In-Grain Deformation Zone Evolution

It is known that the origin of recrystallization textures can be found already in the deformed state [Herbst 1978]. This fact points out the importance of the description and analysis of the deformed state focusing on the prediction of recrystallization nucleation. Preferred sites for nucleation commonly found in aluminium alloys are deformation inhomogeneities, such as transition bands, grain boundaries, shear bands or the deformation zones in the particle surrounding. Recently, there have been many approaches experimentally as well as by simulation, to predict such inhomogeneities [van Houtte 1995, Bate 1999, Radhakrishnan 2000, Humphreys 2003]. One type of deformation inhomogeneities which play an important role in the processing of commercial aluminium alloys are the deformation zones developed during deformation in the vicinity of second-phase particles (mostly present from casting, so-called constituents). They provide in some cases random texture components, but in other cases very specific texture components, such as the P texture component $\{011\}\langle 111\rangle$ and the 22°ND rotated Cube texture component $\{001\}\langle 310\rangle$ during recrystallization as shown in the previous section. With respect to deformation inhomogeneities and their strong impact on recrystallization a more detailed description and the modeling of those deformation inhomogeneities is certainly required for more exact recrystallization texture predictions (as presented later on in Chap. 8). In the current work a model to predict the deformation zone texture as well as the particle-stimulated texture was required to enable modeling of the effects during recrystallization mentioned above.

All Taylor type deformation models including the Grain InterAction model (GIA) [Crumbach 2005] assume that each grain internally deforms homogeneously. In the present work the *Grain InterAction – Deformation Zone* model (GIA-DZ) was developed to predict the orientations developing during inhomogeneous deformation within the deformation zone. It describes the evolution of a deformation zone depending on strain and material properties.

5.3.1 Model setup and general model behavior

The scheme of the GIA-DZ model is outlined in Fig. 5.14. To include the inhomogeneous deformation for one grain with orientation g_i the following steps are carried out:

The deformation zones surrounding particles of different shape are simulated using FEM (Fig. 5.14a). Characteristic strain paths (Fig. 5.14a, box on the right) of specific elements (marked as A, B, C, D, ... Fig. 5.14a left) covering the most important parts of the deformation zone are extracted from FEM output. To represent the deformation zone texture correctly, different weights for the considered locations within the deformation zone are required. That means a corresponding strain path is considered more frequently than others. The weights depend on the size of a certain location (which is characterized by a deformation modulus indicated in Fig. 5.22).

Those characteristic strain paths are used as an input into a standard GIA model together with the grain orientation g_i . The grain i is at the beginning subdivided in eight initially identically oriented sub-regions (Fig. 5.14b right). This grain with its eight sub-regions is then treated as an ‘eight-grain aggregate’ in the GIA-model. All output-orientations from the GIA-simulations for grain i are summarized in one file and represent the microtexture developed in a deformation zone within this grain. Those orientations are direct input for the particle-stimulated nucleation model as a part of the recrystallization model CORE; respectively they can be summarized in individual input files for specific ideal grain orientations (11 orientation classes are handled in CORE).

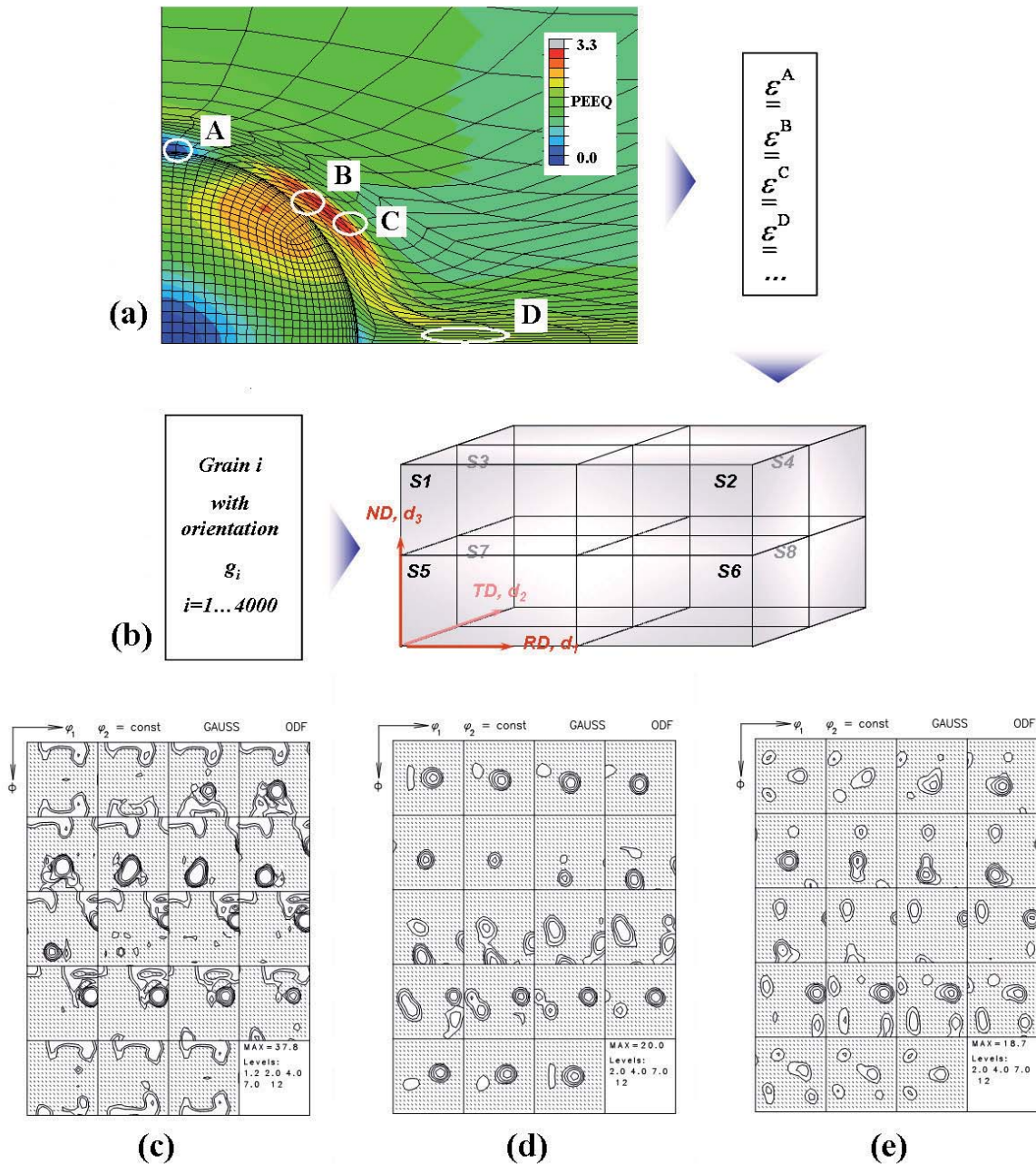


Fig. 5.14: Scheme of the GIA-DZ model to simulate in-grain deformation zones. (a) Step 1 - FEM modeling and providing characteristic strain paths ϵ for different locations A,B,C...; (b) Steps 2,3 - GIA simulation for each grain i using strain paths from step 1. (c)-(e) GIA-DZ simulation results presented as ODF for the case of 70% plane strain deformation in AA3103 for (c) an initial Cu, (d) S/R, (e) Brass oriented input texture.

The GIA-DZ model needs the same input texture as the GIA model, discretized in a list of single grain orientations. Unlike in the GIA model where from this list eight grains are each taken randomly and configured to eight grain aggregates, in the GIA-DZ model each grain is taken *separately* and subdivided in sub-regions of the same orientation. With the random choice criterion in case of the Taylor ambiguity [Crumbach 2005] the orientations of the eight grain regions may develop differently due to the activation of different slip system combinations, which are computed according to the GIA-modeling procedures. The above outlined scheme is applied as many times as required from the number of single grain orientations, in which the initial texture has been discretized. Since the GIA-DZ model uses the GIA model as a subroutine, like the GIA-Split-up model [Crumbach 2005], it requires the same input data as the GIA model and can as well be used

interactively with 3IVM+ [Gurla 2007, Mohles 2008]. Therefore all material and process influences of the GIA model do not only alter the predicted deformation texture but also the evolution of the deformation zones and hence the nucleus spectrum for particle-stimulated nucleation. For demonstration a typical hot rolling texture was discretized in components with e.g. Cu, S or Brass orientation +/- a deviation of 15° from the exact orientation. The obtained orientation lists were then subjected to a simulation with GIA-DZ. Typical texture components developed within the deformation zone of such initial orientations are shown in Fig. 5.14c-e. In case of an initial Cu oriented texture a 22° ND rotated Cube component is obtained within the deformation zone texture (Fig. 5.14c). For an initial S/R or Brass oriented initial texture the desired P component is obtained (Fig. 5.14d, e). This is in good agreement with literature [Engler 1997a] and with the experimental observations shown in Sec. 5.2. If now the volume fraction of constituent particles is known e.g. from experiments, the volume fraction of their deformation zones can be estimated and a new deformation texture after e.g. cold rolling can be calculated, composed of the texture components evolving during homogeneous deformation plus the texture components within the deformation zones in case of locally heterogeneous deformation.

The orientations developed within the deformation zones for each individual grain g_i serve at the same time as input for particle-stimulated nucleation in the respective grain during recrystallization simulations with CORE (see Sec. 5.5). For future applications, the setup of the GIA-DZ model could be also used in order to describe for instance inhomogeneities at grain boundaries. Hence, FEM simulations should be carried out for various combinations of orientation pairs (Cube/S, Cu/S, etc.). The strain paths obtained close to the grain boundary could be then used to calculate the rotations occurring as a result of the friction between two grains during e.g. rolling. This would provide further the local scatter of, for instance, grain boundary nuclei dependent on the deformation degree.

5.3.2 FEM modeling

Prior to the modeling of the deformation zone with GIA-DZ the local strain states were computed by FEM. One might expect that crystal plasticity FEM (Finite Element Modeling) would be most appropriate for this purpose. However, in such case only special orientations could be investigated whereas there are many differently oriented grains with particles in real materials. Therefore, a random orientation distribution, respectively a hot rolling texture around the particles was assumed as orientation input. The FEM simulations were mostly focused on the development of specific strain components during deformation. By this we obtain a statistical average of potential orientation changes which can be converted to texture information. For this purpose the strain path of certain characteristic elements within the deformation zone was calculated. The observed strain path was then used for deformation texture predictions with GIA-3IVM. For each element individual simulations were carried out. Details of the finite element model can be found in [Schäfer 2009].

After the FEM simulation the node displacements computed by FEM were transformed to a displacement gradient tensor, which can be used to compute the deformation texture by a Taylor type model. For this study the grain interaction model GIA was used. The exact work-hardening data as input for GIA can also be found in [Schäfer 2009].

5.3.3 Strain evolution in the particle vicinity

The strain evolution in the vicinity of the particle was tracked during plane strain compression of the sample by means of FEM, in particular for specific locations within the deformation zone. For the FEM simulations a spherical particle shape was assumed and the particle-containing domain was deformed up to a macroscopic strain of 1.2. Other particle shapes were investigated as well.

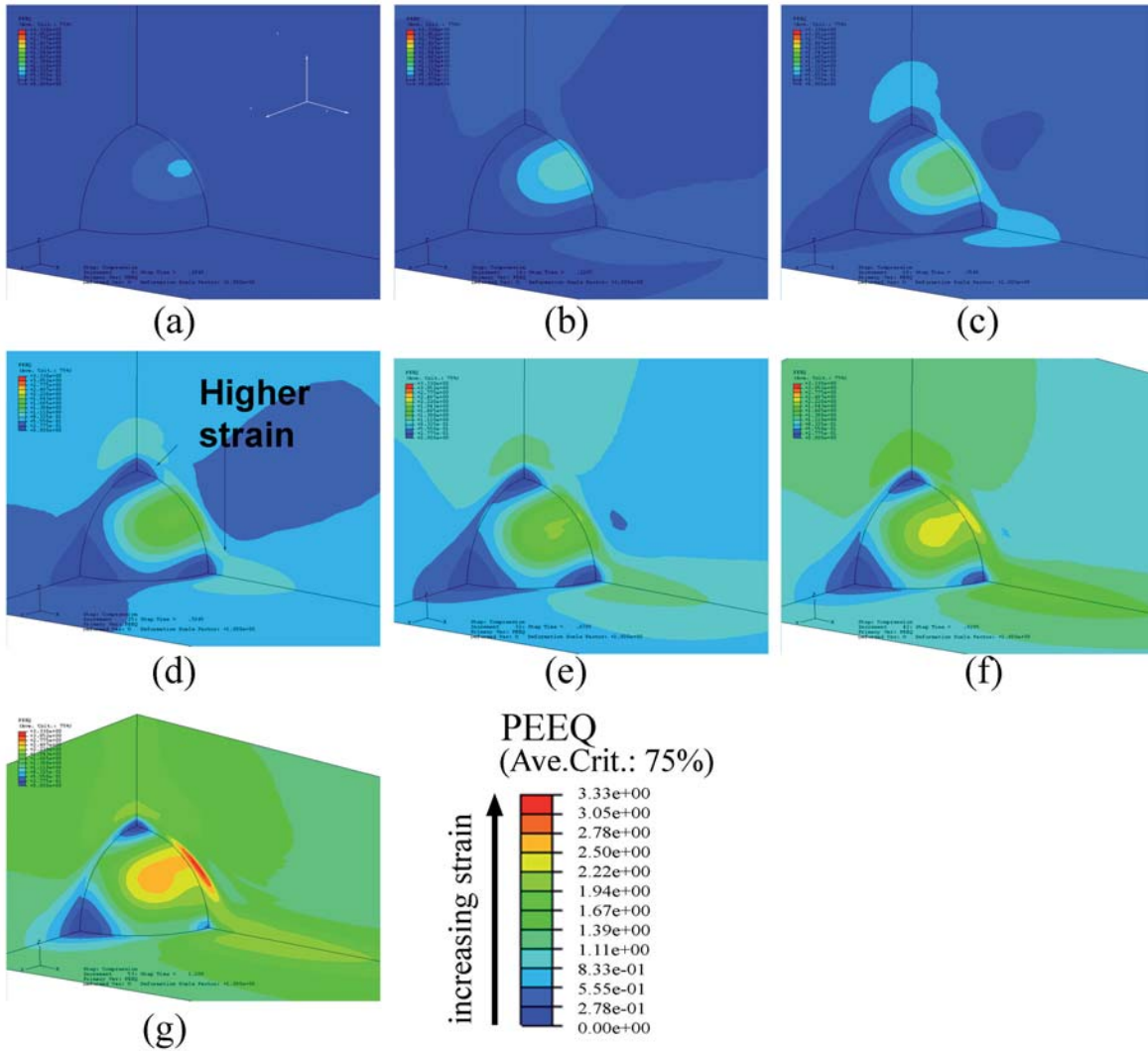


Fig. 5.15: Evolution of the equivalent plastic strain in the deformation zone around a spherical particle.

The evolution of the equivalent plastic strain is shown in Fig. 5.15. Already at low degrees of deformation, the evolution of a strain maximum close to the particle surface becomes evident. The maximum of equivalent plastic strain occurs under 45° to the x-direction, because at this location the shear components reach very high values. The evolution of the deformation zone starts under 45° and becomes elongated in x-direction as soon as a thickness reduction of 45% is reached.

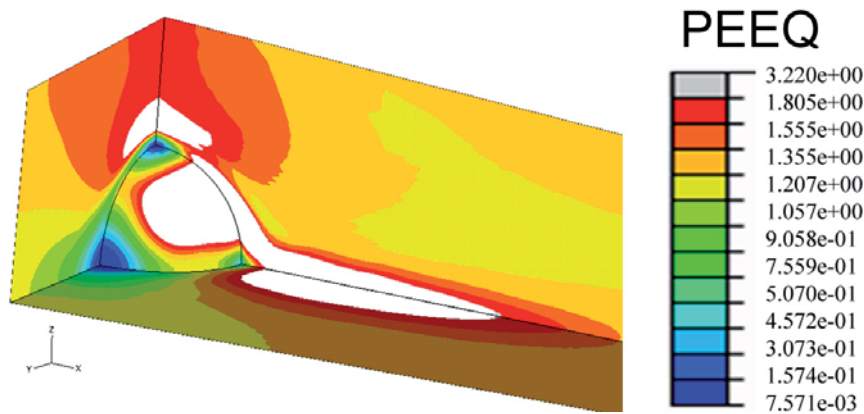


Fig. 5.16: Deformation zone highlighted in white as defined by criterion $\epsilon_{crit} = 1.5 \cdot \bar{\epsilon}$.

Such an extension of the deformation zone in y-direction was not observed. In z-direction only a slight strain increase can be noticed. At the maximum imposed deformation, $\varepsilon_{zz}=1.2$, strain minima had developed at the intersection of the particle surface with the coordinate axes in y- and z-direction (Figs. 5.15d-g). These zones are called dead zones and were also reported by other authors [Humphreys 2004]. The overall shape of this zone was elliptical with its largest extension in x-direction in the xz-plane (Fig. 5.15g). To define the size of the deformation zone, a critical strain $\varepsilon_{crit}=1.5\cdot\bar{\varepsilon}$ was introduced, where $\bar{\varepsilon}$ is the strain developed in the matrix during homogeneous deformation, i.e. here: $\varepsilon_{crit}=1.5\cdot1.2=1.8$. Fig. 5.16 reflects a deformation zone defined by this criterion (highlighted in white). The deformation zone size in RD, TD and ND is later on an input to the recrystallization model. Within the deformation zone later nuclei can grow comparatively faster than in the matrix and thus, gain a growth advantage over other nuclei originating at other nucleation sites. The size of the deformation zone was measured for different deformation degrees. The obtained results are displayed in Fig. 5.17.

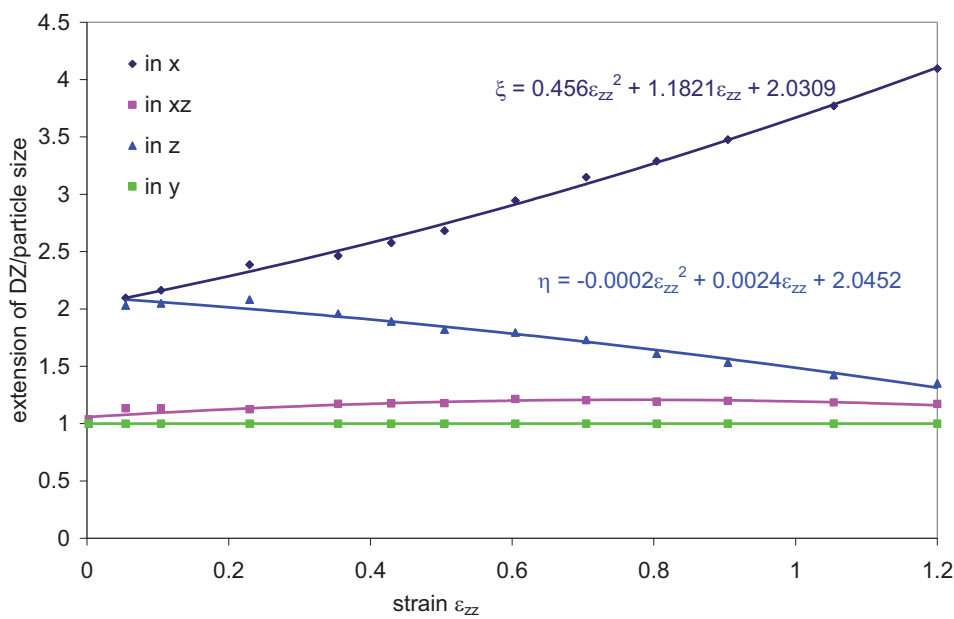


Fig. 5.17: Extension of deformation zone in different directions, η in z-direction, ξ in x-direction.

With increasing degree of deformation the size of the deformation zone in x-direction grew substantially and slightly also in y-direction (Fig. 5.17). The evolution of a deformation zone was observed only after the imposed strain exceeded $\varepsilon_{zz}=0.7$.

5.3.4 Texture evolution in the particle vicinity

The presentation of the texture evolution within the deformation zone will be restricted to spherical particles only. Simulations have shown that the evolution of textures in the vicinity of cuboidal / elliptical particles is similar to the case of spherical particles [Schäfer 2009]. The deformation zone incorporated a large number of finite elements, but only elements in specific positions of particular interest were investigated with respect to texture evolution (Fig. 5.18).

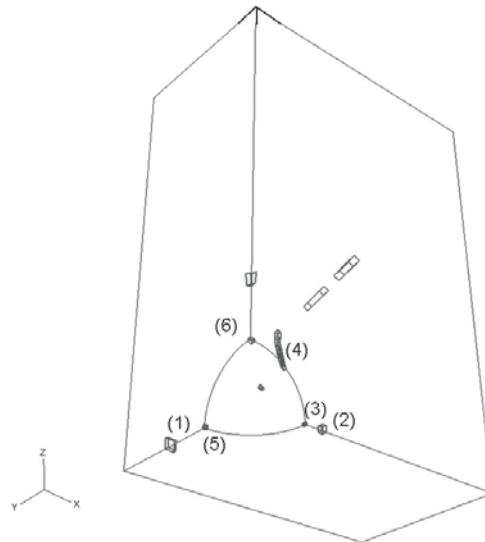


Fig. 5.18: Location of characteristic finite elements in the FEM model.

The corresponding texture evolution was predicted with GIA-3IVM calculations using the modeled strain paths from FEM as input. Beside the displacement gradient tensor, the texture model GIA-3IVM requires also the initial texture. As initial texture input a hot rolling texture of alloy AA3103 and a random texture were chosen. Fig. 5.19 a-b shows the results of the texture evolution based on both initial textures for certain characteristic locations in the vicinity of the particle.

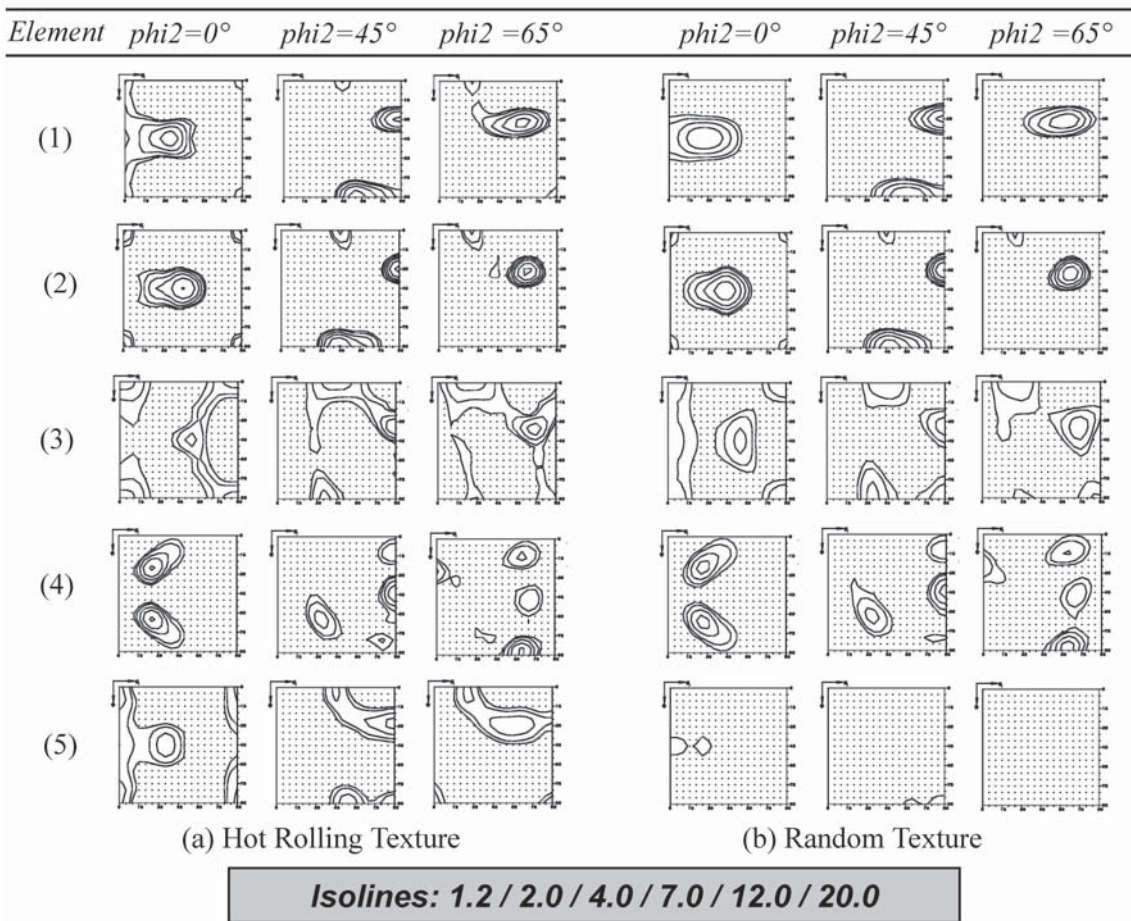


Fig. 5.19: (a) initial hot rolling texture (b) initial random texture – the numbers in brackets denote the element positions as indicated in Fig. 5.18.

As expected, the texture evolution in the deformation zone is affected by the locally different deformation states. The elements located in front of the particle display in particular Cube orientations as well as the so-called P-orientation (see Figs. 5.19.2, 5.19.3). This was observed for both initial textures. Far away from the particle in x-direction or y-direction a pure plane strain state was found and caused the development of a typical plane strain texture comprising essentially orientations of the β -fiber (Fig. 5.19.1). In the so-called dead zones, at the intersections of the particle with the y- and z-axis nearly no texture change was observed (Fig. 5.19.5) and the initial texture preserved. Near the strain maximum (Fig. 5.19.4) components with Euler angles $(25^\circ, 25^\circ, 0^\circ)$ and $(65^\circ, 25^\circ, 0^\circ)$ were observed. As obvious from the calculations the initial texture had little influence on texture evolution, since the evolution of essentially the same orientations was observed in both cases. The two special texture components (P and 45° ND rotated Cube) observed in these studies are found in recrystallization texture of heterogeneous alloys and are usually associated with PSN [Engler 1996, Engler 1997a, Tangen 2004, Sjølstad 2003].

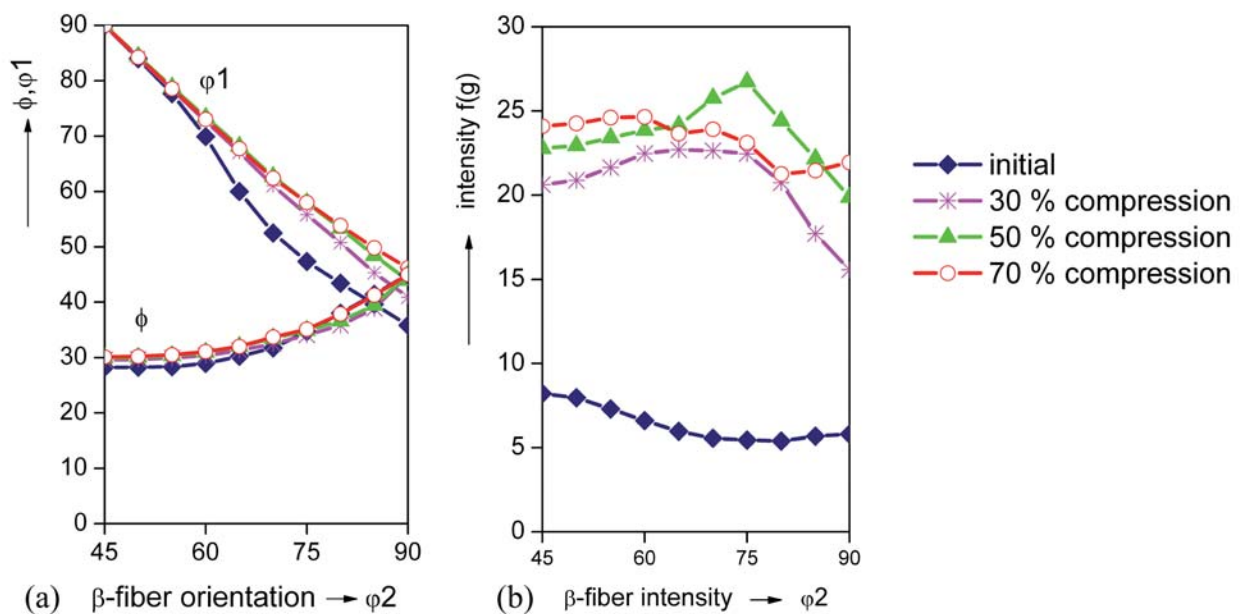


Fig. 5.20: GIA-3IVM output calculated with the FEM strain paths based on an initial hot rolling texture. (a) β -fiber max. density; (b) β -fiber orientation for element (3) in Fig. 5.18. A shift of the β -fiber to higher values of ϕ_1 was observed with increasing compression.

The development of the texture components in the course of deformation is shown in Fig. 5.20 in terms of skeleton plots. Already after 30% plane strain compression the intensities along the β -fiber have characteristically changed. With increasing thickness reduction the β -fiber is shifted to higher ϕ_1 values (Fig. 5.20b), which promotes the development of the P-orientation. Also the development of the ND rotated Cube component reveals a clear tendency. Prior to deformation the texture contains an exact Cube orientation. Already after small thickness reductions the intensity of 45° ND rotated Cube increased, and the exact Cube had completely vanished (Fig. 5.21).

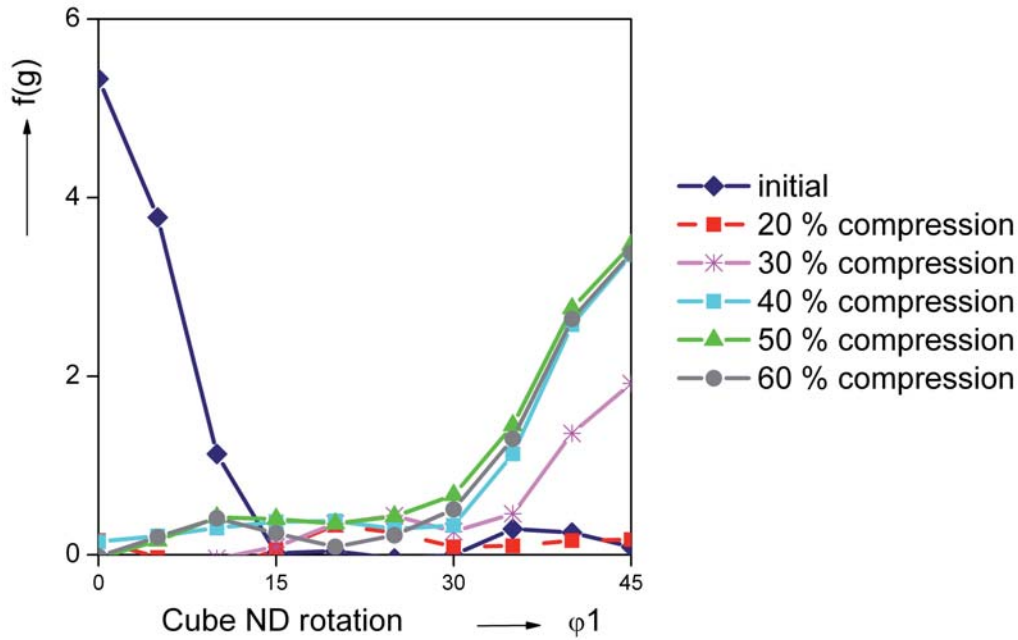


Fig. 5.21: GIA-3IVM output. Cube intensity evolution with strain in element (4) as indicated in Fig. 5.18.

Fig. 5.22 summarizes the observed deformation modes in the deformation zone. In front of the particle, where the deformation zone reached its largest extension, mainly a tensile strain was observed, which caused the appearance of the P-component, as known from tensile deformation of fcc materials. The tensile strain ahead of the particle can be understood from the material flow starting above the particle towards x-direction. Since the particle is assumed to have a high strength it does not undergo a significant thickness reduction during compression. Accordingly, the material flows from regions above the particle and is relocated to the front of the particle. Since the largest amount of material arrives close to the x-axis at the interface, a tensile strain is generated.

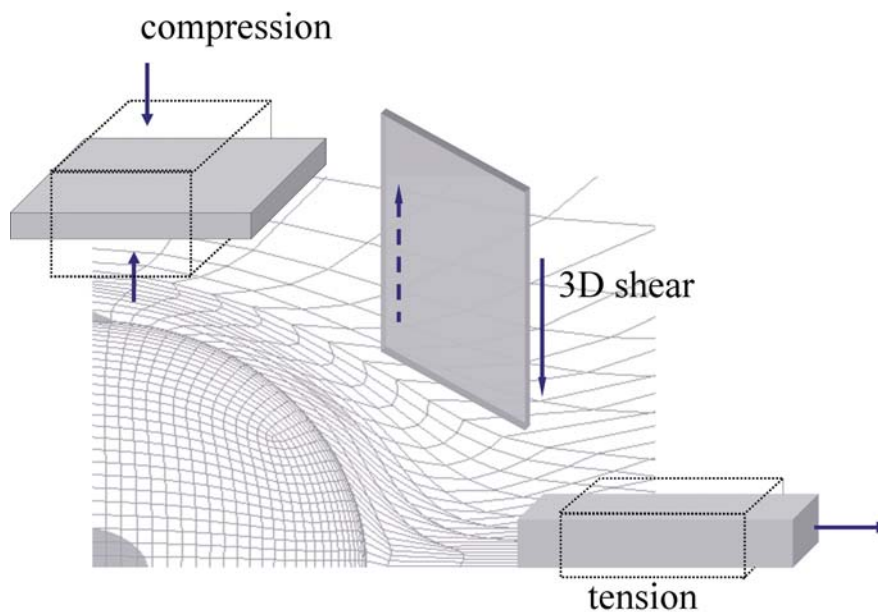


Fig. 5.22: Main deformation states in the deformation zone.

Far away from the particle, the material is deformed by plane strain like in the case of homogeneous deformation. Under 45° to the x-direction a 3D-shear state will occur, since the material flows along

the particle interface towards the x-direction. Under approximately 45° to the x-direction in the yz-plane, orientations with Euler angles $(25^\circ, 25^\circ, 0^\circ)$, respectively $(65^\circ, 25^\circ, 0^\circ)$ were observed in the computed textures, which can be attributed to the strong shear deformation near the interface.

The so-called dead zones (zones with a minimum strain) at the intersection of the particle with the coordinate axes, which remain without change in texture were caused by the boundary conditions, which suppressed material flow in y-direction as evident in plane strain compression tests and also typical for rolling with sufficiently high ratio of width to thickness of a rolling sample.

Fig. 5.23 reveals the orientation distribution in the $\varphi_2=0^\circ$ section of Euler space. It contains the P-component and 45° ND rotated Cube, which were found in the reported texture simulations. The texture components, found in the deformation zone by calculation are in excellent agreement with experimental observations [Engler 1996, Engler 1997a, Tangen 2004, Sjølstad 2003]. The location of the P- and 45° ND rotated Cube component within the deformation zone are further in excellent agreement with experimental observations in Figs. 5.10, 5.11.

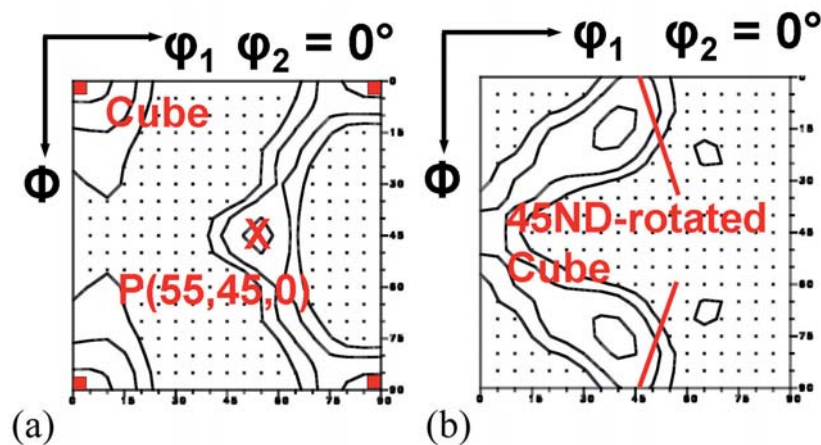


Fig. 5.23: Selected typical texture components in the vicinity of particles (a) for element position (3);(b) for element position (4)(see Fig. 5.18).

Also, these texture components are typical orientations of the recrystallization texture of particle-containing aluminum alloys. The current study substantiates that these orientations are generated in the deformation zone around particles and therefore, can be attributed to PSN. Furthermore, the investigation demonstrates that the orientation distribution in the deformation zone around particles is not random as frequently tacitly assumed. The simulations give valuable information on the possible orientation spectrum for recrystallization nuclei during annealing of rolled aluminum sheet with constituent particles. Hence, the results lend themselves to be fed into recrystallization models.

5.3.5 Texture evolution in ideal orientations

The different deformation paths were further applied to single crystal orientations such as Cube, Goss, Brass, S, Cu. This example should demonstrate the overall influence of a deformation zone (combination of the different considered deformation paths) in a virtual single crystal. The setup for these simulations is mainly an eight-grain aggregate representing a single oriented grain with 8 sub-regions, the separation in different sub-regions is purely artificial. These 8-grain aggregate can be used for a GIA-3IVM simulation. In fact, for each ideal orientation several GIA-3IVM calculations were carried out using 14 selected strain paths extracted from the deformation zone as modeled with FEM. From the sum of all orientations obtained for one initial starting orientation an orientation distribution function was calculated. Fig. 5.24 displays the results obtained for various ideal starting orientations in the $\{111\}$ -polefigure. The poles of the ideal orientations are displayed as well and were connected by lines. This calculation was basically done in order to compare the model output to other simulations or experiments in literature.

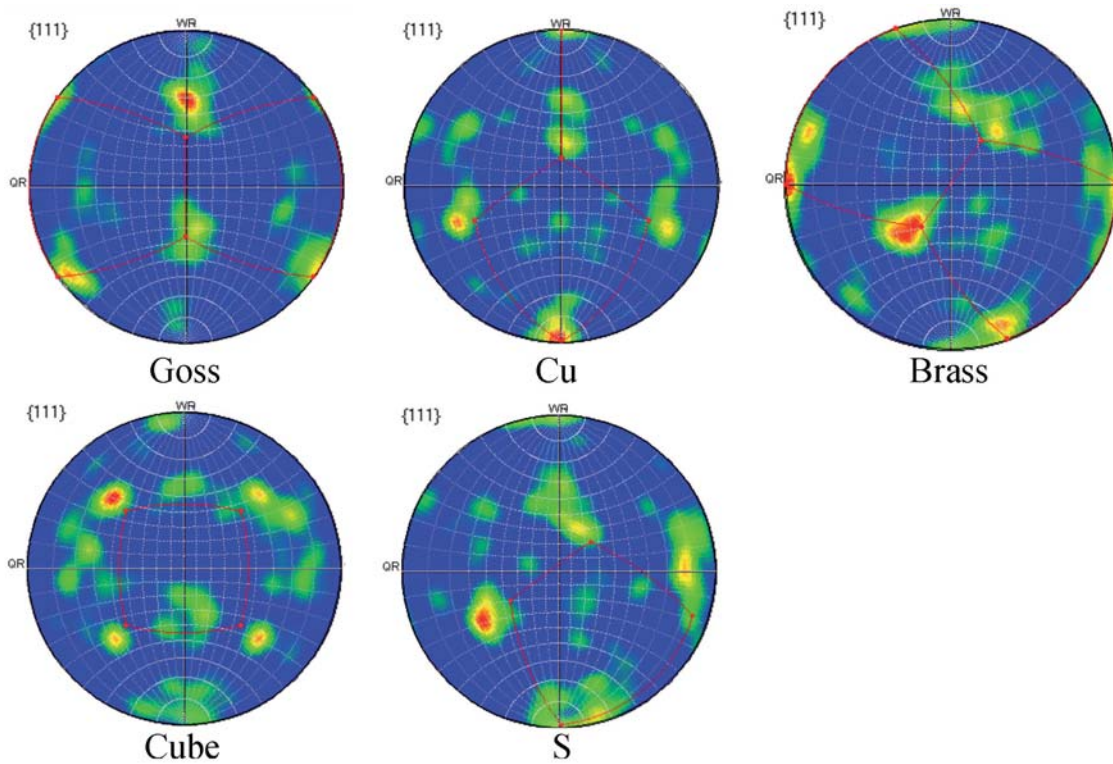


Fig. 5.24: $\{111\}$ polfigures showing the evolution of a deformation zone within single crystals of the indicated orientations as calculated with the GIA-DZ model.

For the Goss single crystal the orientations in the deformation zone are rotated around TD-direction. This is in good agreement with simulations by [Radhakrishnan 2000]. For a deformation degree of $\epsilon=1.2$ a maximum misorientation of 30.8° was observed. For the considered Cu orientation $\{112\}\langle 11\bar{1}\rangle$ also a rotation about TD is observed with a maximum misorientation of 26.6° . For the Brass, Cube and S orientation the rotations cannot easily be attributed to a certain axis. Especially in case for the Cube and Cu orientation a quite large scatter is obtained. The maximum and average misorientations obtained from the simulations are displayed in Fig. 5.25.

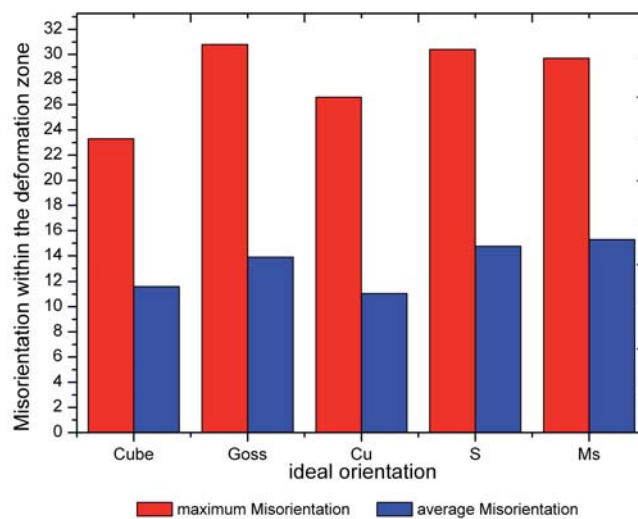


Fig. 5.25: Misorientations in the deformation zone depending on the initial single crystal orientations. The simulations were carried out with the GIA-DZ model.

5.4 Modeling the Evolution of the Deformation Zone in fcc Materials

5.4.1 Influence of deformation degree, temperature and initial texture

In the following the deformation zone evolution is modeled in case of fcc materials. The focus is here laid not on the tracking of certain texture components as in previous section but rather on the general impact of the deformation zones on the overall macrotexture evolution during cold or hot rolling in particle-containing alloys.

For this purpose the GIA-DZ model is applied to simulate the effect of different strains on the deformation zone evolution in AA3103 (Fig. 5.26). In this section basically the texture evolution is considered since it causes a major impact during subsequent recrystallization texture simulations.

From the ODF (orientation distribution function) plots it can be seen that the orientations scatter quite a lot, however this tendency is decreasing for higher rolling reductions. From the ODFs it is very striking that obviously a very high scatter of the components can be observed, such as the rotation around transverse direction of the Cu component towards the 45° ND Cube component. This is in very good agreement with observations from EBSD as shown in Fig. 5.8 for the frequency of the ND rotated Cube component. Further a quite large orientation scatter was also obtained for the Brass and S component in agreement with experiments (Sec. 5.2).

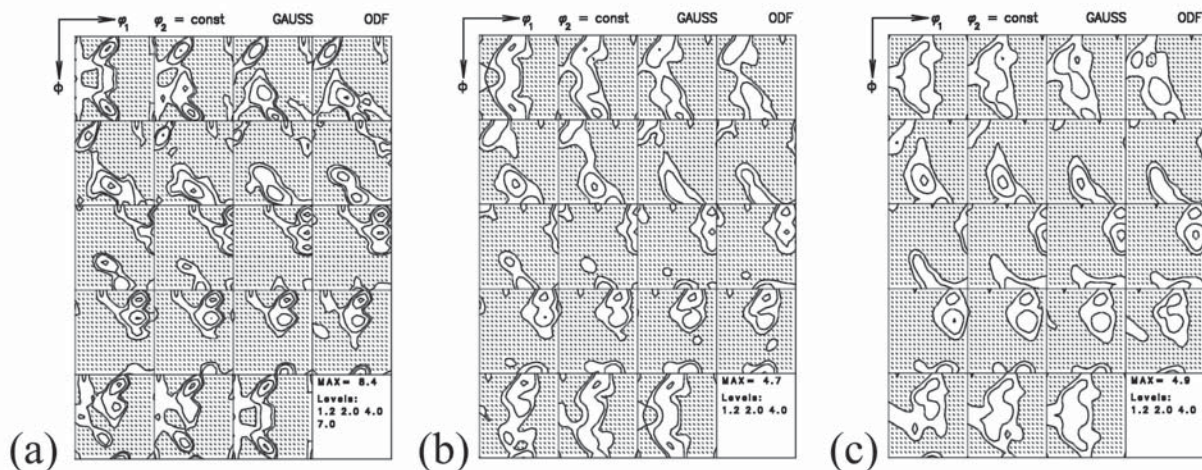


Fig. 5.26: ODFs of the overall texture developed within deformation zones after different applied strains: (a) after 30% thickness reduction, (b) after 50% and (c) after 70% thickness reduction. The calculations are based on a discretized hot rolling texture. As material parameters the 3IVM+-fitting set as presented in Chap. 9 was used. The used material was the commercial aluminum alloy AA3103.

The use of the GIA-3IVM+ for computation allows further the consideration of the effect of different deformation temperatures, such as for cold and hot deformation. Hence, the effect of different deformation temperatures can be indirectly considered in the GIA-DZ model and the effect of the deformation texture evolution can be studied. It was shown, that the deformation temperature, respectively the number of active slip systems has a rather negligible influence on the texture evolution within the deformation zone.

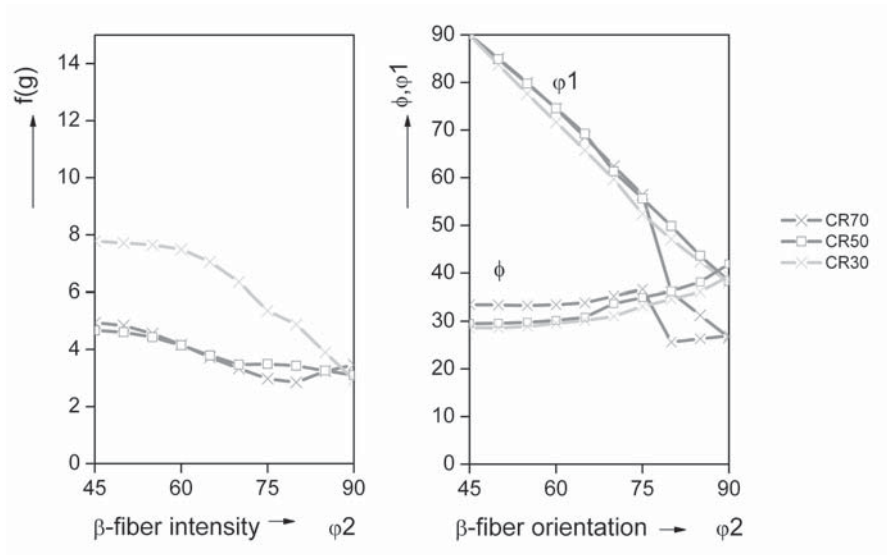


Fig. 5.27: Skeleton Plots of the above ODFs, showing the beta-fiber intensity and orientation of the orientations within the modeled deformation zones after cold rolling reductions of 30%, 50% and 70%.

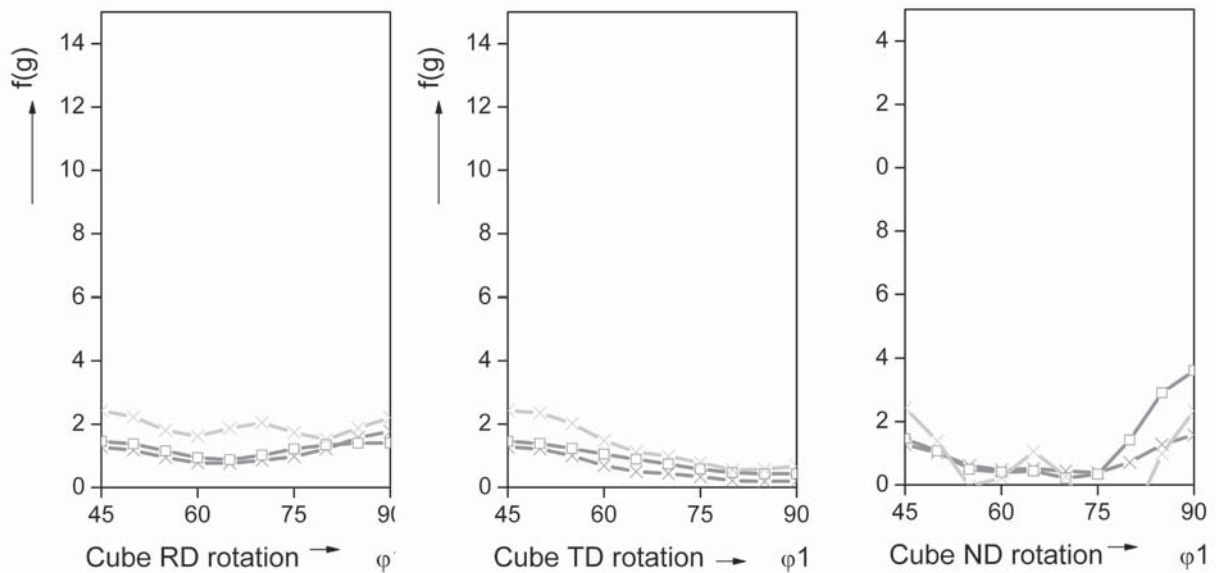


Fig. 5.28: Skeleton Plots of the Cube rotations within the modeled deformation zones after 30%, 50% and 70% cold rolling reduction.

Depending on the prior thermo-mechanical heat treatment also different initial textures can be obtained prior to cold rolling. It is known from [Crumbach 2005] that the initial texture has an influence on the deformation texture evolution. Thus, the deformation zone texture was computed for different initial textures. The following Figs. 5.29 a,b display the deformation zone textures obtained after 70% plane strain deformation for an initial strong Cube texture, respectively a random texture.

It could be shown that the influence of the starting texture is not so pronounced. However, in case of a strong Cube texture as starting texture, a certain fraction of the Cube component is preserved within the deformation zone, e.g. in particular during hot deformation. This can be understood from the existence of the dead zones introduced previously, where the Cube texture component can survive during the cold rolling process.

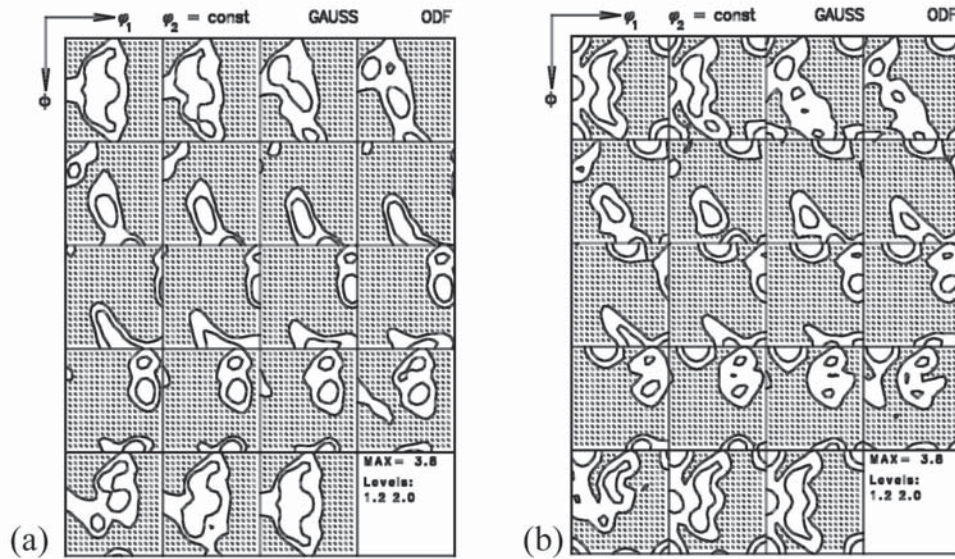


Fig. 5.29: Deformation zone texture developed after a plane strain deformation of 70% in AA3103. As initial starting texture (a) a random texture and (b) a strong Cube texture were used.

5.4.2 Comparison to experiments

Besides modeling the deformation zone starting from ideal orientations it is also possible to consider a polycrystalline material. First of all, a deformation simulation of an initially randomly textured sample with GIA-3IVM+ is carried out. From this calculation a list of 4000 orientations is obtained. For each of those 4000 orientations an individual deformation zone is calculated. The orientations obtained within the individual deformation zones are then recombined again in an ODF. Fig. 5.30 shows the obtained result along with the experimentally measured texture within the deformation zone for a 70% cold rolled AA3103 alloy.

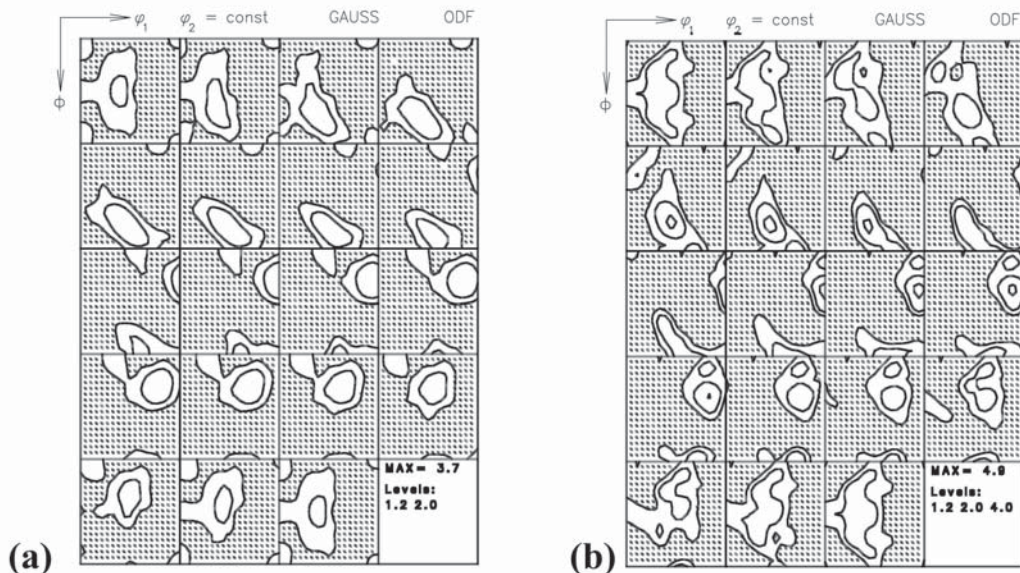


Fig. 5.30: Comparison between (a) measured microtexture within the deformation zones of a 70% cold rolled AA3103 and (b) the deformation zone texture of a macroscopic sample after 70% cold rolling reduction for the same material calculated with GIA-DZ.

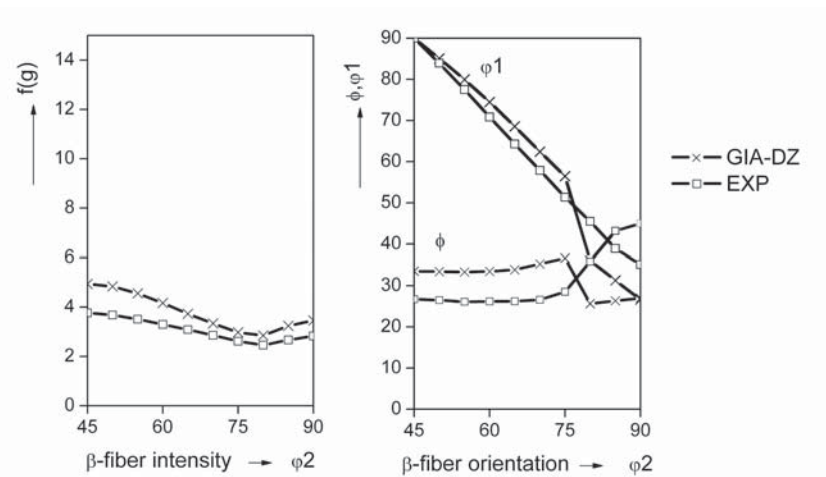


Fig. 5.31: Skeleton plots showing the intensity and orientation of the β -fiber of the measured and modeled deformation zone texture after a rolling reduction of 50% for AA3103 (\square experiments \times GIA-DZ).

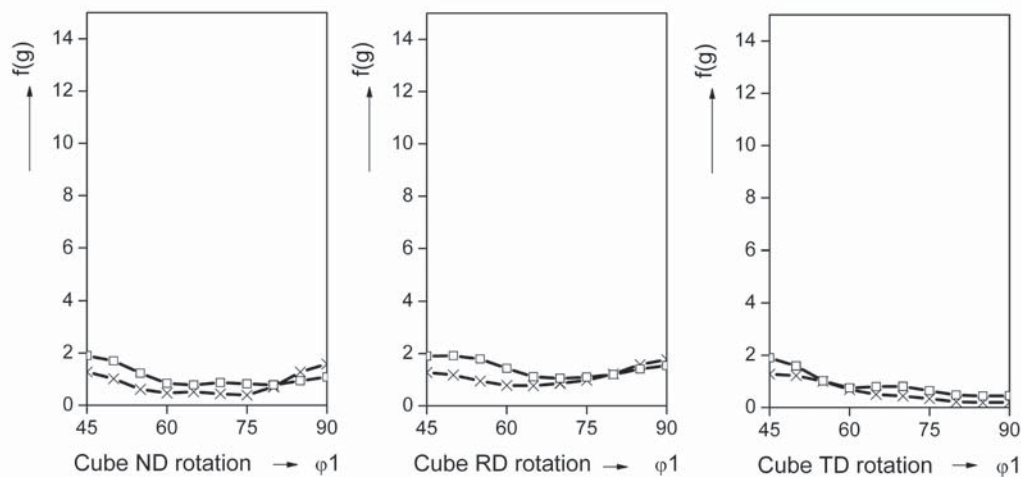


Fig. 5.32: Skeleton plots showing the rotations of the Cube components of the measured and modeled deformation zone texture after a rolling reduction of 70% for AA3103 (\square experiments \times GIA-DZ).

The ODFs obtained from experiment and simulations show excellent agreement. The strong scatter of orientations along the β -fiber observed from experiments (very pronounced for the Brass peak in the ODF) was captured very well by the calculations. The good agreement between experiment and simulations can be clearly seen from the skeleton plots in Figs. 5.31 and 5.32. The small fraction of Cube texture component observed from experiments was not predicted in the simulations since a random initial texture was assumed instead of a hot rolling texture (containing small fractions of Cube texture component).

The deformation zone model proposed here is different from those reported in literature, since the nucleation at particles is treated spatially resolved. In most approaches nucleation at particles is modeled with focus on the final recrystallization texture. Hence, the main interest is in providing the nucleus texture for particle-stimulated nucleation. This is in most cases done by a $40^\circ\langle 111 \rangle$ transformation of the initial deformation texture [Pospiech 1979, Engler 1996]. The corresponding nucleation efficiency is in those cases provided from empirical approaches, respectively experiments. A different approach was proposed by Humphreys and Ardakani [Humphreys 1994] who developed a model to describe the deformation texture close to the particle by blocking one or more of the 5 slip systems that are necessary to deform the crystal plastically according to Taylor theory. Van Houtte [Rabet 1996, Rabet 1997] presented an approach to model the deformation zone texture by means of a Taylor model. The modeling was restricted to a single component, the Cube

texture. The advantage of the present approach is the additional consideration of the work-hardening behavior as well as the consideration of a whole orientation distribution function ODF as input rather than selected ideal orientations. It shows excellent agreement with experimental results.

5.5 A Nucleation Model for Particle-Stimulated Nucleation

5.5.1 Implementation of particle-stimulated nucleation

In the previous sections basically the modeling of the deformation zone was considered. The obtained data, however, can be used for recrystallization modeling. This requires a proper implementation of the respective nuclei. The main input parameters for the nucleation model are the deformation zone texture components within each individual grain, the size of the deformation zone which basically depends on the particle size, the constituent particle distribution and information on the dislocation density increase and misorientations found within the deformation zone. The misorientation gradient in the particle vicinity, determines the preferred nucleus orientation, i.e. those orientations which can grow in the particle vicinity. The required parameters for particle-stimulated nucleation in the cellular automaton are summarized in Tab. 5.1.

Tab. 5.1: Set of input parameters for the particle-stimulated nucleation model (DZ = deformation zone).

<i>Parameter</i>	<i>Origin of parameter</i>
particle distribution	Experiment
particle size/shape	Experiment
Particle volume fraction	Experiment
size/ shape of deformation zone	FEM
Dislocation density increase within DZ	Experiment / FEM
nucleus texture / deformation zone texture	GIA – DZ

The resolution of the cellular automata is basically sufficient to resolve the constituent particles which have an effect on recrystallization nucleation. But the resolution is not sufficient to map each detail of a deformation zone as observed in experiment. Thus, a certain degree of abstraction is required in order to capture the features of particle-stimulated nucleation within a cellular automaton.

Nevertheless, the particles were introduced as a new structural component into the cellular automaton. Beside the particles also the surrounding deformation zone was established by a dislocation density gradient from the particle interface towards the surrounding matrix. The locally increased dislocation density within the deformation zone leads naturally to a higher nucleus number and a higher growth rate. In general, 0-1 nuclei per particle are calculated (Sec. 3.9.3) in agreement with experimental results. The mimicking of a deformation zone by an increased dislocation density and a reduced Zener drag under certain circumstances ensures also a growth advantage of particle-stimulated nuclei. Fig. 5.33 shows the scheme of the implementation of particle-stimulated nucleation in a cellular automaton.

First and most important is the nucleus orientation placed within the deformation zones, because it can significantly influence the final recrystallization texture (see Chap. 8). From literature it is known that particle-stimulated nuclei originate somewhere within the deformation zones [Kalu 1988]. Their orientations are restricted to those present in the deformation zones. However, it was observed that the orientations obtained in the final recrystallized texture were in many cases stronger than the orientation spectrum measured in the deformation zone or in the resulting nucleus texture [Chan 1984]. To properly account for this in the simulations, the local arrangement in the mother orientation of the nuclei is of major importance. For the model the nucleus orientations were taken from the orientation list of the respective grain's deformation zone as provided by GIA-DZ. It is stressed here that it is of major importance that particle-stimulated nuclei are not randomly

distributed throughout the microstructure. Since, the nucleus- / deformation zone orientations are calculated for a respective deformed grain, they should also be placed within this grain during the recrystallization process. This initial surrounding is important, since the deformation zone creation was based on it, and hence provides the right growth environment during a subsequent recrystallization process. Nuclei are understood to be activated by recovery processes, like subgrain growth, during annealing. In some cases subgrain growth might be hindered by Zener or impurity drag. This was considered in the simulations as well as will be introduced later on.

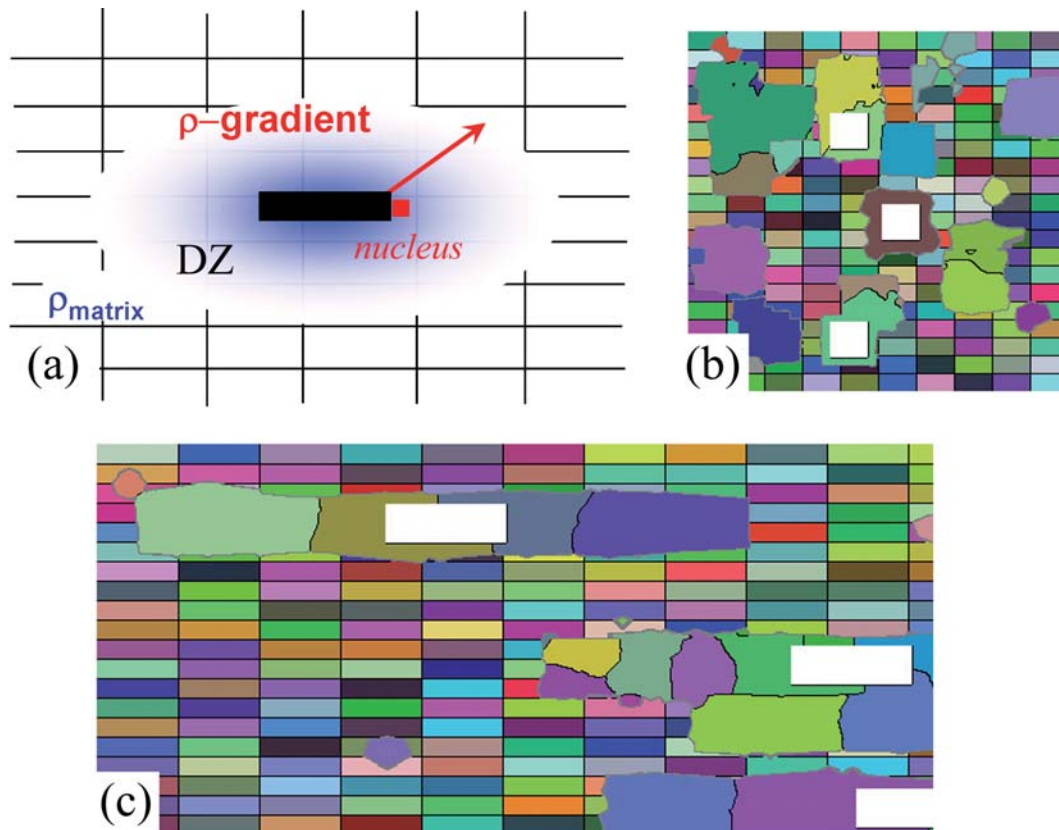


Fig. 5.33: (a) Scheme for particle-stimulated nucleation showing the arrangement in the cellular automaton and the considered features. Appearance of PSN in the cellular automaton and the growth of the newly developed nuclei in the vicinity of particles (white) is shown in rolling (b) and transverse direction (c), nuclei not related to particles are comparatively smaller.

From experimental observations we know in general that the growth of nuclei within the deformation zone does not cease until the whole deformation zone is consumed. This is accounted for in the model by the introduction of an elliptical deformation zone with a locally higher dislocation density and a dislocation density gradient directed away from the particle. At the border of the deformation zone the matrix dislocation density is attained. If the microchemistry and the nucleus orientation are conducive to nucleus growth, the nucleus can extend beyond the size of the deformation zone into the surrounding matrix. This is also reflected in the model in accordance with experiment. The nuclei are in general placed at the tip of the particles where the strain maximum was found in the FEM simulations and where nuclei were detected in experiments in most cases. The local orientation gradient is accounted for implicitly by associating the nucleus with the orientation with highest misorientations to the surrounding matrix as calculated with the GIA-DZ model.

5.5.2 Precipitation free zone

If the nucleation process is accompanied by microchemistry changes, locally a *precipitation free zone (PFZ)* can form in the vicinity of the particles, which can stop the growth of a PSN nucleus

once it reaches the border of the deformation zone. This was considered in the simulations by a deformation zone which is not subjected to Zener drag even if the matrix suffers heavily from it (Fig. 5.34). Under this condition island grains are attained in the fully recrystallized microstructure in accordance to experimental observations.

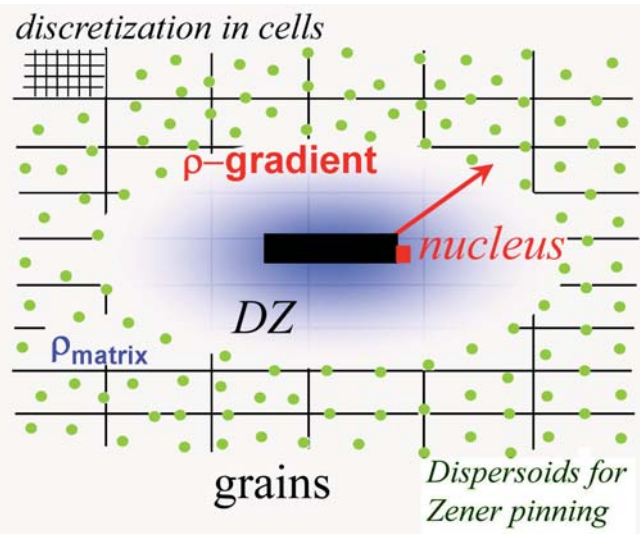


Fig. 5.34: Scheme of particle-stimulated nucleation in case of a precipitation free zone (PFZ) within the deformation zone, the remaining matrix is pinned or influenced by Zener Drag.

The dislocation density gradient in the deformation zone can be either taken from experiment, e.g. by using the measured subgrain size within the deformation zone / matrix and relating it via the principle of similitude to a dislocation density. The ratio of the dislocation densities deformation zone/matrix provides the factor for the maximum dislocation density found inside the deformation zone. This factor can also be taken from FEM simulations by comparing the maximum strain to the average strain. For instance, in case of 70% cold rolled AA3103 (state as presented in Fig. 5.4) the measurement yield a factor of 1.4-2.0 in experiments, and from FEM simulations a factor of 2 is obtained in quite good agreement.

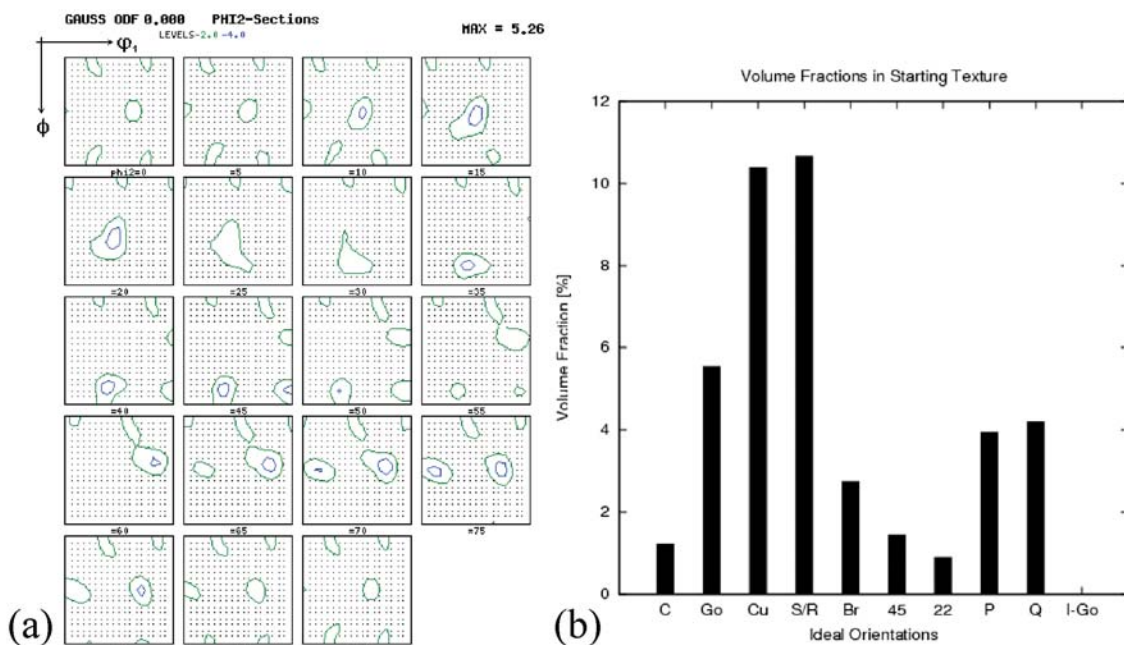


Fig. 5.35: (a) Modeled recrystallization texture in AA3103 under consideration of particle-stimulated nucleation as only nucleation mechanism. (b) Volume fractions of the obtained recrystallization texture components.

Fig. 5.35 shows the result of a CORE simulation (Fig. 5.34). For this simulation only particle-stimulated nucleation was assumed as nucleation mechanism. The nucleus spectrum was modeled with GIA-DZ (Sec. 5.3) and the nuclei were placed in their original deformation zone, respectively grain. The individual nuclei created in the surrounding of particles in a certain grain initially grew into their natural environment and later into other deformed grains. The basis for this simulation was a cold rolling simulation with the deformation model GIA-3IVM+ for 70% thickness reduction in AA3103 as previously introduced.

The obtained recrystallization texture shows excellent results in comparison with experiments for a particle-stimulated texture. It is mainly dominated by 22° ND rotated Cube components as well as the P texture component, which are the components mainly associated with particle-stimulated recrystallization textures. The volume fraction plot (Fig. 5.35b) shows that also other texture components are present, which are not discernible in the ODF due to their strong scatter as typical for the texture components within the deformation zone. The overall texture intensity is weak as often reported for particle-dominated textures.

5.6 Conclusions

The focus of this chapter was to extend the already existing nucleation model ReNuc (Sec. 3.3.2) for the mechanism of particle-stimulated nucleation (PSN), which is essential for prediction of recrystallization in commercial alloys.

First, experimental results on particle-stimulated nucleation in the alloy AA3103 were presented. They were obtained by means of EBSD to characterize the deformation zones in the particle vicinity (microtexture, extension, subgrain size) as well as during later annealing. In this study further the origin of the P- and ND-texture component was located within the deformation zones and their frequency specified.

Second, the deformation zone was modeled by means of the Finite element Method (FEM) to extract the local strain paths which cause the development of the, for PSN, characteristic texture components (P-texture and ND-rotated Cube texture component).

This information was made applicable in the deformation model GIA- DZ which describes the local deformation zone (DZ) evolution. The influence of different initial parameters on the GIA-DZ output was studied. Finally, the implementation of PSN in the recrystallization model CORE was outlined, using among other inputs the data predicted with GIA-DZ. The application of the PSN-model is demonstrated in later chapters (7-9).

Chapter 6

Influence of Recovery on Recrystallization

6.1. Introduction

The major effects on recrystallization studied in the current work are caused by precipitation. However, also the softening due to recovery which proceeds prior and concurrent to recrystallization seriously impacts the recrystallization behavior [Humphreys 2004]. Recovery is the rearrangement and annihilation of dislocations and thus reduces the driving force for recrystallization. The consideration of recovery is particularly important in high stacking fault materials [Gottstein 1998], such as in the used Al-1 wt% Mn alloy.

Recovery as precursor of recrystallization further influences recrystallization nucleation. Since there is a correlation between the initial grain orientation and the characteristics of the deformation substructure [Liu 1998], the modeling of orientation-dependent (locally resolved) recovery rates [Ridha 1982, Rajmohan 2000] is important for the prediction of *incubation times* and *nucleation rates*.

Most current recrystallization models lack the power to predict recrystallization kinetics beyond the range for which they were developed and tested [Zurob 2006]. This is due to the fact that recrystallization is a complex phenomenon that involves a number of influence factors. One of these crucial influence factors is the nucleation step which can up to now hardly be described by physical equations capturing all the required details. Nucleation thus remains a topic of ongoing experimental research [Lauridsen 2000, Gundlach 2004, Sabin 2003, Albou 2010] and unfortunately very few models address the calculation of the incubation time. One exception is the incubation time model for single phase materials developed by Zurob et al. [Zurob 2006].

The incubation time is the time for the first recrystallization nuclei to develop, respectively to be activated. In aluminum, the incubation time is strongly dependent on the recovery kinetics and thus nucleation in Cube oriented grains in fcc metals is favored. This was reported e.g. by Ridha and Hutchinson [Ridha 1982]. Orientation dependent recovery can also be seen in stored energy data [Rajmohan 2000], which reveal that after cold rolling the Cube orientation recovers fastest.

Hence, in this chapter an approach is presented to describe an incubation time based on the locally resolved recovery rates. The purpose of this approach is not the quantitative prediction of incubation times, but rather the prediction of their trends with temperature and strain.

The structure of this chapter is as follows. In Sec. 6.2 the general influences of recovery as modeled by 3IVM+ [Gurla 2007, Mohles 2008] are demonstrated. In Sec. 6.3 a criterion for prediction of incubation times as based on the orientation-dependent recovery rates is presented.

6.2 Appearance of Recovery accompanying Recrystallization

In this section, at first, general influences on recovery as modeled with CORE-3IVM+ (Sec. 3.6) are outlined. Then, results of recrystallization simulations under consideration of the demonstrated recovery behavior are presented.

6.2.1 Temperature-dependence of recovery

The recovery behavior is modeled with 3IVM+ [Gurla 2007, Mohles 2008] according to the equations in Sec. 3.6 as dependent on temperature and orientation. The 3IVM+ parameter data set was obtained by fitting to the experimental flow curves for the Al-Mn alloy AA3103 (see also Sec. 9.2). Fig. 6.1 demonstrates the evolution of the dislocation density within the cell walls during recovery for a temperature range of 240°C to 400°C for the Al-Mn alloy AA3103. For low temperatures the predicted softening curves agree reasonably well with experimental data derived from hardness measurements (indicated by squares in Fig. 6.1). For this purpose, the hardness measurements were at first converted to a yield stress according to [Cahoon 1970] and further related to a dislocation density by using $\sigma \sim \alpha \cdot G \cdot b \cdot \sqrt{\rho}$. The obtained dislocation densities were scaled with respect to the initial dislocation density computed with GIA-3IVM+. However, these values can only serve as a rough estimation of the dislocation density.

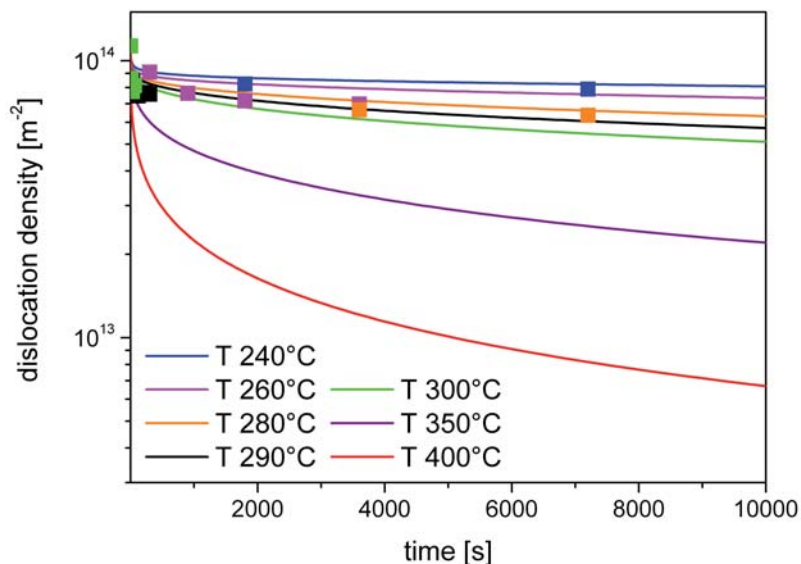


Fig. 6.1: Influence of temperature on the recovery behavior within the cell walls. The initial dislocation density within the cell walls corresponds to GIA-3IVM+ predictions for AA3103 after 70% cold rolling reduction. The activation energies are for climb $Q_{climb} = 1.38$ eV [Volin 1968] and for cross slip $Q_{cross} = 2.1$ eV. Experimental results are indicated by squares for the lower temperatures.

As to be expected a logarithmic decrease of the dislocation density was obtained. With increasing temperature, the dislocation density is reduced faster and to lower final values.

6.2.2 Orientation-dependence of recovery

The orientation dependence of the recovery behavior has its origin in the different stored dislocation densities after deformation. Such dislocation densities can be obtained as a direct output of the GIA-3IVM+ model [Crumbach 2005]. The stored dislocation densities after deformation are strongly depending on the initial orientation of the grains in a polycrystal prior to deformation. Hence, during deformation different slip systems are activated and a certain amount of slip is accomplished on them. During deformation, this leads to a different accumulation of dislocation densities in the differently oriented initial grains. Beside this orientation dependence caused by the prior deformation, also the climb activity of dislocations itself depends on orientation. Eq. (3.14) in 3IVM / 3IVM+ for annihilation by climb (Sec. 3.6) shows a dependency on the number of activated slip systems N_{GLS} [Roters 2000, Mohles 2008]. The number of activated slip systems N_{GLS} is different for all types of orientations, since it depends on the initial grain orientation prior to deformation. The influence of orientation on recovery for grains of different initial orientation as modeled with CORE-3IVM+ (Sec. 3.6) is shown in Fig. 6.2 for the dislocation densities in the cell walls, respectively cell interiors.

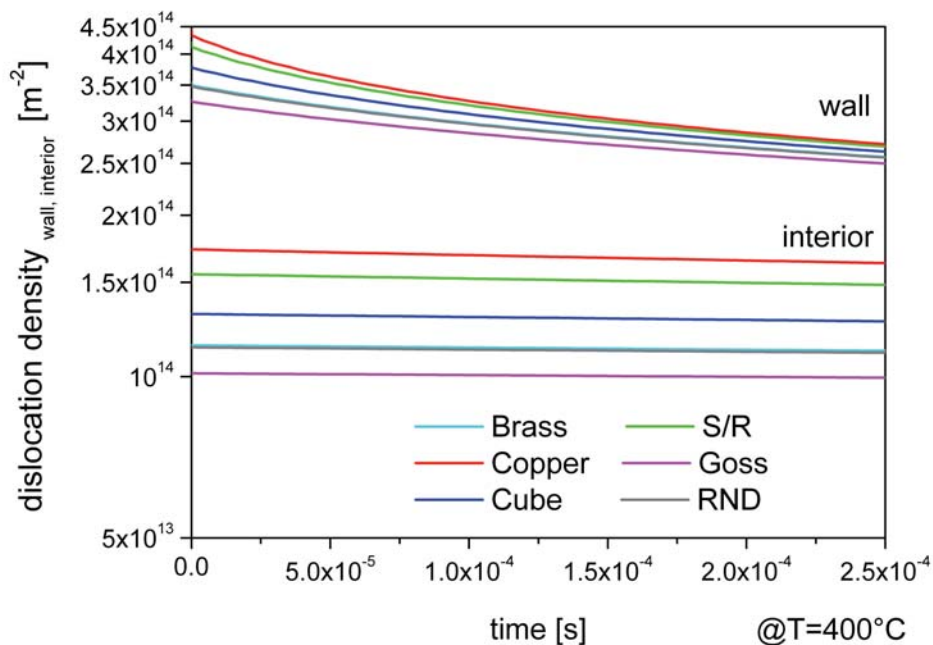


Fig. 6.2: Influence of initial grain orientation on the recovery behavior. The evolution of the dislocation densities in the cell walls and in the cell interiors is displayed over time. The initial dislocation densities after deformation were taken from a GIA-3IVM+ simulation.

As to be expected, the Cu and S/R texture component show the highest initial dislocation density which is subsequently reduced with increasing annealing time. The initial dislocation density of the Brass orientation is relatively low and comparable to the dislocation density of the Cube orientation prior to recovery. Similar observations were made experimentally by Guiglionda et al. [Guiglionda 2004] for a cold-rolled Al-Mg alloy. They found that the S texture component has the highest stored energies when compared to the Cube, Brass and Goss orientation.

6.2.3 Effect of recovery on recrystallization growth

An independent modeling of recovery and recrystallization was not intended in the present work due to the fact that recovery is not the main issue here, but rather its impact on recrystallization. If for instance recrystallization proceeds more slowly than recovery, it can happen that nucleus growth within a grain ceases before the material is completely recrystallized. The exact amount of

recovered volume and the connected texture changes are strongly dependent on the speed of both processes.

The most basic influence of recovery on recrystallization is demonstrated in Fig. 6.3. For these simulations the most important recovery parameters of the 3IVM+ model were altered: the activation energies. With decreasing activation energies for climb and cross slip the driving force for recrystallization is reduced. It was found that the recrystallization kinetics are shifted to longer times, when lower activation energies are assumed (Fig. 6.3a). In this case lower Avrami exponents of about two were obtained (Fig. 6.3b). Experimentally found Avrami exponents in the order of one to two are quite common, e.g. as determined from experimental studies on aluminum [Perryman 1955a, 1955b, Laurent 1952a, 1952b].

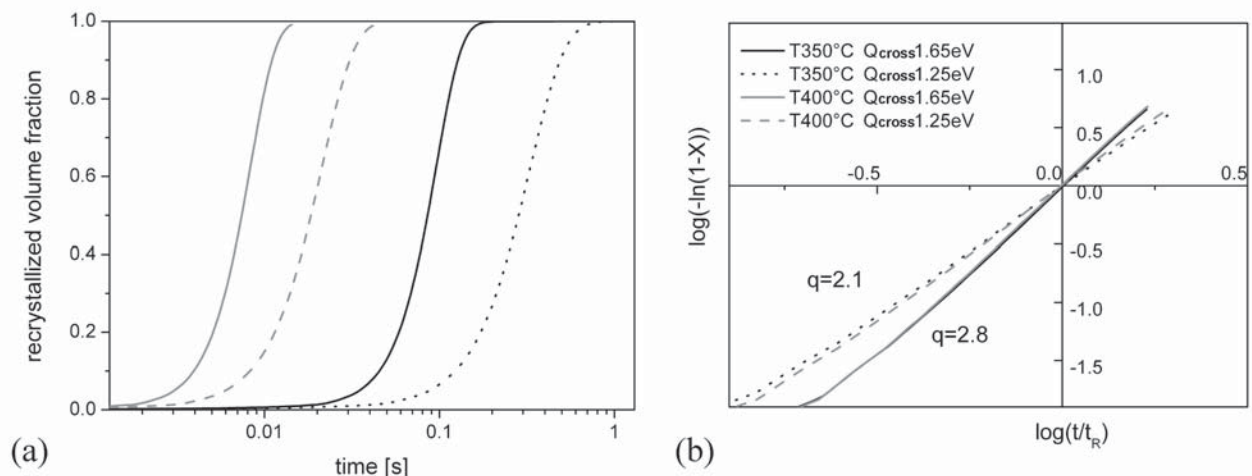


Fig. 6.3: Influence of the strength of recovery on the recrystallization behavior. (a) Recrystallization kinetics; (b) Avrami plot (Q_{climb} = activation energy for climb; Q_{cross} = activation energy for cross slip). In the present case is $Q_{climb} = 1.21$ eV.

A discussion of the Avrami exponent with respect to mechanisms involved in recrystallization is a little arbitrary, since an explicit distinction between the various influences is not possible from experiments. It is, for instance, reported in literature that deviations from the JMAK-plots to lower Avrami exponents can be also the result of a non-uniform dislocation distribution in the cold worked matrix and non-random distribution of nucleation sites [Vandermeer 1962, Price 1989].

In the CORE model, however, such different influences can be clearly distinguished and independently tested. The effect of orientation dependent stored energies and the consideration of different nucleation sites on recrystallization were already validated in Secs. 4.3.5 and 4.3.7.

Recovery does not only influence the recrystallization kinetics, but can also significantly influence the final microstructure and texture. Fig. 6.4 demonstrates the effect of recovery on recrystallization for a constant temperature, but allowing for a much stronger recovery than in the previous case (Fig. 6.3). Fig. 6.4 reflects besides the recrystallization kinetics also two typical textures developed in the course of recrystallization (Fig. 6.4b, c). After a certain time, different recrystallized volume fractions were obtained for the four considered cases (Fig. 6.4a). For high activation energies, and thus negligible influences on recrystallization a fully recrystallized microstructure was obtained. The accompanying texture is mainly comprised of the Cube texture component (Fig. 6.4a, b). In case pronounced recovery takes place (low activation energies), partial recrystallized microstructures were obtained. In this case the final recrystallization texture displayed in addition to the previously observed Cube texture component also remaining fractions of orientations along the β -fiber (Fig. 6.4a, c). The amount of unrecrystallized microstructure and thus the volume fraction of remaining deformation texture components directly depend on the strength of recovery (activation energies chosen for climb and cross slip). In extreme cases, thus also recrystallization in-situ (extended recovery) can be obtained [Gottstein 1998]. Since for the initial grains a homogeneous

orientation rather than orientation gradients are provided from GIA-3IVM+, the effect of texture sharpening in the course of recovery was not considered.

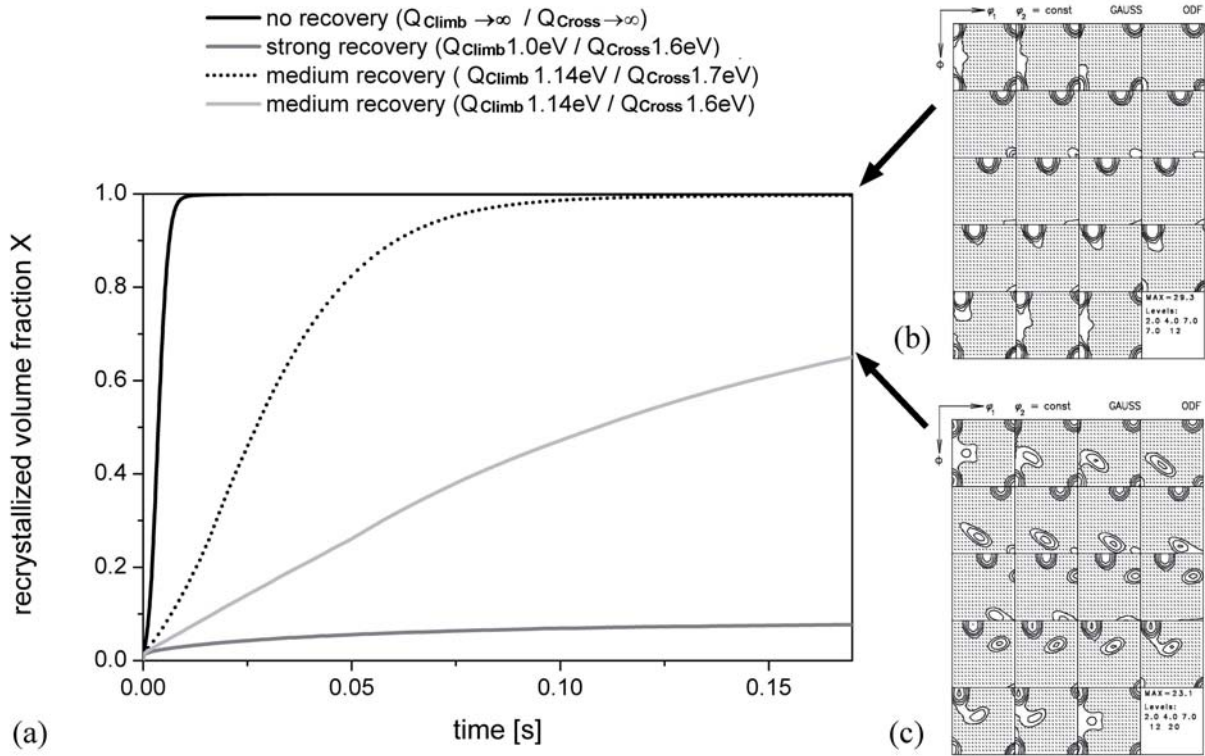


Fig. 6.4: Recrystallization kinetics and textures as influenced by recovery. (a) Effects on Recrystallization kinetics; (b) recrystallization texture – no effect of recovery; (c) recrystallization texture influenced by pronounced recovery, the recovered volume fraction amounts to 30%.

Experiments in the course of this work (Chap. 7) have shown that very low Avrami exponents are encountered in the used Al-Mn alloy (AA3103). The Avrami exponents can be as low as approximately one. Therefore, it was attempted to model recrystallization under consideration of recovery only, with the objective to predict very low Avrami exponents. For the simulations the 3IVM+ parameter set was kept unmodified except for the activation energy for cross slip, which was varied to tune the recovery kinetics. The results are presented in Fig. 6.5.

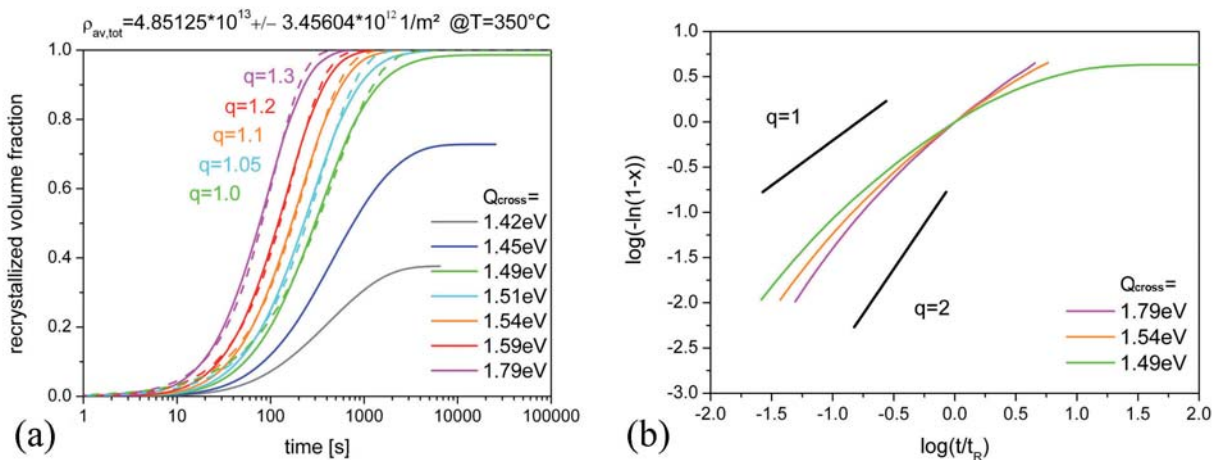


Fig. 6.5: (a) Recrystallization Kinetics under consideration of recovery, the dashed lines represent JMAK-Fits. (b) Avrami plots obtained for recrystallization influenced by recovery.

With decreasing activation energy for cross slip, recovery was more pronounced and hence, slower recrystallization kinetics were obtained (reduced driving force) (Fig. 6.5a). However, when recovery is too pronounced, e.g. for $Q_{\text{cross}} = 1.42 \text{ eV}$, 1.45 eV or 1.49 eV , recrystallization could not proceed to completion, since the effective driving force reached a value of zero all over the microstructure. As a consequence recrystallization was interrupted. It should be kept on mind that in experiments the geometrical necessary dislocations remain in the material and are not recovered as assumed in the 3IVM+ model.

A further decrease of the activation energy, and hence, faster recovery kinetics lead to even lower recrystallized volume fractions (Fig. 6.5a).

The corresponding Avrami plots for the more than 98% recrystallized microstructures are presented in Fig. 6.5b. With increasingly faster recovery kinetics a reduction of the Avrami exponents (slope) down to 1.0 is observed. However, as the activation energy for recovery is lowered, a departure from linearity becomes more obvious, which is equivalent to a retardation of the recrystallization process. Such a behavior was obtained e.g. by Vandermeer [Vandermeer 1963] from experiments in zone-refined aluminum. This shows that by exclusive consideration of recovery, Avrami exponents in the order of experimental findings [Perryman 1955a, 1955b, Laurent 1952a, Laurent 1952b] can be modeled (Fig. 6.5b).

6.2.4 Comparison to empirical approaches for recovery

The recovery description with CORE-3IVM+ (Sec. 3.6) was further compared to an empirical equation which in general yields good agreement with experimental data [Kuhlmann 1949] (Eq. (6.1)). This was done to ensure the applicability of CORE-3IVM+ for the simulation of recovery effects on recrystallization. Eq. (6.1) reads:

$$\rho = \rho_0 - \alpha \cdot \ln(1 + \beta t) \quad (6.1)$$

where ρ_0 is the initial dislocation density at time zero, t the time and α , β constants. The decrease of the driving force due to recovery according to 3IVM+ and Eq. (6.1) is indicated in Fig. 6.6.

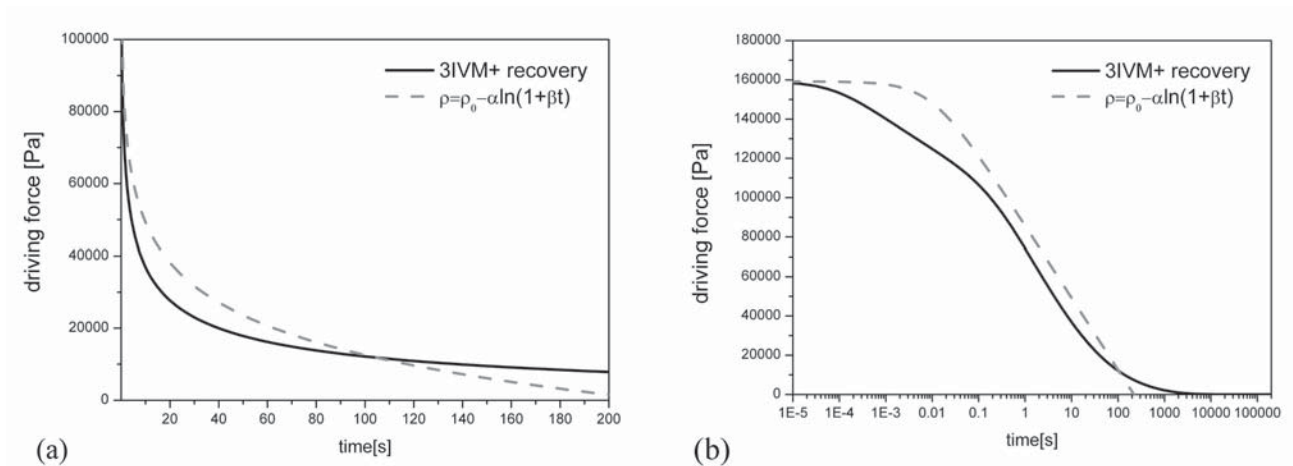


Fig. 6.6: Recrystallization driving force as reduced by recovery on (a) a linear time scale, (b) logarithmic time scale ($\rho_0 = 1.44 \cdot 10^{14}$, $\alpha = 10^{13} \text{ m}^{-2}$, $\beta = 0.01 \text{ s}^{-1}$).

From the presentation on a logarithmic time-scale it becomes obvious why recrystallization can actually be suppressed. The recovery kinetics as described by both approaches lead to entirely vanishing dislocation densities after a finite recovery time (Fig. 6.6b). In such cases, the disruption of recrystallization kinetics is inevitable, since the driving force simply vanishes (Fig. 6.5).

6.3 Modeling Incubation Times

After deformation the dislocation density is non-uniformly distributed in the microstructure, among areas of high dislocation density, the cell walls, and areas of comparatively low dislocation concentration, the cell interiors [Cotterill 1976a, Cahn 1983, Nes 1995, Humphreys 2004]. This structure developed during deformation depends strongly on the stacking fault energy. Most aluminum alloys, however, represent a clearly defined cell structure, besides a few exceptions, e.g. in Al-Mg [Hughes 1993]. Owing to the low driving force for recrystallization in a thermodynamical sense, a nucleus of critical size must be already present in the deformed microstructure [Gottstein 1998]. To initiate the recrystallization process an already existing nucleus needs to be activated by recovery.

Upon annealing the tangled cellular dislocation structure transforms gradually into a subgrain structure comprised of low angle grain boundaries. In this process, the cell walls (or cell boundaries) sharpen and the cells grow larger, while their cell interiors become further depleted of dislocations [Cahn 1983]. This way the cell structure is transformed step by step into a subgrain structure, where the orientation gradient in the cell walls builds up to form sub-grain boundaries. Subsequently, subgrain growth is observed in some materials [Nes 1995]. The annealing time, till the onset of recrystallization, is commonly referred to as incubation time. For high-angle grain boundaries, the structure of the boundaries between deformed grains undergoes rapid and extensive rearrangements during the earliest stages of the recrystallization anneal. For instance, close to high angle grain boundaries a clearing of excess dislocations was observed by means of transmission electron microscopy, such that the remaining dislocations were incorporated into a modified intrinsic grain boundary structure [Jones 1977].

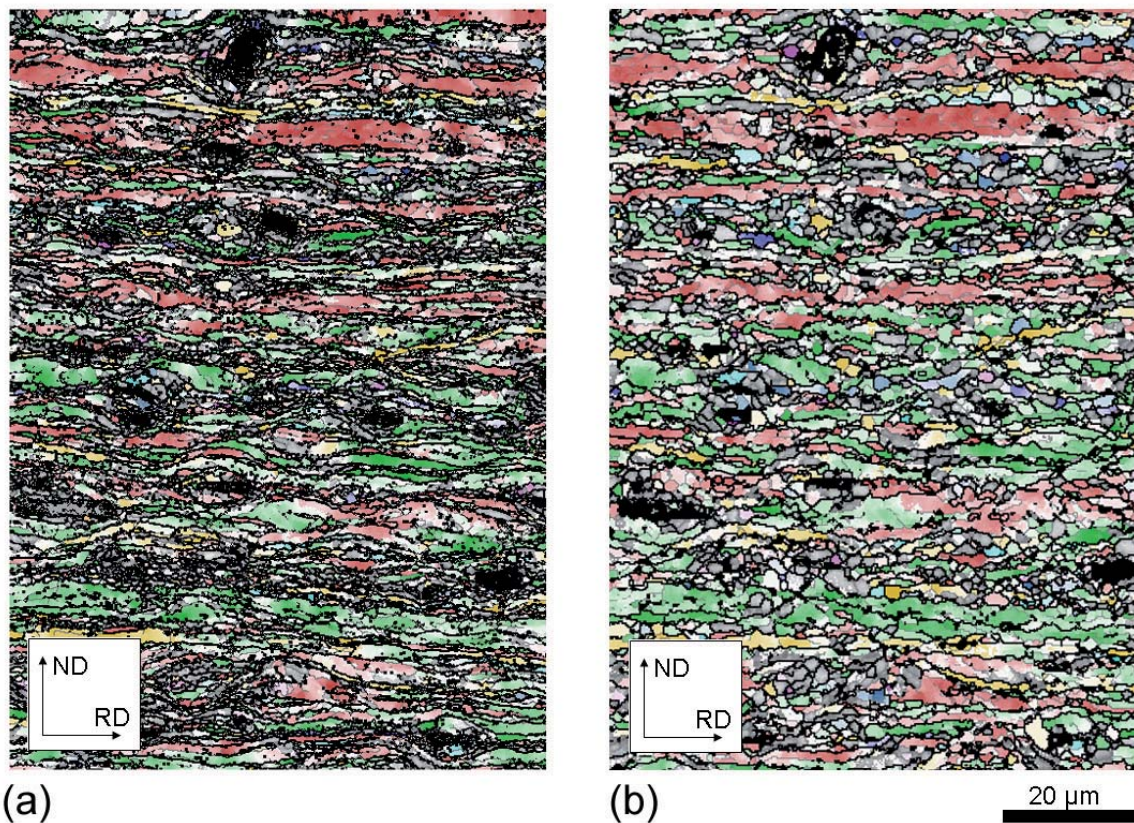


Fig. 6.7: EBSD micrographs of the same spot showing the changes in substructure during early stages prior to the onset of recrystallization in AA3103 cold rolled 70%. (a) Deformed, (b) annealed at $T=290^{\circ}\text{C}$ for $t=15\text{min}$. Grain boundaries with misorientations larger than 5° are indicated in grey and grain boundaries with misorientations larger than 15° are indicated in black.

In the present work the incubation time was assumed to be solely controlled by the sharpening of the cell structure into a subgrain structure, e.g. as indicated by the EBSD micrographs in Fig. 6.7 (neglecting subgrain growth). The micrographs indicate the microstructure changes just prior to the onset of recrystallization in the Al-Mn alloy AA3103. Fig. 6.7a shows a deformed microstructure with relatively undefined grain boundaries (black) and sub-boundaries (grey). Upon short annealing the microstructure has cleared off, and sharp, well defined sub- and grain boundaries are developed (Fig. 6.7b).

6.3.1 Two models for incubation times

The essence of an incubation time model is that a region of high dislocation density, and thus of high strain gradient, turns into a strain-free cell by a process of dislocation climb and rearrangement [Cahn 1983].

The work-hardening / softening model 3IVM+ distinguishes between dislocations in cell walls and interiors, whereas the mobile dislocations are neglected in this context. The coupling of CORE and 3IVM+ makes it possible to track the change of the dislocation densities in the cell walls and in the cell interiors prior to the onset of recrystallization within each grain.

So, if a deformed cellular structure is assumed as initial state after deformation, it contains beside the geometrically necessary dislocations also random dislocations in the cell interiors and cell walls. To activate these cells for nucleation (predict incubation times) those excess dislocations need to be removed. Afterwards, the substructure would basically consist of the remaining geometrically necessary dislocations. This predicted incubation time precedes nucleation and nucleus growth. In some alloys, the incubation time might also include subgrain growth, which was not considered in the present case.

Fig. 6.8 shows the temporal evolution of these two types of dislocation densities (in cell walls and interiors) for different temperatures. It was found that both types of dislocations converge to a quasi-static state, respectively to a hardly changing difference. This relative deviation of the two types of dislocation densities (in the cell interiors and walls) was in the following used as a measure for the incubation time (Eq. (6.2)). The exact value to which the dislocation densities were allowed to drop is the only model parameter. This parameter was adjusted for one temperature and kept constant during further modeling at modified temperature. This tacitly presumes an unchanged microchemistry state in the material during the recovery treatment.

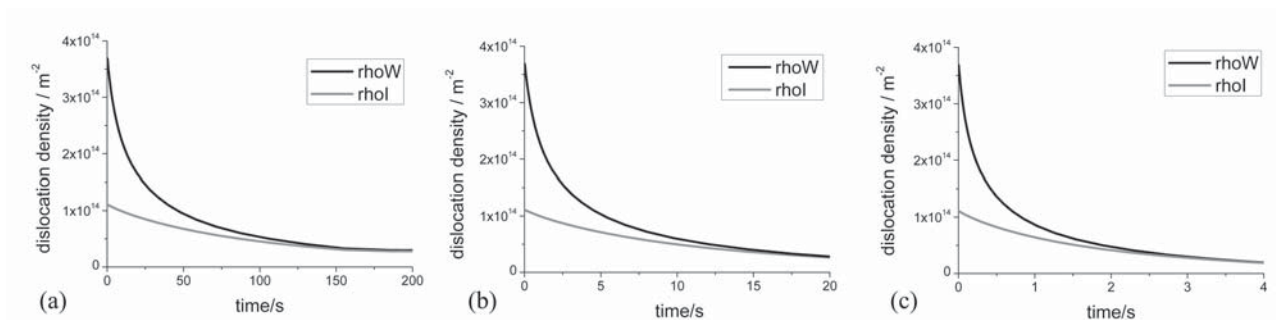


Fig. 6.8: Evolution of the dislocation density in the cell interiors and cell walls for different temperatures (a) 300°C, (b) 350°C and (c) 400°C in the alloy AA3103 cold rolled to 70%.

Fig. 6.9 indicates schematically the transition from a cellular structure to an actual subgrain structure, accompanying the dislocation density evolution in cell interiors and walls.

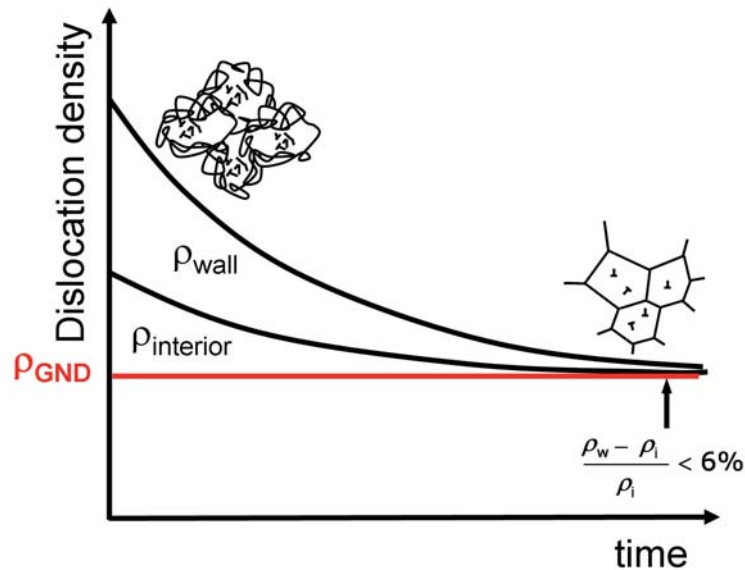


Fig. 6.9: Schematic of the dislocation density evolution over time and the corresponding formation of a cell structure into a subgrain structure. The black lines correspond to the convergence approach, the red line to the SplitUp approach. (ρ_{GND} = geometrical necessary dislocation density, ρ_w = dislocation density in the cell walls, ρ_i = dislocation density in the cell interiors).

The incubation time is therefore expressed by the following criterion:

$$\frac{\rho_w - \rho_i}{\rho_i} \leq \eta_{conv} = \text{constant} \quad (6.2)$$

where ρ_w , ρ_i are the dislocation densities in the cell walls, respectively cell interiors and η_{conv} is a parameter. This criterion provides a measure of how long it takes until the cell structure after deformation has converted into a subgrain structure from which recrystallization can be immediately initiated. It is assumed that the incubation time introduced here is the time to uncover the substructure from excess dislocation, so that finally only geometrical necessary dislocations remain. This criterion will be in the following referred to as *convergence approach*.

A second independent criterion for the incubation time prediction (Fig. 6.9, ρ_{GND}) assumes the creation of a stable substructure, mainly consisting of geometrically necessary dislocations. The incubation times represent then the time to reach a fixed geometrical necessary dislocation density. The geometrically necessary dislocation densities required for this purpose were calculated from the average misorientation as predicted by GIA-Split-up [Crumbach 2004, Crumbach 2006a]. From these resulting misorientations the geometrical necessary dislocation density was computed. This criterion will be in the following referred to as the *SplitUp approach*.

6.3.2 Application of the incubation time criterion

The proposed criterion for the prediction of incubation times is in the following compared to incubation times obtained from experiments in the alloy AA3103 for 70 % cold rolling reduction. To determine the incubation time from experiments different techniques were used: hardness measurements, macrotexture measurements, light microscopy and EBSD.

The hardness measurements (red) in Fig. 6.10a indicate at first a slight drop of the hardness value with time, which can be attributed to recovery. After an incubation time, a sudden hardness drop is observed, which is due to incipient recrystallization (concurrent progress of recovery and recrystallization). The evolution of the hardness values over time can give, however, only a rough

estimation of the time window for recrystallization. A better method to determine the onset of recrystallization more precisely is the use of macrotexture measurements. From macrotexture measurements (evaluation according to Bunge) a strengthening of the β -fiber volume fraction is observed during recovery which is due to the transformations of the cell structure into a subgrain structure. Correspondingly, the diffuse X-ray scattering at cell boundaries is reduced in the course of dislocation annihilation, which causes an increase of the volume fraction of deformation texture components along the β -fiber. When recrystallization is initiated the β -fiber volume fraction is drastically reduced, since the respective texture components become consumed by the growing recrystallization nuclei. Hence, a peak in the β -fiber volume fraction evolution over time is obtained, which allows further confining the time window for the beginning of recrystallization. Within this time window EBSD measurements were carried out with the prospect of finding the first new nuclei. Such different microstructures taken at different temperatures indicating early stages of nucleation are shown exemplarily in Fig. 6.10b,c. The use of these methods allows a quite reliable determination of the onset of recrystallization. The onset of recrystallization is indicated in Fig. 6.10a with the beginning of the grey shaded area. The EBSD-micrographs in Fig. 6.10b,c provide evidence that recrystallization is at its very beginning at this point.

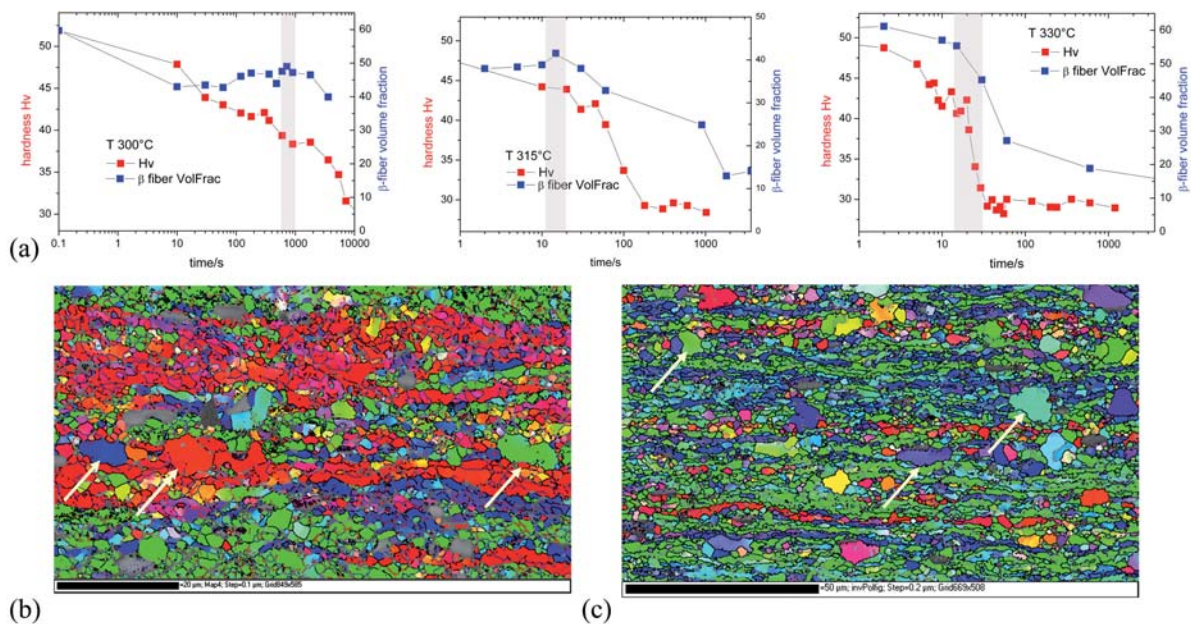


Fig. 6.10: Experimental results for incubation time determination in alloy AA3103. (a) Hardness and macrotexture results vs. time for three different temperatures. (b) EBSD micrograph of material isothermally annealed at $T=300^{\circ}\text{C}$ for $t=15$ min, (c) EBSD micrograph of material isothermally annealed at $T=330^{\circ}\text{C}$ $t=27$ s. The material was previously cold rolled to 70%. Some nuclei in the EBSD micrographs (b) and (c) are indicated by white arrows. The grey shaded areas in (a) indicated the range over which new nuclei are appearing.

The incubation times obtained from experiments were compared to the incubation times predicted with the convergence criterion (Eq. (6.2)) introduced above. Fig. 6.11 shows that an overall good agreement was obtained with experiments (red). However for lower annealing temperatures a larger deviation is obtained. This may be attributed to the change of the microchemistry state in the used material during annealing at $T=300^{\circ}\text{C}$. The initial manganese content in solution of 0.28 wt% decreased to 0.24 wt% during annealing. Therefore, it is likely that already at lower temperature during incipient recovery small precipitates develop which significantly influence the recovery behavior.

Subgrain growth was not considered in the convergence approach. The error bars attached to the average incubation times predicted with the convergence criterion (Fig. 6.11a, blue) originate from

the use of different parameter sets as provided from different 3IVM+-Fits and the corresponding incubation times obtained with them.

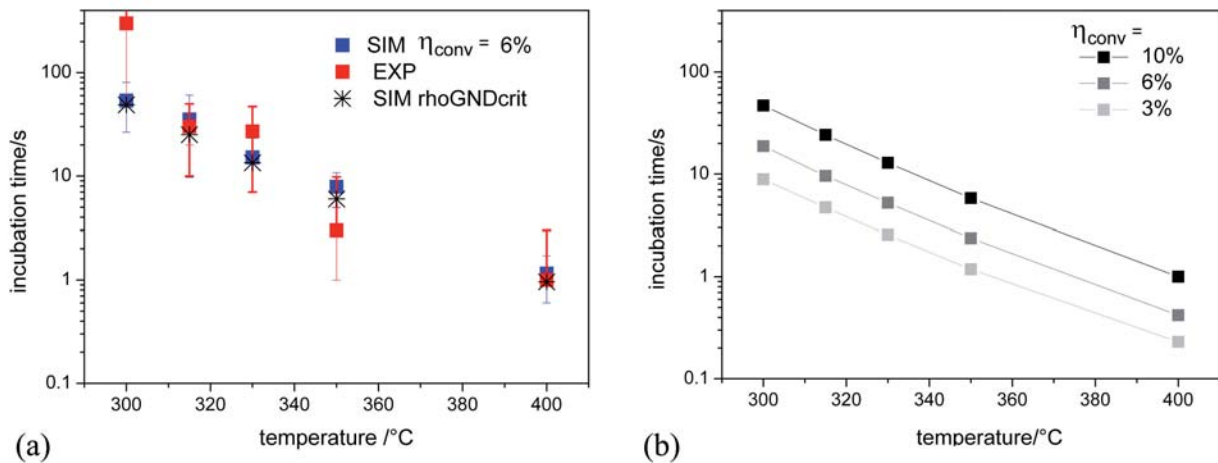


Fig. 6.11: (a) Experimental and modeled incubation times, (b) Predicted incubation times dependent on the chosen value η_{conv} .

The incubation times were also computed with the SplitUp approach. The SplitUp approach (Fig. 6.9) assumes the creation of a stable substructure, mainly consisting of geometrically necessary dislocations as introduced above. Therefore, also the times required to reach a fixed geometrical necessary dislocation density were computed as previously outlined. It was found that both models (convergence approach, SplitUp approach) predict the experimental values pretty well. In principle, a truly correct prediction of the geometrically necessary dislocation density can only be obtained from the 3IVM+ model; since the misorientation created in a GIA-Split up simulation solely reflects a tendency of a grain to split up, rather than quantitative values. However, the information of geometrically necessary dislocations as predicted by the work-hardening model 3IVM+ is at present not available. Nevertheless, the comparisons done in this section are sufficient to ensure a reasonable prediction of incubation times in the present work (Chap. 8) in light of experimental errors. It is very likely that the dislocation densities reached according to the convergence criterion in Eq. (6.2) correspond to the geometrical necessary dislocation density, which would be obtained with such an improved 3IVM+ model (extended to compute geometrical necessary dislocations). This needs to be proven as soon as geometrically necessary dislocations can be computed with 3IVM+.

The critical value η_{conv} (Eq. (6.2) to which both dislocation densities converge is a model parameter. Its influence is demonstrated in Fig. 6.11b. By changing the cutoff value η_{conv} the overall tendency with temperature is preserved. In the present work this cutoff value η_{conv} was set for one temperature in agreement with experiments, and then kept unmodified for simulations at other temperatures.

6.3.3 Modeling nucleation rates

If we replace the average incubation time after which nucleation is initiated at once in all grains (site saturation) by individual orientation-dependent incubation times, a nucleation rate is mimicked. The computed average incubation times for the alloy AA3103 are indicated in Fig. 6.12 (after 70% cold rolling). The scatter of the values in Fig. 6.12 indicates the maximum and minimum incubation times obtained for a certain temperature. It is observed that with decreasing temperature the nucleation of individual grains is activated over longer time intervals.

Hence, significant changes of texture are more likely to occur at lower temperatures, since early nucleated grains receive much larger growth advantage over those nucleated later on. This growth advantage is less pronounced at high temperatures because the absolute time interval for nucleation is smaller (Fig. 6.12). The scatter of the incubation times is particularly pronounced at the lowest

temperature of $T = 300^{\circ}\text{C}$. Here, incubation times are found that amount to 5% of the total recrystallization time. This is, however, absolutely comparable to experimental results by Lauridsen et al. [Lauridsen 2000]. These authors observed in an aluminum alloy AA1050 (containing Al₃Fe-particles) by use of in-situ techniques, incubation times of up to about 15% of the total recrystallization time.

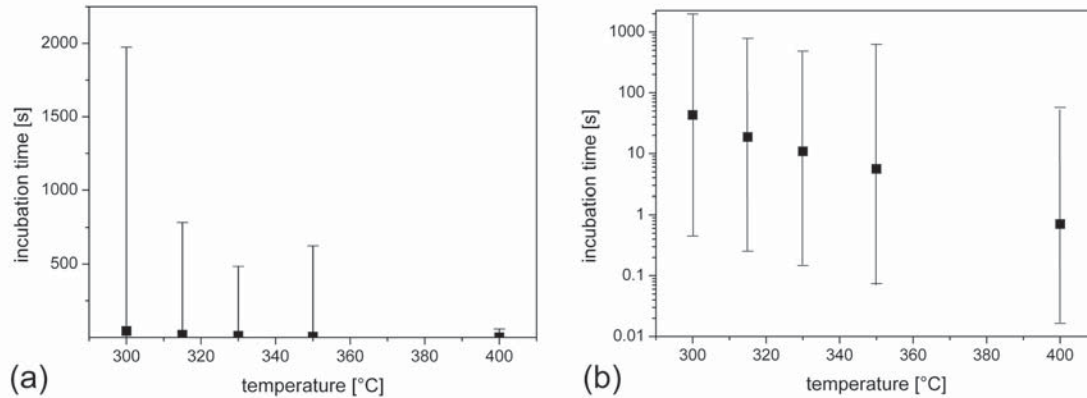


Fig. 6.12: Calculated incubation times dependent on temperature displayed (a) on a linear scale; (b) on a logarithmic scale. The incubation times were calculated for each grain orientation. Beside the average incubation times further the range between the absolute maximum and minimum is indicated. The calculations were based on a data set of AA3103 for 70 % cold rolling.

The incubation time of differently oriented grains strongly depends on the as-deformed dislocation density stored within these grains. A nucleation rate predicted with the incubation time approach naturally affects the grain size distribution and recrystallization texture. For high heating rates this effect on texture and grain size distribution is negligible, since all grains are nucleated within a short time interval (comparable to site-saturation). For low heating rates, however a huge influence can be expected. The grain size distributions resulting from the assumption of site-saturation and nucleation rates are compared in Fig. 6.13 (see also Chap. 8).

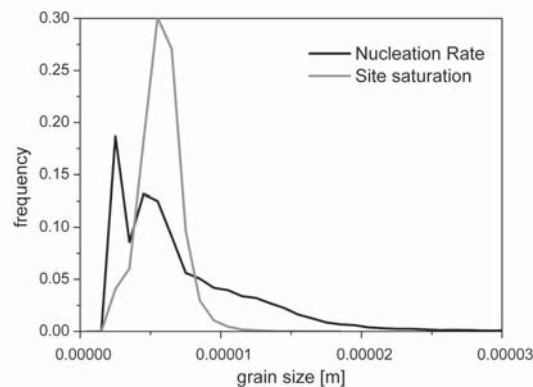


Fig. 6.13: Influence of nucleation rate on the grain size distribution in case of a heating rate of 35°C/h .

For heating rates, respectively nucleation rates a much larger grain size combined with a wider grain size distribution was obtained. It is pointed out that the distribution is clearly non-symmetric in contrast to the results obtained for site-saturation. This effect is strongly pronounced for low heating rates, respectively under consideration of a nucleation rate since in these cases other mechanisms are significantly involved in recrystallization (recovery, precipitation). When the recrystallization kinetics is fast enough compared to other mechanisms, it is then not important whether or not a nucleation rate is considered.

The consideration of incubation times as introduced above influences also slightly the recrystallization kinetics (Fig. 6.14). For the demonstration of this effect, the impact of recovery

was assumed to be less pronounced to ensure full recrystallization. The results are presented for two different temperatures assuming high and low activation energies for recovery (Fig. 6.14).

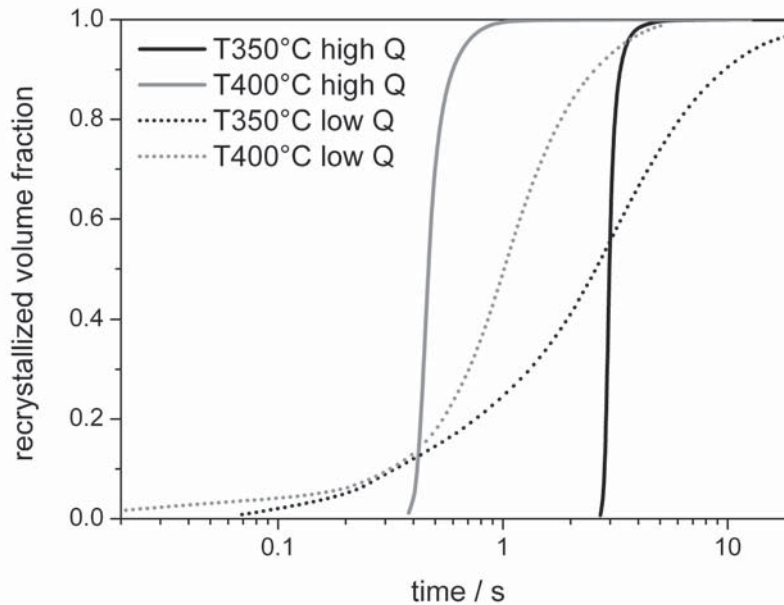


Fig. 6.14: Impact of recovery on the recrystallization behavior for different incubation times (strong recovery: $Q_{\text{cross}} = 1.65 \text{ eV}$, $Q_{\text{climb}} = 1.24 \text{ eV}$ - dotted line, weak recovery: $Q_{\text{cross}} = 1.85 \text{ eV}$, $Q_{\text{climb}} = 1.44 \text{ eV}$ - continuous line).

If the activation energy for recovery is very high, hardly any influence on the recrystallization kinetics is observed (continuous line, Fig. 6.14). If however, pronounced recovery is considered, the incubation time is reached earlier, and recrystallization is initiated earlier. Under this condition recrystallization kinetics with a lower slope are observed which means that during the recrystallization process the stored dislocation density is reduced rapidly due to the fast recovery processes. Hence the driving force for recrystallization drops rapidly, and recrystallization proceeds more and more slowly with increasing time. Since the incubation time directly depends on recovery, the shift of the onset of recrystallization is always accompanied with a different slope of the recrystallization kinetics in a logarithmic plot (Fig. 6.14). This is particularly affected by temperature changes, since the temperature influences the individual processes, recrystallization and recovery differently and therefore impact the extent to which they can occur.

Besides the effect on the recrystallization kinetics, no pronounced effects on grain size distribution and recrystallization texture were observed in the present case.

6.4 Conclusions

This chapter was focused on the influence of recovery on recrystallization. After introducing the coupling of CORE and the work-hardening / softening model 3IVM+ in Sec. 3.6, in this chapter the corresponding model behavior was validated. The introduction of orientation-dependent recovery rates is essential for the individual evolution of single deformed grains and hence for the final volume fractions of the various texture components of the recrystallization texture. These orientation-dependent recovery rates were then interpreted for the modeling of incubation times. The introduced incubation time criteria were shown to predict results in good agreement with experiments in AA3103. These orientation-dependent incubation times were further utilized to mimic nucleation rates during recrystallization with excellent effect on the overall recrystallization kinetics and grain sizes. Particularly, the modeled grain size distribution yielded strongly improved predictions in comparison to experiments.

Chapter 7

Recrystallization Behavior influenced by Precipitation

7.1 Introduction

This chapter is focused on modeling recrystallization considering *concurrent precipitation* during *isothermal heat treatments*. Beside the changes in microchemistry also recovery was taken into account, which plays a minor role compared to precipitation. This case study should reveal the applicability of the various models (CORE, GIA [Crumbach 2005], 3IVM+ [Gurla 2007, Mohles 2008], ClaNG [Schneider 2006]) and in particular their mutual interactions. To investigate the effects of smallest variations in microchemistry a *laboratory* processed aluminum alloy AA3103 was chosen as material, rather than an *industrial* processed one. In general those laboratory processed alloys behave quite sensitive to variations in thermo-mechanical processing compared to those alloys used in industry.

Simulations were carried out for different deformation degrees and isothermal annealing treatments and compared to experiments. Temporal changes of the relevant microchemistry quantities were taken into account.

The structure of this chapter is as follows. Sec. 7.2 summarizes mostly experimental results, which are to be compared later on with the simulation results (Sec. 7.4). Sec. 7.3 gives an overview of the input data required for the recrystallization model CORE as obtained from other models (GIA-3IVM+, GIA-SplitUp [Crumbach 2004, 2005, 2006a], GIA-DZ, ClaNG, 3IVM+). In Sec. 7.4 the predicted recrystallization behavior is presented in terms of the modeled quantities: *recrystallization kinetics*, *microstructure* and *texture*. A detailed analysis of the modeling of recrystallization kinetics is outlined in Sec. 7.5. Whereas the sensitivity of the crucial CORE inputs has already been evaluated in Chap. 4, in Sec. 7.5 the sensitivity of the ClaNG inputs [Schneider 2006] is one important point of discussion. The main purpose of this section is however the critical evaluation of the individual influences (recovery, precipitation) on the recrystallization kinetics, finally proposing a new approach of how to deal with the combined effect of recovery and precipitation on recrystallization.

7.2 Experimental Data and Evaluation

7.2.1 Homogenization treatment for initial material

The material used for this study was an Al-Mn alloy AA3103, which was provided by industry as hot rolled strip. The hot rolled strip was subjected to a homogenization treatment for 14 hours at $T = 610\text{ }^{\circ}\text{C}$ in an air-circulating furnace followed by quenching in water in order to keep a very high content of manganese in solid solution (Fig. 7.1).

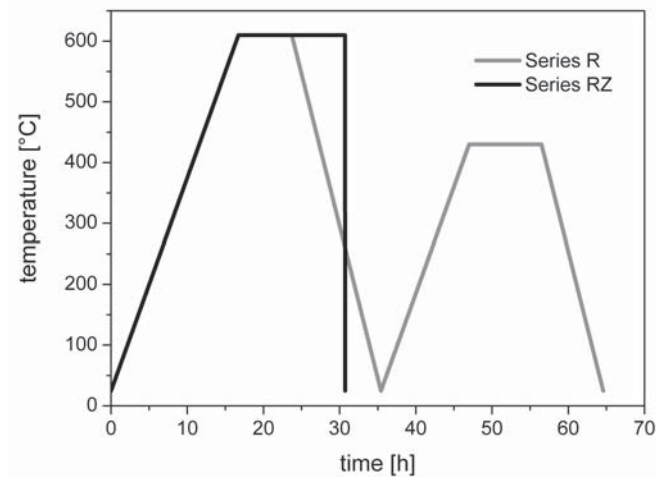


Fig. 7.1: Temperature profile as a function of time during homogenization for series R and RZ.

For series RZ a solute content of 0.4427 wt% manganese and for series R 0.281 wt% manganese was obtained. The material of series RZ was used in the current study (the material of series R was used in Chap. 9). The particle structure obtained after homogenization in series RZ is shown in Fig. 7.2. Beside large constituents, also numerous smallest particles, so-called dispersoids are initially present (indicated by the point-like etch marks).

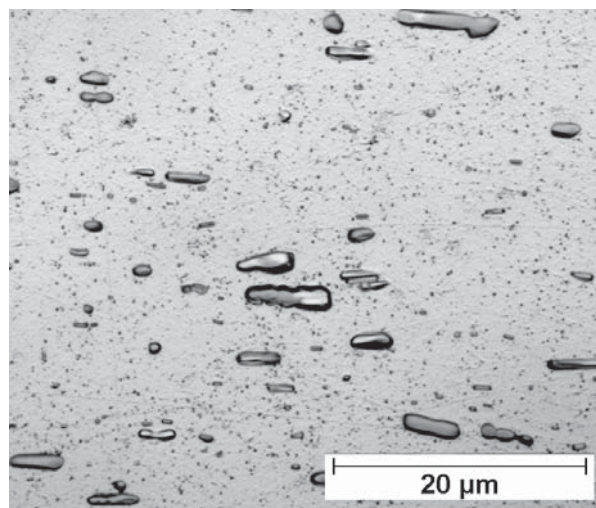


Fig. 7.2: Particle structure in alloy AA3103 after the homogenization treatment for series RZ, large particles are constituent particles, and small particles represent dispersoids. The appearance of the particle size is influenced by the etching time, which was kept as short as possible.

7.2.2 Cold rolling of the homogenized material

After homogenization, the material was cold rolled on a laboratory mill to 50 %, 70 % and 85 % thickness reduction. The typical evolution of microstructure with increasing cold deformation is

illustrated by the EBSD micrographs in Fig. 7.3. At a true strain of 0.7, the original grains were flattened and elongated in rolling direction. At higher rolling reductions a defined substructure became apparent in the grain interior. From the micrographs also the evolution of the deformation zones in the particle vicinity was visible. While the deformation zones (see also Chap. 5, Fig. 5.1) were hardly developed after cold rolling reductions of 50 %, they were very pronounced at 85 % cold rolling reduction.

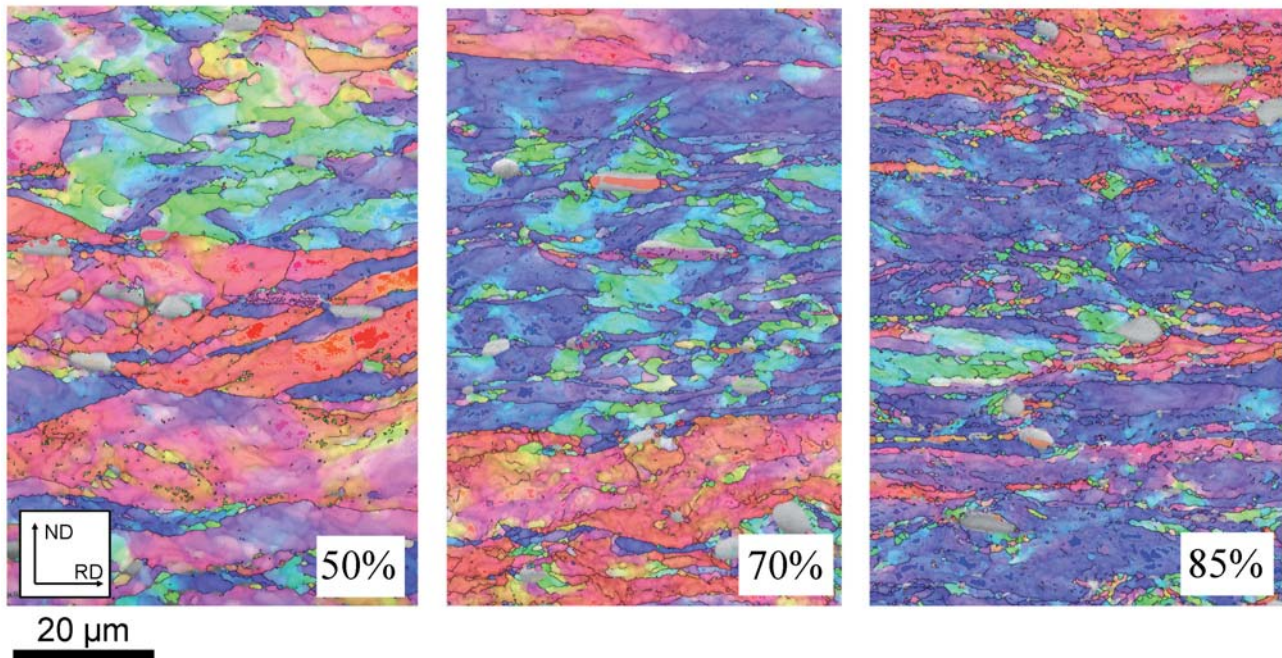


Fig. 7.3: Microstructure evolution during cold rolling. From left to right the cold rolling reduction is increasing from 50%, 70% to 85%. The different colors indicate different orientations; the grey areas represent the constituent particles. The micrographs are presented in the transverse plane.

7.2.3 Characterization of the heat treated material (data for grain size and texture)

Samples with different cold rolling degree were subsequently subjected to annealing treatments in a sand bath at temperatures of $T = 350\text{ }^{\circ}\text{C}$ and $T = 400\text{ }^{\circ}\text{C}$. The corresponding microstructure evolution for the three deformation degrees is shown in Fig. 7.4.

At low temperatures, the microstructure is rather inhomogeneous, displaying large grains and comparatively small grains. At higher temperatures, a very fine, equiaxed grain size was obtained. With increasing rolling degree a finer grain size is obtained for both temperatures. It is pointed out that the grain boundaries at lower temperatures are not smooth. This indicates that the material is strongly affected by Zener pinning during recrystallization. This effect was particularly pronounced for the samples annealed at a low temperature. At lower temperatures, precipitation occurred preferentially at the high angle grain boundaries. And in this case, vastly longer annealing time was required for the material to be recrystallized as presented later on. The observation of larger and more elongated grains in the case of concurrent precipitation (Fig. 7.4a-c) was also reported by various authors for Al-Mn alloys [Furrer 1978, Tangen 2002]. At high temperatures, the obtained microstructure was fine-grained. Recrystallization proceeded almost unaffected by the precipitation process within a short time.

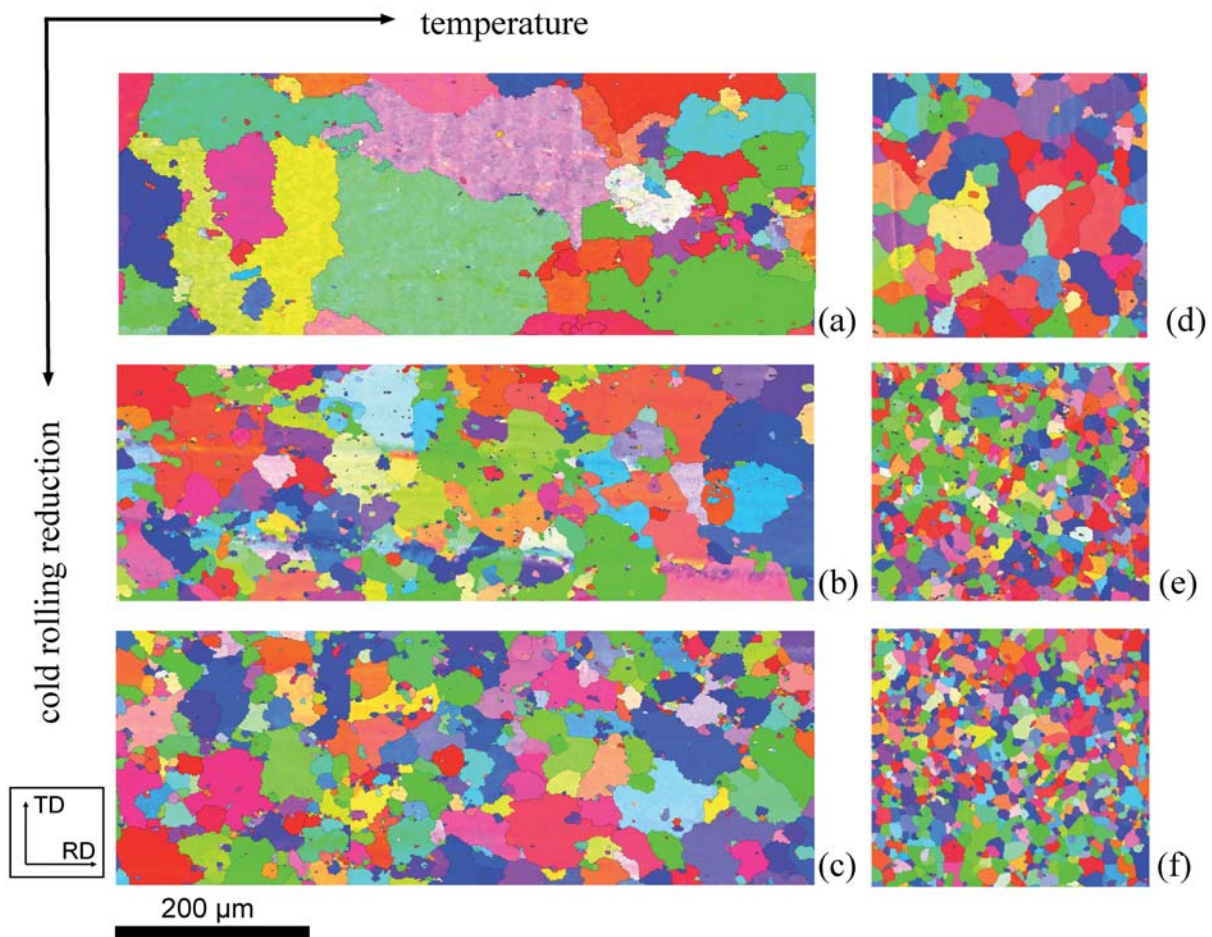


Fig. 7.4: EBSD micrographs of fully recrystallized microstructure after sand bath annealing in AA3103 series RZ. (a)-(c) increasing rolling reduction from 50%, 70% to 85% at $T=350^{\circ}\text{C}$, (d)-(f) increasing rolling reduction from 50%, 70% to 85% at $T=400^{\circ}\text{C}$. The EBSD micrographs were taken in normal direction.

For the differently heat treated samples grain size measurements were carried out by means of stereographic procedures. The grain size was measured from EBSD data by evaluation of the area-equivalent circle diameter, and from optical micrographs, by using the line intercept method. The obtained values with their respective scatter are presented in Fig. 7.5.

It was observed that with increasing initial rolling reduction the grain size decreased as to be expected. A reduction of grain size was also obtained by increasing the annealing temperature. This indicates that different physical mechanisms are taking place at the different temperatures chosen. It was reported in literature that in Al-Mn alloys containing 0.45 wt% manganese in solute solution precipitation sets in at temperatures lower than $T = 350^{\circ}\text{C}$, whereas at higher temperatures the recrystallization kinetics is much faster than the precipitation kinetics [Tangen 2002]. The temporal occurrence of recrystallization and precipitation strongly depends in this case on the manganese content in solid solution as well as on temperature and deformation degree.

However, a large deviation between grain size measurements from EBSD and optical microscopy was observed in particular for the grain sizes measured from the sample annealed at a lower temperature. In this case the EBSD data and the results from the optical micrographs scattered strongly and resulted in large standard deviations. The reason for the wide grain size distributions is not an insufficient statistics, but rather the effect of a locally effective Zener pinning. Thus, resulting, particularly at lower temperatures, in a preferential growth of some grains, where other grains remain as island grains in between. As a consequence a wide grain size distribution is obtained (error bars Fig. 7.5). This was also reported by Furrer for an Al-1wt% Mn alloy [Furrer 1979].

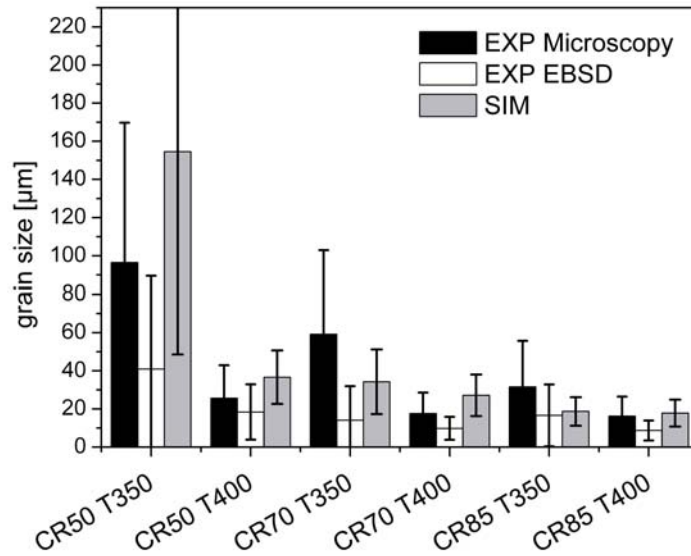


Fig. 7.5: Comparison of average grain sizes as obtained from experiments and simulation for the indicated samples of AA3103, series RZ.

7.2.4 Data for recrystallization kinetics

To compare the modeled recrystallization kinetics with experiments, the recrystallized volume fraction as a function of time was determined. Since in the current case extended recovery took place (Fig. 7.6a), the measured hardness data was not sufficient to determine the recrystallization kinetics. Additionally, macrotexture measurements were carried out for different annealing times, rolling reductions and temperatures. The texture data was calculated from polefigures according to the Bunge method and was then analyzed with respect to the volume fraction of the different texture components. The orientations Brass, S/R and Cu were comprised in the β -fiber volume fraction. The softening behavior as measured from hardness, respectively texture is presented in Fig. 7.6.

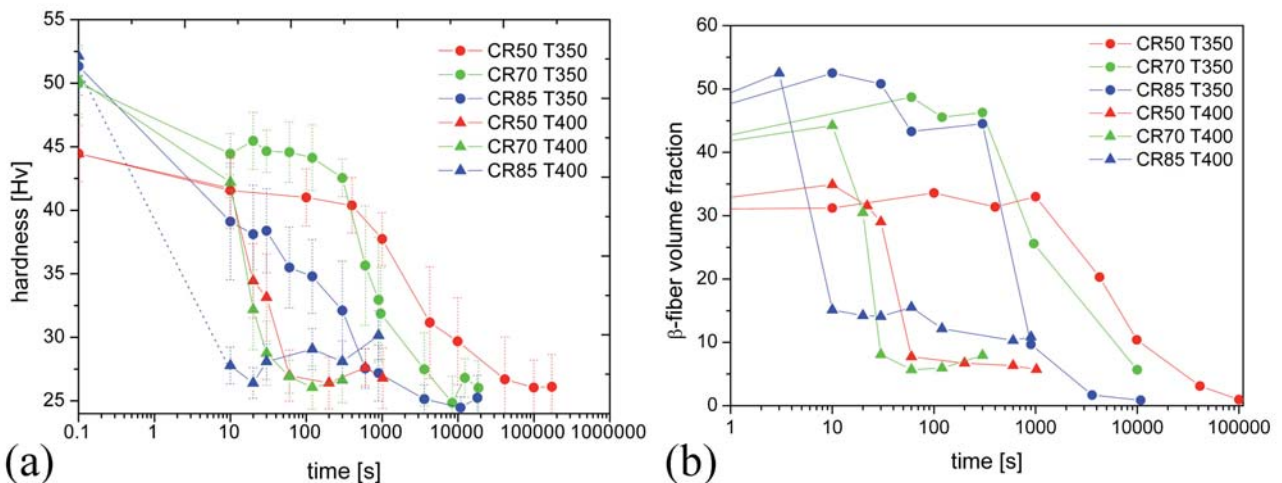


Fig. 7.6: (a) Hardness evolution over time in AA3103-RZ (b) Evolution of β -fiber volume fraction over time in AA3103-RZ.

With increasing deformation degree the onset of recrystallization took place earlier. The effect of temperature on the recrystallization behavior was however much more pronounced. By a decrease of the annealing temperature to $T = 350^\circ\text{C}$, the onset of recrystallization was shifted to longer annealing times by a factor of 1000 (Fig. 7.6a,b indicated by filled circles). It is known from

literature [Sjølstad 2003] that this shift depends on the amount of manganese in solid solution prior to the annealing rather than on the annealing temperature itself. In the present case (series RZ - initial Mn content 0.4427 wt%) the transition in the recrystallization behavior was observed between $T = 350\text{ }^{\circ}\text{C}$ and $T = 400\text{ }^{\circ}\text{C}$ (Fig. 7.6), in contrast to the industrial material (series R - initial Mn content 0.281 wt%) addressed in Chaps. 8, 9, where the transition is observed between $T = 300\text{ }^{\circ}\text{C}$ and $T = 330\text{ }^{\circ}\text{C}$. Connected with the change in recrystallization kinetics is the change from a narrow grain size distribution to a wide grain size distribution, which was also observed in the current experiments as introduced previously (Fig. 7.5).

From the evolution of the β -fiber volume fraction over time finally the recrystallized volume fraction was determined. The recrystallized volume fraction X as a function of time was calculated according to the following equation:

$$X = \frac{f_0 - f_t}{f_0 - f_{END}} \quad (7.1)$$

where f_0 is the initial β -fiber volume fraction just before the onset of recrystallization. f_t is the β -fiber volume fraction after the considered time t , and f_{END} is the final β -fiber volume fraction obtained after complete recrystallization. The calculated recrystallized volume fractions are indicated in Fig. 7.7 by open / filled squares. The derived recrystallization kinetics for $T = 350\text{ }^{\circ}\text{C}$ are presented in Fig. 7.7.

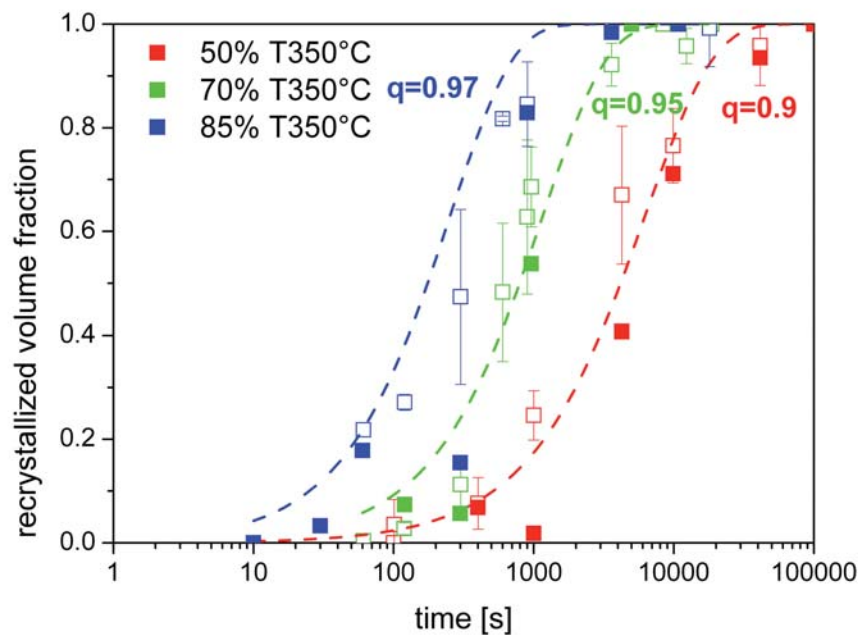


Fig. 7.7: Recrystallization kinetics as determined from hardness and texture measurements in AA3103-RZ. The dashed lines represent the JMAK Fits of the data with the corresponding Avrami exponents q (open square = hardness measurements, filled squares = texture measurements).

At a temperature of $T = 350\text{ }^{\circ}\text{C}$ an Avrami exponent of about one was obtained for the recrystallization kinetics, which is not unusual for cases where pronounced recovery or precipitation occurs. It is in fact very unusual to find experimental data which, on detailed analysis, show good agreement with JMAK kinetics. Either the JMAK plot is non-linear or shows Avrami exponents less than 3. Perryman [Perryman 1955b] reported values between 1.1 and 1.6 for super-purity Al and Al-Mg. Laurent and Batisse [Laurent 1952a, 1952b] found by analysis based on Avrami's theory values for aluminum between 1 and 1.7.

7.2.5 Precipitation during annealing

Beside influences of recovery during recrystallization, the precipitation behavior is of major concern. The temporal precipitation behavior was modeled with the ClaNG model [Schneider 2006]. Since ClaNG contains intrinsic model parameters, they need to be fitted first by comparison to experiments (Sec. 7.3). The solute content of manganese serves for comparison of the later presented precipitation predictions. To determine the solute content of manganese as a function of annealing time, thermo-electric power measurements were carried out for selected samples.

Tab. 7.1: Thermoelectric power and resistivity measurements for series RZ of alloy AA3103 [courtesy of Hydro Aluminium Bonn].

<i>name</i>	<i>solid solution content Mn [wt%] from TEP</i>	<i>R4.2K [mΩ]</i>
<i>homogenized</i>	<i>0.4427</i>	<i>0.03738</i>
<i>cold rolled 80%</i>	<i>0.501</i>	<i>0.18156</i>
<i>CR 80 % + T350°C 50min</i>	<i>0.2245</i>	<i>0.19010</i>
<i>CR 80 % + T400°C 5min</i>	<i>0.3996</i>	<i>0.15477</i>

7.3 Input for Recrystallization Modeling

As outlined in Sec. 3.4, the recrystallization model CORE requires a considerable amount of input parameters. This section summarizes the predicted inputs for the recrystallization simulations, which are sorted according to main topics (deformation, nucleation parameters, precipitation, growth and recovery parameters).

7.3.1 Deformation simulations

A main input for the recrystallization simulations is the stored dislocation density after deformation, since it provides the driving force for recrystallization. Other deformation-related sizes required for recrystallization are the deformed grain size and the deformation texture for initialization of the CORE model.

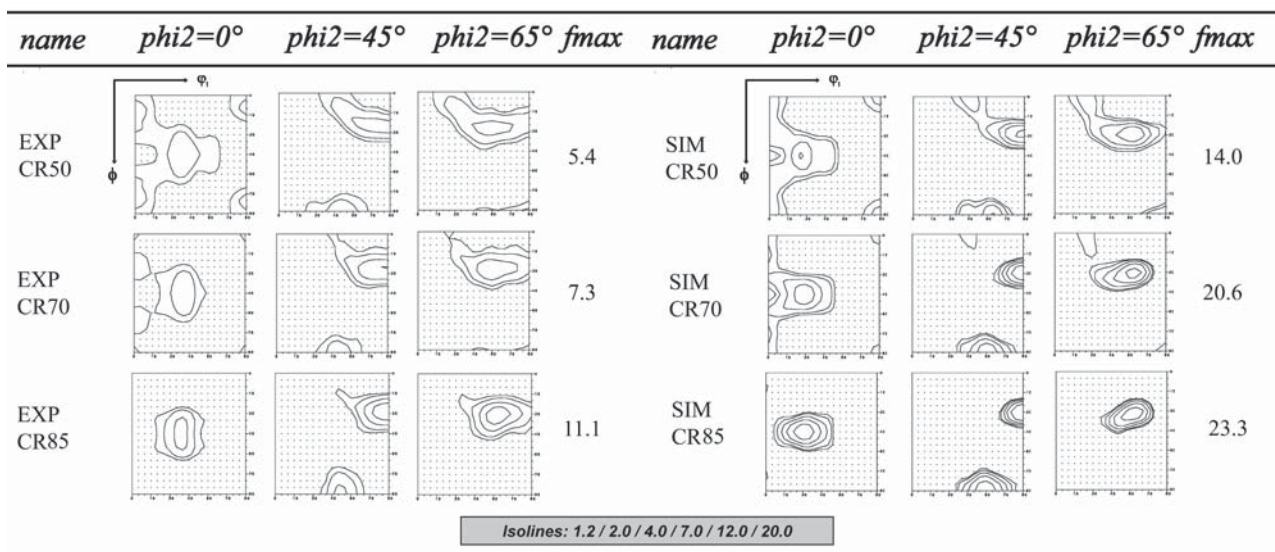


Fig. 7.8: Experimental (left) and simulated deformation textures (right). Displayed are selected sections through the Euler space.

For the modeling of the deformation behavior, the experimental flow curves were fitted with the 3IVM+ fitting model. The obtained fitted data set served as input to describe the work-hardening during deformation of the chosen material, homogenized according to Fig. 7.5 (series RZ). Subsequently the three different rolling reductions 50%, 70% and 85% were modeled with the deformation model GIA. The results are displayed in Fig. 7.8 in comparison to experiments.

The simulated deformation textures are in good qualitative agreement with the experimental data. They show slightly higher maximum intensities than measured from experiments, as frequently observed for textures modeled with GIA [Crumbach 2005]. The average dislocation density obtained for each orientation class is indicated in Fig. 7.9a.

7.3.2 Sub-structural quantities and nucleation

The output of the GIA model was further analyzed with respect to relevant sub-structural quantities for nucleation (ReNuc [Crumbach 2004, Crumbach 2006a, Crumbach 2006b]). To address the orientation dependency of the sub-structural quantities, the single grain data of the GIA-3IVM+ and GIA-Split-Up [Crumbach 2004, 2006a] models was broken down into main texture classes (Tab. 3.9), allowing a scatter of $\pm 15^\circ$ for the Cube, Goss, Copper, S, Brass and the rotated Cube components. The quantities analyzed with respect to these texture components were then averaged and plotted (Fig. 7.9).

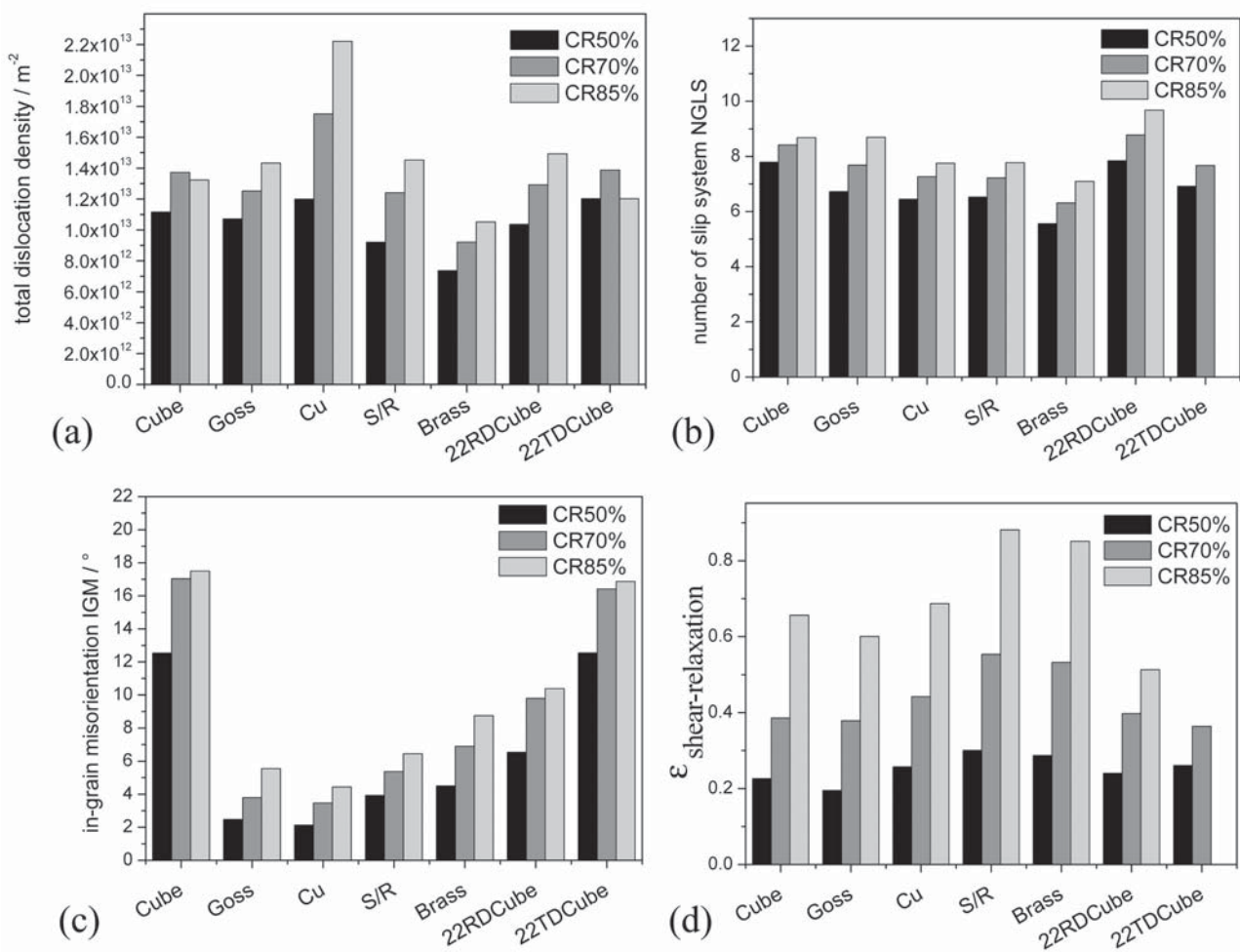


Fig. 7.9: Statistical analysis of (a) stored dislocation density, (b) number of activated slip systems, (c) in-grain misorientation gradients, (d) amount of shear relaxation in main texture components provided by the GIA-3IVM+ model for the alloy AA3103 RZ for three different rolling reductions.

Fig. 7.9a reflects the predicted densities of statistically stored dislocations. It was observed that their absolute values increase with increasing strain, as to be expected. They are further in a reasonable order of magnitude ($6 \times 10^{12} \text{ m}^{-2}$ to $2.2 \times 10^{13} \text{ m}^{-2}$). The relative distribution of statistically stored dislocations densities among the different deformation texture components is of major interest. Since the stored dislocation densities are a measure for the stored energy, their distribution determines which orientations are consumed first during recrystallization. In case of the higher deformation degrees, GIA-3IVM+ predicted the highest values for the Cu orientation, which is hence consumed first during early stages of recrystallization. The Brass component showed the lowest statistically stored dislocation densities. For the Goss, S/R and Cube components, similar intermediate values of statistically stored dislocation densities are found.

Grain Boundary Nucleation

The total number of slip systems N_{GLS} activated during the entire deformation resolved for the individual orientation types is presented in Fig. 7.9b. According to Crumbach [Crumbach 2005] this number is correlated with the relative orientation dependent kinetics of static recovery (ODR). The absolute values of N_{GLS} are increasing with increasing cold rolling reduction, since the higher degree of deformation is connected to larger rotations of the grains and thus to an increased probability to change the active slip systems in them. The Cube orientations have the highest N_{GLS} values and the β -fiber orientations have notably lower values with a minimum in the Brass orientation (Fig. 7.9b). This means that Cube grains will recover faster than e.g. Brass grains, even though the Cube orientation has not the lowest statistically stored dislocation densities. This leads to an earlier formation of viable GB-nuclei in Cube grains compared to, e.g. Brass grains.

Transition band Nucleation

In-grain orientation gradients within grains are developed when the in-grain misorientation (IGM) values predicted by the GIA-Split-Up model [Crumbach 2004, 2006a] are higher than a critical value (Fig. 7.9c). This critical value is the average IGM according to the ReNuc model. The obtained IGM values for the different initial grain orientations (prior to deformation) are plotted in Fig. 7.9c. The IGM values are given for the different initial grain orientations prior to deformation, since based on these orientations later transition band nuclei are formed with an orientation spectrum related to the pre-deformed grain orientation. The absolute IGM values do increase with increasing level of cold rolling. A maximum of 12° misorientation is obtained after 50% cold rolling and about 18° misorientation after 85% cold rolling. These values represent average values for all grains belonging to a specific texture component. For individual misorientations thus values of up to 40° can be obtained. This is in agreement with observations by Humphreys et al. [Humphreys 2004], who observed values up to 40° within single grains for higher deformation degrees. The relative distribution of the IGM value among the different texture components demonstrated again the special behavior of the Cube orientation. It shows together with the 22° ND rotated Cube component by far the highest IGM values, in contrast to very low values found in case of β -fiber grains. This means that Cube nuclei do not only form by GB-nucleation but also by TB-nucleation.

Shear Band Nucleation

The amount of shear relaxation $\varepsilon_{vM}^{shear-relax}$ is considered in Crumbach [Crumbach 2005] to be a strong indicator for inhomogeneous deformation of grains. It was interpreted to be a representative quantity to reflect the probability of a grain for shear banding. The $\varepsilon_{vM}^{shear-relax}$ values presented in Fig. 7.9d show an increase with increasing deformation, since $\varepsilon_{vM}^{shear-relax}$ is summarized over the various strain steps. With respect to the orientation dependency of shear banding it is found that Cube related orientations and Goss grains have lower values of $\varepsilon_{vM}^{shear-relax}$ than β -fiber grains. Thus, again, Cube oriented grains show a different behavior than the deformation texture components. In

the ReNuc model this would lead to the creation of more randomly oriented nuclei in case of β -fiber grains.

7.3.3 Precipitation behavior

Beside the deformation simulations with GIA-3IVM+ also simulations of the precipitation behavior with the classical nucleation and growth model ClaNG were carried out. It is known that the initial amount of defects, such as dislocations after cold deformation can enhance the precipitation behavior due to heterogeneous nucleation at dislocations or dislocation tangles. Therefore the different stored statistical dislocation densities after deformation and their evolution over annealing time were used as input for the ClaNG model. The decrease of dislocation density over time was derived from the hardness value, which were related via a simplified relationship to the macroscopic stress and hence to shear stress and dislocation density [Cahoon 1971] (see also Chap. 8).

The initial dislocation density as input for ClaNG was obtained as output from the respective GIA-3IVM+ simulation. Other parameters of the ClaNG model were adjusted by fitting to the target solid solution content of manganese, which was measured from experiment (Tab. 7.1). From the ClaNG calculations presented in Fig. 7.10 only minor changes dependent on the deformation degree were observed. The predicted solid solution content of manganese is in good agreement to experimental results obtained from thermo-electric power measurements (indicated by black squares in Fig. 7.10). The precipitation behavior was modeled with ClaNG starting from the initial homogenization treatment rather than with only the final annealing treatment. This was done to ensure the same initial condition for all simulations and to prevent additional experimental input of rather complex particle-size distribution in the downstream process. The results of the ClaNG predictions are indicated in Figs. 7.10, 7.11.

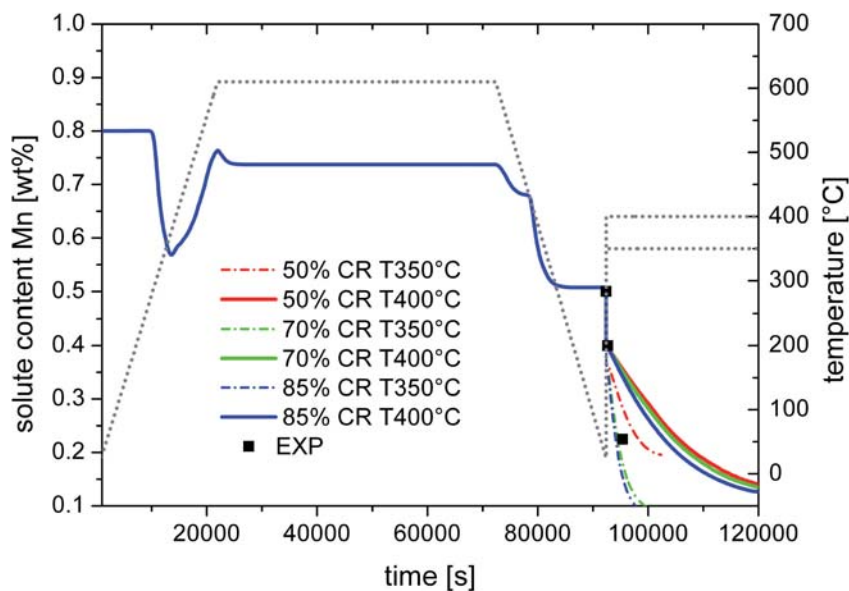


Fig. 7.10: Simulated evolution of manganese in solid solution along the whole production route. Solid square = experimental values from thermo-electric power measurements (TEP) for final annealing temperatures of $T = 350^\circ\text{C}$ and $T = 400^\circ\text{C}$ and cold rolling reduction of 85% rolling reduction.

During the final isothermal annealing treatment, the solute content of manganese (Fig. 7.10) is reduced strongly in particular for the lowest temperature ($T = 350^\circ\text{C}$). This is reasonable, since recrystallization is in this case initiated at longer annealing times, so that still higher dislocation densities were present at the beginning of the precipitation modeling. These higher dislocation densities promote precipitation by heterogeneous nucleation.

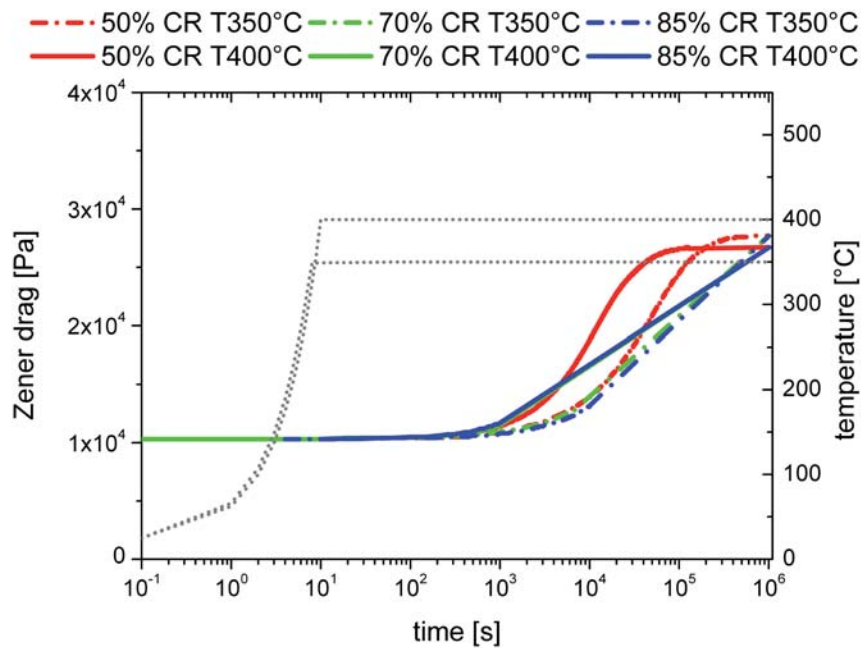


Fig. 7.11: Simulated evolution of Zener drag during the final heat treatment at $T = 350^{\circ}\text{C}$, respectively $T = 400^{\circ}\text{C}$ for alloy AA3103 with different rolling reductions (50%, 70%, 85%).

The precipitation of new particles becomes obvious from the evolution of the Zener drag (Fig. 7.11), as predicted from the ClaNG model. At higher temperatures the maximum value of Zener drag was obtained comparatively faster. In the present investigation only Al_6Mn dispersoids were considered for further recrystallization simulations, since according to Yang [Yang 1999] only those were frequently observed in an AA3103, whereas Al_{12}Mn was observed only occasionally. This agrees very well with the ClaNG predictions, which forecast a very low amount of Al_{12}Mn particles.

The huge difference between this material (series RZ) and the industrial material (series R) used for the case study in Chap. 9, is the shift in the onset of recrystallization to longer times and consequently the more pronounced precipitation. Compared to the industrial processed material where the precipitation sets in after recrystallization is completed, in the present study concurrent precipitation prevails as indicated by the much lower Avrami exponents observed from experimental recrystallization kinetics.

It was further considered that the deformation zones surrounding particles provide locally a higher dislocation density, which further increases with increasing deformation (see Chap. 5).

In the previous work of Mukhopadhyay [Mukhopadhyay 2005] the influence of microchemistry on recrystallization kinetics was shown exemplarily solely considering changes in the solute content.

7.3.4 Growth and recovery parameters

Beside, the above presented inputs; CORE has further parameters with respect to growth and recovery, which require adjustment prior to the simulation. However, these parameters were kept constant for all simulations. In detail, these are the activation energies for growth (i.e. grain boundary migration), which are taken as an average from literature data [Gottstein 1999, Molodov 1999, Winning 2005], as well as activation energies for the recovery processes cross slip and climb. In the current model recovery is considered via the incremental coupling with the improved work-hardening model 3IVM+ (Chap. 3). Basically the 3IVM+ parameter set was kept as obtained from the flow curve fit with 3IVM+ (Chap. 9). The activation energy for climb corresponds to the activation energy of self diffusion, i.e. the sum of the energy for formation and migration of vacancies. The activation energy for cross slip is comparatively high, since it is not

decreased by external stresses, which means that cross slip plays a minor role in the recovery considered here.

Tab. 7.2: Kinetic Parameters in CORe (HAGB = high angle grain boundaries, LAGB = low angle grain boundaries)

Parameter	Value
Activation Energies Growth	$Q_{\max} 1.0\text{eV} / Q_{\text{HAGB}} 1.1\text{eV} / Q_{\text{LAGB}} 1.6\text{eV}$
Recovery	$Q_{\text{climb}} 1.54\text{eV} / Q_{\text{cross}} 1.73\text{eV}$

Based on the local resolved recovery rates, an orientation-dependent incubation time according to the convergence criterion introduced in Sec. 6.3 was considered. This leads to the modeling of a nucleation rate rather than site-saturated nucleation.

7.4 Results of the Recrystallization Predictions

In the following the predicted microstructure, kinetics and textures considering simultaneous recovery and precipitation on recrystallization are presented and evaluated.

7.4.1 Simulated grain size and grain size distributions

The microstructures obtained from the recrystallization simulations are displayed in Fig. 7.12.

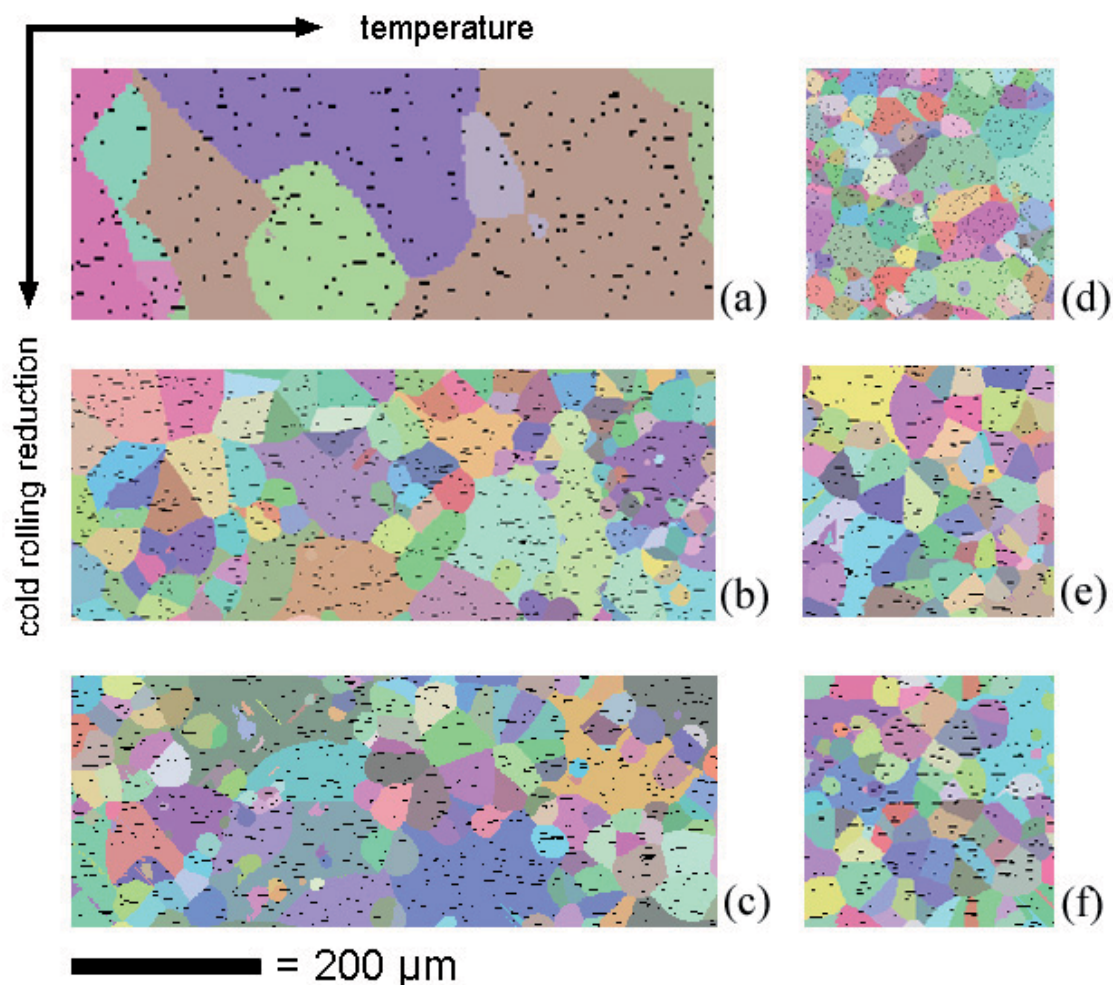


Fig. 7.12: Simulated microstructures in sheet normal direction for (a) - (c) cold rolling reductions 50 %, 70 %, 85 % at $T = 350\text{ °C}$, (d) - (f) cold rolling reductions 50 %, 70 %, 85 % at $T = 400\text{ °C}$, black = particles. Only selected microstructure sections are shown for comparison with experimental results.

A comparison of the predicted microstructures with those results obtained from EBSD measurements shows good agreement (Figs. 7.4 and 7.12). The predictions captured the tendencies observed from experiments. With increasing rolling reduction a finer grain size was observed from the simulations in the considered temperature range, as would be expected. This is due to the increase in grain boundary area with increasing cold rolling reduction. An increase from 50 % to 85 % cold rolling deformation lead to an increase in the grain boundary area by a factor of three, which directly influenced the absolute nucleus number obtained from GB- and TB-nucleation. The general influence of cold rolling reduction on the final grain size was already demonstrated in Chap. 3. In the present context further local deformation zones in the particle vicinity were considered. The increase of the dislocation density with increasing deformation is particularly pronounced in the deformation zones (Chap. 5). Hence, the modeled nucleation density is further increased with increasing deformation by particle-stimulated nucleation in the particle vicinity. Thus the grain size became increasingly smaller with increasing deformation.

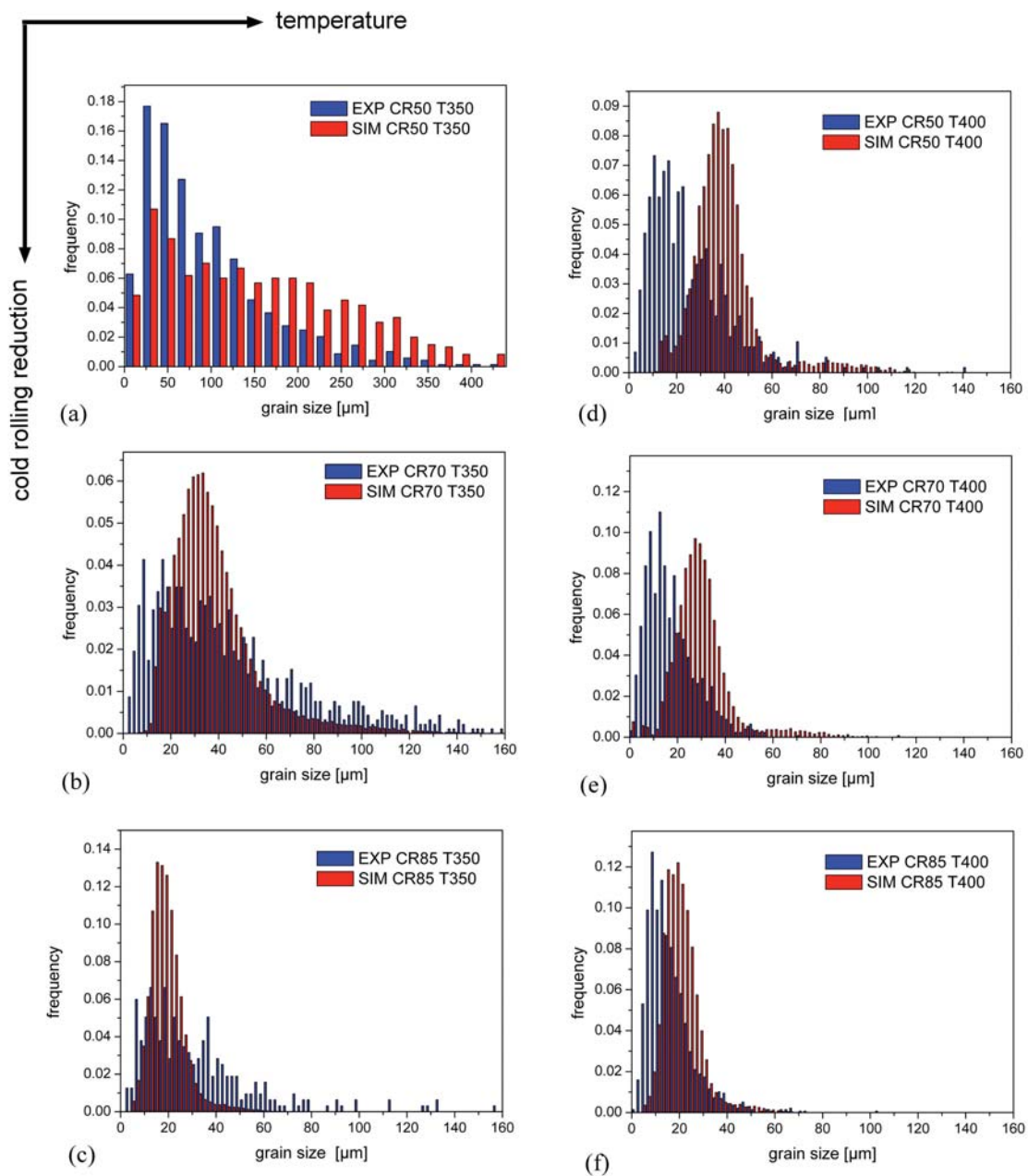


Fig. 7.13: Distribution of the simulated grain sizes in comparison to the experimental measurements. (a) - (c) cold rolling reductions 50%, 70%, 85% at $T=350^{\circ}\text{C}$, (d) - (f) cold rolling reductions 50%, 70%, 85% at $T=400^{\circ}\text{C}$.

The predicted grain sizes are also presented as grain size distributions in Fig. 7.13. For low rolling reductions a significantly larger grain size was observed with a much larger scatter width as observed at higher rolling reductions. This is in agreement to experiments (Fig. 7.13 a, d) and can be explained by a combination of two facts. First, a low population of nuclei results at all nucleation sites, distributed throughout the microstructure. With exception of shear band nucleation, which is assumed to appear randomly in the corresponding grain, nucleation basically starts from preferred locations such as grain boundaries, transition bands or particles. These last three nucleation mechanisms depend directly on the interface area, which is smaller at low rolling reductions than at higher rolling reductions. Hence, in case of a low rolling reduction a low nucleus density was observed. Second, with decreasing nucleus density a larger grain boundaries' free path (before impingement) was observed.

Beside the rolling reduction also the temperature causes significant changes in the grain sizes in the present study. As outlined in Sec. 7.2, 7.3 a stronger Zener drag was predicted from the ClaNG simulations particularly for the low temperature. Thus, grain boundary motion is strongly impeded and thus only orientations with a good growth relationship grow. The microstructures in Fig. 7.12a-c and the grain size distributions in Fig. 7.13a-c reflect this behavior. For lower temperatures a larger grain size with a larger scatter width was obtained in agreement with experiments (Figs. 7.4, 7.5, 7.13). For higher temperatures a more narrow grain size distribution (Fig. 7.13d-f) is obtained with a scatter width of the grain size distributions comparable to experiments. The smallest grain sizes predicted from the simulations are slightly under estimated.

For a better comparison of the average grain sizes with their corresponding scatter, please refer to Fig. 7.5 (error bars indicate scatter width). The grain size distributions for the lower temperature match the experimental distribution quite well, even if the grain sizes obtained from experiments show a slightly larger scatter. Such deviations can be also attributed to the different methods for grain size determination introduced in Sec. 7.2. Especially, at the low temperature large deviations between these techniques are expected. With the chosen modeling setup the basic tendencies on temperature and cold rolling reduction were reproduced and an overall good agreement with experiments was found.

7.4.2 Simulated recrystallization textures

Prior to the recrystallization simulation the nucleation spectra for the different rolling reductions and temperatures were modeled based on the sub-structural quantities analyzed in Sec. 7.3. The final recrystallization textures based on these nucleus textures are shown in Fig. 7.14 in comparison to the experimental textures. After a cold rolling reduction of 50 % and an annealing treatment at $T = 350\text{ }^{\circ}\text{C}$ the material is very coarse grained (see Figs. 7.4, 7.12), which is also obvious from the non-smooth iso-intensity lines in the experimental and simulated texture plots (Fig. 7.14). At higher rolling reductions the ND rotated Cube texture component is not as pronounced as obtained from experiments. This deviation originates in the predictions made with the transition band nucleation model. It is observed from experiments that with increasing rolling reductions a larger scatter from the original Cube orientation resulted, which is not considered by the used nucleation model for transition band nucleation (GIA-SplitUp). The implementation of a strain-dependence of the developing misorientations in the aforementioned sub-model seems to be of importance in the present case. Orientations close to the P- respectively inverse Goss orientation can be found in both experimental and simulated textures. The predicted textures show good qualitative agreement with the experiments.

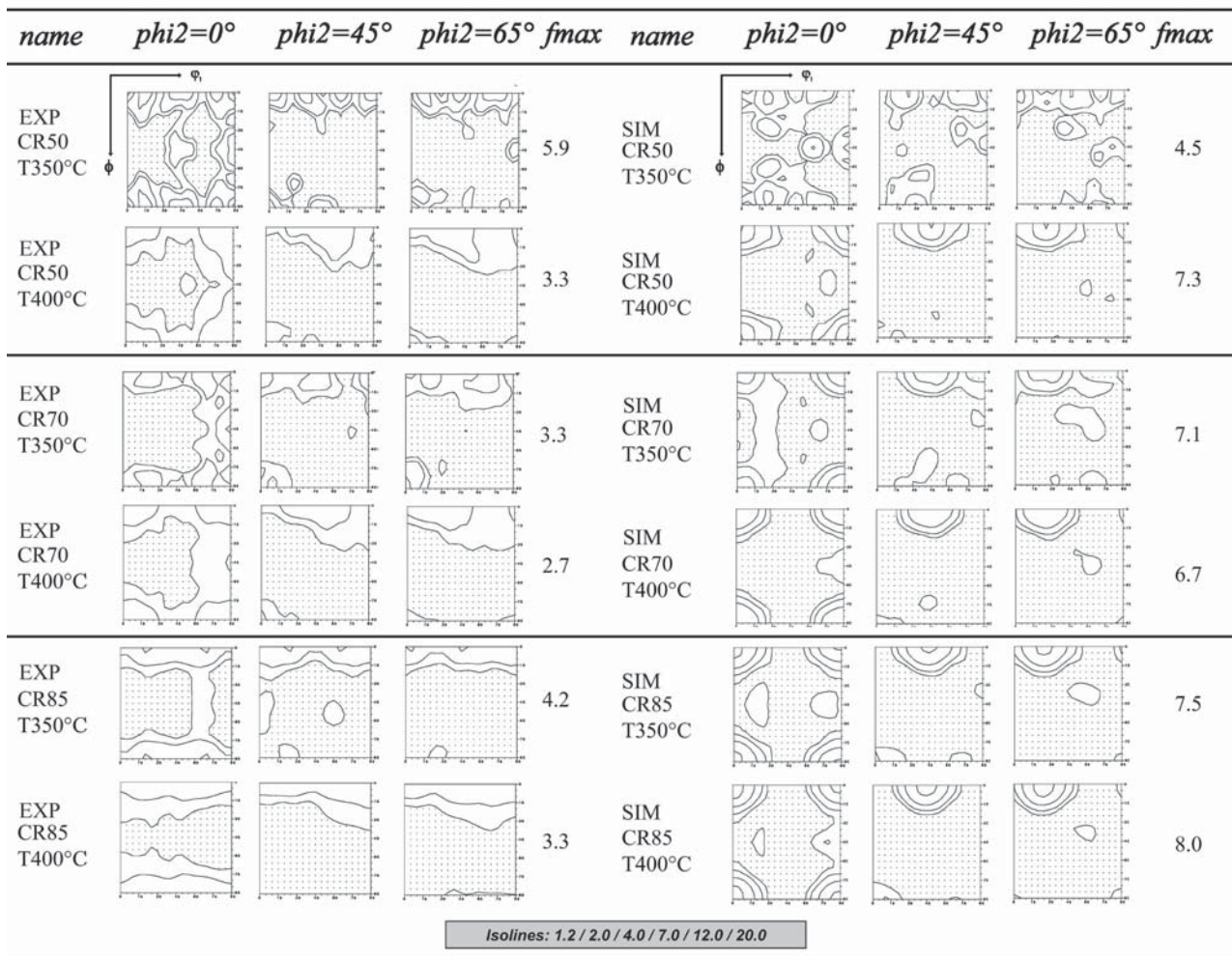


Fig. 7.14: Experimental and simulated recrystallization textures. Displayed are selected sections through Euler space. The experimental textures were measured on fully recrystallized samples.

7.4.3 Simulated recrystallization kinetics

For the simulation of the recrystallization behavior only the incubation time parameter (recovery) was adjusted for different temperatures (Tab. 7.2), all other parameters were kept constant. Fig. 7.15 demonstrates the differences arising in the simulated recrystallization behavior as based on the different input data sets (different cold rolling reduction and individual microchemistry evolution as modeled with ClaNG, different temperatures). Fig. 7.15 summarizes the results obtained for the recrystallization kinetics.

It was found that the recrystallization behavior at high temperatures could be predicted satisfyingly with the used modeling setup. However, a satisfactory prediction of the recrystallization kinetics at low temperatures was not possible with the present modeling setup (combination GIA, CORE and ClaNG). The very low Avrami exponents ≤ 1 as determined from experiments indeed suggest strong recovery processes, Zener drag or a combination of both. As outlined before, all those effects were incorporated in the model. If the Zener drag is considered as suggested in Eq. (3.11) using the predictions from ClaNG the recrystallization ceases very soon after reaching very low recrystallized volume fractions (continuous red lines in Fig. 7.15). These recrystallization kinetics are barely visible in Fig. 7.15a-c. However, it should be highlighted that they provide the desired lower slopes as indicated from experiments. In order to obtain 100 % recrystallization the Zener drag was reduced step by step to 25 % - 40 % of the original value (dotted red lines in Fig. 7.15). This, however, leads to very steep recrystallization kinetics, which are in contradiction to the experimental recrystallization kinetics. The recrystallized volume fractions obtained from

experimental data (hardness and texture measurements) are indicated in Fig. 7.15a-c by open, respectively filled squares.

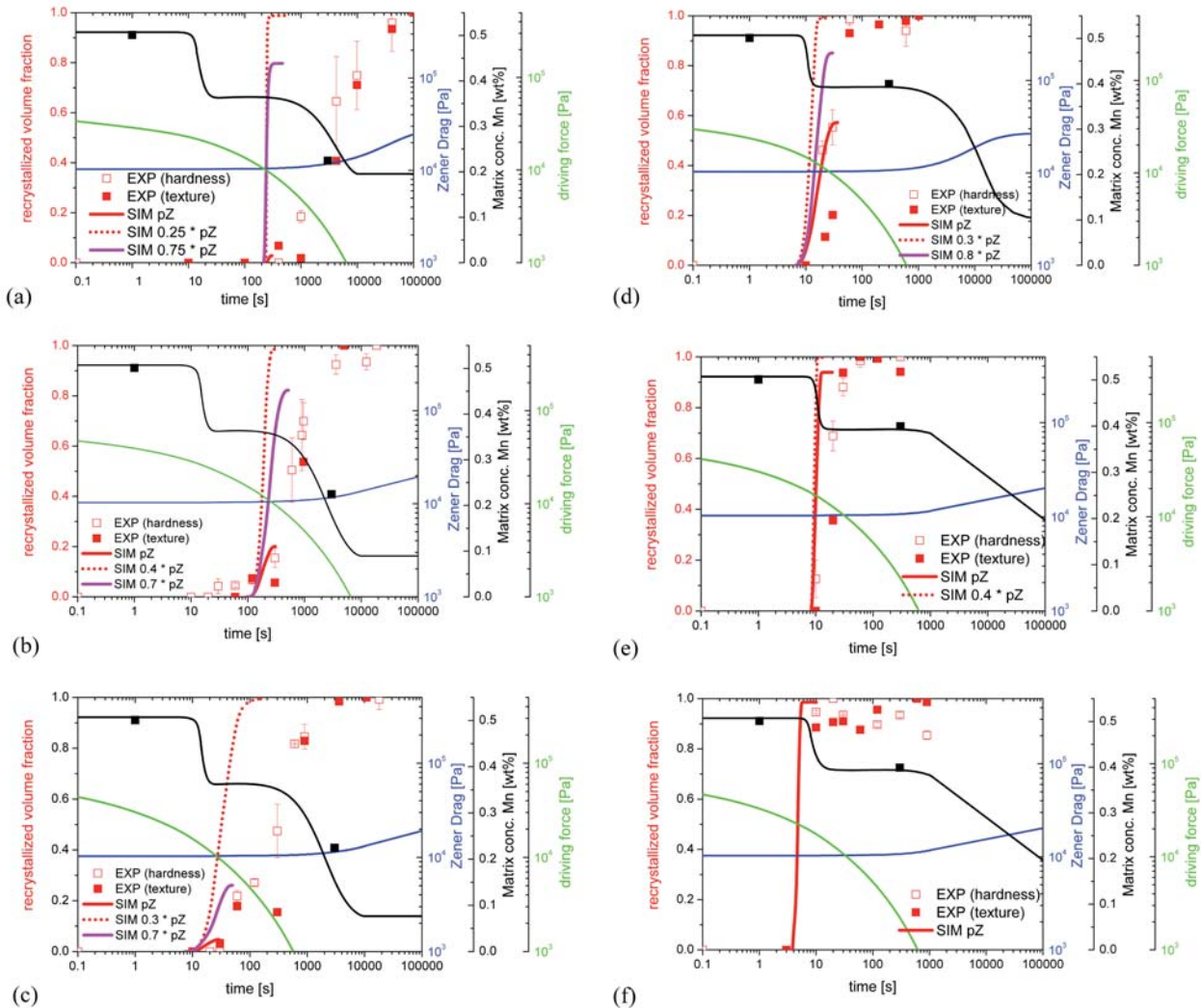


Fig. 7.15: Simulated recrystallization kinetics for AA3103 for (a) - (c) cold rolling reductions 50%, 70%, 85% at $T = 350^{\circ}\text{C}$, (d) - (f) cold rolling reductions 50%, 70%, 85% at $T = 400^{\circ}\text{C}$. The change in solute content of manganese and the evolution of Zener drag over time are presented as well. The driving force averaged over all 4000 grains is indicated as comparison for the Zener drag.

In order to clarify the individual influences of recovery and Zener drag and their interrelationship on recrystallization, the different approaches are discussed independently in the following section. Later on an approach is presented which allows the combined consideration of recovery and precipitation.

7.5 Discussion of Recrystallization Kinetics

Important influences on the recrystallization kinetics are the recovery process, which leads to a reduction of the driving force and the precipitation, which causes the evolution of dispersoids. These dispersoids can hinder or, even suppress grain boundary migration. The crucial point in modeling the recrystallization kinetics is the relative speed of the recovery and precipitation kinetics. As observed from Fig. 7.15, simultaneously modeled precipitation (ClANG) and recovery (3IVM+) always lead to a disruption of the recrystallization kinetics in the present case, since the effective driving force $p_{\text{eff}} = p(t) - p_z$ is reduced almost immediately to zero.

7.5.1 The influence of recovery

The main influence of recovery on recrystallization is the reduction of the driving force for recrystallization growth. As a consequence, a lower slope of the recrystallization kinetics is observed. Recovery was considered by incrementally coupling the work-hardening model 3IVM+ to the recrystallization model CORE (Chap. 3). A basic validation of the influences of recovery on recrystallization was given in Chap. 6. In Chap. 6 the results of the coupling CORE-3IVM+ were further compared to another recovery approach, which usually describes excellent agreement with experiments. It was found that the exclusive consideration of recovery as concurrent process to recrystallization can lead to Avrami exponents down to values of 1.0 according to the experimental ones found in the present experiments (Sec. 7.2). Hence, the observed experimental recrystallization behavior can be simulated by solely consideration of recovery. The only disagreement occurs in the prediction of experimental recrystallization textures and microstructures, since experiments clearly indicate a fully recrystallized material. Hence, the only consideration of recovery in the present study is insufficient, so that influences of precipitation require further consideration.

7.5.2 Accuracy of ClaNG predictions

The general influence of Zener and solute drag and various temporal changes of both were already discussed in detail in Chap. 4. It was shown that the temporal evolution of those quantities can be quite complex, so that the precipitation model ClaNG was applied in the current study to guarantee a consistent treatment of those effects. Due to the importance of microchemistry changes for the recrystallization behavior a short excursus on the accuracy of the ClaNG predictions is required. Input for the ClaNG model is the temporal evolution of dislocation densities during the annealing treatment. Hence, in the following various dislocation density evolutions as interpreted from hardness measurements were used as input (trial 1-3, Fig. 7.16a). Besides the dislocation density evolution over time, all other parameters within the ClaNG model were kept constant (Fig. 7.16a). Figs. 7.16b, c demonstrate the predictions from the precipitation model ClaNG.

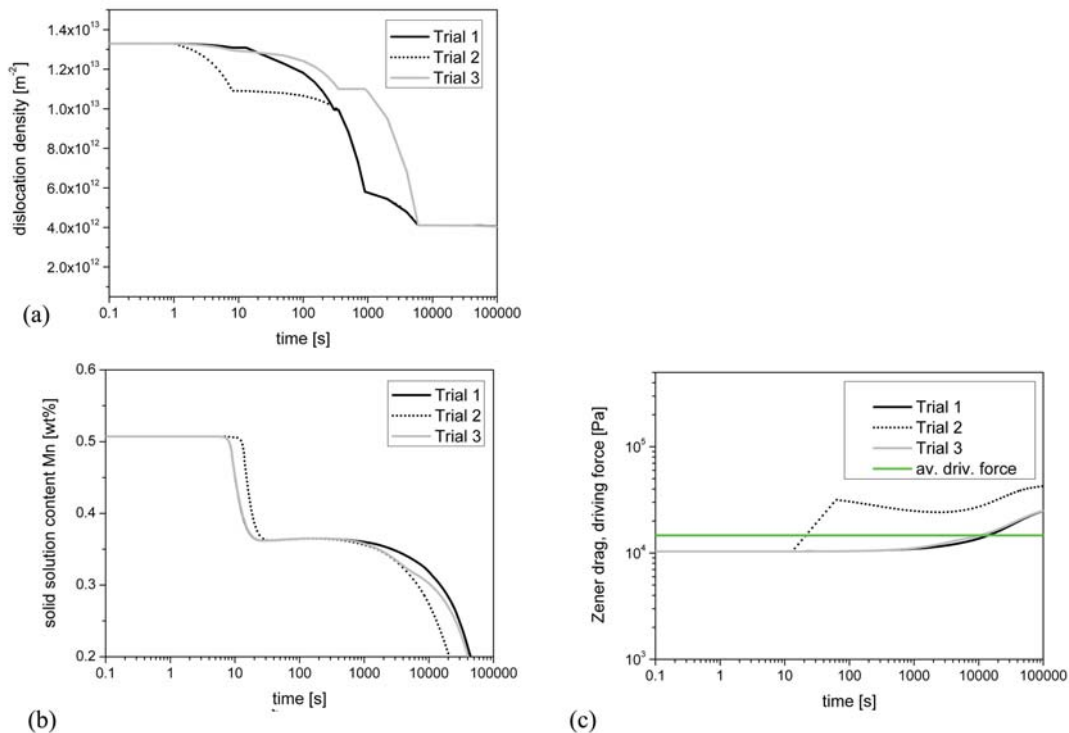


Fig. 7.16: Sensitivity of the ClaNG model to variations in the (a) input data. The response of the ClaNG model is shown in (b) for the solute content of manganese and (c) for the Zener drag. The average driving force is displayed without influence of recovery.

Fig. 7.16b indicates the predicted evolution of the solid solution content of manganese. The modeled curves are all within the range of error of experimental data. So in principle they could all be used for recrystallization simulations with the CORE model. A consideration of Fig. 7.16c demonstrates however that this might not be true for the Zener drag. It can be seen that trial 2 would not lead to any recrystallization, since the Zener drag is much higher than the driving force (green line, Fig. 7.16c) even before recrystallization is initiated. Comparing the initially similar input dislocation density evolutions of trial 1 and 2, the predicted totally different Zener drags are rather surprising. By contrast, the much stronger difference in the chosen input data between trial 1 and 3 is hardly visible in the predicted Zener drag output (Fig. 7.16c). A comparison with Fig. 7.15 shows that the obtained difference in back-driving forces of a factor 3 between the various trials can cause recrystallized volume fractions between 0 % and 100 %, which is a serious effect. This means, that the ClaNG simulations if used for the recrystallization simulations are very sensitive to the user input and thus have to be treated with great care.

The observed sensitivity of ClaNG dependent on the initial inputs is reasoned below. In the presented case study, ClaNG is used to model a discrete nucleation event, rather than coarsening or dissolution of particles. Hence, during the heat treatment suddenly new phases are nucleated and grow. Since precipitation nucleation occurs preferentially heterogeneous at dislocation tangles, the nucleation stage is particularly dependent on the dislocation density evolution. This information is difficult to access from experiments. As an approximate measure of the dislocation density evolution, the relative hardness change as measured from experiments is used. However, the true dislocation density evolution within the remaining unrecrystallized microstructure is not accessible with the available methods. This might lead to a behavior as indicated by the peak in the Zener drag evolution (Fig. 7.16c). Another reason for the sensitivity of the model, connected to the dislocation density evolution and the precipitation nucleation, is the description of nucleation in the ClaNG model itself, which is not dependent on the substructure, and might thus lead to an overestimation of nucleation, so that very stronger Zener drags are predicted particularly during precipitation nucleation. This might explain why the Zener drag modeled with ClaNG is initially too high and thus lead to the disruption of the recrystallization under simultaneous consideration of recovery. To prevent that, the Zener drag was gradually decreased by a certain factor in the simulations in Fig. 7.15 to allow a completion of the recrystallization process. However, this did not lead to the intended lower slopes in the recrystallization kinetics. To demonstrate that indeed lower slopes can be reached by solely consideration of precipitation, particle coarsening is discussed in the following.

7.5.3 Particle coarsening

For this purpose, the complicated precipitation behavior predicted by ClaNG was replaced by the consideration of pure coarsening to reduce the variety of parameters. Various time-dependent Zener drags and their effects on the recrystallization kinetics were already evaluated in Chap. 4 (Figs. 4.35-4.39). In the following, it is assumed that the Zener drag was high at the beginning of the simulation and was reduced with time due to the coarsening of particles. The driving force was kept constant throughout the simulations within each grain (no recovery). Still a variation of the driving force from grain to grain as obtained due to the orientation-dependent stored energies from GIA was allowed (grey shaded area in Fig. 7.17a). Particle coarsening was assumed according to

$$p_z \propto \frac{1}{r} = \frac{1}{\sqrt[3]{r_0^3 + A \cdot t}} \quad (7.2)$$

where r_0 is the initial particle radius at time $t=0$, and A is a kinetic constant. The resulting Zener drag was calculated according to Eq. (3.11) and is indicated for three different cases in Fig. 7.17a (colored lines).

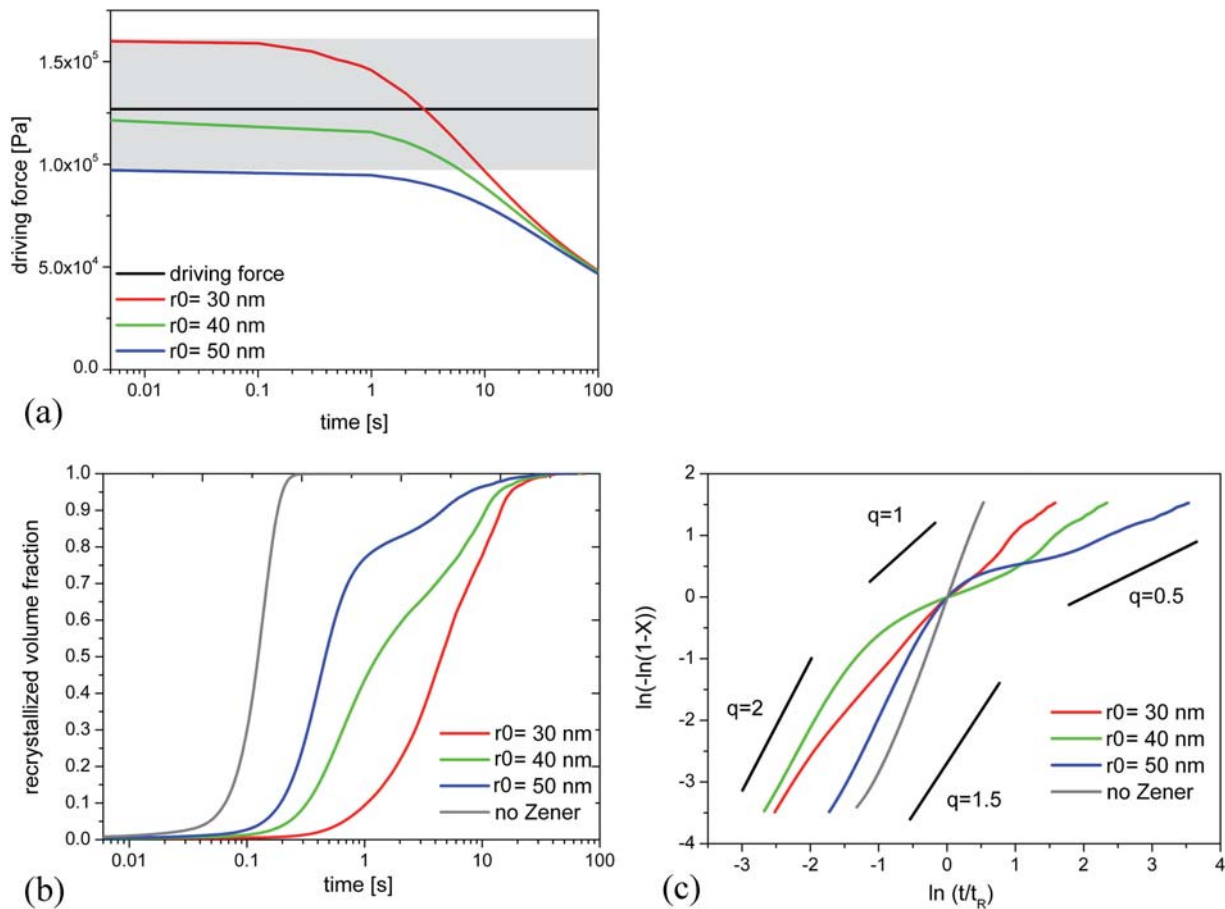


Fig. 7.17: (a) Temporal evolution of driving and back-driving forces. (b) Recrystallization kinetics under consideration of Zener drag. (c) Avrami plots for recrystallization influenced by Zener drag. (q =Avrami exponent, $A=10^{-23}$ m³/s). The grey shaded area indicates the scatter of the stored dislocation densities from grain to grain. The black line indicates the in average stored dislocation density.

In case of low Zener drag (blue curve, Fig. 7.17a), the driving force in all grains is sufficient to guarantee growth in all microstructure grains. The recrystallization kinetics was basically shifted on the logarithmic time scale. If the Zener drag is in the order of the driving force (which has a certain scatter dependent on the orientation, grey shaded area in Fig. 7.17a), in some grains a very low or even zero driving force is obtained. That means recrystallization proceeded only in those grains where the driving force was sufficient. Finally only those grains with the lower driving forces remained, they were consumed at a lower speed. An interruption of the recrystallization process was not observed since the effective driving force increased with time due to the assumed particle coarsening. Even, if the driving force was temporarily zero in a few grains, they could continue recrystallizing after the particles had coarsened sufficiently.

Fig. 7.17b demonstrates the effect on the recrystallization kinetics. A flattening of the curves was observed towards the end, which indicated the very low effective driving force in the remaining grains. In these cases, the observed Avrami exponents (found by fitting to the JMAK equation) could also reach values in the order of one, as suggested by the experiments (Sec. 7.2).

Hence, it cannot be definitely decided whether the effect observed from experimental Avrami exponents in the order of one can be attributed to recovery or Zener drag. It is more likely that both effects may contribute at the same time as supported by experiments.

7.5.4 Concurrent progress of precipitation coarsening and recovery

In the following the difficulty of modeling the concurrent effect of recovery and Zener drag on recrystallization kinetics is discussed. Fig. 7.18a shows the driving force as influenced by recovery (black) and the corresponding curves for Zener drag evolution according to Eq. (7.2) using different parameter sets. The used parameters are indicated in the graphs (Fig. 7.18a, b). No matter which parameter set is chosen for the evolution of the Zener drag (colored curves), it was not possible to obtain very low slopes of the recrystallization kinetics and at the same time a 100% recrystallized material (Fig. 7.18b). As soon as a very low effective driving force was obtained (causing a low slope) it decreased very rapidly to zero (because precipitation and recovery kinetics already intersected). However, in this particular case it was not possible to obtain very low Avrami exponents.

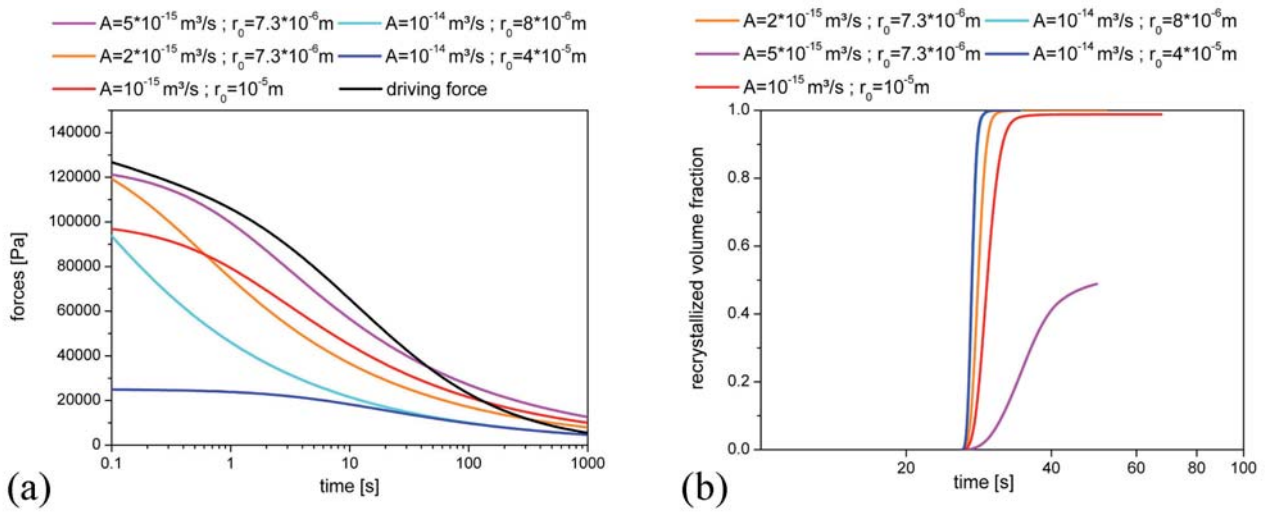


Fig. 7.18: (a) Temporal evolution of driving and back-driving forces. (b) Recrystallization Kinetics under consideration of recovery and Zener drag. In case recovery and precipitation kinetics intersect before recrystallization is completed, only partial recrystallization is obtained.

The evolution of Zener drag and recovery and their mutual interaction is very difficult to control (recovery and precipitation kinetics should not intersect) and is very sensitive with respect to the recrystallization kinetics. The desired results were not obtained even with adjusted precipitation (coarsening) and recovery kinetics to obtain kinetics which resemble each other. In order to obtain low Avrami exponents, but fully recrystallized material, the effective driving force $p_{eff} = p - p_Z$ needs to be small during a longer time interval, but should never reach zero. Hence, the convergence of the precipitation and recovery kinetics is absolutely indispensable for recrystallization kinetics with a low slope.

7.5.5 Introducing a new kinetics

Experimental data suggests the simultaneous occurrence of recovery and precipitation, as already described in Sec. 7.2. Both effects were considered in the above presented recrystallization simulations. Fig. 7.15 indicates that a simultaneous description of recovery and precipitation considering complete recrystallization was not satisfactory. Fig. 7.19a clarifies this situation. The recrystallization behavior under solely consideration of Zener drag was already taken into account in Chap. 4. In Fig. 7.19a the driving force was additionally reduced due to recovery. As soon as the driving force amounts to the Zener drag ($p = p_Z$), the effective driving force for recrystallization $p_{eff} = p(t) - p_Z$ becomes zero. Fig. 7.19b indicates the velocity as a function of the effective driving force p_{eff} . If p equals to p_Z , the simulation is disrupted (velocity = 0) and a partial recrystallized state is predicted (Fig. 7.18b, Fig. 7.19b). This, however, does not agree with the experimental observations, which describe a fully recrystallized material (Figs. 7.4, 7.14). A possible explanation

for this contradiction is the model description itself. In the following, in particular the description of Zener drag in the recrystallization model is questioned.

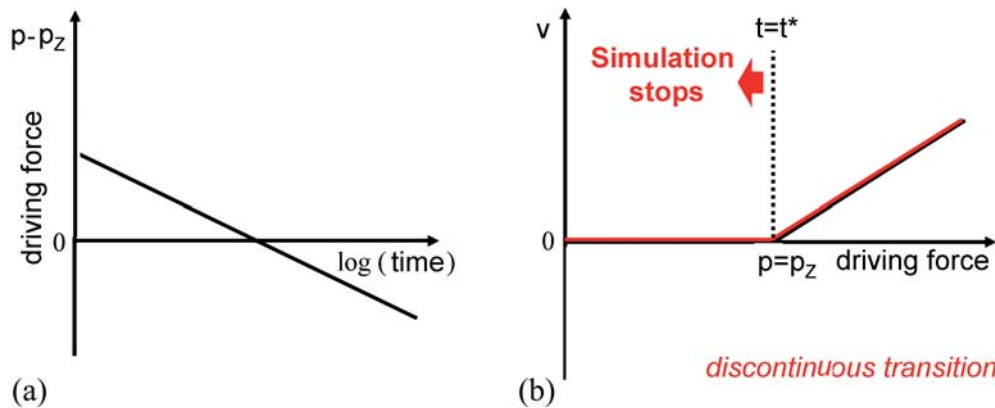


Fig. 7.19: Influence of Zener drag on the recrystallization behavior according to the classical approach (Eq.3.10) ; (a) evolution of driving force p and Zener drag p_z , (b) resulting velocity under consideration of a constant Zener drag.

Zener drag was assumed as a statistical quantity (random distribution of spherical particles) applied to all grains in the same fashion. Nevertheless, a locally resolved Zener drag can have a pronounced effect as described in literature. In that case the effective driving force p_{eff} is not reduced to zero, as shown by the following examples:

(1) Anselmino [Anselmino 2007] observed so-called “Jerky Motion” of grain boundaries during recrystallization by means of in-situ SEM experiments. Here, the particle distribution and dispersoid size were pointed out as the most important influence factors. If the boundary is locally hindered by particles, grain boundary motion is inhibited (Fig. 7.20a,b). After a certain time particles have coarsened or dissolved, and the boundary moves on (Fig. 7.20a,b). Thus, a kind of *Stop and Go* motion (“Jerky Motion”) is obtained, which was locally observed in the microstructure. This can be in principle described by Eq.(7.3).

$$\frac{1}{v} = \frac{1}{v_{free}} + \frac{1}{v_{particle}} \quad (7.3)$$

The velocity of the boundary is depending on the velocity of the freely migrating boundary with the velocity v_{free} and on the velocity of the particles $v_{particle}$. Thus, the grain boundary motion would be locally quite heterogeneous, proceeding with fast speed and then again with low speed, if the boundary is stopped at obstacles.

(2) Another consideration of theoretical nature is the assumption of mobile particles [Gottstein 1993]. It is assumed that a particle size distribution always contains also smallest and hence mobile particles, which are dragged along with the grain boundaries (Fig. 7.20c). This would lead to a continuous description of the velocity as a function of the driving force (Fig. 2.3b), in contrast to the often described discontinuous behavior (Fig. 2.3a) (discontinuous transition from the loaded to the free boundary). Hence, the boundary velocity is locally very small, but never reaches zero.

(3) Furthermore, an orientation dependence of Zener drag was identified by Humphreys et al. [Humphreys 1996]. An orientation dependence would lead to locally very different values of Zener drag, so that in some grains recrystallization continues, where in other grains it is temporarily

inhibited. If in the meantime, the dispersoids dissolve or coarsen, afterwards recrystallization can continue in the not yet recrystallized regions as well.

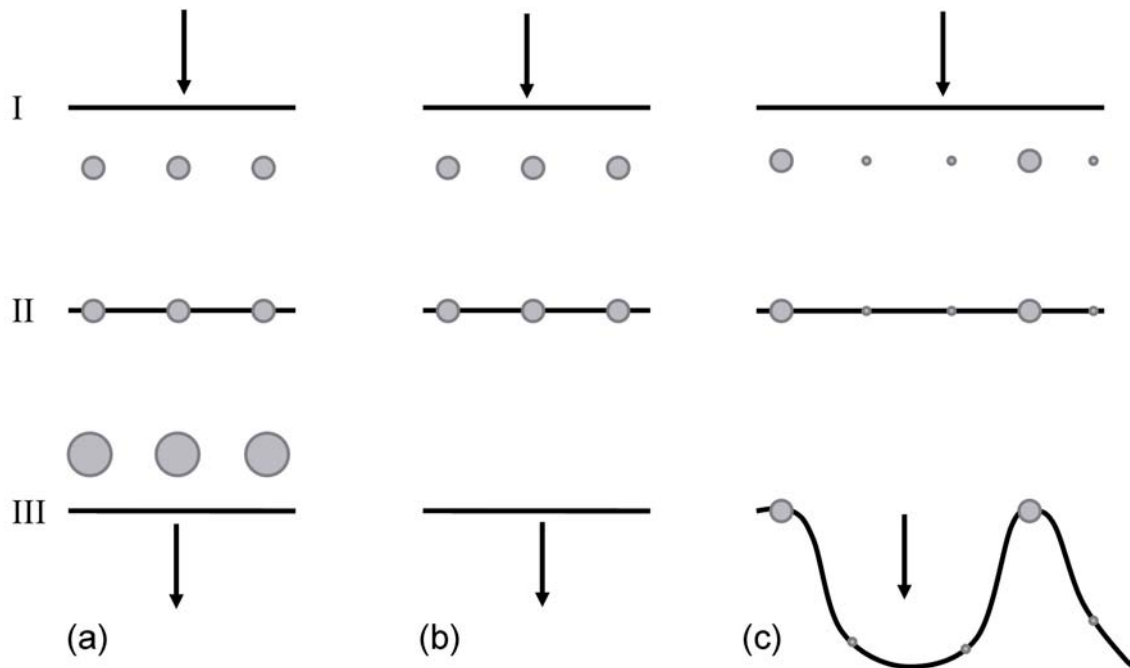


Fig. 7.20: Scheme indicating the different stages of boundary-particle interaction. (I) Boundary is migrating freely, (II) boundary is interacting (pinning), (III) boundary overcomes the particles. The overcoming of particles is obtained in (a) by particle coarsening, (b) by particle dissolving, (c) by dragging along smallest particles. Hence, the boundary is locally moving freely.

Such local phenomena described above, respectively details of the particle distribution cannot be captured with the hitherto existing description for Zener drag in the recrystallization model. Nevertheless, to describe the combined effect of recovery and precipitation on recrystallization, a new kinetics was introduced describing the interplay of recovery and Zener drag. Hence, different grain boundary velocities originating from the phenomena (1)-(3) can be modeled. Such an approach would describe an effective driving force which in case $p = p_Z$ approaches zero very slowly, so that if the driving force is smaller than the Zener drag $p < p_Z$ still a very small, but positive finite effective driving force is obtained. Fig. 7.21 visualizes such an approach (red line).

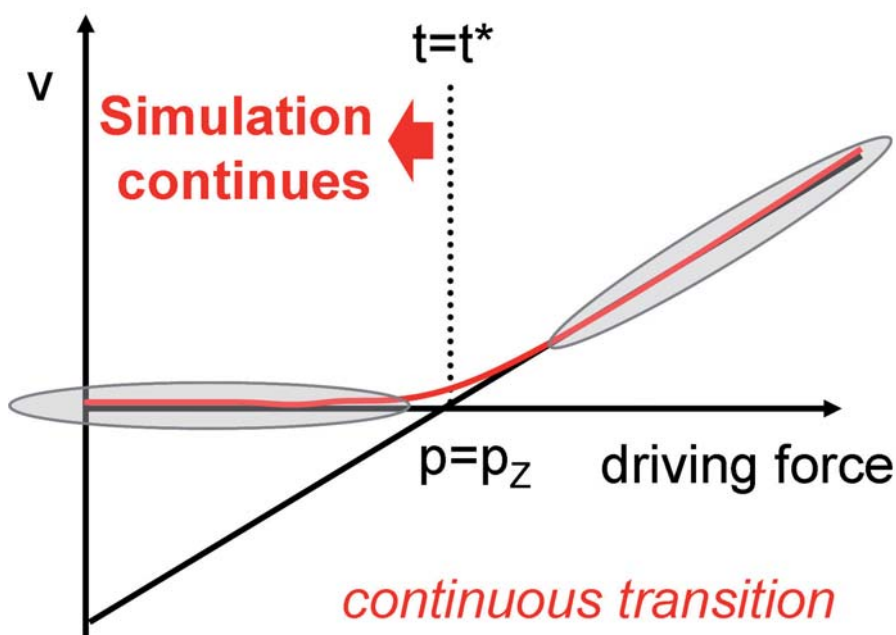


Fig. 7.21: Influence of Zener drag on the recrystallization behavior according to approach in Eq. (7.4).

A corresponding approach to describe such a behavior (red line, Fig. 7.21) can be written as

$$p_{\text{new}} = p_z \left[\sqrt{0.257 \cdot \left(\frac{p}{p_z} - 1 \right)^2 + 1.308 \cdot \left(\frac{a}{p_z} \right)^2} + 0.518 \cdot \left(\frac{p}{p_z} - 1 \right) \right] \quad (7.4)$$

where p is the driving force, p_z the back-driving force due to Zener drag and a a parameter describing the rapidity of the change between the two regimes (grey encircled areas in Fig. 7.21). The parameter a contains information, such as on the width of the particle distribution. It can be seen that the velocity approaches the regime of the free boundary in the grey encircled area to the right, as well as of a loaded boundary in the grey encircled area to the left. For the loaded boundary still a finite velocity is obtained, which becomes very small in case of low driving forces, but always remains positive.

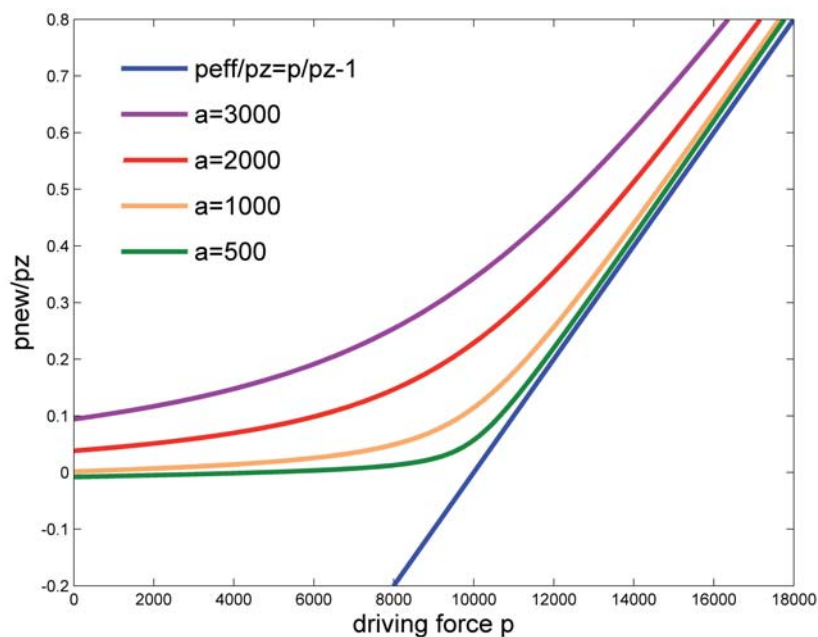


Fig. 7.22: Zener drag according to the modified approach for Zener drag dependent on the a -parameter.

Fig. 7.22 indicates the velocity in dependence of the driving force for different parameters a . With this new approach considering parameters a smaller than 1000 the recrystallization kinetics in Fig. 7.15 were recalculated and the results are shown in Fig. 7.23. It is further pointed out that the presented approach was found by trial and error and that its physical justification was not yet proven. Nevertheless, it accounts for the expected behavior.

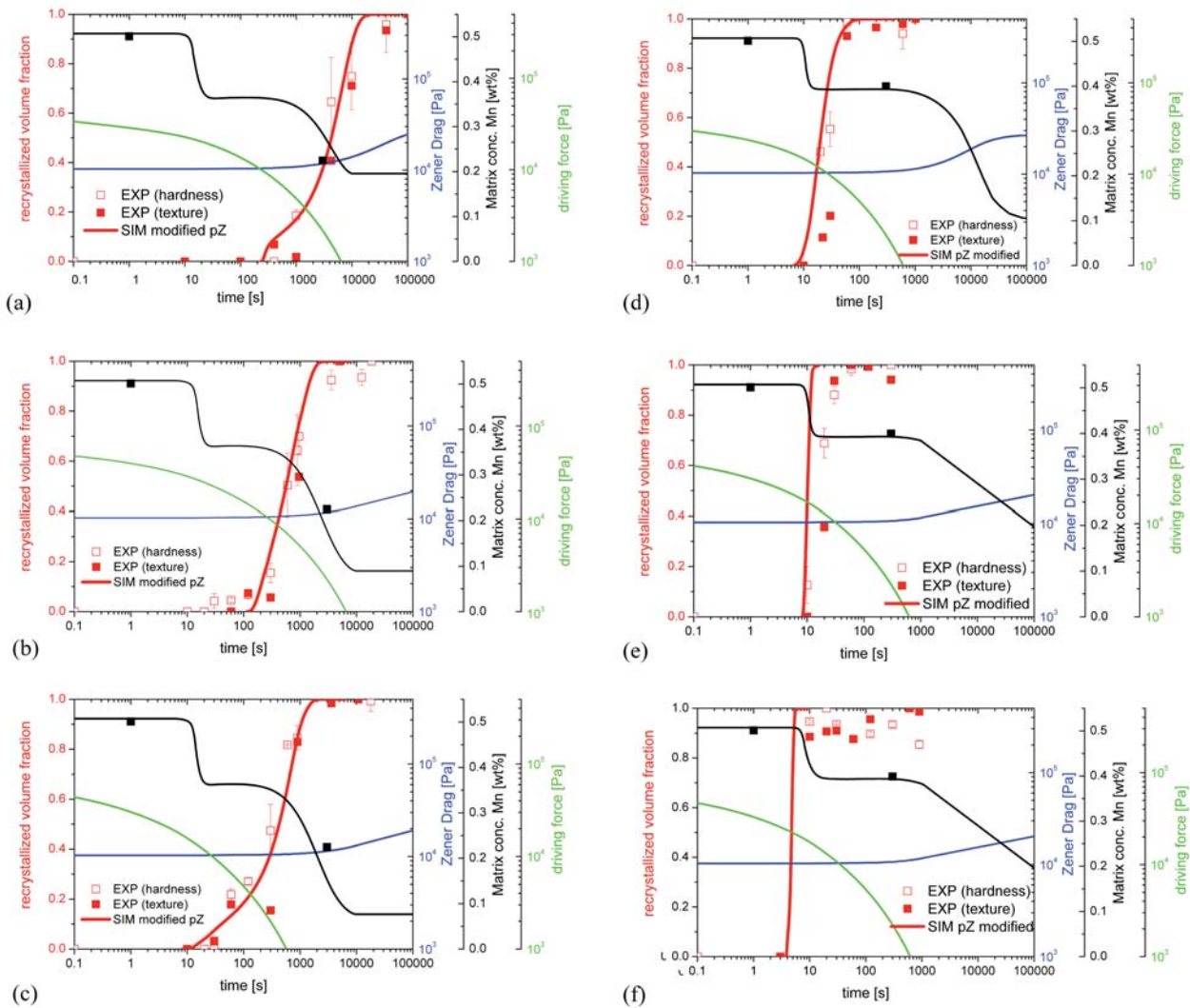


Fig. 7.23: Simulated recrystallization kinetics for AA3103 using the new kinetics approach for (a) - (c) cold rolling reductions 50%, 70%, 85% at $T=350^{\circ}\text{C}$, (d) - (f) cold rolling reductions 50%, 70%, 85% at $T=400^{\circ}\text{C}$. The change in solute content of manganese and the evolution of Zener drag over time are presented as well. The driving force averaged over all 4000 grains is indicated as comparison for the Zener drag.

An overall excellent description of the recrystallization behavior was obtained. Further, with this approach the desired lower Avrami exponents in the order of one were obtained ($q=0.98$ for CR50, $q=1.45$ for CR70, $q=1$ for CR85), as already indicated by the much lower slopes of the recrystallization kinetics particularly at low temperatures.

7.6 Conclusions

In this chapter the influence of concurrent precipitation and recovery on recrystallization was studied during iso-thermal heat treatments. Recovery was in this case described by 3IVM+ [Mohles 2008] and precipitation by ClaNG [Schneider 2006]. Various cold rolling reductions and temperatures were considered and their effect on microstructure, kinetics and texture evolution modeled using a single input data set.

The microstructure and texture predictions yielded good agreement with experimental results (particularly for low rolling reduction and low temperature). To further improve the texture predictions with respect to the rotated Cube components, it is concluded that the transition band nucleation model requires further advances, such as the introduction of a dependency on strain.

The predictions of the recrystallization kinetics using CORE - ClaNG yielded unsatisfactory results. It was shown that the simultaneous consideration of recovery and precipitation, as suggested by experiments, was not possible within the existing model and lead to a disruption of recrystallization. An independent consideration of one of the two effects (any), completely suppressing the other one, yielded good agreement with experimental recrystallization kinetics. The price to pay when only recovery is considered is a wrong prediction of recrystallization textures. The reasons of failure are summarized as follows:

- The chosen recovery model predicts a zero driving force after finite annealing times. That is not realistic, since the geometrically necessary dislocations should remain at least.
- The predictions from ClaNG are highly sensitive to variations in the inputs (e.g. dislocation density for precipitation nucleation).
- An interaction of the recovery model (3IVM+) and the precipitation model is not considered, but it cannot be neglected in the present study.
- The simplification that Zener drag is constant within the whole microstructure cannot hold.

Nevertheless, a simultaneous consideration of recovery and precipitation without a disruption of recrystallization was enforced with a modified description of the effective driving force. This new approach implies a more complicated interaction of particle and moving grain boundary (Sec. 7.5.5) than suggested by the common approach for Zener drag in Eq. (3.11). With this modified approach, which was found by trial and error, an excellent agreement with experimental recrystallization kinetics was yielded (Fig. 7.23). The physical justification of the newly introduced approach has still to be proven and will be topic of further investigations.

Chapter 8

Influence of Heating Rates on the Recrystallization Behavior

8.1 Introduction

It is known from literature that heating rates have a strong effect on recrystallization [Nes 1976, Furrer 1978, Bampton 1982, Tangen 2004, Liu 2008]. The main difference to an isothermal heat treatment in a physical sense is the huge time window for recovery and precipitation reactions to take place prior or concurrent to recrystallization. Three different scenarios can occur: (1) Recrystallization is completed before any significant precipitation sets in; in this case, recrystallization proceeds completely unaffected by precipitation. (2) Precipitation occurs before the onset of recrystallization, then the substructure may be pinned by the dispersoids, and only recovery can take place (recrystallization in-situ). (3) Recrystallization and precipitation occur concurrently. Scenarios (1) and (3) introduced above can be observed in the Al-1 wt% Mn alloy AA3103 [Nes 1976, Furrer 1978, Morris 1980, Bampton 1982, Daaland 1996, Somerday 2003, Tangen 2004] by choosing different heating rates as shown in this study. Hence, recrystallization during annealing with *different heating rates* is affected by both *recovery* and *precipitation*. Recovery does not lead to significant changes in the texture, in contrast to recrystallization. However, it reduces the driving force for recrystallization and for phase transformations (reduction of heterogeneous nucleation sites at dislocation tangles). Precipitation can strongly hinder, or even suppress recrystallization. The overall effect of recovery and precipitation on recrystallization (nucleation and nucleus growth) lead to significant changes in the recrystallization textures, microstructure and kinetics in the considered alloy.

To model recrystallization under *non-isothermal conditions* various approaches are available from literature, mainly concentrating on the modeling of recrystallization kinetics. The modeling approach presented by Dunlop [Dunlop 2007] considers the influences of recovery but precipitation reactions were not considered, since it deals with a single-phase material. Ruitenberg [Ruitenberg 2001] compared further the Johnson-Mehl-Avrami-Kolmogorov equation for isothermal and linear heating rates. Woldt [Woldt 1992] and Krüger [Krüger 1993] derived the JMAK-equation for non-isothermal heat treatments and related it to the one for isothermal conditions.

Besides the modeling of recrystallization kinetics also the microstructure and texture are of importance for the final material properties. The 3D recrystallization model CORE (Cellular Operator for Recrystallization), which was developed at the Institute of Physical Metallurgy and Metal Physics (IMM), can predict those quantities, but up to now only isothermal heat treatments were modeled [Mukhopadhyay 2007].

Since isothermal heat treatments are rarely encountered during industrial thermo-mechanical processing, the recrystallization model CORE was extended in this work. The following section focuses on the consideration of heating rates during the recrystallization simulations and their effect on *texture*, *grain size* and *kinetics*.

To model the above outlined complex recrystallization behavior during non-isothermal conditions, the following improvements of the CORE model were included:

- A nucleation criterion based on strain induced grain boundary migration *SIBM* (Strain Induced Boundary Migration) according to Derby and Ashby [Ashby 1978].
- Individual nucleation mechanisms with their respective nucleation spectra. The nucleus spectrum for particle-stimulated nucleation was provided from modeling the deformation zones in the respective grains with the GIA-DZ (GIA-deformation zone) model introduced in Chap. 5.
- A model for prediction of incubation times based on the formation of a stable subgrain structure out of a cell structure (Chap. 6.3).
- A decrease of the average stored dislocation density within the deformed grains owing to recovery was taken into account by the coupling with 3IVM+ [Gurla 2007, Mohles 2008] as introduced in Chaps. 3 and 6.
- The changes in microchemistry were considered as dependent on time (solute concentration, size and volume fraction of precipitates). The coupling to the precipitation model ClaNG (Classical Nucleation and Growth model for precipitation) [Schneider 2006] to consider the time-dependent changes in microchemistry was described in Chap. 3. A basic evaluation of the combination CORE-ClaNG was demonstrated in Chap. 7.

The extended CORE model was applied to predict the recrystallization behavior during annealing with various heating rates in a commercial Al-1 wt% Mn alloy (AA3103). The corresponding experimental data is outlined in Sec. 8.2. In Sec. 8.3 the input data for the recrystallization model CORE is summarized and the corresponding simulation results are presented in Sec. 8.4. The discussion of the results is comprised in Sec. 8.5 and conclusions are drawn in Sec. 8.6.

8.2 Experimental Data

The experimental data shown in this section provides partly data for validation of the simulations as well as for deeper understanding of the involved physical mechanisms. Starting from industrial processed material, non-isothermal annealing treatments were carried out. Precipitation during recrystallization and the influence on nucleus growth were studied in more detail.

8.2.1 Characterization of the industrially processed material

The material used in the current study is an industrially processed Al-1 wt% Mn alloy AA3103. The alloy contains the following major impurity contents in wt% (Tab. 8.1).

Tab. 8.1: Composition of the used commercial Al-Mn alloy AA3103 in wt%.

Si	Mn	Fe	Ti	Zn	Cu	Mg	Zr	Other	Al
0.12	1.10	0.45	0.015	0.025	<0.01	<0.01	<0.01	<0.01	rest

After casting and homogenization the material was break-down rolled, hot rolled, coil cooled, and cold rolled to a thickness reduction of 70%. The corresponding microstructure and texture evolution during the processing is shown in Fig. 8.1. After break-down rolling the material was completely recrystallized with a Cube texture, during hot rolling the grains were flattened and a typical hot rolling texture developed. The final cold rolled material was characterized by a microstructure with elongated bands and a texture showing a typical cold rolling texture with orientations along the β -fiber. This cold-rolled material was the starting material for the current investigation.

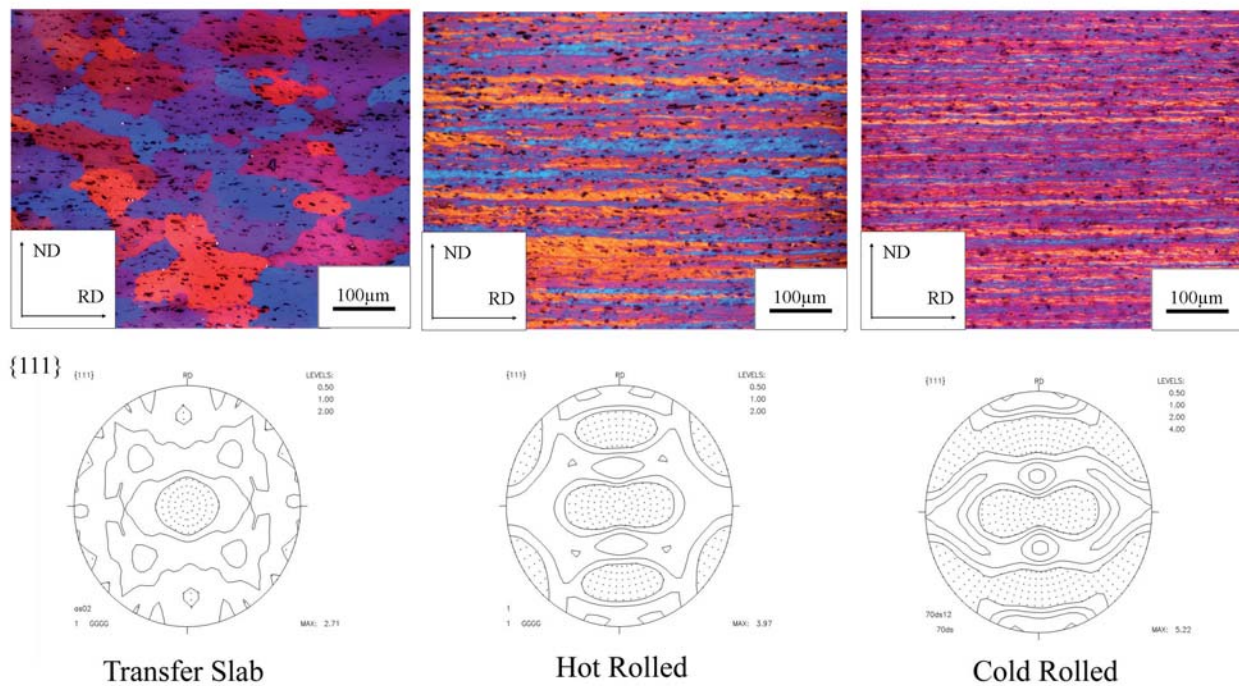


Fig. 8.1: Microstructure and texture evolution in AA3103 during material processing in the transverse plane. Constituents are indicated as the larger black particles in the micrographs. The texture evolution is indicated by representation in $\{111\}$ -polefigures.

8.2.2 Considered time-temperature curves

The purpose of the different annealing treatments (Fig. 8.2) was to control the mechanisms occurring simultaneously in the material. Hence, a fast heating rate was chosen to provide a material state mainly influenced by recrystallization which by-passes the precipitation regime. This treatment is referred to as flash annealing, abbreviated in the following as *FA* with a heating rate of 20 K/s, which corresponds to annealing in a salt bath. In contrast, lower heating rates such as 0.02 K/s, respectively 0.01 K/s, are more comparable to industrial heat treatments and therefore referred to as batch annealing (*BA 0.01 K/s* and *BA 0.02 K/s*). In general, batch-annealing is an industrial term used to describe heat-treatments where the materials are heated with a relatively slow heating rate to the target temperature. During those treatments concurrent precipitation is observed for Al-Mn alloys [Tangen 2004, Furrer 1978]. In order to prevent significant precipitation reactions, so-called step annealing treatments were carried out. The material is hereby annealed at a low temperature such as $T = 180\text{ }^{\circ}\text{C}$ or $T = 290\text{ }^{\circ}\text{C}$ to obtain solely recovery. After quenching, the material is recrystallized $T = 350\text{ }^{\circ}\text{C}$. These step annealing treatments are in the following abbreviated as *Step 180* and *Step 290*.

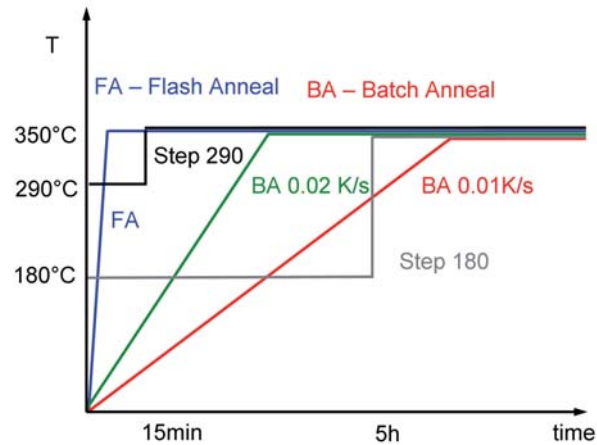


Fig. 8.2: Five different temperature- time curves used to investigate the effects of different heating rates on recrystallization.

8.2.3 Characterization of the heat-treated material (data for grain size and texture)

The 70% cold rolled material was subjected to the outlined annealing treatments at $T = 350^{\circ}\text{C}$ with different heating rates, by either annealing in a sand bath or in an air circulating furnace with programmable heating rates (Fig. 8.2). The following heating rates were used: *FA 20 K/s*, *BA 0.02 K/s* and *BA 0.01 K/s* as well as step annealing treatments to introduce a certain amount of recovery in the material prior to recrystallization.

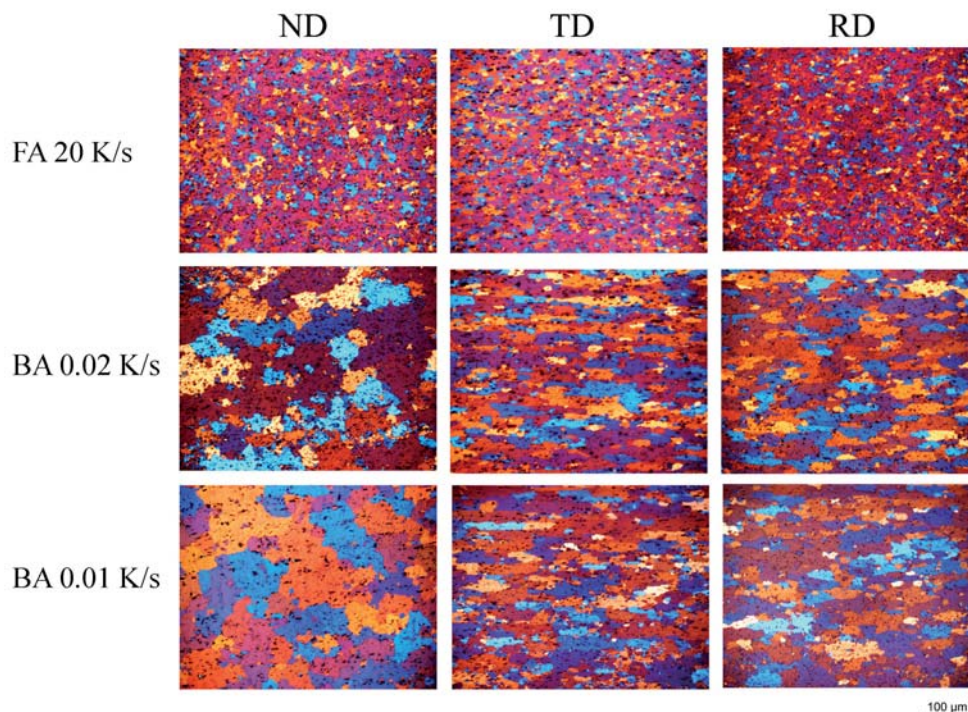


Fig. 8.3: Microstructure Evolution for the different heating rates after 70 % cold rolling, displayed in rolling, transverse and normal direction. Small black particles indicate mainly constituents. The results of the step annealing treatments Step 180 and Step 290 are similar to the fine structure obtained for a heating rate of *FA 20 K/s*.

Different microstructures were obtained dependent on the heating rate (Fig. 8.3). For high heating rates the obtained grain size was small, and the microstructure was very homogeneous

corresponding to scenario (1) described in section 8.1. Upon lowering the heating rates the grain size increased and the grain morphology became increasingly anisotropic with its largest extension in rolling direction as shown in Fig. 8.2 (concurrent precipitation, scenario (3)). These observations agree very well with literature data in Al-Mn alloys [Furrer 1978, Bampton 1982, Tangen 2004, Liu 2008]. The observations of a smaller grain size for lower heating rates by Morris [Morris 1980] can be explained by the fact that in their case smallest dispersoids were presented already prior to the annealing treatments, so that they could significantly coarsen during the annealing at low heating rates so that a finally smaller grain size was obtained than for the fast heating rates. However, in the case discussed in this chapter new precipitates formed during annealing at lower heating rates, so that they had maximum effect on nucleation and precipitation. EBSD maps and macrotextures are presented later on in Sec. 8.4 in direct comparison with the simulation results.

8.2.4 Data for recrystallization kinetics

To characterize the temporal evolution of recrystallization in the present material and for comparison with the simulated recrystallization kinetics in Sec. 8.4, the recrystallized volume fraction is calculated. For this purpose the hardness as well as the β -fiber volume fraction, as obtained from texture measurements, were measured over time. The corresponding softening behavior as obtained from hardness measurements is indicated in Fig. 8.4. During the annealing treatments with linear heating rate (Fig. 8.4b) concurrent precipitation takes place. To clearly distinguish the influence of recovery, so-called step annealing treatments were carried out as indicated in Fig. 8.4a. Hereby, the material is annealed at lower temperatures, so that exclusively recovery can take place. After quenching, the material is rapidly heated to $T = 350^\circ\text{C}$ for recrystallization.

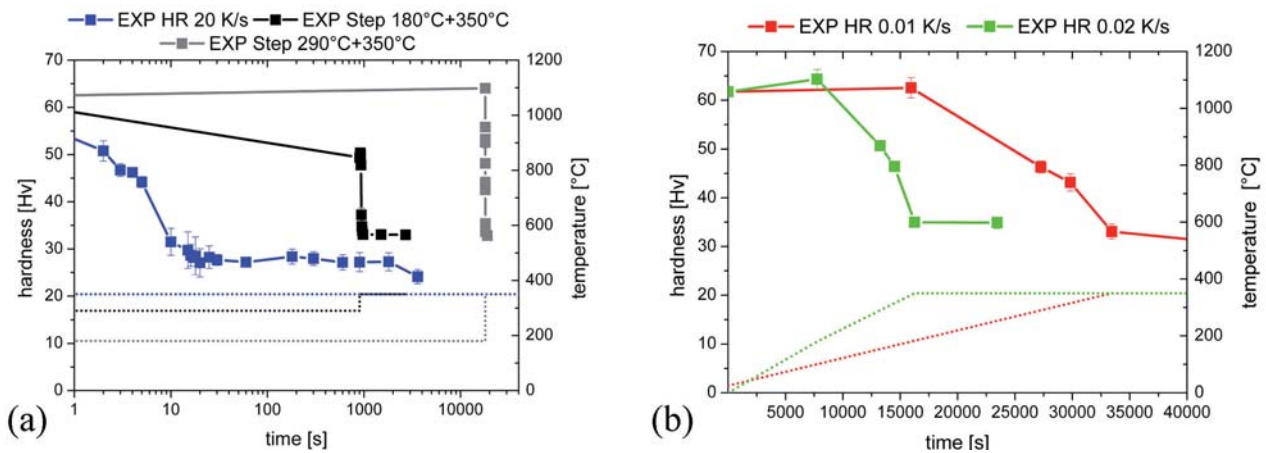


Fig. 8.4: Hardness over time for different heat treatments for initially 70% cold rolled AA3103. The heat treatments are indicated by dotted lines. (a) Heuristic T -profiles: artificial annealing steps are introduced to investigate the effect of recovery; (b) industrial relevant linear heating rates ($HR =$ heating rate).

From the hardness curves in Fig. 8.4, the recrystallized volume fraction X as a function of time was calculated according to the following equation:

$$X = \frac{H_{v,0} - H_{v,t}}{H_{v,0} - H_{v,End}} \quad (8.1)$$

where $H_{v,0}$ is the initial hardness before the onset of recrystallization as interpreted from EBSD (and not the initial hardness after deformation). $H_{v,t}$ is the hardness after the considered time t , and $H_{v,End}$ is the final hardness obtained after complete recrystallization. For Eq. (8.1) a linear dependency

between recrystallized volume fraction and hardness was assumed after recrystallization was initiated.

For the heating procedures in Fig. 8.4a recrystallization is initiated immediately, whereas for the lower heating rates recrystallization is initiated at approximately $T \sim 290^\circ\text{C}$ (Fig. 8.4b). By comparing the hardness values at the onset of recrystallization it can be seen that the heating rate affects the extent of recovery. A lower annealing rate favors a more pronounced reduction of the dislocation density due to recovery (lower hardness values at the onset of recrystallization).

The procedure for conversion of the β -fiber volume fractions into recrystallization kinetics was detailed in Sec. 7.2. The calculated experimental recrystallized volume fractions from hardness and texture are compared in Sec. 8.4 to the simulated recrystallization kinetics.

8.2.5 Precipitation during annealing

Beside influences of recovery during recrystallization, the precipitation behavior is of major concern and thus will be considered in the following. The solute content lowers the boundary mobility by solute drag, whereas second-phase particles, so-called dispersoids cause a back driving force (Zener drag) on the boundaries. The dispersoids are of major importance since they can hinder or even suppress recrystallization.

After initial cold rolling, the manganese solute content was determined by thermo-electrical power measurements to 0.282 wt% (courtesy of Hydro Aluminium Bonn). Further manganese was contained in long elongated constituent particles, which were aligned in rolling direction after 70% thickness reduction (black particles in Fig. 8.1). Their composition corresponded to Al_6Mn and $\alpha\text{-AlFeSi}$. Those large particles (constituents) play a role for particle-stimulated nucleation and thus enhance recrystallization.

Tab. 8.2: Manganese solid solution content in [wt%] as obtained from thermo-electric power measurements for different temperatures in the alloy AA3103. The material at $T = 25^\circ\text{C}$ was deformed to 70% cold rolling reduction [courtesy of Hydro Aluminium Bonn].

temperature [$^\circ\text{C}$]	25	290	315	350
BA (0.01 K/s)	0.282	0.17	0.15	0.12
FA (20 K/s)	0.282	-	-	0.25

During the subsequent annealing treatments, there is sufficient time at elevated temperatures for precipitation reactions to take place as evident from measurements of the solute level which decreased significantly in case of a lower heating rate (Tab. 8.2). Accompanying to the drop in the solute content is the evolution of precipitates in case a low heating rate is used. This is demonstrated in the micrographs from scanning electron microscopy (SEM) in Fig. 8.5. The material was investigated on a transverse section. In the deformed state (Fig. 8.5a) a very low number of dispersoids was found in specific spots along the grain boundaries. An annealing treatment at 290°C for 25 min did not cause significant precipitation as visible from Fig. 8.5b (*Step 290*). However, when the material was heated with a sufficiently low heating rate of e.g. BA 0.01 K/s, significant precipitation took place. This is visible in Fig. 8.5c, where in a certain distance to the constituents newly developed precipitates could be found with sizes of about 100 nm (indicated by white arrows).

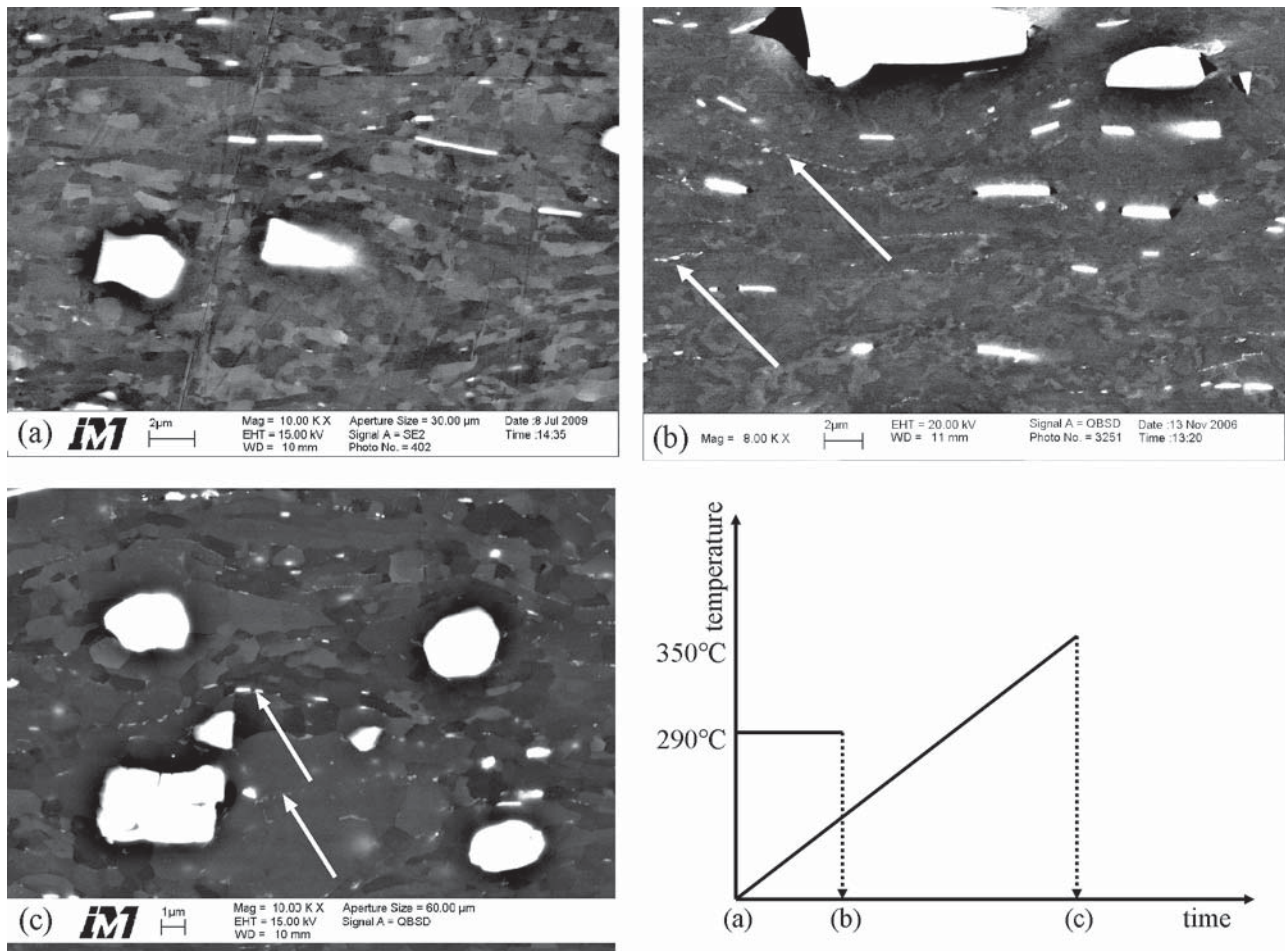


Fig. 8.5: SEM micrographs showing precipitation state (a) 70% cold rolled; (b) additionally annealed at $T=290^{\circ}\text{C}$ $t=25$ min; (c) additionally annealed with heating rate 0.01 K/s at $T=350^{\circ}\text{C}$. Particles are indicated in white color (constituents – large particles, dispersoids – smallest particles). Some dispersoids are additionally marked by white arrows.

The measured solute content and the observed precipitation behavior enable later the validation of the precipitation behavior predicted with ClANG.

8.2.6 Growth selection of P-oriented nuclei

Precipitation does not only influence the microstructure, but also the macrotexture. It is reported in literature that specific texture components are associated with particle-stimulated nucleation [Lücke 1990, Engler 1996, Daaland 1996, Engler 1997a, Liu 2003, Tangen 2004, Liu 2008], namely the P-texture component and the 22°ND -rotated Cube component. How strong these texture components are represented in the final recrystallization texture depends strongly on the chosen heat treatment.

Since the P-texture component is predominant during non-isothermal annealing treatments and due to its importance for the final recrystallization texture, its nucleation and growth behavior was studied in more detail by means of EBSD. In order to detect a P-oriented nucleus by Electron Backscatter Diffraction (EBSD) and its later evolution during the annealing treatment, at first a large area was scanned by means of EBSD. Initially the material was measured in the purely deformed state. Subsequently, the sample was removed from the SEM and was heat treated in an air circulating furnace in order to initiate recrystallization. Afterwards, the same sample was reintroduced into the SEM without further sample preparation in order not to destroy the area of interest. Then, the same area was measured again by EBSD to track microstructure changes. This procedure was repeated several times during the recrystallization process.

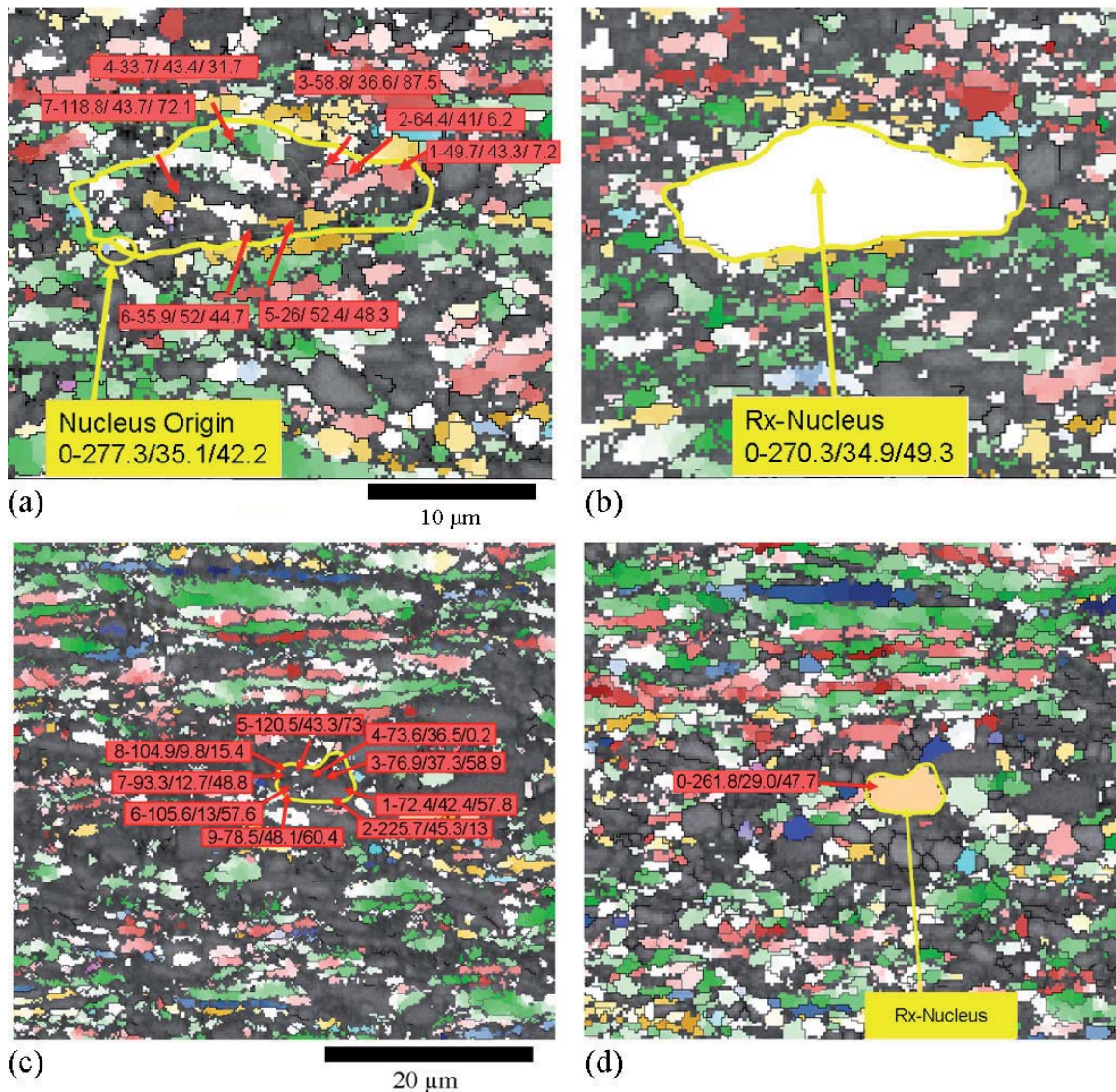


Fig. 8.6: EBSD micrographs showing two examples of the evolution of a P-oriented nucleus (yellow) and its growth in the deformed matrix. The area of interest is encircled in yellow. All samples were previously cold rolled to 70% (a) $T=290\text{ }^{\circ}\text{C}$ 25 min, (b) $T=290\text{ }^{\circ}\text{C}$ 40 min; (c) deformed; (d) $T=290\text{ }^{\circ}\text{C}$ 5 min. The chosen colors indicate different orientation types (green- S/R orientation, red-Copper orientation, yellow- Brass orientation, blue-Cube orientation). For the determination of the orientation relationship between P-oriented nucleus and deformed matrix, the three Euler angles are indicated in the red, respectively yellow boxes.

From the EBSD data, areas of interest were selected and evaluated with respect to nucleation (encircled by yellow line, Fig. 8.6). In Fig. 8.6b, d the appearance of a P-oriented nucleus is indicated. The prior unrecrystallized area (Fig. 8.6a, c) is shown as well for comparison and evaluation of the growth relationship between the P-oriented nucleus and its former surrounding. With the help of HKL software the orientation relationship between the nucleus orientation and the previously deformed orientations, which are later consumed by the growing P-oriented nucleus, could be evaluated. In the graph several grain orientations prior to recrystallization are indicated exemplarily in terms of their Euler angles (in red / yellow boxes, Fig. 8.6) in the area of interest. It was found that an initial P-oriented nucleus will grow into areas which are partially misoriented by up to 25° - 50° around a $\langle 111 \rangle$ axis.

This is considerably more than the range found in literature for high purity aluminum [Gottstein 1999]. These observations were considered for the modeling of recrystallization as presented in Sec. 8.4.

8.3 Input for Recrystallization Modeling

It was already outlined in Sec. 3.4 that the recrystallization model CORE requires a considerable amount of input parameters. This section summarizes the inputs for the recrystallization simulations, as predicted from other models. The inputs are sorted according to main topics (deformation, nucleation and precipitation input). Tab. 8.3 gives in advance an overview of the parameters described in this section.

Tab. 8.3: Main input parameter set for CORE (LAGB=Low angle grain boundary; HAGB=High angle grain boundary, RD=rolling direction, TD=transverse direction, ND=normal direction, N_{GLS} =number of activated slip systems, IGM=in-grain misorientation, $\varepsilon_{crit}^{shear-relax}$ =shear relaxation)

parameter	value	origin
<i>Deformation parameters:</i>		
Orientation dependent dislocation densities	$1.30437 \cdot 10^{14} \text{ m}^{-2}$	GIA-3IVM+, former GIA-3IVM [Crumbach 2001]
Initial texture	Cold rolling texture	GIA-3IVM+, former GIA-3IVM [Crumbach 2001]
Average grain size in RD, TD, ND	$1000 \mu\text{m} * 200 \mu\text{m} * 300 \mu\text{m}$	GIA-3IVM+, former GIA-3IVM [Crumbach 2001]
Nucleation Efficiencies	$N_{GLS,crit}=8$ $IGM_{crit}=1.23$ $\varepsilon_{crit}^{shear-relax} = 0.18$	ReNuc [Crumbach 2004, 2006a,b], GIA-3IVM+/ former GIA-3IVM [Crumbach 2001]
<i>Growth parameters:</i>		
activation energy/ preexponential factor for $40^\circ \langle 111 \rangle$	1.0 eV/ $3.0 \text{ m}^3/\text{N}\cdot\text{s}$	CORE settings
activation energy/ preexponential factor for HAGB	1.1 eV/ $3.0 \text{ m}^3/\text{N}\cdot\text{s}$	CORE settings
activation energy/ preexponential factor for LAGB	1.6 eV/ $1000 \text{ m}^3/\text{N}\cdot\text{s}$	CORE settings
<i>Recovery Parameters:</i>		
activation energy climb	1.4 eV	[Lundy 1962]
activation energy cross slip	$\rightarrow \infty$	(unused)
activation volume cross slip	97.94 b^3	3IVM+ Fit
<i>Model for Particle Stimulated Nucleation:</i>		
Deformation zone size	$5 * 2 * 2$ cells	experiment
Factor of increase of dislocation density in the particle vicinity	2	experiment
constituent particle volume fraction	2.5 %	experiment
average constituent radius	$4 \mu\text{m}$	experiment
Texture particle-stimulated nucleation		GIA-DZ [Chap. 5]
<i>Precipitation Parameters:</i>		
solute content c_{ss}		ClANG [Schneider 2006], EXP
Dispersoid radius & volume fraction f_p		ClANG [Schneider 2006]

8.3.1 Deformation modeling

One of the main inputs required for the recrystallization simulations are the results of a prior deformation texture simulation. These simulations were carried out with the Taylor-type multi-grain approach model GIA-3IVM+ [Crumbach 2001]. The deformation texture simulation was conducted assuming plane strain deformation up to 70% thickness reduction. This rolling simulation provides one of the major inputs for the recrystallization simulation: the dislocation density. The initial texture was an experimental hot rolling texture (Fig. 8.1a) composed of orientations along the β -fiber as well as Cube orientation. The results of the cold rolling simulation are shown in Fig. 8.7b in comparison to the experimental texture in Fig. 8.7a.

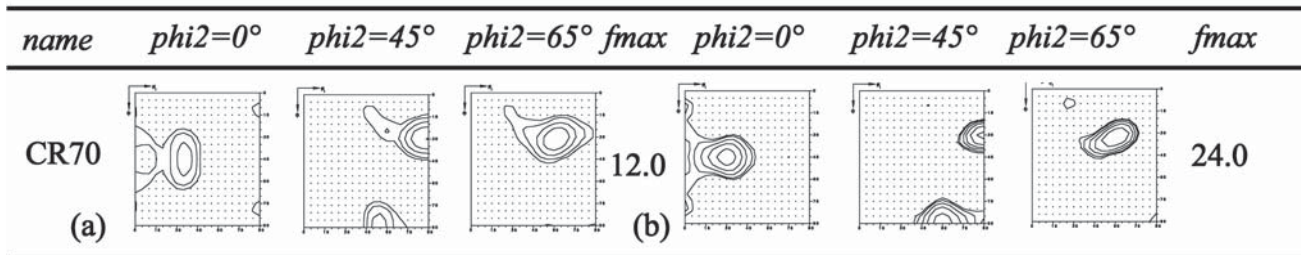


Fig. 8.7: Experimental (a) and simulated (b) macro textures from GIA-3IVM+ calculations close to sheet center layer.

After 70% cold rolling reduction the experimental texture displayed a typical cold rolling texture with orientations along the β -fiber (Fig. 8.7a) and no remaining Cube component. The simulated deformation texture reflected the same tendencies; only that the overall intensities were slightly higher. This could be explained by the homogeneous nature of the model used. In experiments, deformation zones are created in the particle vicinity during deformation. These deformation zones provide mostly random oriented texture components which make the overall experimental deformation texture more random and thus, lead to a decrease in the overall intensities. Such inhomogeneities are not considered in GIA, but can be treated in principle with GIA-DZ (Secs. 5.3 and 9.5). The output data of GIA-3IVM+ served as input for the recrystallization simulations in CORE, by providing the initial average grain size, orientation-dependent stored dislocation densities, and grain orientations for the initial microstructure configuration in CORE.

8.3.2 Sub-structural quantities and nucleus orientations

Sub-structural Quantities

The deformation data was further utilized to estimate the nucleation probabilities for recrystallization (Fig. 8.8). Information on the efficiency of single grains for shear band, transition band and grain boundary nucleation have been obtained by applying the ReNuc model [Crumbach 2006a, Crumbach 2006b]. Parameters of interest were the critical number of activated slip systems ($N_{GLS,av} + ODR\text{-offset} = 8$) during deformation, the total amount of shear-relaxation per grain $\epsilon_{crit}^{shear-relax} = 0.18$, or the critical in-grain misorientation gradients $Misori_{crit} = 1.23$ formed within a grain during deformation [Crumbach 2006a, Crumbach 2006b]. Orientations which reach these critical values will set off nucleation of the considered type in the respective grain (Fig. 8.8). A more detailed discussion of those parameters is given in Chap. 7.

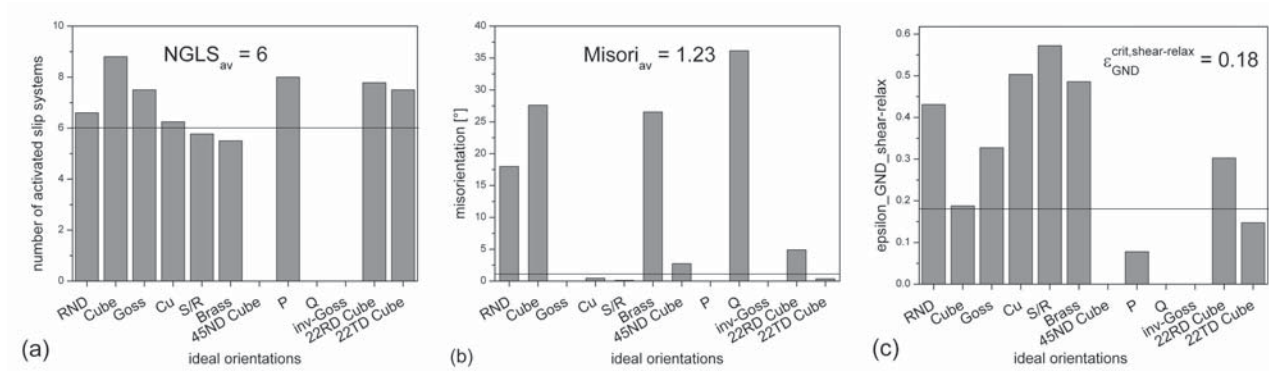


Fig. 8.8: Nucleation relevant parameters classified according to ideal orientation classes for (a) grain boundary nucleation (based on the deformed grain orientations); (b) transition band nucleation (based on the pre-deformed grain orientations) ; (c) shear band nucleation.

Besides nucleation at shear bands, which provides random oriented nuclei, the nuclei at grain boundaries and transition bands are derived by scatter of the initial grain orientations. In case of transition band nuclei the initial grain orientations are those prior to deformation. The orientations for grain boundary nucleation are based on the deformed orientations. For the description of particle-stimulated nucleation a separate nucleation spectrum is required.

Since GIA can only predict homogeneous deformation behavior, the GIA-DZ model was introduced to model the evolution of deformation zones and the related orientations (Chap. 5). The obtained orientation spectra in the deformation zones (Fig. 8.9) agree very well with the measured microtexture within deformation zones found for AA3103 after a cold rolling reduction of 70% as shown in Chap. 5. The nucleus spectrum for particle-stimulated nucleation was derived from this spectrum considering different heating rates and thus orientation-dependent incubation times.

The particle-stimulated nucleation model for CORE was outlined in Sec. 5.5. For this, further a particle volume fraction of 2.5 %, as measured in the hot rolled state, was taken into account. The size of the particles was measured and assumed in the model to range between 1 μm - 12 μm as measured in the hot rolled state, since further changes in the particle distribution during cold rolling are negligible. Additional data for particle-stimulated nucleation can be found in Tab. 8.3.

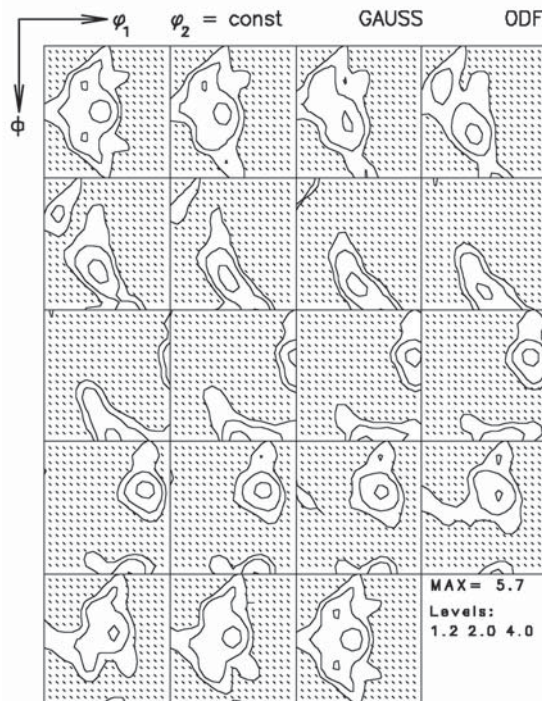


Fig. 8.9: Nucleus spectrum in the deformation zones as obtained from deformation zone model GIA-DZ. This spectrum will provide the nucleus orientations for particle-stimulated nucleation.

The above discussed sub-structural quantities provide the nucleus spectra at grain boundaries, transition bands, shear bands and particles. The effective nucleus quantities and thus resulting nucleus textures are computed in CORE as dependent on the time-temperature curves and interface area.

Nucleus Orientations

Since a nucleus rate was defined in the present simulations, Fig. 8.10 shows the total nucleus spectrum irrespective of the times the nuclei were activated. The nucleus spectrum includes nuclei originating from the different nucleation sites as discussed in the previous section. The nucleus textures do not show significant differences. They are mostly dominated by an exact Cube component. The Cube intensity decreased however with decreasing heating rate. The nucleus orientations obtained close to the β -fiber scattered strongly owing to their proximity to the particles in the deformation zone.

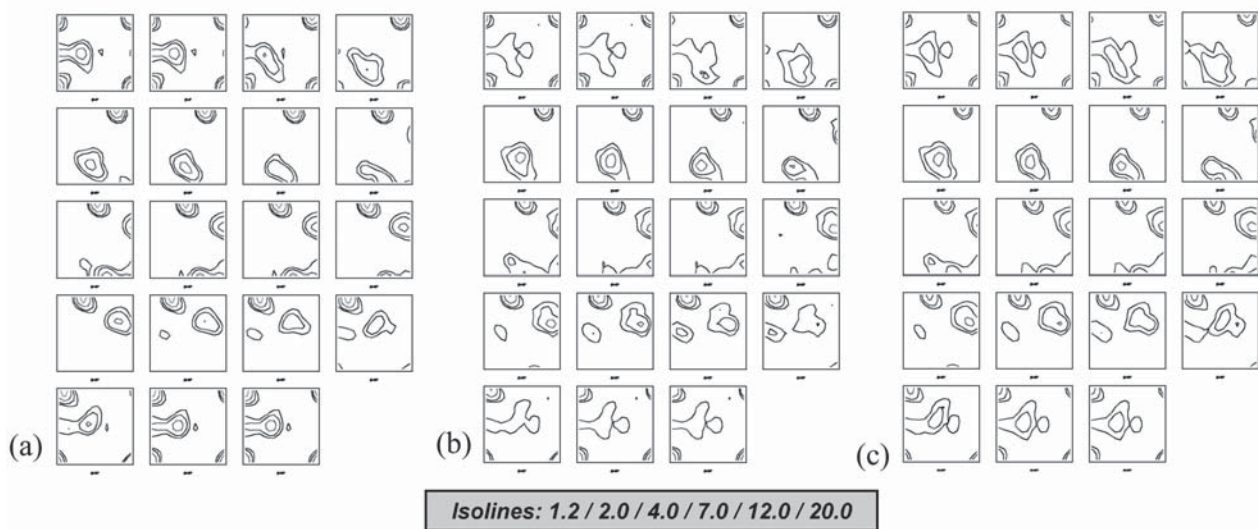


Fig. 8.10: Total nucleus spectra for different heating rates: (a) FA 20 K/s; (b) BA 0.02 K/s; (c) BA 0.01 K/s. The nucleus spectrum for Step 180 and Step 290 are similar to case (a). For the presented nucleus spectra all nucleation mechanisms were considered. The nucleus spectra are depending on the chosen temperature profile.

8.3.3 Precipitation input

Beside the input from deformation texture simulations, also the precipitation behavior was an input for the CORE model. In reality, precipitation and recrystallization proceeded concurrently to each other. Since ClaNG [Schneider 2006] and CORE [Mukhopadhyay 2007] have not been incrementally coupled so far, the microchemistry relevant quantities were calculated a priori. Second-phase particles do not only have an effect on recrystallization nucleation, they also impact nucleus growth. Solute elements further strongly influence the grain boundary mobility, which can drastically change the recrystallization behavior.

In the present work the CORE model was further modified to take also time-dependent microchemistry changes of the sample into account (Sec. 3.7). To provide the input for CORE, simulations with ClaNG were carried out in order to provide the evolution of the solid solution concentration of manganese and the evolution of the dispersoid volume fraction and radius as a function of time and temperature. To validate the simulation results for the solid solution content, thermo-electric power measurements were carried out to provide such data (Tab. 8.2).

The decrease in dislocation density over time served as input to this precipitation model, too. To provide this evolution, measured hardness values were converted into a dislocation density [Cahoon 1971] via a simple relation.

$$\tau = \alpha \cdot G \cdot b \cdot \sqrt{\rho} \quad (8.2)$$

$$\tau = m \cdot \sigma \quad (8.3)$$

$$\sigma = 3 \cdot H_v \quad (8.4)$$

Here, σ is an interpreted macroscopic flow stress, τ the shear stress in the slip system, m the Schmid factor, G the shear modulus, b the magnitude of the Burgers vector, ρ the dislocation density and H_v the Vickers hardness. As initial dislocation density, the average total dislocation density as obtained from GIA-3IVM+ calculations in case of 70% cold rolled material was used. The annealing treatments chosen in this study are indicated in Fig. 8.9. For the different time-temperature paths, of course, different ClaNG simulations were carried out.

The results of the precipitation model ClaNG are shown in Figs. 8.11-8.13. In Fig. 8.11 the comparison between the solid solution content and the values obtained from thermo-electric power measurements is shown. Since ClaNG contains unknown intrinsic parameters it was necessary to adjust these parameters to the present alloy and heat treatments [Schneider 2006]. Figs. 8.11, 8.12 show the result. The area where the material recrystallized for the chosen heat treatment is shaded. It can be observed that for the isothermal annealing treatment no change in microchemistry is observed (FA) in the respective time frame. A drop in the solid solution content of manganese for the low heating rates (BA 0.01 K/s, BA 0.02 K/s) is observed in the regime where recrystallization is initiated. Hence, concurrent to recrystallization, also precipitation reactions take place.

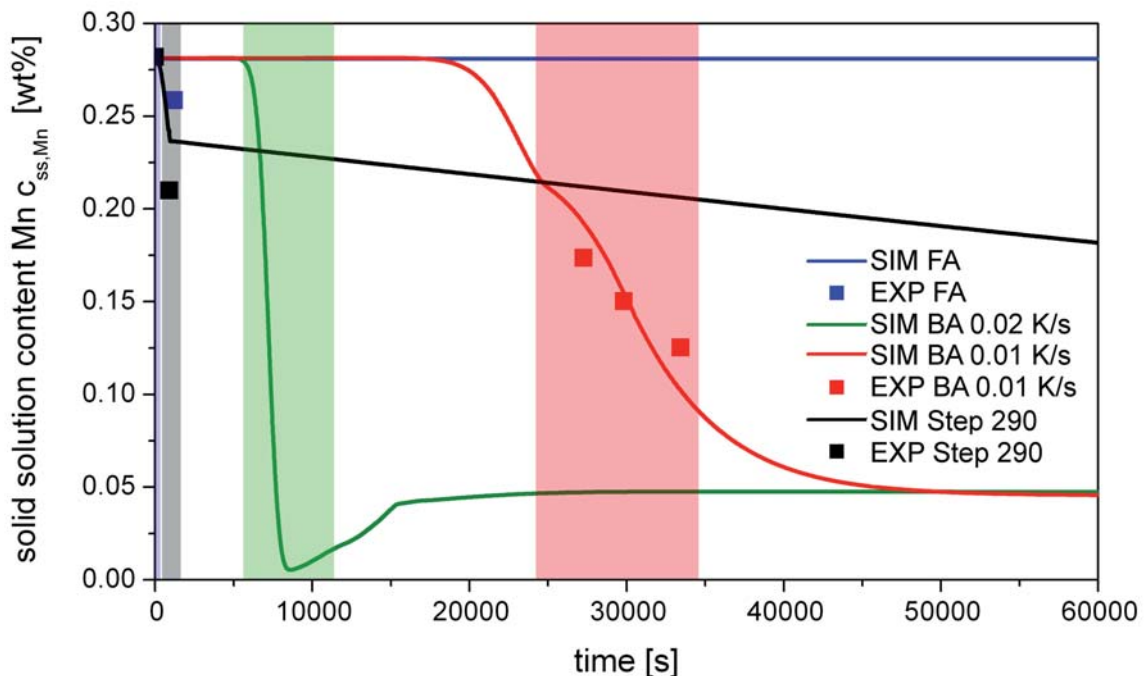


Fig. 8.11: Evolution of manganese solute content for heating rates FA (blue), BA 0.01K/s (red), BA 0.02 K/s (green) and Step 290 (black) as modeled with the classical nucleation and growth model ClaNG. The results for Step 180 are not shown, since there was a negligible effect. The shaded areas indicate the time range where recrystallization takes place.

The evolution of the volume fraction and particle radius was modeled consistent with the solid solution content by means of ClaNG (Fig. 8.12). The variation in the degree of precipitation with

heating rate is in agreement with experimental observations in AA3103 [Tangen 2004]. Tangen et al. observed that the electrical conductivity and consequently the degree of precipitation increased considerably with decreasing heating rate in AA3103.

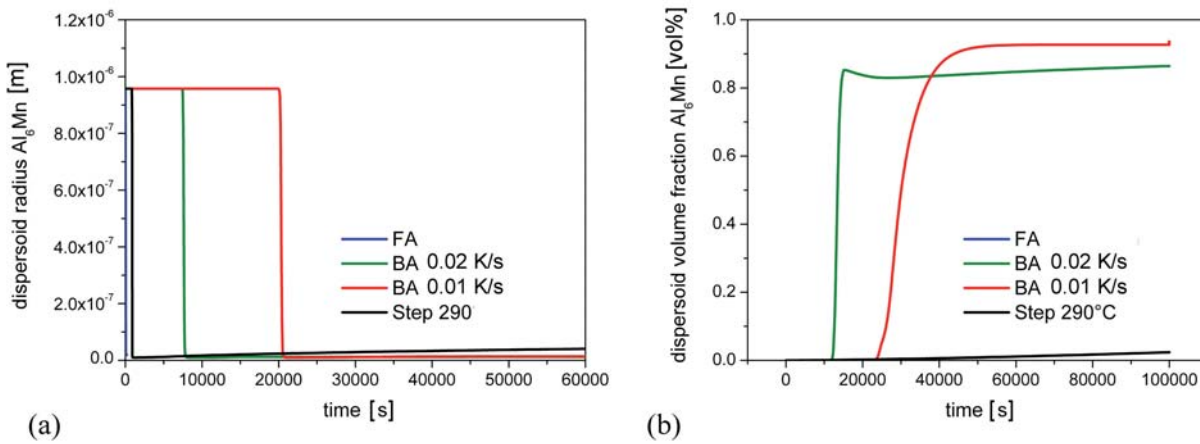


Fig. 8.12: Simulated precipitate radii and volume fractions dependent on time in the alloy AA3103, for different heating rates. The results for Step 180 are not shown; they resemble the results for Step 290.

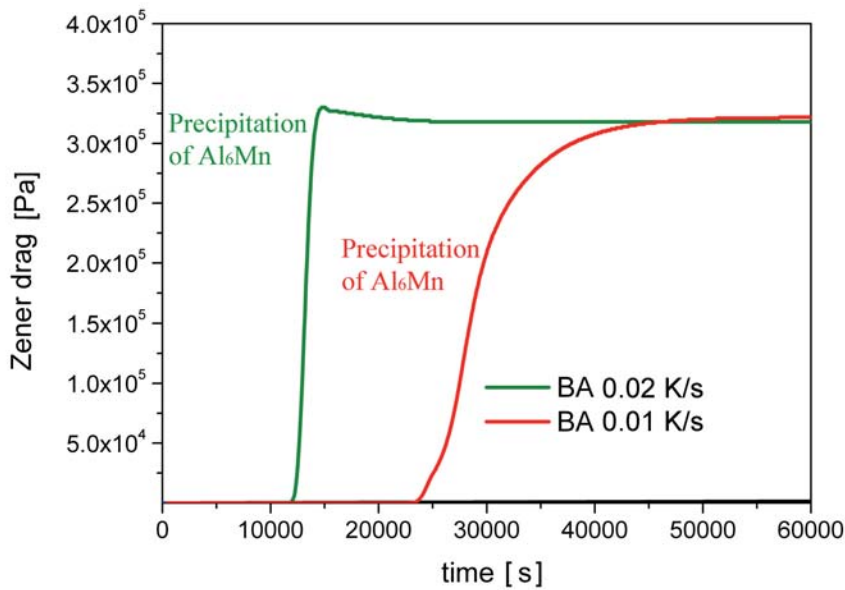


Fig. 8.13: Modeled evolution of Zener drag for heating rates BA 0.01 K/s (red) and BA 0.02 K/s (green). The results for the heat treatments FA, Step 180 and Step 290 are not displayed, since the Zener drag is negligible in these cases.

For the recrystallization simulations with CORE only the solid solution content of manganese and the Zener drag are important. Hence, the Zener drag was calculated based on the particle volume fraction and radius according to Eq. (3.11). The result is displayed in Fig. 8.13.

For the modeling of the Zener drag only the appearance of Al₆Mn dispersoids was considered, even though nucleation of Al₆Mn and α -phase was considered in the ClaNG simulations. But the predicted volume fraction of the α -phase was negligible. The consideration of Al₆Mn as the only dispersoid type is in agreement with literature [Goel 1974]. The calculated Zener drag as obtained from the evolution of particle volume fraction and radius for the heat treatments FA, Step 180, Step 290 is comparatively small so that it has neither an influence on recrystallization nucleation nor on the growth process. For the lower heating rates (BA 0.01 K/s, BA 0.02 K/s) recrystallization nucleation and growth behavior is heavily influenced by Zener drag. This concurrent precipitation can be also seen from the overlap of recrystallization and the simultaneous drop in the solute

content of manganese in Fig. 8.11 (shaded areas). The same tendencies were also observed from experimental observations as discussed in Sec. 8.2 (Fig. 8.5).

Fig. 8.14 summarizes the dependence of the precipitation reactions on the heating rate by means of a schematic TTT-diagram (TTT = time temperature transformation) for precipitation in AA3103. The precipitation kinetics depends strongly on the heating rate (slope of dashed lines) and whether the precipitation phase field is intersected, suggesting that precipitation reactions take place. This is very probable in particular for low heating rates (red line, Fig. 8.14). In contrast, for very high heating rates (blue line, Fig. 8.14) precipitation does not occur, and the recrystallization process remains unaffected by the precipitation reactions, i.e. Zener drag.

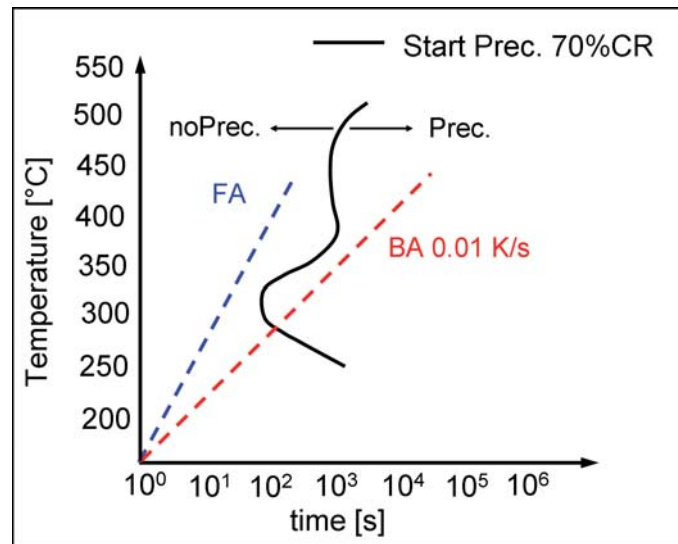


Fig. 8.14: Schematic TTT-diagram relating the precipitation behavior and the different annealing treatments. Heating rates for FA (blue), BA (red). Schematic diagram constructed according to experimental data [Tangen 2002, 2004].

8.4 Recrystallization Simulations

In the following section the recrystallization simulations obtained with CORE under consideration of the inputs in Sec. 8.3 are shown and discussed focusing on the recrystallization texture, kinetics and grain size.

8.4.1 Recrystallization textures

Based on the modeled nucleus textures (Fig. 8.10) the recrystallization textures were computed (Fig. 8.15). For a more precise consideration of the P-texture component in the final recrystallization texture the growth selection was modified from a $35^\circ\text{-}45^\circ\langle 111 \rangle$ to a $25^\circ\text{-}55^\circ\langle 111 \rangle$ growth selection as observed from experiments (Sec. 8.2). In the model deviations from the exact $\langle 111 \rangle$ rotation axis were allowed up to 15° .

Fig. 8.15 displays the simulated textures in comparison to the experimental ones. From experiments (Fig. 8.15a) a significant change in the texture is observed when changing from a high to sufficiently low heating rates. For high heating rates (FA 20 K/s) a weak Cube textures is obtained, whereas for lower heating rates (BA 0.02 K/s, BA 0.01 K/s) P- and ND-rotated Cube components dominate the textures. Similar experimental tendencies were observed by Tangen and Liu [Tangen 2002, Liu 2008] in the aluminum alloys AA3103 and AA3105. Liu further stated that the final texture after fast heating further depends on the final temperature, which was also observed in this thesis (recrystallization textures, Chap. 9).

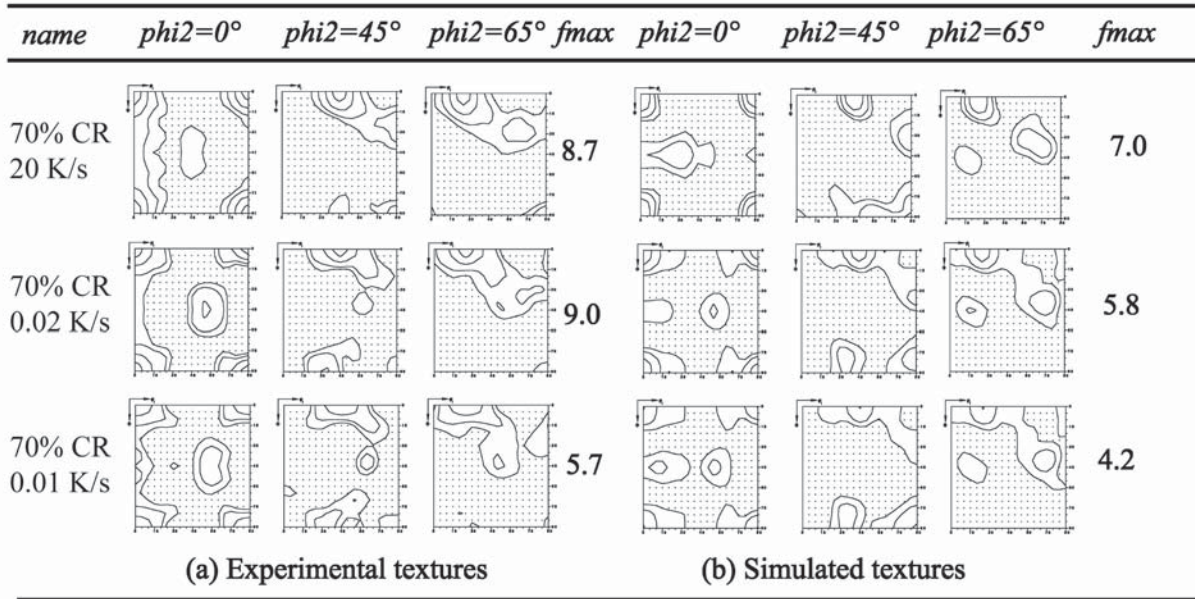


Fig. 8.15: Macrottextures for the sheet center layer from (a) experiments, (b) CORE simulations in terms of selected sections through Euler space.

As to the simulated recrystallization textures (Fig. 8.15b), they reflected the same texture transition found in experiments. For a high heating rate (FA 20 K/s) basically a Cube texture was attained in agreement with the experiment. For lower heating rates the simulated textures were dominated by the ND-rotated Cube component and the P-texture component as a result of concurrent precipitation predicted with ClaNG and CORE.

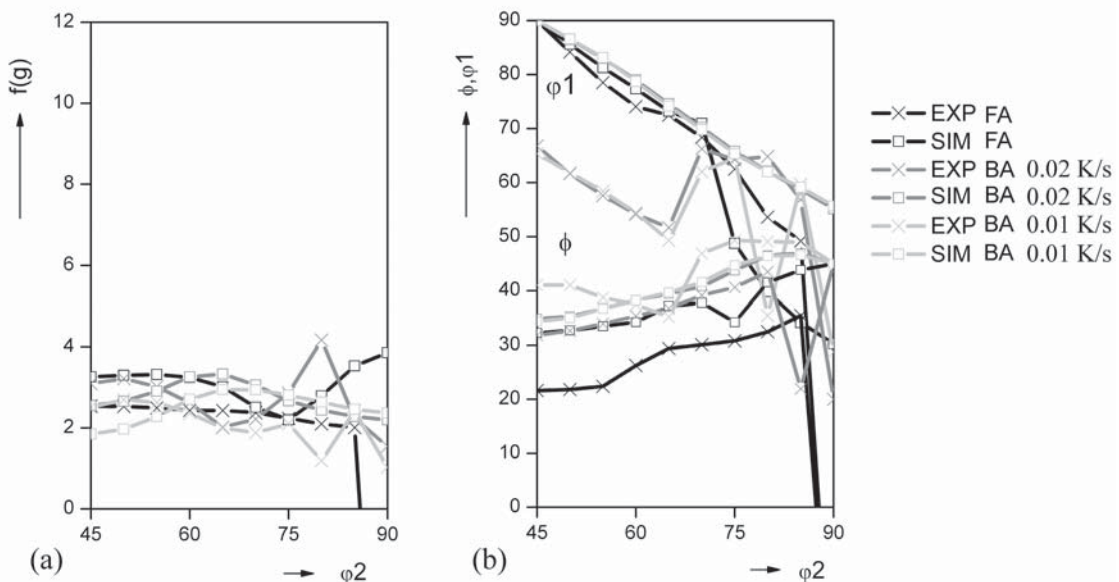


Fig. 8.16: Skeleton Plots: (a) β -fiber intensity, (b) β -fiber orientation of experimental and simulated macrottextures at different heating rates: FA 20 K/s (bold black, BA) 0.02 K/s (grey), BA 0.01 K/s (light-grey); X EXP □ SIM

The skeleton plots in Fig. 8.17 reflect the good agreement of the maximum Cube intensities observed from experiments and simulations. Their relative change in dependence of the heating rate is in agreement with experimental observations. From the skeleton plots (Fig. 8.16) the occurrence of the P-orientation is clearly indicated by a shift of the ϕ_1 values to higher values (for $\phi_2=90^\circ$).

Although the scatter of the Cube component in normal direction was slightly smaller and the P-orientation showed a lower volume fraction than in experiment, a quite good agreement with the experimental texture was achieved at low heating rates.

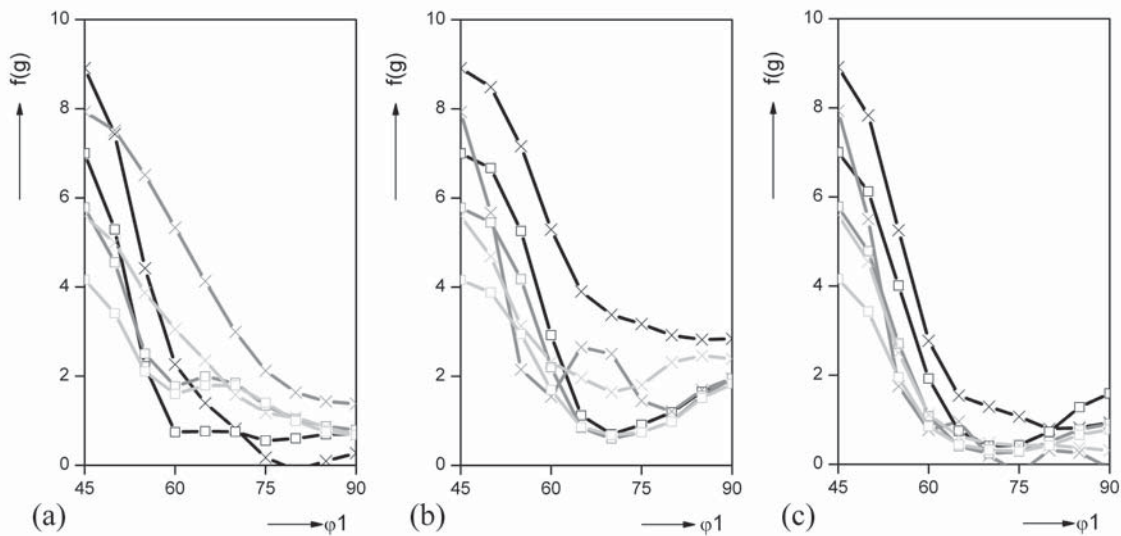


Fig. 8.17: Plots for the Cube intensity: (a) Cube ND rotation, (b) Cube RD rotation, (c) Cube TD rotation, CR70% $T = 350^{\circ}\text{C}$ for different heating rates; black: FA 20 K/s; grey: BA 0.02 K/s; light-grey: BA 0.01 K/s; X EXP \square SIM

Apparently with higher heating rate, both in simulation and experiment, the intensity of the Cube orientation increased (Fig. 8.17). Since during the low heating rate significant precipitation reactions occurred, nucleation was strongly hindered. The advantage of P and ND-rotated Cube component thus can be attributed to the in general lower nucleus number in the case of low heating rates. Further, selected preferred nucleation sites, such as at particles, were activated first (due to higher local dislocation densities in the deformation zones). Thus, these nuclei can already grow and destroy other nucleation sites which might have been activated later, by consuming the respective area. Additionally, when fewer nuclei are created more space is available for those few nuclei. They can grow to large sizes and hence, provide larger volume fractions.

8.4.2 Recrystallization kinetics

To predict the onset of recrystallization, an incubation time was modeled resolved for each microstructure grain according to the approach presented in Sec. 6.3. Accordingly, recrystallization is initiated in the CORE model as soon as the substructure has been cleared off of excess dislocations (representing a state with only geometrically necessary dislocations). The reduction of the dislocation density for different temperatures, as present during a non-isothermal heat treatment was taken into account (coupling to 3IVM+). The predicted recrystallization kinetics are displayed in Fig. 8.18.

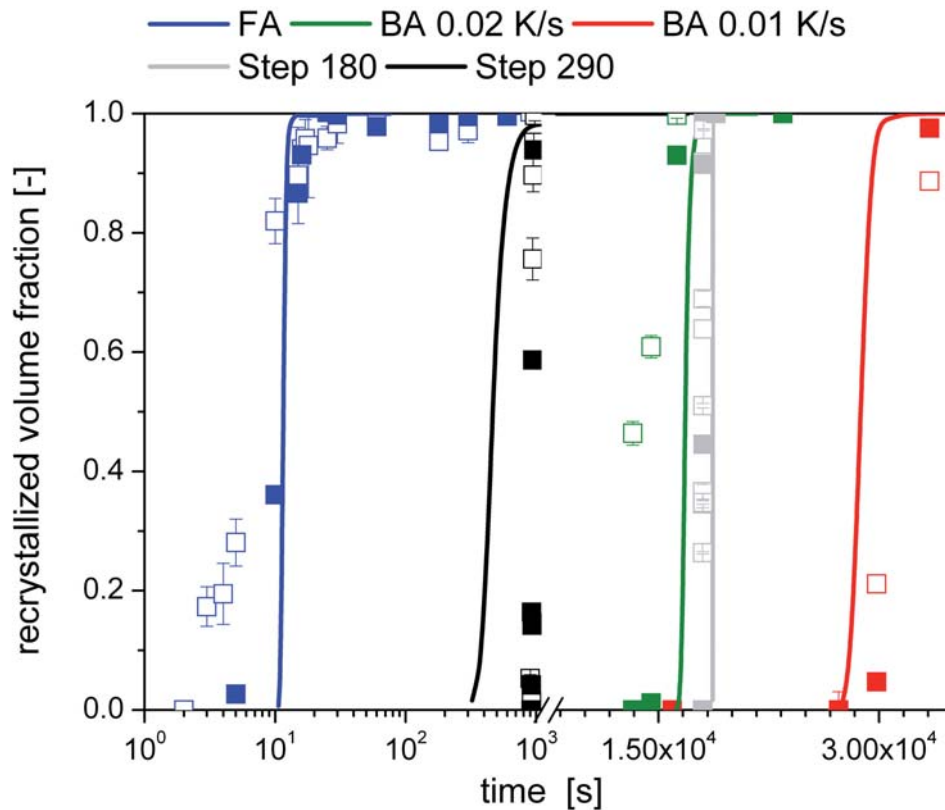


Fig. 8.18: Recrystallization kinetics for different heat treatments of a 70% cold rolled AA3103. The open squares indicate experimental measurements from hardness; full squares indicate values calculated from texture measurements. The x-axis is separated into a partly logarithmic scale and partly linear scale to display all kinetics at the same time.

The modeled curves were compared to experimental data from hardness and texture measurements (open and filled squares, Fig. 8.18, Fig. 8.4). A good agreement was obtained for a large range of different heat treatments. The presented recrystallization kinetics from simulation were obtained using *one single* parameter set. An individual perfect data fit is always possible, but not intended in the present study, since not the numerical agreement but the trends given by the underlying physical mechanisms were of primary concern. It is striking that the dependencies considered in the model seem to predict real recrystallization behavior very well.

From the recrystallization simulations (Fig. 8.18) the incubation time and hence the temperature at the onset of recrystallization can be determined. In case of the low heating rate *BA 0.01 K/s* recrystallization is initiated at $T = 284^{\circ}\text{C}$, for the heating rate of *BA 0.02 K/s* the incubation time was over after a temperature of $T = 276^{\circ}\text{C}$ was attained. These results agree very well with the onset of recrystallization at $T \sim 290^{\circ}\text{C}$ observed from optical microscopy and EBSD (Sec. 8.2).

Since the stored dislocation density within the deformed grains depends on orientation (as predicted from the deformation model GIA-3IVM+), each grain has its individual recovery kinetics and hence incubation time (COfRe-3IVM+). That means, with the incubation time model (Sec. 6.3) a nucleation rate is mimicked.

From literature it is well known that the nucleation rate is non-constant [Anderson 1945, Perryman 1955b, Lauridsen 2003, Humphreys 2004]. It was observed that initially the nucleation rate is low, rises to a very high value after the onset of recrystallization and drops quite fast again to very small values [Cahn 1950, Mould 1967] (Fig. 8.19d).

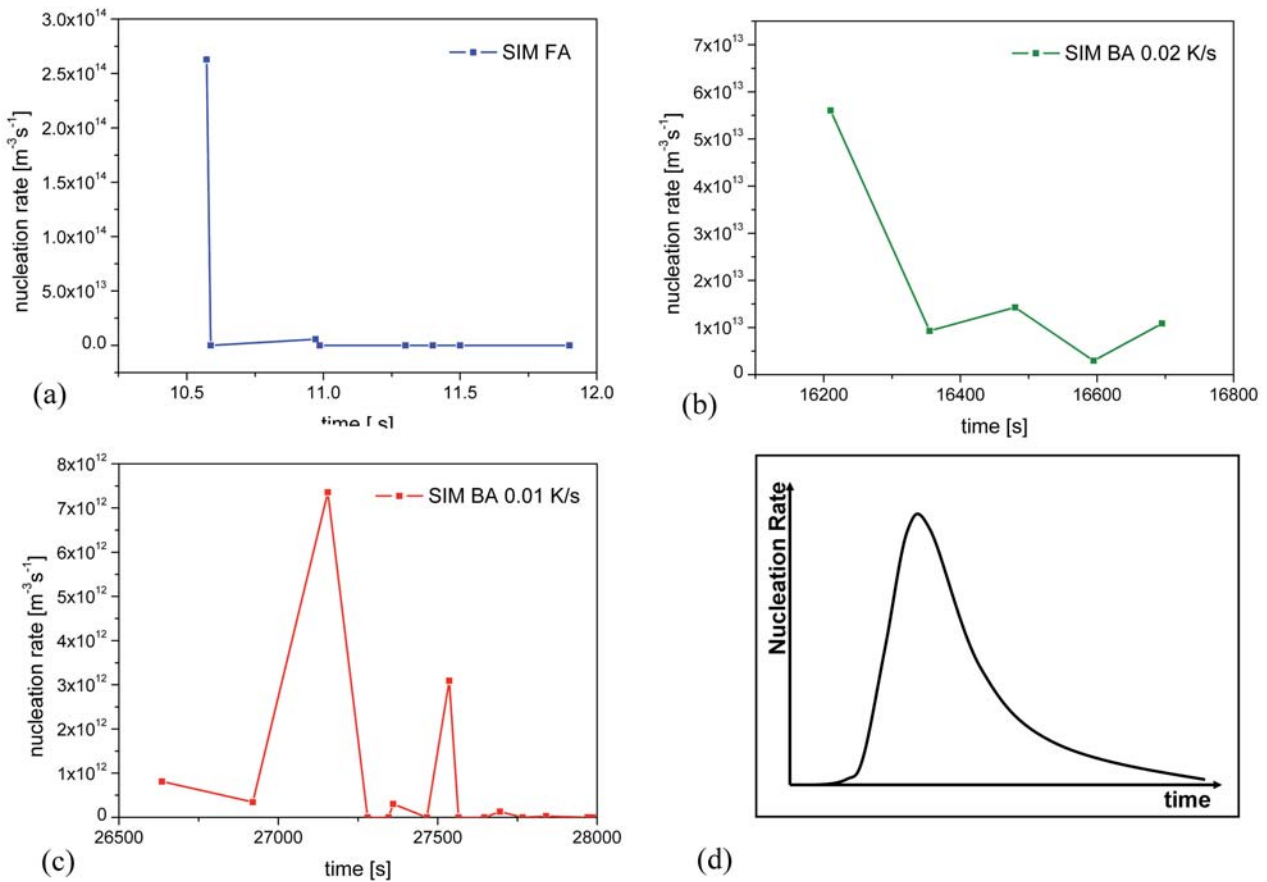


Fig. 8.19: Nucleation rates for different heat treatments of a 70% cold rolled AA3103. (a) Heating rate 20 K/s; (b) 0.02 K/s; (c) 0.01 K/s; (d) schematic of nucleation rate [Cahn 1950, Mould 1967].

The nucleation rates computed for the different heating rates are presented in Fig. 8.19. For the highest heating rate *FA* (Fig. 8.19a) nucleation is initiated immediately, and later on no significant new nuclei are developed. This is due to the destruction of further nucleation sites by the fast consumption of the volume. For a heating rate of *BA 0.02 K/s* the total number of nuclei generated in each time step is already significantly lower. For the lowest heating rate (*BA 0.01 K/s*), at first a very low nucleus number is nucleated, increases temporarily and is decreased to zero towards the end of the recrystallization process.

How fast the nucleation rate increases and decreases is strongly dependent on the heating rate in case of the simulations. After initiation with low nucleus numbers, the nucleation rate rises temporarily to higher rates. In all cases the nucleation rate is very low towards the end of the recrystallization treatment. The nucleation rate described here resembles in some points the nucleation rates often described in literature [Cahn 1950, Mould 1967]. However, the jagged curves are a direct consequence of the discretization of the cellular automaton, as well as of the input data. In general, also a strong decrease of the total nucleus number was observed with decreasing heating rate.

The overall influence of the incubation time, respectively the nucleation rate can be seen from the predicted recrystallization kinetics in Fig. 8.18 and further in the predicted recrystallized microstructures, where it influences significantly the grain size. The step annealing treatments (*Step 180*, *Step 290*) will be discussed in context with the grain sizes.

8.4.3 Grain size distribution

The modeled grain size distributions after the different annealing treatments are presented in Fig. 8.20. The grain size distributions are compared to experimental data obtained from optical

microscopy by using the line intercept method in the section perpendicular to the normal direction. The average grain sizes obtained from EBSD (by calculating the equivalent circle diameter) are indicated in brackets, as well. The x-axis in the grain size plots was adjusted in some cases for better visibility.

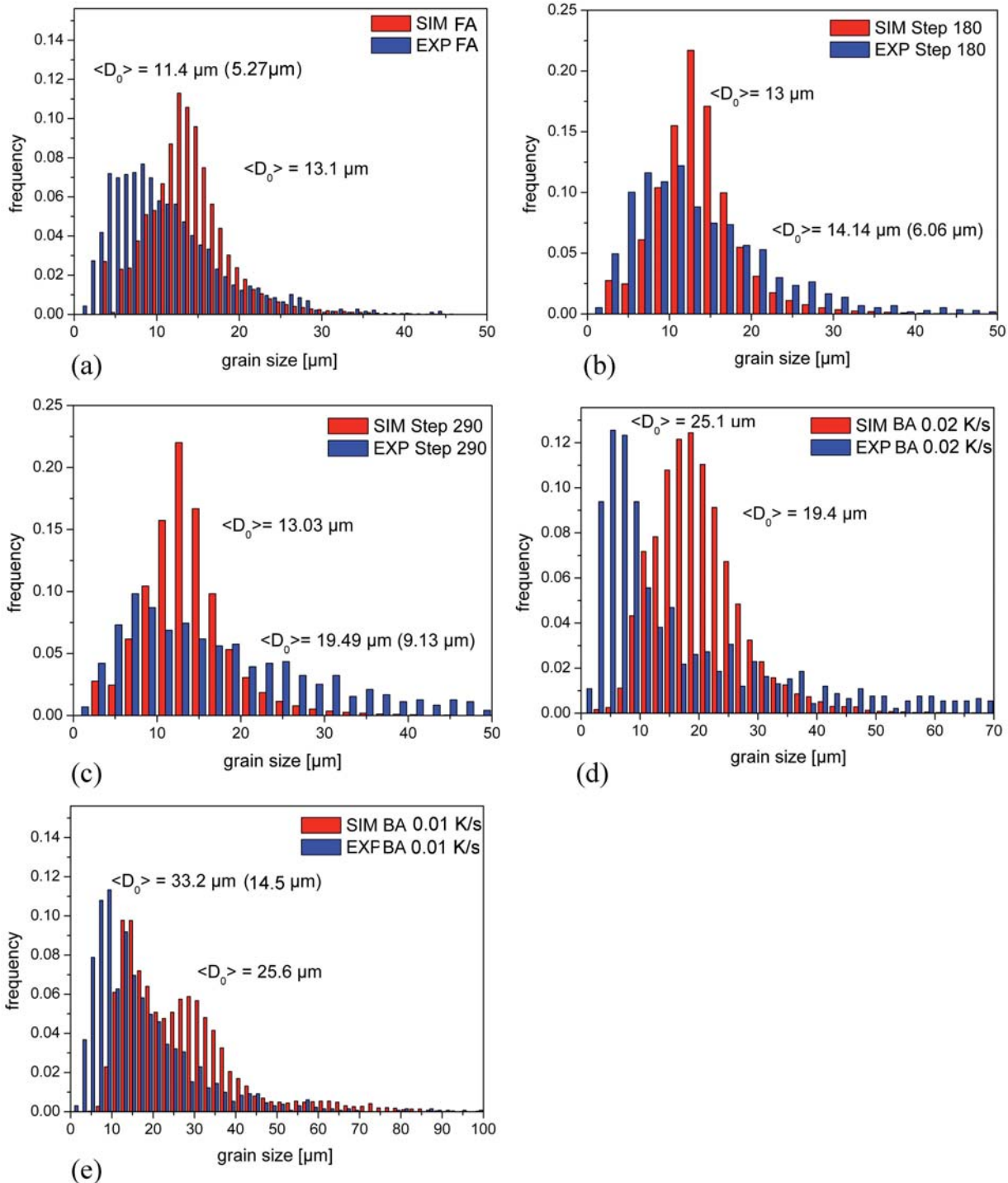


Fig. 8.20: Grain Size distributions for different heating rates (a) FA; (b) step annealing at 290°C for 15 min and 350°C; (c) Step annealing at 180°C for 5 h and 350°C; (d) heating rate BA 0.02 K/s; (e) heating rate BA 0.01 K/s for the 70% cold rolled alloy AA3103. The experimental grain size distributions were measured from optical microscopy. The average grain sizes measured from EBSD are indicated in brackets.

The modeled grain size distributions became wider for lower heating rates (BA 0.02 K/s and BA 0.01 K/s). This is in good agreement with experimental observations as well as with literature data [Tangen 2002, Liu 2008]. This was obtained as a direct result of the nucleation rates (Fig. 8.19)

considered in the model (based on orientation-dependent recovery, Sec. 6.3). According to those nucleation rates, nucleation is set off within the grains as soon as their incubation time is reached. Those nuclei can then instantaneously grow and consume the surrounding deformed microstructure, thereby destroying other nucleation sites which have not yet been activated. The result are huge pancake shaped grains and locally small island grains (Fig. 8.21f). This effect is particularly pronounced at low heating rates so that an overall lower nucleus number was predicted by the model.

The micrographs in Fig. 8.21 demonstrate the changes in microstructure owing to decreasing heating rates. The orientation images obtained by EBSD as well as the simulated microstructures are displayed in a transverse section, i.e. on a plane perpendicular to the transverse direction.

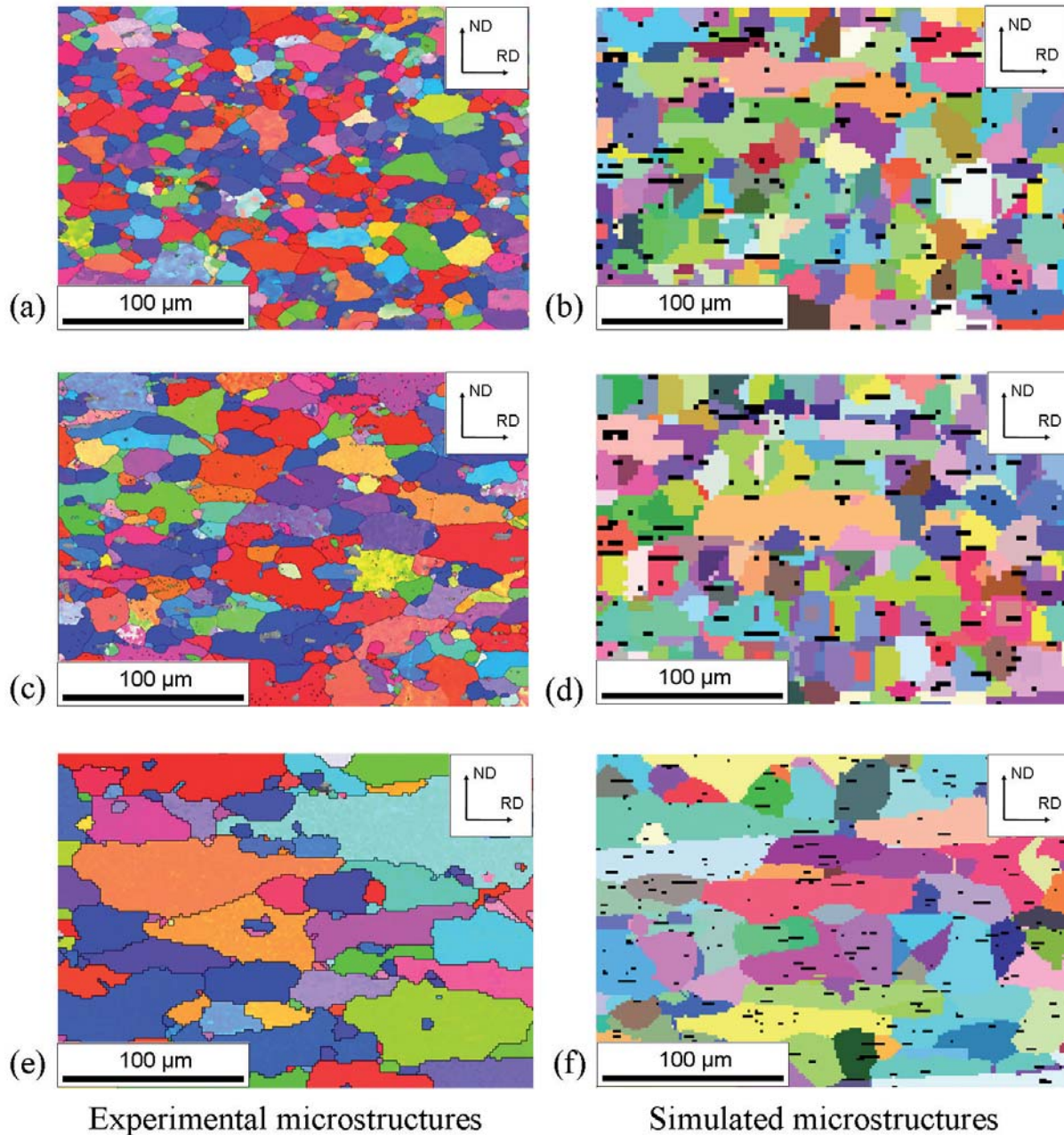


Fig. 8.21: Experimental and simulated microstructures after heat treatments with different heating rates for the alloy AA3103 (a,b) FA; (c,d) Step 290, similar microstructure for Step 180; (e,f) BA 0.01 K/s, similar microstructure for BA 0.02 K/s. For better visibility the grain orientations are indicated in random color. The EBSD maps can also be compared to the micrographs in Fig. 8.3.

It can be observed that with decreasing heating rate, the grain size becomes more elongated and pancake shaped, with their smallest extension in normal direction and the longest in rolling direction.

With respect to the average grain sizes, it is found that for a heating rate $FA\ 20\ K/s$ a very fine grain size was obtained in experiment and simulation (Figs. 8.20a, Fig. 8.21a, b). An additional recovery treatment did, however, hardly influence the final grain size in the experiments (Sec. 8.2). The same tendency was predicted by the simulations with a prior recovery treatment (*Step 180* and *Step 290*) (Figs. 8.20a, b and Figs. 8.21c, d). For very low heating rates ($BA\ 0.02\ K/s$ and $BA\ 0.01\ K/s$) significantly higher average grain sizes were predicted in accordance to experiments (Figs. 8.20d, e and Figs. 8.21e, f).

In case of the lower heating rates, in particular the nucleation stage is strongly influenced by Zener pinning, as can be seen from Fig. 8.13 ($BA\ 0.02\ K/s$ and $BA\ 0.01\ K/s$). This caused a reduction of the initial nucleus density. The nucleation rate further enables a growth advantage for those grains nucleated during incipient recrystallization. This growth advantage is the more pronounced the lower the heating rate is. In case of a lower heating rate nucleation was initiated first in the particle vicinity. During progressing recrystallization, Zener drag further increased for $BA\ 0.02\ K/s$ and $BA\ 0.01\ K/s$, causing grains with a growth advantage to grow even larger. Hence, in particular at lower heating rates larger maximum grain sizes were obtained, as visible from the microstructure in Fig. 8.21 f.

In general, the grain size predictions show a good overall tendency. However, the absolute quantities are topic for further improvements. It can be concluded, that the modeling of incubation times and thus nucleation rates leads to significant improved grain size predictions.

8.5 Effect of Orientation Dependent Growth Rates

It is also of major interest how sensitive various models along the modeling chain are to slight variations of the used input parameters. It was already shown in Chap. 7 that the microchemistry evolution is strongly dependent on the chosen model parameters and the input values used. In contrast, the deformation texture simulations predicted with GIA-3IVM+ are, however, not subject to major changes when the input parameters are slightly modified.

The sensitivity analysis in this chapter focuses more on the growth and nucleation parameters in the CORE model rather than on a sensitivity analysis of the various model inputs (ClANG, GIA). In Sec. 4.2.2 it was already discussed that the growth parameters have a significant influence on the recrystallization kinetics. It is shown in the following that they also have an effect on the grain size distribution. Fig. 8.22 displays the grain size distribution of sample $BA\ 0.01\ K/s$, where a pronounced change in microstructure occurred as previously discussed. If a nucleation rate instead of site-saturation is considered, significant changes of the grain size distribution are obtained as indicated in Fig. 8.22. Instead of a one-peak distribution as for site-saturation (Fig. 8.22c, e), a two-peak distribution is obtained (Fig. 8.22b, d). The grain size distribution (b) in Fig. 8.22 obtained with a nucleation rate resembles much more the real grain size distribution as obtained from experiments (a). However, the distributions show two peaks (Fig. 8.22 (e)), which is not observed from experiments. These two peaks are attributed to the chosen growth selection. It was previously demonstrated (Chap. 4) that the strength of growth selection (ratio between highest mobility for selected boundaries and mobility of high angle grain boundaries) has only a minor effect on the grain size distribution for the case of site-saturation. However, when a nucleation rate is considered a significant influence is observed. In case of strongly different mobilities a two-peak distribution was obtained where the two peaks are clearly separated and hence visible. The smaller the ratio between the mobilities of high angle grain boundaries and special boundaries, the smoother the transition and thus, a single peak distribution with a wide scatter width as comparable to experimental results is obtained.

With this effect in principle more realistic grain size distributions can be considered, proving that especially for lower heating rates the assumption of site-saturation is definitely wrong.

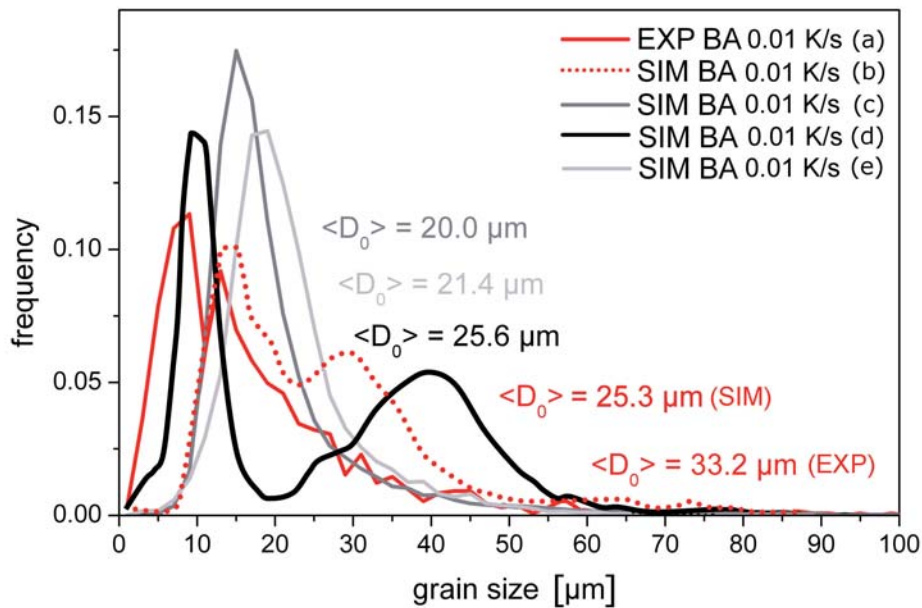


Fig. 8.22: Grain size distribution in the final recrystallized state for a heating rate 0.01 K/s in 70% cold rolled AA3103, different growth modi were considered. (a) Experiments, (b) $m_{GS}/m_{HAGB} = 1.0eV/1.1eV$, nucleation rate, (c) $m_{GS}/m_{HAGB} = 1.0eV/1.1eV$, site-saturation, (d) $m_{GS}/m_{HAGB} = 1.0eV/1.05eV$, nucleation rate, (e) $m_{GS}/m_{HAGB} = 1.0eV/1.05eV$, site saturation.

8. 6 Conclusions

In this study the influence of different heating rates on recrystallization was modeled. The effects caused by varying linear heating rates can be attributed to recovery and precipitation. A lower heating rate means a higher extent of recovery and further allows a sufficiently large time frame at elevated temperatures for diffusion processes, so that precipitation can occur before the onset of recrystallization. These dependencies were considered as outlined in the introduction (Sec. 8.1).

In the course of this study it was found that in order to capture the right tendencies in *recrystallization texture* evolution (occurrence of the particle-related texture components (P-and 22°ND rotated Cube)) when different heating rates are applied, the model must be capable of accounting for sufficiently detailed information on the nucleation spectrum from particle-stimulated nucleation. The most important contribution to the occurrence of these components was provided by the locally resolved modeling of the deformation zones with the GIA-DZ model. Thus, the modeled deformation zone components are placed in the respective grain (where they were modeled), instead of being randomly distributed throughout the microstructure. Without the consideration of the nucleation spectrum for particle stimulated nuclei (as introduced in Chap. 5) the presented recrystallization texture predictions would have not been possible. A modification of the growth selection with respect to larger misorientation angles in the range 25°-55°, instead of 35°-45° as considered so far, improved the predictions clearly. The consideration of a precipitation free zone in the particle vicinity further allowed the growth advantage of particle-stimulated nuclei, which is particularly important for lower heating rates when the total nucleus number is low.

For the prediction of more realistic *grain size distributions* the modeling of a nucleation rate was essential. This required the modeling of an orientation-dependent recovery and thus the modeling of

orientation-dependent incubation times. Further, the absolute nucleus quantity is strongly influenced by the consideration of particle-stimulated nucleation, which is the dominating nucleation mechanism in the present study. In contrast, the variation of the growth parameter had a minor effect on the width of the grain size distribution.

The modeling of the *recrystallization kinetics* required all effects outlined in the introduction (Sec. 8.1). The interplay between recovery and precipitation was already discussed in Chap. 7. In this chapter, it was highlighted that the nucleation rate and the heating rate rank among the major influences.

The tendency of all modeled quantities (microstructure, kinetics and texture) caused by a variation of heating rates in AA3103 can be adequately captured by the used modeling set-up and the combination of effects included. There is an overall good agreement between the prediction of the model and the experimental data shown. It is pointed out that the simulated quantities were not modeled independently but in conjunction. This indicates that the model has captured the essential ingredients required to describe the recrystallization behavior in a physically realistic and predictive manner.

Chapter 9

Through-Process Modeling of AA3103 Sheet Fabrication

9.1 Introduction

The aim of this section is the *through-process modeling* of texture and microstructure evolution during processing of the commercial Al-Mn alloy AA3103. It requires a most complex modeling setup including alternating cycles of deformation and annealing. Within this framework, the previously introduced and described recrystallization model CORE, which was linked to the deformation model GIA-3IVM+ and the microchemistry model ClaNG, was used to simulate the progress of recovery and recrystallization and the accompanying texture and microstructure changes. It is pointed out that the presented setup enables data transfer on the grain scale between deformation and recrystallization cycles. In this context, CORE is a preferred choice to model the inter-stand (or inter-pass) recrystallization between subsequent tandem hot rolling passes due to its temporal and spatial resolution.

9.1.1 Process description

Fig. 9.1 illustrates the conventional fabrication route for aluminum sheet. It consisted of casting of large ingots, a homogenization treatment, break-down hot rolling to 28-30 mm transfer slab gauge, tandem hot rolling to 4.2 mm hot strip, and subsequent cold rolling, resulting in the final gauge sheet with a thickness of 1.2 mm. Before the actual break-down rolling the material was preheated to 610°C. Hereby internal stresses were relaxed and elements in solid solution (e.g. Mn, Fe, Si, Cr, etc.) were precipitated. Soluble phases in the material were dissolved and micro segregation was reduced by diffusion processes while constituent phases changed their shape and were partially redissolved. After homogenization the material was cooled down to room temperature and then reheated to 430°C. After holding for some time at 430°C, the material was break-down rolled and then transferred to the hot rolling mill, which it enters at 330°C. These last annealing treatments may lead to further precipitation and growth of the existing phases and changes in the composition of constituents (from β -Al₆(Mn,Fe) to α -Al₁₅(Mn,Fe)₃Si₂). It is pointed out that the microstructural

state of the slab before hot rolling has significant influences on the down-stream microstructure and texture evolution, and thus on the final properties. The tandem rolling was carried out in three steps, followed by cold rolling and finalized with various annealing treatments. During hot rolling the initially coarse as-cast structure was transformed into a structure of considerably finer grain size. The coarse constituents were crushed and aligned in rolling direction. During cool down, further precipitation occurred from the supersaturated Al matrix, promoted by the additional deformation introduced during hot rolling. The corresponding texture and microstructure changes during processing are indicated in Fig. 9.1. The texture evolution is represented in $\{111\}$ polfigures close to center layer. The finished hot-rolled strip of 4.2 mm thickness displayed a typical hot rolling texture after coil cooling (Fig. 9.1).

9.1.2 Modeling Setup

The through-process modeling presented in this chapter started with hot rolling and took the transfer slab material as input. The corresponding microstructure was fully recrystallized and provided a low hardness of 28 Hv and, consequently, a very low dislocation density. The tandem rolling was carried out in three passes, each with 50% thickness reduction (alternating cycles of rolling and annealing) starting from a fully recrystallized as-cast transfer slab texture. After hot rolling the material was cold rolled to 50% and 70% and annealed at temperatures between $T = 300\text{ }^{\circ}\text{C} - 400\text{ }^{\circ}\text{C}$.

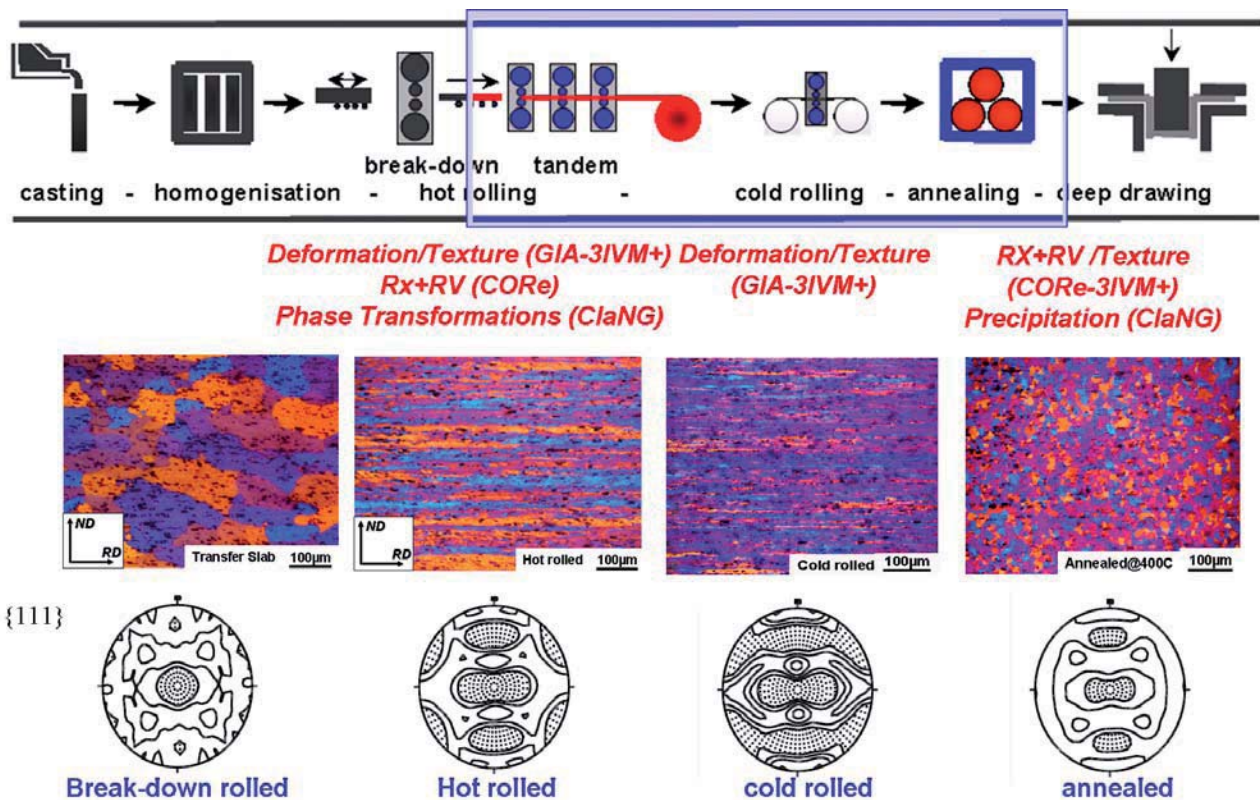


Fig. 9.1: Industrial process chain for sheet metal fabrication for the Al-1wt% Mn alloy (AA3103) from casting to deep drawing. The corresponding through-process microstructure and texture evolution is also shown. The process chain simulated in this chapter is highlighted.

For the modeling of deformation steps the advanced deformation texture model GIA-3IVM+, based on a multi-grain approach which incorporates the work hardening behavior in terms of the evolution of dislocation densities, was utilized. The influence of precipitation during annealing was considered by linking the recrystallization model to the precipitation model ClaNG, which allows tracking potential changes in Zener drag and solute drag. The material softening due to recovery was modeled with the work-hardening/softening model 3IVM+ during inter-pass and final annealing [Gurla 2007, Mohles 2008]. The ReNuc model (Sec. 3.9, [Crumbach 2006a]) and the

PSN model (Chap. 5) were used to provide the nucleation related information for the CORE model. Fig. 9.2 indicates the various interactions between the applied models.

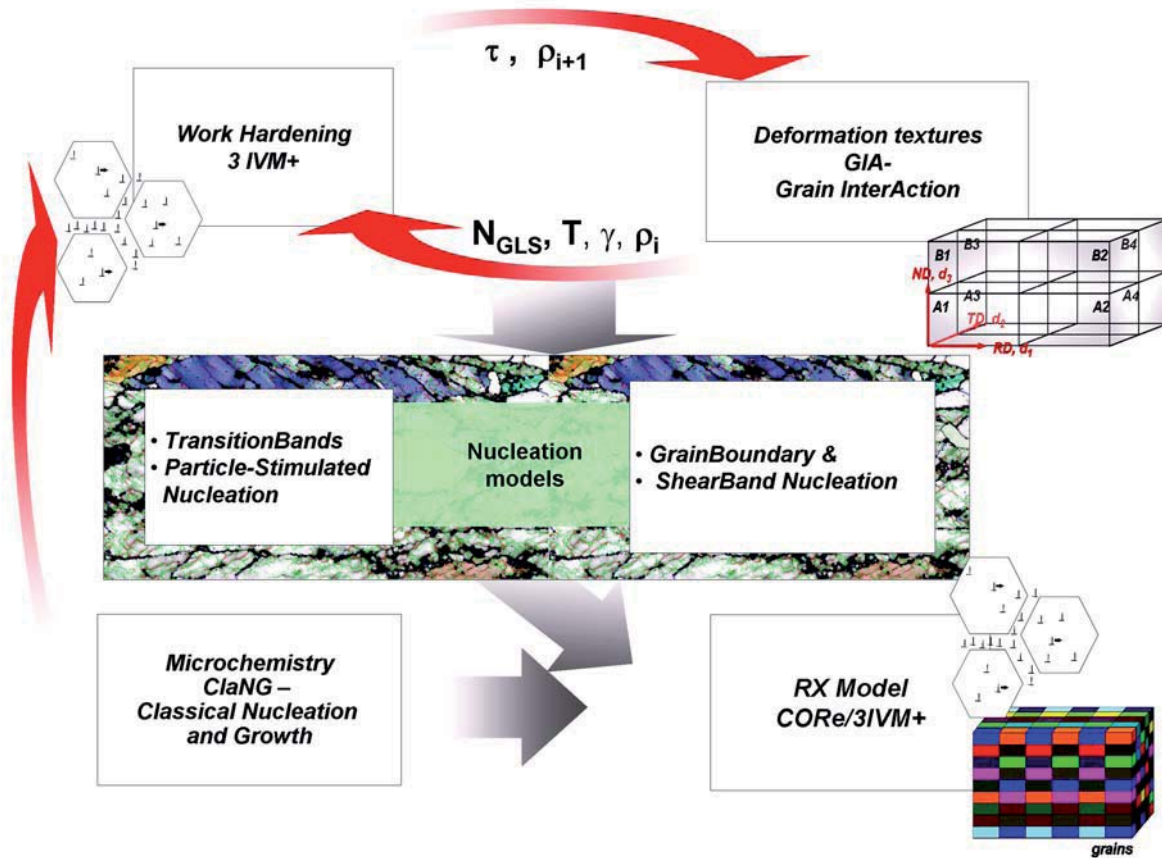


Fig. 9.2: Through-Process Modeling setup showing the interaction between the different models.

A detailed description of the input data required for CORE can be found in Sec. 3.4.

9.2 Work-hardening behavior

For deformation modeling via GIA-3IVM+ ([Crumbach 2005], Chap. 3), at first a parameter set for the work-hardening behavior of the chosen alloy AA3103 was created. For this purpose compression tests were carried out in the temperature range of $T = 25^\circ$ - $T = 400^\circ\text{C}$ for strain rates from 10^{-3} to 10^{+2} s^{-1} . The experimental flow curves were afterwards fitted using the 3IVM+-fitting program to determine the unknown model parameters. The results of the flow curve fits are presented in Fig. 9.3, and the corresponding parameter set can be found in Tab. 9.1. The work hardening behavior required for subsequent modeling of the deformation textures (GIA-3IVM+) at different temperatures and strain rates was based on this parameter set obtained from the above 3IVM+ fits (Tab. 9.1).

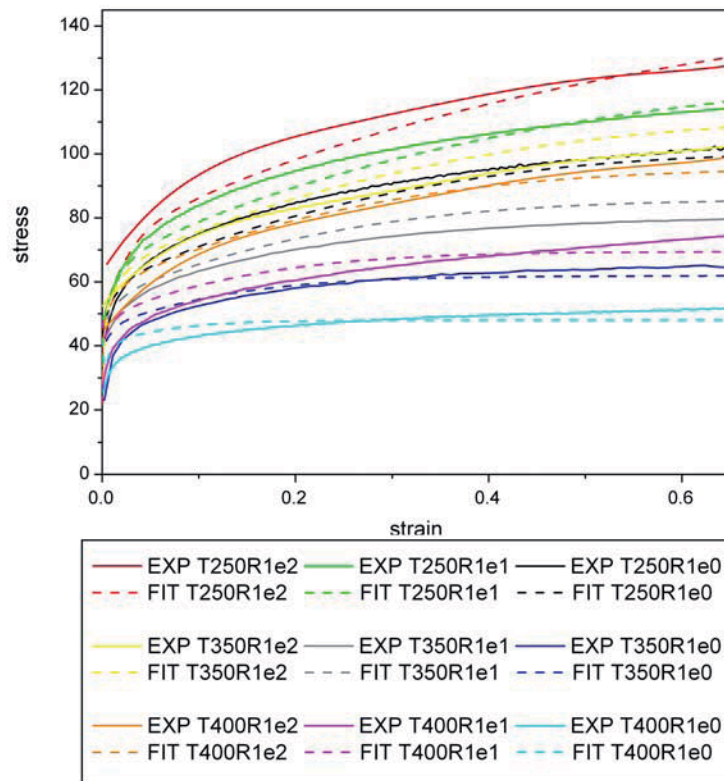


Fig. 9.3: Experimental and fitted flow curves (3IVM+) from hot compression tests for the alloy AA3103.

Tab. 9.1: 3IVM+ Fit Parameter Set as obtained from the flow curve fitting

Parameter	3IVM+ Hot Rolling Value	3IVM+ Cold Rolling Value
dAnnihil	1 b	1 b
dLock	1.14 b	1.08 b
dImmob	0.56 b	0.91 b
dClear	1.90 b	3.51 b
dClimb	5.71 b	0.75 b
volFracWall	0.18	0.17
betaLeffIntern	71.81	99.85
betaLeffWall	107.36	140.65
Alpha Taylor	0.5	0.5
D0solute	1b	1b
Vcross	66.86 b ³	75.95 b ³
Qcross	1.382 eV	1.447 eV
Qclimb	1.22 eV	1.144 eV
Rhomobil 0	4.748*10 ¹⁰	3.125*10 ¹¹
Rhointern0	6.638*10 ¹⁰	2.383*10 ¹⁰
Rhowall0	6.951*10 ¹³	6.166*10 ¹³
thermSolStrength	50.84	247.52
thermSolStrength2	1	1
athermSolStrength1	5.60	5.48
athermSolStrength2	1	1
Particle Strength	1000	1000
numActivePlanes	3	3

9.3 Hot Rolling

The texture evolution during hot rolling was simulated by using the deformation texture model GIA-3IVM+ according to strain paths provided by FEM [courtesy Institut für Bildsame Formgebung, RWTH Aachen]. For hot deformation as modeled with GIA-3IVM+ additionally the activation of non-octahedral slip systems of type $\{001\}\langle 011\rangle$ was taken into account.

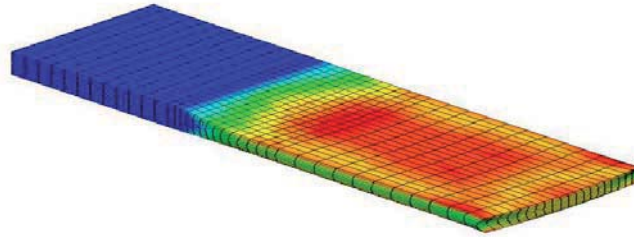


Fig. 9.4: FEM simulation showing gradient of temperature during hot rolling.

Two specific sample locations were of interest with respect to the microstructure gradient developed during experimental hot rolling. Fig. 9.4 reflects the temperature gradient developed during hot rolling from surface to center layer. Accordingly, elements close to the sheet center ($s=0.2$) and close to the surface layer ($s=0.8$) were selected in the FEM output, and the corresponding pathline files were transferred to GIA-3IVM+ to accurately model the deformation texture using a texture discretization into 4000 single orientations. The simulations were carried out in two subsequent passes as indicated in Fig. 9.5. The recrystallized volume fraction and texture at inter-stand times were modeled with CORE. In the following three different variants of virtual thermo-mechanical processing are suggested (Fig. 9.5). As initial texture for the 1st pass served the transfer slab texture in Fig. 9.6. It is mainly comprised of the Cube texture component, which is slightly scattered along normal direction with an intensity of about 7.3.

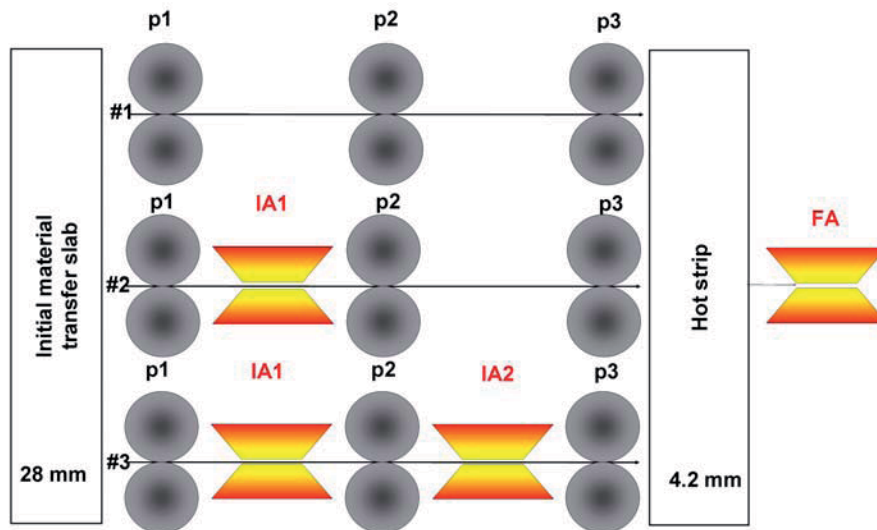


Fig. 9.5: Modeling scheme for the tandem rolling. Three modeling variations are presented. For the validation of CORE a final annealing step (FA) is included which is not part of the through-process scheme. (IA = Interannealing; p=pass).

All textures presented further on are displayed as sections through the Euler orientation space for $\varphi_2=0^\circ, 45^\circ, 65^\circ$, to reveal the characteristic features.

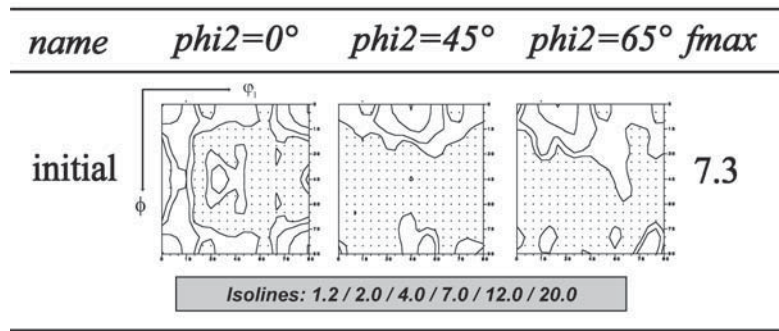


Fig. 9.6: Initial Texture of transfer slab before tandem hot rolling. This is the initial texture input for the deformation texture simulations, presented are characteristic sections through Euler space.

After the 1st hot rolling pass, inter-pass recrystallization was modeled with CORE. In order to obtain the required information on transition band nucleation for subsequent recrystallization modeling, a GIA Split Up analysis [Crumbach 2004a, 2005] was performed. Nucleation data associated with other nucleation mechanisms was generated according to the procedure outlined in Secs. 3.9 and 5.5. Beside the different nucleation parameters, also the deformation texture after different rolling passes, the respective dislocation densities, and the average grain size were used as input data for the CORE model.

The recrystallization simulations were carried out under the assumption of growth selection with preference of $40^\circ\langle 111 \rangle$ relationships. During hot rolling some changes in microchemistry can occur, causing Zener drag and solute drag. Both effects can hinder recrystallization, or even suppress recrystallization completely. In order to consider both drag effects, the solute content of 0.317 wt% manganese as measured from TEP measurements (see Tab. 9.3) was assumed, and the dispersoid relevant data was taken from the ClaNG simulations shown below (Figs. 9.18-9.20). Accordingly, for the Zener drag a particle volume fraction of 1.34 vol % and an average dispersoid radius of 862 nm were assumed at the beginning of the simulation. The temperature at the beginning of hot rolling simulations was $T = 330^\circ\text{C}$ and approximately $T = 315^\circ\text{C}$ at roll exit.

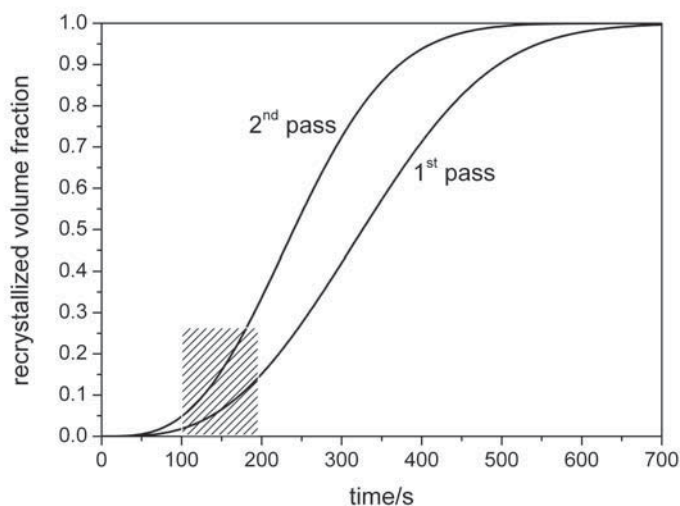


Fig. 9.7: Recrystallization kinetics as modeled with CORE for inter-pass recrystallization during hot rolling of AA3103.

Fig. 9.7 reflects the kinetics for the inter-pass recrystallization during the 1st and 2nd, respectively between the 2nd and 3rd pass modeled with CORE. It shows that during reversible rolling, which allows a time window of 100 s-200 s for inter-pass recrystallization, a maximum amount of 20% volume fraction can be recrystallized. The recrystallization in the 2nd pass was hereby faster than in

the 1st pass, since the higher deformation already stored from the previous pass lead to a higher number of nucleation sites, likewise growth and therefore faster kinetics. The obtained recrystallized volume fraction is in good agreement with experiments. From an analysis of the experimental hot rolling microstructure a maximum degree of 20% recrystallization at inter-stand times can be estimated, since the microstructure displays basically long elongated bands, which are very unlikely to be caused by recrystallization (Fig. 9.12a).

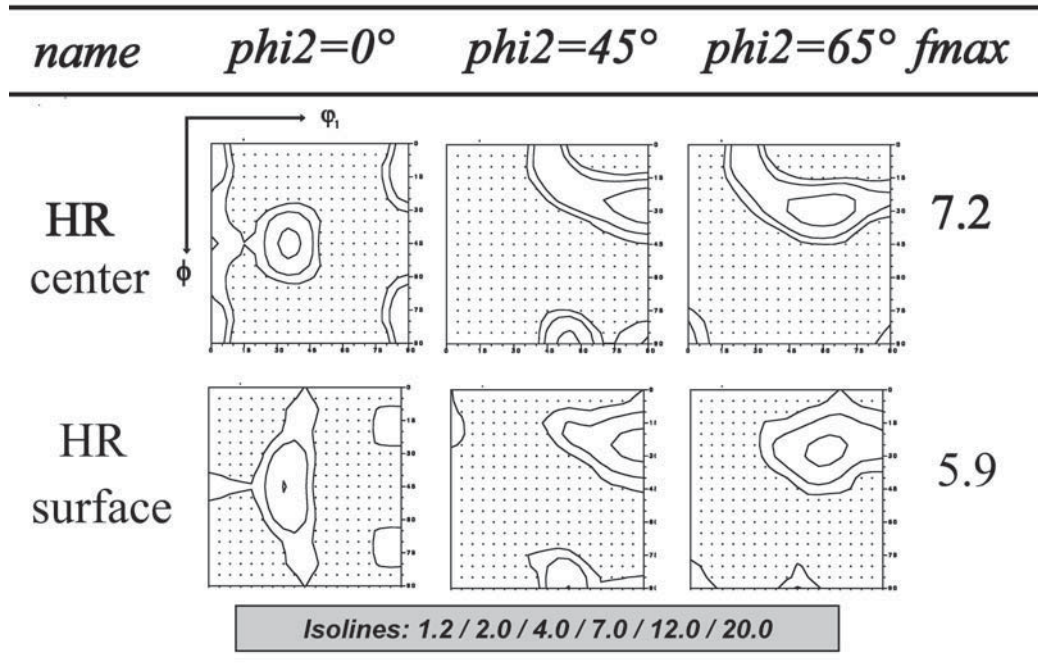


Fig. 9.8: Experimental texture after hot rolling (HR) close to the center layer ($s=0.2$) and close to the surface ($s=0.9$), serves as reference for the simulations of tandem hot rolling, presented are characteristic section through the Euler space.

Fig. 9.8 illustrates the experimental hot rolling textures at two different locations of the cross section. Starting from the center layer, the texture represents mainly orientations along the β -fiber and some Cube component, the texture close to the surface suggested shear texture components, close to the 45° ND rotated Cube component.

Fig. 9.9 shows the results for the modeled hot rolling textures. Fig. 9.9a displays the final hot rolling texture close to the surface layer. Compared to experimental results a good agreement in the modeled texture components and maximum intensities was obtained. The simulated textures close to the center layer, however, show much stronger intensities along the β -fiber compared to experiments (Fig. 9.9b). The predicted hot rolling textures in the sheet center layer differ in the amount of remaining Cube component.

For route 2 (Fig. 9.9b Route #2) with a recrystallized volume fraction of 20% during the 1st and 2nd pass similar results were obtained as for route 1, without any inter-pass recrystallization. Route 3 considered hot rolling with inter-pass recrystallization (20% Rx) between each pass. Of the chosen modeling variations for hot rolling, route 3 gave the best agreement with the experimental texture (Fig. 9.8 $s=0.2$, Fig. 9.9b Route #3). In none of the simulations a TD rotated Cube component was found. This can be attributed to the lack of such grain orientations after deformation texture simulations with GIA. Thus, these texture components are not available as nuclei for the recrystallization simulations with CORE.

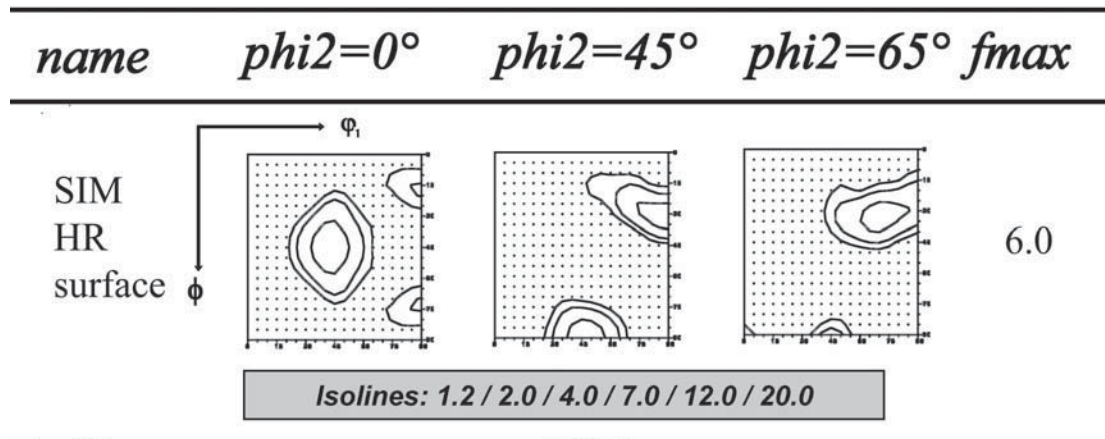


Fig. 9.9a: Simulated textures after hot rolling close to the surface. Since it is sure that interpass recrystallization takes place close to the surface layer 100% recrystallization was modeled at interpasses.

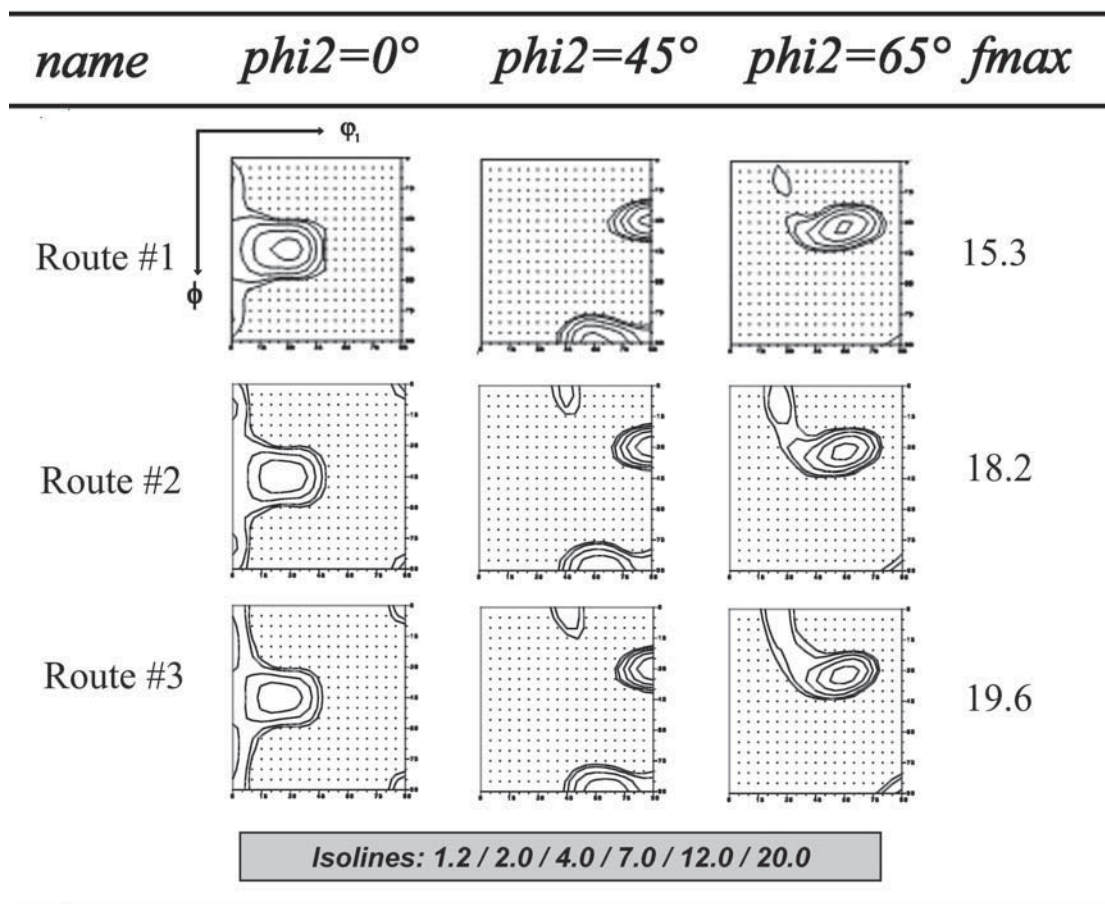


Fig. 9.9b: Simulated textures for different hot rolling routes.

For a better comparison of the chosen hot rolling procedures the fiber plots (Fig. 9.10) are indicated as well. The best agreement with experiment was obtained for route 3, since it reveals a Cube intensity similar to experiments. The overall β -fiber intensity was higher in all three cases compared to experimental observations. This is commonly observed for deformation textures modeled with GIA [Crumbach 2005].

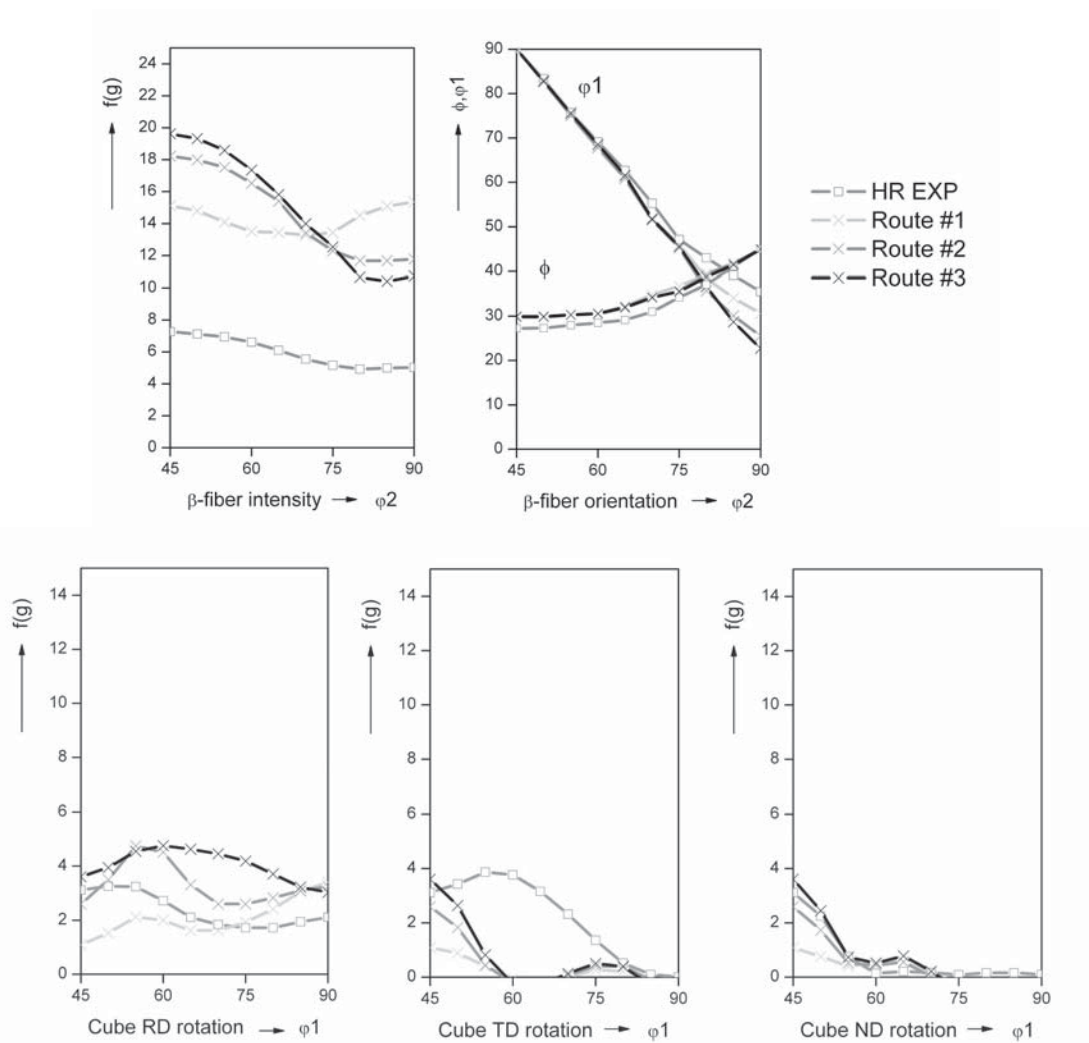


Fig. 9.10: Skeleton plots of the modeled hot rolling textures (with respect to max. Cube and β -fiber intensities), compared to the experimentally measured hot rolling texture for alloy AA3103. Route #3 gives the best agreement with experiments.

9.4 Coil Cooling

Starting from the modeled hot rolling textures (Fig. 9.9), subsequently recrystallization texture simulations were performed at $T = 400^\circ\text{C}$ for routes 1 and 3. This step was carried out for validation reasons only, to select the appropriate hot rolling procedure for further modeling. This additionally coil cooling step was not considered in the subsequent through-process modeling as outlined in Sec. 9.1. For the recrystallization simulations in case of coil cooling the input data from the last GIA-3IVM+ rolling step was used. The considered quantities were the grain orientations, dislocation densities and average grain size from GIA, and information on nucleation sites (ReNuc, GIA-DZ (Sec. 5.3)). For the recrystallization modeling, also growth selection, Zener drag and solute drag were taken into account. The parameters were the same ones as used for the previously demonstrated hot rolling simulations. Fig. 9.11 displays the modeled recrystallization textures after coil cooling in comparison to the experimental texture. Route 1 revealed a weak rolling texture with no remaining Cube component. This is due to the more random nucleus texture obtained after hot rolling simulation without inter-pass recrystallization. Route 3 however, showed more Cube components with a volume fraction of 5.5% compared to 9% in the experimental texture.

The texture seemed less smooth than the experimental one due to a smaller calculate number of recrystallization nuclei than suggested from the experimental grain size obtained after

recrystallization as indicated in Fig. 9.12b. However, the main features of the recrystallization texture were captured (Fig. 9.11), and the overall texture intensity for route 3 was in good agreement with experimental data.

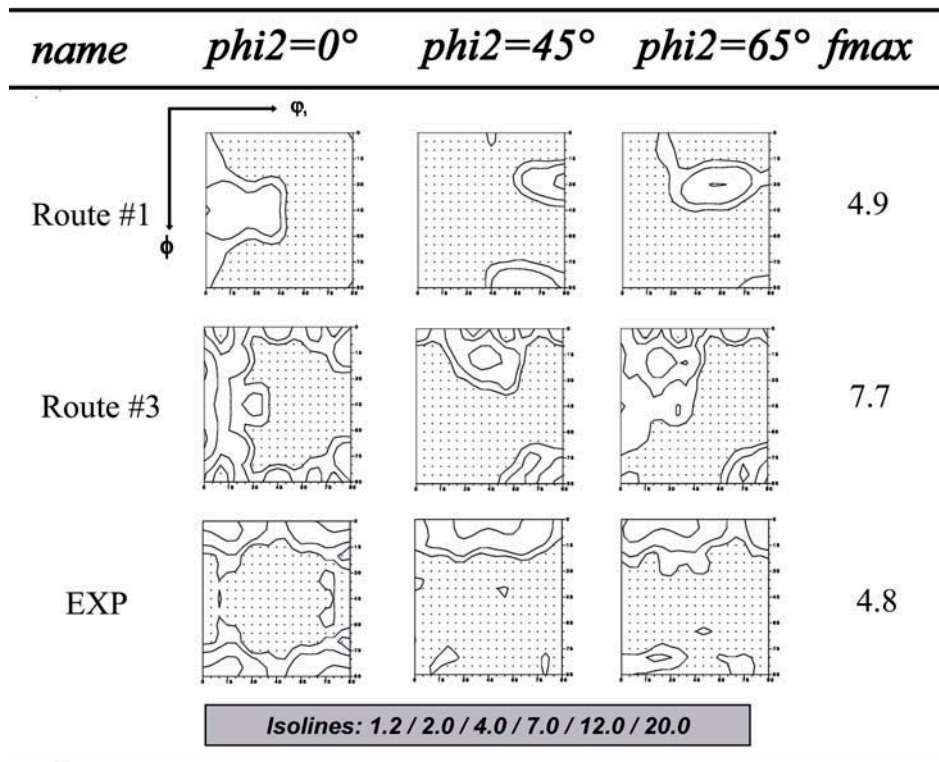


Fig. 9.11: Simulated annealing textures for different hot rolling routes in comparison to experimental texture at 400°C. Route #2 was not presented, since it resembles route #1 (EXP = experiment).

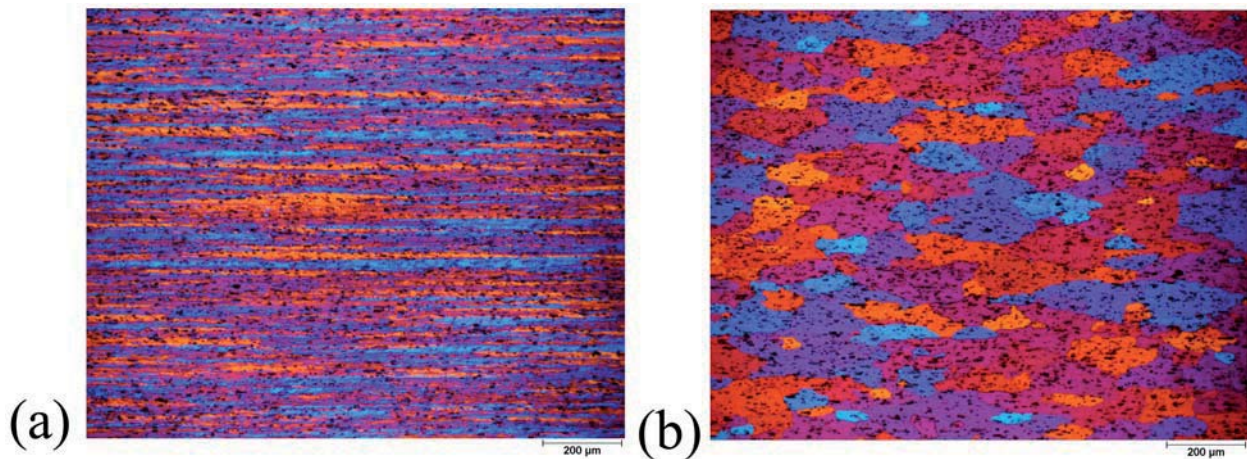


Fig. 9.12: Microstructure of (a) hot rolled microstructure and (b) hot rolled material annealed at $T=400^\circ\text{C}$ for 1 h. The microstructures are shown in the RD-ND plane (RD= rolling direction, ND = normal direction).

As discussed in Sec. 9.3, the modeled hot rolling texture rendered too high intensities of rolling texture components. This is probably due to the fact that coil cooling after hot rolling was not considered. During coil cooling, recovery and recrystallization processes are likely to occur and thus reduce the deformation texture components. However, the missing presence of the Cube component for route 1 cannot be explained by this fact. Without inter-pass recrystallization (Fig. 9.9b Route #1), only rolling texture components were observed in the final recrystallization texture (Fig. 9.11 Route #1). The intensity of the Cube orientation decreased slightly throughout the

hot rolling process modeled with GIA, even though, non-octahedral slip systems were considered. Of course, the Cube intensity decrease happened much more slowly than during cold rolling.

This observation indicates that at least small amounts of recrystallization need to occur during inter-stand times to promote the Cube component. Inter-pass recrystallization indeed prevents a strong degradation of the initial Cube component during rolling, as confirmed by the texture evolution for route 3 (inter-pass recrystallization with a recrystallized volume fraction of 20%), which showed some retained Cube component. The modeled recrystallization texture (Fig. 9.11 Route #3) after hot rolling was in good agreement with the experimental texture.

It should be noted that the results of multi-step simulations can be very sensitive to small variations in prior processing steps. This holds especially for the Cube component as seen from the results presented in this section.

The crucial point to be shown with this additional annealing treatment was that Cube orientations are actually present in the modeled recrystallization texture. This is seen as a mandatory validation of the CORE model.

9.5 Cold Rolling

In this section, the modeling of the through-process chain is continued based on Sec. 9.3. After hot rolling (route 3), without intermediate recrystallization, the material was deformed by plane strain to $\varepsilon_{VM} = 0.7$ and 1.2, respectively 50% and 70% thickness reduction.

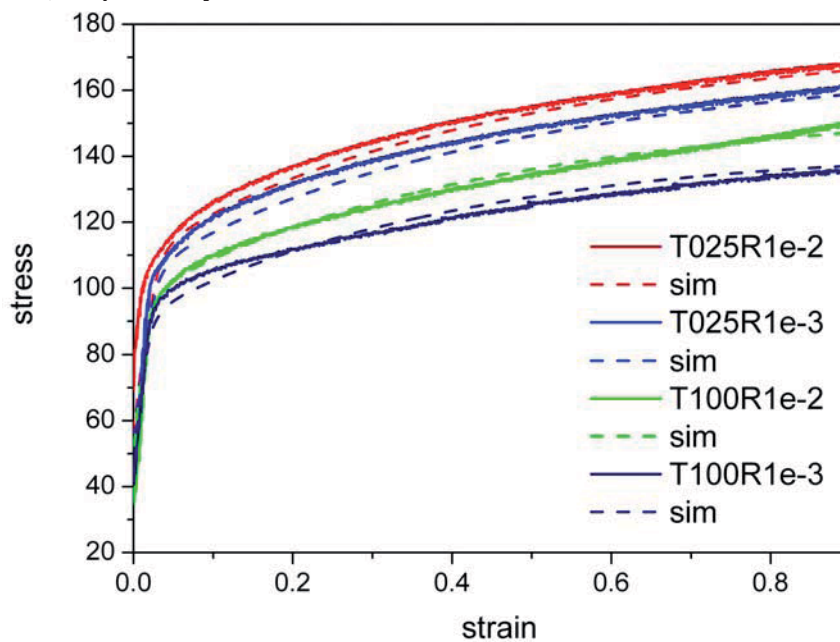


Fig. 9.13: Fitted (3IVM+) and experimental flow curves from cold compression test for alloy AA3103. The parameter set can be found in Tab. 9.1.

The simulated hot rolling data (Fig. 9.9b Route #3) (essentially the texture) was used as input for a cold rolling simulation with the GIA-3IVM+ model for cold rolling reductions of 50% and 70%, respectively. The setup ensures that the texture, the number of slip systems N_{GLS} that had been activated previously and the accumulated in-grain misorientations IGM [Crumbach 2005] are used continuously throughout all rolling steps. The work hardening behavior was fitted with the improved 3IVM+ on experimental flow curves in the range of $T = 25\text{ }^{\circ}\text{C} - 100\text{ }^{\circ}\text{C}$ and strain rates of 0.1 s^{-1} , 0.01 s^{-1} and 0.001 s^{-1} (Fig. 9.13). Fig. 9.14 displays the macrotextures obtained after 50% and 70% cold rolling reduction. The skeleton plots in Fig. 9.15 show the corresponding β -fiber orientations and intensities.

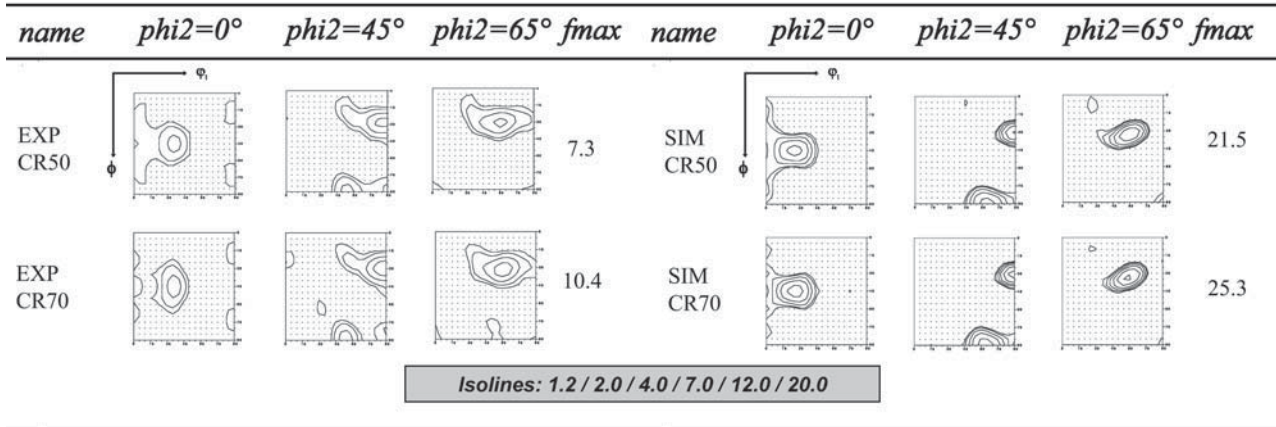


Fig. 9.14: Experimental and modeled deformation textures represented in selected sections through the Euler space showing the main deformation texture components. Compared are the results for cold rolling reductions of 50% and 70% in the material AA3103 (EXP = experimental textures, SIM = simulated textures).

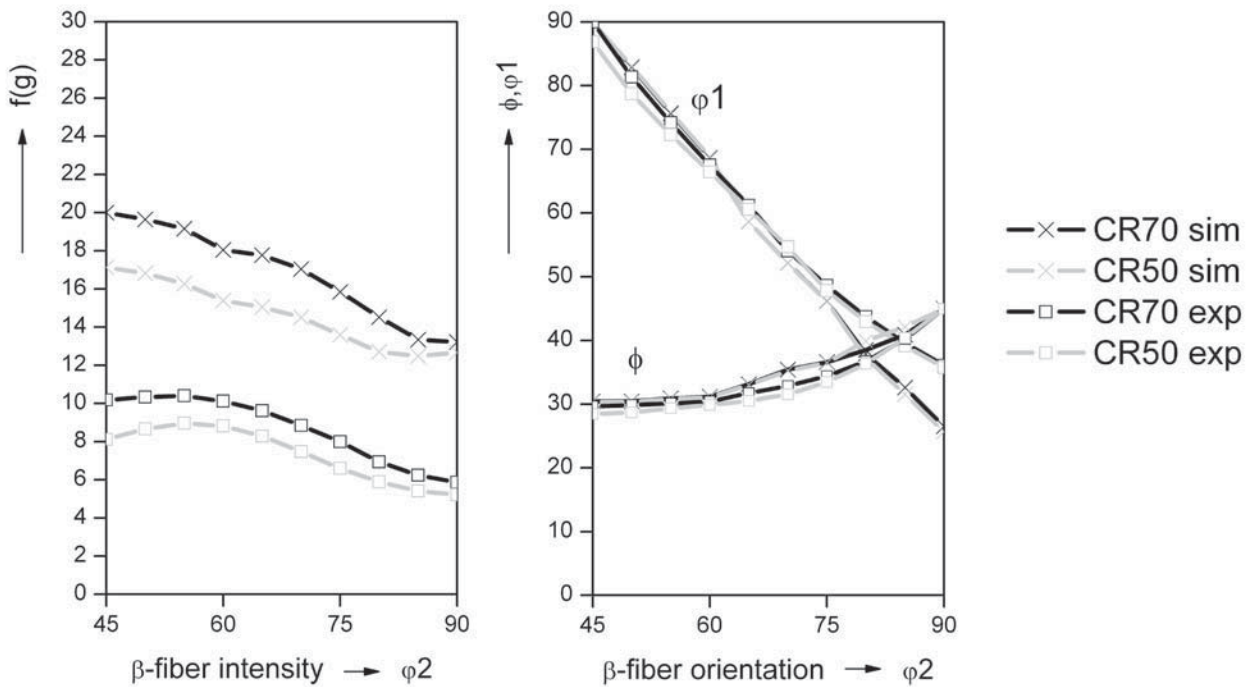


Fig. 9.15: β -fiber intensities and orientation for cold rolling reductions of 50% and 70% for experimental and simulated textures.

The deformation textures predicted with GIA-3IVM+ show good agreement with the measured deformation textures after cold rolling. The advantage of considering the whole through-process setup (sim TPM) over cold rolling textures modeled from experimental hot rolling textures (sim EXP) is reflected in Fig. 9.16a. It shows that the distribution of the main deformation texture components is different than observed in experiments, e.g. the Cu-intensity is overemphasized and the Brass-intensity is underestimated compared to experiments (Fig. 9.16a). In contrast, the predictions made based on the through-process modeled deformation texture are significantly better and in much better agreement with experiments.

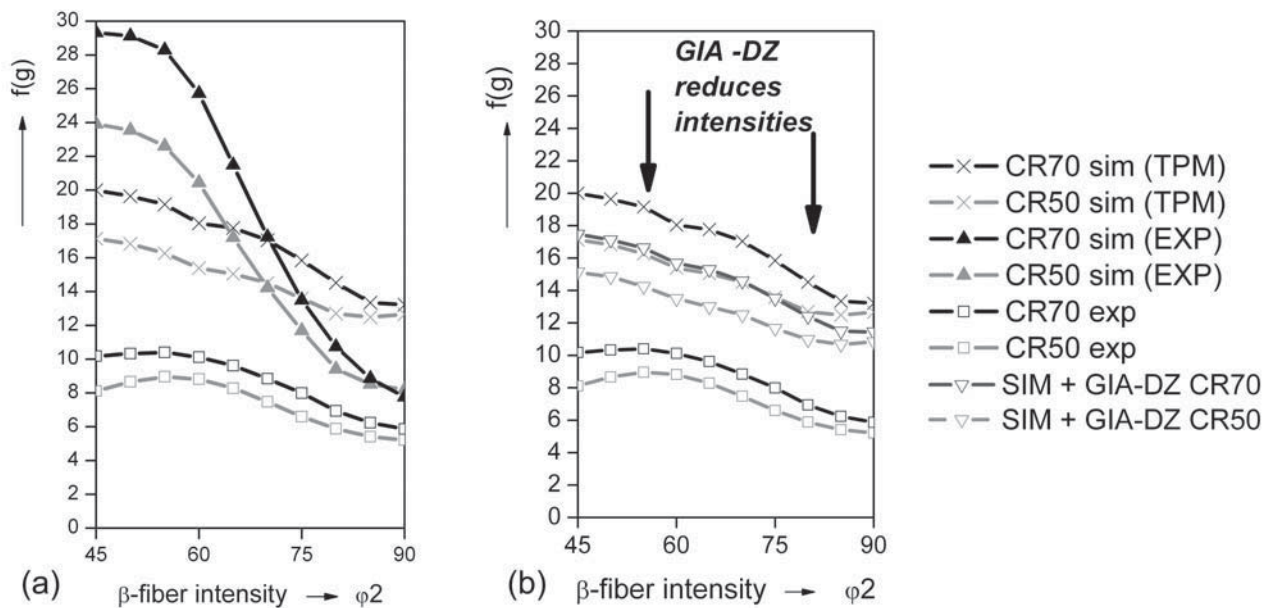


Fig. 9.16: (a) β -fiber intensity for rolling textures predicted from a through-process setup (TPM) and those modeled from an experimental hot rolling texture (EXP) (b) β -fiber intensity showing the improved intensities under consideration of using GIA-DZ for a description of the deformation zones developing during deformation in the vicinity of constituent particles.

To turn back to the through-process modeling: It can be observed from Fig. 9.15 that the intensities of the deformation texture components are still higher than experiments suggest. The reason is that the more inhomogeneous deformation in the deformation zones cannot be captured by the present deformation texture model since it is a model based on homogeneous deformation within the grains. In Chap. 5 the GIA-DZ model was proposed to take such inhomogeneities into account. Fig. 9.16b reflects that the additional consideration of the deformation zones leads to a significant improvement in the deformation texture prediction in terms of intensities. By considering the local rotations within the deformation zones as calculated with the GIA-DZ model (Sec. 5.3) causing a randomization of texture, an improved deformation texture prediction was obtained (Fig. 9.16b).

For further simulation of the final annealing, however, the results without GIA-DZ were used, since data for the number of activated slip systems N_{GLS} cannot be predicted with GIA-DZ. For further improvements of the deformation texture predictions in the framework of a TPM chain, the orientations from GIA-DZ could be provided with the maximum number of activated slip systems (24 for fcc) accounting for the strain localization. Thus, the deformation textures modeled under consideration of strain inhomogeneities could be considered further during recrystallization simulations.

9.6 Final Annealing

For modeling the final recrystallization textures, at first the deformation texture simulations were analyzed with respect to nucleation relevant data [Crumbach 2005, 2006a]. Beside the discretized deformation texture and the deformed grain size after the cold rolling simulations, further the dislocation densities, number of slip systems activated during deformation N_{GLS} and the in-grain misorientation IGM were analyzed (Fig. 9.17). Within the ReNuc model those parameters represent sub-structural quantities that are related to the nucleation efficiency (Chap. 3).

It was observed that the highest stored dislocation densities after deformation evolved in the deformation texture components as to be expected. It is further pointed out that higher initial dislocation densities are obtained as a result of through-process texture modeling than when an experimental hot rolling texture is used as input for the cold rolling simulations, e.g. for 50 % cold

rolling ($5.71 \cdot 10^{13} \text{ m}^{-2}$ instead of $2.389 \cdot 10^{13} \text{ m}^{-2}$) and for 70 % cold rolling ($8.34 \cdot 10^{13} \text{ m}^{-2}$ instead of $3.081 \cdot 10^{13} \text{ m}^{-2}$).

The highest number of activated slip systems during the hot rolling and cold rolling process was found for the Cube orientation, which will thus have a high probability to develop nuclei during subsequent recrystallization simulations. The highest in-grain misorientation *IGM* was obtained for the S/R orientation, which means that those grains preferentially develop transition band nuclei. Fig. 9.17 summarizes the analyzed sub-structural quantities for the different rolling reductions resolved according to orientation classes.

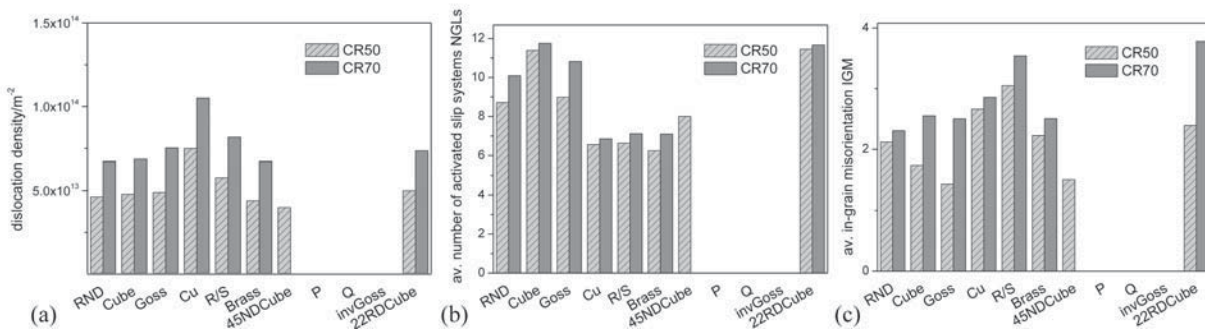


Fig. 9.17: Characteristic parameters as input for the recrystallization model CORE analyzed with respect to the ideal orientations presented as average values of (a) dislocation density, (b) number of activated slip systems during deformation (NGLs), and (c) in-grain misorientation gradients (IGM).

9.6.1 Precipitation Modeling

As presented in Chap. 3, various input data is required for a recrystallization simulation with the CORE model. Besides deformation related data this includes also the temporal evolution of microchemical quantities during the heat treatment. In the following only isothermal annealing treatments were considered. The microchemistry changes in terms of manganese solute content, dispersoid volume fraction and radius were modeled first. To predict the microchemistry changes during the final annealing treatment the whole thermo-mechanical treatment of those samples starting from homogenization at $T = 610 \text{ }^\circ\text{C}$, preheating at $T = 430 \text{ }^\circ\text{C}$ over break-down rolling, hot rolling, cold rolling to the final annealing treatment was modeled. The initial elements in solid solution are given in Tab. 9.2.

Tab. 9.2: Initial matrix composition of the alloy AA3103 as used as input for the ClaNG simulations.

<i>Al</i>	<i>Cr</i>	<i>Cu</i>	<i>Fe</i>	<i>Mg</i>	<i>Mn</i>	<i>Si</i>	<i>Ti</i> [wt%]
<i>rest</i>	<0.01	<0.01	0.03	<0.01	0.9	0.062	0.011

The microchemistry changes were modeled with the classical Nucleation and Growth model ClaNG [Schneider 2006] according to the solute content of manganese as measured from thermo-electric power measurements TEP and resistivity measurements (Tab. 9.3) (courtesy of Hydro Aluminium). Precipitation was modeled for the case of 70% cold rolled material. Since previous calculations had shown that the effect of different initial dislocation densities for the precipitation behavior is negligible under the given circumstances, the same input was used for the recrystallization simulations after 50% cold rolling reduction (Chap. 7).

Tab. 9.3: TEP and resistivity measurements for samples of AA3103 at different processing conditions [courtesy of Hydro Aluminium].

name	TEP css, Mn [wt%]	R4.2K[mΩ]
transfer slab	0.317	0.03188
hot rolled	0.2811	0.02287
cold rolled 70%	0.282	0.08115
CR70 + T400°C 5min	0.2532	0.07609
CR70 + T350°C 30min	0.2586	0.07181
CR70 + T330°C 45s	0.2155	0.07707
CR70 + T315°C 45s	0.2038	0.07746
CR70 + T300°C 5min	0.2496	0.07335
CR70 + T290°C 15min	0.2191	0.06767
CR70 + T290°C 25min	0.2209	0.07012

For a consideration of the impact of the deformation steps during thermo-mechanical processing, the hardness values were related to a yield stress. From the yield stress dislocation densities were interpreted, which are furthermore used as input for the ClaNG model. The reduction of dislocation density due to softening during annealing was derived analogously. The corresponding graphs displaying the simulated evolution of solute content, dispersoid radius, and volume fraction are presented in Figs. 9.18 to 9.20.

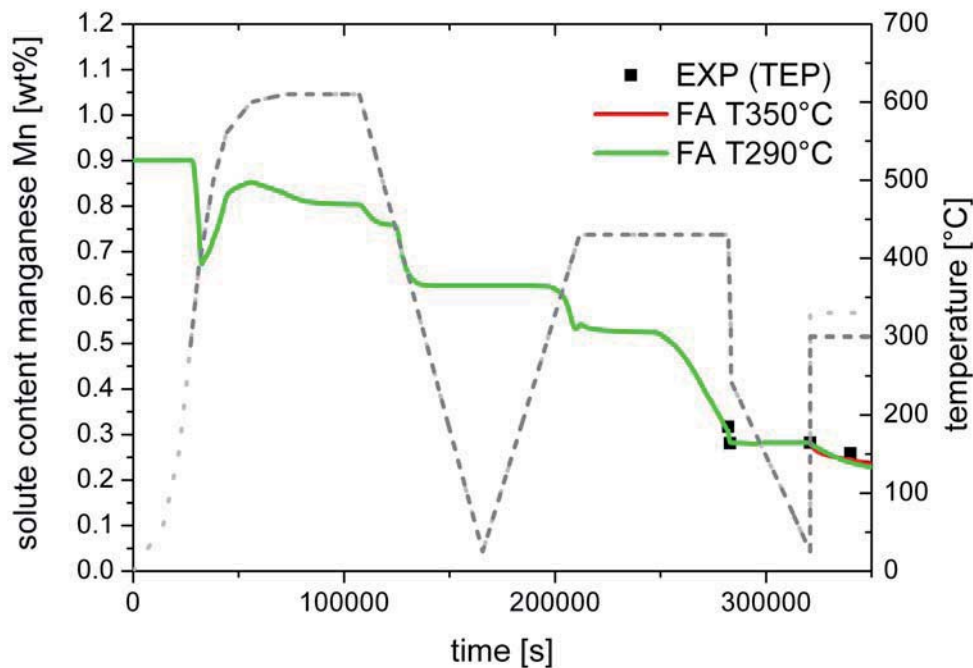


Fig. 9.18: Solute content as calculated with ClaNG for two different rolling reductions 50% and 70%. The Mn solute content is displayed over time for two different temperatures $T=290^{\circ}\text{C}$ and $T=350^{\circ}\text{C}$. Experimental data from thermo-electric power measurements is indicated by black squares. The grey dotted / dashed lines indicate the corresponding temperature profiles.

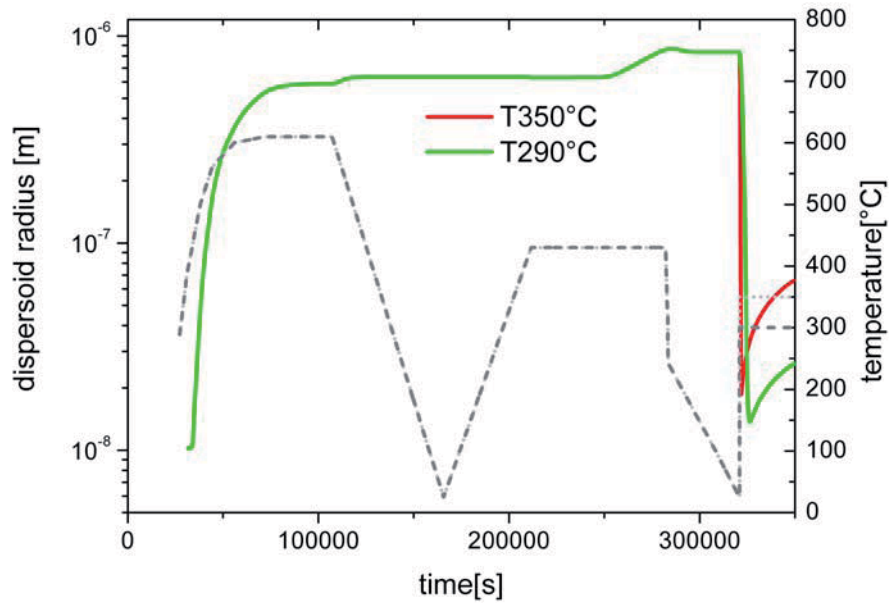


Fig. 9.19: Dispersoid radius as calculated with ClaNG for two different rolling reductions 50% and 70%. Evolution of dispersoid radius of the phase Al_6Mn .

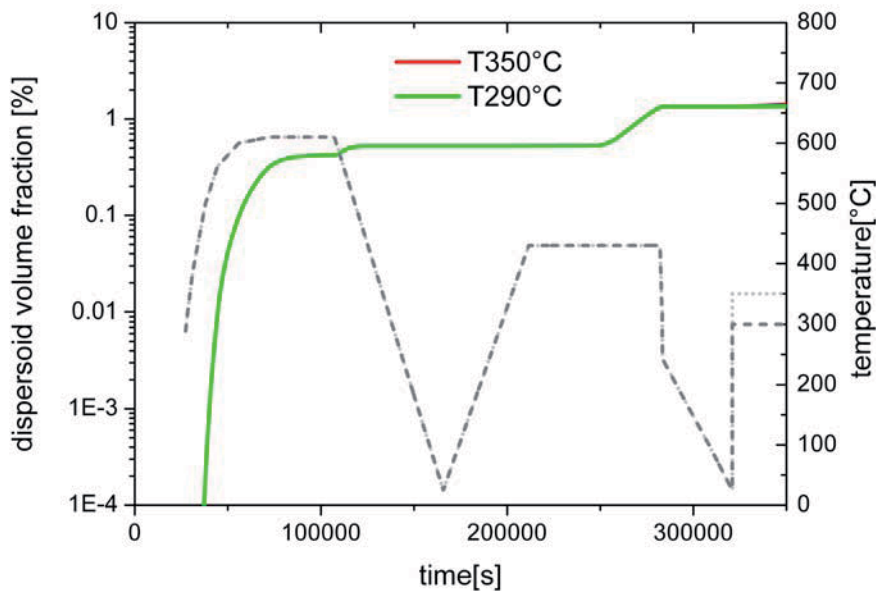


Fig. 9.20: Dispersoid volume fraction as calculated with ClaNG for two different rolling reductions 50% and 70%. Evolution of the volume fraction of the phase Al_6Mn .

Individual precipitation simulations were carried out for the different final annealing temperatures used. In Fig. 9.18 the solute content is shown exemplarily for only two quite different annealing temperatures.

During thermo-mechanical processing the solute content changes. Of particular interest is here the drop of the manganese content during the final anneal, since manganese is known to have a pronounced effect on the recrystallization behavior. It can be concluded that no strong influence of the annealing temperature on the evolution of the solute content was observed. The simulations were compared to experimental values from thermoelectric power measurements (for details see Tab. 9.3). A very pronounced difference for annealing at different temperature, however, was observed for the evolution of the dispersoid radii. It is obvious that for lower temperatures, smaller dispersoid radii were developed, since the diffusion processes for the coarsening of dispersoids are slowed down at lower temperature. This small difference is not reflected in the dispersoid volume

fractions. The corresponding evolution of Zener Drag as presented in Fig. 9.21 was calculated on the basis of the statistical approach presented in Chap. 3 (Eq. (3.11)). A significant difference in the absolute magnitude of the Zener drag was observed for the different temperatures (only $T = 290\text{ }^{\circ}\text{C}$ and $T = 350\text{ }^{\circ}\text{C}$ shown in Fig. 9.21).

The solute content change, as well as the Zener drag evolution as dependent on time (Figs. 9.18, 9.21), were subsequently used as input for CORE.

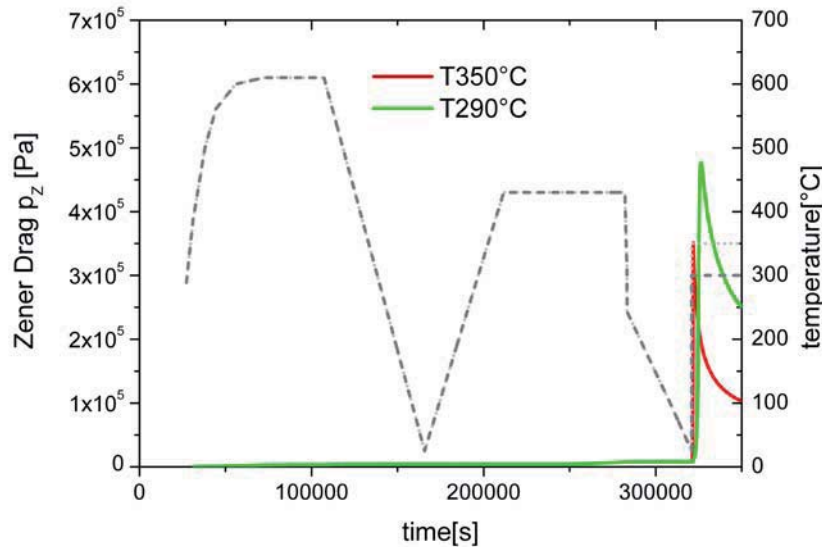


Fig. 9.21: Zener drag evolution over time for two different temperatures as calculated from the modeled dispersoid radii and volume fractions.

9.6.2 Modeling of recovery and growth

Further inputs to the CORE model (Chap. 3) are the parameters for recrystallization growth which are given in Tab. 9.4. Mobility ratios $m_{GG} : m_{HAGB} : m_{LAGB}$ of 1483 : 72 : 1 (for $T = 300\text{ }^{\circ}\text{C}$) were used for fast growing grains, high angle grain boundaries and low angle grain boundaries. The mobility and driving force were considered in dependence on the solute content c_{ss} , respectively the dispersion degree f/r (Chap. 3). At the same time the driving force was reduced owing to concurrent recovery. Within CORE recovery parameters are required, to model the incubation time and the softening due to recovery as presented in Chap. 6. For a better fit of the recovery behavior with experiments the activation energy for cross slip was adjusted from 1.44 eV to 1.63 eV (Tab. 9.1 for cold rolling). These values were obtained by fitting experimental data at $T = 290\text{ }^{\circ}\text{C}$. To enable this, the measured hardness values were converted into dislocation densities as described in Sec. 6.2 (Fig. 6.1).

Tab. 9.4: Recrystallization parameters for CORE for alloy AA3103 (HAGB = high-angle grain boundary, LAGB = low angle grain boundary, FB = fast boundaries, TB = transition band, GB = grain boundary, SB = shear bands, PSN = particle-stimulated nucleation, CR = degree of cold rolling, m_0 = pre-exponential factor of mobility, E_A = activation energy of mobility).

Temp. [° C]	CR [%]	av. total disloc. density ρ [m^{-2}]	Nucleation Frequencies				Growth Parameters	
			TB	GB	SB	PSN	m_0 [m^4/Js]	E_A [eV]
300	50	$5.705 \cdot 10^{13}$					3	0.95 (FB)
to	&		0.3	$6 \cdot 10^{-4}$	0.7	0.7	3	1.1 (HAGB)
400	70	$8.344 \cdot 10^{13}$					1000	1.6 (LAGB)

9.6.3 Modeling of recrystallization kinetics

Starting from the simulated cold rolling textures predicted by GIA-3IVM+, recrystallization simulations with CORE were carried out using the output of the rolling simulations (50% and 70% cold rolling reduction). The microchemistry changes as predicted with ClANG were considered as introduced in Sec. 9.6.1. Besides microchemistry further recovery was considered with the parameters introduced above (Sec. 9.6.2). The modeled recrystallization kinetics under consideration of the microchemistry changes and recovery are presented in Figs. 9.22 and 9.23 for the previously 50%, respectively 70% cold rolled material.

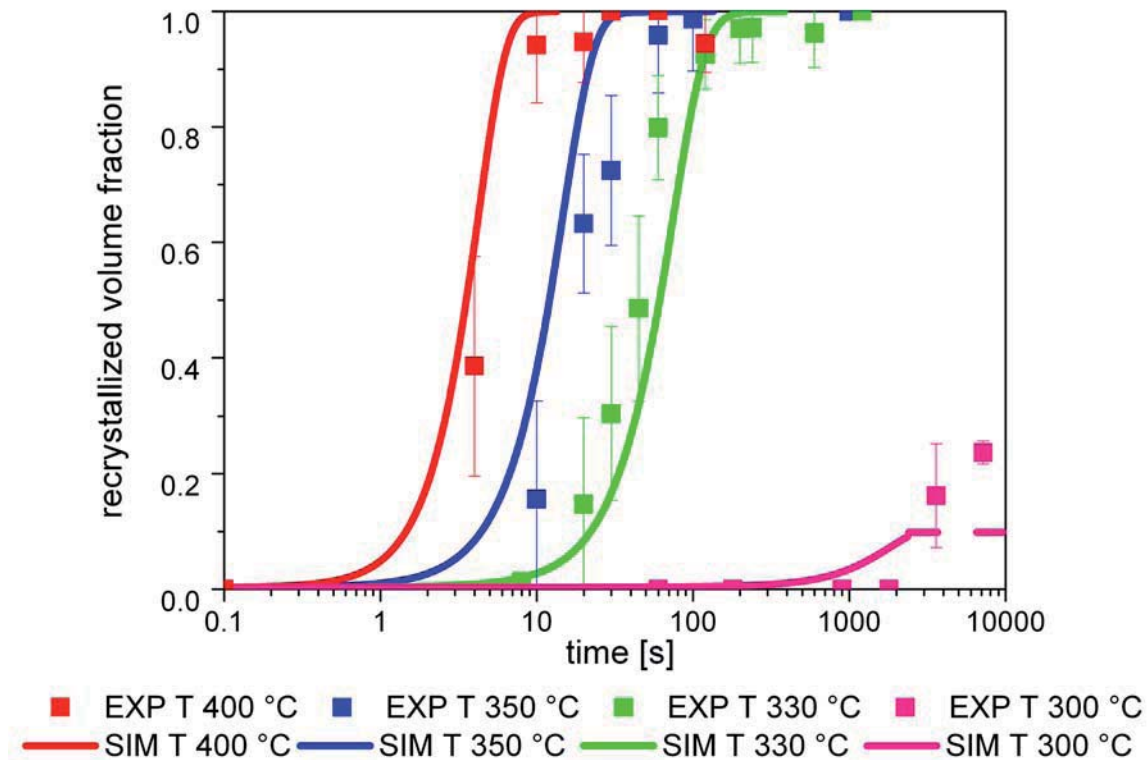


Fig. 9.22: Recrystallization kinetics for the alloy AA3103 after a cold rolling reduction of 50%. For $T = 300$ °C the recrystallization simulation stopped at a recrystallized volume fraction of $X = 10\%$, since the effective driving force became zero due to recovery.

The recrystallization kinetics in Figs. 9.22, 9.23 were obtained by simultaneous consideration of recovery and incubation times, Zener and solute drag. The isolated influences of each of these mechanisms were already demonstrated in Chap. 4 and thus are not detailed further. The simulated recrystallization kinetics after 50% and 70% cold rolling show good agreement with experiments over the chosen temperature range. With decreasing temperatures a non-linear shift of the recrystallization kinetics to longer annealing times was predicted with CORE on the logarithmic time scale. The prediction of this effect is in good agreement with the experiment. Particularly at lower temperatures, a pronounced shift to longer annealing times is predicted. However, for the lowest temperature, the kinetics were not only shifted to longer annealing times, but they were further disrupted before reaching 100% recrystallization.

The procedure to receive such an agreement with experiments is not trivial. It will be outlined in the following for the recrystallization kinetics predicted after 70% cold rolling (Fig. 9.23). At first, a recrystallization simulation is carried out for an intermediate temperature. This curve (70% cold rolling $T = 350$ °C) in Fig. 9.23 was then fitted to experimental data (parameter for incubation time, recovery activation energies). A high temperature was chosen, since at higher temperatures the predicted effect of microchemistry influences is small, since recrystallization proceeds faster than

the precipitation reactions. To obtain a reasonable value for the onset of the recrystallization kinetics, the parameter η_{conv} for the incubation times (Eq. (6.2), Chap. 6) and the connected changes in recovery (activation energies) were adjusted (Sec. 9.6.2).

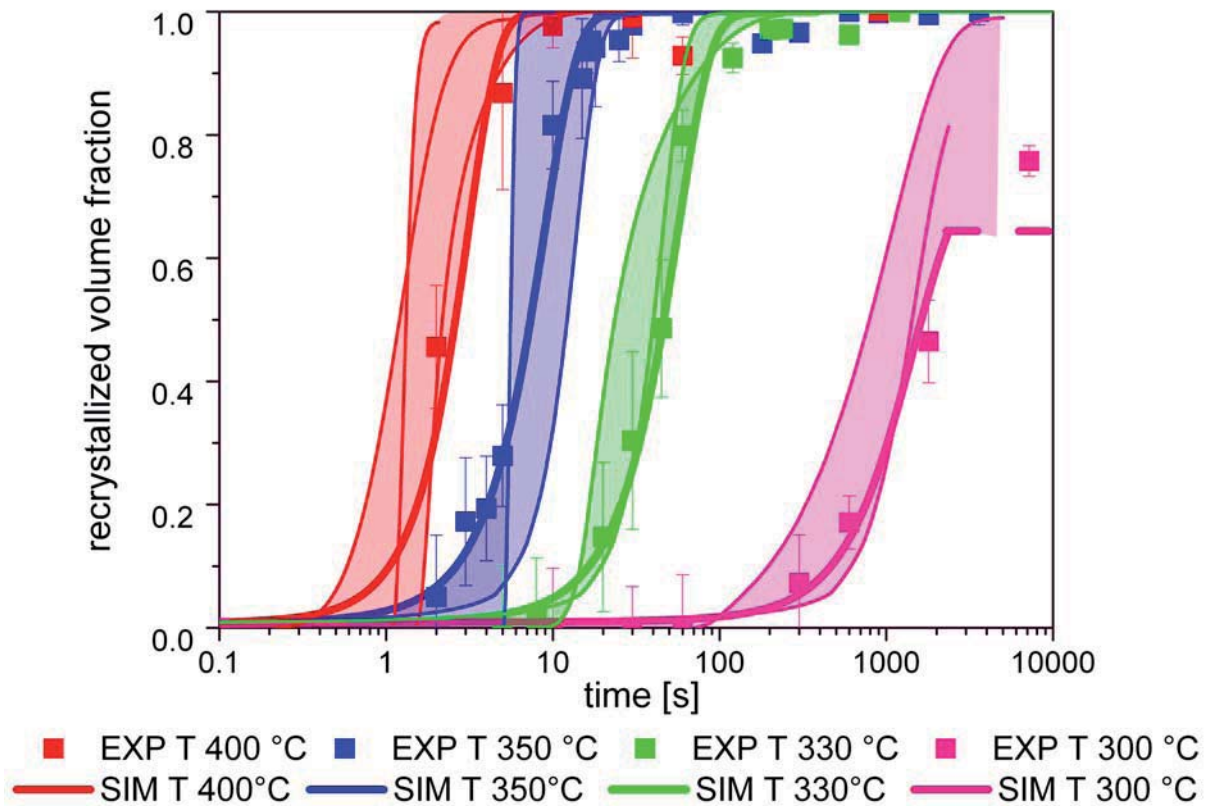


Fig. 9.23: Recrystallization kinetics for the alloy AA3103 after a cold rolling reduction of 70%. For $T = 300\text{ °C}$ the recrystallization simulation stopped at a recrystallized volume fraction of $X = 64\%$, since the effective driving force became zero due to recovery. The bold lines indicate the final simulation. Within the shaded area, further examples of recrystallization kinetics are given with slightly altered parameters (modifications were: activation energies for growth or the parameter for the incubation time η_{conv}).

The obtained values were applied to the simulation of all other curves correspondingly. If the temperature is changed keeping these parameters constant, a shift of the recrystallization kinetics to lower, respectively higher temperatures is obtained. However, this shift in temperatures did agree reasonably well for the higher temperatures, but did not receive satisfying agreement for the lowest temperatures. Without consideration of microchemistry basically a linear shift on the logarithmic time scale is obtained (Chap. 4).

The additional consideration of microchemistry changes occurring at lower temperatures as measured from experiments is thus required (Tab. 9.3). To capture these effects on recrystallization the drop in solute content of manganese was predicted with the ClaNG model in Sec. 9.6.1. From the ClaNG output further the Zener drag was derived, which was found to be very pronounced at lower temperature (Fig. 9.21). Another important aspect in the successful modeling of the recrystallization behavior is that the increase of Zener drag did overlap with the time window for recrystallization, which was not the case for the higher temperatures (see Fig. 9.24). For the higher temperatures the Zener drag remained constant ($\sim 10^4\text{ Pa}$) during recrystallization. Whereas for lower temperatures an increase of the Zener drag is observed during the recrystallization, finally leading to a disruption of the recrystallization kinetics. For better visualization the overlap of precipitation and recrystallization is indicated by the shaded overlays in Fig. 9.24 in the corresponding colors. It can be concluded that the consideration of microchemistry was definitely required for the modeling of the lower temperatures.

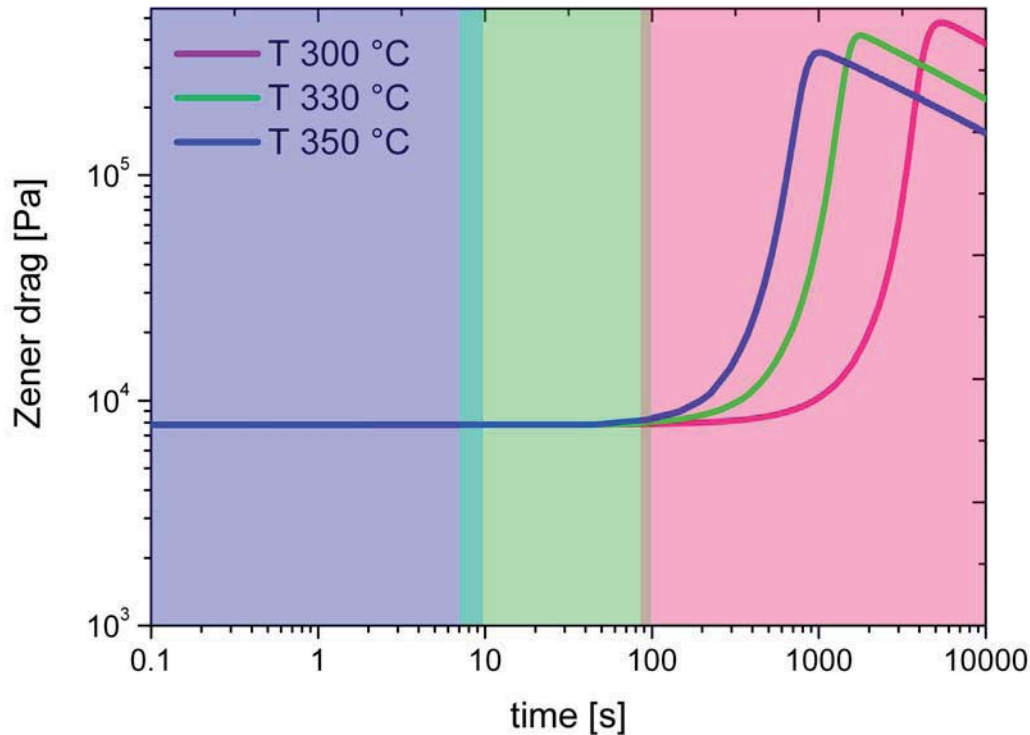


Fig. 9.24: Time window for evolution of Zener drag and recrystallization. The time window for recrystallization is reflected by the shaded areas (blue: $T = 350\text{ }^{\circ}\text{C}$, green: $T = 330\text{ }^{\circ}\text{C}$, red: $T = 300\text{ }^{\circ}\text{C}$). Only for the lowest temperature the increase of Zener drag coincides with the time frame for recrystallization.

Besides the onset of recrystallization also the slope of the kinetics is in good agreement with the experimental values. To obtain this agreement recrystallization was modeled considering Zener drag according to (Eq. (7.4)). The shadowed areas in Fig. 9.23 indicate the range for recrystallization kinetics predicted considering slightly altered parameters. The recrystallization kinetics with the very steep slopes were, for instance, obtained using the “normal” Zener drag approach in Eq. (3.11). In particular, the curve for the lowest temperature was significantly improved with the modified Zener approach (Eq. (7.4)).

The recrystallization kinetics in Fig. 9.23 were also computed independently using incubation times from experiments. Since from experiments two different activation energies were obtained for the low and high temperature regime also a non-linear shift of the recrystallization kinetics on a logarithmic scale was obtained similar to the one presented in Fig. 9.23.

In the present case the rolling simulations were the result of through-process modeling. When the rolling simulations are based on experimental hot rolling textures, instead lower average dislocation densities are obtained at the beginning of the recrystallization simulations. Hence, the recrystallization kinetics are comparatively slower. The effect of microchemistry changes on the recrystallization kinetics can be classified as being very important with respect to the outcome of the recrystallization simulations. The effects on texture and grain size are demonstrated below.

9.6.4 Modeling of recrystallized grain sizes

Figs. 9.25 and 9.26 show exemplarily the microstructures obtained from experiments and simulation for different FA -temperatures and different rolling reductions. The micrographs at higher temperatures indicate a fully recrystallized microstructure, whereas at the lowest temperature only partially recrystallized microstructures were obtained in agreement with experiments.

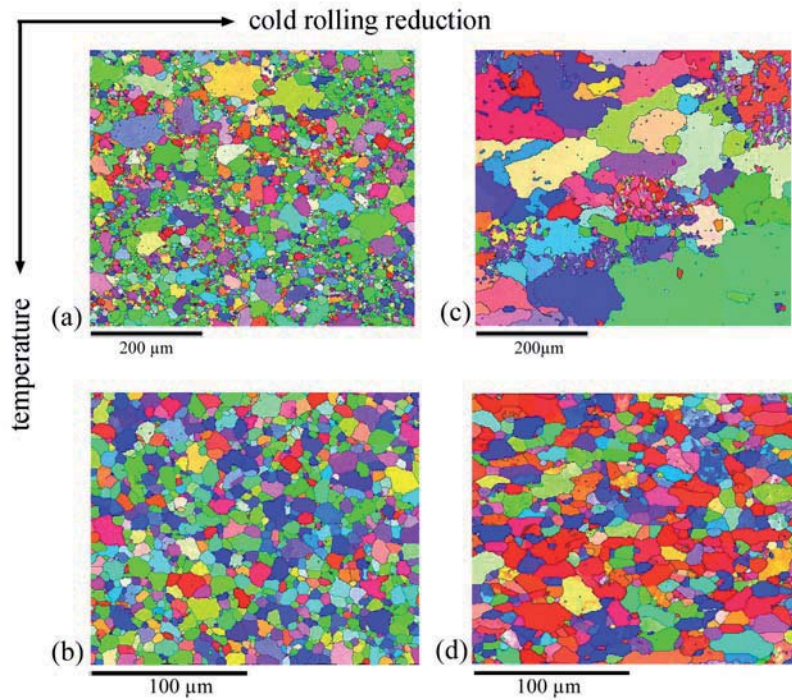


Fig. 9.25: EBSD micrographs of the microstructure of alloy AA3103 after cold rolling reduction 50% (a,b), and 70% (c,d). The temperatures were $T=300^{\circ}\text{C}$ (a,c), $T=400^{\circ}\text{C}$ (b,d). The annealing times were different. In (a) and (c) the microstructure was not completely recrystallized after $t=4.5\text{d}$ annealing.

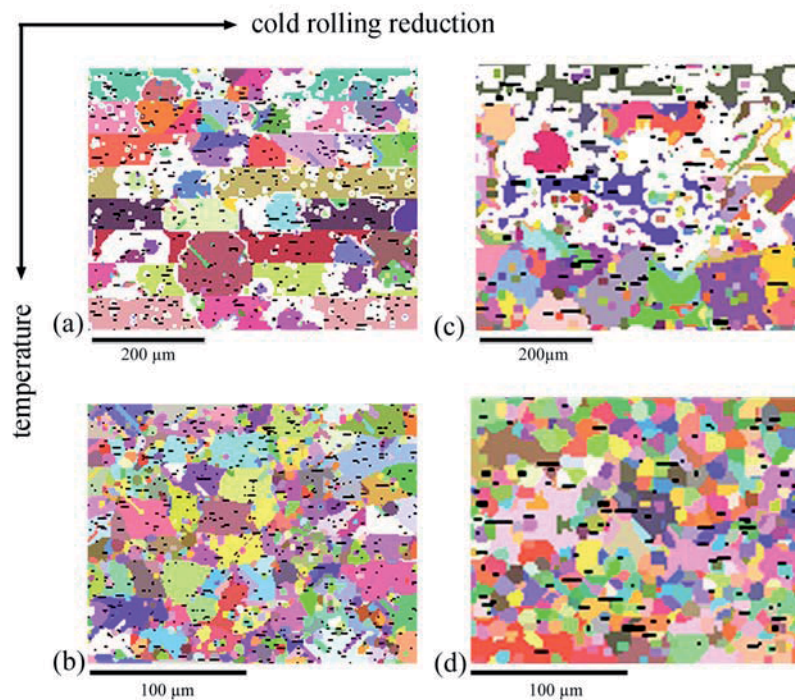


Fig. 9.26: Simulated microstructures after cold rolling reduction 50% (a,b), and 70% (c,d). The temperatures were $T=300^{\circ}\text{C}$ (a,c), $T=400^{\circ}\text{C}$ (b,d). In (a) and (b) the microstructure was not completely recrystallized after the simulation stopped. The white area reflects the cells which are currently calculating (recrystallized volume fraction < 1).

The corresponding grain size distributions are indicated in Fig. 9.27. All grain size predictions are in the right order of magnitude, typically the maximum deviates by less than a factor of two. For lower temperatures the simulations predicted also large recrystallized grains comparable to experimental observations, which is a direct result of the interrupted recrystallization kinetics leading to partial recrystallized microstructures (see also Fig. 9.26 a,c). For higher temperatures grain size distributions with a smaller width are predicted in contrast to experiments. This is

attributed to the site saturated modeling of nucleation. Hence, most grains have a similar grain size and only very few which were subject to growth selection grew much larger (Fig. 9.26 a,c).

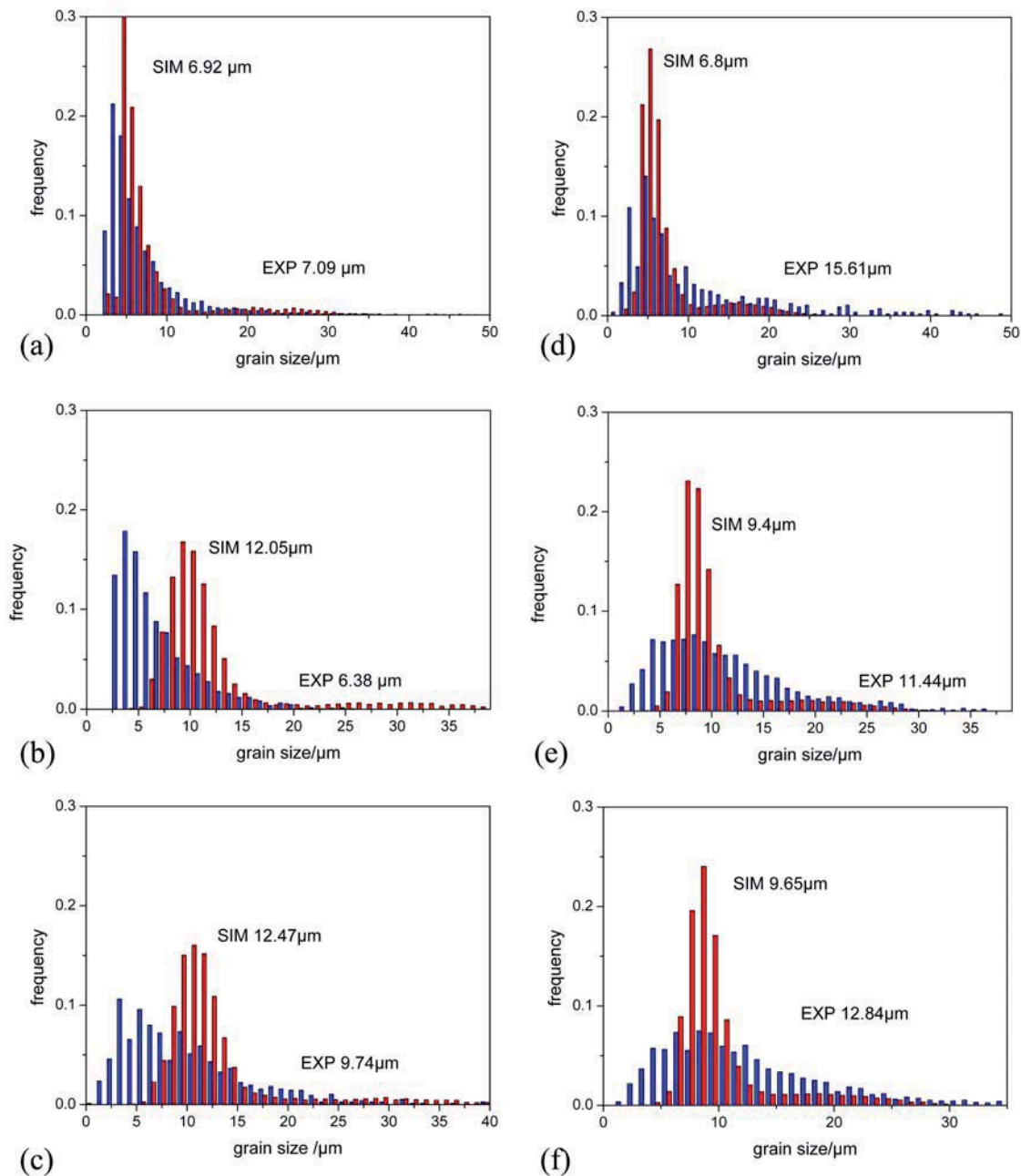


Fig. 9.27: Final grain size distributions after maximum recrystallization for alloy AA3103 for rolling reduction 50% (a-c), and 70% (d-f). The temperatures were $T=300^{\circ}\text{C}$ (a,d), $T=350^{\circ}\text{C}$ (b,e), $T=400^{\circ}\text{C}$ (c,f). The annealing times were different. In (a) and (d) the microstructure was not completely recrystallized after $t=4.5\text{d}$ annealing.

The overall evolution of the grain size during all processing steps is indicated in Fig. 9.28. Beside the grain sizes accessible from experiment, also the grain size evolution during hot rolling is displayed. The experimental grain size in normal direction continuously decreased during the various process steps. The only significant alteration of the grain size was observed during final annealing (Fig. 9.28a), when new grains appeared which consumed the microstructure completely. It is pointed out that even during hot rolling the new recrystallized grain size is strongly dependent on the size of the formerly deformed grains in normal direction, since high angle grain boundaries are frequently encountered during the growth in normal direction (see, e.g. blue recrystallized grains in Fig. 9.28b).

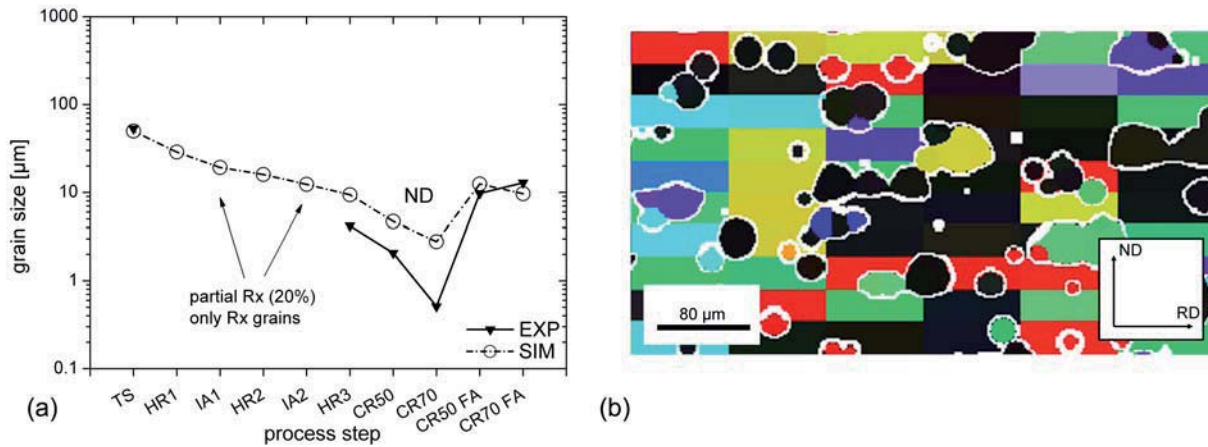


Fig. 9.28: (a) Grain size evolution in normal direction through all process steps compared to experiments if accessible. (b) Microstructure after 20% inter-pass recrystallization during hot rolling. The growth of nuclei is slightly hindered in normal direction due to the high-angle grain boundaries encountered in normal direction (the colors correspond to crystallographic orientations: red- Cu, green- S/R, bronze – Brass, blue – Cube, black – random orientation).

9.6.5 Modeling of recrystallization textures

Fig. 9.29 compares the recrystallization texture simulations with experimental macrottextures for initially 50% cold rolled material subjected to salt bath annealing at different temperatures. Correspondingly, the recrystallization textures after annealing of the 70% cold rolled material are indicated in a similar fashion in Fig. 9.30. The modeled recrystallization textures show good agreement with experimental results with respect to absolute intensities and volume fractions (Fig. 9.31). It was however found that the RD rotated Cube component was missing in the modeled recrystallization textures after 50% cold deformation. As already observed from the recrystallization kinetics at low temperatures only partial recrystallized textures were obtained for both rolling reductions. In this case recrystallization textures resulted, showing beside the Cube component, also retained deformation texture components.

Tab. 9.5: Relative nucleus frequency from different nucleation mechanisms and average absolute nucleus numbers/grain used for final annealing FA. (The ReNuc parameters remained unchanged for this consideration).

deformation degree degree [%]	grain boundary nuc. parameter GB	transition band nuc. parameter TB	shear band nuc. parameter SB	particle-stimulated nuc. parameter PSN
	nuclei [%]	nuclei [%]	nuclei [%]	nuclei [%]
50	0.5-0.6	11.8-12.8	3.4-3.6	83.2-84.0
70	4.9-5.3	18.1-18.5	1.7-1.8	74.7-75.0
	av. nuclei/grain	av. nuclei/grain	av. nuclei/grain	av. nuclei/particle
50	0.34	7	1	0-1
70	5.88	25	1	0-1

All recrystallization textures shown in this section were based on the same nucleation parameters (ReNuc, Tab. 9.4). Since in CORE the nucleus number calculation (Sec. 3.9) depends significantly on the interface area, different fractions of the considered nucleus types were obtained (Tab. 9.5). Beside the frequency also the average nucleus number per grain and mechanism is displayed. As obvious from Tab. 9.5, the number of grain boundary and transition band nuclei increased with increasing deformation degree, because the interface/volume ratio drastically increased. Beside the increase of interfacial area, also the different stored dislocation density dependent on orientation

type cannot be neglected as can be seen from the number of particle-stimulated nuclei, which increased with increasing deformation degree.

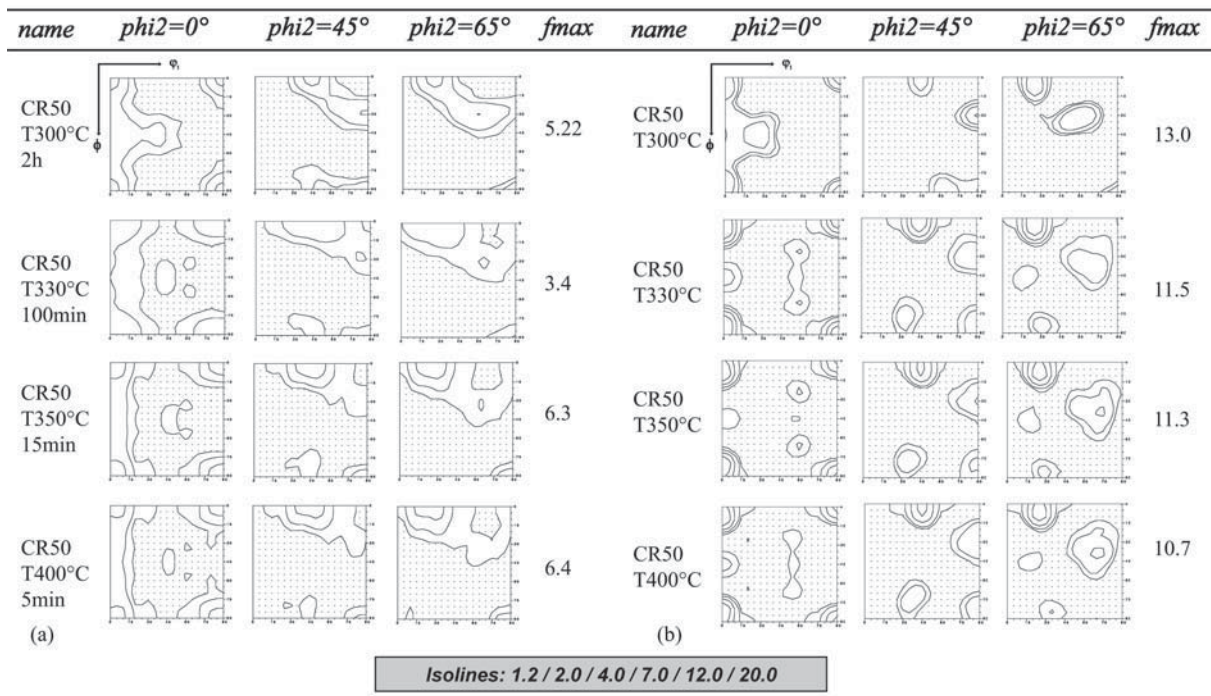


Fig. 9.29: Recrystallization textures after a cold rolling reduction of 50%. (a) Experimental, (b) simulated textures.

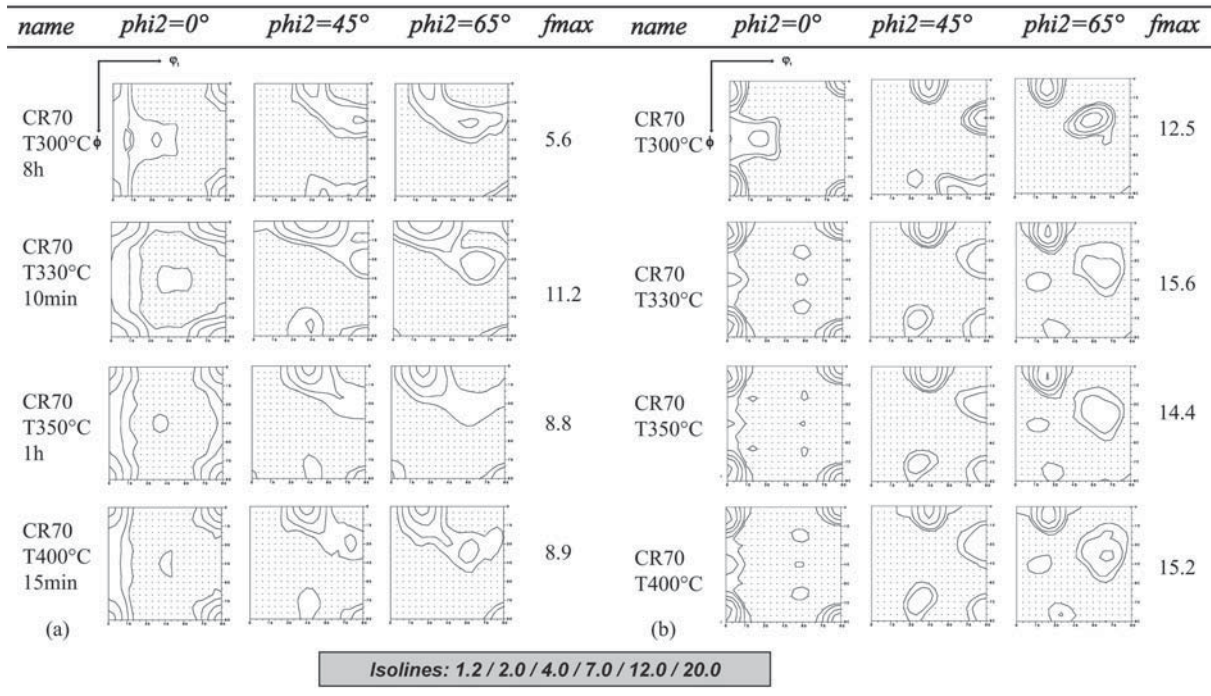


Fig. 9.30: Recrystallization textures after a cold rolling reduction of 70%. (a) Experimental, (b) simulated textures.

The modeled volume fractions of selected recrystallization textures show with almost no exception comparatively higher volume fractions than found in experiment (Fig. 9.31). This owes to the too low fraction of random orientations in the simulations. But the overall tendencies of temperature and strain agree quite well with the experiment.

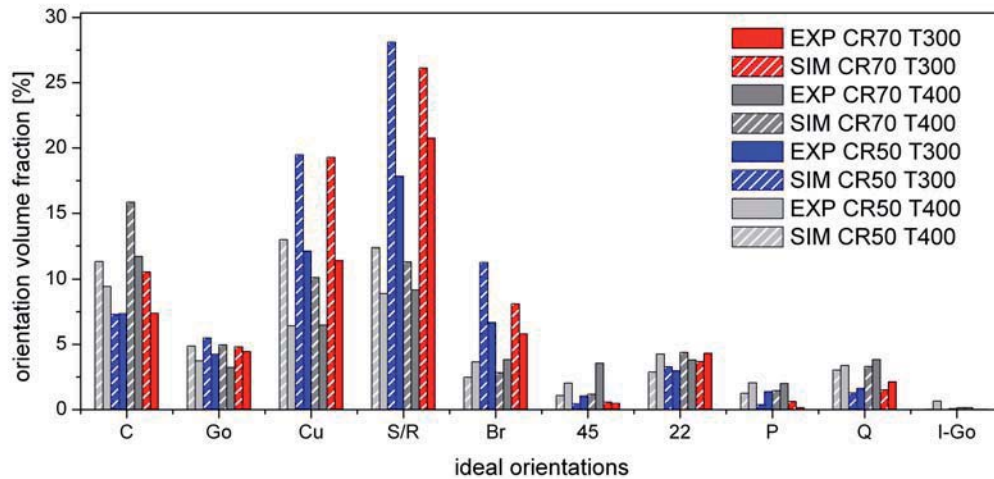


Fig. 9.31: Volume fraction of texture components for selected recrystallization textures as measured or modeled with CORE after final annealing FA.

Through-Process Development of Cube Orientation: Fig. 9.32 presents by means of volume fractions of the main texture components a comparison of measurement and simulation for all process steps.

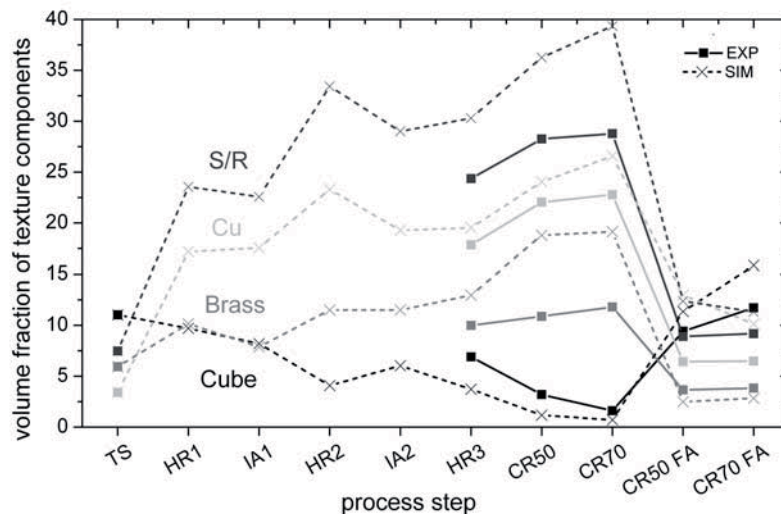


Fig. 9.32: Predicted and experimental volume fractions of ideal texture components in all process steps close to the center layer ($S=0.2$). (TS = transfer slab, HR = hot rolling, IA = Inter-annealing, CR = cold rolling, FA = final annealing).

Commencing from the hot strip texture one observes a parallel evolution of the volume fractions throughout the process, demonstrating the very good match of all subsequent simulations with the measurement. In the cold rolling textures, always the S-orientation dominates, followed by a lower Copper and even lower Brass orientation volume fractions. During the (inter-) anneals during hot rolling the volume fractions of the deformation texture components drop only slightly, but since the material is predicted to recrystallize only partially, still the S-orientation dominates the textures. The most interesting feature of this plot is the steady decrease of the Cube volume fraction starting from the hot strip values. During cold rolling this decrease is due to the instability of the Cube orientation. Only during final annealing the Cube volume fraction increases again, due to preferred growth of this component. It was pointed out above that with increasing rolling reduction the Cube volume fraction increased due to a higher number of potential nucleation sites at prior grain

boundaries. The overall volume fractions of deformed and Cube components are captured well by the TPM.

Accuracy of complete Through-Process Texture Prediction: The quality of the texture simulations at all stages of the process is represented in terms of the texture difference index ρ [Engler 2005] given in Fig. 9.33. The through-process textures (squares) at the center layer are simulated with satisfying accuracy. The average rho Index of 0.4 is mainly caused by the relatively strong texture intensities predicted from the deformation texture simulations. However, the cold rolling predictions significantly improve when the deformation zones as predicted with the GIA-DZ model (Sec. 5.3.1) are considered (stars). Also the cold rolling textures predicted as based on the experimental hot rolling texture yielded slightly better predictions (circles). It can be further observed that the deviations from the deformation texture models did not accumulate and further played no significant influence on the final recrystallization textures because a drop was observed in the rho index during final annealing. Considering the fact that the main purpose of the present through-process modeling setup was the simultaneous modeling of various recrystallization quantities (recrystallization textures, kinetics and grain sizes) an overall good result was obtained.

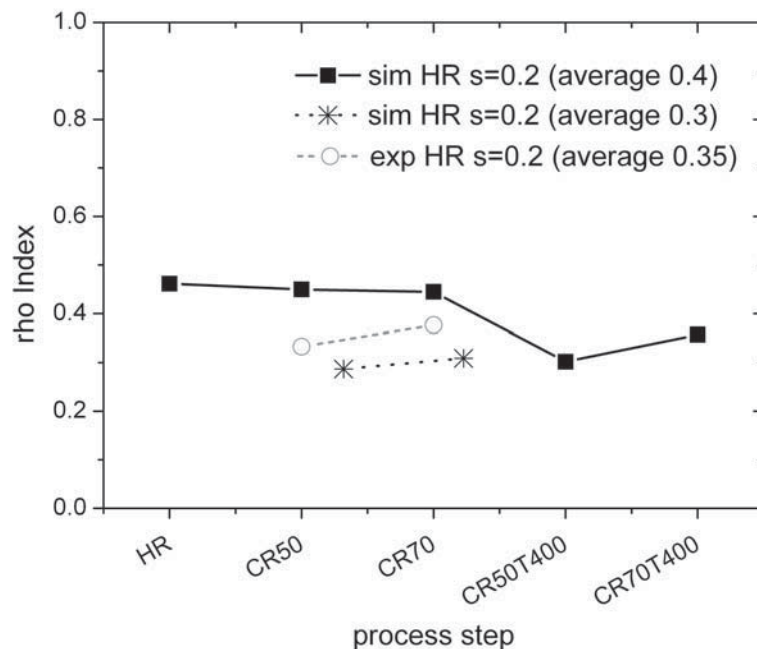


Fig. 9.33: ρ parameter for the simulated textures at sheet centre ($S=0.2$) in all process steps accessible for experimental texture measurement (HS=hot strip, CR=cold rolling pass, T=temperature).

9.7 Assessment of through-process predictions

The present through-process modeling scheme was successfully applied to the processing of Al-alloy AA3103. The use of the physical mechanisms listed below captures reasonably well the complex situation during any annealing treatment:

- deformation = $f(\text{temperature, deformation degree, chemistry})$
- precipitation = $f(\text{dislocation density})$
- recovery = $f(\text{prior deformation, microchemistry, temperature})$
- incubation time = $f(\text{recovery})$

But it still remains an open question whether the modeling scheme can be applied to other alloys as well and whether it will still work for a significantly altered thermo-mechanical process. To answer

this, it is pointed out and shown that by changing the amount of inter-pass recrystallization the Cube volume fraction could be significantly tuned with dramatic consequences for final annealing. It was further shown that the consideration of changes in microchemistry during final annealing can alter significantly the outcome of a recrystallization simulation. Particularly, at lower temperatures minute changes can decide whether the material becomes fully recrystallized or if recrystallization is interrupted earlier. However, if microchemistry becomes modified during processing, the ClaNG model proposed in [Schneider 2005] will capture these changes. Hence, a consideration of such different microchemistry leads to different recrystallization simulations. It was, however, shown that especially recrystallization kinetics are quite sensitive to modifications in microchemistry. Grain size and texture are only in particular cases (partial recrystallization) significantly affected.

Summary

The present work deals with the modeling and simulation of the recrystallization behavior in commercial aluminum alloys considering microchemistry influences. The technical relevance of recrystallization originates from the complete regeneration of the microstructure and texture connected with a massive change in the material properties. Hence, recrystallization is one of the outstanding means for selective adjustment of desired material properties. However, microchemistry changes have severe consequences for the texture and microstructure evolution during recrystallization and thus for the material properties. A modification of the solute content, for instance, has minute consequences and can change the grain boundary mobility by several orders of magnitude [Masing 1956, Detert 1956, Lücke 1957]. In addition, the precipitation of second phases (dispersoids) causes a strong time- and orientation dependent hindering of grain boundary motion by Zener drag. In contrast, the presence of large particles (constituents, primary phases) prior to deformation enhances nucleation at such particles (PSN – particle stimulated nucleation) during subsequent annealing.

Since experimental methods are very laborious and time-consuming, simulation seems to be the method of choice to study these complex interactions. The tendency goes particularly towards physically-based models, since empirical models are restricted to the range for which they were calibrated. The modeling technique used in the present work is based on the principles of cellular automata. As the name already suggests, the smallest units are the cells, by which the progression of recrystallization is determined based on deterministic rules. This method is favored, since it allows a temporal and spatial resolved description of grain boundary motion during recrystallization. During recrystallization the recrystallization front sweeps over the deformed area, leaving behind a recrystallized area of lower energy. Since the already recrystallized areas are not important for the further recrystallization process, only areas located at the recrystallization front are considered for calculation („front tracking“). Such a cellular automaton for the prediction of textures, microstructures and kinetics already existed at IMM [Mukhopadhyay 2005] (Cellular Operator for Recrystallization (CORE)). In that version, the CORE model contained very basic and mostly time-invariant descriptions of the involved physical phenomena. A description of local inhomogeneities was not considered; the related quantities were treated as average values in a qualitative rather than quantitative manner. The new developments and improvements, which were implemented in the course of the present work, are outlined in the following.

To begin with, a major point was the derivation of deformation-related information and its application for recrystallization nucleation modeling. The importance of nucleation can be

understood from the fact that the nucleus number and orientations determine strongly the final recrystallized grain size, respectively texture. Since in commercial alloys the nucleation at particles is of outstanding importance, the understanding and modeling of particle-stimulated nucleation and the resulting conclusive explanation of the evolving texture components was an important advancement.

For this purpose, a deformation model (GIA-DZ (Chap. 5)) was developed to describe the evolution of a particle deformation zone dependent on the initial deformed grain orientation. The model is based on continuum-mechanic simulations (FEM) of the individual deformation paths, which as a whole describe the evolution of a deformation zone. The model was tested for different initial textures and deformation conditions. An excellent agreement was obtained with statistical data collected from EBSD experiments and literature [Engler 1997a]. The observation of the P-texture component $\{011\} \langle 11\bar{1} \rangle$ and the ND-rotated Cube texture component $\{001\} \langle 310 \rangle$, as often observed in the context with particle-stimulated nucleation [Lücke 1990, Engler 1996, Daaland 1996, Engler 1997a, Liu 2003, Tangen 2004, Liu 2008], was fundamentally explained by the outcome of the simulations.

For the locally resolved consideration of particle-stimulated nucleation in CORE, first the structural quantity of particles and the surrounding deformation zone was introduced as local inhomogeneities into CORE. Second, the calculation of the respective nucleus numbers was directly related to the inhomogeneous deformation. The model for particle-stimulated nucleation (PSN) represents an extension of the existing nucleation model ReNuc (a collection of sub-models) [Crumbach 2006a], which did up to now consider PSN only as an arbitrary random volume fraction in the final texture. The presented approach further differs significantly from the consideration of a $40^\circ \langle 111 \rangle$ transformation of the rolling texture for prediction of a particle-stimulated nucleus spectrum [Pospiech 1979, Engler 1997b]. In contrast to previous approaches, in the present approach the number and type of nuclei is in direct relation to the initial orientation, which is locally modified by the presence of particles (deformation zone). It was shown, that a local resolved calculation of the deformation texture is inevitable for the successful prediction of textures, which are dominated by particle-stimulated nucleation, e.g. during annealing with low heating rates (Chap. 8). With this new nucleation model the PSN spectrum can be predicted for different initial textures and materials.

The CORE model itself was outlined in detail and its numerous modeling parameters were studied separately, discussed and classified according to their importance. One of the major extensions of the CORE model was the implementation of non-isothermal time-temperature profiles and the connected temperature-dependency of all involved physical processes (recovery, precipitation).

For the temperature-dependent modeling of recovery, for instance, an incremental coupling with the improved dislocation-density based work-hardening/softening model 3IVM+ [Mohles 2008] was carried out to describe the softening concurrent to recrystallization. This enables the computation of orientation-dependent recovery rates for each grain. An absolute requirement for the modeling of non-isothermal recrystallization was further the consideration of incubation times. A criterion for the incubation time, based on the relative evolution of the dislocation densities in the cell walls and cell interiors with the objective to create a stable substructure, was introduced. By means of this criterion, nucleation rates were defined. It was shown that the consideration of nucleation rates significantly improved the prediction of grain size distributions within CORE.

For the temperature and time-dependent modeling of precipitation, the CORE model was successively coupled to the precipitation model ClaNG [Schneider 2006]. The evolution of solute contents, particle volume fractions and dispersoid radii were thus modeled time- and orientation-dependent. The resulting effect of these microchemistry changes on recrystallization was studied systematically (different homogenization, temperatures and rolling reductions).

Equipped with these different time-dependent mechanisms, the CORE model offers in the current state a high flexibility, but also numerous parameters. To reveal the complexity of the

interactions the obtained extremely powerful model was tested in realistic case studies (Chaps. 7-9). The required material data for the modeling and simulation were determined from experiments, some of them from extensive EBSD studies. The individual case studies demonstrate the flexibility of the model, but also point out the application limits. For instance, it was shown that the model is flexible enough for the application in industrial tasks, respectively for industrial materials, but in this case a simultaneous consideration of the various implemented effects was indispensable. A realistic case study that required the simultaneous modeling of recrystallization, recovery and precipitation, was for instance presented in Chap. 8 for the alloy AA3103 using different heating rates. Hereby, special focus was laid on the correct modeling of specific texture components in dependence on the heating rate, which showed the successful application of the deformation and nucleation model for particles developed in this work (Chap. 5).

A particular problem, encountered in case of very strong interactions of recovery and precipitation with recrystallization, was that recovery and precipitation could not be modeled independently. By means of a laboratorial produced Al-Mn alloy, it was shown that both processes rather need to be modeled with respect to each other. A solution strategy for the simultaneous consideration of recovery and precipitation was presented and applied.

The integration of various physical and semi-empirical models, its testing, validation and evaluation, allowed to identify still open questions in other models, e.g. the description of recovery kinetics, which outputs a dislocation density of almost zero during long annealing times instead of a remaining geometrically necessary dislocation density; or the precipitation nucleation which is very sensitive to changes in the dislocation densities.

Finally, the applicability of the cellular automaton for the modeling of a through-process chain was demonstrated for the alloy AA3103 in Chap. 9. In cooperation with colleagues within large research projects (SFB-370 und TFB-63 financed by the German Research Foundation) the recrystallization model CORE was further connected to macroscopic finite element simulations, and applied for other industrial aluminum alloys.

Zusammenfassung

In der vorliegenden Arbeit wurde das Rekristallisationsverhalten unter Einfluss der Mikrochemie in kommerziellen Legierungen modelliert und simuliert. Die technische Bedeutung der Rekristallisation begründet sich auf der kompletten Erneuerung der Mikrostruktur und Textur, verbunden mit einer massiven Änderung der Werkstoffeigenschaften. Aufgrund dessen ist sie eines der bedeutendsten Mittel um die gewünschten Werkstoffeigenschaften gezielt einzustellen. Effekte, die in kommerziellen Legierungen von Bedeutung sind, sind solche, durch die im Laufe des Prozesses eine sich ändernde Mikrochemie verursacht wird. Eine Änderung der in Lösung befindlichen Elemente hat direkte Konsequenzen für die Korngrenzenbeweglichkeit und kann die Korngrenzenmobilität um mehrere Größenordnungen ändern [Masing 1956, Detert 1956, Lücke 1957]. Zusätzlich kann die Ausscheidung von Teilchen zweiter Phase (Ausscheidungen, Dispersoide) weiterhin bei ausreichend kleiner Teilchengröße zu einer starken zeit- und orientierungsabhängigen Behinderung der Korngrenzenbewegung durch Zener drag führen. Sind die zweiten Phasen hingegen ausreichend groß und bereits während der Verformung anwesend, so wirken sie stimulierend für die Keimbildung (PSN – particle stimulated nucleation) durch die Präsenz starker lokaler Gradienten der Versetzungsdichte und Misorientierung.

Da experimentelle Untersuchungen sehr zeitintensiv sind und empirische Modelle zur Vorhersage sehr auf den validierten Bereich beschränkt sind, werden Ansätze mit stärker physikalischem Charakter bevorzugt. Zur Modellierung der Rekristallisation wurde im Rahmen dieser Arbeit die Methode der zellulären Automaten verwendet. Wie der Name bereits sagt, bestehen zelluläre Automaten aus kleinsten Einheiten, den Zellen. An Hand dieser Zellen kann das Voranschreiten der Rekristallisation, basierend auf deterministischen Regeln, beschrieben werden. Diese Methode wurde bevorzugt, da es eine zeitliche und räumliche aufgelöste Beschreibung der Korngrenzenbewegung während der Rekristallisation erlaubt. Das durch die vorhergehende Verformung eingestellte Ungleichgewicht, wird im Zuge der Rekristallisation durch die Rekristallisationsfront überstrichen und somit in einen energetisch günstigeren Zustand überführt. Da die bereits rekristallisierten Gebiete für den weiteren Rekristallisationsprozess nicht von Bedeutung sind, werden während der Berechnung nur solche Zellen betrachtet, die unmittelbar an der Rekristallisationsfront liegen („Front Tracking“). Solch ein zellulärer Automat existierte bereits am IMM [Mukhopadhyay 2005] (Cellular Operator for Recrystallization (CORe)). In dieser Version, beinhaltet das CORe Model eine sehr grundlegende und größtenteils zeitunabhängige Beschreibung der berücksichtigten physikalischen Phänomene. Eine Beschreibung lokaler

Inhomogenitäten wurde nicht berücksichtigt, die entsprechenden Größen wurden als Mittelwerte in einer mehr qualitativen, als quantitativen Art und Weise behandelt. Die im Rahmen dieser Arbeit verwirklichten Modellentwicklungen und -verbesserungen werden im Folgenden beschrieben.

Ein Hauptpunkt war zunächst die verstärkte Ableitung von Informationen aus der Verformungsstruktur und deren Übertragung auf die Simulation der Rekristallisationskeimbildung. Die Bedeutung der Keimbildung versteht sich aus der Tatsache, dass die Keimzahl und die Keimorientierungen sehr stark die Endkorngröße und Endtextur beeinflussen. Da in kommerziellen Legierungen die Keimbildung an Teilchen von herausragender Bedeutung ist, war das Verständnis und die Modellierung von teilchen- induzierter Keimbildung, und die sich daraus ergebende schlüssige Erklärung der sich entwickelnden Texturkomponenten ein entscheidender Fortschritt.

Zu diesem Zweck, wurde zunächst ein Verformungsmodell (GIA-DZ, Kap. 5) entwickelt, das die Entstehung einer Verformungszone in beliebigen Orientierungen beschreibt. Das Modell basiert auf kontinuumsmechanischen Simulationen (FEM) der individuellen Verformungspfade, die in ihrer Gesamtheit die Entwicklung einer Verformungszone beschreiben. Das Modell wurde für verschiedene Anfangstexturen und Verformungsbedingungen getestet. Es wurde eine exzellente Übereinstimmung mit statistischen Daten aus EBSD Experimenten und Literatur [Engler 1997a] erreicht. Die im Zusammenhang mit PSN häufig beobachteten Lagen, P-Lage $\{011\} \langle 1\bar{1}\bar{1} \rangle$, sowie die ND rotierte Würfellage $\{001\} \langle 310 \rangle$ konnten mit Hilfe der Simulationsergebnisse grundsätzlich erklärt werden [Lücke 1990, Engler 1996, Daaland 1996, Engler 1997a, Liu 2003, Tangen 2004, Liu 2008].

Für die lokal aufgelöste Betrachtung der teilchen-stimulierten Keimbildung in CORE, wurde zunächst die strukturelle Größe der Teilchen und die umgebenden Verformungszone als lokale Inhomogenitäten berücksichtigt. Als nächstes wurde die Berechnung der entsprechenden Keimzahl direkt zur inhomogenen Verformung in Beziehung gesetzt. Das Modell zur teilchen-stimulierten Keimbildung stellt eine Erweiterung des existierenden Keimbildungsmodells ReNuc (eine Sammlung von Submodellen) dar [Crumbach 2006a], indem bisher PSN nur als beliebiger zufälliger Volumenanteil in der Gesamttextur betrachtet wurde. Dieser Ansatz unterscheidet sich weiterhin signifikant von den bisherigen Ansätzen, bei denen zumeist ein Spektrum angenommen wird, das die besagten Komponenten bereits enthält, aber nicht vorhersagt, z.B. transformierte Walztextur zur Vorhersage der PSN Textur [Pospiech 1979, Engler 1997b]. Der vorgestellte Ansatz unterscheidet sich davon grundsätzlich, da die Anzahl und Art dieser Keime in direkter Beziehung zur Anfangskornorientierung stehen, die lokal durch die Anwesenheit von Teilchen modifiziert wird (Verformungszone). Es hat sich gezeigt, dass eine lokal aufgelöste Berechnung der Verformungstextur für eine erfolgreiche Vorhersage von Texturen, die durch Teilchen bestimmt sind, unerlässlich ist, wie am Beispiel der linearen Heizraten gezeigt wurde (Kap. 8). Mit diesem neuen Keimbildungsmodell kann das PSN-Keimspektrum für verschiedene Materialien und Anfangstexturen vorhergesagt werden.

Das CORE Modell selbst wurde detailliert dargelegt und die Vielzahl der Modellparameter wurde einzeln beschrieben, diskutiert und klassifiziert. Eine der Haupterweiterungen des CORE Modells war die Implementierung von nicht-isothermen Zeit-Temperatur Profilen und die damit verbundene Temperaturabhängigkeit der involvierten physikalischen Prozesse (Erholung, Ausscheidung).

Für die zeitabhängige Modellierung von Erholung, beispielsweise, wurde eine inkrementelle Kopplung mit dem verbesserten versetzungsdichte-basierten Verfestigungs- / Erholungsmodell 3IVM+ [Mohles 2008] durchgeführt um die Entfestigung parallel zur Rekristallisation zu beschreiben. Dies ermöglicht die Berechnung orientierungsaufgelöster Erholungsraten für jedes einzelne Korn. Eine absolute Notwendigkeit für die Modellierung von nicht-isothermen Temperatur-Zeit-Profilen während der Rekristallisation, war die Berücksichtigung von Inkubationszeiten. Hierzu wurde ein Kriterium für die Inkubationszeit eingeführt, das auf der relativen Entwicklung der Versetzungsdichte in den Zellwänden und im Zellinneren beruht, mit dem Ziel der Bildungen einer stabilen Substruktur. Mit Hilfe dieses Modells wurden Keimraten

definiert. Es wurde gezeigt, dass die Betrachtung von Keimraten die Vorhersage der Korngrößenverteilungen in CORE sichtbar verbessert.

Für die Temperatur- und zeitabhängige Ausscheidungsmodellierung wurde das CORE Modell sukzessive mit dem Ausscheidungsmodell ClaNG [Schneider 2006] verbunden. Die Entwicklungen des Lösungsgehaltes, der Volumenbruchteile und Radien der Partikel wurden hiermit zeit- und außerdem orientierungsabhängig modelliert. Die Auswirkungen der Änderungen in der Mikrochemie auf die Rekristallisation wurden systematisch untersucht (verschiedene Homogenisierungen, Temperaturen und Walzgrade).

Durch die verschiedenen physikalischen Mechanismen, die im Modell Berücksichtigung fanden, bietet das Modell im gegenwärtigen Zustand eine hohe Flexibilität, aber auch eine Vielzahl von Parametern. Um die Komplexität der Wechselwirkungen zu zeigen, wurde das nun extrem leistungsstarke Modell in realistischen Fallstudien getestet. Die notwendigen Werkstoffdaten für die Modellierung und Simulation wurden experimentell, zum Teil sehr aufwendig durch umfangreiche EBSD Studien, ermittelt. Die individuellen Fallstudien demonstrieren die Flexibilität des Modells, aber weisen zugleich auch seine Grenzen auf.

Die Flexibilität des Modells konnte durch die erfolgreiche Anwendung auf industrielle Fragestellungen, bzw. industriell verwendete Materialien, gezeigt werden. Hierfür war jedoch eine gleichzeitige Betrachtung der Rekristallisation, Erholung und Ausscheidungsreaktionen unausweichlich. Die gleichzeitige Modellierung dieser verschiedenen Effekte wurde am Beispiel der Al-Mn Legierung AA3103 (Kap. 8) unter Verwendung nicht-isothermer Heizraten demonstriert. Hierbei wurde ein spezielles Augenmerk auf die erfolgreiche Modellierung der auftretenden Texturkomponenten in Abhängigkeit von der Heizrate gelegt. Es handelt sich hierbei um das gleichzeitige Auftreten von Rekristallisation und Ausscheidungsreaktionen, die sogen. „Concurrent Precipitation“. Das neu entwickelte Verformungs- und Keimbildungsmodell für Partikel (Kap. 5) fand in diesem Zusammenhang direkte Anwendung.

Ein spezielles Problem trat bei der parallelen Modellierung von Erholung und Ausscheidung während der Rekristallisation auf. Es wurde gezeigt, dass eine unabhängige Betrachtung von entweder Erholung oder Ausscheidung nicht zwangsläufig ausreichend ist. An Hand einer labormäßig hergestellten Al-Mn Legierung wurde gezeigt, dass beide Prozesse in Abhängigkeit zueinander modelliert werden müssen. Eine Lösungsstrategie für die gleichzeitige Betrachtung von Erholung und Ausscheidung wurde vorgestellt und angewendet.

Die bereits zuvor dargestellte Kopplung der verschiedenen physikalischen und halbempirischen Modelle wurde im Rahmen dieser Arbeit ausgiebig getestet, validiert und bewertet. Entsprechend konnten noch offene Fragestellungen im Bezug auf andere Modelle identifiziert werden, so beispielsweise die Beschreibung der Erholungskinetiken in 3IVM+, die eine verschwindend geringe Versetzungsdichte, statt einer verbleibenden geometrisch notwendigen Versetzungsdichte für lange Glühzeiten vorhersagen; oder die recht empfindliche Reaktion des Ausscheidungsmodells ClaNG auf Veränderungen in der Versetzungsdichte als Eingangsparameter.

Abschließend, wurde die Anwendbarkeit des CORE Modells für die Modellierung einer durchgängigen Prozesskette am Beispiel der Legierung AA3103 gezeigt. In Zusammenarbeit mit Kollegen innerhalb großer Forschungsprojekte (SFB-370 und TFB-63 finanziert durch die deutsche Forschungsgemeinschaft) wurde das Rekristallisationsmodell auch an makroskopische Finite Element Simulationen angeknüpft, sowie auf verschiedene industrielle Legierungen angewendet.

References

- [Albou 2010] A. Albou, S. Raveendra, P. Karajagikar, I. Samajdar, C. Maurice and J.H. Driver, *Scripta Mater.* 62 (2010) 469.
- [Ardakani 1994] M. G. Ardakani, F. J. Humphreys, *Acta Metall.* 42 (1994) 763.
- [Ashby 1966] M. F. Ashby, *Phil. Mag.* 14 (1966) 1157.
- [Ashby 1970] M.F. Ashby, *Phil. Mag.* 21, (1970) 399.
- [Avrami 1939] M. Avrami, *J. of chemical physics* 7 (1939) 1103.
- [Avrami 1940] M. Avrami, *J. of chemical physics* 8 (1940) 212.
- [Avrami 1941] M. Avrami, *J. of chemical physics* 9 (1941) 177.
- [Bailey 1960] J.E. Bailey, *Phil.Mag.* 5 (53) (1960) 485.
- [Bailey 1962] J. E. Bailey, P. B. Hirsch, *Proc.Roy.Soc. A* 267 (1962) 12.
- [Bampton 1982] C. C. Bampton, J. A.Wert, M. W. Mahoney, *Metall. Trans. A* 13 (1982) 193.
- [Barrett 1940] C. S. Barrett, *Trans. AIME* 137 (1940) 128.
- [Bate 1997] P. Bate, B. Hutchinson, *Scripta Mater.* 36 (1997) 195.
- [Bate 1999] P. Bate, *Phil.Trans. R. Soc. Lond. A* 357 (1999) 1589.
- [Bate 2001] P. Bate, *Proc. Int. Conf. on Recrystallization and Grain Growth*, Aachen, eds. G. Gottstein, D. Molodov, Springer Verlag, Berlin (2001) 39.
- [Bay 1979] B. Bay, N. Hansen, *Metall. Trans. A* 10 (1979) 279.
- [Beck 1950] P. A. Beck, P. R. Sperry, H. Hu, *J. Appl. Phys.* 21 (1950) 420.
- [Beck 1952] P. A. Beck, H. Hu, *Trans. AIME* 194 (1952) 83.
- [Beck 1953] P. A. Beck, *Acta metall.* 1 (1953) 230.
- [Beck 1954] P. A. Beck, *Advances in Physics* 3 (1954) 245.
- [Bellier 1977] S. P. Bellier, R. D. Doherty, *Acta Metall.* 25 (1977) 521.
- [Blum 1993] W. Blum: in *Plastic Deformation and Fracture of Materials*, ed. H. Mughrabi, vol. 6 *Mat. Sci. and Techn.*, R. W. Cahn, P. Haasen, E. J. Kramer, eds., VCH Verlagsgesellschaft, Weinheim (1993) 359.
- [Bragg 1947] L. Bragg, J. F. Nye, *Proc. R. Soc. Lond. A* 190 (1947) 474.
- [Brown 1971] L. M. Brown, R. K. Ham, in *Strengthening Methods in Crystals*, ed. A. Kelly, R.B. Nicholson, Elsevier, London (1971) 9.
- [Brown 1971] L. M. Brown, W. M. Stobbs, *Phil.Mag.* 23 (1971) 1201.
- [Burgers 1931] W. G. Burgers, P. C. Louwarse, *Z. Physik* 67 (1931) 605.
- [Burgers 1941] W.G. Burgers in *Rekristallisation, Verformter Zustand und Erholung*, Akademische Verlagsgesellschaft Beckers & Erler, Leipzig (1941).
- [Burgers 1951] W. G. Burgers, Y. H. Liu, T. J. Tiedema, *Proc. Kon. Ned. Akad Wet. B* 54 Amsterdam (1951) 459.
- [Burgers 1957] W. G. Burgers, C. A. Verbraak, *Acta Metall.* 5 (1957) 765.
- [Burke 1952] J.E. Burke, D. Turnbull, *Prog. Metal Phys.* 3 (1952) 220.

- [Cahn 1950] R.W. Cahn, *Proc. Phys. Soc. A* 63 (1950) 323.
- [Cahn 1962] J. W. Cahn, *Acta Metall.* 10 (1962) 789.
- [Cahn 1978] R. W. Cahn: in *Recrystallization of Metallic Materials*, ed. F. Haessner, Dr.Riederer Verlag, Stuttgart (1978) chapter 3.
- [Cahn 1983] R. W. Cahn, in *Physical Metallurgy*, eds. R.W.Cahn, P. Haasen, Elsevier (1983) chapter 25.
- [Cahn 1996] J. W. Cahn, in *Thermodynamics and Kinetics of Phase Transformations*, Materials Research Society Symposia Proceedings, Materials Research Society, Pittsburgh, PA 398 (1996) 425.
- [Cahoon 1971] J. R. Cahoon, W. H. Broughton, A. R. Kutzak, *Metall. Trans.* 2 (1971) 1979.
- [Chan 1984] H. M. Chan, F. J. Humphreys, *Acta metall.* 32 (1984) 235.
- [Chopard 2005] B. Chopard, M. Droz, *Cellular Automata Modeling of Physical Systems*, (2005), Cambridge University Press.
- [Cotterill 1976a] P. Cotterill, P.R. Mould, *Recrystallization and Grain Growth*, Chapter 7, Surrey University Press (1976) 180.
- [Cotterill 1976b] P. Cotterill, P. R. Mould, *Recrystallization and Grain Growth in Metals*, Chapter 4, Surrey University Press (1976) 60.
- [Cottrell 1953] A. H. Cottrell, in *Progress in Metal Physics 4*, (ed. by B. Chalmers), Pergamon Press LTD, London (1953) 251.
- [Crumbach 2001] M. Crumbach, G. Pomana, P.Wagner, G.Gottstein, in *Proc.1st Int. Conf. on recrystallization and Grain Growth*, (eds. G.Gottstein, D.A.Molodov), Springer,Berlin (2001) 1053.
- [Crumbach 2004] M. Crumbach, M. Goerdeler, G. Gottstein, *Mat. Sci. Forum* 467-470 (2004) 617.
- [Crumbach 2004a] M. Crumbach, M. Goerdeler, G. Gottstein, L. Neumann, H. Aretz, R. Kopp, *Modell. Simul. Mater. Sci. Eng.* 12 (2004) 1.
- [Crumbach 2005] M. Crumbach, *Through-Process texture Modeling*, Doctoral Thesis, IMM, RWTH Aachen, Der andere Verlag Osnabrück Germany (2005).
- [Crumbach 2006a] M. Crumbach, M. Goerdeler, G. Gottstein, *Acta Mater.* 54 (2006) 3275.
- [Crumbach 2006b] M. Crumbach, M. Goerdeler, G. Gottstein, *Acta Mater.* 54 (2006) 3291.
- [Daaland 1996] O. Daaland, E. Nes, *Acta Mater.* 44 (1996) 1413.
- [Davidson 1979] A. P. Davidson, D. R. F. West, *Met. Sci.* 13 (1979) 170.
- [Derby 1987] B. Derby, M. F. Ashby, *Scripta Metall.* 21 (1987) 879.
- [Detert 1956] K. Detert, K. Lücke, *The Influence of Defined Small Amounts of Impurities on the Recrystallization of Aluminium*, Brown. Univ. Report. #AFOSR-TN-56-103;AD-82016-March, (1956).
- [Detert 1965] K. Detert, J. Ziebs, *Trans AIME* 233 (1965) 51.
- [Dillamore 1967] I. L. Dillamore, C. J. E. Smith and T. W. Watson, *Met. Sci.* 1 (1967) 49.
- [Dillamore 1972] I. L. Dillamore , P. L. Morris, C. J. E. Smith, W. B. Hutchinson, *Proc. R. Soc. Lond. A* 329 (1972) 405.
- [Dillamore 1974] I. L. Dillamore, H. Katoh, *Metal Sci.* 8 (1974) 73.
- [Doherty 1962] R. D. Doherty, B. A. and J. W. Martin, *J. Inst. Metals* 91 (1962-63) 332.
- [Driver 2000] J. H. Driver, H. Paul, J.-C. Glez, C. Maurice, *Proc. 21st Risø Int. Symp. on Material Science, Recrystallization – Fundamental aspects and relations to*

- deformation micorstructure*, (eds. N. Hansen, X. Huang, D. Juul Jensen, E. M. Lauridsen, T. Leffers, W. Pantleon, T. J. Sabin, J. A. Wert) , Risø, Denmark, 35.
- [Dunlop 2007] J. W. Dunlop, Y. J. M. Bréchet, L. Legras, H. S. Zurob, *J. Nuclear Mater.* 366 (2007) 178.
- [Engler 1995a] O. Engler, J. Hirsch, K. Lücke, *Acta Metall. Mater.* 43 (1995) 121.
- [Engler 1995b] O. Engler, *Textures and Microstructures*, 23 (1995) 61.
- [Engler 1995c] O. Engler, P. Yang, *Proc. of the 16th Riso Int. Symp. on Mat. Sci* (eds. N. Hansen, D. Juul Jensen, Y. L. Liu, B. Ralph), Risø National Lab, Roskilde, Denmark (1995) 335.
- [Engler 1996] O. Engler, P. Yang, X. W. Kong, *Acta Mater.* 44 (1996) 3349.
- [Engler 1997a] O. Engler, X. W. Kong, P. Yang, *Scripta Mater.* 37 (1997) 1665.
- [Engler 1997b] O. Engler, *Scripta Mater.* 37 (1997) 1675.
- [Engler 1997c] O. Engler, *Textures and Microstructures* 28 (1997) 197.
- [Engler 1997d] O. Engler, *Proc.of ReX'96 , 3rd Int. Conf. on Recrystallization and Related Phenomena*, (ed. T.R. McNelley) (1997) 503.
- [Engler 1998] O. Engler, H. E. Vatne, *JOM* 50 (1998) 23.
- [Engler 1999] O. Engler, *Textures and Microstructures* 32 (1999) 197.
- [Engler 2005] O. Engler , M. Crumbach, S. Li, *Acta Mater.* 53 (2005) 2241.
- [Every 1974] R. L. Every and M. Hatherly, *Texture* 1(1974) 183.
- [Faivre 1979] P. Faivre, R. D. Doherty, *J. Mat. Sci.* 14 (1979) 897.
- [Ferry 1996a] M. Ferry, F. J. Humphreys, *Acta Mater.* 44 (1996) 3089.
- [Ferry 1996b] M. Ferry, F. J. Humphreys, *Mat. Sci. Forum* 217-222 (1996) 493.
- [Frost 1987] H. J. Frost, C. V. Thompson, *Acta Metall.* 35 (1987) 529.
- [Fruhstorfer 2002] B. Fruhstorfer, V. Mohles, R. Reichelt, and E. Nembach, *Phil. Mag. A* 82 (2002) 2575.
- [Furrer 1978] P. Furrer, H. Warlimont, *Aluminium* 54 (1978) 135.
- [Furrer 1979] P. Furrer, G. Hausch, *Metal Sci.* (1979) 155.
- [Gawne 1971] D. T. Gawne, R. A. Higgins, *J. Mater Sci.* 6 (1971) 403.
- [Gleiter 1969] H. Gleiter, *Acta Metall.* 17 (1969) 1421.
- [Goel 1974] D. B. Goel, U. P. Roorkee, P. Furrer, H. Warlimont, *Aluminium* 50 (1974) 511.
- [Goerdeler 2007] M. Goerdeler, *Application of a Dislocation Density Based Flow Stress Model in the Integrative Through-Process Modeling of Aluminum Production*, Doctoral Thesis, Shaker Verlag, Aachen (2007).
- [Gottstein 1984 a] G. Gottstein, *Rekristallisation metallischer Werkstoffe*, Deutsche Gesellschaft für Metallkunde, Oberursel (1984).
- [Gottstein 1984 b] G. Gottstein, *Acta Metall.* 32 (1984) 115.
- [Gottstein 1992a] G. Gottstein, L. S. Shvindlerman, *Scripta Metall.* 27 (1992) 1515.
- [Gottstein 1992b] G. Gottstein, L. S. Shvindlerman, *Scripta Metall.* 27 (1992) 1521.
- [Gottstein 1993] G. Gottstein, L. S. Shvindlerman, *Acta Metall. Mater.* 41, 11 (1993) 3267.
- [Gottstein 1998] G. Gottstein, *Physikalische Grundlagen der Metallkunde*, Springer Heidelberg (1998).

- [Gottstein 1999] G. Gottstein, L. S. Shvindlerman, *Grain Boundary Migration in Metals: Thermodynamics, Kinetics, Applications*, CRC Press, Boca Raton, Florida (1999).
- [Gottstein 2001] G. Gottstein, R. Sebald, *J. Mater. Process. Tech.* 117, Issue 3 (2001) 282.
- [Guiglionda 2004] G. Guiglionda, A. Borbély, J. H. Driver, *Acta Mater.* 52 (2004) 3413.
- [Gundlach 2004] C. Gundlach, W. Pantleon, E. M. Lauridsen, L. Margulies, R. D. Doherty, H. F. Poulsen, *Scripta Mater.* 50 (2004) 477.
- [Gurla 2007] P.V.S.S. Gurla, *An Improved Dislocation Density Based Work Hardening Model for Al-Alloys*. Doctoral Thesis, IMM, RWTH Aachen (2007).
- [Haessner 1978] F. Haessner, *Recrystallization of Metallic Materials*, Dr. Riederer Verlag, Stuttgart (1978).
- [Henderson 1979] D. W. Henderson, *J. Non-Cryst. Sol.* 30 (1979) 301.
- [Henderson 1979] D. W. Henderson, *J. Thermal. Anal.* 15 (1979) 325.
- [Herbst 1978] P. Herbst, J. Huber, in *Texture of Metallic Materials* (eds. Gottstein and Lücke), Springer Verlag Berlin 1 (1978) 453.
- [Hesselbarth 1991] H. W. Hesselbarth, I. R. Göbel, *Acta Metall.* 39 (1991) 2135.
- [Hesselbarth 1992] H. W. Hesselbarth, *Simulation von Versetzungsstruktur- und Rekristallisation und Kriechschädigung mit dem Prinzip der zellulären Automaten*, TU Braunschweig, Doctoral Thesis (1992).
- [Higginson 1997] R. L. Higginson, M. Aindow, P. S. Bate, *Mat. Sci. Eng. A* 225 (1997) 9.
- [Hirsch 1969] P. B. Hirsch, F. J. Humphreys, in *Physics of Strength and Plasticity* (ed. A. Argon) MIT Press, Cambridge MA (1969) 189.
- [Hjelen 1991] J. Hjelen, R. Ørsund, E. Nes, *Acta Metall.* 39 (1991) 1377.
- [Holm 1970] K. Holm, E. Hornbogen, *J. Mat. Sci.* 5 (1970) 655.
- [Hornbogen 1978] E. Hornbogen, U. Köster, in *Recrystallization of Metallic Materials*, (ed. J. Haessner) (1978) 159.
- [van Houtte 1994] P. van Houtte, *Acta Metall. Mater.* 43 (1995) 2859.
- [Hu 1962] H. Hu, in *Recovery and Recrystallization of Metals* (ed. L. Himmel), Interscience Publishers, New York, (1962) 311.
- [Hu 1963] H. Hu, in *Recovery and Recrystallization of Metals* (ed. L. Himmel), J. Wiley and Sons, New York (1963) 311.
- [Hughes 1993] D. A. Hughes, *Acta Metall. Mater.* 41 (1993) 1421.
- [Humphreys 1977] F. J. Humphreys, *Acta Metall.* 25 (1977) 1323.
- [Humphreys 1979] F. J. Humphreys, *Acta Metall.* 27 (1979) 1801.
- [Humphreys 1983] F. J. Humphreys, *Proc. 4th Riso Symp.* (1983) 41.
- [Humphreys 1986] F. J. Humphreys, D. Juul. Jensen, *7th Riso* (1986) 93.
- [Humphreys 1992] F. J. Humphreys, *Scripta Metall. Mater.* 27 (1992) 1557.
- [Humphreys 1994] F. J. Humphreys, M. G. Ardakani, *Acta Metall. Mater.* 42 (1994) 749.
- [Humphreys 1996] F. J. Humphreys, M. G. Ardakani, *Acta Mater.* 44 (1996) 2717.
- [Humphreys 2003] J. F. Humphreys, P. Bate, *Scripta Mater.* 48 (2003) 173.
- [Humphreys 2004] F. J. Humphreys, *Recrystallization and related annealing phenomena*, Elsevier, 2nd edition, 2004.
- [Hurley 2003] P. J. Hurley, F. J. Humphreys, *Acta Mater.* 51 (2003) 3779.

- [Hutchinson 1978] W. B. Hutchinson, B. J. Duggan, *Met. Sci.* 12 (1978) 372.
- [Hutchinson 1992] W. B. Hutchinson, *Scripta Metall.* 27 (1992) 1471.
- [Ibe 1966] G. Ibe, K. Lücke, in *Recrystallization, Grain Growth and Textures*, (ed. H. Margolin), A.S.M. Metals Park, OH, (1966) 434.
- [Inokuti 1978] Y. Inokuti, R. D. Doherty, *Acta Metall.* 26 (1978) 61.
- [Jazaeri 2004] H. Jazaeri, F. J. Humphreys, *Acta Mater.* 52 (2004) 3251.
- [Jensen 1992] D. Juul Jensen, *Scripta Metall. Mater.* 27 (1992) 1551.
- [Jensen 1995] D. Juul Jensen, *Acta Metall. Mater.* 43 (1995) 4117.
- [Jensen 1997] D. Juul Jensen, *Metall. and Mater. Trans. A* 28 (1997) 1073.
- [Jones 1977] A. R. Jones, P. R. Howell, B. Ralph, *Phil.Mag.* 35 (1977) 603.
- [Jones 1980] A. R. Jones, N. Hansen, *Proc. 1st Riso Int Symp.*, Roskilde, Riso (1980) 13.
- [Kalu 1988] P. N. Kalu, F. J. Humphreys, *Icotom 8* (eds. Kallend, G. Gottstein) TMS Warrendale (1988) 511.
- [Karduck 1983] P. Karduck, G. Gottstein, H. Mecking, *Acta Metall.* 31 (1983) 1525.
- [Kohara 1958] S. Kohara, M. N. Parthasarathi, P. A. Beck, *Trans. AIME* 212 (1928) 875.
- [Kolmogorov 1937] A. N. Kolmogorov, *Izv. Akad. Nauk. U.SSR Ser. Matemat.* 1 (1937) 355.
- [Krüger 1993] E. Krüger, *J. Phys. Chem. Solids* 54 (1993) 1549.
- [Kuhlmann 1949] D. Kuhlmann, G. Masing, J. Raffelspieper, *Z. Metallkunde* 40 (1949) 241.
- [Laptyeva 2009] G. Laptyeva, C. Schäfer, K. Karhausen, V. Mohles, G. Gottstein, *Light Metals 2010: Proc. TMS 2010 Annual Meeting and Exhibition*, 585.
- [Laurent 1952a] P. Laurent and N. Batisse, *Révue de Metallurgie* 49 (1952) 485.
- [Laurent 1952b] P. Laurent and N. Batisse, *Révue de Metallurgie* 49 (1952) 593.
- [Lauridsen 2000] E. M. Lauridsen, D. Juul Jensen, H. F. Poulsen, U. Lienert, *Scripta Mater.* 43 (2000) 561.
- [Lee 1995] D.N.Lee, *Scripta Metall. Mater.* 32 (1995) 1689.
- [Lee 1996] D. N. Lee, *Proc. ICOTOM 11* (1996) 503.
- [Lei 2008] Lei Hu, Master Thesis, IMM, RWTH Aachen (2008).
- [Lens 2005] A. Lens, C. Maurice, J. H. Driver, *Mat. Sci and Eng. A* 403 (2005) 144.
- [Li 1962] J. C. M. Li, *J. Appl. Phys.* 33 (1962) 2958.
- [Liebmann 1956] B. Liebmann, K. Lücke, G. Masing, *Z. Metallkde.* 47 (1956) 57.
- [Liu 1998] Q. Liu, D. J. Jensen, N. Hansen, *Acta Metall. Mater.* 46 (1998) 5819.
- [Liu 2003] J. T. Liu, Y. S. Liu, J. G. Morris, *Mat. Sci Tech.* 19 (2003) 1498.
- [Liu 2005] W. C. Liu, J. G. Morris, *Metall. and Mater. Trans. A* 36 (2005) 2829.
- [Liu 2008] W. C. Liu, Z. Li, C.-S. Man, *Mat. Sci. Eng. A* 478 (2008) 173.
- [Lloyd 1982] D. J. Lloyd, *Metal Sci.* 16 (1982) 304.
- [Löchte 2004] L. Löchte, M. Schneider, G. Gottstein, *Aluminum* 80 (2004) 685.
- [Lücke 1957] K. Lücke, K. Detert, *Acta Metall.* 5 (1957) 628.
- [Lücke 1962] K. Lücke, H. P. Stüwe, in *Recovery and Recrystallization of Metals*, (ed. L. Himmel), Interscience London (1962) 171.
- [Lücke 1974] K. Lücke, *Canadian Met. Quart.* 13 (1974) 261.

- [Lücke 1990] K. Lücke, O. Engler, *Mat. Sci. Tech.* 6 (1990) 1113.
- [Lundy 1962] T. S. Lundy, J. F. Murdock, *J. Appl. Phys.* 33 (1962) 1671.
- [Marthinsen 1989] K. Marthinsen, O. Lohne, E. Nes, *Acta Metall.* 37 (1989), 135.
- [Marx 1995a] V. Marx, D. Raabe, in *Proc. 16th Riso International Symposium on Materials Science: Microstructural and Crystallographic Aspects of Recrystallization*, (eds. N. Hansen, D. Juul Jensen, Y. L. Liu and B. Ralph), Riso National Laboratory, Roskilde, Denmark (1995) 461.
- [Marx 1995b] V. Marx, D. Raabe, G. Gottstein, in *Proc. of the 4th European Conference on Advanced Materials and Processes*, Euromat 95, Symposium F-Materials and Processing Control, published by Associazione Italiana di Metallurgia, Milano, Italy 3 (1995) 395.
- [Marx 1996] V. Marx, D. Raabe, G. Gottstein, in *Proc. of the 11th International Conference on Textures of Materials*, Sept 1996, Xian, China, eds: Z.Liang, L.Zuo, Y.Chu, International Academic Publishers, Beijing 100010, China 1 (1996) 515.
- [Marx 1999] V. Marx, F. R. Reher, G. Gottstein, *Acta Mater.* 47 (1999) 1219.
- [Masing 1956] G. Masing, K. Lücke, P. Nölting, *Z. Metallkunde* 47 (1956) 64.
- [Messenger 1960] C. Messenger, O. Dimitrov, *Cpt. Rd. Acad. Sc.* 251 (1960) 88.
- [Meyers 1978] M. A. Meyers, E. L. Murr, *Acta Metall.* 26 (1978) 951.
- [Mohles 2007a] V. Mohles, E. Jannot, C. Schäfer, G. Gottstein, in *Schweißtechnik und Füge-technik Schlüsseltechnologien der Zukunft*, 10th Int. Aachener Schweißtechnik Kolloquium (ASTK), (ed. U. Reisgen), Shaker-Verlag Aachen (2007) 151.
- [Mohles 2007b] V. Mohles- Private Communication.
- [Mohles 2008] V. Mohles, X. Li, C. Heering, G. Hirt, S. Bhaumik, G. Gottstein, in *Proc. of 11th Int. Esaform Conf. on Material Forming*, INSA de Lyon, CD, Springer (2008).
- [Molodov 1995] D. A. Molodov, U. Czubyko, G. Gottstein, L.S. Shvindlerman, *Scripta Metal. Mater.* 32 (1995) 529.
- [Molodov 1999] D. A. Molodov, *Migration of High Angle Grain Boundaries in Metals*, Shaker Verlag, Aachen (1999).
- [Morris 1978] P. L. Morris, B. J. Duggan, *Metal Sci.* (1978) 1.
- [Morris 1980] P. L. Morris, M. D. Ball, in *Proc. 1st Riso Int. Symp. on Material Science*, Roskilde, Denmark, Riso National Laboratory, (ed. N. Hansen et al.) (1980) 97.
- [Mould 1967] P. R. Mould, P. Cotterill, *J. Mater. Sci.* 2 (1967) 241.
- [Mukhopadhyay 2005] P. Mukhopadhyay, *Simulation of Primary Static Recrystallization with Cellular Operator Model*, Doctoral Thesis (2005).
- [Mukhopadhyay 2007] P. Mukhopadhyay, M. Loeck, G. Gottstein, *Acta Mater.* 55 (2007) 551.
- [Nembach 1996] E. Nembach, *Particle Strengthening of Metals and Alloys*, Wiley, New York (1996).
- [Nes 1975] E. Nes, J. D. Embury, *Z. Metallkunde*, 66 (1975) 589.
- [Nes 1976] E. Nes, *Aluminium* 52 (1976) 560.
- [Nes 1985] E. Nes, N. Ryum, O. Hunderi, *Acta Metall.* 33 (1985) 11.
- [Nes 1995] E. Nes, *Acta Metall. Mater.* 43 (1995) 2189.

- [Park 1997] Y. B. Park, D. N. Lee, G. Gottstein, *Mater. Sci. Tech.* 13 (1997) 289.
- [Parthasarathi 1961] M. N. Parthasarathi, P. A. Beck, *Trans. AIME* 221 (1961) 831.
- [Perryman 1955a] E. C. W. Perryman, *Trans. AIME* 203 (1955) 369.
- [Perryman 1955b] E. C. W. Perryman, *Trans. AIME* 203 (1955) 1053.
- [Pospiech 1979] J. Pospiech, K. Lücke, *Z. Metallkunde* 70 (1979) 567.
- [Porter 1979] J. R. Porter, F. J. Humphreys, *Metal Sci.* 13 (1979) 83.
- [Potts 1952] R. B. Potts, *Proc. of the Cambridge Philosophical Society*, 48 (1952) 106.
- [Price 1989] C. W. Price, *Scripta Metall.* 23 (1989) 1273.
- [Raabe 1998] D. Raabe, *Computational Materials Science: The Simulation of Materials Microstructures and Properties*, Wiley-VCH, Weinheim (1998).
- [Raabe 1999] D. Raabe, *Phil. Mag. A* 79 (1999) 2339.
- [Raabe 2000] D. Raabe, *Modell. Sim. Mater. Sci. Eng.* 8 (2000) 445.
- [Rabet 1996] L. Rabet, P. Ratchev, B. Verlinden, P. van Houtte, *Mat. Sci. Forum* 217-222 (1996) 465.
- [Rabet 1997] L. Rabet, P. Ratchev, B. Verlinden, P. van Houtte, *Proceedings of Rex '96, 3rd Int. Conf. on Rex and Relat. Ann. Phen.* (eds. Terry R. McNelley) (1997) 487.
- [Radhakrishnan 2000] B. Radhakrishnan, G. Sarma, H. Weiland, P. Baggethun, *Model. Sim. Mater. Sci. Eng.* 8 (2000) 737.
- [Rajmohan 2000] N. Rajmohan, J. A. Szpunar, *Acta Mater.* 48 (2000) 3327.
- [Ray 1975] R. K. Ray, W. B. Hutchinson, B. J. Duggan, *Acta Metall.* 23 (1975) 831.
- [Reher 1998] F. R. Reher, *Simulation der Rekristallisation auf der Basis orientierter Keimbildung und orientierten Keimwachstums mittels modifizierter zellularer Automaten : Morphologie, Textur, Kinetik*, Doctoral Thesis, RWTH Aachen, (1998).
- [Ridha 1982] A. A. Ridha, W. B. Hutchinson, *Acta Metall.* 30 (1982) 1929.
- [Rios 2009a] P. R. Rios, E. Villa, *Acta Mater.* 57 (2009) 1199.
- [Rios 2009b] P. R. Rios, E. Villa, *Acta Mater.* 57 (2009) 3714.
- [Roters 2000] F. Roters, D. Raabe, G. Gottstein, *Acta Mater.* 48 (2000) 4181.
- [Ruitenberg 2001] G. Ruitenberg, E. Woldt, A. K. Petford-Long, *Thermochimica Acta* 378 (2001) 97.
- [Russell 1970] K. C. Russell, M. F. Ashby, *Acta Metall.* 18 (1970) 891.
- [Sabin 2000] T. J. Sabin, G. Winther, D. Juul Jensen, *Acta Mater.* 51 (2003) 3999.
- [Saeter 1997] J. A. Saeter, H. E. Vatne, S. Benum, E. Nes, *Proc. of ReX'96* (ed. T.R.McNelley) (1997) 307.
- [Schäfer 2007] C. Schäfer, G. Gottstein, *Mat. Sci. Forum* 558-559 (2007) 1169.
- [Schäfer 2009] C. Schäfer, J. Song, G. Gottstein, *Acta Mater.* 57 (2009) 1026.
- [Schäfer 2009a] C. Schäfer, G. Pomana, V. Mohles, G. Gottstein, O. Engler, J. Hirsch, Recrystallization Modeling of AA8XXX Alloys with Cellular Automata Considering Recovering Kinetics, *Advanced Engineering Materials* 12 (2010) 131.
- [Schäfer 2010a] C. Schäfer, V. Mohles, G. Gottstein, Modeling the effect of heating rate on recrystallization texture evolution in AA3103, *Advanced Engineering Materials* 12 (2010) 981.

- [Schneider 2006] M. Schneider, *Modellierung und Validierung zeitabhängiger mikrochemischer Prozesse in Aluminium Knetlegierungen*, Doctoral Thesis, IMM, RWTH Aachen (2006).
- [Sebald 2002a] R. Sebald, G. Gottstein, *Acta Mater.* 50 (2002) 1587.
- [Sebald 2002b] R. Sebald, *Modellierung der Rekristallisationstextur: Wechselwirkung zwischen Keimbildung und Keimwachstum*, Doctoral thesis IMM, RWTH Aachen, Shaker Verlag, Aachen (2002).
- [Sircar 1994] S. Sircar, F. J. Humphreys, in *Proc 4th Int. conf. on Aluminium* (eds. Sanders and Starke), Chan Atlanta 1 (1994) 170.
- [Sjølstad 2003] K. Sjølstad, *Deformation and softening behaviour of commercial AlMn-alloys*, Doctoral Thesis, NTNU Trondheim (2003).
- [Sommerday 2003] M. Somerday, F. J. Humphreys, *Mat. Sci. Tech.* 19 (2003) 20.
- [Srolovitz 1986] D. J. Srolovitz, G. S. Grest, M. P. Anderson, *Acta Metall.* 34 (1986) 1833.
- [Tangen 2002] S. Tangen, K. Sjølstad, E. Nes, T. Furu, K. Marthinsen, *Mat. Sci. Forum* 396-402 (2002) 469.
- [Tangen 2004] S. Tangen, *Deformation and annealing behavior of commercial non-heat treatable aluminium alloys*, Doctoral Thesis, NTNU, Norway (2004).
- [Taoka 1965] T. Taoka, K. Suzuki, A. Yoshikawa, M. Okamoto, *Acta Metall.* 13 (1965) 1311.
- [Vandermeer 1962] R. A. Vandermeer, P. Gordon, in *Recovery and Recrystallization of Metals*, (ed. L. Himmel), Interscience London (1962) 211.
- [Vandermeer 1963] R. A. Vandermeer, in *Recovery and Recrystallization of Metals* (ed. L. Himmel) US, Society of AIME (1963) 211.
- [Vatne 1996a] H. E. Vatne, T. Furu, R. Orsund, E. Nes, *Acta Mater.* 44 (1996) 4463.
- [Vatne 1996b] H. E. Vatne, S. Benum, O. Daaland, E. Nes, *Textures and Microstructures* 26-27 (1996) 385.
- [Vatne 1997] H. E. Vatne, O. Engler, E. Nes, *Mat. Sci. and Tech.* 13 (1997) 93.
- [Vázquez 2000] J. Vázquez, P. L. López-Alemány, P. Villares, R. Jiménez-Garay, *J. Phys. Chem. Sol.* 61 (2000) 493.
- [Verbraak 1960a] C. A. Verbraak, *Z. Metallkunde.* 51 (1960) 646.
- [Verbraak 1960b] C. A. Verbraak, *Acta Metall.* 8 (1960) 56.
- [Volin 1968] T. E. Volin, R. W. Baluffi, *Phys. Stat. Sol.* 25 (1968) 163.
- [Walter 1963] J. L. Walter, E. F. Koch, *Acta Metall.* 11 (1963) 923.
- [Wauthier 2007] A. Wauthier, H. Réglé, R. Brenner, *Mat. Sci. Forum* 550 (2007) 205.
- [Weiland 1995] H. Weiland, *Proc. 16th Int Riso Symp.* (eds. Hansen et al.) (1995) 215.
- [Winning 2007] M. Winning, *Grain Boundary Mechanics, interactions between mechanical stresses and grain boundaries – New approaches to microstructure control and materials design*; Cuvillier Verlag, Göttingen, Germany (2007).
- [Woldt 1992] E. Woldt, *J. Phys. Chem. Solids* 53 (1992) 521.
- [Wolfram 2001] S. Wolfram, *A new kind of science*, General Science, Canada (2001).
- [Yang 1999] P. Yang, O. Engler, H. J. Klaar, *J. Appl. Cryst.* 32 (1999) 1105.
- [Yoshida 1959] H. Yoshida, B. Liebmann, K. Lücke, *Acta Metall.* 7 (1959) 51.
- [Zener 1949] C. Zener, private communication to C.S. Smith, *Trans AIME* 175 (1949) 15.
- [Zurob 2006] H. S. Zurob, Y. Bréchet, J. Dunlop, *Acta Mater.* 54 (2006) 3983.

Curriculum Vitae

Zur Person

Name: Carmen Schäfer
Geboren am: 01.06.1980 in Saarbrücken
Familienstand: ledig
Staatsangehörigkeit: deutsch

Schulbildung

1986 - 1990 Grundschole Köllerbach
1990 - 1996 Realschole Heusweiler
1996 - 1999 Wirtschaftswissenschaftl. Gymnasium Saarbrücken
17 / 06 / 1999 Abitur

Studium

10 / 1999 - 03 / 2002 Werkstoffwissenschaften, Universität des Saarlandes
04 / 2002 - 11 / 2004 Metallurgie und Werkstofftechnik, RWTH Aachen
11 / 11 / 2004 Diplom, RWTH Aachen

Beruf

01 / 2005 - 12 / 2008 Wissenschaftliche Angestellte am Institut für Metallkunde und Metallphysik der RWTH Aachen
01 / 2009 - 03 / 2010 Stipendiatin der German Research School for Simulation Sciences, Aachen-Jülich

Auszeichnungen

06 / 2005 Springorum Gedenkmünze, RWTH Aachen
12 / 2007 Posterpreis "Innovation", NIMR conference, Niederlande

